The Marine Geology of the Aliwal Shoal, Scottburgh, South Africa

by

Charl Bosman

Submitted in fulfilment of the academic
requirements for the degree of
Doctor of Philosophy in the
Faculty of Science and Agriculture
School of Agricultural, Earth and
Environmental Sciences
University of KwaZulu-Natal
Durban

JANUARY 2012

As the candidate's supervisor I have/have not approved this thesis for submission.

Signed: _____ Name: _____ Date: _____

ABSTRACT

This study represents the first detailed geological, geophysical and geochronological investigation of the continental shelf surrounding the Aliwal Shoal, ~5 km offshore of Scottburgh, in southern KwaZulu-Natal. Mapping of the seafloor geology using geophysics and direct observations from SCUBA diving transects were integrated with the seismic stratigraphy and constrained by new geochronological data.

Four seismic stratigraphic units (A to D**)** were identified and interpreted with the subsequent sequence stratigraphic model consisting of four incompletely preserved stratigraphic sequences separated by three sequence boundaries (SB1 - SB3) comprising complex reworked subaerial unconformity surfaces. Sequence 1 is the deepest, subdivided by a basin-wide marine flooding surface (MFS1) into a lower Campanian (and possible Santonian) TST and an upper Maastrichtian combined regressive systems tract comprising HST/FRST deposits. SB1 follows Sequence 1 and spans most of the Tertiary representing multiple erosional events. Shelf sedimentation resumed during the Late Pliocene to early Pleistocene with deposition of Sequence 2, the shelf-edge wedge, which again was followed by erosion and non-deposition during the high frequency and amplitude Early to Middle Pleistocene sea-level fluctuations resulting in the formation of SB2. Sequence 3 consists of coast-parallel, carbonate cemented aeolianite palaeo-shoreline ridges of various ages overlying Sequence 1 and 2.

Sequence 4 unconformably overlies all the earlier sequences and comprises a lower TST component displaying characteristic retrogradational stacking patterns and an upper local HST clinoform component showing progradation and downlapping. Inner and middle shelf TST units constrained between Sequence 3 ridges form thick sediment deposits showing a progression from lagoonal and lower fluvial-estuarine deposits, overlain by foreshore and shoreface sands, documenting the changing depositional environments in response to a sea-level transgression. Laterally, in the absence if Sequence 3 ridges, TST sediments comprise only a thin transgressive sand sheet.

The upper HST component comprises a prograding shore-attached subaqueous-delta clinoform sediment deposit, the *Mkomazi Subaqueous-Delta Clinoform* (MSDC) which evolved in four stages. An initialization and progradation stage (Stage 1) (9.5 to 8.4 ka cal. B.P.) was interrupted by retrogradation (Stage 2) and backstepping of the system due to rapid sea-level rise between 8.4 to 8.2 ka cal B.P. Stage 2 backstepping of the clinoform controlled the subsequent overlying topset morphologies resulting in later stages inheriting a stepped appearance upon which shoreface-

connected ridges (SCR's) are developed. Stages 3 (8.2 to 7.5 ka cal. B.P.) and 4 (7.5 to 0 ka cal. B.P) show a change from 'proximal' topset aggradation to 'distal' foreset progradational downlap, linked to a change in the dominant sedimentary transport mechanism from aggradational along-shore to progradational cross-shore related to variations in accommodation space and the rate of sediment supply. Morphologically the MSDC is characteristic of sediment input onto a high energy storm-dominated continental shelf where oceanographic processes are responsible for its northward directed asymmetry in plan-view, for the lack of a well defined bottomset and for the re-organisation of its topset into very large SCR's.

The SCR's are 1 - 6 m in height, spaced 500 to >1350 m apart and vary from 3 km to >8 km in length, attached on their shoreward portions to the shoreface between depths of -10 m to -15 m (average at -13 m) and traceable to depths exceeding -50 m, although the majority occur on the inner shelf between -20 m to -30 m. Several individual crests can be identified forming a giant shoreface-connected sand ridge field with a sigmoidal pattern in plan-view postulated to be a surficial expression of the subjacent retrogradational phase (MSDC Stage 2).

SCR's development occurred in two stages. Stage 1 involved deposition of sediment on the shoreface and ridge initiation during the MSDC Stage 2 retrogradational event. Sediment was reworked during sea-level rise generating clinoforms with proximal along-shore aggradation and distal across-shore progradation. This occurred during the last post-glacial sea-level rise from ca. 8.4 ka cal. B.P. SCR Stage 2 represents modern maintenance of the SCR system which is continually modified and maintained by shelf processes and consists of two physical states. State 1 considers SCR maintenance during fair-weather conditions when transverse ridge migration is dominant and driven by the north-easterly flowing counter current shelf circulation. State 2 considers SCR development during storm conditions when longitudinal ridge growth is suggested to occur as a result of storm return flows. Following the storm, the regional coast-parallel current system is restored and the fair-weather state then moulds the SCRs into a transverse bedform. Deposition on the MSDC is ongoing on a continental shelf that is still in a transgressive regime.

The exposed seafloor geology comprises late Pleistocene to Holocene aeolianite and beachrock lithologies, deposited as coastal barrier and transgressive shoreface depositional systems. Extensive seafloor sampling was combined with a multi-method geochronological programme, involving the U-series, C14 and optically stimulated luminescence (OSL) to constrain the evolution of the aeolianite and beachrock complex.

The Aliwal Shoal Sequence 3 ridge comprises three distinct aeolianite units (A1 to A3) which represent different types of dune morphologies deposited during the climatic and associated sea-

level fluctuations of MIS 5. Units A1 and A2 deposited during the MIS 6/5e (~134 to ~127 ka cal. B.P.) transgression represent contemporaneous evolution of a coastal barrier system which consisted of two different dune forms associated with a back-barrier estuarine or lagoonal system. Unit A1 most likely originated as a longitudinal coastal dune whilst Unit A2 comprised a compound parabolic dune system that migrated into the back-barrier area across an estuary mouth/tidal inlet of the back-barrier system. The coastal barrier-dune configuration established by Unit A1 and A2 was most likely re-established during similar subsequent MIS 5 sea-level stands which during MIS 5c/b resulting in the formation of the back-barrier dune system of Unit A3.

Palaeoclimatic inferences from Units A1 and A2 aeolianite wind vectors indicate a change from cooler post-glacial climates (lower Unit A1) to warmer interglacial-like conditions more similar to the present (upper Unit A1 and Unit A2). Unit A3 palaeowind vector data show variability interpreted to be related to global MIS 5c climatic instability and fluctuations.

For Units A1, A2 and A3 pervasive early meteoric low-magnesium calcite (LMC) cementation followed shortly after deposition protecting the dune cores from erosion during subsequent sea-level fluctuations. Sea-spray induced vadose cementation in Units A1 and A2 may have been a key factor in stabilising dune sediment before later phreatic meteoric cementation. The final preserved Late Pleistocene depositional event in the study area was that of the storm deposit of beachrock Unit B5. Induration followed shortly after deposition by marine vadose high-magnesium calcite (HMC) cementation. Following deposition and lithification, Units A1, A2, A3 and B5 underwent a period of cement erosion associated with decementation and increased porosity due to either 1) groundwater table fluctuations related to the high frequency MIS 5 sea-level fluctuations and/or 2) carbonate solution due to complete subaerial exposure related to the overall MIS 4 - 2 sea-level depression towards the LGM lowstand. In addition to the decementation and porosity development Unit B5 also experienced inversion of the original unstable HMC cement to LMC. During MIS 4 to 2 the Aliwal shelf comprised an interfluve area which was characterised by subaerial exposure, fluvial incision of coast-parallel tributary river systems and general sediment starvation.

Beachrock Units B1 to B4 were deposited in the intertidal to back-beach environments and subsequently rapidly cemented by marine phreatic carbonate cements comprising either aragonite or HMC. Unit B1 was most likely deposited at 10.8 ka cal. B.P., B2 at 10.2 ka cal. B.P, B3 at 9.8 ka cal. B.P and B4 <9.8 ka cal. B.P. thereby indicating sequential formation during the meltwater pulse 1b (MWP-1b) interval of the last deglacial sea-level rise.

Unit B3 marks the change from a log-spiral bay coastal configuration established by Units B1 and B2 to a linear coastline orientation controlled by the trend of the pre-existing aeolianite units. This change in the morphology of the coastline is also documented by the shape of the underlying transgressive ravinement surface (reflector TRS, Sequence 4) which again was controlled by the subjacent sedimentary basin fill architecture and subsequent transgressive shoreline trajectory (Sequence 4).

Sea-level rose at an average rate of 67 cm/100 years from B1 to B2 and 86 cm/100 years from B2 to B2 indicating an acceleration in the rate of sea-level rise supporting enhanced rates of sea-level rise during the MWP-1b interval which also seemed to have altered the coastal configuration and resulted in the closure of the southern outlet of the back-barrier estuarine system. Two cycles of initial aragonite followed by later HMC cement are tentatively linked to two marine flooding events related to different pulses of enhanced rates of sea-level rise during MWP-1b which are considered responsible for significant changes in the marine carbon reservoir ages.

Comparisons of the U-series, C14 and optically stimulated luminescence (OSL) methods have shown OSL to be the most reliable method applied to dating submerged aeolianites and beachrocks. OSL not only provides the depositional age of the sediment but also does not suffer from open system behaviour, such as marine reservoir changes and contamination.

Acoustic classification of the unconsolidated sediment samples resulted in the demarcation of 3 major acoustic facies, C to E, interpreted with sample analyses as *quartzose shelf sand* (C), *reef-associated bioclastic-rich sand* (D) and an *unconsolidated lag and debris deposit* (E). Grain size distribution patterns of the unconsolidated seafloor sediments indicate that the SCR system delivers fine and medium sand to the inner and middle shelf and imparts a general N-S trending pattern to the gravel and sand fractions. In addition grain size distributions support selective erosion of the seaward flank of the *Sandridge* with the remobilised sediment deposited in the *Basin* as low amplitude bedforms over the Facies E lag and debris pavement. The mud fraction is interpreted to be deposited by gravity settling from buoyant mud-rich plumes generated by river discharge. Integration of acoustic mapping, field observations and sample analyses indicate that the present distribution of the unconsolidated sediment is the result of a highly variable distribution of modern and palimpsest sediments which are continually redistributed and reworked by a complex pattern of bottom currents generated by the interaction of opposing oceanographic and swell driven circulation patterns.

PREFACE

The research represented by this thesis was carried out in the Joint Council for Geoscience/University of KwaZulu-Natal Marine Geoscience Unit under the supervision of Prof. Ron Uken.

The project was primarily funded by the Council for Geoscience with additional financial assistance from Prof. Ron Uken and the University of KwaZulu-Natal aiding in sample analysis and various logistic expenses. This research was initiated in June 2001 as a part-time Master's dissertation which was subsequently upgraded to a full-time Doctoral dissertation in August 2007 following the recommendation of an independent examiner.

DECLARATION 1 - PLAGIARISM

I, Charl Bosman declare that

1. The research reported in this thesis, except where otherwise indicated, is my original research.
2. This thesis has not been submitted for any degree or examination at any other university.
3. This thesis does not contain other person's data, pictures, graphs or other information, unless specifically acknowledge as being sourced from other persons.
4. This thesis does not contain other person's writing, unless specifically acknowledge as being sourced from other researchers. Where other written sources have been quoted, then:
    a. Their words had been re-written but the general information attributed to them has been referenced.
    b. Where their exact words have been used, then their writing has been placed in italcs and inside quotation marks, and referenced.
5. This thesis does not contain text, graphics or tables copied and pasted from the Internet, unless specifically acknowledged and the source being detailed in the thesis and in the References sections.

Signed: _____

DECLARATION 2 - PUBLICATIONS

DETAILS OF CONTRIBUTION TO PUBLICATION

Publication 1 (Appendix III)

Bosman, C., Uken, R. and Smith, A.M. (2005). The bathymetry of the Aliwal Shoal, Scottburgh, South Africa. *South African Journal of Science*, **101**, 255-257.

C. Bosman: Collected, processed and interpreted all the data, made all the maps and figures and was the primary and decisive author for all sections.

R. Uken: Is the candidate's supervisor and as such provided conceptual guidance throughout the study and manuscript editing.

A.M. Smith: Contributed to the morphology section by providing guidance on the bedform feature named 'the Sandridge' and undertook general editing of the manuscript.

Publication 2 (Appendix X)

Bosman, C., Uken, R. and Ovechkina, M. (2007). The Aliwal Shoal revisited: New age constraints from nannofossil assemblages. *South African Journal of Geology*, **110**, 647-653.

C. Bosman: Collected all the samples, made Figure 1, interpreted the data and was the primary and decisive author for all sections.

M. N. Ovechkina: Extracted and identified all the nannofossil forms, wrote a part of the methodology section and provided Figures 2 and 3.

R. Uken: Is the candidate's supervisor and as such provided conceptual guidance throughout the study and manuscript editing.

Signed: _____

AUTHOR'S PUBLICATION LIST

(Topics related to the thesis)

INTERNATIONAL REFEREED JOURNAL PAPERS

Bosman, C., Uken, R. and Smith, A.M. (2005). The bathymetry of the Aliwal Shoal, Scottburgh, South Africa. *South African Journal of Science,* **101**, 255-257.

Bosman, C., Uken, R. and Ovechkina, M. (2007). The Aliwal Shoal revisited: New age constraints from nannofossil assemblages. *South African Journal of Geology*, **110**, 647-653.

CONFERENCE ABSTRACTS

Bosman, C. and Uken, R. (2004). Sea-level fluctuations and submerged coastal dune systems: The geology and evolution of the Aliwal Shoal. *Extended Abstracts, Postgraduate Research Day, University of KwaZulu-Natal, Howard College, Durban, South Africa, 1pp.*

Bosman, C. and Uken, R. (2005). Sea-level fluctuations and submerged coastal dune systems: The geology and evolution of the Aliwal Shoal. *Extended Abstracts, 4th Annual Meeting of the Geological Society of South Africa (Geo2005), Durban, South Africa, 1pp.*

Bosman, C. and Uken, R. (2005). Sea-level fluctuations and submerged coastal dune systems: The geology and evolution of the Aliwal Shoal. *Extended Abstracts, 12th South African Marine Science Symposium, Durban, South Africa, 1pp.*

Bosman, C. and Uken, R. (2007). Sea-level fluctuations and submerged coastal dune systems: Rapid Quaternary environmental change as documented by the Aliwal Shoal. *Extended Abstracts, 17th Biennial Congress of the Southern African Society for Quaternary Research (SASQUA), Howick, South Africa, 1pp.*

Bosman, C., Smith. A.M. and Uken, R. (2008). Shoreface-connected ridges from the Aliwal Shelf, KZN. *Extended Abstracts, 13th South African Marine Science Symposium, Cape Town, South Africa, 1pp.*

REPORTS

Bosman, C. (2003). Cruise Report for the Aliwal Shoal Geophysical Survey, Umkomaas, South Africa. Phase 2: Seismic Surveys. *Council for Geoscience Report*, **2003-0046**, 32pp.

Bosman, C. (2003). Aliwal Shoal geophysical survey, Umkomaas, South Africa: Project update & preliminary geophysical data interpretation report (2002-2003) - Bathymetry and side-scan sonar. *Council for Geoscience Report*, **2003-0133**, 28pp.

Bosman, C. (2006). Seismic stratigraphy of the continental shelf in the vicinity of the Aliwal Shoal, South Africa. *Council for Geoscience Report*, **2006-0157**, 73pp.

Bosman, C. (2007). Aliwal Shoal geochronology programme: 1. Radiocarbon and Uranium Series analyses (Results and initial interpretation). *Council for Geoscience Report*, **2007-0146**, 13pp.

Bosman C. and Leuci R. (2001). Cruise report for the Aliwal Shoal geophysical survey, Umkomaas, South Africa. Phase 1: side-scan sonar and bathymetry. *Council for Geoscience Report*, **2001-0072**, 15pp.

POPULAR PAPERS

Bosman, C. (2004). The marine geology of the Aliwal Shoal, Scottburgh, South Africa, *Geoclips*, **9**, 1pp.

Bosman, C. (2006). Marine geology of the Aliwal Shoal. In: Goldberg, J. (Ed.), *Aliwal Shoal Dive Guide*. WWF Special Publication, 4pp.

Bosman, C. (2009). Brief geology of Cracker Reef. *Ultimate Spearfishing*, **Summer 2009**, 1pp.

ACKNOWLEDGEMENTS

My life, as far back as it is worth remembering (~0.025 ka cal.), has been fundamentally interwoven with the ocean, first through my total devotion to the pursuit of riding waves (surfing) and later also through my endeavours as a marine geologist. The latter, was kindly brought about by Dr. Peter J. Ramsay, whom first changed my life in 1999 by employing me as a marine geologist and training me in the commonly perceived 'dark arts' of marine geophysics and secondly in 2001, by giving me Council for Geoscience Statutory Project 0612 - *The Marine Geology of the Aliwal Shoal*, thereby inadvertently setting my course for the next decade. As a consequence of the nature and extended duration of this research project numerous people were involved and hence needs to be acknowledged for the foundation they provided.

Firstly, this thesis could not have been completed were it not for the following people; my wife Thale Westad Bosman whom sacrificed much over the years, my supervisor and mentor Prof. Ron Uken, colleague and friend Rio Leuci and Dr. Peter Ramsay. The sincere support and interest from my mom and long time friends, Ryan Lemmer, Craig Verdon, Gerry Wessels amd Mawson Croaker saved this thesis numerous times from being terminated. To you all I dedicate this thesis and will forever owe a great debt of gratitude.

The Durban Marine Geoscience Unit (MGU) for the Council for Geoscience is sincerely thanked not only for funding this research project but also for granting me permission to use the seafloor geophysical data to complete this project after my resignation.

The collection of geophysical data and seafloor sampling are not individual pursuits but heavily dependent on other people. As such my former colleagues at the Marine Geoscience Unit were instrumental in the various stages of this study. My utmost gratitude goes to Mr. Rio Leuci, Mr. Craig Verdon, Mr. Wade Kidwell, Mr. Doug Slogrove, Mr. Phil van den Bossche and Mr. Juan Loggenberg for facing dangerous boat launches through the surf zone, heaving seas, faulty equipment, *Tethys*' carbon monoxide poising and exhaustion during the numerous seafloor surveys. Commander Blake from the SA Navy kindly provided a mine hunter vessel for the first phase of seismic surveying. Dr. Peter Ramsay and Mr. Warwick Miller from Marine GeoSolutions (PTY) Ltd are sincerely thanked for providing a hydrophone array for the second phase of boomer surveying.

In 2003, the first of two SCUBA diving ground-truthing campaigns was initiated on the dangerous Aliwal Shoal shelf setting a new benchmark in underwater seafloor sampling and observation. The huge success of these campaigns is directly attributable to the knowledge, commitment and experience of Mr. Wade Kidwell and Mr. Rio Leuci. My sincerest appreciation is also extended to the remaining dedicated and fearless members of the dive team; Dr. Alan Smith, Mr. Paul Young, Mr. Andrew Richardson (who rather would have drowned than drop a full sample bag) and Dr. Andrew Green. Our boat skipper Juan Pereira is especially commended for his professionalism and impressive knowledge of the reef and of course for always finding us after a dive.

Onland field assistance for palaeosea-level surveys were provided by Mr. Zane Thackeray, Dr. Billy Ansell, Mr. Andrew Richardson, Dr. Andrew Green, Dr. Samantha Perritt and Dr. Matthew Brayshaw. Random Saturday trigonometric beacon searches in the Umkomaas back-country were kindly accompanied by Mr. Zane Thackeray and Mr. Andrew Richardson. Mr. Rio Leuci of Environmental Mapping and Surveying is thanked for grain size analyses for both the sediment samples and the digested GC-samples series. Andrew Richardson and Wade Kidwell are thanked for assisting with drill cores from the large GC sample blocks. Hayley Cawthra is profusely thanked for digitizing the seafloor contours of the shoreface-connected ridges and for helping with references and many other administrative issues. Mr. Paul Young is thanked for sharing his knowledge all things GIS and computers with me over the years and especially for helping me obtain critical references in the dying minutes of this PhD match. The staff members at the School of Geological Sciences are thanked for all their assistance over the years which ranged from thin section preparation to sorting out long-distance registration issues - Prof. Steve McCourt is especially thanked in

this regard. Ms Sharon Eggers of the Electron Microscopy Unit is thanked for providing assistance with the SEM imagery of the various carbonate cements.

All my gratitude and appreciation is extended to Dr. Zenobia Jacobs for taking a personal interest in this project and not only providing the OSL analyses and personally covering the luminescence costs at the University of Wollongong, but also for her enduring and resolute commitment to complete the project. The results from this study would not have made sense without the precise geochronological framework that the OSL ages provided.

Many thanks to Dr. Maria Ovechkina whom painstakingly extracted and identified all the nannofossil forms.

Many fruitful discussions were had with numerous knowledgeable persons over the years. Thank you for your constructive input which helped to make my way clearer; Prof. Ron Uken, Mr. Rio Leuci, Dr. Alan Smith, Dr. Peter Ramsay, Mr. Warwick Miller, Prof. Mike Watkeys and Prof. Rodney Maud. Prof. Andrew Cooper and Prof. Dr. Burgh Flemming provided much needed references, useful background information and helpful suggestions.

Through my long association with the department (first the University of Natal, Durban's Department of Geology and Applied Geology, renamed to the School of Geological and Computer Sciences during merger with the Pietermaritzburg Department and renamed again to the School of Geological Sciences post University of Durban-Westville merger), certain members of staff and Postgrads contributed (mostly unknowingly) to my development as not only a geologist but also as a person. They are Prof. Fred Bell, the late Mrs. Carol Forbes (our departmental student mother), Prof. Mike Watkeys, Prof. Tavener-Smith, Prof Saggerson, Prof. Tom Mason, Prof. Ron Uken, Dr. Michael Duane, Dr. Nick Richards, Prof. Rodney Maud, Prof. Johan Krynauw and the legendary postgrads comprising Dr. Ian Basson, Mr. Carl Haycock, Mr. Kevin Pietersen and the only normal one in the bunch, Mrs. Audrey Pietersen. You left a positive impression in my life and will always be remembered fondly.

Cheers to my friends whom always had an interest in my academic undertakings; Gerry Wessels, Craig Verdon, Ryan Lemmer, Mawson Croaker, Rio Leuci, Daniel Aitchison, Zane Thackeray and all the others not mentioned here.

I am sincerely grateful to all the MGU colleagues and students which made my 9 years with the Unit an unforgettable period in my life which I will always treasure and hold dear. Thank you Peter Ramsay, Warwick Miller, Ian Wright, Wade Kidwell, Doug Slogrove, Jaun Loggenberg, Rio Leuci, Phil van den Bossche, Ron Uken, Paul Young, David Sinclair, Craig Verdon, Samantha Perritt, Andrew Green, Zane Thackeray, Andrew Richardson, Hayley Cawthra, Dylan Blake, Rasmus Blomqvist, Neil Tinmouth, Brett Ayres and Andrea Zanin.

A final word of thanks is extended to Mr. Warwick Miller and Dr Peter Ramsay from Marine GeoSolutions (PTY) Ltd for their most kind assistance in printing free of charge examination copies of this thesis. Mr. Zane Thackeray and Mr. Rio Leuci from Environmental Mapping and Surveying are also gratefully thanked for additional printing assistance.

In the end, if I may leave one comment on this thesis it will be;

> *this PhD is not unlike the sedimentary record of the continental shelf it studies - an almost old affair interrupted with long and frequent hiatuses, documenting properly only the most recent events which are, as it turns out, novel and quite anomalous in their nature.*

Finally, all my love and appreciation to Thale, Zoe and Stella which paid a high price for this book.

TABLE OF CONTENTS

ABSTRACT ..... **I**

PREFACE ..... **V**

DECLARATION 1 - PLAGIARISM ..... **V**

DECLARATION 2 - PUBLICATIONS ..... **VI**

AUTHOR'S PUBLICATION LIST ..... **VII**

ACKNOWLEDGEMENTS ..... **IX**

TABLE OF CONTENTS ..... **XI**

CHAPTER 1

INTRODUCTION **1**

1.1 BACKGROUND 1
1.2 LOCALITY 2
1.3 PURPOSE AND AIMS 3
1.4 THESIS FORMAT 4
1.5 PREVIOUS WORK 6

CHAPTER 2

REGIONAL PHYSIOGRAPHY AND MORPHOLOGY **9**

2.1 CLIMATE 9
2.1.1 Rainfall and Temperature *9*
2.1.2 Wind *10*
2.2 COASTAL HYDRODYNAMICS 11
2.2.1 Tides *11*
2.2.2 Swell *12*
2.3 OCEANOGRAPHY 13
2.3.1 Agulhas Current *13*
Current Meanders 15
Salinity and Temperature 15
Geological History of the Agulhas Current 16
2.3.2 Study Area Circulation *17*
2.3.3 Hinterland Topography and Drainage *20*
2.2 CONTINENTAL MARGIN MORPHOLOGY 23
2.2.1 Introduction *23*
2.2.2 Morphology of the KwaZulu-Natal Margin *24*
2.2.3 Morphology of the Continental Shelf in the Vicinity of Aliwal Shoal *27*

CHAPTER 3

REGIONAL GEOLOGY **30**

3.1 INTRODUCTION 30
3.2 BASEMENT ARCHITECTURE AND CONTINENTAL MARGIN DEVELOPMENT 32
3.2.1 Gondwana Breakup *32*
3.2.2 Coastal Faulting in KwaZulu-Natal *37*
3.3 CRETACEOUS BASINS 40
3.3.1 Zululand Basin *42*
3.3.2 Durban Basin *43*
3.3.3 Mzamba Deposits *44*
3.3.4 St Johns Basin *45*

3.3.5 Igoda Estuary/Needs Camp Deposits *46*
3.4 POST CRETACEOUS/CENOZOIC SEQUENCES 47
3.4.1 Tertiary *47*
Maputaland Group 50
3.4.2 Quaternary *50*
Pleistocene 52
Bluff Formation 52
Berea Formation 54
Offshore Aeolianite Ridges 56
Holocene 57
Onshore 57
Offshore 58
Sediment Supply to the continental shelf 60

CHAPTER 4

QUATERNARY SEA-LEVEL CHANGES 63

4.1 INTRODUCTION 63
4.2 CLIMATE AND LATE QUATERNARY SEA-LEVEL CHANGES 63
4.3 PROCESSES CONTROLLING SEA-LEVEL CHANGE 65
4.4 THE RECORD OF PAST SEA-LEVEL CHANGES 67
4.4.1 The Oxygen Isotope Record *67*
4.4.2 Sea-Level, Raised Coral Terraces and Meltwater Pulses *72*
4.5 THE KWAZULU-NATAL SEA-LEVEL RECORD 76

CHAPTER 5

METHODOLOGY 83

5.1 INTRODUCTION 83
5.2 GEOPHYSICAL DATA COLLECTION 83
5.2.1 Navigation and Coordinate Systems *83*
Survey Positioning 83
Coordinate System 85
5.2.2 Single Beam Echo-Sounding *86*
5.2.3 Side-Scan Sonar *87*
5.2.4 Boomer Seismic Profiling *89*
5.3 GEOPHYSICAL DATA PROCESSING 92
5.3.1 Introduction *92*
5.3.2 Bathymetric Data *93*
Collected Data 93
Seismically Derived Data 94
Captured Archival Data 95
5.3.3 Side-Scan Sonar *97*
5.3.4 Boomer Seismic Profiles *99*
5.4 SEAFLOOR SAMPLING 100
5.4.1 Introduction *100*
5.4.2 Sample Site Selection *101*
5.4.3 Positioning *101*
5.4.4 Geological Observation and Photography *103*
5.5 SAMPLE ANALYSES - LABORATORY PROCEDURES 104
5.5.1 Rock Samples *104*
Transmitted light microscopy 104
Scanning Electron Microscopy 105
Acid Dissolution 105
Grain Size Distribution 105
Carbonate Content 106
5.5.2 Sediment Samples *106*
Grain Size Distribution 107
Carbonate Content 107
Petrography 107

CHAPTER 6

SEISMIC AND SEQUENCE STRATIGRAPHY 108

6.1 INTRODUCTION 108
6.2 PREVIOUS SEISMIC STUDIES 109
6.2.1 Birch's Seismic Stratigraphy 109
6.2.2 Martin and Flemming's Seismic Stratigraphy 111
6.2.3 Cawthra's Sequence Stratigraphy 112
6.3 ALIWAL SHOAL SEISMIC STRATIGRAPHY 114
6.3.1 Unit A 124
Interpretation and Correlation 125
6.3.2 Unit B 126
Interpretation and Correlation 127
6.3.3 Unit C 127
Interpretation and Correlation 128
6.3.4 Unit D 128
Interpretation 132
Correlation 136
6.4 SEQUENCE STRATIGRAPHIC INTERPRETATION 137
6.4.1 Introduction 137
6.4.2 Sequence Stratigraphic Terminology 139
6.4.3 Sequence- and Chronostratigraphic Model 140
Sequence 1 144
Sequence Boundary 1 (SB1) 146
Sequence 2 146
Sequence Boundary 2 (SB2) 147
Sequence 3 147
Sequence Boundary 3 (SB3) 149
Sequence 4 150
Unit Ds: Antecedent geology, TST sedimentation and the transgressive ravinement surface 153
The Mkomazi Subaqueous-Delta Clinoform 158
6.5 SYNTHESIS 163

CHAPTER 7

SEAFLOOR MORPHOLOGY 168

7.1 INTRODUCTION 168
7.2 HIGH RESOLUTION COLLECTED BATHYMETRIC DATASET 168
7.2.1 Seafloor Morphology 169
7.2.2 Comparison to the Durban Bluff dune system 176
7.3 SEISMICALLY DERIVED BATHYMETRIC DATASET 180
7.3.1 Continental Shelf Morphology 180
7.3.2 Continental Shelf Classification 185
7.4 ARCHIVAL BATHYMETRIC DATASET 186
7.4.1 Shoreface-Connected Ridge Morphology 187
7.4.2 Shoreface-Connected Ridges 196
Models for the origin of SCRs 199
7.4.3 Aliwal Shoal SCR System 202
Aliwal SCR Formation Model 203
Stage 1: Ridge initiation 205
Stage 2: Modern maintenance 208

CHAPTER 8

SEAFLOOR GEOLOGY 211

8.1 INTRODUCTION 211
8.2 SIDE-SCAN SONAR MOSAIC AND ACOUSTIC FACIES 212
8.3 SEAFLOOR LITHOLOGIES 217
8.3.1 Lithological Sampling 217
8.3.2 Brief Introduction to Aeolianites and Beachrocks 220

8.3.3 Aliwal Shoal Aeolianites *224*
Unit A1 - The Main Ridge Aeolianites 226
Geomorphology 226
Sedimentary Structures and Features 229
Unit A2 - The Parabolic Aeolianites 234
Geomorphology 234
Sedimentary Structures and Features 236
Unit A3 - The Plateau Aeolianites 240
Geomorphology 240
Sedimentary Structures and Features 241
Aeolianite Petrography 244
Composition and Texture 244
Cementation 250
8.3.4 Aliwal Shoal Beachrocks *260*
Geomorphology and Sedimentology 260
Unit B1 263
Unit B2 263
Unit B3 266
Unit B4 270
Unit B5 272
Beachrock Petrography 274
Composition and Texture 274
Cementation 280
8.3.5 Discussion *287*
Model of Aeolianite and Beachrock Carbonate Diagenesis 287
Aeolianite Diagenesis 288
Beachrock Diagenesis 293
Aeolianite and Beachrock Formation Models from Submerged Deposits 298
8.4 UNCONSOLIDATED SEAFLOOR SEDIMENTS 300
8.4.1 Seafloor Sedimentary Characteristics *300*
8.4.2 Acoustic Facies and Sedimentary Distribution Patterns *305*
Facies C 305
Facies D 310
Facies E 313
8.4.3 Summary and Conclusions *315*
8.5 SYNTHESIS 317

CHAPTER 9

GEOCHRONOLOGY AND SHELF EVOLUTION 319

9.1 INTRODUCTION 319
9.2 THE AGE OF THE ALIWAL SHOAL 319
9.3 METHODS 320
9.3.1 Field Sampling and Sample Preparation *320*
9.3.2 Geochronological Programme Rationale *323*
9.4 RESULTS 324
9.4.1 Nannofossil Biostratigraphy *324*
9.4.2 Optically Stimulated Luminescence (OSL) *324*
9.4.3. Uranium Series *325*
9.4.4. Radiocarbon *329*
9.5. DISCUSSION 332
9.5.1 Dating Aeolianites; OSL vs. U-Series *332*
9.5.2 Dating Beachrocks; OSL vs. Radiocarbon *335*
9.5.3 Aeolianite and Beachrocks Ages *338*
Aeolianite Ages 338
Beachrock Ages 339
Correlation 339
9.5.4 Quaternary Sea-Level Changes as Documented by the Aliwal Shoal *340*
Indicative Meaning of the Aliwal Shoal Data 340
Sea-Level and Aeolianite Deposition 341
The Holocene Sea-Level Rise 344
9.5.5 Wider Implications *348*
9.6. CONCLUSIONS: EVOLUTION OF THE ALIWAL SHOAL CONTINENTAL SHELF 350

9.6.1 Cretaceous to Early Pleistocene Shelf Evolution *350*
9.6.2 Late Pleistocene Shelf Evolution *351*
9.6.3 The Last Deglacial Sea-Level Rise and Holocene Sediment Wedge *352*
Transgressive systems tract (TST) sediments 352
Highstand systems tract (HST) sediments 354
9.7 RECOMMENDATIONS 356

REFERENCES **358**

APPENDIX 1* **387**
APPENDIX II* **413**
APPENDIX III* **425**
APPENDIX IV **428**
APPENDIX V **434**
APPENDIX VI **442**
APPENDIX VII **447**
APPENDIX VIII **452**
APPENDIX IX **459**
APPENDIX X* **463**
APPENDIX XI* **471**
APPENDIX XII* **555**
APPENDIX XIII* **561**
APPENDIX XIV **565**

**** Designate appendices found in digital format attached to the back cover***

CHAPTER 1
INTRODUCTION

1.1 BACKGROUND

Continental shelves are continually shaped by sea-level changes, undergoing submergence during warmer interglacial periods and emergence during glacial periods. The morphology and sedimentary architecture of continental shelves provide a record of tectonic processes active during continental fragmentation and continental margin formation with subsequent sedimentation and erosive events driven by marine transgressions and regressions. In addition, continental shelves world-wide are biologically productive, supporting a recreational and commercial fisheries industry and a source of most of the worlds hydrocarbons. In South Africa, the Quaternary evolution of the continental shelf is also closely linked to the emergence of modern man (Marean *et al*., 2007; Fisher *et al.*, 2010; Compton, 2011).

This study represents the first detailed geological, geophysical and geochronological investigation of the continental shelf of the Aliwal Shoal in southern KwaZulu-Natal and follows on from a similar study undertaken by Ramsay (1991) in Sodwana Bay on the northern KwaZulu-Natal shelf (Figure 1.1). The Aliwal Shoal and the Sodwana Bay reefs represent submerged aeolianite and beachrock complexes that form part of a more extensive series of aeolianite ridges at various depths on the KwaZulu-Natal continental shelf (Martin and Flemming, 1988). More recent studies by Richardson (2005) and Cawthra (2006, 2010) offshore from Durban provided a detailed seafloor geology and seismic stratigraphic record of the shelf in that area (Figure 1.1).

Of particular importance is that this study integrates the seafloor geology with precise geochronological data providing robust age constraints on the late Pleistocene evolution of the Aliwal Shoal continental shelf. Mapping of the seafloor geology using geophysics and direct observations from SCUBA diving transects were integrated with the seismic stratigraphy and constrained by new geochronological data. Precise geochronological ages were determined using a multi-method geochronological programme, involving U-series, C14 and, for the first time, applying the luminescence dating technique to this type of submerged deposits. Results show that the Aliwal Shoal encompasses a drowned coastal barrier system the evolution of which documented by a sequence of submerged aeolianites, beachrocks and transgressive sediments representing one of the best preserved underwater archives of rapid environmental change that occurred along the southeast African continental shelf during the Late Pleistocene and Holocene.

1.2 LOCALITY

The research area (Figure 1.1) occupies 65 km^2 of continental shelf situated offshore between the towns of Umkomaas and Scottburgh, approximately 50 km southwest of Durban on the KwaZulu-Natal south coast. Three overlapping data sets were used: 1) the detailed study area, 2) the seismic study area and 3) the shoreface-connected ridge study area. The detailed study area constitutes the focus of this thesis and is covered by side-scan sonar, seismic and bathymetric data as well as seafloor mapping and sampling coverage.

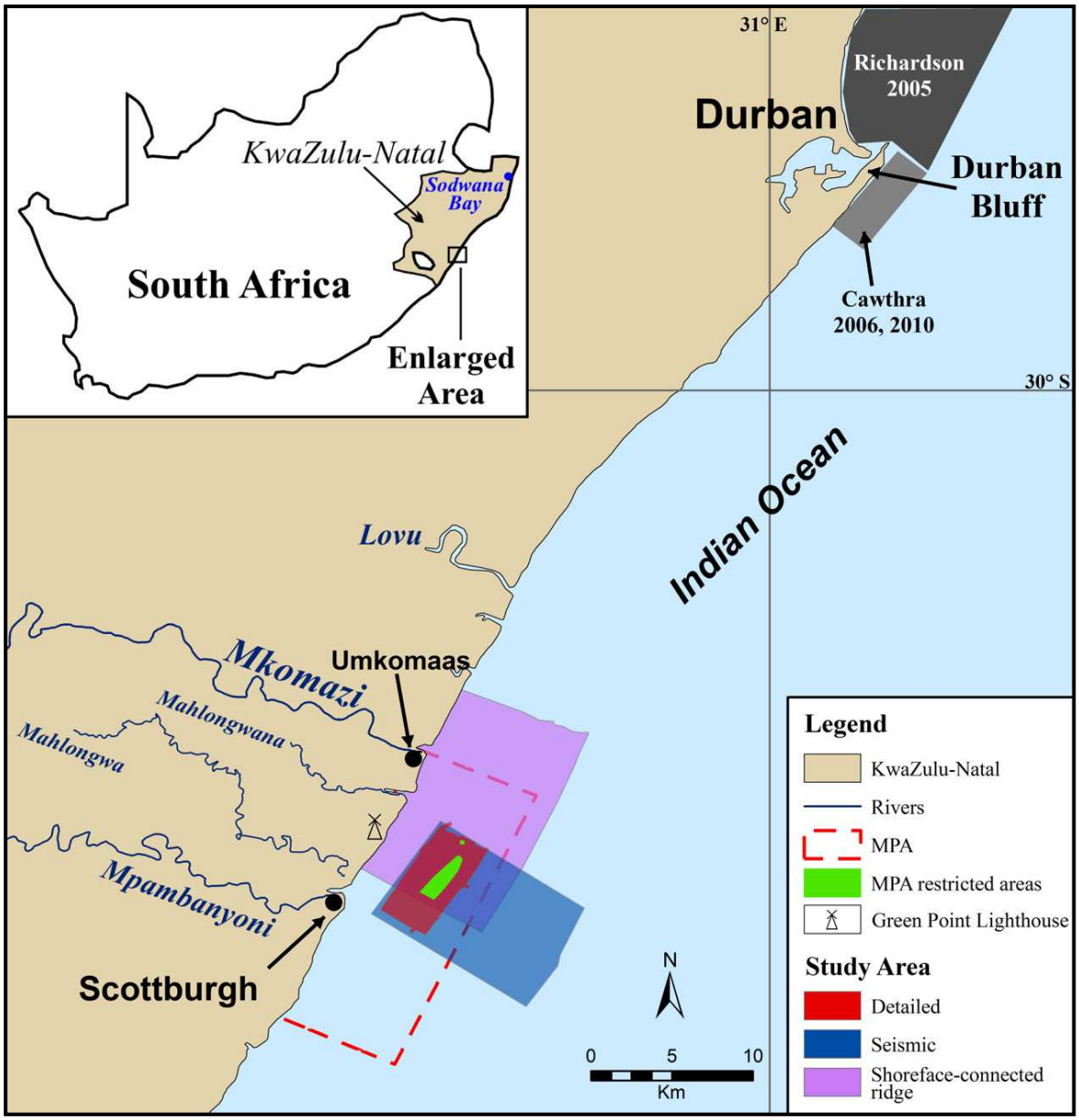

Figure 1.1 Locality map of the study area showing the three overlapping data sets, the MPA and the restricted zone of the MPA, the Durban Bluff and Sodwana Bay (inset) study site of Ramsay, 1991.

The seismic study area represents the area of shelf covered by high resolution boomer seismic profiles, whereas the shoreface-connected ridge study area comprise only a archival bathymetric dataset.

The detailed study area is located within a Marine Protected Area (MPA). It comprises an approximately 18 km^2 section of continental shelf and includes the infamous Aliwal Shoals. After Sodwana Bay (Ramsay's study area), the Aliwal Shoal is the best known and most popular SCUBA diving destination in South Africa. Thirty to fifty thousand recreational SCUBA dives are undertaken each year on the Aliwal Shoal reef which is rated as a world class dive site. The attraction for these divers is the fact that the Aliwal Shoal reef complex serves as a gathering ground for ragged-tooth sharks during their annual northward breeding migration from the Cape waters to the warmer tropical waters off KwaZulu-Natal and Mozambique (Cliff, 1999).

Due to the uniqueness and popularity of the shoal it was declared a Marine Protected Area by Marine and Coastal Management (MCM). MCM is part of the national government and is a division of the Department of Environmental Affairs and Tourism (DEAT). Bathymetric and seafloor interpretation maps generated by this study proved to be an extremely valuable asset to MCM as these maps were used to accurately delineate the boundaries of the restricted zone of the MPA around the reef complex. This was a direct result from the acquisition of the high resolution geophysical dataset, which provided accurate information on the nature of the seafloor in the MPA, which is critical in any MPA, as it forms the baseline dataset whereupon other data types (biological, fishery, oceanography etc.) can be plotted and modelled. The integration of all the datasets (biological, oceanography and geological) will facilitate the development of an environmental management plan which is vital for the sustainable development of the Aliwal Shoal MPA (Bosman *et al*., 2005).

1.3 PURPOSE AND AIMS

This project initially formed part of the Council for Geoscience Marine Geoscience Unit's annual statuary program. It arose from the lack of detailed geophysical and geological studies on the eastern continental shelf of South Africa. The continental shelf in the vicinity of the Aliwal Shoal was chosen particularly for its proximity to Durban (Figure 1.1), its unique shallow marine setting between the depths of 6 m to 34 m and due to the increase interest in the Aliwal Shoal as a natural resource but without any baseline studies performed in the area. The aims of this study were broadly:

1. to acquire high resolution geophysical datasets including seismic, side-scan sonar and echo-sounding data of the seafloor to produce accurate geophysical interpretations and maps of the study area;
2. to undertake SCUBA diving to map and ground-truth the geophysical survey data and collect geo-referenced samples of the seafloor;
3. to undertake precise geochronological dating on samples collected to complement the mapping and geophysical interpretation and,
4. to propose a model for the geological evolution of the continental shelf with reference to the Aliwal Shoal.

1.4 THESIS FORMAT

The thesis is subdivided into 9 chapters beginning with the physiography, regional geological setting and a review on Holocene sea levels changes, which are particularly relevant to this study. This is followed by a review of the various methods applied in this study, a detailed account and interpretation of the seismic stratigraphy and sea floor geology, ending with the integration of precise ages into the sequence stratigraphic framework and seafloor geology culminating in a proposed model for the evolution of the Aliwal Shoal.

The following outline the content of each chapter in more detail:

Chapter 2 - Physiography and Morphology
Review of the setting of the study area in terms of the climate, oceanography and continental margin physiography.

Chapter 3 - Regional Geology
This chapter represents a comprehensive review of the regional geology of the South African eastern continental shelf, offshore basins and associated onshore geology with reference to the study area. It provides the necessary regional geological context that is required for the thesis.

Chapter 4 - Quaternary Sea-Level Changes
Chapter 4 describes Quaternary sea-level changes and explore the link between Quaternary climate and sea-level change. The processes controlling sea-level change and the record of sea-level change is also briefly discussed to provide a background for reviewing South African and more specifically the East Coast record of relative sea-level change during the Pleistocene and Holocene.

Chapter 5 - Methodology

This section provides a brief theoretical background to and describes the various geophysical methods that were used to survey the continental shelf. It also provides information on the survey methodology, data processing procedures and sample analysis techniques. Appendix I contain accounts of theoretical background deemed too detailed for inclusion in the main text.

Chapter 6 - Seismic and Sequence Stratigraphy

Seismic data collected for this study is first described and interpreted in terms of seismic stratigraphy, the results of which were then used to develop the first sequence- and chrono-stratigraphic model of continental margin development for the Aliwal Shoal shelf. The newly proposed sequence stratigraphic model is compared and contrasted with previous studies. Many new insights are presented; the most novel relating to the development of the Holocene sediment wedge including identification and naming of the Mkomazi subaqueous-delta clinoform and the recognition of the control antecedent geology exerted on the subsequent sedimentary basin fill architecture, ravinement processes and formation of beachrock. The chapter is concluded by a summarised synthesis of postulated continental shelf evolution.

Chapter 7 - Seafloor morphology

The seafloor morphology in the study area is described using several bathymetric databases. Three dimensional (3D) models and contour plots were produced and aid description, visualisation and classification of the continental shelf morphology and dynamics. The occurrence of shoreface-connected ridges (SCRs) is documented for the first time from the southeast African shelf. A model of SCR formation linked to the Mkomazi subaqueous-delta clinoform is proposed.

Chapter 8 - Seafloor geology based on side-scan sonar interpretation and ground-truthing

Chapter 8 describe the seafloor geology and sedimentology based on the interpretation of the side-scan sonar mosaic and an extensive ground-truth SCUBA diving observation and sampling program. The seafloor is first interpreted according to the acoustic facies concept and then geologically in terms of the lithological units based on ground-truthing and sample analyses. Petrographical analyses allowed for the development of a model of carbonate cementation and interpretation of diagenetic environments of the aeolianite and beachrocks of the Aliwal Shoal. The unconsolidated shelf sediments are only very briefly reviewed in terms of the effect the Aliwal Shoal exerts on the sediment dynamics.

Chapter 9 - Geochronology and Shelf Evolution

Four different analytical methods were used to constrain the age of the various lithological units as precisely as possible. This included the radiocarbon, Uranium series, optically stimulated luminescence and nannofossil biostratigraphy methods. This geochronological programme is unique and represents the first application of the OSL method to this type of submerged deposits. It represents a benchmark study in successfully dating offshore aeolianite and beachrock complexes stranded on the South African shelf. The results from the geochronology analyses finally provided a precise age for the Aliwal Shoal after ~45 years of debate, contributed new palaeosea-level index points to the recalibrated and reinterpreted local relative sea-level curve and presented new inferences on age constraints of the strata underlying the Aliwal Shoal, all of which, allowed for the development of a chronological framework and subsequent model of evolution for the Aliwal Shoal. The thesis is concluded with a summation of the geological history of the Aliwal Shoal continental shelf and recommendations for similar future studies.

1.5 PREVIOUS WORK

The Aliwal Shoal first received attention from the scientific community when Belderson (1961) suggested an aeolian origin. Belderson (1961) also noticed that the Aliwal Shoal depth contours are similar to the Durban Bluff topography and suggested that the coast parallel offshore reefs on the eastern continental margin of South Africa are calcareous cemented coastal sand dunes that formed during lower sea levels. The subject of the origin of Aliwal Shoal was revisited - literally - when in 1963 the freighter *Aimee Lykes* grounded upon the shoal (Turner, 1988). Once in the dry dock M.J. McCarthy extracted rock samples from the damaged hull of the vessel. McCarthy subsequently published a paper in 1967 correlating the Aliwal Shoal with the on-land 'Bluff beds' in Durban. This important publication suggested a revision of the post-Cretaceous stratigraphy in the Durban area and also provided an explanation of the later geological history involving major sea-level changes since the late Tertiary.

Carter (1966) undertook a foraminiferal study on the Aliwal Shoal sample collected by M.J. McCarthy and for comparative purposes also on samples from the Durban Bluff, offshore Durban sands and sediment dredge from the Durban harbour. His study showed that the calcareous sandstones of the Durban Bluff and the Aliwal Shoal have similar foraminiferal assemblages and are distinguished from modern offshore and harbour sediments by the absence of *Ammonia beccarii*. Carter reported that the foraminifera are of probable Pliocene-Recent age with some reworked lower Miocene age species present. Carter however favoured a Pliocene age for the Aliwal Shoal. McLachlan & McMillan (1979) reviewed Carter's (1966) data and revised the age

to Late Pleistocene and preferred an age between 135 000 and 30 000 BP years. Most recently Cooper and Liu (2006) proposed the Aliwal Shoal Formation and adopted the earlier Pliocene age, associating it with one of the early Pliocene regressive sea-level phases.

A regional seabed mapping programme was initiated by the Geological Survey, University of Cape Town group and was continued by the Marine Geoscience Division of the National Research Institute for Oceanology (N.R.I.O.). The N.R.I.O. in collaboration with the Council for Scientific and Industrial Research (C.S.I.R.), employed the research vessel *Meiring Naude* to conduct several geophysical cruises on the southeastern continental shelf during the period 1978 to 1983. Side-scan sonar, bathymetry and reflection seismic profiling data were collected. A brief account will be given of the research that has been done in the vicinity of the current study area and the vast amount of geological information gathered during these six years of intensive data collection.

Birch (1981), investigated the bathymetry and geomorphology of the continental shelf and upper slope between Durban and Port St Johns. This regional study delineated the gross morphological features of the continental shelf including the aeolianite ridges, which form part of the extensive offshore relict coastal dune system. In 1996 Birch used seismic profiling data for the purpose of defining the Quaternary sedimentation off the east coast of southern Africa (Cape Vidal to Cape Padrone). The data was collected during 1978 & 1979, but only published in 1996. Due to the nature of the study (regional investigation) and the considerable extent of Birch's study area, the spacing between the survey lines was very wide. None of Birch's airgun seismic data plot in the present study area, however, two other seismic lines exists - one to the north and one south of the present study area. The reader is referred to the seismic stratigraphy section (Chapter 6) of this thesis for a locality map of these lines.

Martin and Flemming (1986) discussed the formation and sedimentary characteristics of the Holocene shelf sediment wedge off the south and east coasts of South Africa. They proposed a facies model for the Holocene sediment wedge located on the inner continental shelf. Martin and Flemming (1988) synthesised numerous publications and discussed the geological evolution and structure of the Natal continental shelf. Side-scan sonar data was collected and interpreted by Flemming (1978, 1980 and 1981) from which he subsequently derived a sedimentary process-response model for the southeast African continental margin. Flemming (1981) also described the offshore aeolianite ridges. Hay (1984) investigated the sediment dynamics on the continental shelf between Durban and Port St. Johns. Her study focused on the distribution and dynamics of modern shelf sediments on the southeast continental margin. The integration of Flemming and Hay's work provided an unsurpassed benchmark summary publication (Flemming and Hay, 1988) on the sediment dynamics offshore of the KwaZulu-Natal margin.

The most recent study of the Aliwal Shoal prior to this investigation was conducted by Ramsay (1998). Ramsay (1998) undertook a purely geophysical study and surveyed a portion of the Aliwal Shoal under contract for the Oceanographic Research Institute with the aim of distinguishing between different seafloor bottom types (reef or sediment) for benthic survey studies (Schleyer *et al*., 2006). The data for Ramsay's 1998 report was collected in 1997 and the survey consisted of the collection of bathymetry and analogue side-scan sonar records, no seafloor samples were obtained and no side-scan sonar mosaic was produced. The present study utilised more advanced digital geophysical instrumentation whose resolution far exceeds those used by the N.R.I.O. workers and even that of Ramsay's 1997 survey and integrate this with numerous seafloor samples.

CHAPTER 2
REGIONAL PHYSIOGRAPHY AND MORPHOLOGY

2.1 CLIMATE

Oceanic and climate has changed significantly during the development of the continental shelf, and since the evolution of the Aliwal Shoal. It is thus useful to compare climate proxies recorded in the Aliwal Shoal to the present day, particularly the palaeowind regime for the aeolianites and palaeosea surface temperatures.

The present day climate along the coastal belt of the KwaZulu-Natal (KZN) is dominated by the southern subtropical high pressure belt (STHP) which has a mean position situated on the 30° south latitude (Schulze, 1965; Hunter, 1988). There is a seasonal shift in the position of this belt; typically occupying a position south of the sub-continent in summer and migrating 3° - 4° north and often overland in winter (Hunter, 1988). This system produces a humid sub-tropical climate in the region with warm wet summers. Onshore climate data are provided by the South African Weather Bureau (SAWB) and offshore observations are from Voluntary Observing Ships (VOS) that supply the data to the South African Data Centre for Oceanography (SADCO).

2.1.1 Rainfall and Temperature

Rainfall is highly seasonal in the KwaZulu-Natal coastal region reaching a maximum in the summer months of November to March (Hunter, 1988). Mean annual precipitation along the KwaZulu-Natal coast varies between 1000 - 1100 mm annually (Hunter, 1988). With the exception of St Lucia which displays anomalous winter rainfall figures the rest of the coastal belt winter monthly rainfall figures are typically less than 30% of the summer values (Hunter, 1988). Temperatures are characterised by a relatively low seasonal change which is due to the moderating effect of the adjacent warm ocean (Hunter, 1988). On the diurnal scale large variations may occur especially during bergwind conditions (Hunter, 1988). The VOS dataset shows that the absolute minimum temperature offshore approach 10 °C and maximum values between 33 °C and 35 °C (Hunter, 1988). This is in contrast with the onshore absolute minimum of 2.8 °C (Durban International Airport), 4 °C (weather site influenced by marine conditions) and absolute maximum of 42 °C illustrating the moderating effect of the ocean and warm Agulhas Current (Hunter, 1988).

2.1.2 Wind

A characteristic feature of the seasonal wind roses for the KwaZulu-Natal coastal belt are the high frequency of strong winds blowing parallel to the north-northeast - south-southwest trending coastline (Figure 2.1) (Hunter, 1988). North-easterly winds are typically the result of ridging of the South Indian Ocean High (SIOH) pressure over the east coast of Southern Africa, whilst the south-westerly winds are closely related to northward migrating low pressure cells and associated cold fronts (Hunter, 1988).

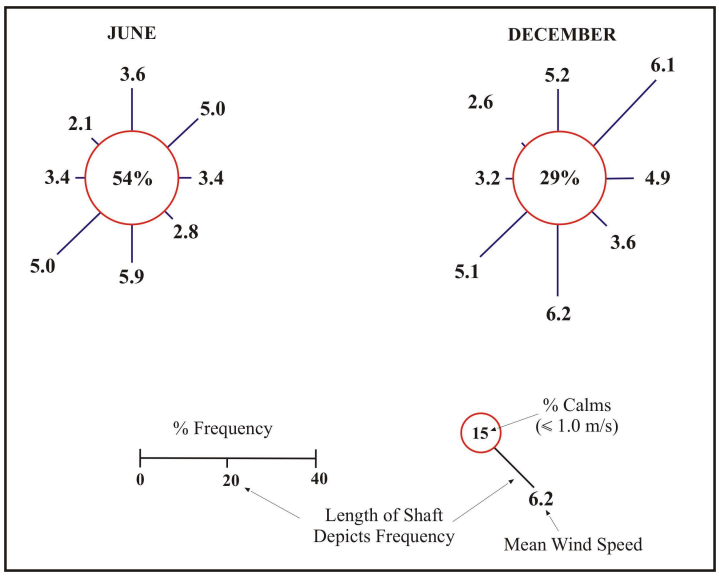

Figure 2.1 Average wind conditions at Durban International Airport for June (winter) and December (summer) for 1956 to 1970 (modified from Hunter, 1988).

The SAWB data show that summer north-easterly winds attain higher velocities than the winter southerly winds (Figure 2.1) with the highest hourly (average) wind speed measured at 24 ms^{-1} (Hunter, 1988). The majority of offshore flow (west winds) occurs in winter and is related to the nocturnal land breeze whereas northwesterlies are associated with bergwinds (Hunter, 1988). Significantly the warm Agulhas Current drives a strong land breeze circulation, reaching 60 km off the coast with wind speeds of 9 ms^{-1}, due to the strong temperature gradient between the coast and the current (Hunter, 1988). The SADCO dataset shows that south-westerly through southerly winds generally have the highest wind speeds (Figure 2.2) although offshore wind conditions may vary greatly to those reported onshore. At sea the land breeze can attain velocities of more than 30 ms^{-1} as opposed to the 9 ms^{-1} measured from terrestrial weather stations (Figure 2.2). Even more striking is the highly bimodal distribution of the wind out to sea. The high coast-parallel dune barrier formed along most of the KwaZulu-Natal coastline attest to the volume of coastal aeolian

sediment transport which were facilitated by the unique combination of coastline orientation and dominant wind directions being parallel. Eroded remnants of Pleistocene aeolianites display planar cross-bedding indicating similar palaeowind directions (Section 8.3.3) suggesting that the present dominant wind directions were a well established feature in the Late Pleistocene.

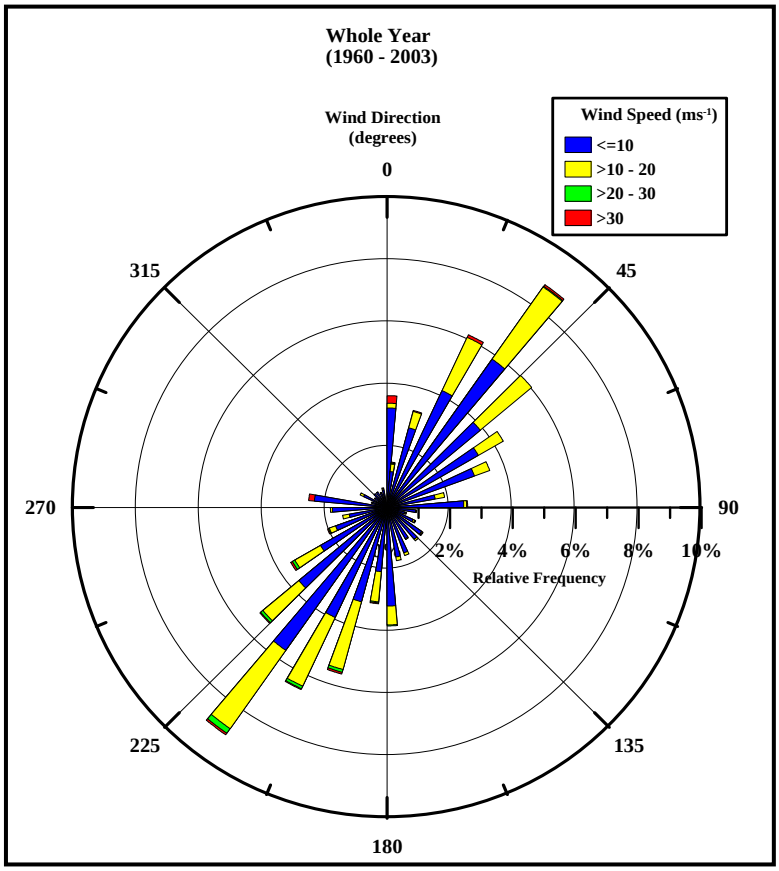

Figure 2.2 The strongly bimodal wind direction and speed for the area between 30° - 30.9° S and 30.3° - 30.9° E as derived from the SADCO database for the period 1960 to 2003.

2.2 COASTAL HYDRODYNAMICS

2.2.1 Tides

The tidal range averages 2 m (Schumann and Orren, 1980) classifying the coast as high microtidal (Davies, 1964) or low mesotidal (Hayes, 1979). Microtidal coasts typically show narrow and steep beach profiles with offshore bars and an offshore-fining trend as represented by the Aliwal shoal area. Since this shelf is also narrow, tidal currents are negligible. Most analyses place an amphidromic point for the dominant M_2 tide to the south of Africa, with the cotidal lines orientated

nearly parallel to the coast with little phase difference between the tides to the north and the south of the region (Schumann, 1988). For this reason tides change simultaneously along the whole KwaZulu-Natal coast and the tidal conditions for the study area were determined from predicted tidal elevations for Durban (Table 2.1) and these corrections applied to the bathymetry data in this study (refer to Section 5.3.2 for a detailed description).

Table 2.1 Predicted tidal levels for Durban (from the Hydrographic Office, 2001) for 2001 (year of data collection) with respect to chart datum (-1.113 m relative to land levelling datum for 2001 and -0.913 m for 2004). Levels based on more than 19 years' observation. LAT = lowest astronomical tide; MLWS = mean low water springs; MLWN = mean low water neaps; ML = mean level; MHWN = mean high water neaps; MHWS = mean high water springs; HAT = highest astronomical tide.

Durban	LAT	MLWS	MLWN	ML	MHWN	MHWS	HAT
2001	0	0.21	0.87	1.11	1.36	2.01	2.3

2.2.2 Swell

The east coast is dominated (40 % of the year) by persistent high-energy waves and prevailing large amplitude southern swells (Figure 2.3; Begg, 1978; Swart and Serdyn 1981; Rossouw 1984 and Ramsay, 1996). These swells become refracted by the shelf to produce a dominant south-easterly direction whereas north-easterly to easterly onshore swells prevails for a further 40 % of the time (van Heerden and Swart, 1986).

The north-easterly to easterly swell is of a low amplitude and short period and is superimposed on the southerly swell. Only when the north-easterly wind blows for a considerable period of time does this become the dominant swell direction (Ramsay, 1991). The average significant deep-sea wave height is 1.57 m, with the average significant breaking wave height being 2.6 m (Dunkley *et al*., 1998). The average wave period for the east coast is 9 s with a maximum of 14 s (Cooper, 1991a).

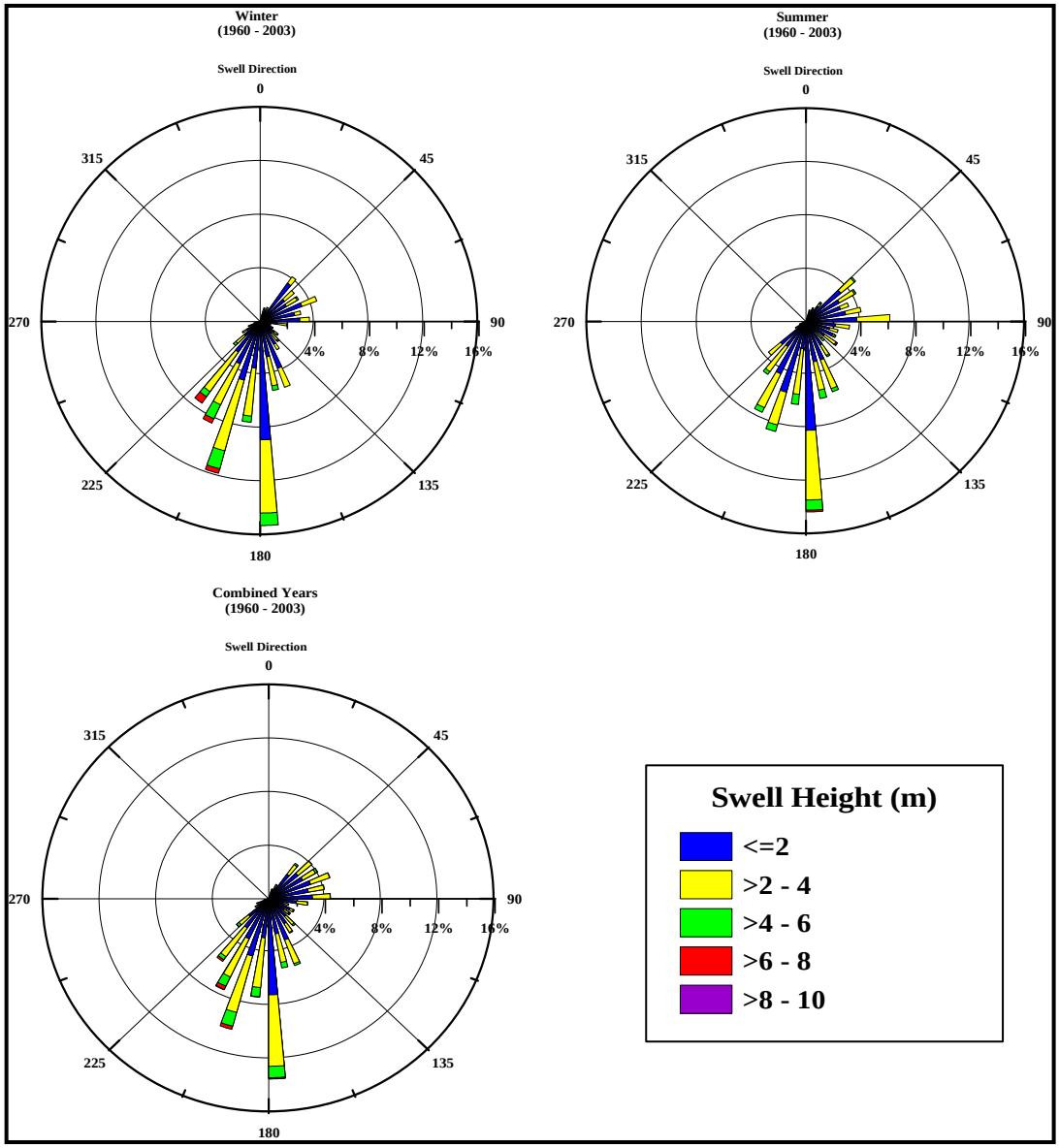

Figure 2.3 Combined yearly, winter (June, July, August) and summer (December, January, February) plots of swell direction and swell height for the area between 30° - 30.9° S and 30.3° - 30.9° E as derived from the SADCO database for the period 1960 to 2003.

2.3 OCEANOGRAPHY

2.3.1 Agulhas Current

The most important large-scale oceanographic feature on the east coast shelf is the Agulhas Current forming part of the western boundary current system of the south-western Indian Ocean. It is generally accepted that it originates off the northern KwaZulu-Natal/Mozambique coast (Figure 2.4a) from the confluence of waters which follow complex paths in the Mozambique

Channel and south of Madagascar (Lutjeharms *et al*., 1981; Flemming, 1981 and Gründlingh and Pearce, 1984). The southward flowing Agulhas Current sweeps polewards with a core, generally situated just off the continental shelf break (Schumann, 1987).

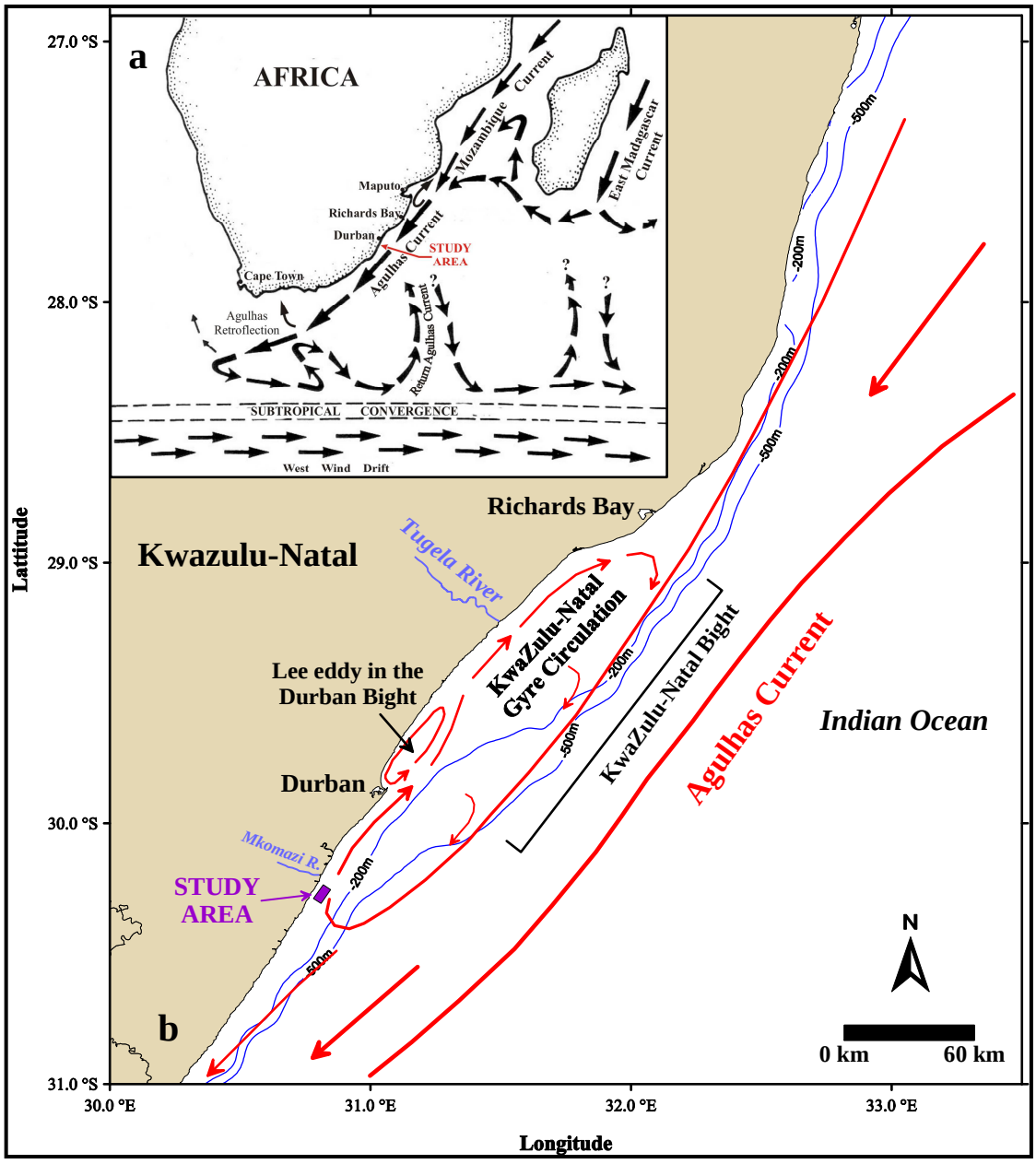

Figure 2.4 **(a)** The regional setting of the Agulhas Current system (modified from Flemming, 1981). **(b)** Simplified representation of the mean circulation of the Agulhas Current off KwaZulu-Natal and in the vicinity of the study area (modified from Gründlingh and Pearce, 1990).

Surface current velocities of >2.5 ms^{-1} have been recorded and bottom velocities of 0.34 ms^{-1} are common (Martin and Flemming, 1986; Flemming, 1981). Off Durban, the core of the current can be located anywhere from 15 km to 100 km offshore (Pearce, 1974; 1976; 1978) and a mean

current width of 100 km and a depth to more than -1000 m (Pearce *et al*., 1978). On average, the inshore edge of the Agulhas Current is located 20 -30 km offshore from the coast (Pearce, 1978). Gründlingh (1980), calculated a volume transport of ~70 x 10^6 m^3/s extrapolated over the total depth and width of the current. At present there is insufficient evidence to indicate whether or not seasonal variability exists in the Agulhas Current (Schumann, 1988) although wind stresses and bottom topography are known influences (Schumann, 1988; van Ballegooyen *et al*., 1991).

Current Meanders

The narrowing of the shelf south of the Tugela River, and the fact that the shelf break off Durban becomes very diffuse, causes a degree of instability in the core of the Current as it tries to re-establish its position close to the shelf edge (Gill and Schumann, 1979). This results in a meandering Current and the formation of semi-permanent clockwise eddies or gyres (Pearce *et al*., 1978, Gründlingh and Pearce, 1990 and Schumann, 1981). In the lee of structural offsets, such as south of Richards Bay where the coast and shelf is offset to the west (Figure 2.4b), semi-permanent gyres or cyclonic eddies (flow reversals) are induced (Flemming, 1978; Flemming, 1981; Martin and Flemming, 1986; Gründlingh and Pearce, 1990 and Gründlingh, 1992).

One of these, the Natal Gyre (Luthjeharms and Roberts, 1988), renamed the KwaZulu-Natal Gyre (Bosman *et al*., 2007) is developed south of Richards Bay within the KwaZulu-Natal Bight, extending as far south as the study area (Figure 2.4). Here the increased width of the shelf and the change in orientation of the coast relative to the southward-flowing Agulhas Current results in the generation of the gyre (Flemming, 1978, 1981, Martin and Flemming, 1986; Gründlingh and Pearce, 1990 and Gründlingh, 1992). Variability in the current regime is most pronounced on the wider shelf north of Durban, away from the dominating influence of the Agulhas Current. Previous workers suggested that it is highly unlikely that a single well-defined clockwise circulation, on the scale of the Bight (~200 km), is a permanent feature (Figure 2.4B). It is more probable that at any one time eddies (on a variety of scales) are generated in the region by meteorological forcing or shear processes (Pearce *et al*., 1978; Schumann, 1981). However, Bosman *et al*. (2007) showed that the KwaZulu-Natal Gyre exerted a strong sedimentological control on the shelf and might be more permanent than previously thought.

Salinity and Temperature

The only major river onshore from the study area is the Mkomazi River (Figure 1.1) with little overall influence on the vertical density structures and currents (Schumann, 1988) except during

heavy rains or floods when sediment and significant fresh water produces an extensive turbid plume extending kilometres out to sea. Such situations are generally short-lived but in summer, water with slightly lower salinity values are found and terrigenous silt can be detected in the circulation systems further offshore (Schumann, 1988). Shelf water is dominantly of tropical or sub-tropical origin, brought into the area by the Agulhas Current (Schumann, 1988) although cold, deep water can be introduced at times by up-welling mechanisms. Surface salinity varies between 35.3 and 35.5 parts per thousand with the higher salinity values linked to sub-tropical water from the mid-latitude Indian Ocean and lower values linked to tropical water from the equatorial Indian Ocean.

A well-mixed regime is indicated by the fairly uniform vertical temperature structure. In the shallower inshore region there is an approximate 4 °C temperature change between summer and winter, with a maximum temperature of 25 °C in February. Surface temperature of the current varies from 22 °C to 26 °C off Durban but as it flows southwards there is a 1°C decrease per ~500 km due to heat loss to the atmosphere (Pearce, 1978).

Geological History of the Agulhas Current

Changes in sedimentation occurred in the Natal Valley in the Cenomanian/Turonian and Cretaceous/Tertiary boundary which *may* have been due to changes in the Agulhas Current regime (Martin, 1981a,b). Clear evidence for enhanced current action dates from the Lower Oligocene which marks a major alteration in current strength or its main core location (Martin *et al*., 1982). During the Late Miocene - Early Pliocene flow paths, broadly similar to those of today, were established (Martin, 1981a,b; Dingle *et al*., 1983) with an eastward movement of a counter-current and cyclonic eddy off Maputo in the Pliocene - Recent (Martin *et al*., 1982).

The Agulhas Current response to Pleistocene global climate is well established. Foraminifera and sedimentological studies of a core taken on the Agulhas Bank (Agulhas Current retroflection zone) by Rau *et al*. (2002) indicate a major oceanographic change at 200 - 250 kyr B.P. to warmer surface water conditions and a link to glacial - interglacial cyclicity in the Middle Pleistocene. During the Late Pleistocene seasonal changes in circulation may have been even more pronounced (Hutson, 1980). This is supported by the sedimentological data of Martin (1981b) which indicates fluctuations in the Agulhas Current system in response to Pleistocene glacial periods. During the last glacial period, the summer Agulhas Current existed as a warm southward flowing current similar to today but with higher salinities (Hutson, 1980) but during the winter months southwards flow either decreased, shifted or was replaced by a cool high salinity current from the south (Hutson, 1980). Bè and Duplessy (1976) provided the most compelling evidence of Agulhas

Current weakening during glacial and interglacial stages. Their records span the last 540 ka and are based on isotopic and micropaleontological analyses of mid-latitude sediment cores (one core located 500 km southeast of Durban in 3308 m water depth) taken from opposite margins of the Indian Ocean. This showed a northward fluctuation of the Subtropical Convergence Zone (SCZ) to a position north of Durban during glacial periods. They also calculated sea-surface temperatures (SST) for this time interval which indicated that present day mean summer SST only occurred approximately 1% of the time off southeast Africa. Bè and Duplessy (1976) considered the northward migration of the SCZ and much lower SST off southeastern Africa as a reflection of a generally weaker Agulhas Current.

Holocene Agulhas Current temperatures were much higher and present day temperatures were only reached during four short intervals (marine isotope stages 5, 9, 11 and 13) during the last 540 ka (Bè and Duplessy, 1976). Hutson (1980) also inferred that oceanographic conditions during the Holocene were similar to modern conditions with estimated temperatures slightly higher and salinities slightly lower than those observed today.

2.3.2 Study Area Circulation

Three distinct circulation systems influence the study area viz; the outer shelf southerly flow, the southern limit of the return flow gyre and the northwards flowing longshore drift (Figure 2.5). The dominant circulation patterns are mainly the result of the Agulhas Current and consist of alternating but opposing southerly flow in the offshore regime and northwards return flow in the inshore regime. As a result of the return flow gyre,the Agulhas Current plays an important role in the inshore circulation and hence sediment movement in the study area (Schumann, 1981).

Flow direction studies (Table 2.2) off Umkomaas have indicated a strongly bimodal directional character (Anderson *et al*., 1988) with southerly flow slightly more common (Table 2.2). Dominance of the southerly flow might be attributable to the narrow continental shelf which is subjected to a stronger influence from the southerly flowing Agulhas Current. Gill and Schumann (1979) have shown that the return flow forces the water to move inshore and then northwards (Figure 2.5; Table 2.2). Current meter data confirmed a general onshore flow at depths of 200 m at a position immediately south of Green Point (Pearce *et al*., 1978).

The oceanographic data are in agreement with Hay (1984) and Flemming and Hay's (1988) bottom current patterns inferred from sediment distribution analysis and bedforms patterns which

identified an outer shelf flow regime dominated by the Agulhas Current and an inner return flow gyre (Figure 2.6).

Table 2.2 Variation in the flow direction offshore from Umkomaas (from Harris, 1978; Schumann, 1979 in Hay, 1984).

Distance Offshore (km)	% North Flowing	% South Flowing	% Onshore Flow
1	42	51	7
2	39	43	9.1
3	47	50	1.5
4	50	44	3.8
5	40	50	7.1

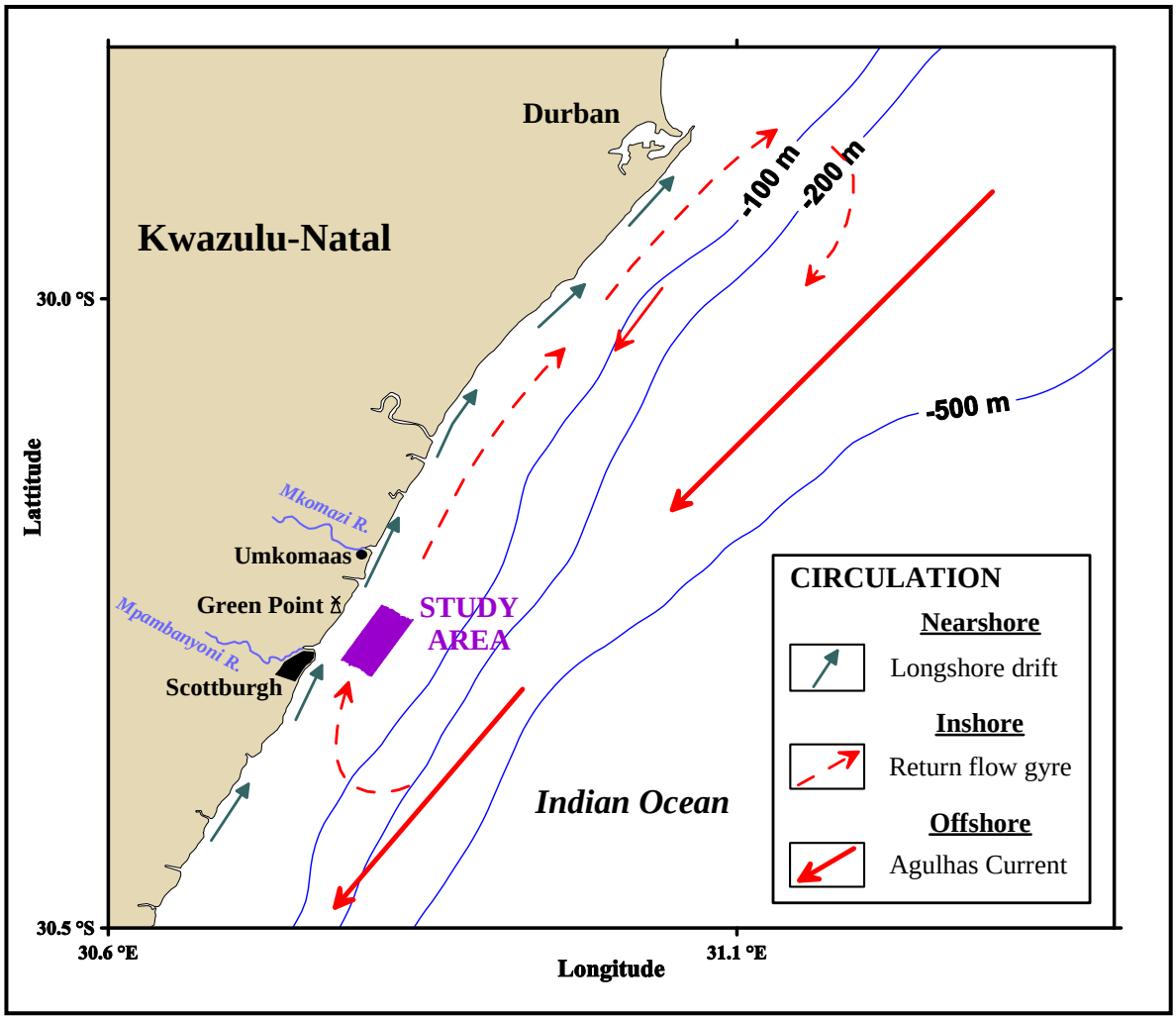

Figure 2.5 Simplified diagram of the mean current circulation patterns in the vicinity of the study area (modified from Gründlingh and Pearce, 1990 and Schumann, 1987).

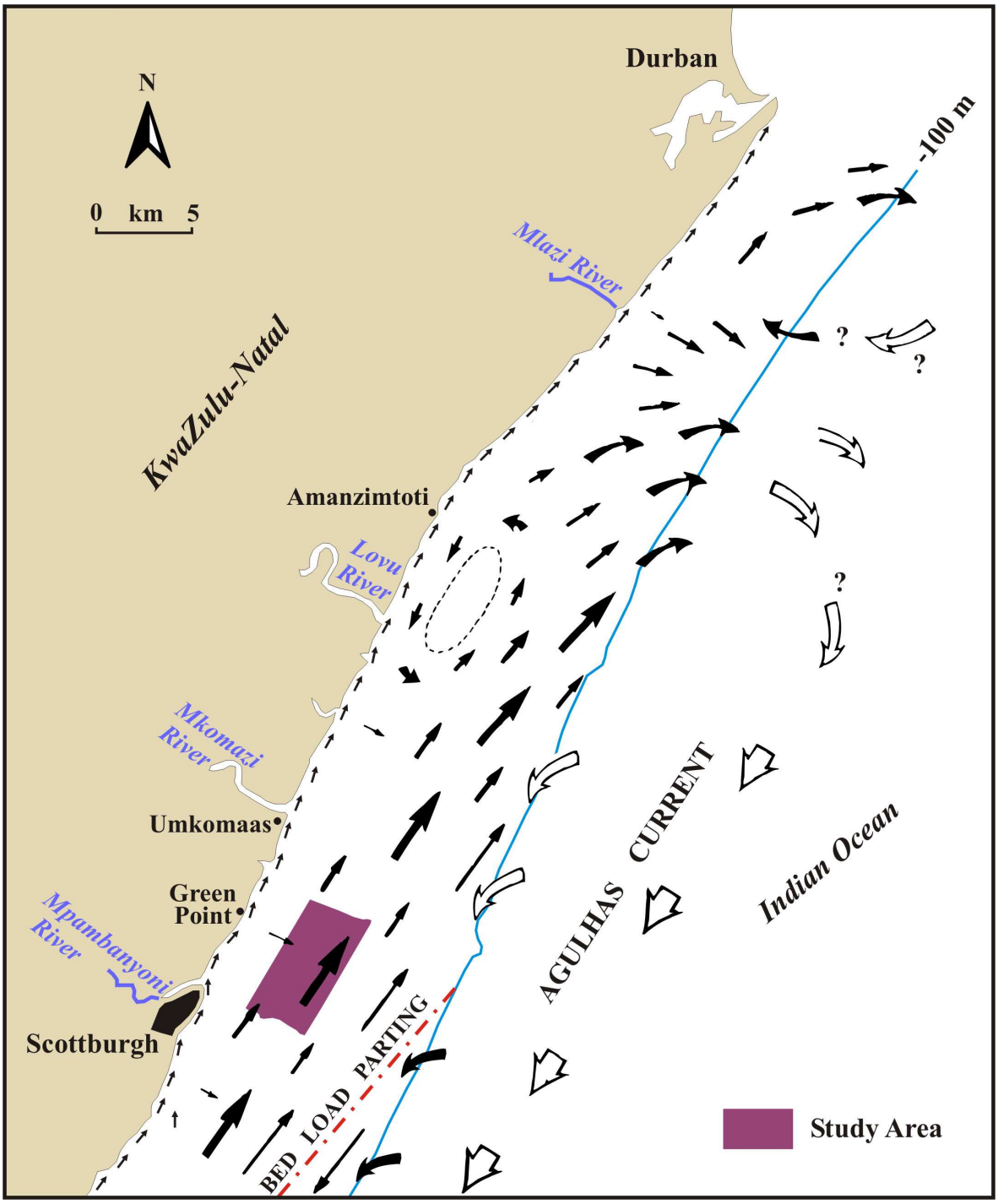

Figure 2.6 Schematic bottom current patterns in the vicinity of the study area inferred from sediment dispersal and bedform patterns (modified from Hay, 1984 and Flemming and Hay, 1988). Note the dominant shelf counter current and the Agulhas Current along the continental slope. The bedload parting zone is strongly migratory depending on the relative positions of the Agulhas Current and counter current.

To the SE of the study area a bedload parting zone (zone of opposing current, hence sediment transport) is present (Figure 2.6) marking the divide between the south flowing Agulhas Current and north flowing counter-current return gyre. Bedload parting zones are normally situated at the southern limits of large clockwise eddy systems and can shift tens of kilometres periodically up and down the shelf (Flemming and Hay, 1988). This indicates that, as for the KwaZulu-Natal Gyre, the return flow gyre is a semi-permanent feature controlled by variations in intensity and the flow path of the Agulhas Current (Flemming and Hay, 1988).

Through the many SCUBA dives conducted on the Aliwal Shoal the author has noticed that a strong northerly flow is coupled with a coastal low system and associated strong south-westerly winds, indicating the possibly of the return gyre also having a wind-forced origin. Boomer seismic data (Chapter 6, Bosman, 2003b) confirms the sparker seismic data of Martin and Flemming (1986) indicating a northward migration of unconsolidated sediment north of the study area, controlled by the return flow gyre (also refer to Sections 6.3.4 and 6.4.3). Flemming and Hay (1988) suggested that a small anticlockwise semi-permanent lee eddy is situated inshore from the clockwise return flow gyre, offshore from the Lovu River (Figure 2.6), probably the result of the presence of a large spit-bar complex (Section 2.2.3). The northeast-ward directed longshore drift is active in the nearshore region and is the net result of the combined effects of the orientation of the coastline and incoming swell direction.

2.3.3 Hinterland Topography and Drainage

KwaZulu-Natal is situated on the eastern side of the Great-Escarpment (Figure 2.7) of southern Africa (Cooper, 1991b). The Great Escarpment was formed by the subsequent erosion of a marginal escarpment that occurred as a giant rampant located 50 - 200 km inland of the present coastline and existed during continental fragmentation in the Cretaceous (Partridge and Maud, 2000). The Great Escarpment rises to over 3300 m above sea-level in Lesotho, only 230 km away from the coast (Cooper, 1991b). This results in a steep coastal hinterland with comparatively short drainage systems characterised by high flow velocities (Cooper, 1991b).

As a consequence rivers have little opportunity to coalesce and subsequently drain small, lateral restricted catchments, separated by deeply incised divides with narrow river courses and poorly developed floodplains which offer little storage capacity for sediment (Cooper, 1991b). This combination of a steep hinterland and the lack of a coastal plain have resulted in abundant small rivers forming independent outlets at the coast (Cooper, 1991b).

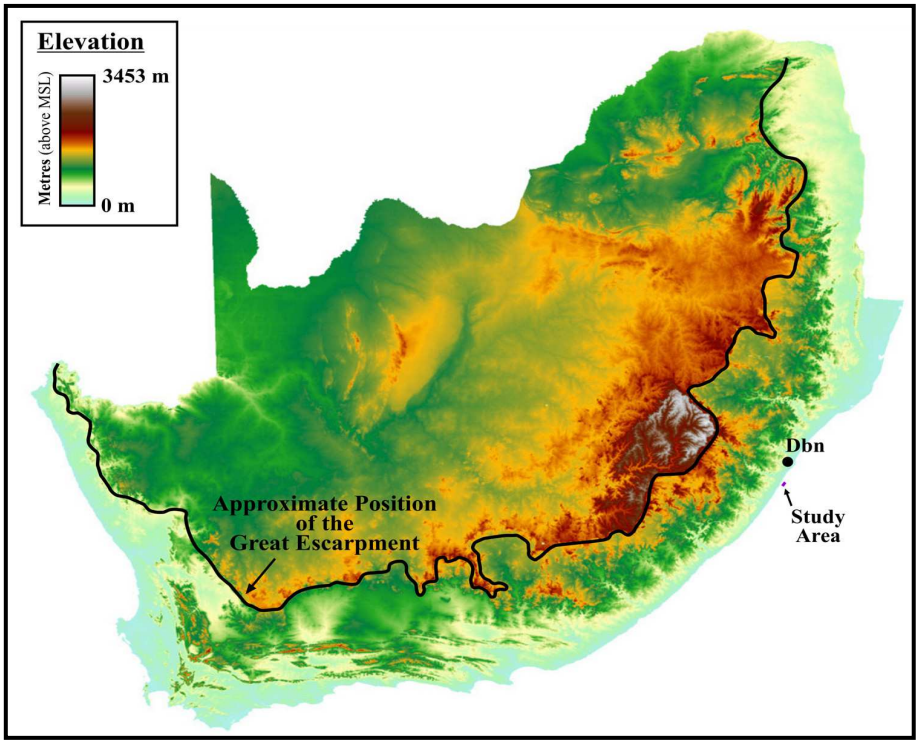

Figure 2.7 Shaded relief map showing the Great Escarpment of South Africa (data courtesy Council for Geoscience). Note the predominantly narrow and linear drainage patterns exhibited by rivers on the East coast. This is as a consequence of the position and elevation of the Great escarpment relative to the coastline. Dbn = Durban.

Onshore from the study area four river systems drains the hinterland viz; the Mkomazi, Mhlongwa, Mahlongwana and Mpambanyoni Rivers (Figures 2.8; 2.9). These are summarised and compared with the Tugela River (largest river in KwaZulu-Natal) in Table 2.3. The Mkomazi River is by far the largest river and is the only major river system in the area with a river course length of ~ 300 kilometres (Figures 2.8; 2.9 and Table 2.3). Hence it is the most influential river to the study area in terms of mean annual runoff (fresh water delivery) and sediment yield to the shelf (Figure 2.8). It has a catchment area of 4310 km^2 and although relatively narrow, extends from the coast to the Great Escarpment, rising to an altitude of more than 2 600 m above mean sea-level (Figures 2.7; 2.8 and 2.9).

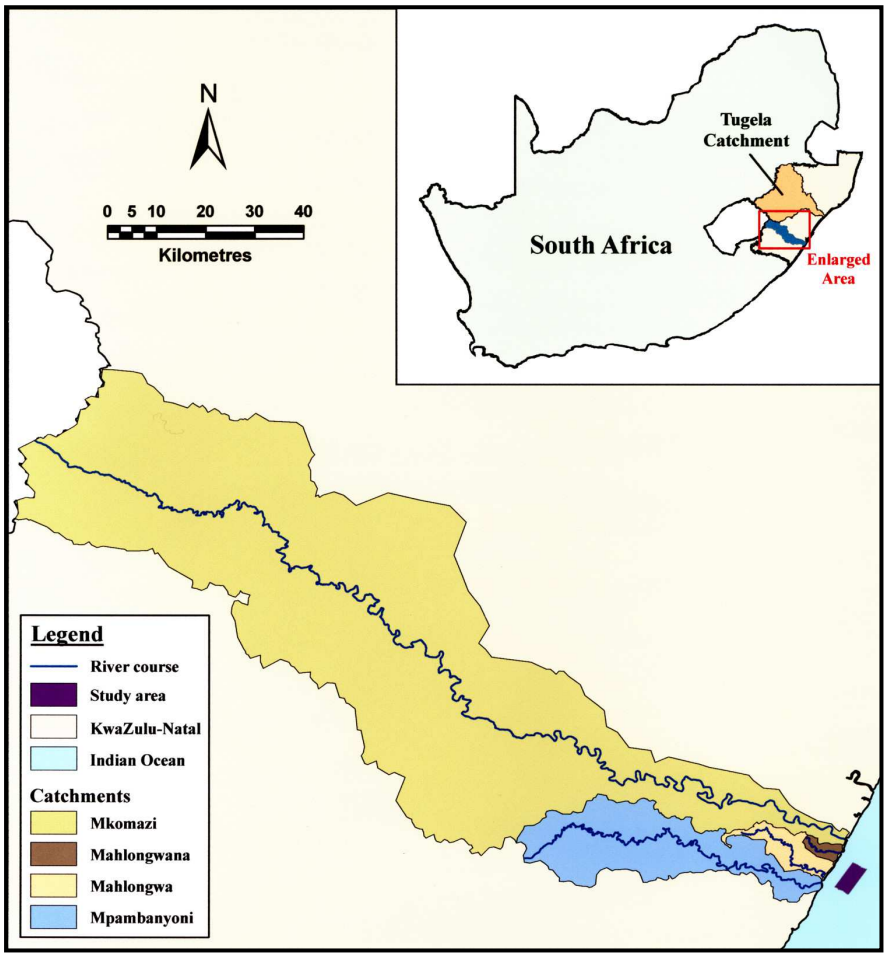

Figure 2.8 River systems and catchments draining the hinterland onshore of the study area (data courtesy Council for Geoscience).

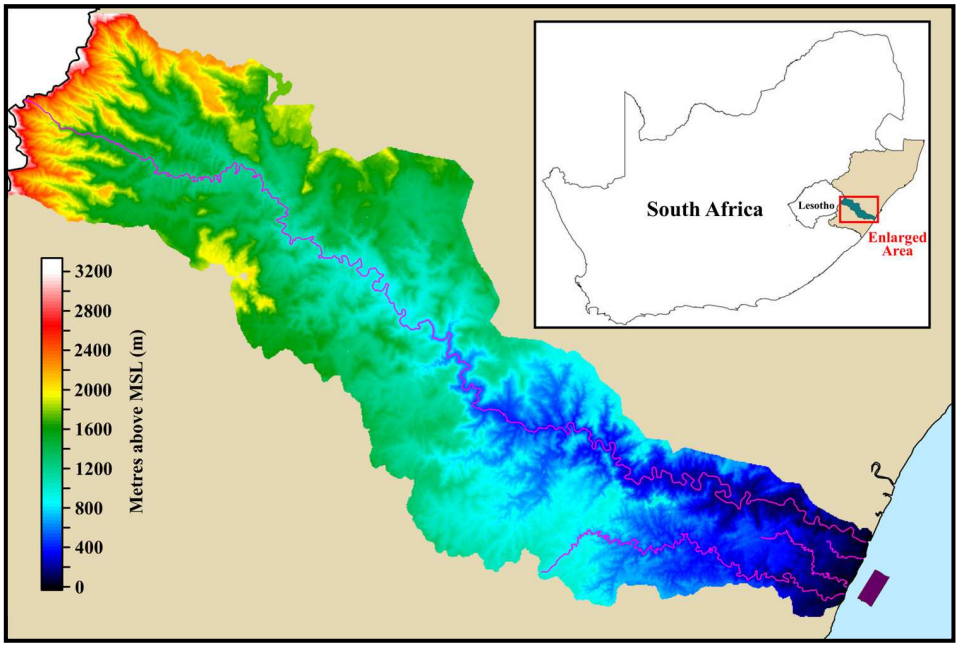

Figure 2.9 Digital elevation model of the topography of the river systems and the associated catchments draining the hinterland onshore of the study area. Refer to figure 2.8 for the respective catchments, river names and scale (data courtesy Council for Geoscience).

Table 2.3 Tabulated data on the main river catchments that drains the hinterland onshore from the study area (after NRIO, 1986). Tugela River data included for comparison.

River	Catchment Area (km^2)	River Length (km)	Elevation of Source (metres a.m.s.l)	Mean Annual Runoff ($m^3 \times 10^6$)	Average Sediment Yield (tonnes/year)
Mkomazi	4 310	298	2 650	1 036.17	1 616 360
Mahlongwana	15	6	218	1.96	6 000
Mahlongwa	92	23	430	12.04	36 800
Mpambanyoni	562	100	962	52.02	184 550
Total	***4 979***	**-**	**-**	***1 102.19***	***1 843 710***
Tugela	29 101	405	3 109	4 594.94	8 798 000

Of the other river systems only the Mpambanyoni River contains a catchment of any notable size (562 km^2), with a total river course length of a 100 km and a source elevation reaching almost 1000 m amsl (Figures 2.8; 2.9 and Table 2.3). Both the Mahlongwana and Mahlongwa Rivers have very restricted catchment areas with the maximum source elevation < 450 m above sea-level. However, relative to the size of their catchments, the average sediment yield for all the rivers onshore of the study area exceeds that of the Tugela River. The rate of erosion is determined by the depth of weathering, the precipitation distribution and amount, the type and density of vegetation and the local topography (Hay, 1984). Fluvial discharge is further influenced by the geology of the source rocks (refer to Section 3.4.2) which in turn control the availability of various grain sizes, the topography of the catchment, the distance between the sediment source and the river mouth (storage capacity) and the transport capacity of the river (Hay, 1984).

2.2 CONTINENTAL MARGIN MORPHOLOGY

2.2.1 Introduction

The general morphology of the seafloor around southeast Africa consists of several ocean basins and ridges (Figure 2.10). The Natal Valley is situated adjacent to the KwaZulu-Natal continental shelf. This north-south trending sediment-filled ocean basin deepens southwards to depths >3000m where it merges with the Transkei Basin (Martin and Flemming, 1988; Goodlad, 1978 and Dingle *et al.*, 1978). It is separated from the Mozambique Basin by the Mozambique Ridge which forms a north-south trending bathymetric high (>1500 m depth). The eastern margin of the

ridge is steep and drops from 2000 m to between 3000 m and 5000 m in the Mozambique Basin (Dingle *et al*., 1978; Goodlad, 1978). The less well defined western flank of the ridge grades northwards into the Central Terrace which again passes into the low-lying coastal plain of Mozambique (Dingle *et al*., 1978). Most of these features either originated or was modified during Gondwana fragmentation which is discussed in Section 3.2.1.

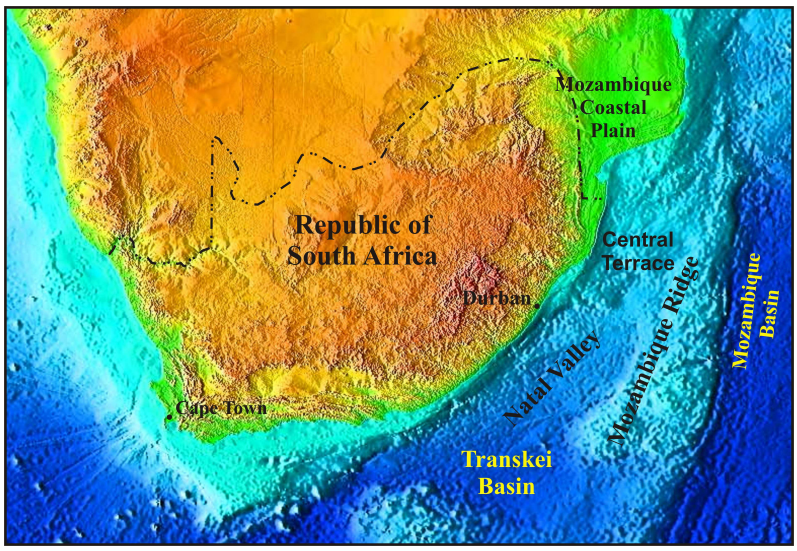

Figure 2.10 Morphology of the seafloor around southeast Africa (digital elevation map from NOAA, 2000).

2.2.2 Morphology of the KwaZulu-Natal Margin

The physiography and morphology of the continental margin and offshore features off the KwaZulu-Natal coast have been well described and documented by several workers (Goodlad, 1978; Dingle *et al*., 1978; Dingle *et al*., 1983; Birch, 1981; Flemming, 1981; Hay, 1984; Goodlad, 1986; Martin and Flemming, 1986 and Martin and Flemming, 1988 etc.). This section aims to introduce the reader to the broader continental margin setting surrounding the study area.

The bathymetry of the KwaZulu-Natal continental margin is shown in Figure 2.11. The KwaZulu-Natal margin is characterised by an extremely narrow (3 - 40 km) and shallow (-100 m) continental shelf (Flemming, 1981; Martin and Flemming, 1986 and Ramsay, 1991) when compared to the global average width of 78 km and an average shelf break depth of 130 m (Kennett, 1982). The development of the narrow continental shelf and straight coastline of KwaZulu-Natal is the result of the extraction of the Falkland Plateau (Dingle and Scrutton, 1974; Martin, 1984) along a transform fault known as the Agulhas-Falkland Fracture Zone (AFFZ; see Section 3.2.1).

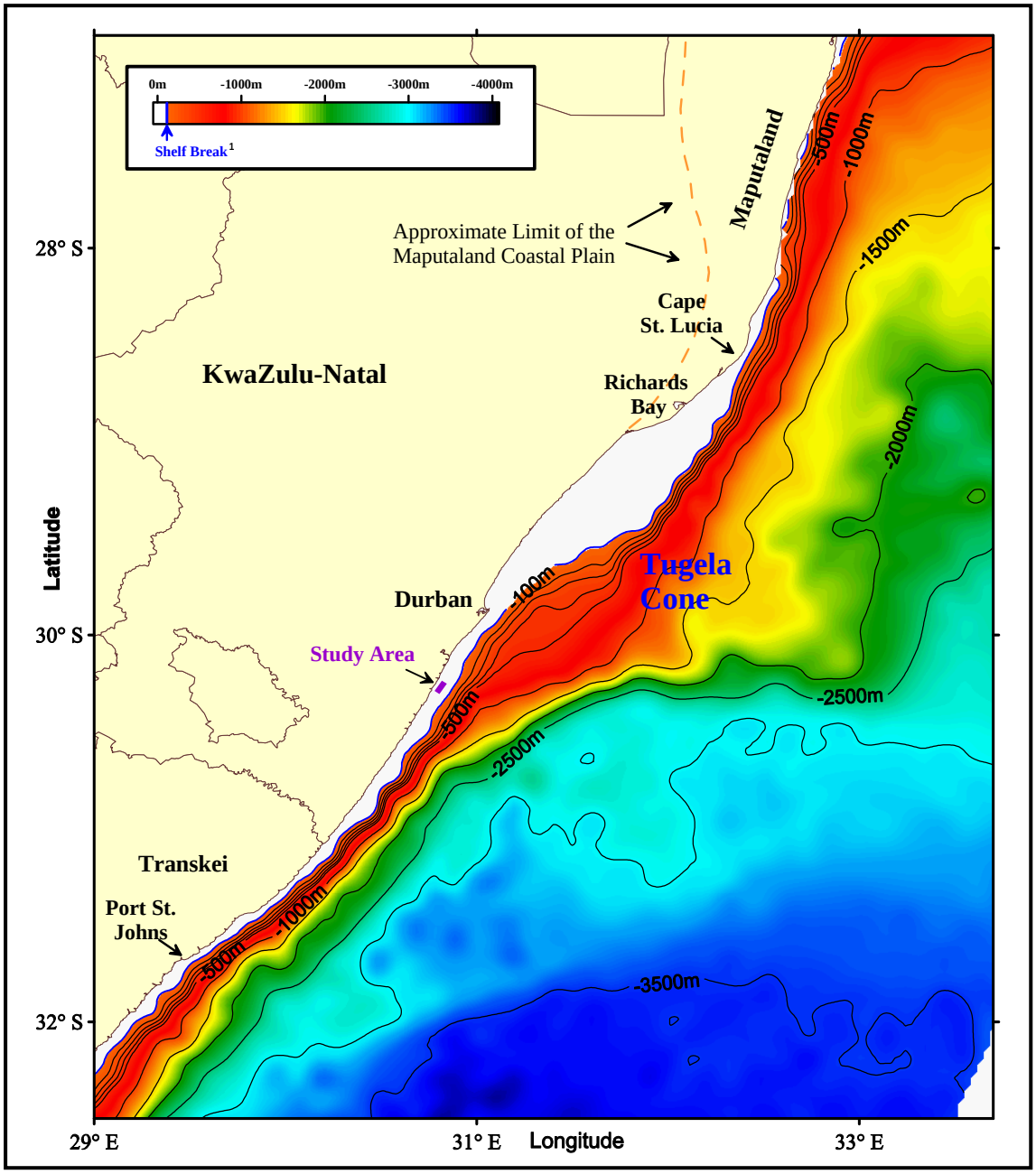

Figure 2.11 Bathymetry of the KwaZulu-Natal continental margin (Data courtesy Council for Geoscience; [1]Goodlad, 1978).

The continental shelf and slope is generally parallel to the NNE - SSW trending coastline (Goodlad, 1978). Exceptions occur where structural offsets change the coastline orientation towards a NE - SW trend. The most conspicuous being the ~55 km structural offset (Dingle *et al.*, 1983) just south of Cape St Lucia. Here the Tugela Cone is situated in the lee of the structural offset. A similar but smaller 3 km offset is present northeast of Port St Johns. Both these offsets are related structural displacement of the entire continental margin (Flemming, 1981; Dingle *et al.*, 1983).

Separation along the AFFZ can be described by a small circle with the pole of rotation situated at 46.75° N, 32.65° W (Martin *et al.*, 1981; Dingle *et al.*, 1983). The trend of the shelf break and coastline south of Durban and in Maputaland closely parallels this small circle (Dingle *et al*., 1983; Hay, 1984) - the area between Durban and St. Lucia being the exception. According to Scrutton (1979), the fundamental cause of steepness along sheared continental margins is the emplacement of oceanic crust against continental crust at transform faults. As opposed to the KwaZulu-Natal coastline and continental margin which has a transform fault origin (Martin, 1984) as far north as Durban (see Section 3.2), the Maputaland offshore submerged crust is deemed continental in origin (Dingle *et al*., 1983; Watkeys and Sokoutis, 1998). If the broad Maputaland coastal plain is considered as the exposed counterpart of the present continental shelf (an emerged shelf), the total shelf width increases to approximate the 45km width of the Tugela Cone (Maud, 1961; Goodlad, 1978). The narrow nature of the margin north Durban must therefore be ascribed to another origin (Shaw, 1998).

Goodlad (1978) divided the shelf into three sub-units; Transkei to Durban (KwaZulu-Natal south coast), Durban to Cape St. Lucia and Cape St. Lucia to the Mozambique border (Maputaland). Martin and Flemming (1988) divided the shelf into two morphological types. Both these schemes subdivided the shelf using the Tugela Cone as the discriminating feature i.e., north and south of the Tugela Cone the continental shelf is narrow and the continental slope is steep (Martin and Flemming, 1988).

The 100 m isobath is generally accepted to represent the shelf break off KwaZulu-Natal (Goodlad, 1978), although deviations from this depth is common. North of St Lucia in Maputaland the shelf is remarkably narrow, averaging approximately 5 km with the shelf break situated at a depth varying between 60 m to 100 m (Goodlad, 1978; Ramsay, 1991). Offshore Maputaland the shelf break generally parallels to the present day coastline, the only exception occurs where the shelf is incised by submarine canyons. These canyons are perpendicular to the shelf trend and in some cases canyon heads are as close as 1 km to the shoreline (Ramsay, 1991, 1994 and Shaw, 1998). North of Durban the shelf break trend changes towards the NE, widening the shelf to a maximum of 45 km opposite the Tugela River (Goodlad, 1978; Martin and Flemming 1988). This broader shelf area is an expression of the Tugela Cone - a major sediment depocentre since at least the Early Cretaceous (Dingle *et al*., 1983). The area of shelf between Transkei and Durban is of special interest to this study. Here the shelf is narrow ranging from 10 - 12 km in width with the shelf break mirroring the coastline and occurring mostly at a depth of 100m (Goodlad, 1978). The continental slope is very steep ranging from 6° - 16° (Hay, 1984) compared to the global average of 3° - 4° (Shepard, 1963). In the vicinity of the study area the shelf is 10.5 km wide with the shelf break occurring at -85 m (Bosman, 2003a).

2.2.3 Morphology of the Continental Shelf in the Vicinity of Aliwal Shoal

The modern shelf morphology in the study area is predominantly the result of Pleistocene sea-level fluctuations with subsequent modification by Holocene sedimentary processes (Flemming, 1978). A more detailed bathymetric map of the continental shelf in the vicinity of this study area (Durban to Scottburgh) is given in Figure 2.12.

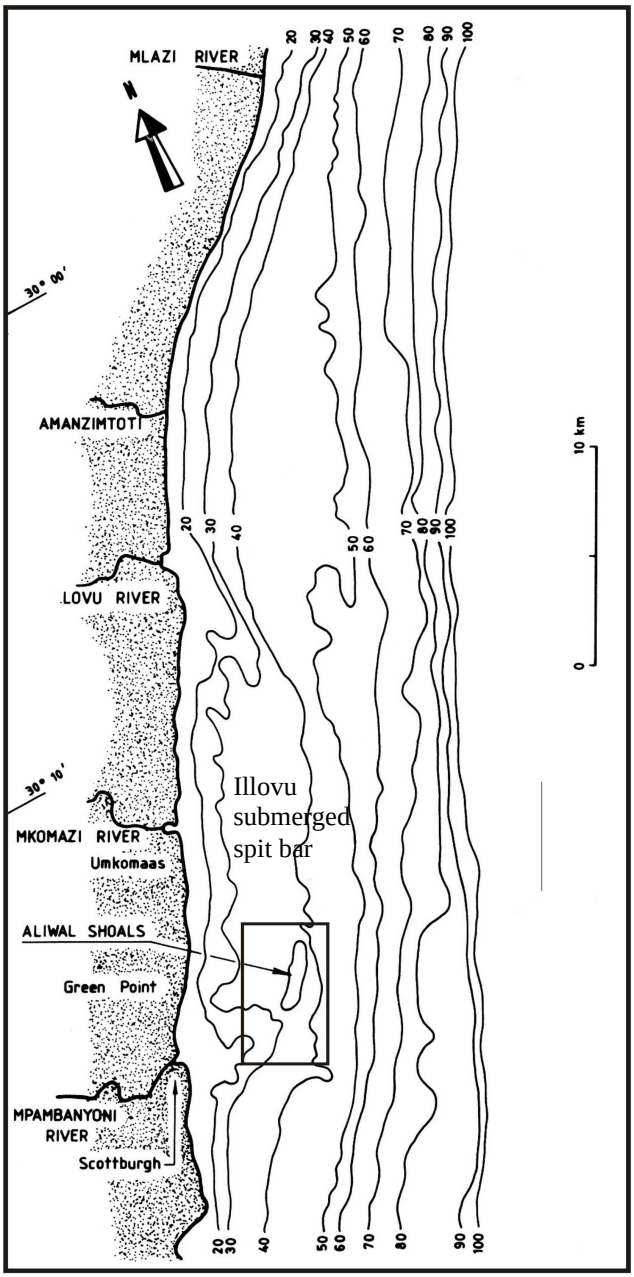

Figure 2.12 Bathymetry of the area surrounding the Aliwal Shoals (from Martin and Flemming, 1986). Rectangle = approximate detailed study area. The sedimentary Illovu submerged spit bar deposit forms a prominent bathymetric feature. Sand ridge bedform structures, represented by the -20 m and -30 m isobaths, are visible in the northern portion of the spit bar. These features are dealt with in Section 7.4.

The following discussion is applicable to the shelf area as per Figure 2.12. Birch (1981) divided the shelf into an inner shelf (0 - 50 m), a middle shelf (50 - 70 m) and an outer shelf (70m - shelf break). Whereas, Flemming (1981), divided the shelf based on two morphological zones - a nearshore and an offshore zone. These two zones are separated by drowned Pleistocene palaeodune ridges present between depths of 40 m - 60 m (Flemming, 1981). These aeolianite ridge complexes are semi-continuous features, sub-parallel to the coastline trend and present along most of the KwaZulu-Natal continental margin (Flemming, 1981; Martin and Flemming, 1988). According to Hay (1984), the morphology of the shelf is strongly influenced by the presence or absence of surficial (unconsolidated) sediments -which is a function of sediment supply and dispersal. The submerged aeolianite ridges again, controls sediment dispersal (Birch, 1981; Flemming, 1981) and act as topographical barriers to cross-shelf sediment movement. These barriers are generally mid-shelf features damming sediment on their shoreward side (see Section 3.4.2, Figure 3.14) since the Flandrian transgression (Hay, 1984). This sediment accumulation imparts a gently undulating and uniformly sloping morphology to the middle shelf (Hay, 1984).

The inner shelf is characterised by a broad topographically high feature between Illovu (or Lovu on Figure 2.12) River and Scottburgh. South of the Illovu River the -40 m isobath swings south-eastwards, widening the inner shelf to ~5 km, the change in orientation coinciding with the steep outer face of a large north-easterly prograding sedimentary body (Figure 2.12) (Hay, 1984; Martin and Flemming, 1986, Martin and Flemming, 1988). Birch (1996 - based on work done in 1978, 1979, and 1980) coined it the ‘Umkomaas sediment deposit’ whereas Martin and Flemming (1986) renamed it the ‘Illovu submerged spit bar’ (Figure 2.12).

The Aliwal Shoal complex is situated on the southern margin of the sediment deposit attaining a maximum relief of ~25 m above the seafloor. Immediately to the north of the sediment deposit is an arcuate mid-shelf terrace with the inverse morphological shape of the sediment deposit. Generally the middle shelf morphology in this area is dominated by aeolianite ridges. The distance offshore, orientation and width of these ridges are variable (Hay, 1984) but not easily discernible due to the scale of the bathymetry map in Figure 2.12. The seaward edge (-50 m to -70 m) of this arcuate terrace is bounded by low relief aeolianite outcrops (Hay, 1984) imparting an erratic pattern to these isobaths.

The outer shelf region in the northern part of the shelf is ~2.5 km wide, narrowing to ~1.5 km off the Illovu River. South of the Mkomazi River the -70 m isobath swings SW widening the outer shelf to ~4.7 km forming an outer shelf terrace. These physiographic zones are better developed south of the study area (Hay, 1984) and reflect strong current action which prevents sediment deposition. Hay (1984) noted that the width and character of these outer shelf terraces are

influenced by the offshore distance of the aeolianite ridge system/s i.e., the closer the ridge to the shelf break (greater offshore distance), the narrower the outer shelf terrace.

The shelf break almost exactly mirrors the NNE - SSW trending coastline, except north of the Amanzimtoti River where the coastline attains a more NE trend. Birch (1981) and Hay (1984) describe the presence of a discontinuous 10 - 15 m high ridge situated close to the shelf break. This was also observed by the author who undertook boomer seismic profiling (Chapter 6) offshore the Aliwal Shoal. Flemming (*pers. comm.*) in Hay (1984) suggested that these elevated areas are not superimposed features (such as aeolianites) on the outer shelf but rather relict eroded parts of the underlying 'basement' strata. However, seismic data from this study suggests that it comprises relict dune ridges almost completely buried by sediments from the modern (Holocene) transgression (see Section 6.3; Figures 6.5 - 6.9).

CHAPTER 3
REGIONAL GEOLOGY

3.1 INTRODUCTION

Prior to the Early Jurassic Period (>180 Ma) southern Africa occupied a central position within Gondwana (Dingle *et al*., 1983; Martin and Hartnady, 1986; Martin and Flemming, 1988; Watkeys and Sokoutis, 1998 and Watkeys, 2002, 2006) and its ultimate fragmentation was controlled by an inherited basement architecture that was re-activated, influencing the rifting process and the generation of the new continental margins (King, 1970, Hobday, 1982; Tankard *et al*., 1982; Cox, 1992; Watkeys and Sokoutis, 1998 and Watkeys, 2002, 2006).

The KwaZulu-Natal coast and specifically the onshore geology of the study area (Figure 3.1) comprises a crystalline basement of the Proterozoic Namaqua Natal Province (NNP; also known as the Namaqua Natal Metamorphic Province, NNMP; Figure 3.1) with a Phanerozoic cover of the Natal Group (Ordovician - Silurian) and Karoo Supergroup (Permian to Jurassic) (Figure 3.1). A detailed account of these sequences is beyond the scope of this study and the reader is referred to the following key publications;

i. for the NNP: Nicolaysen and Burger (1965); Matthews (1972, 1981); Thomas (1988, 1989); Thomas *et al*. (1990); Jacobs *et al*. (1993); Visser (1998) and Cornell *et al*. (2006),
ii. for the Natal Group: Thomas *et al*. (1992); Marshall and Von Brunn (1999) and Marshall (2006) and,
iii. for the Karoo Supergroup: Ryan (1967); Matthews (1970); Stratten (1970); Johnson (1976); Hobday (1973, 1982); SACS (1980); Tankard *et al*. (1982); Dingle *et al*. (1983); Saggerson *et al*. (1983); Encarnación *et al*. (1996); Visser (1998); Watkeys (2002), Duncan and Marsh (2006) and Johnson *et al*. (2006).

For the purposes of this study, the NNP, Natal Group and Karoo Supergroup lithologies form the structural basement to the post-Gondwana sequences that cover and have built the continental shelf and are the focus of this study.

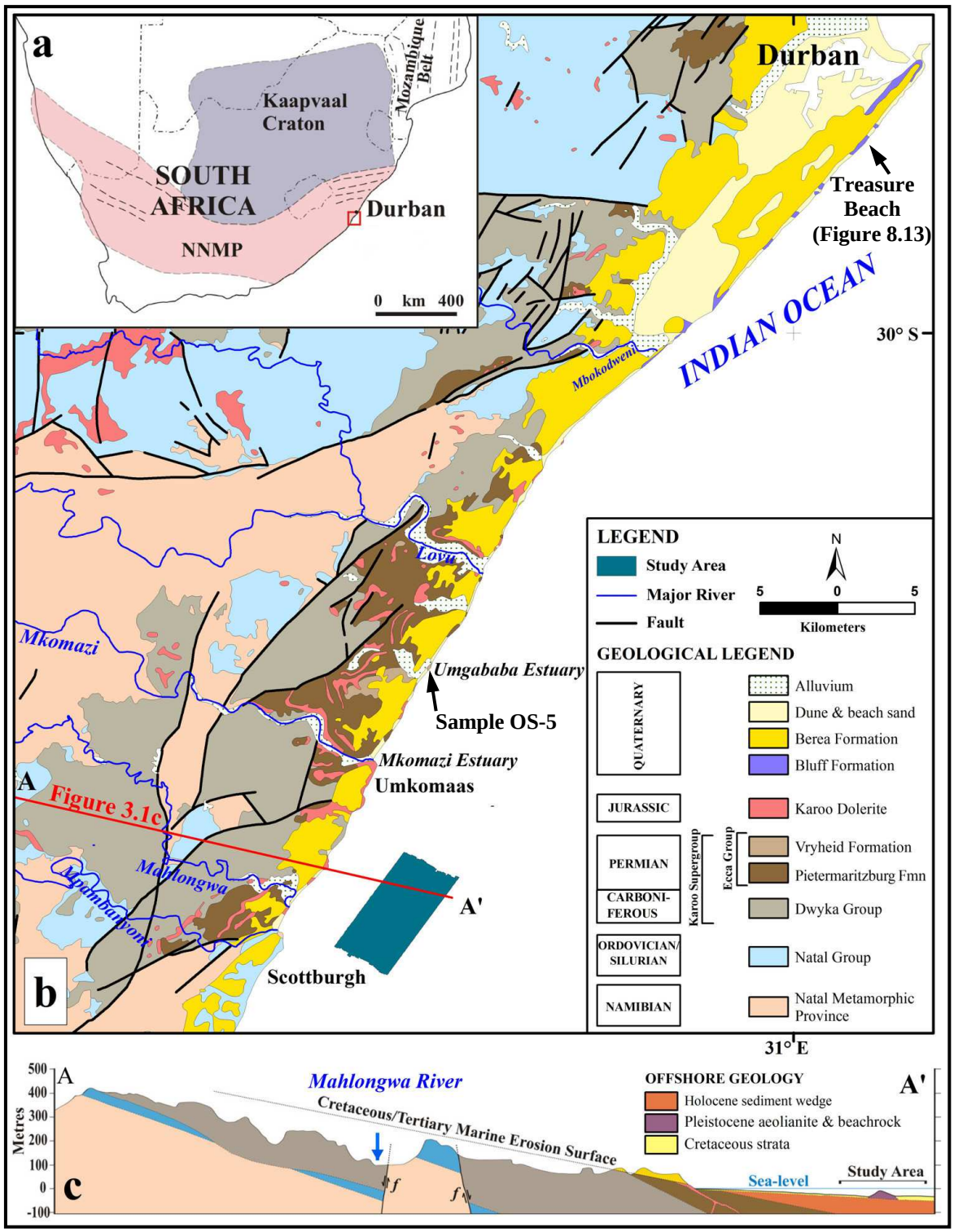

Figure 3.1 (a) Crustal architecture of South Africa (modified from Visser, 1998). NNMP = Namaqua-Natal Metamorphic Province. **(b)** Simplified onshore geological map of KwaZulu-Natal in relation to the detailed study area (data courtesy of Council for Geoscience). Treasure Beach is the locality for a photograph in Figure 8.13. **(c)** Schematic geological cross-section on line A - A' vertical scale exaggerated 5.8x, horizontal scale = 1 : 82 385.

3.2 BASEMENT ARCHITECTURE AND CONTINENTAL MARGIN DEVELOPMENT

Basement architecture played a significant role in the geological evolution of not only the south-eastern African margin but also Gondwana. Re-activation of older structures has played a significant role in determining subsequent geological events as diverse as sediment deposition, basin tectonics and Gondwana rifting.

An approximate north-south zone of crustal weakness existed during Gondwana times, sub-parallel to the present coastline. Both the Dwyka and Ecca Group basins were influenced by the underlying early Palaeozoic trough (Natal Embayment) which had an axis sub-parallel to the present coastline. Although the Ecca and Dwyka basins were slightly offset relative to the Natal Embayment, the parallel trend of their major axes was maintained (Hobday, 1982). The origin of the trough appears to be related to mantle processes which also led to the subsequent breakup of east and west Gondwana (Hobday, 1982). According to Dingle's (1976) 'failed arm' model a long history of linear subsidence without rifting preceded the evolution of the existing coastline of south eastern Africa (Hobday, 1982). Furthermore, this area represents the southern-most extension of a 7000 km zone stretching from the Dead Sea/Red Sea through the East African Rift System (Dingle *et al*., 1983) marking a zone of incipient crustal fracture (Hobday, 1982), active since the early Palaeozoic. Controversy surrounds the nature and underlying causes of this line of crustal weakness but there is general agreement that this lineament is a zone of tension (Dingle *et al*., 1983).

3.2.1 Gondwana Breakup

South Africa's continental margins, coastline and the offshore basins were formed during the fragmentation of the super-continent of Gondwana (Scrutton, 1973; Dingle and Scrutton, 1974; Martin *et al*., 1981; Dingle *et al*., 1983, Martin, 1984; Goodlad, 1986; Martin and Hartnady, 1986; Martin and Flemming, 1988; Marshall, 1994; Watkeys and Sokoutis, 1998 and many more). A detailed discussion of the breakup history of Gondwana falls outside the scope of this thesis and the reader is referred to above references and to Visser (1998); Watkeys (2002) and Watkeys (2006) for an updated summary. Of interest to this study is that pre-existing basement structures controlled the fragmentation of western Gondwana which ultimately not only resulted in the straight KwaZulu-Natal coastline and narrow continental margin, but also the development of the Mesozoic sedimentary basins.

The east coast, including KwaZulu-Natal, is a passive margin with a complex rifting and strike-slip history (Visser, 1998; Watkeys and Sokoutis, 1998). Figure 3.2 shows the palaeogeographical setting whilst Figure 3.3 illustrates the post-breakup crustal architecture of southeast Africa and environs. During the Jurassic (~180-155 Ma) extensional rifting (taphrogenesis) related to extensive Karoo volcanism (Watkeys, 2002) was an initial manifestation of an attempted Gondwana fragmentation. Fracturing took place along several pre-existing basement structures and eventually resulted in the formation of the Lebombo line (Figure 3.3) and coastal faults (Watkeys, 2002). At this stage only the northern or proximal Natal Valley existed and was bounded on four sides; Mozambique Ridge (east and south), Falkland Plateau (west) and continental Mozambique in the north (Dingle *et al*., 1983). Minor sedimentation (Upper Jurassic to Lower Cretaceous) occurred into the proximal Natal valley establishing the proto-Tugela cone (Dingle *et al*., 1983). Similarly, the continental part of the Agulhas Plateau were attached to and extended south of the Mozambique Ridge (Dingle *et al*., 1983). Both the Mozambique Ridge and Agulhas Plateau are considered microcontinental fragments, with at least the latter (if not both) having a composite origin (continental and oceanic crust) (Dingle *et al*., 1983; Visser, 1998).

Actual breakup (Figure 3.2) commenced with the southward separation of the Eastern Gondwana plate (Antarctica, Madagascar, Australia, and India) relative to the Western Gondwana plate (Africa and South America), along a major shear zone (Davies Fracture Zone), from ~155-133 Ma (Watkeys, 2002). At this stage the only basins that existed on the eastern margin were the intracratonic St Johns and Durban basins (Dingle *et al*., 1983; Visser, 1998). Separation of the two Gondwana plates resulted in further rifting and subsequent development of the Zululand Basin which stretched to the south of Durban and subsequently included the Durban Basin. Concurrently, a spreading ridge and oceanic crust in the Mozambique Basin was initiated (Dingle *et al*., 1983; Visser, 1998).

Opening of the Atlantic and initial dextral strike-slip movement along the Agulhas Falkland Fracture Zone (AFFZ) started during the Lower Cretaceous (~133.5 Ma) and signalled the breakup of Western Gondwana (Figure 3.2) (Hobday, 1982; Watkeys, 2002). The driving force behind the seafloor spreading in the Atlantic and hence, the onset of withdrawal of the Falkland Plateau, was the arrival of the Tristan da Cuñha plume beneath the proto-South Atlantic rift at ~137 Ma (Watkeys and Sokoutis, 1998). South-westwards extraction of the continental crust of the Falkland Plateau (containing the Falkland Islands) along the AFFZ resulted in the creation of oceanic crust progressively from north to south in the Natal Valley with synchronous ocean crust emplacement in the southeast Cape basin (Dingle *et al*., 1983; Watkeys 2002). This coincided with the formation of a seafloor spreading ridge between the southern margin of the Tugela Cone and the Falkland Plateau (Martin and Flemming, 1988; Watkeys, 2002) and the creation of new

oceanic basins immediately adjacent to the continental margin (Dingle *et al.*, 1983). This spreading ridge migrated south-westwards along the AFFZ and cleared southern KwaZulu-Natal by 127 Ma (Martin and Flemming, 1988).

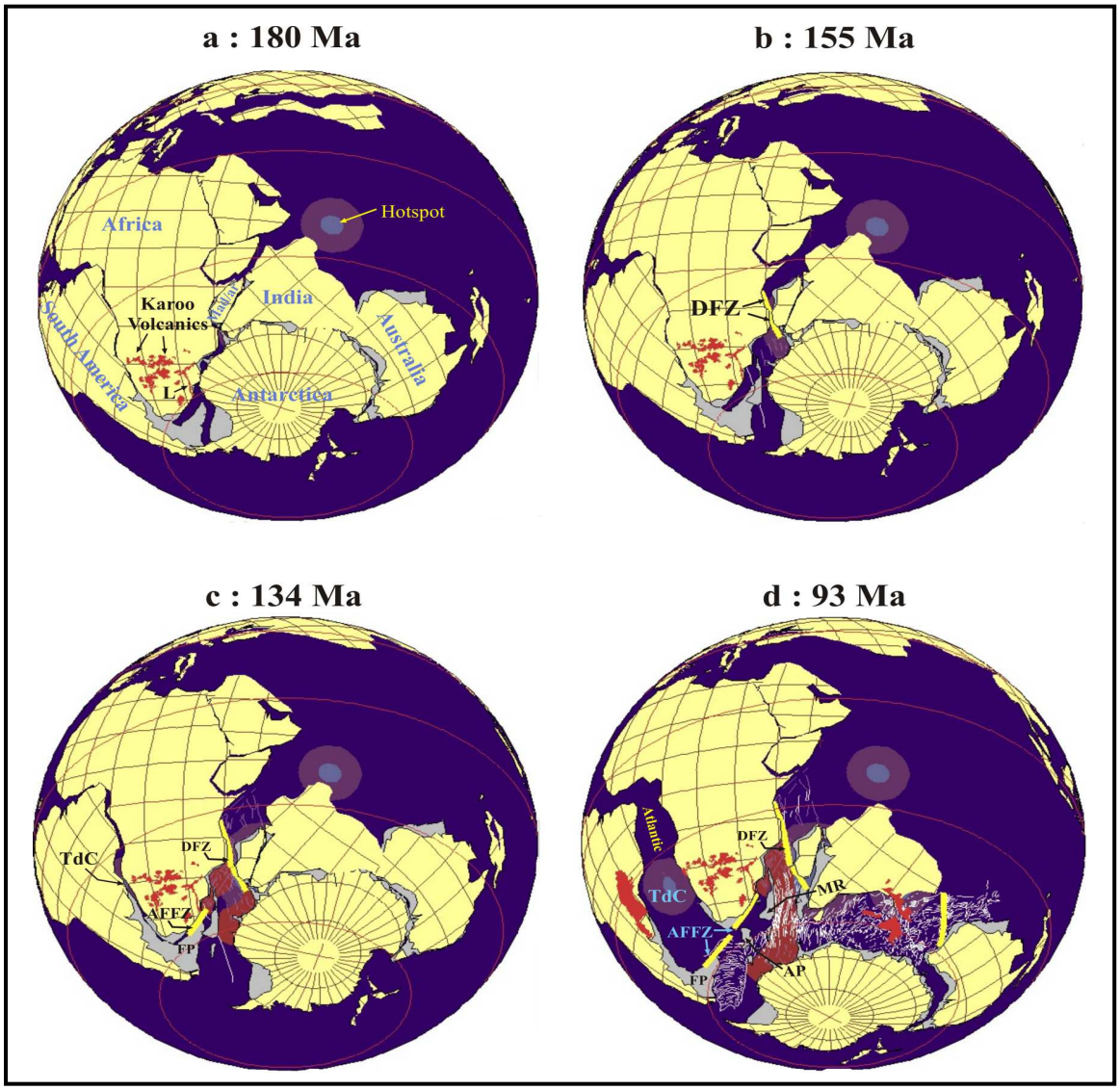

Figure 3.2 Successive maps of Gondwana fragmentation illustrating the palaeogeographic setting of southeast Africa (from http://kartoweb.itc.nl/gondwana/index.html). **a)** Eruption of the Karoo volcanics and early extension along the Lebombo line (L) was an initial manifestation of Gondwana fragementation. **b)** Separation of the Eastern and Western Gondwana plate along the Davies Fracture Zone (DFZ). **c)** Separation of Africa and South America signalled by the opening of the Atlantic and extraction of the Falkland Plateau (FP) along the Agulhas Falkland Fracture Zone (AFFZ), TdC = Tristan da Cuñha plume/hotspot. **d)** Complete continental separation between Africa and South America - also marking the cessation of the coastal faulting along the southeastern African margin, MR = Mozambique Ridge, AP = Agulhas Plateau.

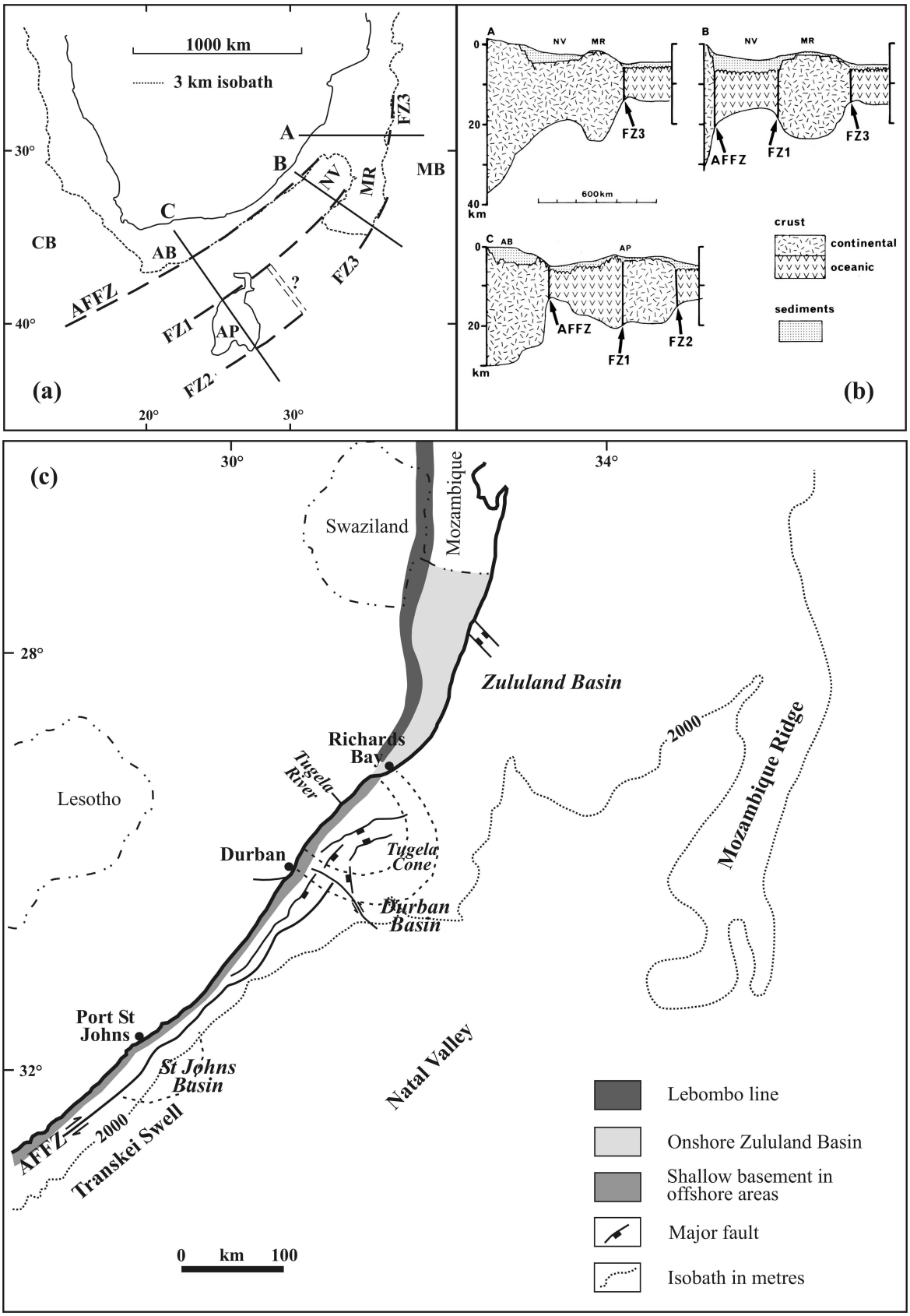

Figure 3.3 **(a)** Plate-tectonic setting of southern Africa. A, B and C indicate positions of cross-sectional lines in Figure 3.3(b), AFFZ = Agulhas Falkland Fracture Zone, AB = Agulhas Bank, AP = Agulhas Plateau, CB = Cape Basin, FZ = fracture zone, MB = Mozambique Basin,

Figure 3.3 (cont.) MR = Mozambique Ridge, NV = Natal Valley, ? = extinct spreading ridge (adapted from Dingle *et al*., 1983 and Visser, 1998). **(b)** Crustal structure off southern Africa (modified from Dingle *et al*., 1983). **(c)** Major structural elements of the East Coast (modified from Dingle *et al*., 1983, van Vuuren *et al*., 1998, and Visser, 1998).

South-westwards movement of the Falkland Plateau along the AFFZ also resulted in the Agulhas Plateau detaching from its position close to the Mozambique Ridge migrating south-westwards along two fracture zones (Figure 3.3). A sector of oceanic crust with an abandoned spreading ridge must therefore occupy the area between the Mozambique Ridge and Agulhas Plateau (Dingle *et al*., 1983).

The AFFZ developed into an intracontinental transform fault ~1200 km long linking the mid Atlantic ridge with the spreading ridge in the Natal Valley (Dingle *et al*., 1983; Watkeys, 2002). On the east coast the effect of this transform fault was to produce a margin characterised by a narrow shelf and continental slope with truncated remnants of the earlier formed Mesozoic Durban and St Johns basins (see Sections 3.3.2 and 3.3.4) remaining (Dingle and Scrutton, 1974). Drifting led to accelerated subsidence in the Natal Valley (Visser, 1998) while tilting and erosion on the adjoining northern continental margin formed the southern margin of the Cretaceous deposits of Maputaland. North of Durban the offshore submerged crust between Maputaland and the Mozambique Ridge (Figure 3.3b) is continental in origin (Dingle *et al*., 1983; Watkeys and Sokoutis, 1998 and Watkeys, 2002). This continental crust continues northwards into Mozambique (including sections of the Mozambique Ridge) where it is highly extended and forms the coastal plain (Watkeys, 2002). At this stage further coast-parallel faulting occurred in KwaZulu-Natal south of the Lebombo and involved reactivation of older structures (Watkeys and Sokoutis, 1998; Watkeys, 2002). According to Dingle *et al*. (1983) the main structural features that developed during the Middle Jurassic to Upper Cretaceous can be summarised as follows:

- N - S and NNW - SSE normal fractures bounding wide horsts and grabens on the continental crust north of Durban,
- NE - SW shear fractures (AFFZ etc.) bounding the Natal Valley south of Durban with similar features bounding the western edge of the Mozambique basin trending N - S,
- arcuate faults between 29° S and 32° S, extending from the coastal zone onto the margin offsetting basement rocks to the east, resulting in a NE deflection of the coastline. The eastward deflection distance of the coastline at these arcuate features increasing from south to north.

The N - S direction is an old Archaean basement structural trend and at the Lebombo line marks the junction between the Kaapvaal Craton and Mozambique Belt (Figure 3.1a) (Hobday, 1982;

Watkeys, 2002). The NE - SW direction is parallel to the major axis of a trough (Natal Embayment/Trough; Ryan, 1967; Hobday, 1982; Tankard *et al*., 1982) active since the early Palaeozoic through to the Permain, also paralleling the Mozambique Belt basement lineation (Figure 3.1a) and the present coastline (Hobday, 1982). The Natal Embayment and Lebombo line forming part of a 7000 km linear zone of incipient crustal fracture (Hobday, 1982; Dingle *et al*., 1983). Interestingly, the northern dislocation boundary of the Falkland Plateau occurred where one of these arcuate faults cut the coast at right angles.

Complete continental separation between the South American and African plates occurred at ~93 Ma (Figure 3.2) and was concurrent with the cessation of faulting along the eastern margin (Watkeys, 2002). During the Aptain/Albian (~121-98 Ma) crustal subsidence and basin development on the continental margins underwent a fundamental change in style (Dingle and Scrutton, 1974; Dingle *et al*., 1983). This was marked by a change from horst/graben basement displacement (taphrogenesis) characterised by narrow and deep sedimentary basins to regional downwarping characterised by bowl-shaped depocentres (epeirogenesis) that transgress the older boundary faults (Dingle *et al*., 1983). At this time the proto-Atlantic was ~1600 km wide with the Natal Valley, Agulhas Plateau, Mozambique Ridge and Basin (Figure 3.3a) as well established geomorphological features (Dingle *et al*., 1983). Due to uplift of the rift flanks which preceding continental separation the newly formed margin had an elevated rift shoulder forming a substantial marginal escarpment. The subsequent erosion of which, formed the offshore marine Cretaceous deposits, ultimately forming the Drakensberg escarpment (Partridge and Maud, 2000). Erosion was facilitated by the humid warm climates of the Cretaceous through the medium of a well developed drainage network (Partridge and Maud, 2000).

3.2.2 Coastal Faulting in KwaZulu-Natal

Structurally the coastal area and continental shelf of KwaZulu-Natal is characterised by numerous faults (Figure 3.4) reflecting the highly fractured nature of this margin. There is little doubt that the coastal faulting is related to the breakup of Gondwana but there is much speculation on the kinematics and evolution of these faults (Maud, 1961; De Swardt and Bennet, 1974; Martin, 1983; von Veh and Anderson, 1990; Watkeys and Sokoutis, 1998 and Watkeys, 2002).

The most significant characteristic of the faults in the coastal zone is their arcuate geometry (Figure 3.1; 3.7). Most of the faults close to the coast strike NE paralleling the coastline with some curving towards the coast along their northern extremities (Visser, 1998) with other minor trends striking N - S and NW - SE. These arcuate faults have downthrows on their convex side

with the strata inside the arcs tilted towards the coast (Maud, 1961; Dingle *et al.*, 1983). Superimposed on this pattern are later coast parallel normal faults (von Veh and Anderson, 1990). Watkeys and Sokoutis (1998) suggested that the overall pattern indicate discrete blocks pulling out towards the ENE, paralleling the trend of the supracrustal rocks in the basement utilising these as zones of weakness.

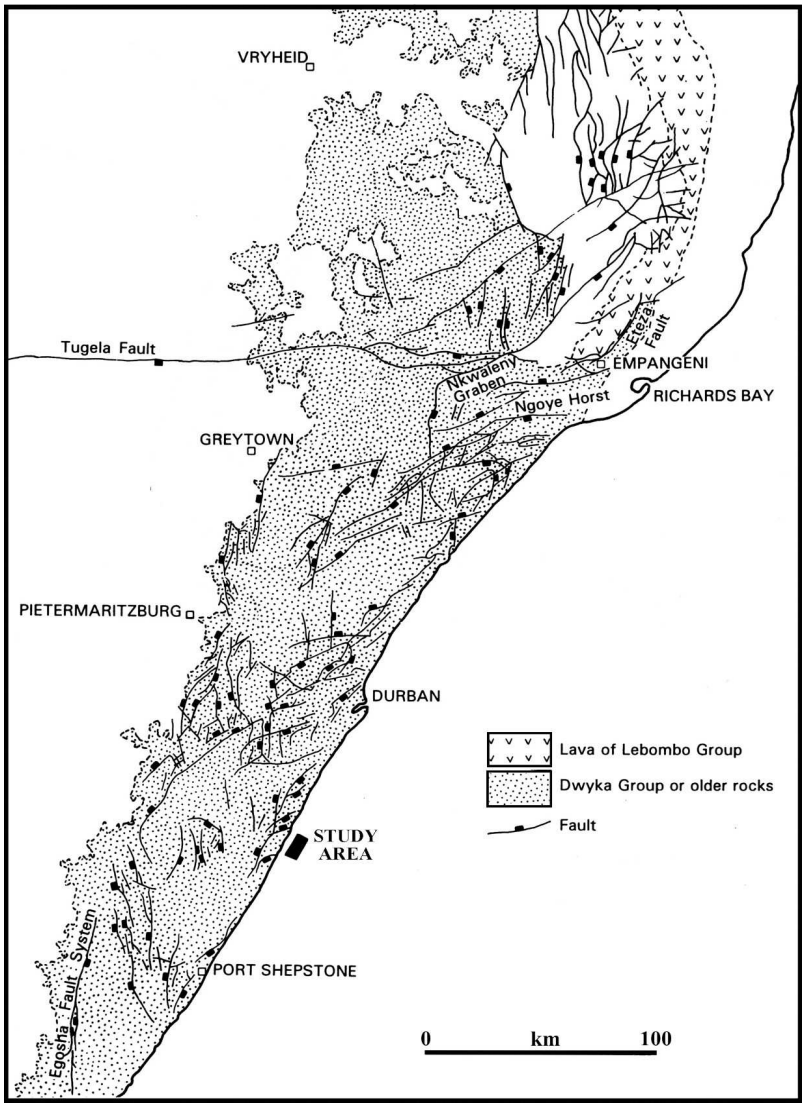

Figure 3.4 Pattern of coastal faulting in KwaZulu-Natal (Modified after De Swart and Bennet, 1974 in Visser, 1998). Note that the study area is located immediately offshore of and probably is situated on a horst structure (also see Figure 3.1b).

Maud (1961) recognised four arcuate fault systems (two of which are inland) where Dingle *et al.* (1983) only recognised two close to the coastline - the latter described here because of the implications for the margin. The northern arcuate (Figure 3.5) feature stretches from inland south of Durban cutting the southern end of the Lebombo line where it curves eastwards and intercepts

the coast (29° S) south of Richards Bay (Dingle *et al*., 1983). This corresponds with a change in continental shelf morphology (narrowing rapidly northwards) and a change in coastline trend from NNE to NE. Here Pre-Cambrian basement of the Natal Metamorphic Province is offset to the east and coincides with a ~55 km eastward deflection of the coastline. The southern arcuate feature lies adjacent to the basement high of the Port Shepstone Arch (Figure 3.5) and extends from ~31° S to the vicinity of Durban where it curves sharply eastwards intersecting the coast perpendicularly. This point coincides with a number of important features namely (Dingle *et al*., 1983);

- a sudden widening of the adjacent continental shelf, also coinciding with a slight easterly offset of the coastline,
- offshore continuation of the arcuate feature forms the Tugela Ridge, terminating structural trends underneath the Tugela Cone. This ridge corresponds to a fundamental change in the crustal structure marking the junction between oceanic crust to the south and thinned continental crust to the north,
- the gravity and bathymetric anomaly marking the AFFZ ceases here thereby marking the continent-ocean boundary relating to the palaeo-position of the Falkland Plateau (Figure 3.2).

It is interesting to note that the eastward deflection of the coastline trend coincides with the point where the northern extent of the arcuate faults cut the coastline (Figure 3.5), commonly corresponding with the eastward offsetting of basement and a subsequent change in continental shelf morphology.

The age of the coastal faulting in KwaZulu-Natal is a contentious issue but most workers agree that the faulting must have occurred between ~190 Ma and ~90 Ma (age of Lebombo lavas) based on the observation that undisturbed Upper Cretaceous sediments overlie these faults (Maud, 1961; Dingle *et al*., 1983; Watkeys and Sokoutis, 1998 and Visser, 1998). It is widely accepted that the faulting formed due to the major tectonic events related to Gondwana breakup, but whether it was due to extensive taphrogenic faulting, or the SW extraction of the Falkland Plateau, or a combination of both is uncertain (Dingle *et al*., 1983). The coastal fracturing was due to tensional stresses but the pattern was determined by pre-existing lines of weakness in the basement (Hobday, 1982).

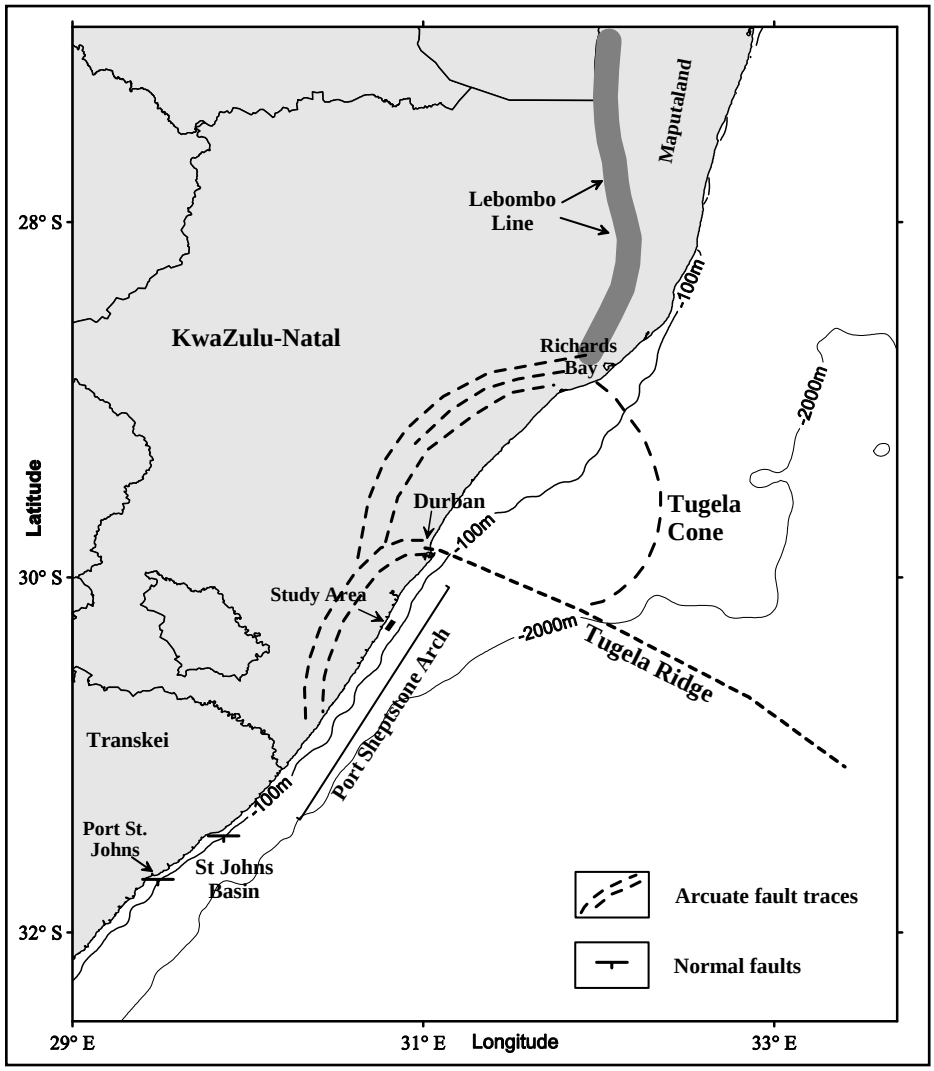

Figure 3.5 Regional tectonic setting showing the two large arcuate fault systems in KwaZulu-Natal (modified after Dingle *et al*., 1983) and their relationship to the Lebombo Line, the Tugela Ridge and Tugela Cone.

3.3 CRETACEOUS BASINS

The east coast (onshore) Cretaceous strata are represented by outcrops in Maputaland, sporadic coastal outcrops on the lower KwaZulu-Natal south coast and as tiny isolated outliers in the Eastern Cape with no exposures found onshore of the study area (Figure 3.6). The Upper Cretaceous transgression was markedly diachronous along the eastern margin and proceeded southwards from the Zululand Basin (St Lucia region; Coniacian in age), reaching the Durban-Mzamba latitudes during the Middle to Upper Santonian and the Needs Camp-Igoda region in late Campanian to early Maastrichtian times. (Dingle *et al*., 1983; Visser, 1998; Shone, 2006).

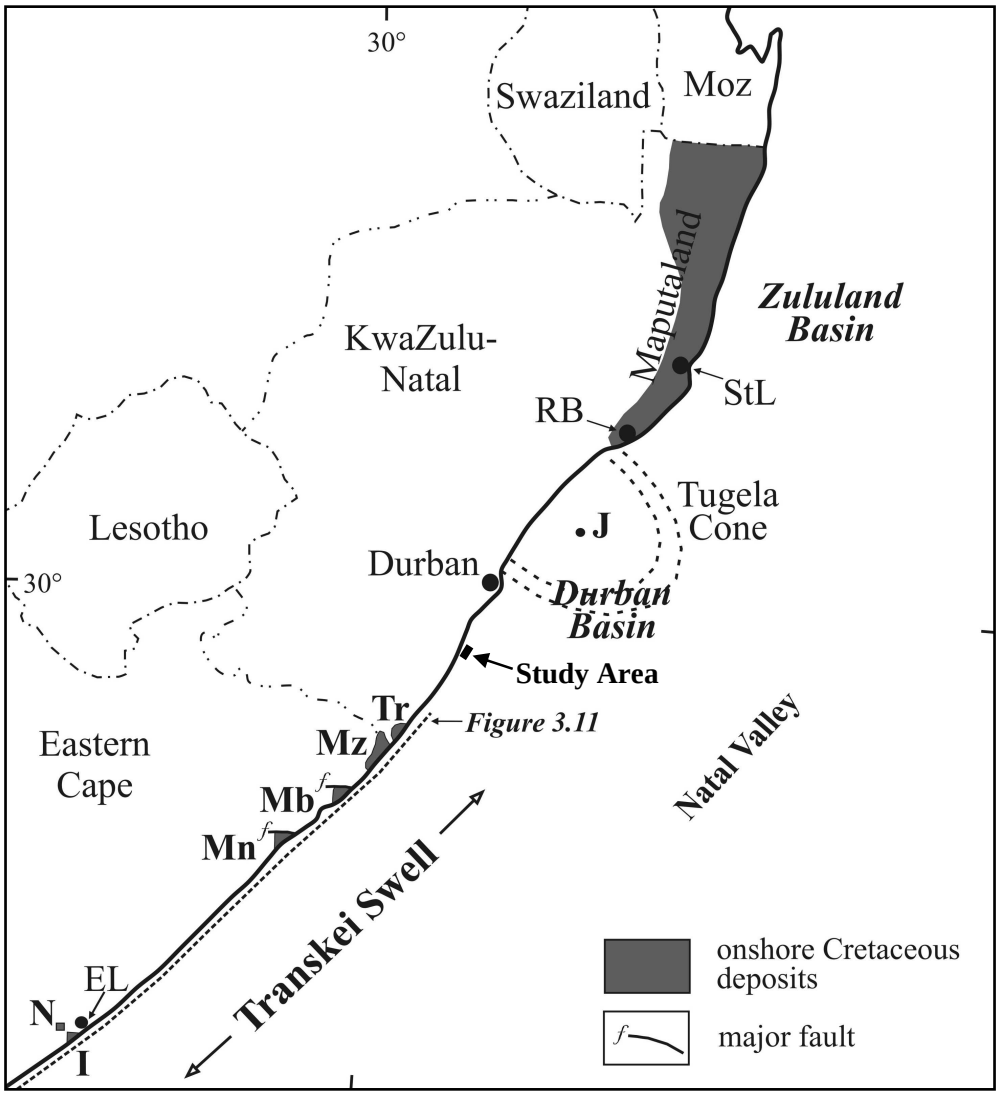

Figure 3.6 Regional distribution of Cretaceous deposits and basins, I = Igoda Estuary, N = Needs Camp, Mn = Mngazana, Mb = Mbotyi, Mz = Mzamba, Tr = Trafalgar, EL = East London, J = J(c)-1 borehole, RB = Richards Bay, StL = St Lucia, Moz = Mozambique (adapted from SACS, 1980 and Dingle *et al*., 1983).

Prior to Gondwana breakup the only known large sedimentary basins on the southeast African margin were the intracontinental St Johns and to a lesser extent the Durban basins (Figure 3.3) (Dingle and Scrutton, 1974). Following Gondwana breakup most sediment on the east coast margin was carried oceanward and deposited in the deep ocean basins because of the lack of suitable receptacles (Dingle and Scrutton, 1974). Sediment basin development during the Jurassic to Lower Cretaceous (taphrogenic) was controlled by major crustal lineaments with two strongly contrasting styles. North of 30° S sediment basins form a series of large graben structures with an approximate N - S trend, whilst south of 30° S depocentres are confined to areas immediately adjacent to and beyond the various continent-ocean boundaries that define the Natal Valley/Transkei Basin, bounded in the east by the Mozambique Ridge (Dingle *et al*., 1983).

During Mid Cretaceous times basin development on the continental margin underwent a fundamental change related to a change in crustal subsidence style from taphrogenesis to epeirogenesis, resulting in sediment deposits transgressing previous fault controlled basin margins (Dingle *et al*., 1983). These structural and depositional modifications in basin development are consequently the result of the two phases of Gondwana breakup.

Cretaceous climates were warm and humid which facilitated rapid erosion of the uplifted newly formed rift margins resulting in the thick marine Cretaceous sequences (Dingle *et al*., 1983; Partridge and Maud, 2000). Thermal modelling of fission track data indicate a minimum of 4.5 km of denudation in the coastal zone of KwaZulu-Natal since formation of the continental margin (~130 Ma), with a marked Early Cretaceous episode of accelerated denudation broadly coincident with Gondwana fragmentation (Brown *et al*., 2002).

3.3.1 Zululand Basin

The Maputaland exposures form part of the Zululand Group which was deposited in the large onshore/offshore Zululand Basin during a marine transgression from the north related to the opening of the Indian Ocean during Gondwana breakup (SACS, 1980; Visser, 1989) (Figures 3.6; 3.9). These Cretaceous sediments accumulated in the newly created basins and continental margin formed by the fragmentation of Gondwana (Section 3.2.1). The onshore Zululand Group succession dips eastwards at ~5° and unconformably overlies titled (20° eastward dip) volcanic rocks from the Lebombo Group (SACS, 1980; Visser, 1998). The Zululand and Durban basins are considered the southern continuation of the Mozambique Basin, which attains a maximum thickness of ~2.5 km thinning southwards to ~1 km in the St Lucia region (Visser, 1998; PASA, 2003a). The onshore Zululand Group is divided into three formations separated by unconformities (SACS, 1980; Wolmarans and Du Preez, 1986).

The basal Makatini Formation (Upper Barremian to the Upper Aptian) consists of non-marine conglomerate, grit and sandstone often interbedded with shallow-water marine siltstones which are finally overlain by fossiliferous marine sandstone (Wolmarans and Du Preez, 1986). The overlying Mzinene Formation consists of shallow marine glauconitic siltstone and fine grained sandstone and range in age from the Albian to the Cenomanian (Visser, 1989). The base of this formation designates the Albian/Aptian boundary and is represented by an erosion surface or a surface of no deposition (non-sequence), characterised by a layer of *Lithodomus* bored concretions (Wolmarans and Du Preez, 1986). The marine St Lucia Formation follows paraconformably on

the Mzinene Formation and comprise a basal conglomerate followed by glauconitic siltstone and interbedded sandstone with fossiliferous beds at various horizons (Visser, 1989). It ranges in age from the Lower Coniacian to the Palaeocene (Danian; ~60 Ma) - which is only present in boreholes in Richards Bay (Visser, 1989). The base of the St Lucia Formation represent a hiatus ranging from the Upper Cenomanian, all of the Turonian and part of the Lower Coniacian (Wolmarans and Du Preez, 1986) and has been linked to a Late Cenomanian regression (Tankard *et al*., 1982). The onshore Zululand Basin contains a maximum of 2200m of Barremian to Maastrichtian age sediments (PASA, 2003b).

Offshore the Zululand Group is virtually unbroken with thick sedimentary sequences preserved but interrupted by local basement highs (SACS, 1980; Dingle *et al*., 1983). Data on the sedimentary sequences in the basin are based on the seismic stratigraphy (Figure 3.7) and limited borehole cores, the most cited being the J(c)-1 core (du Toit and Leith, 1974). The hiatus developed onshore between the Mzinene and St Lucia formations is not present offshore in the J(c)-1 borehole (Figure 3.6) with sedimentation continuing unabated on the continental shelf through the entire Cretaceous and into the Danian (Tankard *et al*., 1982).

3.3.2 Durban Basin

Sedimentation in the Durban Basin (Figures 3.6; 3.9) was initiated prior to Gondwana fragmentation and originally formed an intracratonic basin (Chapter 3.3.1; Dingle *et al*., 1983). Relatively little is known about the basin with most information derived from seismic stratigraphy (Figure 3.7). According to Dingle *et al*. (1983) and PASA (2003a), the lower part of the sequence the sequence is Late Jurassic - Early Cretaceous and forms part of the Tugela Cone, a large submarine fan extending across the shelf to water depths of 3000 m (PASA, 2003a) with distal turbidite deposits in the Natal Vallley (Tankard *et al*., 1982). Sediment comprises a lower sequence of 3.5 km in thickness of Jurrassic to Lower Cretaceous, followed by 1.6 km thick sequence of Upper Cretaceous. Three sediment growth phases are recognised (Figures 3.10); the first two related to syn-rift and early drift sedimentation with a final phase related to renewed progradation in the Tertiary (PASA, 2003a).

At Durban, Cretaceous strata are buried under Cenozoic cover and are described from boreholes (Anderson, 1906; Krige, 1932 and King, 1962a,b) and seismic investigations in the Durban Harbour (Leuci *et al*., 2002; Perritt *et al*., 2003). Here the top of the Cretaceous surface is encountered between the depths of 21 m and 37 m beneath the harbour floor. Strata dips east at ~1° - 2° (Leuci *et al*., 2002; Perritt at al., 2003) indicating a sequence that forms part of a seaward

thickening wedge. Cretaceous strata in Durban are at least a 100 m thick and ascribed a Santonian to Campanian age based on faunal assemblages (Kennedy *et al*., 1973; SACS, 1980; Tankard *et al*., 1982 and Dingle *et al*., 1983; McMillan, 2003). Cawthra (2010) suggested the occurrence of Maastrichtian strata underlying the outer Durban shelf (see Section 6.2.3).

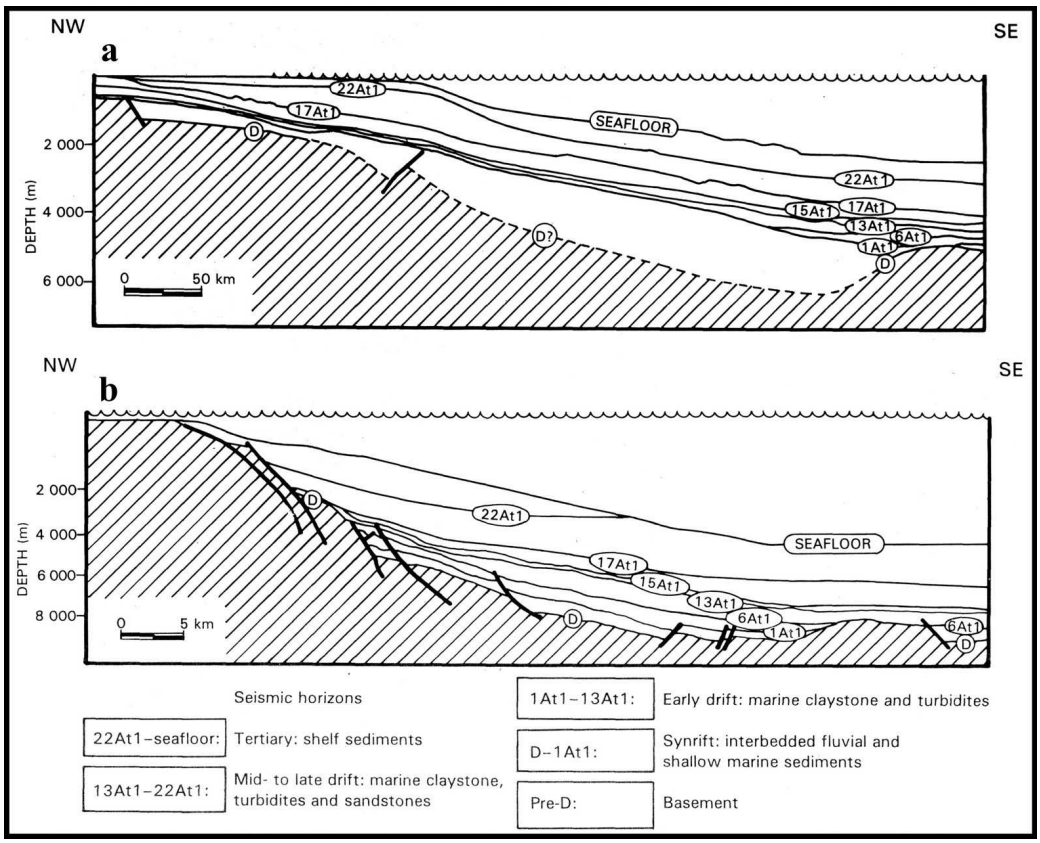

Figure 3.7 Interpreted NW - SE seismic section across the Zululand **(a)** and Durban **(b)** Basins (from Soekor, 1994 in Visser, 1998).

3.3.3 Mzamba Deposits

South of Durban, Upper Cretaceous rocks crop out in two areas (Figure 3.6): sporadically along a 40 km strip of the foreshore from near Trafalgar Beach (KwaZulu-Natal) in the north to 15 km south of Mzamba in the Eastern Cape (Transkei) and near East London (Dingle *et al*., 1983; Thomas, 1989). The former is best exposed in low seacliffs at Mzamba Beach and consists of a ~2 m basal conglomerate with bored silicified logs, ammonites and sharks teeth, followed by ~21 m of fossiliferous (Echinodermata, Foraminifera, Ostracoda, Gastropoda and vertebrate remains) glauconitic fine sand and silts interbedded with discontinuous cross-bedded shelly glauconitic sandy limestone, constituting the Mzamba Formation (SACS, 1980; Dingle *et al*., 1983).

Lithologically and palaeontologically these sediments suggest a transgressive beach and shoreface depositional environment (Tankard *et al*., 1982). The Mzamba Formation rests on basement rocks of either the Natal Metamorphic Province (Trafalgar) or the Natal Group (Mzamba) and has been assigned a Middle Santonian to Early Campanian age based on faunal assemblages (Klinger and Kennedy, 1979).

3.3.4 St Johns Basin

The St Johns Basin (Figures 3.6; 3.9) formed on the Palaeozoic basement high of the Transkei Swell by half graben development (Figure 3.8) along two major E - W trending fault lines (Mngazana and Egosa). The present expression of the basin is limit to two tiny coastal outliers, the Mngazana and Mbotyi outliers (Figure 3.6), situated on the southern side of the large boundary faults (Dingle *et al*., 1983). At Mngazana the Cretaceous strata unconformably overlies Karoo Supergroup rocks (Dingle *et al*., 1983).

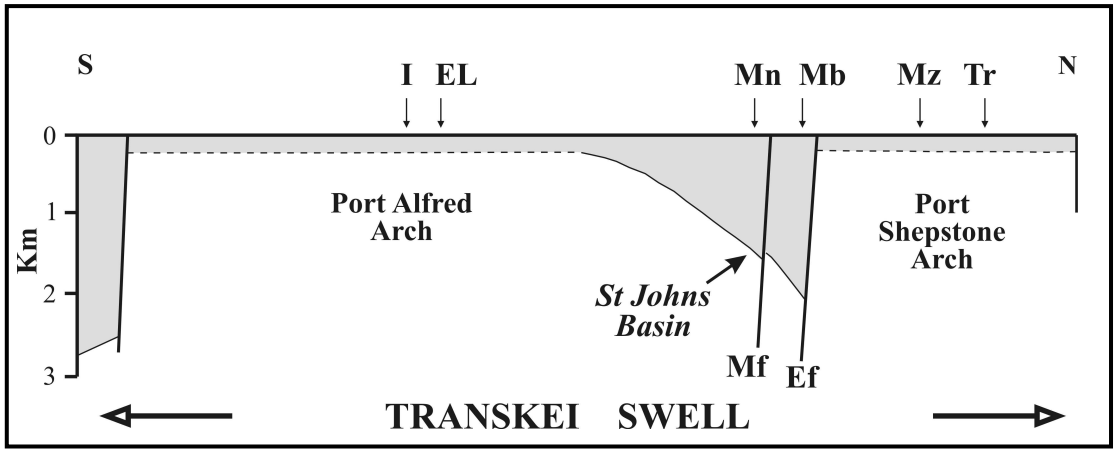

Figure 3.8 N - S continental shelf section (refer to Figure 3.6 for locality) across the Transkei Swell showing the half graben development of the Port St Johns Basin on the collapsed crest of the Transkei Swell (from Dingle *et al*., 1983). Mf = Mngazana fault and Ef = Egosa fault, all other abbreviations as per Figure 3.6. Shaded areas represent Mesozoic basin deposits overlying basement (white) comprising mainly Natal Group and Karoo Supergroup.

These deposits comprise conglomerate alternating grit and fossiliferous limestone (Visser, 1989) and form the Mngazana Conglomerate Formation (SACS, 1980). The succession, dips ENE at 20° and attains a thickness of approximately 100 m and is ascribed a Valanginian age based on the marine fossils (Dingle *et al*., 1983). The Mbotyi outlier is situated north of the Mngazana outcrop

to the south of the Egosa Fault (Visser, 1989), which offsets the coastline and the continental shelf ~3 km to the NE (Dingle *et al*., 1983; Flemming, 1981). Cretaceous rocks unconformably overlie Karoo Supergroup rocks and comprise conglomerates interbedded with sandstone containing sparse wood fragments (Visser, 1989). The strata have been assigned to the Mbotyi Conglomerate Formation and are correlated with the Mngazana Conglomerate Formation based purely on lithological similarity (Dingle *et al*., 1983). The St Johns Basin is separated from the Durban Basin (and subsequent Zululand basin) by the Port Shepstone Arch (Figure 3.8), (Dingle *et al*., 1983).

3.3.5 Igoda Estuary/Needs Camp Deposits

The Cretaceous sediments near East London occur at Needs Camp and in the vicinity of the Igoda River estuary (Figures 3.9; 3.12). The Needs Camp locality is situated 15 km inland from the present coastline with the sediments exposed in two quarries (Figure 3.9) (Dingle *et al*., 1983). These rocks consist of a few metres of polyzoan limestone containing ostracods, benthic and planktonic (rare) foraminifera, Bryozoa and abundant small shells with rare quartz and glauconite grains resting on an erosive surface cut into a Karoo dolerite sill at 367 m above sea level (Dingle *et al*., 1983). The Needs Camp succession is considered to be part of the Mzamba Formation and dated as late Campanian to early Maastrichtian based on planktonic foraminifera (SACS, 1980). The dominance of benthic foraminifera suggests that this locality was not connected to the open ocean when the Upper Cretaceous transgression reached this area - the farthest transgression into the Transkei Swell (Dingle *et al*., 1983).

Cretaceous sediments at the Igoda locality are exposed in cliffs on the SW side of the Igoda River estuary and consist of a ~3 m basal sequence of pebbly sandstone passing into a small-pebble conglomerate which is overlain by ~20 m of arenaceous limestone and calcareous sandstone which are both glauconite rich (Dingle at al., 1983; Visser, 1989). These rocks rest unconformably on rocks of the Karoo Supergroup and are covered unconformably by Tertiary strata (Visser, 1989). Fossils of corals, Bryozoa, Echinodermata, Brachiopoda, Lamellibranchia, ammonites, ostracods, Foraminifera, sharks teeth and remains of Plesiosauria are present in these beds (Visser, 1989). The sediments of the Igoda succession constitute the Igoda Formation and are considered contemporaneous with the Needs Camp beds (based on faunal assemblages) and thus ascribed a late Campanian to early Maastrichtian age (SACS, 1980; Dingle at al., 1983). The erosion surface on which the Igoda Formation rests dips seawards at ~2°, if this surface is projected inland to the vicinity of Needs Camp it gives a height well in excess (600 m) and well above the height at which

the Needs Camp exposure (367 m) occurs, suggesting coastal flexure since the Upper Cretaceous times (Dingle *et al*., 1983).

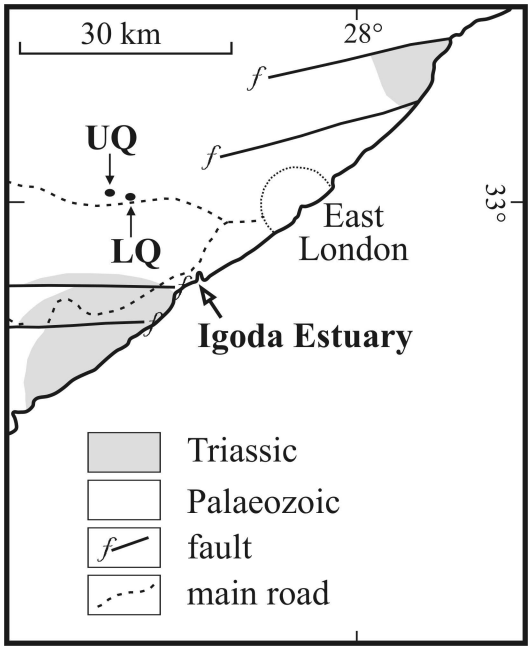

Figure 3.9 The localities of the Cretaceous Needs Camp (UQ = Upper Quarry, LQ = Lower Quarry) and Igoda Estuary deposits (modified from Dingle *et al*., 1983). Also see Figure 3.6.

3.4 POST CRETACEOUS/CENOZOIC SEQUENCES

Cenozoic rocks in KwaZulu-Natal comprise a thin superficial cover of sand, gravel, soft sandstone and limestone (SACS, 1980). Only Quaternary units are present onshore from and in the study area (Figure 3.1), although some controversy exists over the age of the Berea Formation (see below).

3.4.1 Tertiary

Worldwide, the end of the Cretaceous signified a major change in global climates with Tertiary climates representing a progressive sometimes erratic decline in temperatures (Dingle *et al*., 1983; Partridge and Maud, 1987; 2000). Climatic change and aridification during the Tertiary was strongly linked to fundamental changes in global climate and circulation with associated polar glaciations. During the Eocene final separation of Antarctica and Australia (~40 Ma) established the circum-south polar circulation resulting in a gradual decrease in sea water temperature so that Neogene times saw the onset of extensive ice cover in Antarctica and the commencement of the

Arctic glaciation (Dingle *et al*., 1983). The present coastal configuration of southern Africa was established by the end of the Cretaceous and the change from taphrogenic to epeirogenic crustal movements (initiated during the Late Cretaceous) continued into the Cenozoic Era (Tankard *et al*., 1982; Visser, 1998). With the exception of the Maputaland coastal plain the only significant deposits of Tertiary strata in KwaZulu-Natal occur on the continental shelf and slope as a seaward-thickening sedimentary prism with the distribution of the deposits dominated by the major terrigenous input from the Tugela River (Dingle *et al*., 1983). Therefore, as was the case for the Mesozoic (Chapter 3.4.2) maximum Tertiary sediment accumulation on the east coast occurred in the Tugela Cone, with the bulk of the total Tertiary sediments being Palaeogene in age (Dingle *et al*., 1983).

The Tertiary Period is characterised by major eustatic sea-level movements (Figure 3.10, transgression and regressions) with the major regressions accompanied by hiatuses in the sedimentary record (Dingle *et al*., 1983). These sea-level changes resulted from volumetric changes in the ocean basins (related to seafloor spreading rates) and associated changes in climate (Tankard *et al*., 1982, Visser, 1989). Changes in sea-level due to glacio-eustatic effects were only pronounced in the Late Cenozoic when the polar ice sheets were established (Tankard *et al*., 1982).

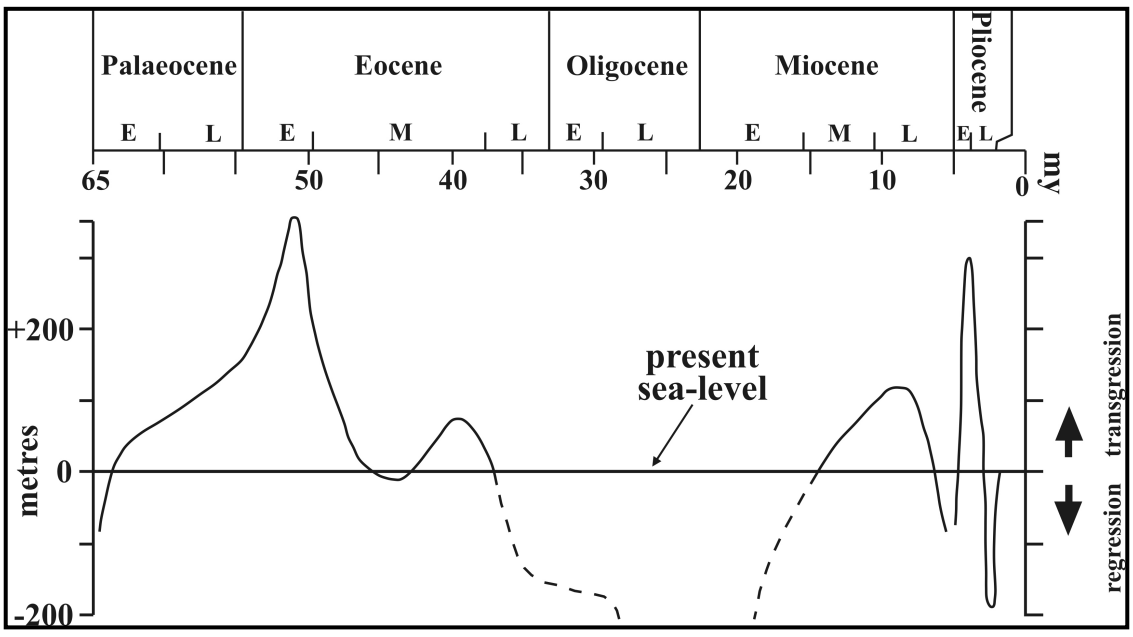

Figure 3.10 Tertiary sea-level movements plotted in relation to present sea-level for South Africa (modified after Dingle *et al*., 1983). E = Early, M = Middle and L = Late.

The Late Cretaceous transgression (peaking in the Maastrichtian; Section 3.3) was followed by a major late Maastrichtian - Early Palaeocene regression (Dingle *et al*., 1983). The only known

Palaeocene rocks onshore in South Africa form part of the Late Cretaceous to Danian St Lucia Formation with the Cretaceous/Palaeocene boundary marked by a non-sequence (Dingle *et al*., 1983; Visser, 1989). This regression was followed by a regional Late Palaeocene - Early Eocene transgression with the only Mid Palaeocene marine sediments on the east coast found on the continental shelf off St Lucia, and at -28 m in a borehole in Richards Bay (Visser, 1998). A major mid Tertiary regression spans most of the Oligocene with sea-levels reaching a maximum of ~530 m below present levels (Dingle *et al*., 1983). The Oligocene regression and associated hiatus was followed by a Middle to Late Miocene transgression (+100 m above present levels) which was interrupted by a brief latest Miocene regressive pulse (~100 m below present levels) before reaching its peak in the Early Pliocene (Dingle *et al*., 1983; Visser, 1998).

The Pliocene sea-level high stand reached either ~90 m (Visser, 1998) or 45-50 m (Maud and Botha, 2000) above present levels on the Maputaland coastal plain as indicated by the sequence of marine limestones of the Uloa Formation. The aforementioned Tertiary sea-level movements are considered gross movements of sea-level around southern Africa with regional uplift or subsidence resulting in relative sea-level changes affecting local areas differently (Dingle *et al*., 1983).

In addition to the sea-level movements, the eastern hinterland was uplifted by more than a kilometre in a series of tectonic pulses (Miocene ~250 m; Pliocene ~850 m) while the establishment of the East Antarctic ice sheet (14 Ma) caused changes in the circulation patterns of the southern oceans which initiated the cold Benguela upwelling system along the Atlantic coast and onshore desertification (Partridge and Maud, 2000). Uplift of the east coast and cooling of the western coast (though not strictly concurrent) resulted in the east - west climatic gradient still present today (Partridge and Maud, 2000). Uplift prevented sediment deposition on the continental shelf, with deposition occurring on the continental slope and basins instead (Dingle *et al*., 1983; Partridge and Maud, 2000).

It is also during the Tertiary that the modern drainage net evolved with major regressions and especially the uplift in the Pliocene producing major incision along the valleys of rivers entering the Indian Ocean (Dingle *et al*., 1983; Partridge and Maud, 2000). Consequently, thick offshore sedimentary sequences correspond to the crustal uplift episodes whereas onshore conditions did not allow for the preservation of strata, except for the limited exposures found on the Maputaland coastal plain (Dingle *et al*., 1983). Clear evidence indicates that the Agulhas Current was a well established oceanographic feature during the Late Miocene - Early Pliocene with flow paths broadly similar to those of today (Martin, 1981a,b; Dingle *et al*., 1983).

Maputaland Group

Lithostratigraphic correlation of onshore Cenozoic strata in KwaZulu-Natal is made extremely difficult by the lack and localised nature of surface outcrops. Establishing a chronostratigraphic framework is also complicated by several phases of uplift and numerous sea-level changes that have affected the region (Botha, 1997). This is further complicated by inconsistent use by numerous workers of the poorly defined stratigraphic units accepted by SACS (1980) and the proliferation of named units, some re-naming existing units which have not been formally proposed nor accepted by SACS (Botha, 1997).

Recent advances in understanding sea-level changes and new radiometric dating techniques resulted in the SACS Cenozoic Task Group to review Botha's (1997) proposed framework for the KwaZulu-Natal coastal region (Maud and Botha, 2000). Botha's (1997) proposed framework comprises the Maputaland Group and includes strata which accumulated in response to eustatic sea-level change and epeirogenic/isostatic uplift of marine planed surfaces during the Neogene and Quaternary (Maud and Botha, 2000). The Maputaland Group (Table 3.1) consists of two Tertiary and five Quaternary formations (Maud and Botha, 2000). However, with the exception of the Pleistocene Isipingo Formation none of the other Maputaland Group formations occur outside of Maputaland and hence will not be further discussed. The relationship between the proposed Maputaland Group and the accepted SACS lithostratigraphic units for the Cenozoic is illustrated in Table 3.1.

3.4.2 Quaternary

The Quaternary Period was characterised by rapid and extensive changes of global climates caused predominantly by fluctuations in the Northern Hemisphere polar ice volume (Bradley, 1999; Pillans and Naish, 2004). As opposed to Cretaceous and Tertiary sea-level change, Quaternary sea-level changes were climatically controlled.

Quaternary deposits of the KwaZulu-Natal coast comprise a veneer of Recent sand, Pleistocene calcified dune (aeolianite) cordons of the Bluff Formation (Table 3.1) and deeply weathered decalcified 'Berea'-type sand forming the Berea Formation (SACS, 1980; Visser, 1989). Together the Berea and Bluff Formations form prominent ridges of predominantly aeolian origin parallel or slightly oblique to the present coastline (Tankard *et al*., 1982). In Maputaland it up to six parallel dune cordons are developed on the wide coastal plain whilst south of Richards Bay (where the

coastline deflects towards the SW) and especially onshore of the study area, these deposits are compressed into a narrow coastal belt (SACS, 1980; Maud and Botha, 2000).

Table 3.1 Lithostratigraphy of the Cenozoic deposits of KwaZulu-Natal. Thick dashed line indicates the Tertiary/Quaternary boundary. Maputaland Group from Maud and Botha (2000) and Porat and Botha (2008). LIG = Last Interglacial.

SACS (1980)		**Age and Lithologies**	**Not necessarily directly correlated**	**Maputaland Group (Botha, 1997, Maud and Botha, 2000)**	**Age and Lithologies**
Berea Formation		Quaternary, inland dune cordons composed of red decalcified sand.		'Berea'-type red sand (informal unit)	Weathering product of Mio-Pliocene and Pleistocene calcareous deposits.
				Sibayi Formation	Post Mid-Holocene composite accretionary coastal dune cordon.
				Kwambonambi Formation	Late Pleistocene and Holocene inland dunes and interdune diatomite and peat.
Bluff Formation	Cave Rock Calcarenite Member	Quaternary, locally Eemian, coastal and offshore dune cordons of calcarenite.		Kosi Bay Formation	Late Pleistocene lignite and dune sand, surficially weathered reddish brown.
	False Bay Coral Limestone Memeber	Eemian fossiliferous limestone containing corals.		Isipingo Formation	Pre- & post-LIG aeolianite and beach deposits.
Port Durnford Formation		Late Middle Pleistocene poorly consolidated sand, silt, clay and lignite containing marine fossils and mammalian bones.		Port Durnford Formation	Middle-to-Late Pleistocene marine or estuarine mudstone and clayey sand deposited on coastal dunes and in lakes.
				Umkwelane Formation	Pliocene aeolianite and calcarenite.
Uloa Formation		Mio-Pliocene coquina and aeolianites - excluding Pleistocene deposits		Uloa Formation	Mio-Pliocene littoral and shallow marine coquina.

Beneath the Recent sand in estuaries and lagoons, muds and clays formed due to higher than present sea-levels during the Late Pleistocene and Holocene (SACS, 1980). Onshore from the study area exposures of the Berea Formation (Figure 3.1) unconformably overlie rocks belonging the Natal Metamorphic Province, Natal Group and Karoo Supergroup (Thomas, 1989).

Pleistocene

Notwithstanding the many inadequacies to the lithostratigraphic subdivision (Table 3.1) of SACS (1980), it will be retained in this section as Botha's (1997) Maputaland Group is not yet recognised by SACS and with the exception of the Isipingo Formation (Table 3.1) most of its formations only occur in Maputaland. By retaining the SACS (1980) subdivisions it will also serve to highlight its insufficiencies and subsequently lend support to a review of the Cenozoic stratigraphy - such as is suggested by Botha (1997).

Bluff Formation

The Bluff Formation is defined as the deposits consisting of coastal and offshore dune cordons of calcarenite or aeolianite (Figures 3.12 and 7.5a) (SACS, 1980). The formation is found along the coastal belt of KwaZulu-Natal and the onshore type locality are the exposures found on the prominent Bluff Peninsula in Durban (Figure 3.11) rising some 120 m above sea-level (SACS,1980). Offshore it forms intertidal platforms whereas on the continental shelf the formation forms a series of reefs such as the Aliwal Shoal (Wolmarans and Du Preez, 1986; SACS, 1980). The formation originated as a series of calcified dunes (aeolianite) formed in part during a marine regression (SACS, 1980; Visser, 1989). Krige (1932) named the calcareous sandstones that form the Bluff and associated outcrops further south and inland the Bluff Beds.

At Durban the Bluff Formation unconformably overlies Cretaceous strata and consists of a lower hard calcarenite composed of predominantly quartz with minor feldspar, pyroxene, amphibole, iron-titanium oxides (heavy minerals) and bioclastics (microfossils, foraminifera, molluscs and bryozoan fragments) cemented with calcium carbonate (Anderson, 1906; McCarthy, 1967). It extends 90 - 100 m below sea-level and is considered the core of the Bluff, characteristically showing large scale planar cross-bedding (Anderson, 1906; McCarthy, 1967; Maud, 1968; SACS, 1980). Eemian and later beach, nearshore and dune facies were welded onto this aeolianite core disconformably forming stranded beach deposits at various levels above and below present sea-level (McCarthy, 1967; Cooper and Flores, 1991, Cawthra, 2010).

These are followed by a poorly consolidated aeolian calcarenite which weathers to a yellow - brown sand which in turn is capped by red sands rich in clay minerals such as kaolin and goethite. Tropical weathering of the iron-bearing minerals imparted the deep red colour to the sand (McCarthy, 1967; Maud, 1968).

The Bluff ridge (Figure 3.12) is a compound dune composed of lithified aeolian sands of various ages with younger dune sands banked against the coastal dune complex during the Late

Pleistocene, with sand accumulation continuing into the Holocene (Cooper and Flores, 1991; Cawthra, 2010). The thickness of the formation is estimated at more than 180 m (SACS, 1980).

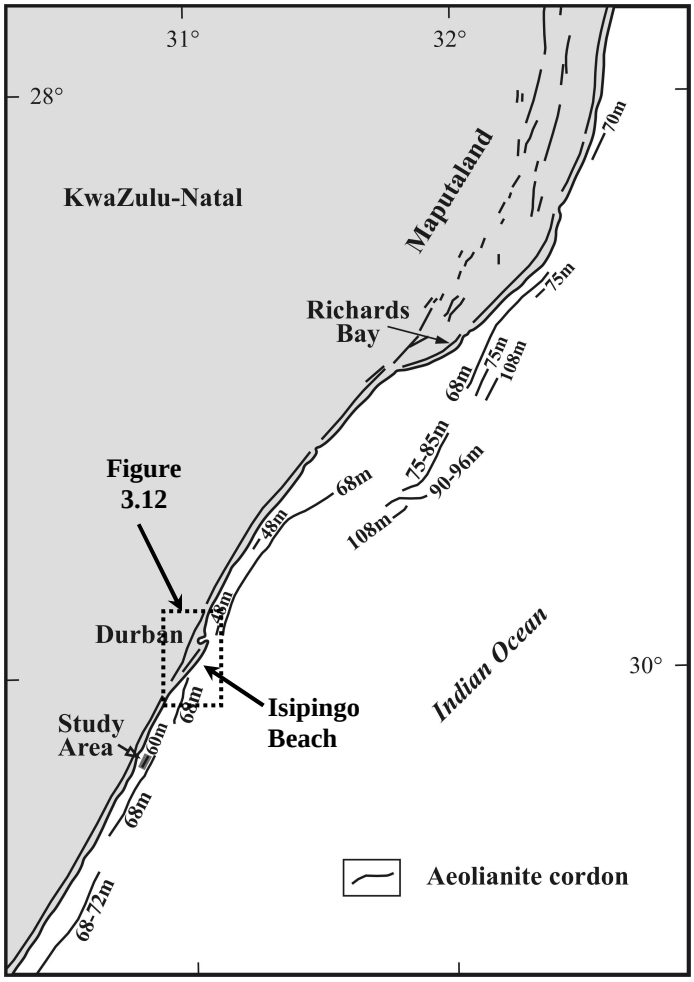

Figure 3.11 Pleistocene aeolianite cordons present onshore and on the continental shelf of KwaZulu-Natal. The numbers refer to the depth of the base of the cordon as established from seismic sections (modified after Martin and Flemming, 1988). Note that the onshore cordons represent both the Bluff and Berea Formations (refer to the section discussing the Berea Formation for explanation) whereas the offshore cordons belongs, *senso stricto*, according to SACS (1980), to the Bluff Formation.

The rocky shoreline of the Bluff is also the type locality for Botha's (1997) Isipingo Formation (Figure 3.12) which conceptually consists of basal aeolianites relating to the transgression from the Penultimate Glacial during the time span ~180 to 135 ka and disconformably overlying nearshore and beach deposits of the Eemian (~125 ka) high sea-level of 4.5 - 5 m amsl (Cooper and Flores, 1991; Maud and Botha, 2000). The Isipingo Formation is thus equivalent to the shoreline exposure of the Bluff Formation at the Bluff (Figure 3.12).

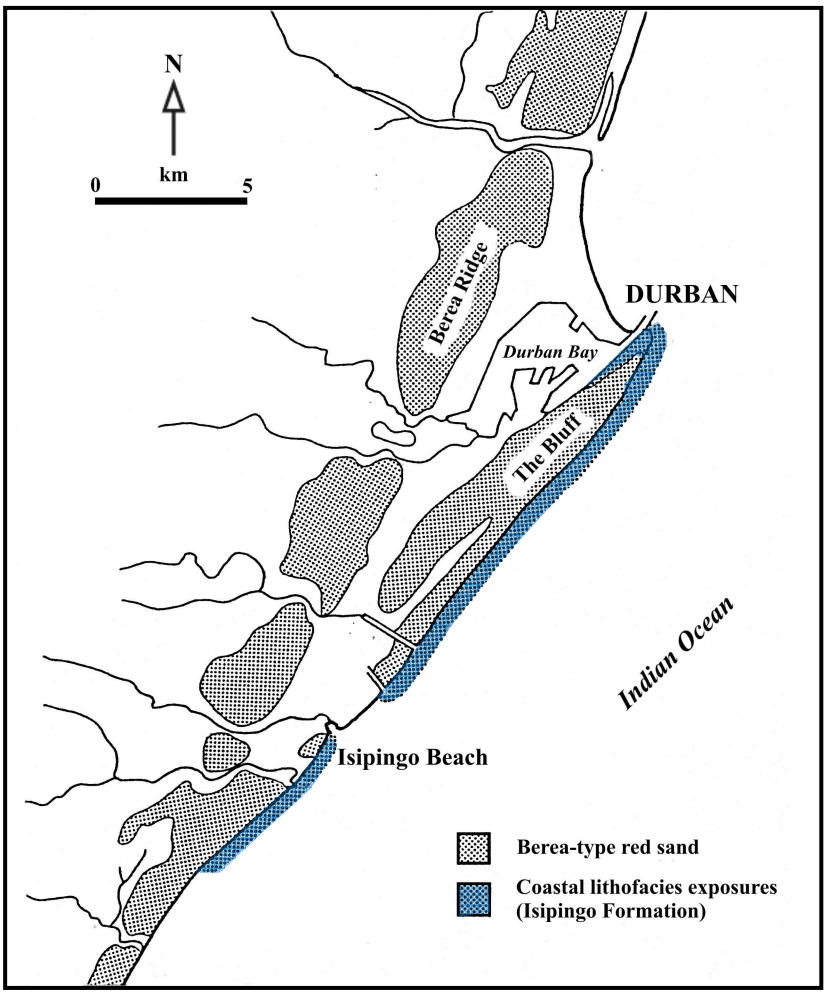

Figure 3.12 Locality map showing the extent of the Berea-type red sand and the coastal lithofacies in the Durban area (modified from Cooper and Flores, 1991). The Isipingo Beach exposures are the type locality for the Isipingo Formation situated on the shoreline of the Durban Bluff (Botha, 1997).

The age of the Bluff Formation is highly controversial. McCarthy (1967) favoured a Pliocene age for the Bluff (and Berea Formation) on the basis of foraminiferal studies by Carter (1966). Other authors preferred a Pleistocene age for the dune (Krige, 1932; Parr, 1958; King and Maud, 1964; Maud, 1968 and McMillian (1987). Ramsay *et al.* (1993) found an elephant tusk embedded at the base of an intertidal rock pool cut into Bluff aeolianite which yielded an average age of 112 ± 23 ka cal. B.P. Subsequent dating of the aeolianite wherein the tusk was found yielded a minimum age of 182 ± 18 ka cal. B.P. for the Bluff aeolianite by dating the aeolianite cement (Ramsay and Cooper, 2002).

Berea Formation

The Berea Formation comprises the inland dune cordons which are usually composed of decalcified sand with a characteristic red colouration (SACS, 1980). In Maputaland several

distinct 'Berea'-type ridges are present on the wide coastal plain whereas further south these ridges are limited to a narrow coastal belt so that a single ridge up to a kilometre wide occurs adjacent to the shoreline (Figure 3.11). The formation is named after the NE - SW trending Berea Ridge (Figure 3.12) which not only forms a prominent Durban landmark but also characterises the coastal zone of KwaZulu-Natal (Jermy and Mason, 1983; McCarthy, 1992). Onshore from the study area the Berea Formation represents a high (>100 m) coastal barrier (Figure 3.1) with Holocene dunes banked against its seaward flank.

The Berea Formation has resulted from the intense weathering of coastal dune sand, with the complete removal of shell fragments by leaching and the alteration of the feldspar grains to kaolin and goethite rich clays (McCarthy, 1988). The distinctive red colouration is derived from oxidation of mafic silicate and other Fe-rich minerals (McCarthy, 1988). At the base of the formation a laterally extensive, thin matrix supported polymictic conglomerate, the 'boulder bed' lies unconformably on eroded pre-Pleistocene seaward-dipping topography (Krige, 1932; King, 1962b; King and Maud, 1964; McCarthy, 1967; McCarthy, 1988; Maud, 1968 and Jermy and Mason, 1983). This boulder bed is interpreted as a basal beach conglomerate deposited during a marine transgression upon which aeolian sand was deposited during the subsequent marine regression (Jermy and Mason, 1983).

In some places the Berea Formation overlies isolated outcrops of carbonate cemented aeolianite bodies which appear to be exactly similar to the aeolianites of the Bluff Formation (Parr, 1958; Frankel, 1965; King, 1962b; McCarthy, 1967; Maud, 1968; Jermy and Mason, 1983). Foraminiferal studies not only assigned a Pleistocene age (Krige, 1932; Parr, 1958; King and Maud, 1964; Frankel, 1965) to these outcrops but also suggested it to be contemporaneous with the Bluff Formation (Krige, 1932 and Parr, 1958). Maud's (1968) study provided evidence that the Berea and Bluff ridges formed at different sea-levels on similar transgressive or regressive cycles during the Early to Middle Pleistocene. McCarthy (1967) considered the basal conglomerate of the Berea Formation and the Bluff Formation Pliocene in age. King (1961) suggested an Eocene age for the Berea Formation. A Pleistocene age is generally accepted for the Berea Formation in Durban although conclusive data still needs to be presented. McCarthy (1967) realised that the Berea Formation is the residual weathering product of underlying aeolianites of various ages. Herein lies the problem with the Berea Formation - it represents a weathered product of different ages of aeolianites. This has led to confusion regarding the distribution and stratigraphic status of 'Berea-type' red sand along the KwaZulu-Natal coast (McCarthy, 1988). Formation rank is not given to the weathered soil profiles of other strata in the geological column but yet this is the case with the Berea Formation (McCarthy, 1988). The Berea Formation is assigned a Quaternary age by SACS (1980) but it also represents the weathered counterparts of

Tertiary aeolianites in Maputaland (McCarthy, 1988), the same formation thus representing Quaternary and Tertiary strata.

It is clear from the foregoing discussion of the Bluff and Berea Formations that although many studies have been undertaken in the past, geochronological control is still very poor. Also, the distinction between the two formations is complicated by the fact that the Berea Formation is a weathering product and in some cases might even represent the weathered product of the Bluff Formation. Future work should include a geochronological program to clarify the age relationship of the various units. Improved knowledge of Pleistocene sea-level fluctuations on the east coast will further contribute to a better understanding of the Quaternary coastal evolution.

Offshore Aeolianite Ridges

Offshore and onshore aeolianite dune cordons (Figure 3.11) extend from Mozambique to the south-eastern Cape (McCarthy, 1967; Maud, 1968; Birch, 1981; Martin and Flemming, 1988 and Ramsay, 1991). Outside of Australia it is the most extensive deposit of carbonate aeolianite in the Southern Hemisphere (Brooke, 2001). The offshore coast-parallel linear aeolianite shoals form some of the most prominent features on the KwaZulu-Natal continental shelf (Martin and Flemming, 1988) and the presence of these deposits occurring to depths greater than -95 m on the continental shelf attests to the magnitude of sea-level oscillations during the Quaternary (Ramsay, 1991).

Ramsay (1991), was of the opinion that the offshore aeolianite and beachrock ridges on the Sodwana Bay continental shelf were developed in a dune and barrier beach complex during lower sea-levels. He defined the sedimentary sequence as regressive and delineated a series of four palaeocoastline episodes characterised by linear coast-parallel aeolianite/beachrock ridges at different depths (-15 m to -95 m). These ranged in age from 117 to 22 ka B.P. and developed during the Late Pleistocene regression leading to the Last Glacial Maximum (Ramsay, 1991). Most recently Cawthra (2010) mapped the Durban Bluff coastal lithofacies and adjacent continental shelf and found two offshore aeolianite units proposed to range in age from ~200 to 60 ka B.P. and thirteen beachrock units proposed to range in age from the last interglacial (MIS 5e) to a successive sequence deposited from ~14 to 0.91 ka B.P. during the Holocene transgression. With the exception of nannofossil biostratigraphy indicating that all lithologies are younger than ~290 ka B.P. and one feldspar optical age range (60 - 70 ka B.P.) on an offshore aeolianite sample, Cawthra's (2010) study lacks robust geochronological control.

Although detailed studies concerned with these offshore aeolianites are almost non-existent the work by Ramsay (1991) and Cawthra (2010) has some chronological control. Conversely, many

workers studied the onshore aeolianites (especially in the Durban region) but the chronological control is extremely poor (Anderson, 1906; Krige, 1932; King, 1962b; King and Maud, 1964; McCarthy, 1967; Maud, 1968; Jermy and Mason, 1983 and Cooper and Flores, 1991).

Holocene

Holocene sediments occur onshore as Recent sand accreted as beaches and dunes forming a complex coastal dune cordon immediately inland of the shoreline and as fluvial channel infill (Maud and Botha, 2000; Martin and Flemming, 1988). The majority of Holocene sediment is found offshore (Figure 3.1c) comprising the inner to mid shelf Holocene sediment wedge or Holocene sand prism (Flemming, 1981; Martin and Flemming, 1986; Birch, 1996; Ramsay *et al*., 1996).

Onshore

Onshore from the study area the coast is characterised by a linear headland-bay complex which receives fluvial sediment input (Figures 2.8; 2.9 and 3.1) from several rivers (Cooper, 1991). The Holocene beaches consist of alternating rocky headlands and concave rock-free sandy beaches forming small embayments which are backed by a generally low Holocene transverse dune barrier banked against the red sands of the Pleistocene coastal dune cordon (Figure 3.13). Most rivers have small estuaries, the mouths of which are for the most part blocked by sandbars (termed mouthbars) constructed from beach sediments. These are breached naturally after periods of heavy rain and/or high swells. The Holocene dune barrier has grown in response to high energy sediment transport during and since the Flandrian transgression (Orme, 1973, Ramsay, 1996).

During the Late Pleistocene times the glacial maxima produced sea-levels of up to -130 m below present such as during the Last Glacial Maximum (LGM) occurring ~18 000 years B.P. (Ramsay and Cooper, 2002). This caused rivers to rejuvenate and incise deep channels into the bedrock, the depth of erosion related to the size of the catchment of the Pleistocene rivers (Orme, 1975). Coring operations in the Umgababa estuary (Figure 3.1) intersected bedrock at levels between -16 m and -21 m below the surface (Grobbler, *et al*., 1988). Bedrock was encountered at -48m below surface in the Mkomazi estuary (Figures 3.1; 8.34a) illustrating the relationship between catchment size and scour depth (Grobbler, *et al*., 1988). A wood fragment found on the bedrock was dated as 9 990 ± 90 years B.P., the age falling within the Flandrian Transgression (Grobbler, *et al*., 1988).

The subsequent Flandrian or Holocene transgression (~18 000 - 9 000 years B.P.) filled the deeply incised river channels with marine, lagoonal and fluvial sediments (Orme, 1975). In general

fluvial deposits characterise the inner portions of the estuary giving way progressively seaward to lagoonal and marine sediments (Orme, 1975). Marine deposits in these estuaries are of two types: either as sediment incursion by wave and tidal action during the transgression, or as sands forming the coastal barriers and spits washed or blown into the estuary by wave and wind action during and since the transgression (Orme, 1975). Scour and fill episodes related to floods events have repeatedly disturbed the earlier Flandrian sedimentary sequence thereby making the stratigraphic correlation of the progress of the Flandrian transgression impossible (Orme, 1975).

Figure 3.13 Holocene dunes accreting onto the older Pleistocene coastal barrier. Stippled line marks the approximate boundary between the Holocene and Pleistocene dune ridges. Arrows indicate red colouration of the Pleistocene barrier. Locality is north of the Mkomazi River estuary and view is towards the NE. The prominent coastal barrier of the Durban Bluff (Figure 3.12) can be seen on the horizon (black arrow).

Offshore

The Holocene sediment wedge is a semi-continuous unconsolidated sediment feature stretching some 1500 km from the east to the south coast along the inner to mid shelf (Martin and Flemming, 1986). The wedge reaches a maximum width of 40 km off the Thukela River but is generally very narrow on the east coast reaching as little as 2 km in width, thus forming a very long nearly continuous sand-stream parallel to the coast (Martin and Flemming, 1986). In the vicinity of the

study area it is only ~6 km in width (Figure 3.14). The major source of terrigenous sediment supply to the sediment wedge is by fluvial discharge from major rivers (Martin and Flemming, 1986).

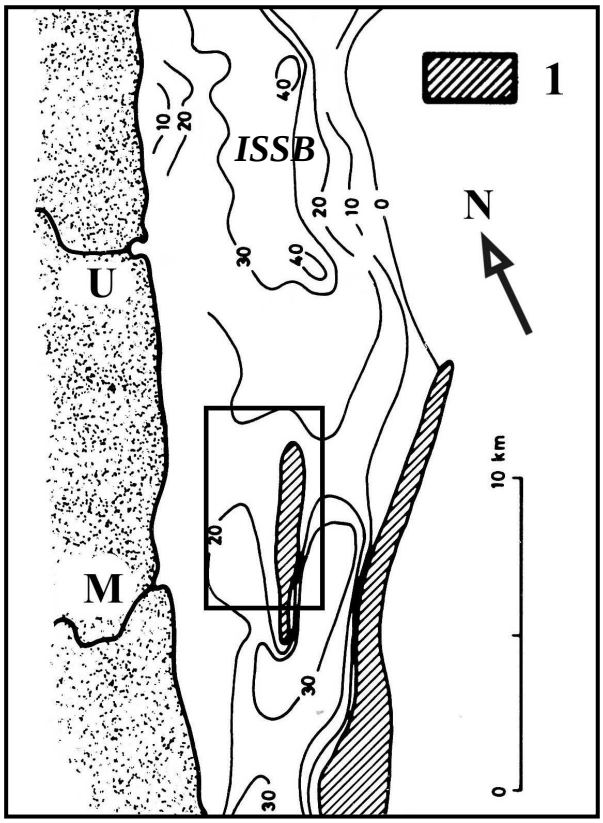

Figure 3.14 Isopach map of the Holocene sediment wedge in the vicinity of the study area (modified from Martin and Flemming, 1986). Rectangle = approximate position of the study area, U = Mkomazi River, M = Mpambanyoni River. Isopachs are at intervals of 10 ms two-way reflection time, to obtain sediment thickness in metres multiply by 0.75. 1 = aeolianite ridges. ISSB = Illovu Submerged Spit-Bar, for details regarding the thick sediment deposit NE of the Mkomazi River refer to Chapters 2.2.3 and 7.4.

Flemming (1980, 1981) divided the offshore Holocene sedimentary sequence into (1) an outer shelf current dominated basal biogenic conglomerate formed during the Flandrian transgression by the reworking of fossil algal-reef bioherms (coined the outer shelf relict carbonate facies), and superimposed on the lag deposit is (2) an inner shelf wave dominated modern terrigenous facies forming the inshore sediment wedge (Flemming, 1980, 1981). The occurrence of subaqueous sand dunes of various sizes in the sediment wedge is well documented (Flemming, 1978, 1980, 1981; Flemming and Hay, 1988, Ramsay, 1994, 1996 and Green, 2009a;c). From this work it is known that sediment dispersal and sedimentary processes on the shelf are dominated by the southerly flowing Agulhas Current (Flemming, 1981; Ramsay *et al*., 1996) whilst the inshore areas are more

strongly influenced by wind and wave driven circulation (Flemming, 1978; Martin and Flemming, 1986). Continental shelf morphology influences the sediment wedge in two ways; (i) it influences the Agulhas Current circulation pattern by creating clockwise eddies or counter-currents in the lee of major coastal and shelf structural offsets resulting in bedload parting zones and (ii) canyons dissecting the shelf break act as mass wasting features interrupting the Agulhas-driven 'conveyor belt' of unconsolidated sediment with sediment funnelled into the canyon heads and ultimately transported to the deep sea environment by turbidity currents (Flemming, 1978, 1980; Martin and Flemming, 1986, 1988).

Offshore submerged coast-parallel linear aeolianite shoals (e.g. the Aliwal Shoal) form some of the most prominent features (Figures 3.11; 3.14) on the KwaZulu-Natal continental shelf (Martin and Flemming, 1988). These remnant Pleistocene palaeostrandlines control sediment dispersal acting as topographical barriers to cross-shelf sediment movement by damming sediment (see Chapter 6) on their shoreward side (Birch, 1981; Flemming, 1981). Considerable thicknesses of sediment (>20 m) may be dammed by these ridges and in some instance aeolianite ridges can be completely buried by the sediment wedge (Birch, 1996).

Sediment Supply to the continental shelf

Possible sediment sources, delivering sediment to the continental shelf include fluvial discharge, coastal and offshore marine erosion, aeolian input, *in situ* authigenic mineralization and biogenic sediment derived from skeletal carbonates (Flemming and Hay, 1988). According to Flemming (1981) and Flemming and Hay (1988), fluvial discharge and biogenic production are the only short-term sediment sources delivering sediment to the KwaZulu-Natal continental shelf.

The continental shelf in the vicinity of the study area receives fluvial sediment input from several rivers (see Section 2.3.3, Figures 2.8 and 2.9). The total sediment yield of these rivers amounts to ~ 1 843 710 tonnes/year (Table 2.3, Section 2.3.3). As fluvial discharge is the most important source of terrigenous material to the continental shelf, the type of sediment delivered to the continental shelf and hence, the Holocene sediment wedge, is therefore strongly influenced by the catchment size and the geology of the respective river catchments. Figure 3.15 shows the geology of the four river systems onland from the study area. Of these four river systems the Mkomazi River is by far the largest and will therefore exert the most influence on the type of sediment delivered to the shelf (Figure 3.15).

The upper and mid reaches of the Mkomazi River drains the lithologies of the Drakensberg Group, the Clarens, Elliot and Molteno Formations, the Beaufort Group and the Dwyka Group (Figure 3.15). With the exception of the basaltic Drakensberg Group all the other units consist essentially of different proportions of shale and fine grained sandstones (Visser, 1989). Due to the combination of the steep and undulating source region and the mostly argillaceous source rocks, it is expected that the bulk of the sediment discharged into the sea by the Mkomazi River is largely medium to fine grained. Although the lower reaches drains the granite-gneisss lithologies of the NNP and medium to coarse sandstones of the Natal Group (refer to Section 3.1), the contribution to the sediment yield is considered negligible according to Hay (1984) due to the subdued topography (Figure 2.9, Chapter 2.3.3) and the restricted drainage of the Mkomazi River in these areas (Figure 3.15). Of the remaining three river systems the Mpambanyoni River has the largest catchment area and hence largest sediment yield (Figure 3.15), although both the Mahlongwana and Mahlongwa Rivers have a greater sediment yield per km^2 (Table 2.3, Chapter 2.3.3). These three river systems all have their origins in the subdued topography of the lower escarpment (Figure 2.7 and 2.9, Chapter 2.3.3), and drain the coarser grained lithologies of the NNP and Natal Group. They are expected to have a lower sediment yield than the Mkomazi and supply a predominantly medium to coarse grained sand to the shelf (Hay, 1984).

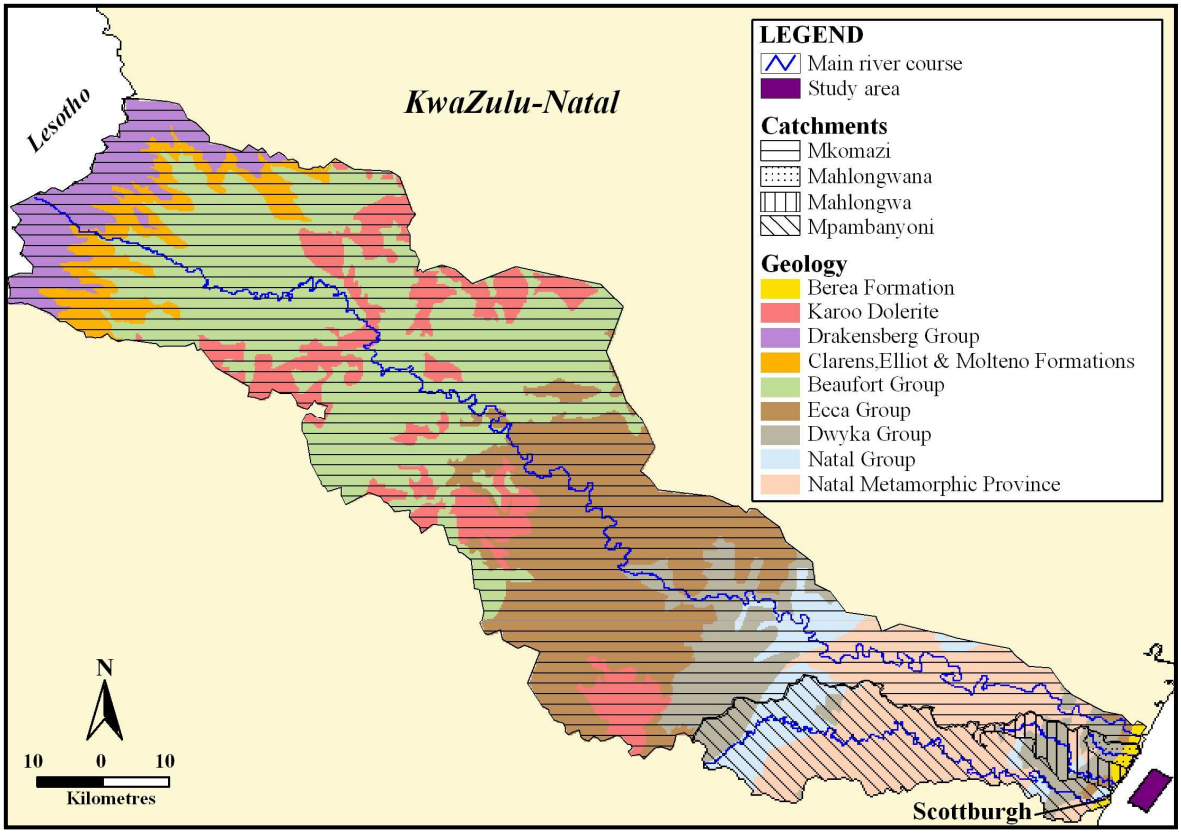

Figure 3.15 Catchment geology of the four drainage systems onshore from the study area (Data courtesy of the Council for Geoscience) with the Mkomazi River by far the most significant.

In addition to the terrigenous sediment supply the only other important source of shelf sediment is biogenic sediment or bioclastic sediment. Flemming (1978) and Flemming and Hay (1988) showed that the carbonate content of shelf sediments off KwaZulu-Natal can range from < 10 % to >90 %, with a general increase in carbonate content with increasing water depth. The middle and outer shelf carbonate sediments are consider relict (relict carbonate facies), whereas the nearshore sediment is dominated by modern terrigenous sediment (Flemming, 1981). The carbonate content of the nearshore sediments is thus linked to biogenic production rates (Flemming and Hay, 1988) with a total annual input to the KwaZulu-Natal continental shelf estimated at 270 000 tonnes (Flemming and Hay, 1988). Ramsay (1991; 1996) indicated that the carbonate content of the bioclastic sediment on the Sodwana Bay shelf (Figure 1.1) ranges from 20 % to 82 %. In addition, he also identified reef-derived and outer shelf-derived bioclastic sediment populations. Closer to the Aliwal Shoal area, Richardson's (2005) study off Durban showed that carbonate content of the shelf sediments range from 3 to 81 % with an increase in carbonate content associated with primary biological productivity on reefs. Cawthra (2010) observed a similar distribution offshore the Durban Bluff (Figure 3.12), south of Richardson's (2005) study, but with maximum carbonate content values only reaching 68 %.

In contrast the carbonate content of the Aliwal Shoal shelf sediments range from 39% - 98%, with an average of 61% (Chapter 8). High carbonate production rates throughout the Pleistocene and Holocene, producing bioclastic-rich sediment, along the KwaZulu-Natal Coast is an important pre-requisite for the generation of aeolianite and beachrock. The carbonate is easily leached, especially during sea-level lowstands, precipitating as a cement to form aeolianites and beachrocks (Section 8.3).

The last and least quantified sediment source supplying sediment to the shelf is that of coastal erosion. Recently, the impact of swell driven coastal erosion has been highlighted by Smith *et al*. (2010), with sediment eroded from the coastal zone shown to be delivered to the shelf by strong storm-return flows.

CHAPTER 4
QUATERNARY SEA-LEVEL CHANGES

4.1 INTRODUCTION

The Quaternary Period is characterised by rapid global climatic fluctuations accompanied by sea-level changes, greater than any other time in the last 60 million years (Maud, 1968; Bradley, 1999). Whereas Cretaceous and Tertiary sea-levels were mainly controlled by tectonic and basin volume changes (tectono-eustacy), Quaternary sea-level changes were and are glacio-eustatic in origin linked to climatic variations and changes in the Northern Hemisphere polar ice volume (Tankard *et al*., 1982; Dawson, 1992; Bradley, 1999; Siegert, 2001; Pillans and Naish, 2004). Southern Africa is particularly well positioned to document these effects as it is considered tectonically stable (see Section 4.5), recording sea-level and palaeoenvironment change on the continental shelf. In addition the coastal environment is intimately associated with the evolution of modern man along the southern African coast (Marean *et al*., 2007; Fisher *et al*., 2010; Compton, 2011).

4.2 CLIMATE AND LATE QUATERNARY SEA-LEVEL CHANGES

Variations in Earth's orbital parameters caused changes in the amount of incoming solar radiation (insolation), which in turn lead to regular fluctuations between warmer (interglacial) and cooler (glacial) global climate. Periodic climatic fluctuations were first described by Croll (1867a,b) and later refined by Milutin Milankovitch (1941), becoming known as Milankovitch theory (Dawson, 1992). The mathematical basis of this theory was further advanced by Vernekar (1972) with Berger (1978, 1979), providing detailed information on past insolation changes. According to Milankovitch theory, climatic variation is due to three astronomical cycles viz (Figure 4.1);

- *Orbital Eccentricity*; this refers to the gradual change in the shape of the Earth's orbit from elliptical to circular orbits. The resultant periodicities are quasi-periodic and include the 95 ka, 123 ka (forming the ~100 ka cycles) and the ~413 ka cycles (Bradley, 1999; Coe, 2003). The average period length over the past 5 Ma years is ~95 800 years (Bradley, 1999).
- *Obliquity*; changes in the angle of tilt of the Earth's axis which has varied from 21.8° to 24.4°, presently it is 23.44°. The periodicity of the obliquity cycle is 41 ka.

- *Precession*; is a 'wobbling' in the Earth's axis of rotation. There are two components to the precession: that related to the axis of rotation and that relating to the elliptic orbit of the Earth (Coe, 2003). The Earth's axis sweeps in a conical manner around a line perpendicular to the orbital plane. The elliptical orbit of the Earth around the Sun also precesses (Coe, 2003). The main resultant periodicities of both these motions are 19 ka and 23 ka with a mean period of 21 700 years (Bradley, 1999; Coe, 2003).

The eccentricity cycle mainly controls the amplitude of the precession cycle (Coe, 2003) and does not affect the amount of solar radiation reaching the Earth during summer or winter, or the total annual insolation received by each hemisphere (Dawson, 1992). Orbital eccentricity increases the contrast in seasonality in one hemisphere and reduces it in the other (Dawson, 1992). An increase in obliquity lengthens the period of winter darkness in polar regions (Dawson, 1992) significantly affecting high latitudes but does not affect the amount if insolation at low latitudes (Dawson, 1992). Oliquity and eccentricity cycles thus affect the distribution of the solar radiation over the Earth's surface (Coe, 2003). Precession controls the timing of the seasons relative to the perihelion (point in orbit where the Earth is at its shortest distance from the sun, Figure 4.1) and aphelion (furthest distance) and hence the total radiative heating in each season (Coe, 2003). Dalgleish *et al*. (2000) calculated that deglaciation events are associated with obliquity and precession rather than changes in eccentricity.

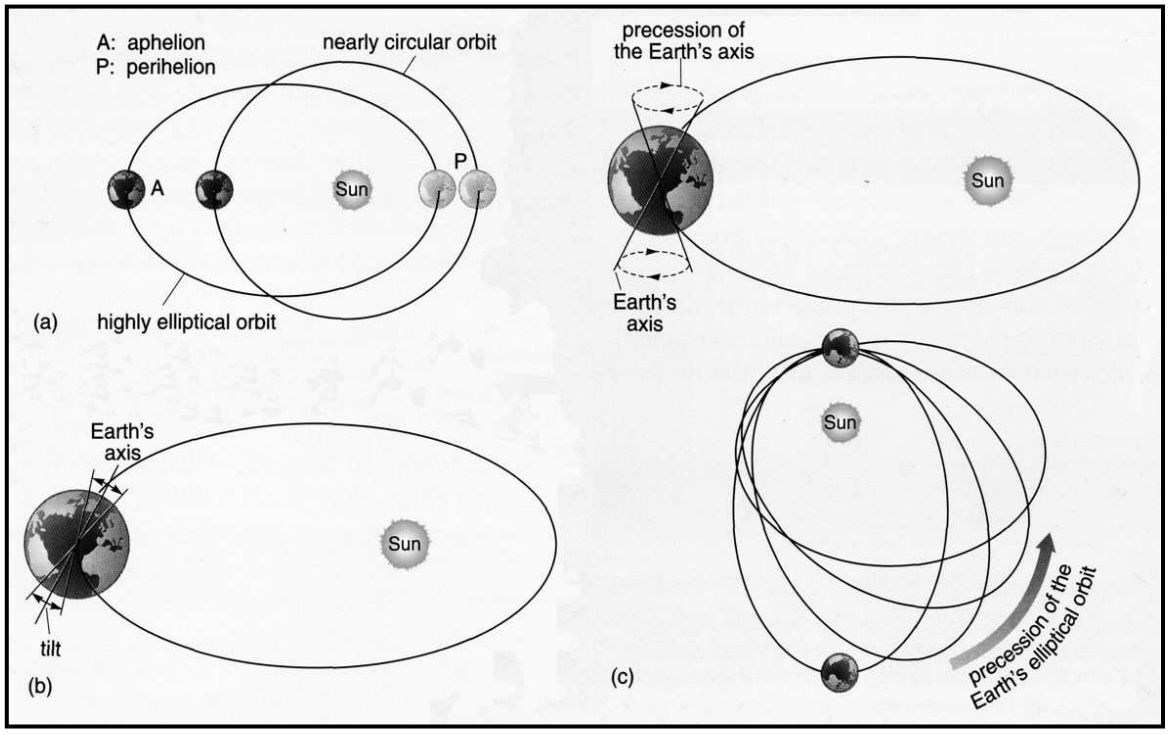

Figure 4.1 The Earth's three orbital parameters which cause orbital-climate cyclicity; (a) eccentricity, (b) obliquity and (c) precession (adapted from Coe, 2003).

The superimposition of the variations in the orbital parameters causes a complex ever-varying pattern of solar radiation receipts to the Earth (Bradley, 1999). The resultant temperature variations drive climate change, which results in the growth and decay of ice-caps, and expansion and contraction of the oceans, which in turn result in global sea-level fluctuations (Coe, 2003). However, Potter *et al*. (2004) illustrated that although the Milankovitch astronomical insolation-forcing theory is able to explain gross features of global climate over broad glacial - interglacial cycles, it is not able to account for rapid suborbital climate fluctuations such as observed during marine isotope stages 5a and 5c. In contrast, evidence of past sea-level oscillations provides a direct estimate of changes in global ice volume and hence global climate (Potter *et al*., 2004). Suborbital millennial-scale climatic shifts - which are mainly due to Dansgaard-Oeschger (DO) cycles which occurred repeatedly over much of the Northern Hemisphere during the Last Glacial period (particularly 12 – 75 ka) - are also recorded by oxygen isotope fluctuations in Greenland ice cores (Grootes *et al*., 1993; Stuiver and Grootes, 2000). Chappell (2002) showed that between 30 and 65 ka the Bond cycle (Atlantic marine sediments DO cycles are grouped in bundles called Bond cycles which terminate with ice-rafted debris horizons known as Heinrich events) bundles of DO cycles were reflected in sea-level changes which are recorded by coral terraces at the Huon Peninsula in Papua New Guinea.

4.3 PROCESSES CONTROLLING SEA-LEVEL CHANGE

Sea-level changes at any location at any point in time are dependant upon a combination of sea surface level changes, any isostatic or tectonic changes and local coastal processes - thus a product of changes in crustal and oceanic variables (Woodroffe and Horton, 2005). Average global or eustatic long term sea-level changes are mainly due to (Figure 4.2);

- *Ocean-Water Volume Changes*; the principal cause of variation in the volume of seawater is through the formation and melting of ice-caps and glaciers and is referred to as *glacial eustasy* (Coe and Church, 2003a). Global ice volume is inversely related to the mean eustatic sea-level. Steric or thermal expansion/contraction is another mechanism for changing the volume of seawater (Woodroffe and Horton, 2005).
- *Ocean Basin Volume Changes*; sea-level changes due to changes in the size or shape of ocean basins - or *tectono-eustasy*. Seafloor spreading can decrease the volume of an ocean basin resulting in transgressions whereas during orogenesis, ocean basin volume will increase resulting in regressions. Tectono-eustasy also includes several other processes such as glacial-isostasy, hydro-isostasy and continental margin tectonics (Dawson, 1992; Coe and Church, 2003a).

- *Ocean-Level Distribution Changes*; regional variations in the Earth's gravity field result in considerable differences in geoidal sea surface altitudes - *geoidal eustasy* (Dawson, 1992). The most important Late Quaternary changes in the Earth's gravity field were caused by the gravitational attraction of ocean water to ice sheets (Dawson, 1992). Mörner (1976) showed a 180 m difference in present sea-level between the geoidal low Maldive Islands and geoidal high New Guinea. During the Last Glacial Maximum (LGM), ice loading at high latitudes caused deformation of the crust resulting in sublithospheric flow away from the centres of load (Woodroffe and Horton, 2005). This created a low latitude gravitational anomaly producing a high in the oceanic geoid. The subsequent LGM deglaciation resulted in ice unloading with associated continental viscoelastic rebound causing the decay of the gravity anomaly and migration of the oceanic geoid from lower to higher latitudes - this process was named equatorial ocean syphoning by Mitrovica and Peltier (1991) (Woodroffe and Horton, 2005).

Geoidal eustasy has the further consequence that published curves of sea-level change may only be of local and not global significance (Mörner, 1976; Dawson, 1992). The notion of a global eustatic curve of sea-level change is therefore questionable (Clark *et al*., 1978; Mörner, 1987). In addition, relative sea-level effects from equatorial ocean syphoning have only been observed for the last 3000 years (Woodroffe and Horton, 2005).

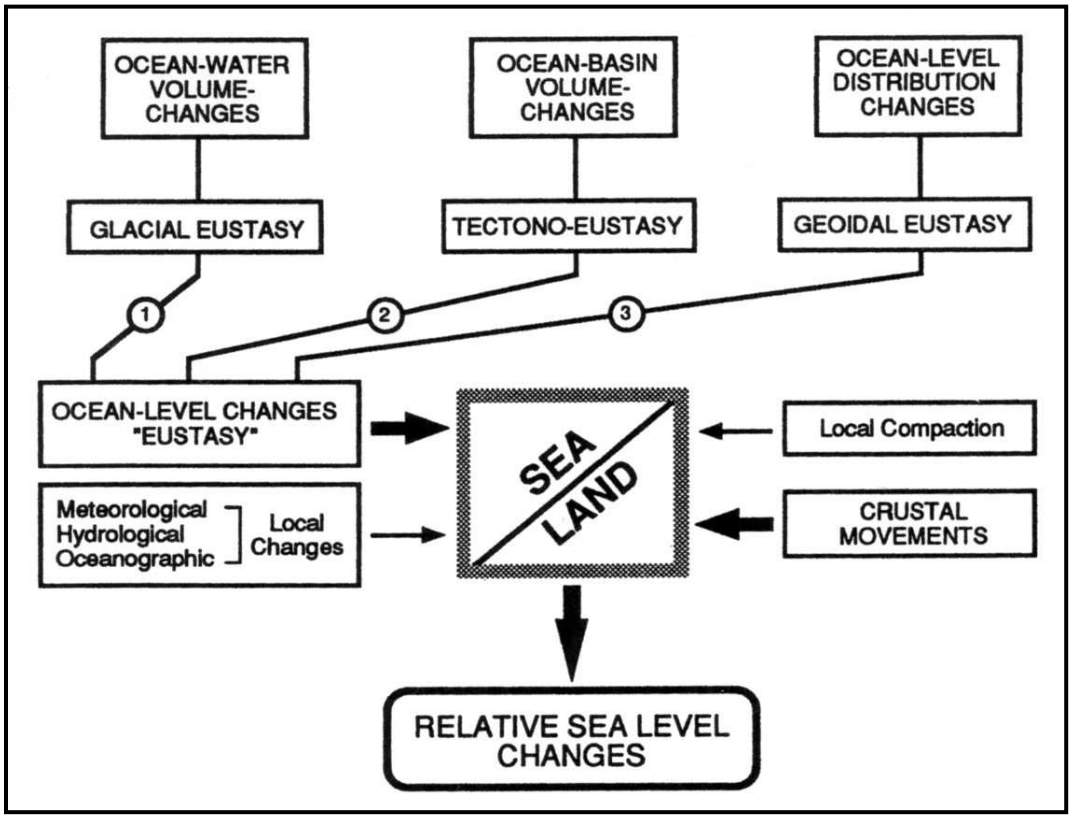

Figure 4.2 (cont) The three eustacy processes (Glacial, Tectono and Geoidal) that when combined with combined with local meteorological, hydrological, oceanographic, compaction and crustal movements result in relative sea-level changes (from Mörner, 1980 in Dawson 1992).

These three types of eustasy thus result in *relative* sea-level change at any one particular location. Relative sea-level change is a useful term as it does not imply that a specific mechanism is responsible for the sea-level change or that it is global in extent (Coe and Church, 2003a). However, Peltier (2002) demonstrated that there are preferred oceanic locations such as Barbados in the Caribbean at which eustatic sea-level is well approximated by the local relative sea-level history. The eustatic function of sea-level change can be approximated from quantifying and adjusting factors resulting in the relative sea-level changes such as tectonic uplift, glacio-hydro-isostasy and by using realistic ice-distribution and earth models (Bassett *et al*., 2005).

4.4 THE RECORD OF PAST SEA-LEVEL CHANGES

There are several methods of estimating ancient sea-level change. The Quaternary record of past sea-level change is predominantly derived from two main sources; namely the oxygen isotope record of deep sea sediment cores obtained by the Integrated Ocean Drilling Program (IODP; previously the Deep Sea Drilling Project since superseded by the Ocean Drilling Program) and from dating of low latitude raised coral reef terraces.

4.4.1 The Oxygen Isotope Record

Oxygen isotope ratios of marine fossils found in deep sea sediments are related to the volume of polar ice sheets which in turn is directly linked to sea-level change (Coe and Church, 2003a). Biogenic oozes form the bulk of all but the deepest of deep sea sediments and are primarily composed of calcareous or siliceous skeletons (Bradley, 1999). These generally provide a continuous record of sedimentation which is only rarely disturbed by erosional events such as submarine landslides and turbidity currents (Dawson, 1992). For oxygen isotope studies the most important are the tests of calcareous foraminifera. Planktonic foraminifera provide information on ocean surface conditions while benthonic species provide information on former deep water environments (Dawson, 1992). Changes in the oxygen isotope composition of seawater are preserved in the calcium carbonate skeletal remains of foraminifera that precipitated from seawater when it was alive. The stable oxygen isotope composition of the carbonates produced by the foraminifera is dependant on the isotopic composition of seawater and also on the temperature of the seawater (Dawson, 1992). The ratio of the stable isotopes ^{16}O and ^{18}O in seawater varies with

salinity, temperature and the volume of polar ice (Dawson, 1992; Bradley, 1999; Siegert, 2001; Coe and Church, 2003a and numerous others). The proportion of ^{18}O isotope to the ^{16}O isotope is determined with respect to a standard in parts per thousand (per mil or ‰) using;

$$\delta\,^{18}O = \frac{\left(^{18}O/^{16}O\right)_{sample} - \left(^{18}O/^{16}O\right)_{standard}}{\left(^{18}O/^{16}O\right)_{standard}} \times 1000 \qquad (2.1)$$

The $\delta^{18}O$ value (i.e. the oxygen isotope composition) can be either positive or negative. Negative values represent lower ratios in the sample (i.e. less ^{18}O than ^{16}O and thus isotopically lighter) and positive values represent higher ratios in the sample (i.e. more ^{18}O than ^{16}O and thus isotopically heavier) (Bradley, 1999). The standard used for carbonate fossils is a Cretaceous belemnite from the Pee Dee Formation of North Carolina, U.S.A (known as the Pee Dee Belemnite; PDB). Most oxygen isotope studies are based on the analyses of planktonic foraminifera. Isotopic variations attributed to water temperature changes need to be separated from those caused by variations in the isotopic composition of seawater - this is known as the temperature effect (Dawson, 1992). The $\delta^{18}O$ signal from benthic foraminifers provides a more accurate measure of palaeoglaciation being less prone to the temperature effect. The reader is referred to Bradley (1999) and Dawson (1992) for a detailed review of the uncertainty and problems associated with oxygen isotope analyses.

During periods of glaciation ocean water is relatively enriched in the heavier ^{18}O isotope. This is mainly due to preferential removal of the lighter ^{16}O isotope from the oceans through isotopic fractionation during evaporation. Thus, when the ^{16}O enriched water vapour in the atmosphere is eventually precipitated as snow in the polar regions, it is depleted in ^{18}O relative to the oceans (Coe and Church, 2003a). Conversely, during interglacials the lighter ^{16}O isotope is returned to the oceans resulting in a relative depletion of ^{18}O in the oceans. Worldwide oxygen isotope analyses indicate that similar isotopic ($\delta^{18}O$) variations are recorded (after making allowance for variations in sedimentation rates, vital effects, temperature effects etc.) in all areas (Bradley, 1999). This is because the primary $\delta^{18}O$ signal recorded is that of ice volume changes on the continents and concomitant changes in the isotopic composition of the oceans (Shackleton, 1987). For this reason, universally recognised isotope stages in marine sediments can be defined (Emiliani, 1955, 1966; Pisias *et al.*, 1984). These are known as marine oxygen isotope stages (OIS) or marine isotope stages (MIS) where warmer periods (interglacials) are assigned odd numbers and colder periods (glacials) are assigned even numbers. This numbering notation is applied from the ‘top down’ with the present interglacial (Holocene) being number 1. As these numbers mostly indicate periods of full glacial and interglacial status, some exceptions, such as MIS 3, exists. Although, MIS 3 is considered a warm stage, it is only recognised as a period of

interstadial status, i.e. a warm period associated with the last glacial (Walker, 2005). In addition, some of the interglacial periods are subdivided into separate warmer and colder episodes i.e. MIS 5 includes 5 substages, with the warmer episodes designated as 5a, 5c, 5e and the cooler episodes assigned as 5b and 5d. Worldwide, the last interglacial is considered to be represented *senso stricto* to the warm substage 5e (Walker, 2005).

Abrupt glacial to interglacial climate shifts and associated rapid isotopic changes are recognised as Terminations. As for the MIS, the number designation is from the 'top down' e.g. Termination 1 refers to the marked $\delta^{18}O$ shift at the end of MIS 2 (Walker, 1995). MIS thus provides a relative chronostratigraphic scheme but absolute dating should also be included. Martinson *et al*. (1987) developed an 'orbital tuned' standard reference chronostratigraphy for the Late Quaternary by 'tuning' the $\delta^{18}O$ signal in marine sediments to the orbital frequencies according to Milankovitch theory. The resulting 'SPECMAP' (Spectral Mapping Project) record (Figure 4.3) allows for other $\delta^{18}O$ records to be corrected and fitted to this reference chronology, even if no dates are available for these records (Bradley, 1999). This method of orbital tuning $\delta^{18}O$ records can now be applied to extend back as far as 2.5 Ma for selected pelagic sediment cores (Bradley, 1999).

A number of important features (Figure 4.4) are apparent from the oxygen isotope record (Bradley, 1999; Dawson, 1992):

- there have been numerous alternating periods of warm and cold climate and many of these fluctuations have been extremely rapid,
- the curve is 'saw-toothed' in character showing a slow increase in $\delta^{18}O$ resulting from the gradual build-up of ice on the continents, followed by a period of rapid deglaciation,
- $\delta^{18}O$ values have rarely been higher than Holocene levels, indicating that there have been few periods with less continental ice than there are at present; these episodes were principally in oxygen isotopes stages 5, 9, 11, 31 and 37 (Figure 4.4),
- from 3.1 Ma to 2.6 Ma B.P. an increase in $\delta^{18}O$ indicates a progressive cooling, probably associated with the growth of the Antarctic ice sheet and continental ice sheets in the Northern Hemisphere,
- only since isotope stage 22 (~ 800 ka ago) have there been episodes of continental glaciation comparable in magnitude to the most recent ice age (MIS 2),
- the record shows the increased importance of variance of the 100 ka (eccentricity) frequency band over the last 1 Ma years.

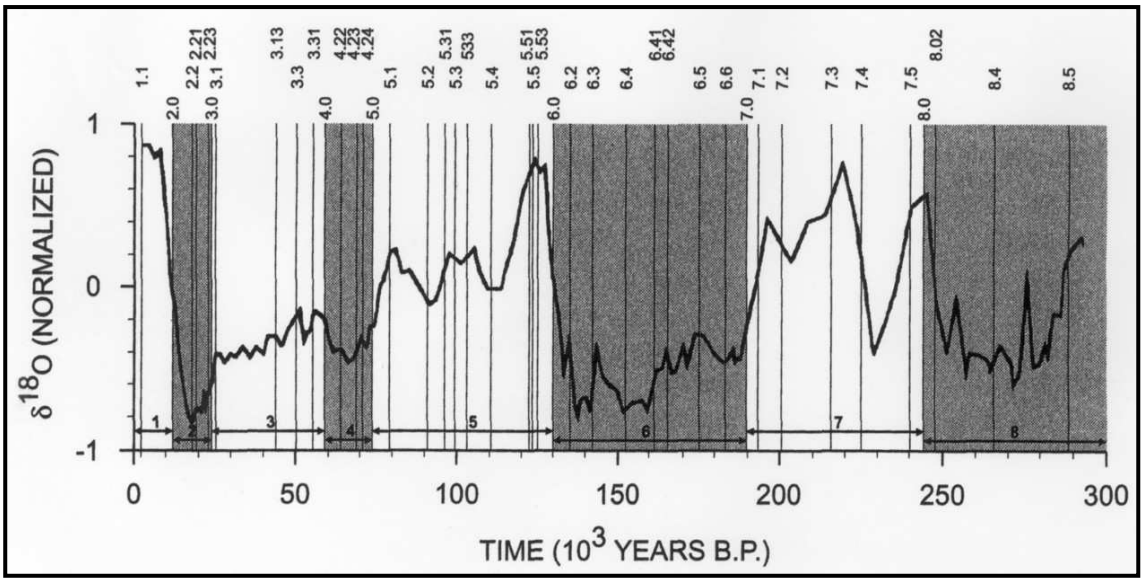

Figure 4.3 Martinson *et al.*'s (1987) SPECMAP record consisting of a composite chronology for a set of seven superimposed $\delta^{18}O$ records from sediment cores obtained from different ocean basins. The chronology is derived from orbital tuning that assumes that the primary forcing mechanism controlling the frequency characteristics are orbital variations, the periodicities of which are described by Milankovitch theory. Numbering refers to the marine isotope stages with the major stadial periods (2, 4,6 and 8) shaded. Vertical lines are defined by Martinson *et al.* (1987) and represent times of transitions between stages or substages; substages 5a to 5e is centred on lines 5.1 to 5.5, respectively (from Bradley, 1999).

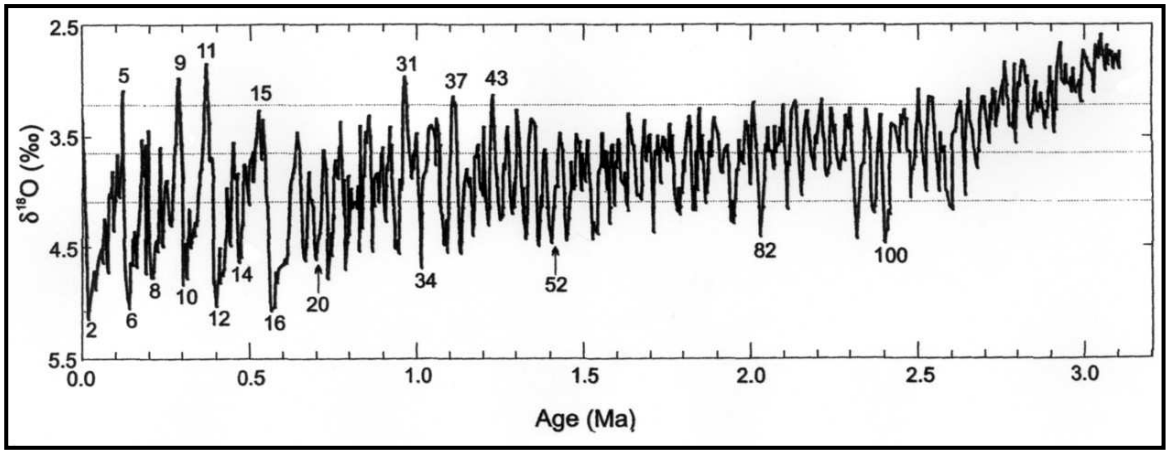

Figure 4.4 3.2 Ma benthic oxygen isotope record from equatorial Atlantic core ODP-607. Numbers refer to the marine oxygen isotope stages and horizontal lines indicate $\delta^{18}O$ values for the Holocene (upper line), stage 5c (middle line), and the stage 2/1 boundary (lowest line), as recorded in this core (from Raymo, 1992 in Bradley, 1999).

As noted earlier $\delta^{18}O$ is predominantly related to isotopic changes of the oceans under the influence of changing continental ice volume. As the ice sheets grew on the continents, $\delta^{18}O$ in the oceans increased and global sea-level fell. The relationship between ice volume and $\delta^{18}O$ is complex and non-linear and the reader is referred to Shackleton (1987), Dawson (1992) and Bradley (1999) for a review of the complexities. Shackleton and Opdyke (1973) used the oxygen isotope data to calculated a probable sea-level curve for the last 130 000 years based on the assertion that a measured variation of 0.1‰ in $\delta^{18}O$ is approximately equal to a 10 m change in global sea-level. The relationship between $\delta^{18}O$ and sea-level has also been considered more recently by Chappell and Shackleton (1986) and Shackleton (1987). Shackleton's (1987) glacio-eustatic curve (Figure 4.5) is based on the analyses of planktonic and benthonic oxygen isotope data and compared to sea-level fluctuations estimated from the most detailed Huon records available at the time.

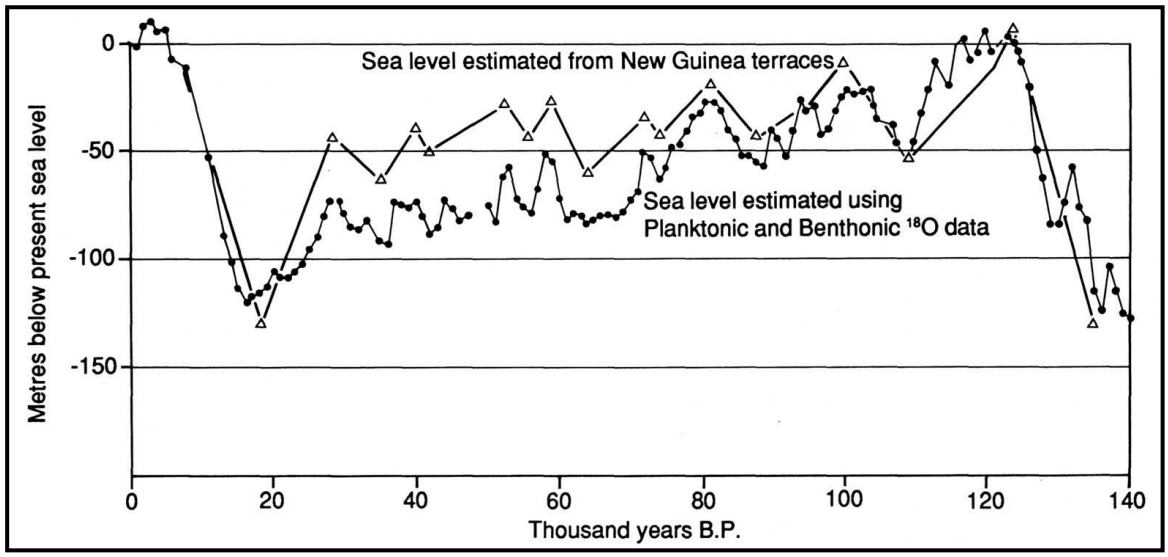

Figure 4.5 Oxygen isotope global sea-level record compared with the sea-level data from New Guinea terraces (from Shackleton, 1987 in Dawson, 1992).

Late Quaternary sea-level data correlated moderately with the glacio-eustatic ($\delta^{18}O$) curve for the last interglacial but showed large discrepancies of up to 60 m between 60 ka to 28 ka (Figure 4.5). Chappell *et al*. (1996) resolved the discrepancy between the sea-level derived from raised coral terraces and oxygen isotopes by redating the Huon terraces. They found that all previous age estimates were too young for this period, with the recalculated sea-levels between 30 and 70 ka lower than previous estimates and hence, closer to the isotopic sea-levels (Chappell *et al*., 1996). Chappell *et al*. (1996) also concluded that their evidence supports the conclusion of Chappell and Shackleton (1986) that the Late Quaternary record of sea-level changes obtained from Huon

represents a global pattern. More recently, Waelbroeck *et al* (2002) produced a relative sea-level curve based on the isotopic records from benthic foraminifera spanning 432 000 years. This curve is used for comparison in Section 4.5 and Chapter 9.

4.4.2 Sea-Level, Raised Coral Terraces and Meltwater Pulses

Past sea-level reconstructions also utilise ancient shorelines that have been tectonically uplifted by dating low latitude raised coral reefs. This is possible as certain species of coral only grow at a specific depth relative to sea-level e.g. *Acropora Palmata* which grows within 5 m of the sea surface (Potter *et al*., 2004). By sampling for example the crest of the terrace deposit the record would represent deposition during a sea-level highstand (Potter *et al*., 2004). The raised coral terraces are found on tectonic active coasts and therefore must also be corrected for tectonic uplift by using a predetermined curve of uplift correction. In some areas the Late Quaternary tectonic uplift is uniform (New Guinea) while other areas show non-uniform uplift (Japan) (Dawson, 1992). Sea-level reconstruction using raised coral terraces has the advantage of not being affected by temperatures changes, which complicate the interpretation of sea-level from marine oxygen isotope records (Chappell, 2002). In many cases the uplift correction is assumed (New Guinea, Bloom *et al*., 1974; Barbados, Bender *et al*., 1979) and some sea-level curves use a combination of raised coral terrace data and oxygen isotope data (Chappell and Shackleton, 1986; Shackleton, 1987) and thus also require some assumptions.

Important raised coral terraces include those in Barbados (Mesolella *et al*., 1969; Fairbanks, 1989; see Schellmann and Radtke, 2004 and Radtke *et al*., 2004 for updated review) and the Huon Peninsula at Papua New Guinea (Bloom *et al*., 1974; Chappell, 1974; Chappell and Shackleton, 1986 and Chappell *et al*., 1996). Figure 4.6 shows the sea-level curve established from the Huon Peninsula which corresponds well to eustatic curves from elsewhere in the world, in particular Barbados (Dawson, 1992).

It is clear from the sea-level curve that sea-level during the last 240 000 years was usually lower than present. The Middle Pleistocene was dominated by three highstands of -10 m at ~240 ka B.P., 213 ka B.P. and 200 ka B.P., collectively constituting the Penultimate Interglacial (Figure 4.6). This interglacial was followed by the Penultimate Glacial at 135 ka B.P. which resulted in eustatic lowering of ~130 m of sea-level (Figure 4.6). Last Interglacial sea-levels are represented by sea-level highstands at ~125 ka B.P. and ~100 ka B.P. interrupted by sea-level lowering to -50 m at ~112 ka B.P (oxygen isotope substage 5d). The sea-level highstand at ~125 ka B.P. (oxygen isotope substage 5e) represents the peak of interglacial warmth with the possible partial

disintegration of the West Antarctic ice sheet which in addition to Northern Hemisphere ice sheet decay might have caused the global sea-level to rise ~6 m above the present level (Dawson, 1992; Siegert, 2001). There is a remarkable correspondence in the high sea-levels of the Last Interglacial from New Guinea, Barbados and other localities illustrating its global significance.(Dawson, 1992; Muhs, 2002; Coyne *et al*., 2007). The sea-level lowstand during substage 5d represents a brief but major period of ice build-up which began at ~120 ka B.P. and terminated at ~115 ka B.P. (Dawson, 1992). It is speculated to be related to the partial disintegration of the West Antarctic ice sheet during isotope substage 5e and the influx of glacial meltwaters causing climatic changes (Dawson, 1992).

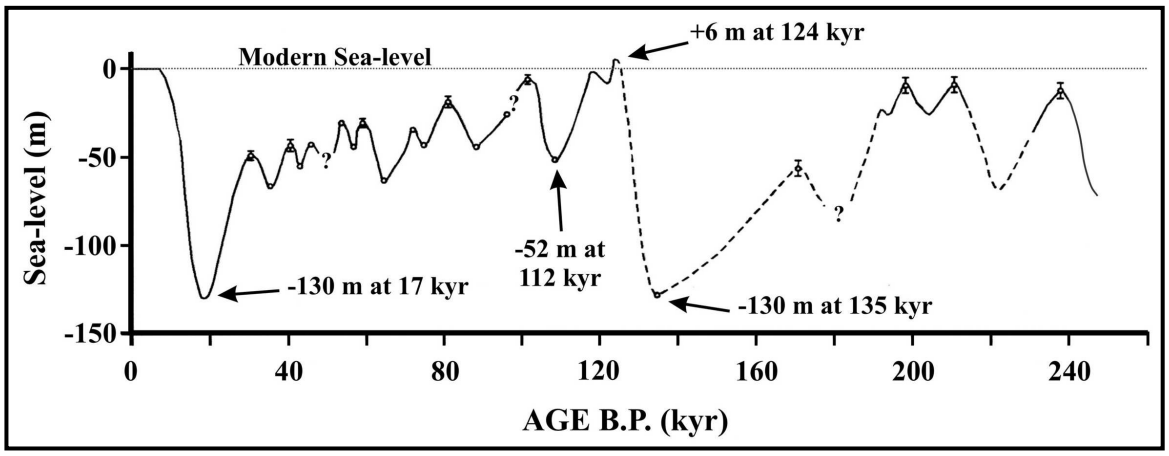

Figure 4.6 Detailed corrected sea-level curve for Site HP2, Huon Peninsula, Papa New Guinea (from Chappell and Shackleton, 1986).

The Last Interglacial was followed by a cold period wherein rapid oscillations in sea-level were superimposed on a gradually falling sea-level (Figures 4.5 and 4.6), which ultimately culminated as the Last Glacial Maximum (LGM). Pre-LGM fluctuations indicate severe climate shifts and are characterised by 10 - 15 m changes in sea-level (Figures 4.5 and 4.6) every ~6 - 7 ka years with the most rapid fall of sea-level prior to the LGM lowstand occurring ~30 000 years ago (Lambeck and Chappell, 2001; Yokoyama *et al*., 2001a). The timing of these rapid change events during marine oxygen isotope stage 3 (MIS3) apparently coincided with Heinrich ice-rafting events in the North Atlantic (Bond *et al*., 1997; Lambeck and Chappell, 2001; Chappell, 2002).

During the LGM (~22 - 19 ka B.P.) ice sheets attained their maximum extend and resulted in global sea-levels ~120 - 135 m lower than present (Chappell and Shackleton, 1986; Shackleton, 1987; Yokoyama *et al*., 2001b; Siegert, 2001; Clark and Mix, 2002; Lambeck *et al*., 2002a and 2002b). Ice sheet expansion occurred predominantly in the mid- to high-latitude Northern

Hemisphere where continental ice sheets expanded across Europe and North America (Siegert, 2001). In Antarctica and Greenland LGM ice sheets grew from ice masses that survived the Last Interglacial, whilst ice expansion also occurred in mountain glacier complexes in the Southern Hemisphere mid-latitudes (e.g. Patagonia, New Zealand and Lesotho) (Siegert, 2001). In the Southern Hemisphere, outside of Antarctica, the lack of continents (and continental shelf) limited the growth of ice sheets (Siegert, 2001).

As mentioned before, ice sheet decay following a glacial period is rapid and the post-LGM sea-level rise was extremely fast and is known as the Flandrian transgression. Many authors modelled the eustatic function of the post-glacial sea-level rise citing sea-level records from 'near-field' (regions once glaciated) and 'far-field' (records from sites distant from major glacial activity) sites. A review of these falls outside the scope of this section and the reader is referred to Mörner (1971), Fairbanks (1989), Fleming *et al*. (1998), Yokoyama *et al*. (2001b), Clark and Mix (2002), Lambeck *et al*. (2002a), Milne *et al*. (2002), Peltier (2002) and Mitrovica (2003), Clark *et al*. (2004), Bassett *et al*. (2005).

By the Holocene, sea-level has risen ~85 m (of the 120 m LGM depression) which is equivalent to the melting of two thirds of the LGM ice sheets - almost all of the meltwater was discharged through the North Atlantic in two short episodes, lasting a total of ~2 500 years (Bradley, 1999). The overall warming trend which brought about the deglaciation was thus punctuated by a series of cold events, the coldest of these being the enigmatic Younger Dryas. This occurred between 10 ka B.P. and 11 ka B.P. (11.7 - 12.9 calibrated ka B.P.) representing a period of climatic deterioration and associated ice advances in NW Europe and the U.S.S.R (Dawson, 1992). Many problems surround the Younger Dryas episode, which essentially involve the forcing mechanisms (orbital forcing is discarded) and the extent (global or not) of this glacial-like event (see Broecker *et al*., 2010). Although the Younger Dryas is well documented for the Northern Hemisphere, its record in the Southern Hemisphere remains elusive (Alley and Clark, 1999) with supporting and contradicting evidence and timing (also see Andres *et al*., 2003).

The sea-level curve obtained from drowned coral reefs off Barbados revealed that the LGM attained a maximum of -121 ± 5 m at ~18 ka B.P (Fairbanks, 1989). As deglaciation set in, sea-level slowly rose by ~20 m during the following 5 ka years. Sea-level then rose rapidly, ~24 m in <1000 years due to a rapid increase in meltwater discharge (meltwater pulse 1a, MWP-1a), at a rate of 16000 km^3a^{-1} (Fairbanks, 1989; Bard *et al*., 1996). This rapid sea-level rise then slowed down markedly for ~1000 years during the Younger Dryas which was followed by a second meltwater pulse (MWP-1b) at ~9.5 ka cal. B.P. resulting in an additional sea-level rise of 28 m in ~1500 years (Bard *et al*., 1996). The precise timing, hemispherical synchronicity and source,

amplitude and importance to the rate of sea-level rise of both meltwater pulses are controversial (Okuno and Nakada, 1999; Peltier, 2005; Peltier and Fairbanks, 2006; Stanford *et al*., 2006). Recently, Stanford *et al*. (2011) used statistical analyses from far-field sites to determine the highest probability sea-level history for the last deglacial sea-level rise and inferred the existence of both MWP-1a (14.3 - 12.8 cal. ka B.P.) and MWP-1b (11.5 - 8.8 cal. ka B.P.). Bard *et al*. (2010) drilled three boreholes in Tahiti specifically to study the existence of MWP-1b and the Younger Dryas event. They confirmed the existence of MWP-1a, the slower Younger Dryas sea-level rise and the reacceleration, but contrary to Stanford *et al*. (2011), could not detect a sea-level jump caused by a MWP-1b (Bard *et al*., 2010).

Liu et al. (2004) based on data from the Yellow River subaqueous delta suggested the existence of various meltwater pulses including a MWP-1c between 9.8 to 9.0 ka cal. B.P. Woodroffe and Horton (2005) also found a meltwater pulse (termed MWP-2) at ~9.1 ka cal. B.P. from Caribbean and north Atlantic records but questioned the global significance of this event. Liu et al. (2007) studying the Shadong Clinoform suggested that the general deceleration of the Holocene sea-level rise following MWP-1c was interrupted by multi-decadal to centennial scale meltwater pulse events which caused abrupt rises in sea-level and were related to climatic fluctuations. The timing of one such event (8.45 - 8.25 ka cal. B.P.) was also confirmed by Hijma and Cohen (2010) in records from the Dutch continental shelf.

Fleming *et al*. (1998) modelled the non-uniform post-LGM rise in eustatic sea-level, showing that the initial rate of rise from ~21 ka B.P to 17 ka B.P was relatively slow with an average rate of ~ 6 m/ka. This was followed by faster average rate of ~10 m/ka for the next 10 000 years but significant departures from these rates occurred during the Younger Dryas. Most of the ice sheet decay was completed by 7 ka B.P. (Fleming *et al*., 1998) and since then, 3 - 5 m of water has been added to the ocean probably as a result of the partial melting of the West Antarctic ice sheet. Lambeck *et al*. (2002a) also modelled the post-LGM sea-level rise using data from seven different regions. Their data indicated that the LGM occurred at 30 ka B.P. and remained constant until 19 ka B.P., with the entry into the LGM characterised by a sea-level fall of 50 m within a few thousand years. Post-LGM sea-level rise was non-uniform and characterised by marked changes in rates with maximum rates of about 15 mm/year occurring for the period 16 ka B.P to 12.5 ka B.P. and again from 11.5 to 9 ka B.P. (Lambeck *et al*., 2002a). These periods of rapid rise were interrupted by the Younger Dryas event which resulted in a nearly constant sea-level for ~1000 years. Similar rates of sea–level changes occurred during oxygen isotope stage 3 (Lambeck *et al*., 2002a).

4.5 THE KWAZULU-NATAL SEA-LEVEL RECORD

To produce a sea-level curve, plotted as a time/depth-elevation graph, geochronologically constrained sea-level index points are needed. Each sea-level index point should have an indicative meaning which is the relationship of the sample to the local environment in which it formed to a contemporaneous reference tide level, with a related error range (Woodroffe and Horton, 2005). This is commonly expressed as a vertical range and the associated reference water level the assemblage is assigned, such as mean sea-level (MSL) (Woodroffe and Horton, 2005).

Although Pleistocene sea-level indicators along the KwaZulu-Natal coast are rare, a result of fluctuations occurring close to the current coastline obliterating earlier records (Ramsay, 1996), the following have been found useful:

- *Beachrocks* on microtidal coastlines are good indicators of sea-level due to their formation 0.1 - 0.2 m below mean sea-level (msl) (Ramsay, 1994; Ramsay; 1995). Whole rock dates give a maximum age for sea-level if the skeletal carbonate constituents are contemporaneous (Ramsay and Cooper, 2002).
- *Aeolianites* are useful as long as a contemporaneous beachrock unit is present to constrain the vertical accuracy of the aeolianite unit (Ramsay *et al*., 1993). Martin and Flemming, 1987) also suggested their use with a vertical accuracy of remnant aeolianite cores that is poorly constrained.
- *Fixed biological indicators* such as barnacles, oysters and fossil calcareous tubeworm encrustations are good sea-level index points. Their known relationship to mean sea-level and occurrence in the inter-tidal zone can indicate the contemporary sea-level with accuracy equal to at least the tidal range or even 0.5 m (Ramsay and Cooper, 2002).

Other less accurate indicators that have been used to construct the local sea-level curve includes contemporary coastal wetlands and incised valley fills (Ramsay and Cooper, 2002). Estuarine sequences are usually developed in coastal wetlands and these normally occur within a few metres of sea-level. Woody debris occurring in incised valley fills can be used to indicate sea-level by assuming that river scour is determined by sea-level (Ramsay and Cooper, 2002).

Published original Late Quaternary sea-level curves available for South Africa include Tankard (1976), Barwis and Tankard (1983), Miller (1991) and Compton (2001, 2006, 2011). The sea-level curve (Figure 4.7) applicable to this study was compiled by Ramsay and Cooper (2002) mainly from aeolianites and beachrocks. Although it spans the last 200 000 years, very little data exists for the period preceding the last 120 000 years. In addition, Uranium series ages, which are calendar ages, were plotted with uncalibrated radiocarbon ages. To this extent the Ramsay and Cooper (2002) radiocarbon data (mostly spanning the Holocene transgression) were calibrated and

reinterpreted for comparison with data from this study (see Chapter 9 for methodology). The Ramsay and Cooper (2002) Uranium series age data were not changed.

This relative sea-level (hereafter RSL) curve (Figure 4.7) is broadly similar to that from other regions (Figures 4.5 and 4.6) and thus is assumed to reflect the general eustatic pattern of Late Quaternary sea-level change as recorded in KwaZulu-Natal with sea-level predominantly lower than present for most of the Late Quaternary (Figure 4.7). Ramsay and Cooper (2002) reported three sea-level highstands. The oldest, constituting a record of the penultimate interglacial, represented by one sample only; an aeolianite with associated beachrock unit dated at 182 ± 18 ka B.P, indicating a sea-level (-3 m) close to present level. Chappell and Shackleton's (1986) sea-level curve showed three highstands during the penultimate interglacial (Chapter 3.4.2), the youngest being at 200 ka B.P., also close (-8 m) to present sea-level (Figure 4.6). Although the Ramsay and Cooper (2002) index point has a large error, it most likely represents Chappell and Shackleton's (1986) youngest penultimate interglacial highstand record. No data exists for the Ramsay and Cooper's (2002) curve (or any other curve for South Africa) between the penultimate interglacial (MIS7) and the Last Interglacial (MIS5) (Figure 4.7). This is probably due to the subsequent interglacial events destroying evidence of former sea-levels.

Sea-level and oxygen isotope records from other localities suggest a worldwide sea-level depression of ca. -130 m, constituting the Penultimate Glaciation (refer Chapter 4.4.2). These records indicate very fast deglaciation with sea-level rising from -130 m to +6 m in <12 000 years (refer to Section 4.4.1). McCulloch and Esat (2000) showed that the fast sea-level rise was in the order of 30 - 50 m within 1000 years from 130 ± 1 ka cal. B.P., equating to 80 m of sea-level rise in the final 1 - 2 ka. This is considerably faster than the 7 ka it took during the Holocene. Recently, Waelbroeck *et al*. (2008) constrained the glacial/interglacial transition at 131 ± 2 ka cal. B.P.

According to Ramsay and Cooper (2002) the Last Interglacial in KwaZulu-Natal represents the warmest climate for the last 260 000 years and is characterised by two sea-level highstands (Figure 4.7). The oldest or Eemian 'high' (MIS 5e) at ~126 ka B.P. has an elevation of +5 m which is followed by the second highstand at ~100 ka B.P. (MIS 5c) with an elevation of +4 m. The two highstands are separated by a lowstand during MIS 5d of -44 m at 117 ka B.P. which is also represented on Chappell and Shackleton's (1986) sea-level curve (Figure 4.6). The substage 5d sea-level lowstand corresponds to a considerable increase in global ice volume (refer Section 4.4.2; Kukla et al., 2002). When compared to the Ramsay and Cooper (2002) curve, the Barbados data shows that substage 5e is higher than substage 5c (Schellmann *et al*., 2004) with differing sea-level elevations. Carr *et al.* (2010) produced new data constraining the amplitude and timing of

the last interglacial highstand (MIS 5e) along the southern South African coastline which also shows a significant departure from the Ramsay and Cooper (2002) curve (see Chapter 9 for comparison).

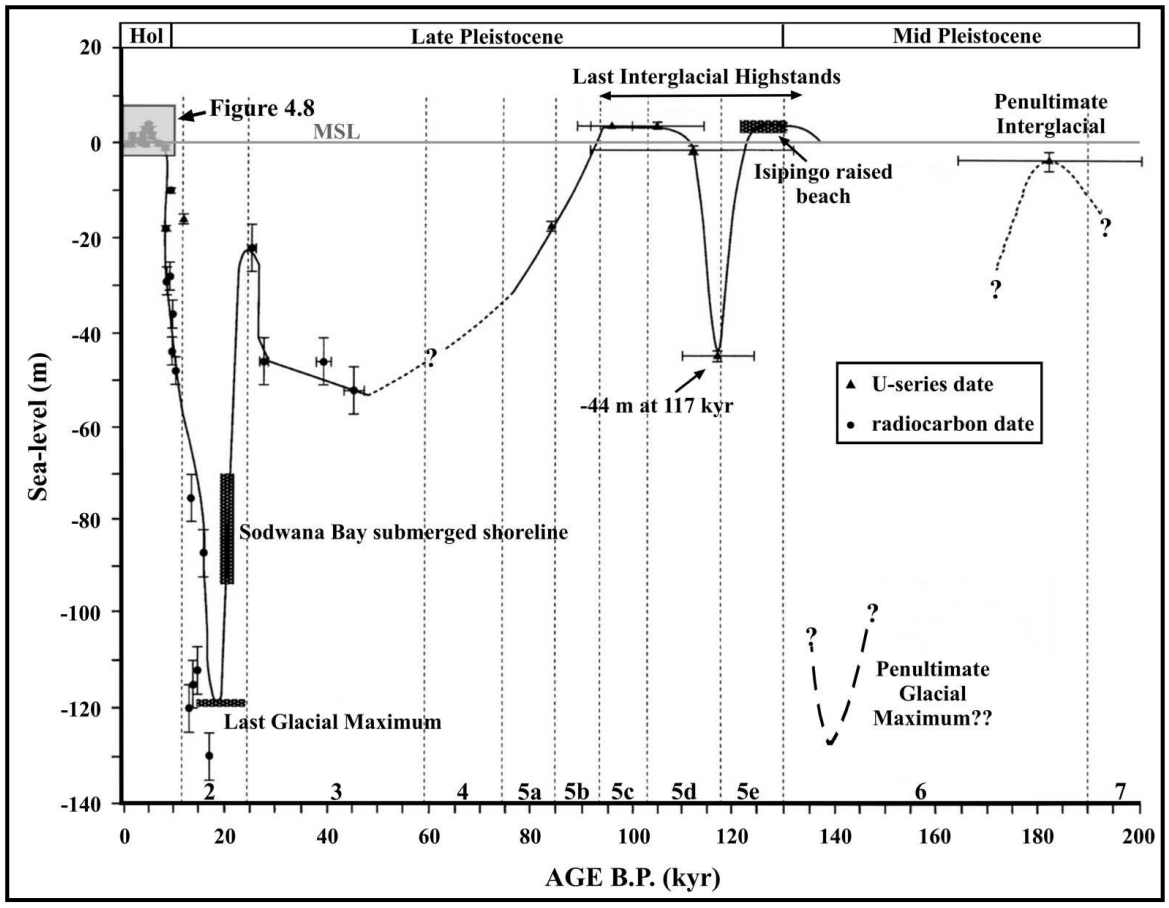

Figure 4.7 Late Quaternary relative sea-level curve for KwaZulu-Natal (from Ramsay and Cooper, 2002). Numbers 2 - 7 refers to the marine oxygen isotope stages (MIS) with substages indicated for MIS 5, Hol = Holocene. A detailed Holocene sea-level curve for the east coast of southern Africa is presented in Figure 4.8. The calibrated and reinterpreted part of the Ramsay and Cooper (2002) sea-level curve spanning the Holocene is presented in Appendix XIV.

According to Ramsay and Cooper (2002) substage 5b highstand ended at ca. 84 000 years B.P. No evidence for sea-levels are available for the period 84 ka years B.P to ~45 ka B.P. (MIS 5a - 4), with sparse data for the latter part of MIS 3, only indicating a general downwards trend towards the LGM (Figure 4.7). Ramsay and Cooper (2002) suggested that this was a period of relative sea-level stability, however, global patterns indicate that this was a period of extreme sea-level instability with rapid sea-level oscillations superimposed on a gradually falling sea-level (refer Chapter 4.4.2, Figures 4.5 and 4.6). Post-Eemian regressions allowed for the formation of

aeolianite ridges (Chapter 3.5.2) such as the Sodwana Bay submerged shoreline sequence on the continental shelf. Although most of these aeolianite ridges remain undated (e.g. Aliwal Shoal) it attests to lower than present sea-levels and in the case of Sodwana Bay, serves to document the progress of the sea-level regression towards the LGM (Ramsay, 1991; 1996).

Corresponding to the global records, the South African evidence similarly shows a rapid fall in sea-level at the end of MIS 3,culminating in the LGM at ~18 ka B.P. with a maximum sea-level depression of between 120 m and 135 m (Green and Uken, 2005) lower than present (Figure 4.7). The maximum LGM depression is controversial because of scarce evidence and varied ice-earth models (Yokoyama *et al*., 2000; Lambeck *et al*., 2002a and Peltier, 2002; Peltier and Fairbanks, 2006). The LGM produced a coastline regression of ~10 km offshore of its present position in the Aliwal shelf area thereby exposing the continental shelf (refer Chapter 2.2.3), revealing pre-existing aeolianite sequences and blanketing these with shifting aeolian sands (Ramsay, 1996). In addition the LGM changed baseline levels rejuvenating rivers and producing deeply incised valleys extending to the outer continental shelf.

As for the Penultimate Glaciation, the post-LGM deglaciation was rapid (Flandrian transgression, 167 cm/100 years; Tankard *et al*., 1982). During the transgression, unconsolidated sediment cover was eroded, exposing and submerging older aeolianite ridges (Ramsay, 1996). Younger coastal lithologies (e.g. beachrocks) and planation episodes, were superimposed onto the pre-existing aeolianite sequences during several sea-level stillstand events which lasted from ~10 - 8 ka B.P. (Ramsay, 1991; 1996). Whether, these should be considered actual sea-level stillstands is debateable. It is more likely that these surfaces are the result of changes in the rate of sea-level rise linked to meltwater discharge (refer Chapter 4.4.2) and climatic events like the Younger Dryas. Deeply incised coastal river valleys, formed during the LGM, were filled with marine, lagoonal and fluvial sediments during the Holocene (Flandrian) or last deglacial transgression (Orme, 1975). Ramsay and Cooper (2002), obtained most of their evidence for the Holocene sea-level rise from back-barrier estuarine fill sequences. In addition, the present east coast dune barrier (up to 180 m high) is postulated to have grown in response to onshore directed high energy sediment transfer during and since the Holocene transgression, sometimes superimposed on remnants of the Pleistocene barrier systems (Orme, 1973).

Ramsay (1995) provided a detailed Holocene RSL curve for the southeast African coast using beachrocks (Figure 4.8). This shows an early Holocene sea-level rise of 8 mm/year between 9 ka B.P. and 8 ka B.P. reaching present sea-level at ~6.5 ka B.P. Sea-level continued to rise, depositing a series of beachrocks at an elevation of 2.75 m above mean sea-level (amsl) between 5 080 B.P and 4 650 B.P. culminating with the mid-Holocene highstand (mH) at 3.5 m amsl at

~4 480 B.P. (Ramsay, 1995). Ramsay (1995) suggested that discrepancy between the predicted ice-earth model mid-Holocene sea-level highstand of +2 m (Clark *et al*., 1978) and +2.5 m (Peltier, 1991) and the observed +3.5 m for the south-eastern African coastline, demonstrated the inadequacies of the geophysical models. He further suggested that the discrepancy is possibly due to higher sea temperatures during the mid-Holocene which may have contributed a steric component and a subsequent volume expansion of the surface waters of the oceans. Following the mHH sea-level regressed to present levels at ~3 380 B.P. whereafter sea-level attained a secondary highstand of 1.5 m amsl at 1 650 B.P. before finally reaching present levels at 900 B.P. (Ramsay, 1995).

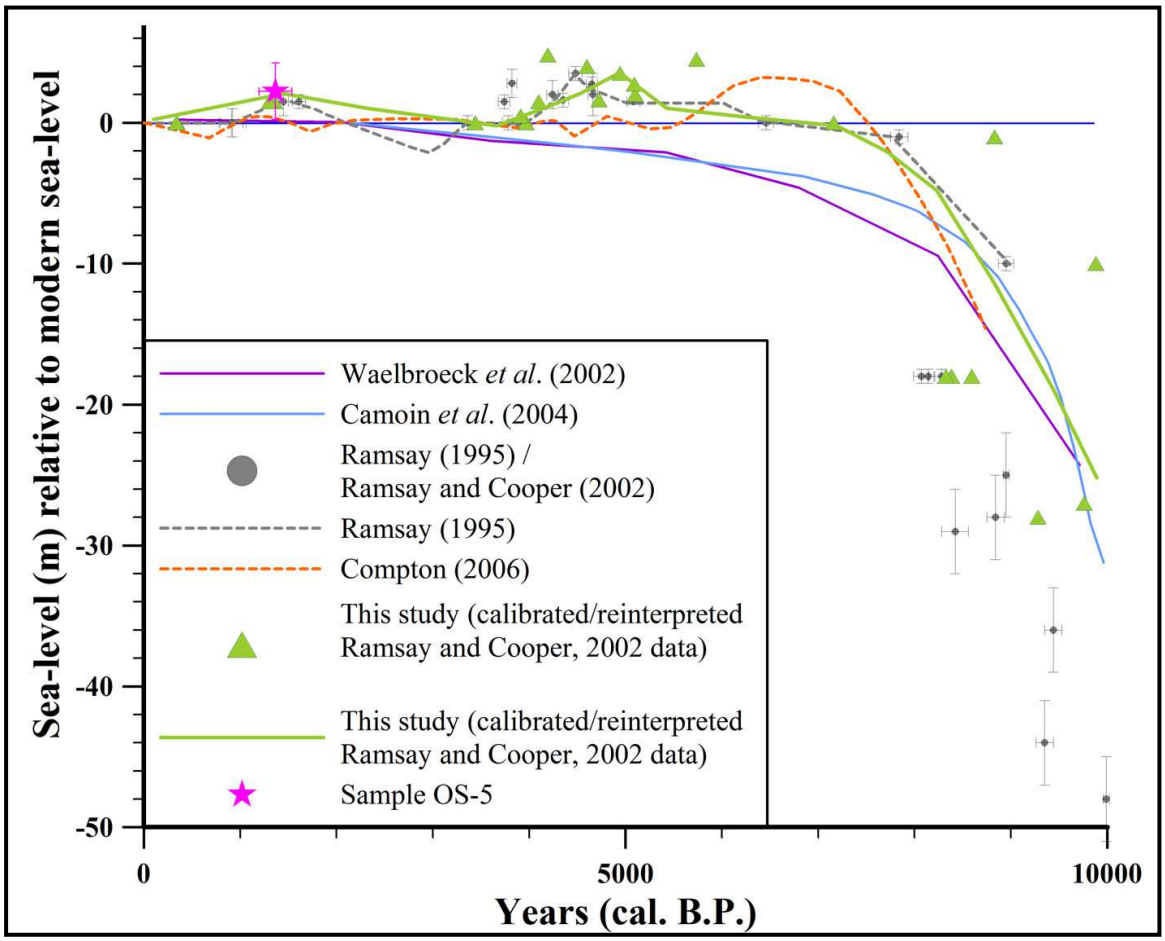

Figure 4.8 Holocene sea-level trends for South Africa as suggested by Ramsay 1995 (adopted by Ramsay and Cooper (2002) for the east coast and Compton (2006) for the west coast. The calibrated and reinterpreted Ramsay and Cooper (2002) data are also presented but without error ranges in the interest of clarity (for error ranges and methodology etc. see Appendix XIV). Despite calibrating the Ramsay (1995) data, significant differences remain between the east and west coast sea-level curves. Also shown for comparison is the global eustatic sea-level curve of Waelbroeck *et al*. (2002) and the postglacial western Indian Ocean sea-level curve of Camoin *et al*. (2004). Sample OS-5 relates to Chapter 9 (Section 9.5.4) and confirms the secondary Holocene highstand observed by Ramsay (1995).

Ramsay's (1995) curve of RSL change along the southeastern African coast departs from the curve of Tankard (1976), Miller et al. (1995) and Compton (2001, 2006; Figure 4.8), especially with regards to the timing and amplitude of the mid-Holocence sea-level highstand. One reason for the discrepancy is that Ramsay's (1995) curve is not calibrated whereas the most recent west coast curve by Compton (2006) is calibrated. However, even the reinterpreted calibrated Ramsay and Cooper (2002) curve (see Appendix XIV for details) differs significantly (Figure 4.8). In essence calibration of the Ramsay (1995) data resulted in a shift towards slightly older values i.e. a mid-Holocene sea-level highstand of 3.5 m was reached at 4943 yr cal. B.P. (4480 yr B.P. in original publication), in agreement with that predicted (3 -5 ka cal. B.P.) for the Western Indian Ocean by Camoin *et al*. (2004). This still is significantly different to the west and south coast mid-Holocene sea-level curves. These show a highstand peak between 7.3 - 5.9 ka cal. B.P. reaching present day levels at ~5500 yr cal. B.P. and oscillating about the present MSL with notable lowstands (~1 m amplitude) at ~4500, 1800 and 700 yr cal. B.P. (Compton, 2006).

Regional scale (Indo-Pacific region) sea-level variability was also observed by Woodroffe and Horton (2005), where the nature of Holocene sea-level change is generally similar, but with major discrepancies related to the mid-Holocene sea-level highstand. As is exemplified by the South African scenario, these differences do not disappear when a more local setting is considered and in some cases variation is large along a particular coastline (Woodroffe and Horton, 2005). Camoin, *et al*. (2004) noted that sea-level records from the western Indian Ocean after 7 ka cal. B.P. can be divided into two broad patterns; 1) continental margins and large islands that generally shows higher than present sea-levels between 6 - 4 ka cal B.P and 2) oceanic islands and ocean basin that typically shows either a continuous rising sea-level or a subdued mid- to late-Holocene highstand.

Since South Africa is situated at relative low latitudes (during the Quaternary) it was unaffected by the influence of ice sheets and is deemed a far-field location with small or no glacio-hydro-isostatic effects. Most workers consider the southeast coast of Africa tectonically stable for most of the Quaternary, with no evidence of Late Pleistocene or Holocene neotectonics (Partridge and Maud, 1987; Miller *et al*., 1993; Gilchrist *et al*., 1994; Ramsay, 1995; Brooke, 2001; Bateman, *et al*., 2004 and Woodroffe and Horton, 2005) and sea-level observations are therefore assumed to provide well constrained glacio-eustasy and hydro-eustasy data (Ramsay and Cooper, 2002; Bateman, *et al*., 2004; Woodroffe and Horton, 2005). In addition, Ramsay (1995) collected evidence for Holocene sea-level changes along a 180 km stretch of coastline and did not observe any evidence for Holocene neotectonics. However, recent published GPS measurements by Mather *et al*. (2009) suggests that the southern African plate is undergoing uplift resulting in differential movement along the South African coastlines. The coastline in the vicinity of the study area (east coast) is suggested to be uplifted at a rate of 1.03 mm/yr (Mather *et al*., 2009).

Unfortunately, Mather *et al*. (2009), erroneously, ascribe this uplift as follows '*..the African plate is subject to motion induced by the plate and rebound movement on account of historical glacial ice sheet loading.'*. Notwithstanding the tectonic stability debate, effects of equatorial ocean syphoning, steric expansion and hydro-isostasy on the local RSL change cannot be discarded, especially in the absence of a local isostatic response study. The lack of evidence for neotectonic activity along the east coast does not necessarily preclude any isostatic emergence. On the contrary, it possibly may indicate that in the area of study, the southeast African plate experienced uniform uplift, as is suggested for the east coast at least by Mather *et al*. (2009). If the uplift observation by Mather *et al* (2009) is correct it might explain the difference observed in the level of mHH deposits and that predicted by geophysical models (Ramsay, 1995) and possibly the inconsistent timing and magnitude of the mHH along the South African coastline.

It is clear from the foregoing discussions that sea-level records obtained from a 'far-field' location, such as South Africa, can contribute valuable information regarding the glacial-eustasy and hydro-eustasy functions of the global or eustatic sea-level. However, only through additional sea-level research coupled with an isostatic response study for the African plate can the controversies surrounding Late Quaternary sea-level change along the southern African coast be resolved. Importantly, as stressed by Woodroffe and Horton (2005), such sea-level studies should focus on collecting and reporting sea-level data using a consistent methodology according to standardised procedures.

CHAPTER 5
METHODOLOGY

5.1 INTRODUCTION

The collection of geophysical datasets was central to this study, providing georeferenced seafloor imagery and serving as a baseline map whereupon other data types were then incorporated, such as the detailed seafloor sampling and observation programme. These data were then combined with laboratory analyses and final geological interpretation. Appendix I, complements this chapter, with a more comprehensive review of the theory and application of the different geophysical methods used in this research.

5.2 GEOPHYSICAL DATA COLLECTION

The author collected geophysical data on four surveys which included single beam bathymetric profiling, high resolution side-scan sonar and boomer seismic profiling (Figure 5.1) A total of approximately 258 line kilometres of geophysical data were collected using a range of vessels (Figure 5.2) between March 2001 and February 2002 (Table 5.1).

5.2.1 Navigation and Coordinate Systems

Survey Positioning

Navigation and position fixing during the geophysical surveys were provided by a Fugro Omnistar 12 channel differential Global Positioning System (DGPS) Operating in the differential GPS mode, the system has a one-second update rate and sub-metre accuracy. DGPS co-ordinates were downloaded, in real time, onto a Pentium notebook computer via a RS-232 serial cable using a programme called *Navlog*. This program performs two main functions; firstly it acquires, distributes, transforms and synchronises incoming positional data, and secondly it provides a heads up display allowing the user to steer the vessel along a predetermined survey track line by displaying the vessel position in real time.

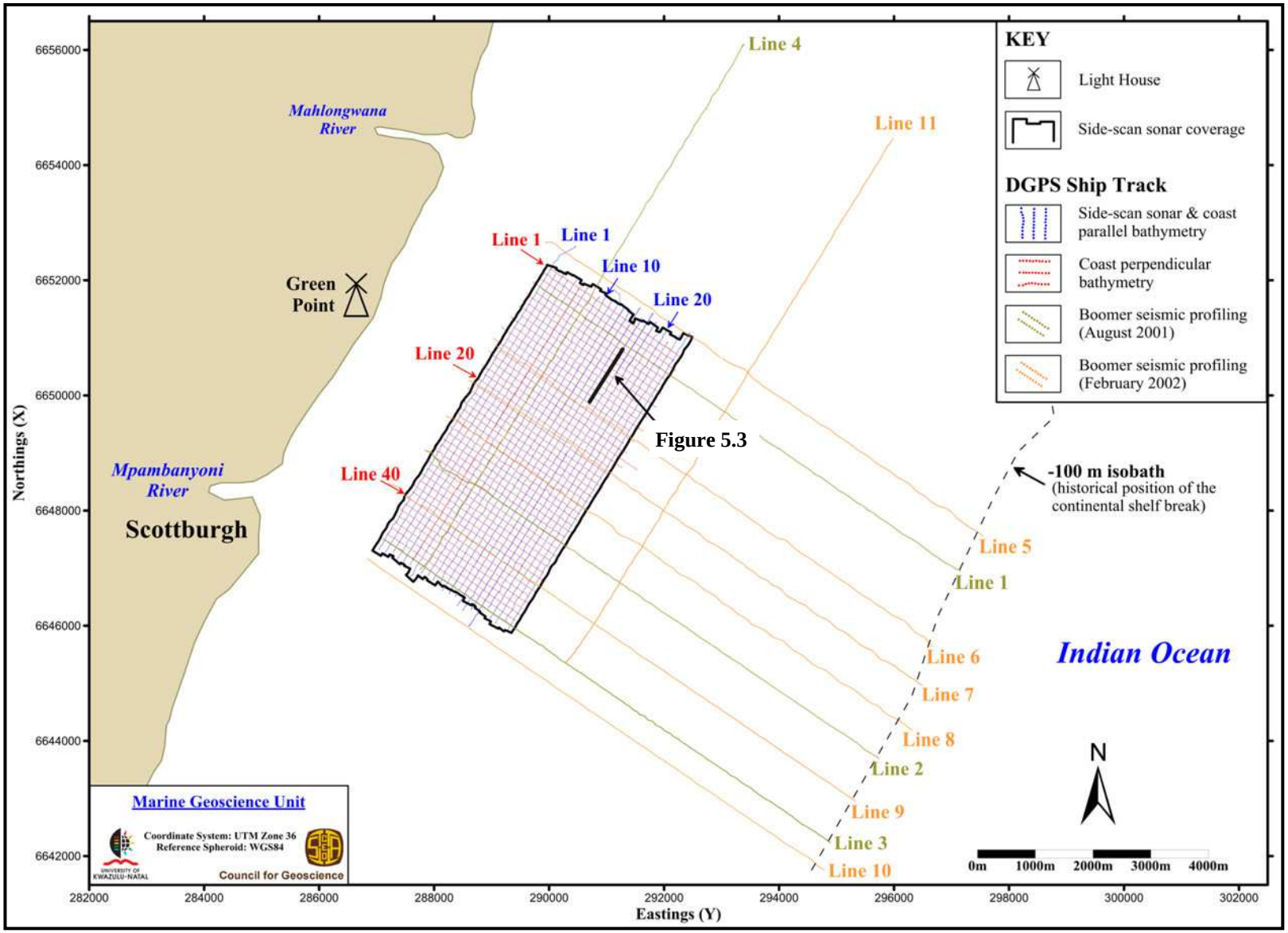

Figure 5.1 Ship track chart derived from the Differential Global Positioning System (dGPS, see Appendix I) navigational fixes for the various instruments used during the various Aliwal Shoal seafloor geophysical survey campaigns.

Table 5.1 Summary of geophysical surveys undertaken on the continental shelf in the vicinity of the Aliwal Shoal.

Cruise	Vessel	Data Acquired	Line Kilometres
March 2001	*Subtech Surveyor*	Side-scan Sonar & coast parallel bathymetry	~132 km
June 2001	*Tethys*	Coast perpendicular bathymetry	~80 km
August 2001	*SAS Umhloti*	Boomer seismic profiling (& derived bathymetry)	~39 km
February 2002	*MV Ocean Mariner*	Boomer seismic profiling (& derived bathymetry)	~69 km

Figure 5.2 Vessels used to collect the geophysical data for this study. i) Subtech Surveyor, ii) Tethys, iii) MV Ocean Mariner and iv) SAS Umhloti. The skiboats *Tethys* and the *Subtech Surveyor* were used because of low cost, suitability for beach launching and rapid deployment.

Coordinate System

The DGPS receives positional data on the geodetic datum WGS84 in latitude and longitude. Since degrees of latitude and longitude do not have a standard length, it is not possible to measure distances or areas accurately or display the data easily on a 'flat' map (Appendix I) and depending on scale, a geographic coordinate system is not ideally suited for geological mapping. For this

reason most maps are produced by using a projected coordinate system. All (unless otherwise stated) processed data and maps presented in this study are projected using the Universal Transverse Mercator (UTM) projection, Zone 36 South (Central Meridian 33° East) on the WGS84 spheroid. For a detailed review of DGPS and coordinate systems the reader is referred to Appendix I.

5.2.2 Single Beam Echo-Sounding

Single beam echo-sounding data were collected during two sea cruises (Table 5.1). The first bathymetric dataset was collected with side-scan sonar (Figure 5.1). Since the optimum tow configuration for side-scan sonar is parallel to bathymetric contours, the orientation of the survey lines was constructed parallel to the coast, which is also parallel to the geological features (Figure 5.1). A second set of bathymetry data was collected perpendicular to the first set for tie-line purposes (Figure 5.1). Combined, these two datasets represent the core of the high resolution bathymetry survey of the Aliwal Shoal. A third bathymetric dataset was derived from two boomer seismic surveys (Figure 5.1). These data covered areas of previous surveys and extended across the continental shelf to beyond the shelf break (Figure 5.1). A detailed description of acquisition and instrument settings for all the bathymetric data is documented in Bosman & Leuci (2001) and Bosman (2003b).

An Odom Echotrac Model 3100 single frequency, digital survey echo-sounder was used to collect the bathymetric data during the survey. The narrow beam (10°) transducer has an operating frequency of 200 kHz and is capable of sounding rates of 20 pulses per second in shallow water surveys. Accuracy is 0.01 % of total water depth, dependant on the accuracy of the velocity of sound value (Odom, 1991). Pulse length is a function of frequency, output power and scale width but the range for the system is between 0.07 to 0.2 milliseconds (ms). The echo-sounder transducer was mounted on a retractable stern mounted bracket. Digital outputs were made via an RS-232 connection with a baud rate of 9600. The survey computer was interfaced to the DGPS and echo-sounder by RS-232 connection and acquired navigation and bathymetry data in ASCII format at 1 second intervals. Analogue charts or echo-sounding profiles (Figure 5.3) were printed by an on-board thermal printer along with annotation which can take the form of automatic event marks or externally generated event marks.

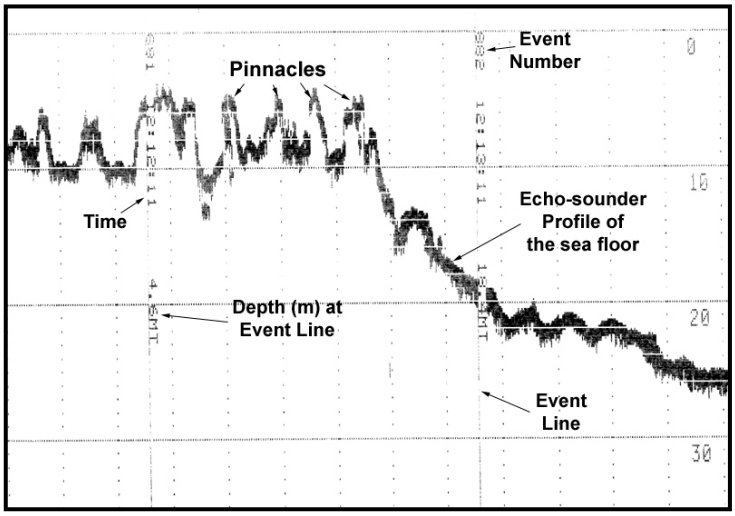

Figure 5.3 A segment of an analogue echo-sounder profile. Note the pinnacles and steep drop-offs. Profile is a segment of line 16, refer to Figure 5.1 for locality.

The analogue record was annotated at 60 second intervals, displaying a unique event number, depth and time. The echo-sounder was calibrated at the start of each day using the "bar-check" method and the calibrated velocity of sound in the water was recorded for each day. The effective horizontal resolution (R_h) of the Odom 3100 echo-sounder is calculated at 0.16 m using equations (1) & (2) in Appendix I and by assuming a sound velocity of 1500 ms^{-1} and an average water depth of 26 m for the study area. Theoretically the system with its pulse length range (0.07 to 0.2 ms) can resolve objects between 0.105 m to 0.3 m apart (Appendix I).

5.2.3 Side-Scan Sonar

The Side-scan sonar survey lines (Figure 5.1) were acquired with a scan range of 75 m and a line spacing of 120 m which resulted in a 30 m (27 %) overlap between adjacent swathes. This overlap was needed to ensure a 100 % coverage of the seafloor at all times, even if the vessel deviated from its predetermined survey line. Survey lines were coast parallel coinciding with the trend of the Aliwal Shoal complex. This configuration is optimal for side-scan sonar requiring minimum tow cable layback changes over the features. A Klein System 2000 digital side-scan sonar was used (Figure 5.4) with an 8 channel (4 sonar channels - Table 5.2), dual frequency (simultaneous 100/500 kHz) capability collecting high resolution image-corrected acoustic data. The topside processor (TSP) incorporates a digital Exabyte drive, a high resolution printer and a full colour (800x600 dpi) video display (Figure 5.6). Sonar data are recorded on a digital exabyte tape drive capable of storing up to 7 Gigabytes of compressed data which translates into five to seven hours of data collection, depending on the scan range. Analogue sonographs were printed in 256 level greyscale using a high resolution (300 dpi) thermal printer.

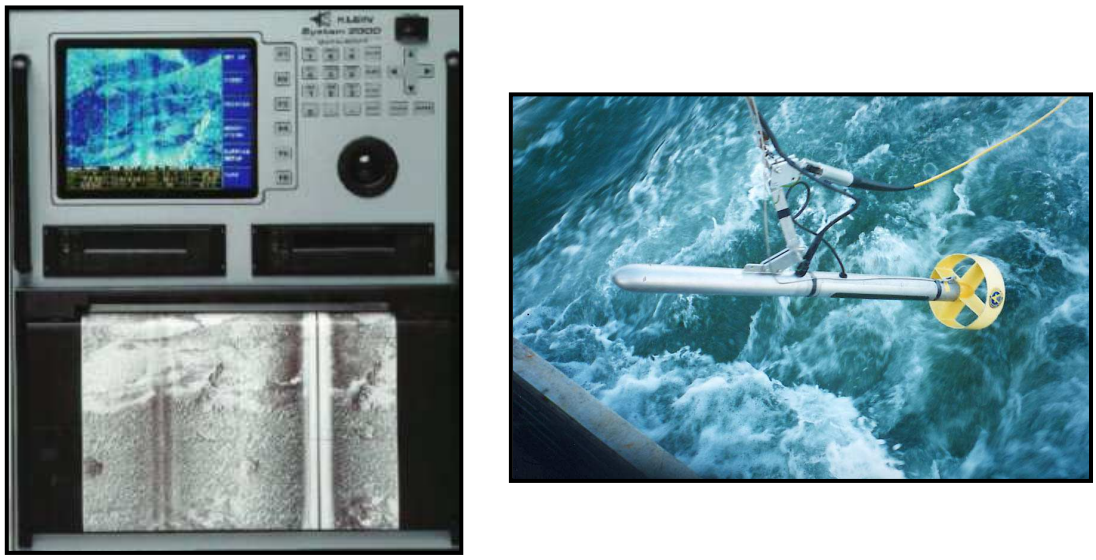

Figure 5.4 The Klein System 2000 side-scan sonar system, consisting of a topside processor (left) and digital towfish (right).

Table 5.2 Channel allocation for the Klein System 2000 side-scan sonar.

Channel	Assignment
1	100kHz – Port
2	100kHz – Starboard
3	500kHz – Port
4	500kHz – Starboard
5	Instrument Telemetry
6	Not Used
X	Auxiliary Channel – external input
S	Sub-bottom Profiler

The Klein sonar system has a 1° beam angle for the 100 kHz frequency and a 0.2° beam angle for the 500 kHz frequency. Pulse width ranges from 25 μs to 500 μs and is either set on the default value for the scan range or is user selectable. Bandwidth for the 100 kHz ranges from 115 - 135 kHz and for 500 kHz ranges from 380 - 420 kHz. A 150 m polyurethane Kevlar reinforced tow cable was used to tow the digital towfish. Towfish altitude was kept at a recommended 20 % of the scan range (15 m), unless seafloor topography dictated otherwise. Towfish transducers were tilted downwards at 15° from the horizontal to minimise surface return echoes. Survey speed was kept between 3.5 and 6 knots, with an average of 4.5 knots, to ensure high quality sonar data and high density along-track bathymetric data. An average speed of 4.5 knots translates into a bathymetry data point every 2.3 m on the seafloor. Printed sonographs were annotated every 60

seconds with an event line containing vessel speed, towfish latitude and longitude, time and towfish altitude. Layback for the towfish was calculated using standard layback formula (Figure 5.5) and applying a correction value for the cable catenary factor (Table 5.3) for the tow cable used. A total of 23 side-scan sonar lines were surveyed insonifying an area of more than 18 km^2 of seafloor (Figure 5.1). The theoretical across-track resolution for the sonar data are 0.0796 m with an along-track resolution of 1.31 m (refer to Appendix I).

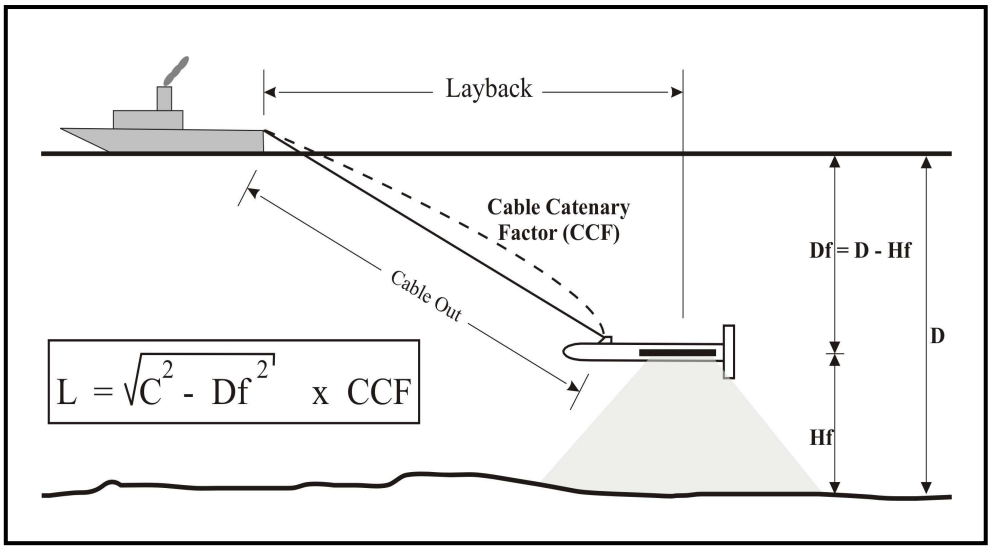

Figure 5.5 Diagram illustrating the calculation of towfish layback (after Klein, 1999). Where L = towfish layback, Df = towfish depth, Hf = towfish altitude and D = water depth. Refer to Table 5.3 for the calculation of the cable catenary factor.

Table 5.3 Catenary correction factors applicable to the tow cable used for this study.

Cable Out	Tow Speed (Knots)					
	1.5	**3.5**	**4**	**5**	**6**	**8**
0 - 30 m	0.85	0.91	0.917	0.934	0.95	0.98
31 - 60 m	0.91	0.95	0.955	0.967	0.98	1.0
61 - 90 m	0.95	0.98	0.983	0.993	1.0	1.0
>90 m	1.0	1.0	1.0	1.0	1.0	1.0

5.2.4 Boomer Seismic Profiling

Two separate seismic surveys, totalling 11 survey lines, resulted in the collection of 108 line kilometres of boomer seismic profiles across the continental shelf in the study area (Figure 5.1; Table 5.1). Boomer seismic coverage was matched length of the sonar and echo-sounding survey

block but extended past the continental shelf break (Figure 5.1). Theoretical background detailing the boomer seismic method is presented in Appendix I. A detailed description of the data acquisition and instrument settings for the boomer seismic profiling is available in Bosman (2003b).

Two vessels were used during the course of the surveys. The first boomer seismic survey was undertaken from a South African Navy vessel, the *SAS Umhloti* (Figure 5.2iv), a 380 ton, 48.1m, River Class Mine-Hunter vessel powered by diesel or electric motors. A wooden hull and the capacity to run "silent" on two Voith-Schneider vertical axis propulsion electric motors, made her an ideal vessel for collecting seismic profiling data. The second boomer seismic survey was undertaken from the vessel *Ocean Mariner* (Figure 5.2iii), a 32.5m steel hull vessel with a displacement of 189 tonnes and a draft of 3.26m. The vessel, powered by a 6 cylinder Ruston Hornsby diesel engine made her acceptably acoustically "quiet". Survey speed was kept between 3.0 - 4.5 knots, and was continually adjusted to optimise the seismic data quality. The instrument configuration, integration and towed array were the same for both of the vessels used during the seismic profiling.

The boomer seismic profiling system used to collect the seismic profiles consisted of the following:

- Applied Acoustic Engineering Model CSP1000 seismic energy source.
- Design Projects 500 Joule (J) MaxiPulse boomer aluminium plate transducer with dedicated catamaran tow vehicle.
- Octopus 360 sub-bottom digital signal processor.
- Design Projects 20 element hydrophone array.

The equipment interfacing for the above mentioned seismic profiling system is schematically illustrated in Figure 5.6.

The Applied Acoustics Engineering Model CSP1000 (Figure 5.6) power supply is a seismic energy source able to deliver up to a 1000 J/second to a source transducer. A 12kV generator provided the power for the seismic energy source, which in turn provided the boomer tow vehicle (Figure 5.6) with energy pulses. The boomer and hydrophone array were towed behind and at opposite sides of the vessel's propeller wash in order to minimise the effect of a direct pulse from the transducer to the hydrophone array, thereby resulting in a 'cleaner' seismic record (Figure 5.7). The Design Projects MaxiPulse 500 J boomer (aluminium plate) produces a short (200 µs), bipolar, stable pulse signature with a centre frequency of approximately 400Hz (Figure 5.8). The transducer plate is spectrally optimised for 500 J and one can effectively trigger the boomer at 500 J twice a second. This system is capable of achieving penetration in excess of 100 milliseconds

(ms) or >75 m. The Octopus 360 sub-bottom digital signal processor controlled all of the data acquisition parameters including the trigger interval, sweep period, sample rate, time variable gain (TVG) algorithms, time variable band-pass filtering and real time signal processing. The trigger rate for the survey was set at 500 ms and was provided directly to the seismic energy source, which in turn triggered the boomer transducer. The boomer was thus fired at an energy level of 500 J every 500 milliseconds (twice/second), translating into a data point or trace spacing of every 1.16 metres on the seafloor (at 4.5 knots). Returned signal traces received by the 20 element hydrophone array were transmitted to the Octopus 360 sub-bottom processor which acquired, processed and stored signals in SEGY format. The data were acquired at a sweep period of 250 ms at a sample rate of 24 kHz.

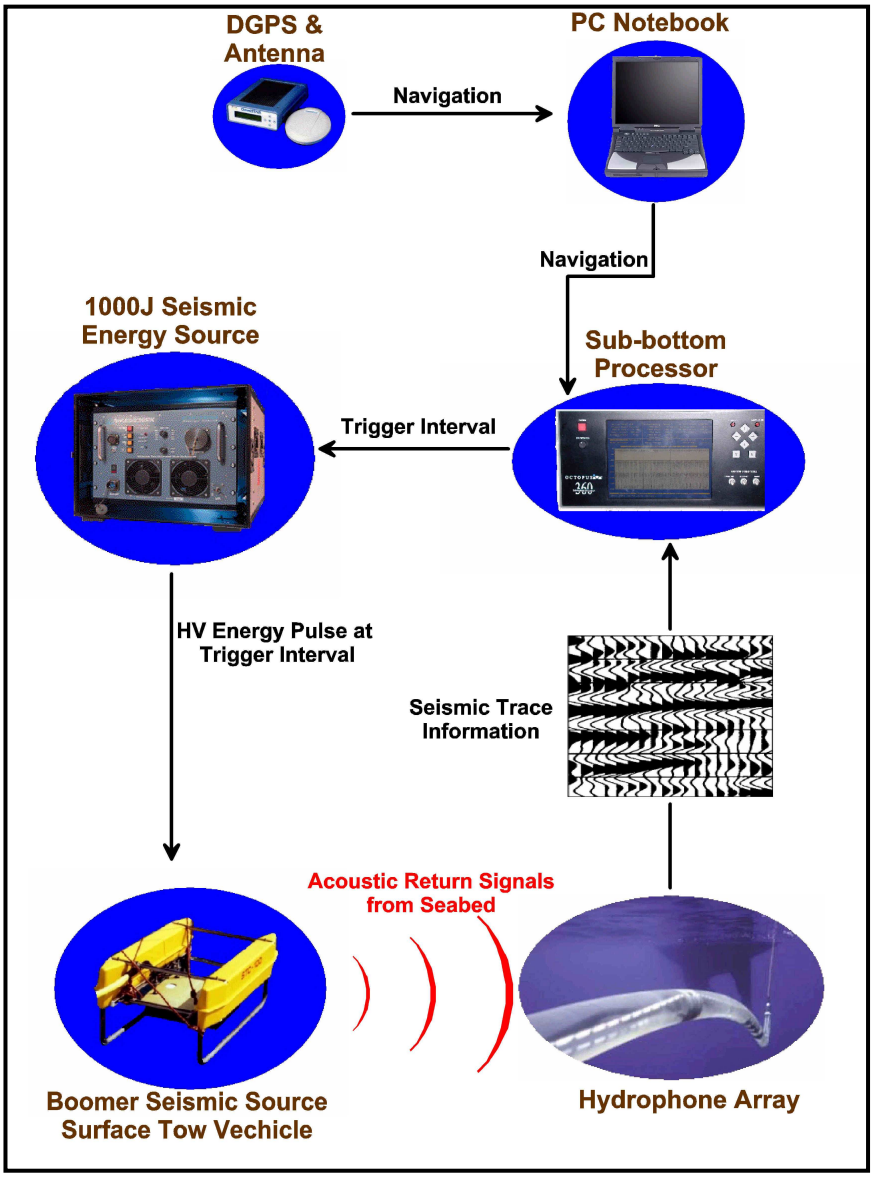

Figure 5.6 Schematic illustrating equipment interfacing for boomer seismic profiling.

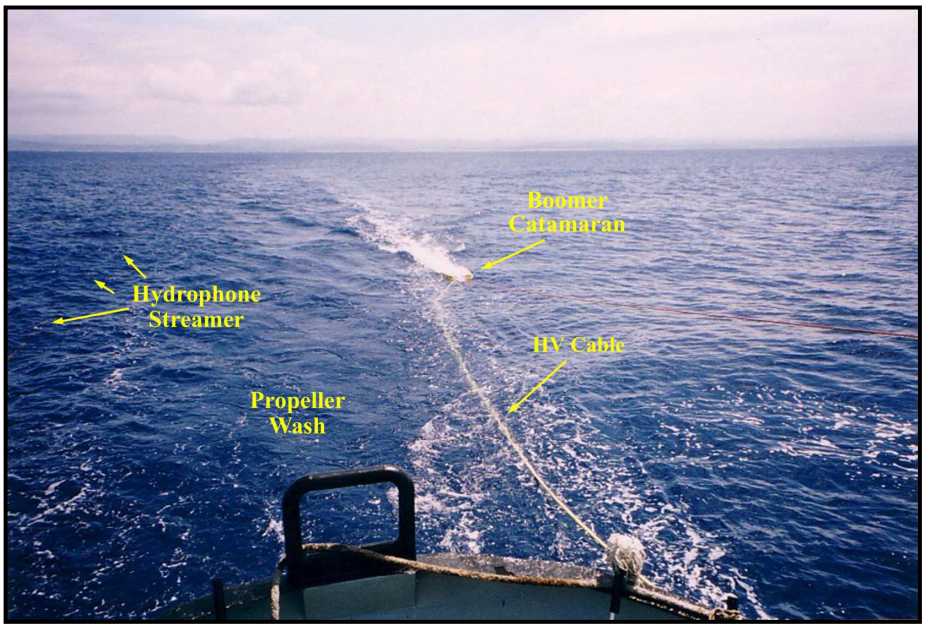

Figure 5.7 Separation between the acoustic source (boomer catamaran) and hydrophone streamer using the acoustic noise (aeration) generated by the propeller wash from the vessel. This separation not only reduces the intensity of the direct pulse from the acoustic source but also aids in diminishing the intensity of the multiples and hence provides cleaner records.

Time varied bandpass filtering was applied to the received acoustic signals at a low pass start of 2000 Hz and a high pass start of 300 Hz. This reflects the "broad band" nature or wide frequency spectrum which is obtainable with a boomer system. Sub-metre accurate navigation data were delivered to the sub-bottom processor from the DGPS via a pc notebook using *Navlog* navigational software. The theoretical vertical resolution (***R***v) for this seismic system is 1 metre (Appendix I). However, from the individual seismic profiles (refer to Chapter 6) it can be observed that the 'bang pulse' and subsequently, the individual reflector packages are approximately 5 - 8 ms in thickness. This translates into a minimum practical resolution of 4 metres (Appendix I).

5.3 GEOPHYSICAL DATA PROCESSING

5.3.1 Introduction

The data processing techniques discussed in this section form part of the standard operating procedure for geophysical data processing techniques developed by Dr. P. Ramsay whilst at the Marine Geoscience Unit for the Council for Geoscience. Processing procedures described in this section are based on the detailed geophysical post-processing manual developed by Ramsay (2001) with later additions by van den Bossche and Bosman (2004).

5.3.2 Bathymetric Data

As discussed in 5.2.2 different bathymetric datasets were collected for this study. This included two single-beam echo-sounding datasets and two bathymetric datasets derived from seismic cruises (Figure 5.1; Table 5.1). Since the methodology for data reduction is different for *collected data* as opposed to *seismically derived data*, these will be discussed separately. Both datasets have the same coordinate system and reference spheroid (Appendix I) with a high positional accuracy. All data were acquired in the Universal Transverse Mercator (UTM) Zone 36 South (Central Meridian 33° East) coordinate system on the WGS84 spheroid. A fifth bathymetric dataset, captured *archived data,* was generated from an unpublished N.R.I.O (refer Chapter 1.5) chart.

Collected Data

The process of producing a bathymetry map consists of several phases from editing the raw data to plotting the final contour map. These phases can be broadly subdivided into two main activities viz: post-processing and gridding and contouring. The purpose of post-processing is to edit the data for any errors that might have been introduced during acquisition, apply post-processing parameters and to attain a standard file format that is both easy to use and easy to transfer between different applications. Data were acquired in a binary format (DLG) containing integrated navigational, depth and time values. Raw binary data files were copied from the survey notebook computer onto a computer at the Council for Geoscience offices. All the original raw data files were archived for safekeeping. This was done not only for data backup purposes but also in the event that for any reason it was deemed necessary to refer to the original data files.

Copied binary files were imported into the integrated navigational software suite, *Navlog*, to correct for any erroneous depth values by using a depth normalizing routine. These depth corrected files were archived and a copy of these files used for the next phase of post-processing, viz. tidal correction. Tidal correction of the data was achieved by using *Navlog*'s tidal correction functionality. Applicable SA Navy South African tide prediction tables (Hydrographic Office, 2001) were imported into *Navlog*. The SA Navy tables give daily predictions of hourly heights of the tide for specific areas in South Africa. As the port of Durban is closest to the field area, the predicted tide tables for Durban were used for correcting the depth data. All the predicted heights are given in metres above Chart Datum, where Chart Datum is standardised as the Lowest Astronomical Tide (LAT) in all ports of the Republic of South Africa and Namibia. LAT is defined as the lowest level, which can be predicted to occur under average meteorological conditions and under any combination of astronomical conditions (Hydrographic Office, 2003).

As LAT is not a practical datum to use all the data were converted to the Land Levelling Datum or, as it is commonly known, Mean Sea Level (MSL). The height of MSL relative to LAT is +1.113m for the port of Durban. The tide corrected files where converted and exported from *Navlog* into ASCII (text) format and then imported into Surfer 7 for final post-processing in spreadsheet format. By using the statistics functionality of the Surfer 7 spreadsheet the data were edited for dilution of precision spikes (dop spikes) and anomalous position readings. After editing all the files for these errors the files were merged into one ASCII format file.

Once post-processing of the data files was completed the corrected merged file was exported in ASCII format into Surfer 7 for gridding. Gridding of data produces a regularly spaced, rectangular array of Z values from irregularly spaced XYZ data i.e. evenly spaced rows and columns. The intersection of a row and column is referred to as a grid node. Gridding generates a Z value at each grid node by extrapolating and interpolating the data values. The data acquired from the bathymetric surveys are considered 'irregularly spaced' data containing areas of no data coverage or 'holes' in the data. Gridding thus fills these 'holes' by extrapolating and interpolating Z values at those locations where no data exists. Several gridding methods are available in Surfer. These methods use weighted average interpolation algorithms (*Surfer 7* manual). This means that the closer a point is to a grid node, the more weight it carries in determining the Z value of the particular grid node (*Surfer 7* manual). A total of 101 433 usable data points were used to generate the bathymetric model. To produce the contour map the data were gridded with a Kriging method, using an octant search, a grid interval of 20 m and a search radius of 180 m. The detailed bathymetric contour map for Aliwal Shoal is presented in Chapter 7.

Seismically Derived Data

Although the seismic system is not a dedicated hydrographical echo-sounder, it produces acoustic signals that can be used to acquire seabed profiles and it is not uncommon to use seismic profiling for bathymetric surveys especially in deep water environments (Jones, 1999). Whereas a shallow water (<-200 m) echo-sounder typically has an operating frequency of 200 kHz, the boomer seismic system has a centre frequency of approximately 400 Hz (0.4 kHz). In all devices that use acoustic signals to acquire data the following relationship applies: the penetration of the acoustic signal into the seabed is inversely proportional to the frequency of the acoustic signal. It must be noted that depending on seabed composition it is possible in some instances for the higher frequency echo-sounder to also achieve limited penetration below the seabed. Thus, by using the echo-sounding properties of the boomer seismic system it was possible to extract seabed depth data from the boomer seismic profiles.

Post-processing of the seismic data to extract bathymetric data is the same as for post-processing of the data to extract seismic profiles. The only difference in the methodology occurs in the final phase of post-processing, or the digitising phase, where the seabed becomes the focus of the digitising and not the sub-bottom layers as per usual. As the post-processing of the seismic data is detailed in Chapter 5.3.4 and the sequence is the same for extracting the seafloor, it will not be discussed any further. Digitised files contained the time, position and seabed depth (m), all of which were corrected for the speed of sound in water/saturated sediment and correcting the navigation for equipment offsets and the depth of the transducer. After application of these corrections the digitised files were exported in ASCII format, tidally corrected to the MSL datum and merged into one XYZ file. Correction of the above mentioned parameters resulted in the digitised data attaining a level of navigational and depth accuracy that is comparable to that of the data collected with a dedicated echo-sounder.

Once post-processing of the data files was completed the corrected merged file was exported in ASCII format into *Surfer 7* for gridding. Gridding methodology is exactly the same as for that of standard bathymetry data previously described under *Collected Data*. A total of 68 646 usable data points were digitised from the boomer seismic survey, producing a contour map from gridded data that were Kriged, using an octant search, a grid interval of 110 m and a search radius of 3000 m. A larger portion of the continental shelf morphology was charted by combining the collected data with the digitised bathymetric data derived from the boomer seismic profiles (Chapter 6). Comparisons between areas of overlap with the collected data show depth compliancy within 1 m. However, the seismic seafloor data are less dense due to the greater survey line spacing and also because of the manual digitizing method. Hence, on integration between the collected data and the seismic derived data, preference was given to the collected data in the areas of overlap. The resultant integrated bathymetric map is thus the best possible resolution that could have been achieved with the available datasets.

Captured Archival Data

Additional bathymetric data were obtained from an archival unpublished map in the form of a 1:10 000 scale hydrographical chart (Figure 5.8). Metadata related to this dataset is limited, but it was surveyed in June 1986 by the N.R.I.O/C.S.I.R on the Lo32 coordinate system (Clarke 1880 datum) and with the depth values reduced to MSL. Contour interval was 1 m with frequent spot depths between the contour lines. Unfortunately no survey track line chart was found which would shed light on the survey line spacing and hence the data density. For single beam echo-sounding it is desirable to have closely spaced survey lines to increase data coverage and bathymetric resolution, but this is not always practical if large areas of seafloor have to be covered. The positional

accuracy of the data are 50 to 200 m and is related to the Decca radar navigation systems used during that period (P. Young, Council for Geoscience, *pers. comm.*). Due to the nearshore location of the dataset, the lower end (~100 m) of the range is preferred. Consequently both the data density and positional accuracy of this chart is inferior to that of the previously discussed datasets.

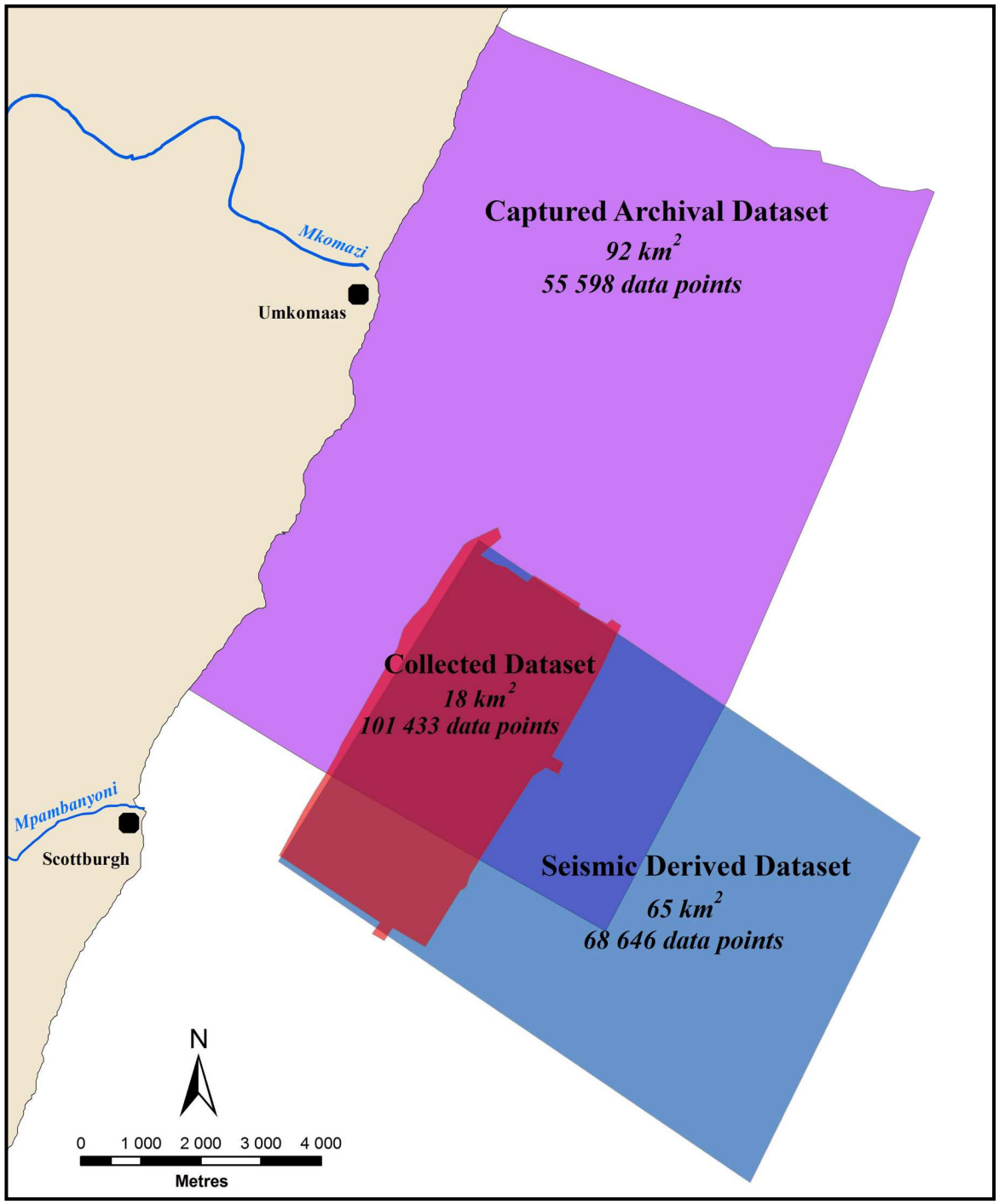

Figure 5.8 Locality map of the captured N.R.I.O. archival bathymetric dataset relative to the collected and seismic derived datasets. Also shown are number of bathymetric data points in each of the coverage areas.

Since the data were in the form of an A0-sized paper chart, the first procedure was to scan the chart into digital format. This was done using an A0-sized scanner from the Architectural Department of the University of KwaZulu-Natal converting the image into TIFF format. The digital image was then imported into *E.R. Mapper 6.1* for georeferencing. A polynomial method with 99 control points was used to georeference the digital image which resulted in very small Root mean square error values (Rms - a measure of spatial accuracy). Small Rms values are indicative of chart consistency and negligible spatial errors due to the paper deformation. Spatial inaccuracies in the chart are thus inherited from the navigation system. Since the surveying coordinate system was different to the one used in this study, the georeference TIFF image was reprojected to the UTM Zone 36S coordinate system on the WGS84 datum. This was achieved using the 'Map to Map Reprojection' utility in *E.R. Mapper 6.1*. For the purpose of this study it was necessary to capture the depth data contained in the map as XYZ values. This was done by digitising the contours and spot depths using Golden Software's *Didger 3* software.

A total of 55 598 data points were digitised covering a depth range from 2 to 70 m below MSL. The gridding methodology is exactly the same as described above for the collected and seismic derived datasets. Data were gridded with a Kriging method, using an octant search, a grid interval of 100 m and a search radius of 3000 m. This dataset was then integrated into the existing datasets. This was achieved by giving priority to the better resolution and positional accuracy data by clipping the captured dataset in areas of overlap. Thus in the areas of overlap, bathymetric data are represented by the collected and seismically derived data. The remaining bathymetric grids were integrated using the grid mosaic tool in *Surfer 8* to produce a final map.

5.3.3 Side-Scan Sonar

Post-processing of sonar data is more complex than for bathymetry data with over 60 Gigabytes of data collected for this study (Figure 5.9). Only a broad description will be given in this section. It is important to note that the processing procedures discussed here are applicable to the time of mosaic production (2001) and have subsequently been slightly modified as set out by van den Bossche and Bosman (2004). Sonar data are acquired in 2KD (Klein 2000) format and stored onto an 8 channel Exabyte tape capable of storing up to 7 Gigabytes of data and printed on thermal paper in real time for backup purposes. The 2KD field data are then download onto a computer using Klein DTS 5000 software which facilitates the conversion of System 2000 tape data to Klein's proprietary 5KD format. The large 5KD format is then converted into Qmips, which is a down sampled, industry standard file format.

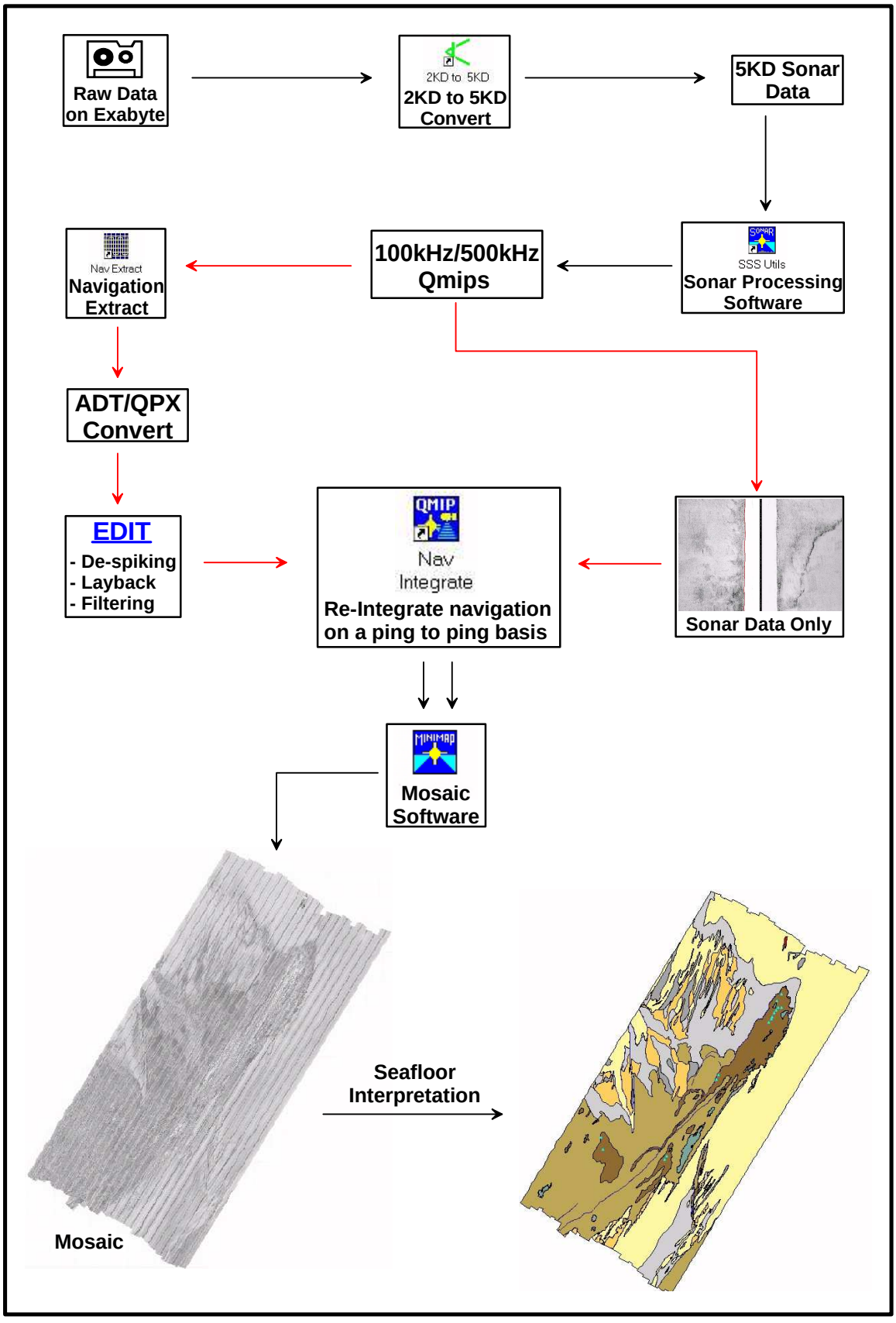

Figure 5.9 Flow diagram illustrating the side-scan sonar post-process procedures.

This is achieved by using a number of modules in the *Navlog* side-scan sonar software suite. The *SS_Kln3* module converts the 5KD file into a 100 kHz or 500 kHz Qmips sonar file which down samples each channel to 1024 data points per channel. This procedure is also used to adjust, bottom tracking, image and data enhancement. Once the sonar files are in Qmips format, the next phase of post-processing involves the extraction of sonar navigation files. These data are written into the 2KD (and thus the 5KD and Qmips) files from the GGA & VTG NMEA sentences sent from the navigation computer. Sonar data records are extracted, edited and then re-integrated using three *Navlog* software modules. Navigational data are extracted from the Qmips files in ASCII (ADT) or binary (QPX) format according to a time selective dump procedure i.e. extraction on a specified time interval e.g. 10 seconds. The editing of files consists of several routines. Navigation data or the track can suffer from jitter, signal dropouts and data mutilations which need to be removed to generate smooth navigation data. Once the navigation files are edited and layback is corrected, data are then re-integrated with the sonar file by replacing the edited navigation data in precisely the correct positions in a new copy of the original sonar data file. This is possible because the navigation fix to ping number relationship is retained throughout all the intermediate operations. The re-integrated sonar files are then inserted into the mosaicing software, *Navlog Mosaic Utilities* to produce a 100 kHz digital side-scan sonar mosaic of the Aliwal Shoal. The digital mosaic was interpreted on an acoustical facies basis and digitised and inserted into a GIS software package to produce a seafloor map of the survey area. A geological map of the seafloor was then produced by obtaining representative samples of each of the acoustic facies (Chapter 8).

5.3.4 Boomer Seismic Profiles

All the seismic lines were interpreted using *Navlog Systems*' *Seismic Data Utilities* software, custom made for the Marine Geoscience Unit. Firstly, all data files were 'bottom-tracked' using the *SegXdp*1 module. This module has an integrated seabed tracking routine and allowed for the position of the seabed to be automatically (and manually) digitised. Seabed position is a critical parameter, influencing the sub-bottom reflector position and subsequent seismic unit thickness calculations. Once all the boomer profiles were 'bottom-tracked' the "*Image DP*" utility was used to enhance and compress the seismic data. Enhancement features include utilities such as TVG (time-varied gain) application, swell correction and filtering. The data were also 'compressed' and 'averaged' to reduce seismic 'noise' and enhance the true seismic signal producing a vertical exaggeration of the seismic line. Basic interpretation was done by digitising seismic reflector terminations and internal reflectors. The "*Interpret*" utility was then used to 'fine tune' the interpretation by obtaining greater detail with respect to internal seismic reflector configurations

and termination patterns. This utility also allowed for applying enhancement features such as TVG, filtering etc. but more importantly allowed the user to zoom into the seismic record and thereby analyse and digitise the section in improved detail. Digitised data were extracted in ASCII format and corrected for the depth of the transducer, antenna and hydrophone array offsets and the speed of sound through water and saturated sediment. Table 5.4 contains the important parameters that were applied to the post-processing of the seismic data. The final correction to the digitised data was that of tidal correction. Applicable surfaces and reflectors were corrected to the MSL datum as required.

Table 5.4. Metadata related to the post-processing parameters for the seismic data.

	Transducer Depth (m)	Bandpass filtering (Hz)		Speed of sound (m/s)	
		Low cut	High cut	Above seabed	Below seabed
Value	0.5	200	900	1500	1650[1]

[1]After Browne (1994).

5.4 SEAFLOOR SAMPLING

5.4.1 Introduction

The primary objective of the sampling program was to collect representative georeferenced rock and sediment samples of all the acoustical facies identified on the side-scan sonar mosaic (Chapter 8) of the study area. Ground-truthing of the acoustic facies was fundamental to the geological classification of the side-scan sonar records. The secondary objective was to collect physical observations of the nature of the seafloor and any geological features present including strike and dip readings from aeolianite and other outcrops, joint readings, sedimentary structures (subaqueous dunes) and palaeosea-level indicators.

The seafloor in the vicinity of Aliwal Shoal is very well suited for SCUBA diving due to the warmth of the water generally good underwater visibility of 10 - 15 m. SCUBA diving ground-truthing and sampling program took 2 years to complete and resulted in the collection of 69 rock and 51 sediment samples. In addition 10 rock samples each averaging ~80 kg were retrieved from critical sites for geochronological analysis. Thus a total of 79 rock and 51 sediment samples were obtained from the Aliwal Shoal and surrounding seafloor.

5.4.2 Sample Site Selection

Sample localities were identified using the high resolution (0.25 m pixel size) side-scan sonar mosaic of the area (Chapter 8). Representative samples from each acoustic facies were prioritized followed by reef sampling transects across the Aliwal Shoal ridge. Both shelf and on-reef sediment samples were obtained. Shelf sediment samples were limited due to the size of the area with a focus on consolidated lithologies (Chapter 8). A sample density of 2.83 samples per km^2 (51 samples/18 km^2) was achieved which compares well to the study of the Durban shelf (Richardson, 2005) where a density of 0.83 samples per km^2 or 118 samples/142 km^2 was used.

5.4.3 Positioning

Since GPS signals cannot penetrate the water column, an alternative method was developed for this study to accurately recored sample positions. The system consists of a Garmin *Etrex* 12 channel splash proof handheld GPS mounted on a weighted float with a transparent plastic waterproof pouch for the GPS and 50 m of dacron rope (Figure 5.10).

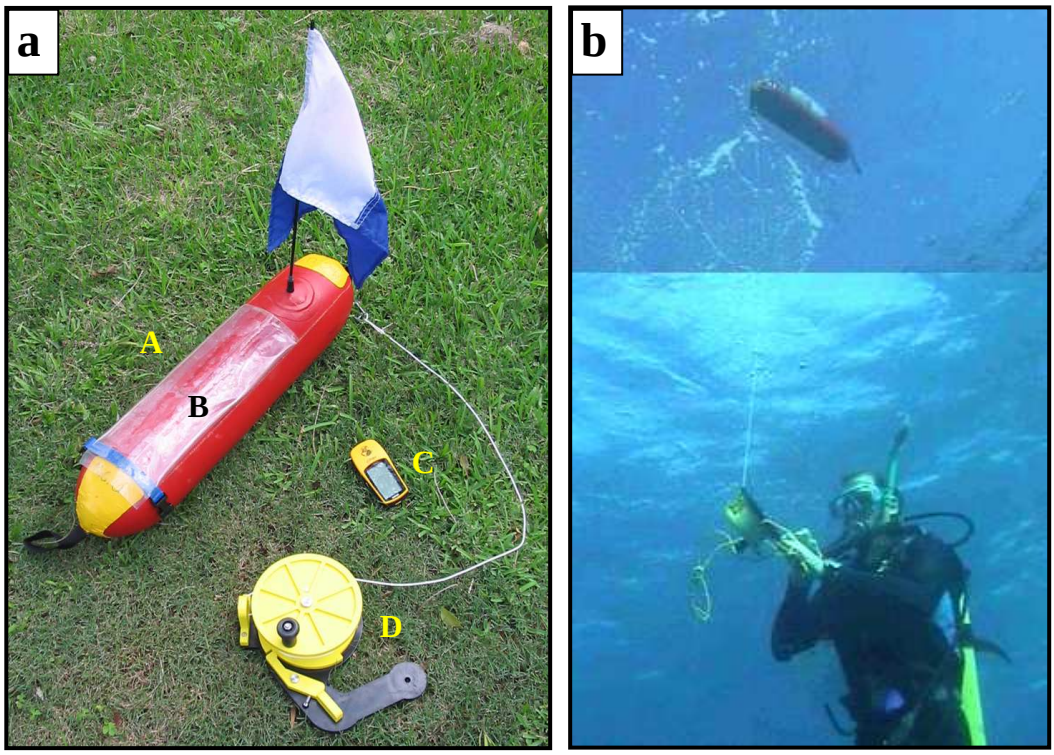

Figure 5.10 **a)** Navigation system devised for seafloor sample positioning (A) Weighted float with Alpha dive flag, (B) waterproof pouch for GPS, (C) Garmin *Etrex* GPS and (D) diver reel and line. **b)** Underwater images of the buoy diver with the hand reel and the float on the sea surface.

To record the dive track and sample positions, all the divers' watches are synchronised with the GPS time. At the dive site, boat engines are switched off and boat drift is recorded with the boat GPS. The dive team enter the water and group together on the surface. The boat skipper activates the tracking function on the GPS float and throws the float overboard. The GPS is now logging positional data every 30 seconds. The dive team descent to the seafloor with member in charge of the reel which connects to the GPS float on the surface. The tether to the GPS float on the surface is kept taut by the diver to keep the float as directly above the dive team as possible but making sure not to submerge the float. Position correction can be made (Figure 5.11) as the depth and the tether length are known. Current velocity and direction is approximated from the drift of the boat established initially.

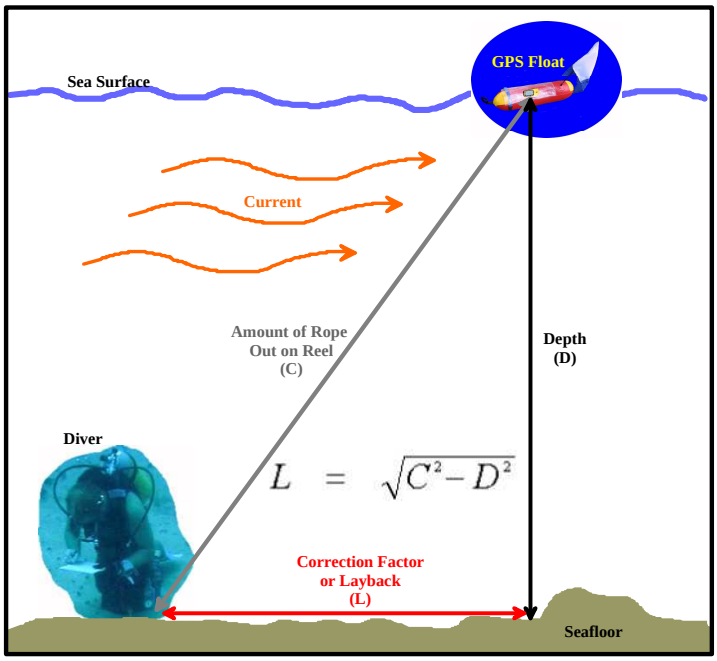

Figure 5.11 A schematic illustration of the procedure followed to correct diver position due to error introduced by currents.

Whenever a sample is taken the time is noted and because the diver's watches are synchronised with the GPS a fairly accurate position can be obtained for the sample. GPS accuracy can be as low as 15 to 20 m. Further error is introduced by current action on the GPS float which, after adjustment using the layback method can be up to 5 m. This translates to a worst case error of up to 25 m. Positional errors can be corrected from diver "tracks" which are plotted onto the high accuracy side-scan sonar mosaic, acquired by DGPS. It is estimated that positional accuracy is between 2 and 5 m for most sample positions.

5.4.4 Geological Observation and Photography

The initial dive team consisted of a four man team, but was increased to a six man team as it was found to be the optimum productive underwater work team for the scope of work. Many tasks had to be performed on each dive which included geological observational note taking (Figure 5.12), video photography, sampling (Figure 5.12) and positioning. A typical dive on the Aliwal Shoal would last between 20 to 30 minutes and for safety and logistical reasons all dives were non-decompression dives. By subdividing the duties, especially the physically challenging activities, an overall longer dive time was achieved for the dive group. At shallow depths it was possible to perform two dives per day, but at depths of greater than 30 m only one dive was done per day.

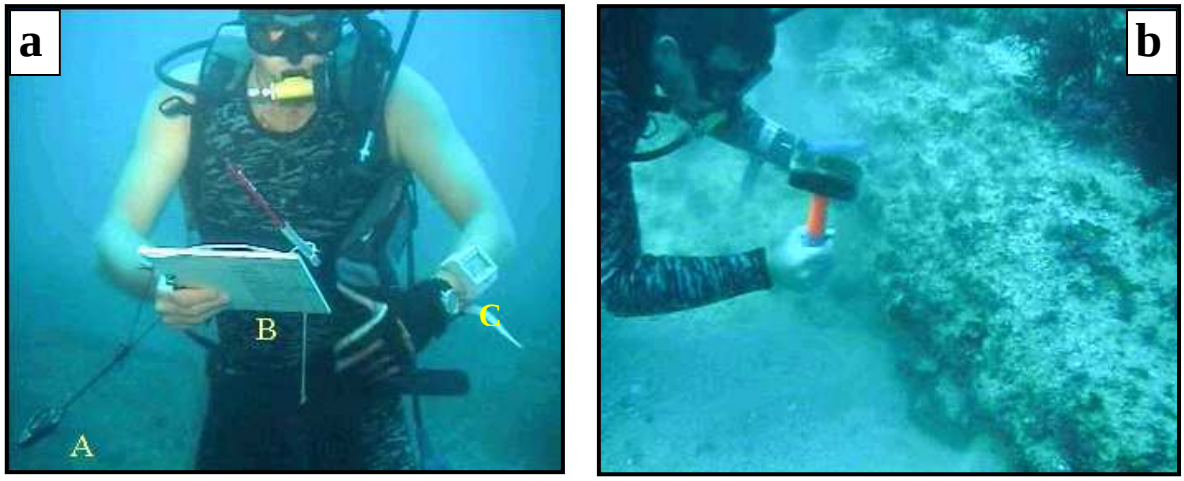

Figure 5.12 Underwater photographs of scientific divers undertaking geological observations and sampling using SCUBA diving. **a)** Observational diver (author) with A) compass-clinometer, B) underwater scribe and C) dive watch and computer. **b)** Sampling diver obtaining a rock sample.

Underwater geological observations were noted on waterproof scribes and azimuth, strike and dip readings were taken using *Silva Ranger Pro* compass-clinometers (Figure 5.12). Each dive was videoed with a digital *Sony* video camera encased in a waterproof housing. Samples were taken at localities picked by the two observational scientists, each accompanied by a dedicated sampling diver. All recordings (sample, geological features etc.), made by the observational scientists had a time and depth entry. The time entry was used to make tide corrections to the depth entry and for synchronisation with the GPS float system. Accurate sample depths are critical for geochronological analysis and palaeosea-level reconstruction.

5.5 SAMPLE ANALYSES - LABORATORY PROCEDURES

All sample analyses, with the exception of the geochronological analyses, were performed using the facilities at the School of Geological Sciences, University of KwaZulu-Natal.

5.5.1 Rock Samples

The laboratory preparation procedure of the rock samples is graphically illustrated in Figure 5.13.

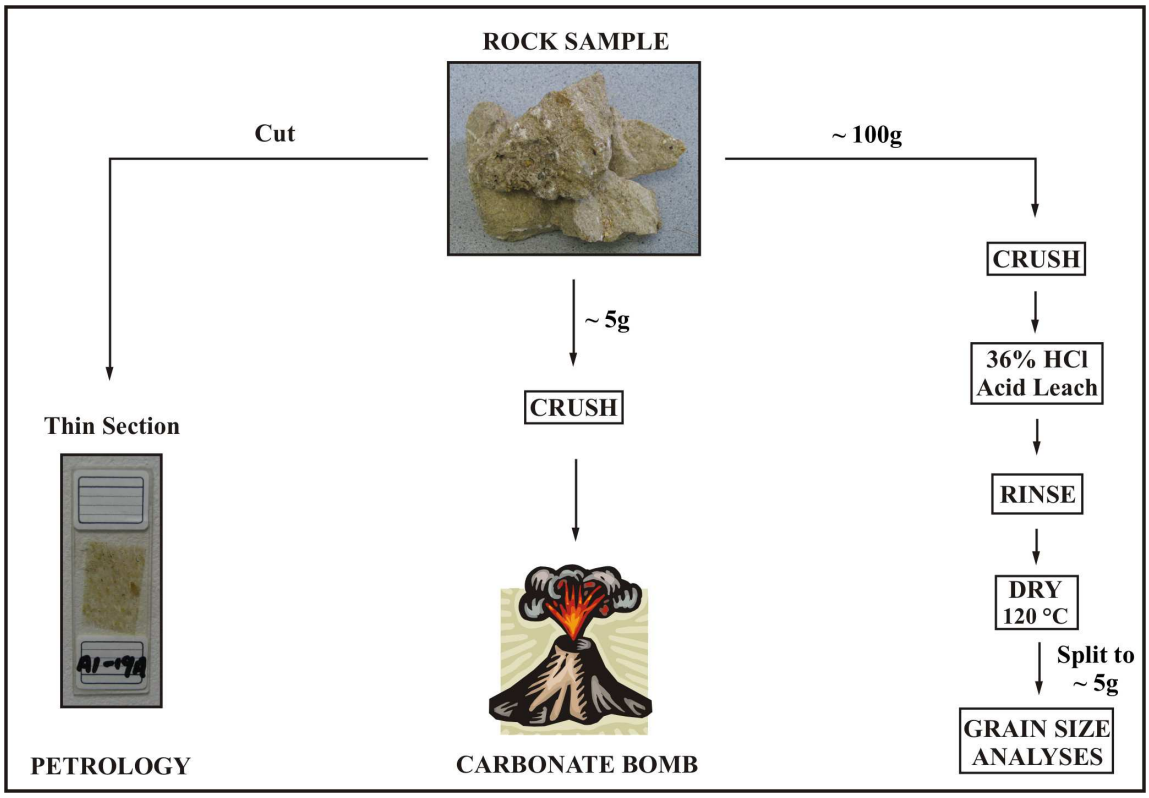

Figure 5.13 Simplified flow diagram illustrating the laboratory procedures for analysing rock samples.

Transmitted light microscopy

Rock samples were sub-sampled for thin section preparation. These were manually cut by the author to maintain sample orientation and integrity. A total of 76 thin sections were made, despite many being very poorly cemented and having a high primary porosity. Differentiating between aeolianite and beachrock lithologies was achieved by combining petrography with observations of primary sedimentary structures and a detailed analysis of the carbonate cement provided a

diagenetic and depositional history for Aliwal Shoal. All geochronological samples (GC-1 to 10) were analysed for lithological composition by point-counting thin sections (average of 419 grains per sample). In addition all samples from Unit A1 were point-counted for control (26 thin sections, total of 8083 grains) whilst the remaining samples were counted by a combination of visual estimation using the comparison chart of Terry and Chilingar (1955) and point-counting.

Scanning Electron Microscopy

All the GC-series of samples were imaged on a Leo1450 scanning electron microscope (SEM) from the University of KwaZulu-Natal's Electron Microscope Unit (EMU). Samples were mounted with carbon tape and gold coated in a vacuum chamber before analyses. The chemical composition of the carbonate phases were analysed using an energy dispersive X-ray microprobe system (EDX) also known as energy dispersive spectroscopy (EDS). Calculation method and results of the mole % MgCO3 of the marine cement phases in the GC-series samples are presented in Appendix VI.

Acid Dissolution

Rock samples were sub-sampled for acid digestion and were acid-leached with 36% hydrochloric acid (HCl) to remove carbonate cement and grains. The cleaned and dried unconsolidated residue was sub-sampled for grain size analyses. Cooper and Flores (1991), Ramsay (1991) and Richardson (2005) all noted that the loss of calcareous grains did not noticeably alter the grain distributions of the original sediment. Nonetheless, this observation is not realistic in, especially the beachrock samples, where carbonate material comprise the coarser grain sizes and as such some differences should be expected.

Grain Size Distribution

Particle size analyses were performed on the digested rock samples to obtain grain size distributions using mechanical sieving. The washed and dried sediment sample from the acid leaching process was thoroughly mixed sub-sampled to ~5 g and sieved trough 10 SABS (South African Bureau of Standards) sieves (2000 µm, 1410 µm, 1000 µm, 710 µm, 500 µm, 355 µm, 250 µm, 125 µm, 90 µm, 63 µm). The size fractionsretained on the sieves was measured on a scale accurate to 0.01 g. Results were plotted on cumulative frequency curves with the grain size parameters derived from these curves used to calculate the median, mean, sorting and skewness

using the methods of Folk and Ward (1957). Results were gridded in Surfer 9 software to produce contour maps for all the major grain size parameters (Chapter 8.4).

Carbonate Content

The carbonate content of the rock samples was determined using a slightly modified version of the 'carbonate bomb' (Schink *et al*., 1978). This method measures the amount of CO_2 liberated by the reaction of HCl with $CaCO_3$. The crushed dried sample is placed in the device which is sealed and into which HCl is added and the release of CO_2 measured on a pressure gauge. The device is calibrated each day by reacting 0.30 g, 0.50 g, 0.85 g, 1.00 g and 1.35 g of analytical $CaCO_3$ and recording the pressure. The resultant 'calibration curve' is used to determine the carbonate content of the sample.

5.5.2 Sediment Samples

The laboratory analyses of the sediment samples are graphically illustrated in Figure 5.14.

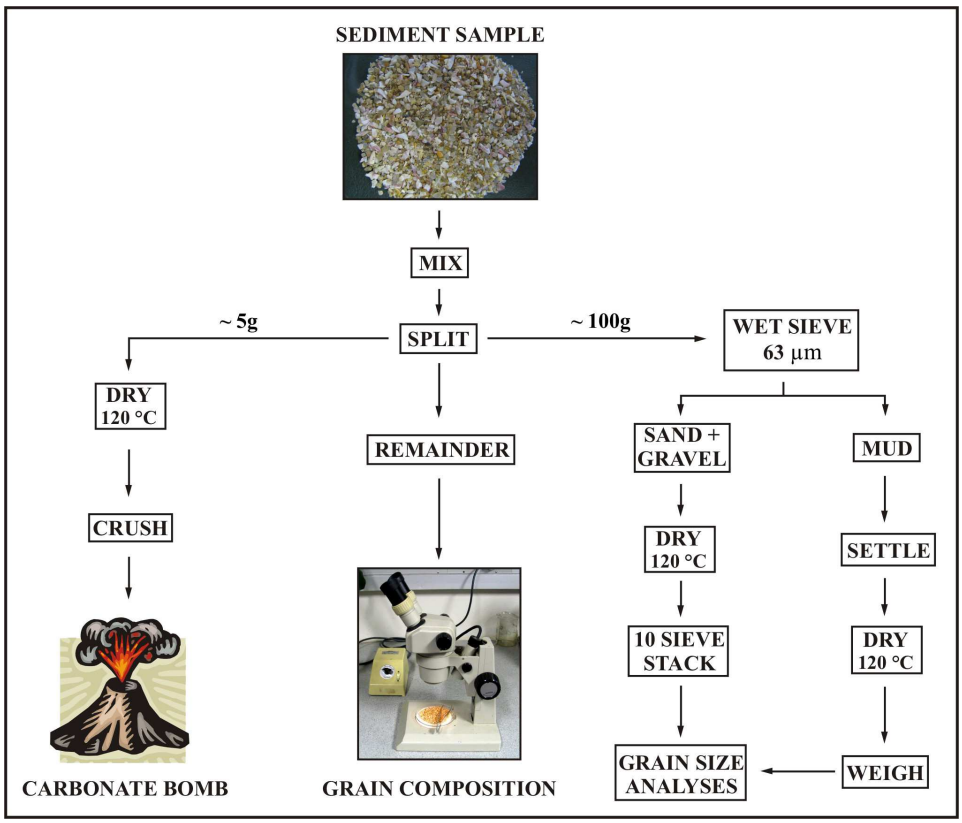

Figure 5.14 Simplified flow diagram illustrating the laboratory procedures for analysing sediment samples.

Grain Size Distribution

As for the acid leached rock samples, particle size analyses of the unconsolidated sediment samples were performed using mechanical sieving. Original samples were thoroughly mixed and by using a splitter sub-sampled to ~100 g (Figure 5.14). Samples were wet sieved through a 63 µm sieve to remove the mud fraction (if present) and to dissolve any salt crystals that might be present. The >63 µm fraction was then dried and dry sieved trough 10 SABS (South African Bureau of Standards) sieves (2 mm, 1.41 mm, 1 mm, 710 µm, 500 µm, 355 µm, 250 µm, 125 µm, 90 µm, 63 µm). Results were plotted on cumulative frequency curves with the grain size parameters derived from these curves using Folk and Ward's (1957) formulae for calculation of median, mean, sorting and skewness.

Carbonate Content

The method for determining the carbonate content of sediment samples is the same as for rock samples (Section 5.5.1 - Carbonate Content).

Petrography

All sediment samples obtained during the seafloor sampling campaign were analysed under a low power binocular microscope to determine grain composition.

CHAPTER 6
SEISMIC AND SEQUENCE STRATIGRAPHY

6.1 INTRODUCTION

Seismic stratigraphy refers to the geological approach applied to the stratigraphic and depositional facies interpretation of seismic sections (Mitchum, 1977; Vail and Mitchum, 1977). It was initially developed in the 1960s and early 1970s by Peter Vail and his colleagues, first at the Carter Oil Company and then subsequently at the Exxon Production and Research Company, as a tool for hydrocarbon exploration and rock unit correlation (Emery and Myers, 1996). The original seismic sequence stratigraphy concepts were devised for siliciclastic sediments in an extensional continental margin tectonic setting and application of these principles revolutionised the science of stratigraphy at the time (Miall, 1997). Since then the concept of sequence stratigraphy has been expanded beyond its original intended purpose and is now more widely used in its application to sedimentary basin analyses including application to drill core sections and surface outcrops (Vail *et al.*, 1977; Emery and Myers, 1996; Miall, 1997; Coe and Church, 2003b). This has led to criticisms of the validity of the method in certain applications (Emery and Myers, 1996; Miall, 1997) but in turn has stimulated further developments and improvements to the technique. Most of the existing controversy surrounds two issues: (1) the notion of the existence of a worldwide sequence framework (globally correlated cycles) and its premise that global stratigraphic successions are primary controlled by eustatic sea-level changes (see Miall and Miall, 2001) and (2) the interpretation of the origins of some types of sequences and sequence surfaces which results in the application of various sequence stratigraphic models (see Coe and Church, 2003b and Catuneanu, 2006).

More recently Catuneanu *et al*., (2009) recommended a standardised set of terms for the often model-dependant nomenclature of systems tracts and sequence stratigraphic surfaces. Although many problems still remain (see Helland-Hansen, 2009; Zecchin, 2010) the validity of sequence stratigraphy, as an indispensable tool in sedimentary basin analysis, and its successful and continued use, is certain.

This chapter presents the seismic stratigraphy and a sequence stratigraphic framework model for the upper continental shelf in the study area. It is supported by limited but significant new geochronological data (Chapter 9) produced from this study.

6.2 PREVIOUS SEISMIC STUDIES

Although deep seismic investigations related to hydrocarbon exploration are common along the eastern seaboard of South Africa, shallow detailed seismic stratigraphical investigations of the continental shelf are limited comprising either regional scale investigations undertaken in the 1980's (Birch, 1996; Martin and Flemming 1986, 1988; Sydow, 1988) or recent detailed but geographically isolated studies (Shaw, 1998; Green, 2009a; Cawthra, 2010). In addition, robust chronostratigraphical ages for the various seismic units from the handful of detailed study sites are lacking thereby further complicating regional correlation between areas already showing highly variable geotectonic evolutionary histories. The particulars of the previous seismic studies relating to the Aliwal Shoal are reviewed below.

6.2.1 Birch's Seismic Stratigraphy

Although superseded by sequence stratigraphic interpretations of the Durban area by Cawthra (2010) and northern KwaZulu-Natal by Green (2009a), Birch (1996) presented the first interpretation (his work was *in prep*. for almost 20 years) of the seismic stratigraphy of the upper continental margin off the east coast of southern Africa in his study of the Quaternary unconsolidated sediments. Line drawings of the seismic section interpretations that are of importance to this study are shown in Figure 6.1a, and an idealised representation of Birch's (1996) seismic stratigraphy is presented in Figure 6.1b.

Birch (1996) identified 4 main seismic units which are denoted as B, M, P and Q for the purpose of this study (Figure 6.1b). The oldest seismic unit identified by Birch (1996) is Unit B which he interpreted as pre-Mesozoic basement strata. Unit B is overlain by Unit M which consists of seaward-dipping reflectors with an apparent onlapping relationship. On all of the seismic sections in Figure 6.1a the geometry of the stratal terminations pattern of Unit M against Unit B is obscured and an apparent onlapping pattern is therefore inferred from adjacent stratal patterns. Birch (1996) interpreted Unit M as a marine sequence of a Cretaceous or Tertiary age. The seaward inclined reflectors of Unit M are easily recognisable on most of the seismic sections and are not only characteristic of Unit M but also confirm the regional distribution of these reflectors. Pleistocene sediments rest unconformably on Unit M. In the diagrammatic representation of Birch's seismic stratigraphy, Unit P is subdivided into two seismic facies viz. P_1 (relict dune ridge) and P_2 (Figure 6.1b).

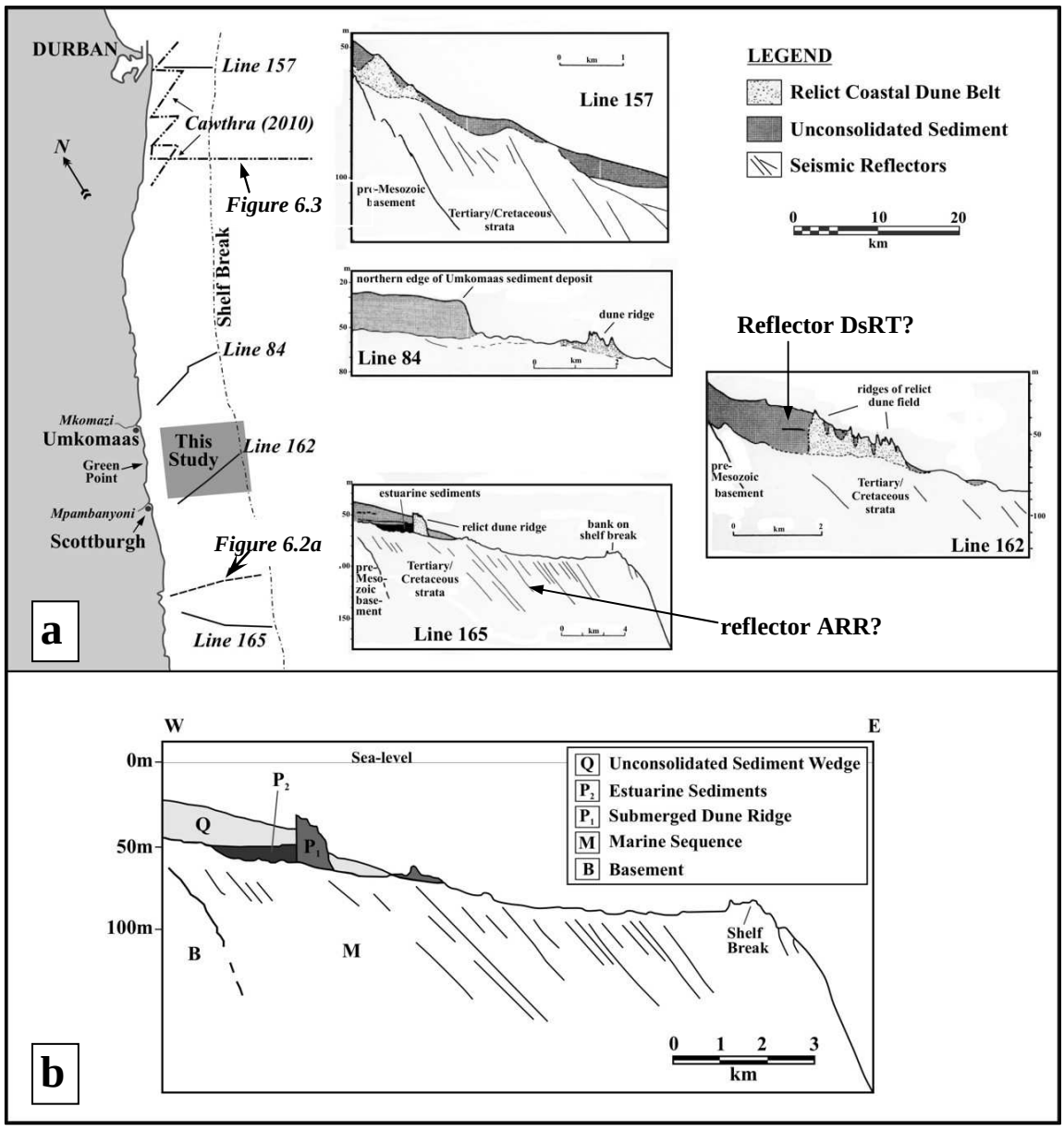

Figure 6.1cont. a) Seismic sections acquired in the vicinity of this study (interpreted line drawings modified after Birch, 1996). **b)** Inferred schematic representation of the generalised shelf seismic stratigraphy for the area between Durban and Scottburgh (compiled from Birch, 1996). For reflectors ARR and DsRT refer to sections 6.3.1 and 6.3.4, respectively.

Facies P_2 was only rarely recognised by Birch which he interpreted - based only on reflector amplitude - to consist of estuarine sediments. As is the case for most of the seismic sections Unit Q also unconformably overlies Unit M and in rare cases Facies P_2 (Figure 6.1a,b). Unit Q is interpreted as the Quaternary unconsolidated sediment wedge and is one of the most easily recognisable units. The thickness of the sediment deposit can exceed 20 m and it is commonly banked against the landward side of the submerged aeolianite ridges on the inner and mid shelf.

6.2.2 Martin and Flemming's Seismic Stratigraphy

Martin and Flemming (1986) presented an interpreted sparker seismic line (Figure 6.2a) which is located north of Line 165 of Birch (1996) and south of this investigation's study area (Figure 6.1a). The similarities between Birch's seismic stratigraphy and Martin and Flemming's are striking. Whereas Birch (1996) recognised at least four seismic units, Martin and Flemming (1986) only recognised three (Figure 6.2a). Unit B of Birch's seismic stratigraphy was not recognised and the oldest seismic unit consists of truncated seaward-dipping strata and was assigned a Palaeozoic to Tertiary or pre-Quaternary age by Martin and Flemming (1986). As for Birch's Unit M, the seaward-dipping reflectors of Martin and Flemming (1986) are easily recognisable and also characteristic, further confirming the regional distribution of these seaward inclined reflectors on the southern KwaZulu-Natal upper continental shelf. This interpreted marine sequence is unconformably overlain by Quaternary formations comprising submerged aeolianite ridge complexes (Birch's Unit P) and unconsolidated sediments (Figure 6.2a). The aeolianites were assigned a Pleistocene age based on micropalaeontological assessments (Martin and Flemming, 1986). The Holocene unconsolidated sediments are banked by the aeolianite ridges (Figure 6.2a) and thus unconformably overlie both the marine sequence and the Pleistocene aeolianites.

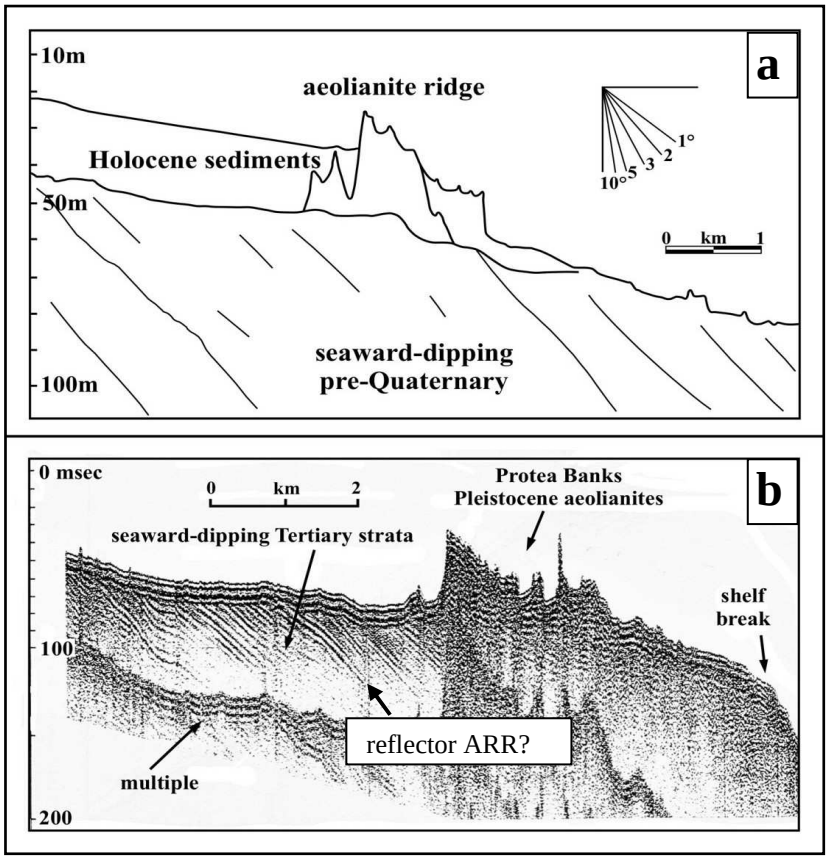

Figure 6.2 a) Interpreted line drawing of a sparker seismic profile collected south of the present study area (from Martin and Flemming, 1986). The location for this line is given in Figure 6.1a. **b)** Sparker seismic

profile of the continental shelf in the vicinity of the Protea Banks, 70 km southwest of the present study area (from Martin and Flemming, 1988). Note that as opposed to **a)**, the seaward-dipping marine sequence is assigned a Tertiary age. Also indicated is a possible reflector ARR which is also identified from the seismic profiles across the Aliwal Shoal. As is the case at Aliwal Shoal, the strata seawards and on top of reflector ARR have a steeper dip than those below. For further details refer to Section 6.3.1.

Martin and Flemming's (1988) sparker seismic line of the continental margin across the Protea Banks (Figure 6.2b) showed only two seismic units (Figure 6.2b); the oldest unit consisting of truncated seaward-dipping strata (Birch's Unit M) unconformably overlain by Pleistocene aeolianites (Birch's Unit P), the seismic units equivalent to Birch's Unit B (pre-Mesozoic basement). However, the equivalent to Birch's Unit Q (Quaternary sediment wedge) is not represented on this section of continental shelf. The seaward-dipping strata are clearly identifiable on the seismic profile, which again confirms the regional extent of this seismic unit. However, whereas this unit has previously been described as a pre-Quaternary or even pre-Cretaceous unit (Martin and Flemming, 1988; Birch, 1996), it is ascribed a Tertiary age by Martin and Flemming (1988). This uncertainty regarding the age of the most common seismic unit on the southern KwaZulu-Natal upper continental margin will be further discussed in terms of the results presented by this study (section 6.3). It is also interesting to note that there seems to be a decrease from north to south of the number of seismic units preserved on the shelf.

6.2.3 Cawthra's Sequence Stratigraphy

Cawthra (2010) undertook a seismic investigation offshore south of Durban and provided a detailed sequence stratigraphic interpretation (Figure 6.3). Although Cawthra (2010) collected data from 8 seismic lines, 7 lines terminated on the mid shelf (above - 50 m) well above the shelf break (Figure 6.1a). Her sequence stratigraphic interpretation (Figure 6.3) is primarily based on one seismic line. In addition to the seismic basement interpreted to be Ecca Group strata, she identified eight seismic units (A-G) assigning these ages ranging from Cretaceous to Holocene (Figure 6.3). Cawthra's (2010) interpretation is comparable to those of Birch (1996) and Martin and Flemming (1986; 1988) albeit more interpretative identifying sequence stratigraphic surfaces such as sequence boundaries (SB), maximum flooding surfaces (MFS) and wave ravinement surface (WRS). Whereas Birch (1996) and Martin and Flemming (1986; 1988) interpreted the truncated seaward dipping strata as one seismic unit, Cawthra subdivided it into four units (A - D) comprising three sequences (1 - 3) ranging in age from Santonian to Late Pliocene/early Quaternary (Figure 6.3). This subdivision of the marine sequence by Cawthra (2010) is not based on any new direct sampling but is based on inference and therefore treated as such in this study.

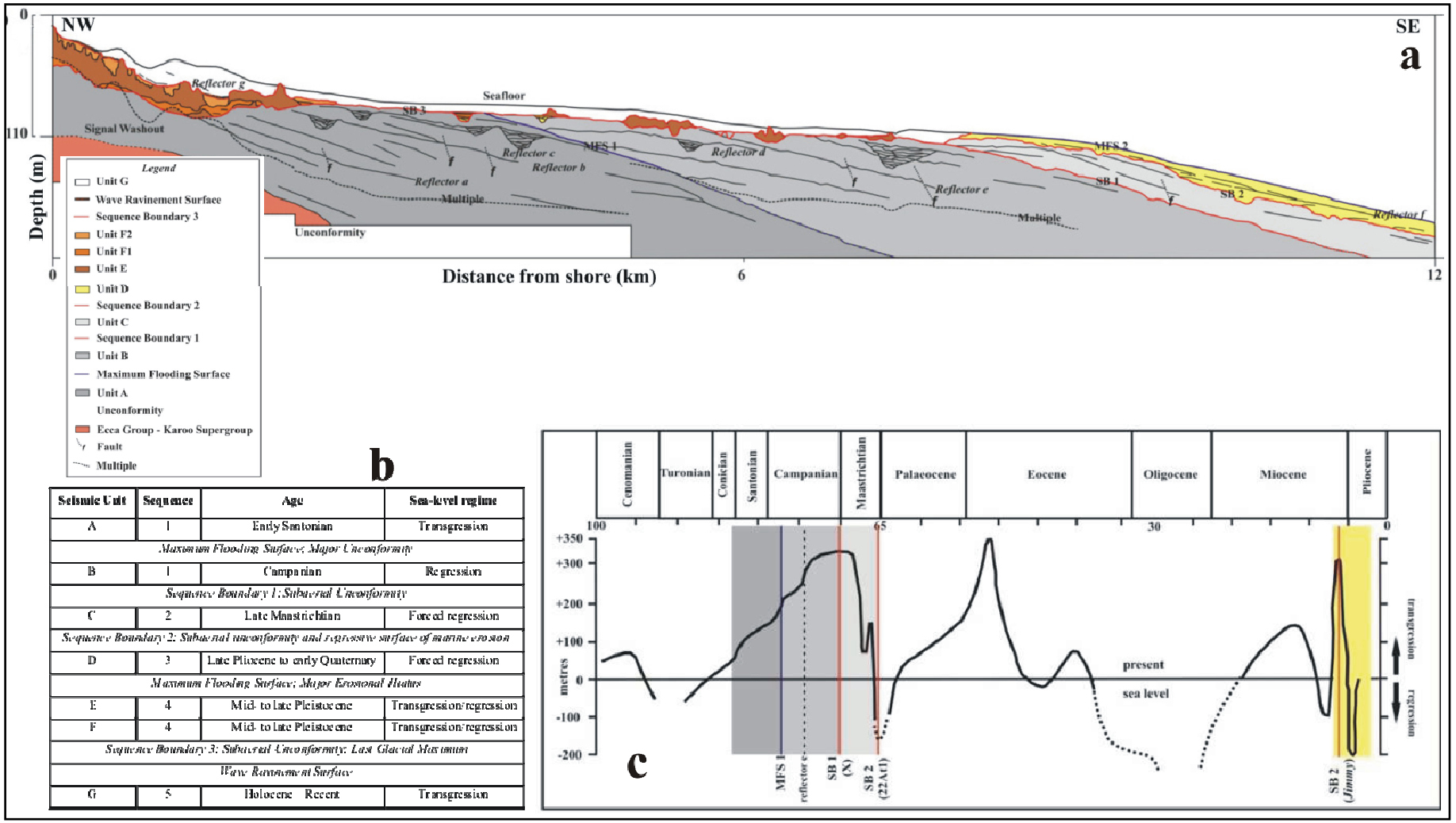

Seismic Unit	Sequence	Age	Sea-level regime
A	1	Early Santonian	Transgression
Maximum Flooding Surface; Major Unconformity			
B	1	Campanian	Regression
Sequence Boundary 1: Subaerial Unconformity			
C	2	Late Maastrichtian	Forced regression
Sequence Boundary 2: Subaerial unconformity and regressive surface of marine erosion			
D	3	Late Pliocene to early Quaternary	Forced regression
Maximum Flooding Surface; Major Erosional Hiatus			
E	4	Mid- to Late Pleistocene	Transgression/regression
F	4	Mid- to Late Pleistocene	Transgression/regression
Sequence Boundary 3: Subaerial Unconformity: Last Glacial Maximum			
Wave Ravinement Surface			
G	5	Holocene - Recent	Transgression

Figure 6.3 **a)** Cawthra's (2010) sequence stratigraphic interpretation for strata located offshore the Durban Bluff (from Cawthra, 2010). Refer to Figure 6.1a for location of the seismic line**.** **b)** Cawthra's (2010) Table 4-2 summarising the sequence- and chronostratigraphic model (from Cawthra, 2010) and **c)** Graphic illustration of Cretaceous and Tertiary sequences and sequence boundaries plotted on the sea-level curve from Dingle *et al*., 1983 (from Cawthra, 2010). SB = sequence boundary. Note that Cawthra (2010) interpreted SB 1 as a subaerial unconformity (see **b** and **c**). This is further discussed in section 6.4.3 below.

This issue is further discussed in section 6.4.3 (Sequence 1). Martin and Flemming (1988) identified a prograding shelf-edge wedge offshore from Durban (not identified from profiles further south) assigning it to a Late Pliocene - Pleistocene age which is equivalent to Unit D of Cawthra (2010). The Pleistocene aeolianites of Birch (1996; Unit P) and Martin and Flemming (1986; 1988) are equivalent to Cawthra's units E and F (Figure 6.3), whereas the Quaternary sediment wedge corresponds to Cawthra's Unit G (Table 6.1)

Table 6.1 Correlation of the major shelf strata recognised by the various seismic studies in the vicinity of the Aliwal shelf. N/R = Not recognised.

Major shelf seismic units	**Birch (1996)**	**Martin and Flemming**		**Cawthra (2010)**
		1986	**1988**	
Sediment wedge	Unit Q; Quaternary	Holocene		Unit G; Holocene
Aeolianite ridges	Unit P; Pleistocene	Pleistocene		Unit E/F; Mid- to late Pleistocene
Shelf-edge wedge	N/R	N/R	Late Pliocene - Pleistocene	Unit D; Late Pliocene to early Quaternary
Seaward prograding strata	Unit M; Tertiary/Cretaceous	Pre-Quaternary	Tertiary	Unit C; Late Maastrichtian Unit B; Campanian Unit A; Santonian
Basement	Unit B: Pre-Mesozoic	N/R	N/R	Ecca Group locally

6.3 ALIWAL SHOAL SEISMIC STRATIGRAPHY

This section describes and interprets the continuous seismic profiles collected in the study area (Figure 6.4). A total of 11 seismic lines were acquired (Figure 5.1) but only five profiles are presented (Figures 6.5 to 6.9) as these adequately display the regional stratigraphy. A 400 Hz boomer seismic system was used which has a theoretical resolution of 1 m, although the practical resolution was ~4 m (Appendix I).

Seismic reflection profiles were interpreted using the established principles of seismic stratigraphy as outlined by Mitchum *et al*., (1977a; b), Mitchum and Vail (1977), Vail and Mitchum (1977), Vail *et al*. (1977), Vail (1987) and Catuneanu (2006). The principles of seismic stratigraphic interpretation as applicable to this study are reviewed in Appendix II. Four seismic units (A to D**)** were identified from the profiles (Table 6.2) based on reflection termination patterns, internal reflection configuration, unconformity or bounding surfaces and external unit geometry.

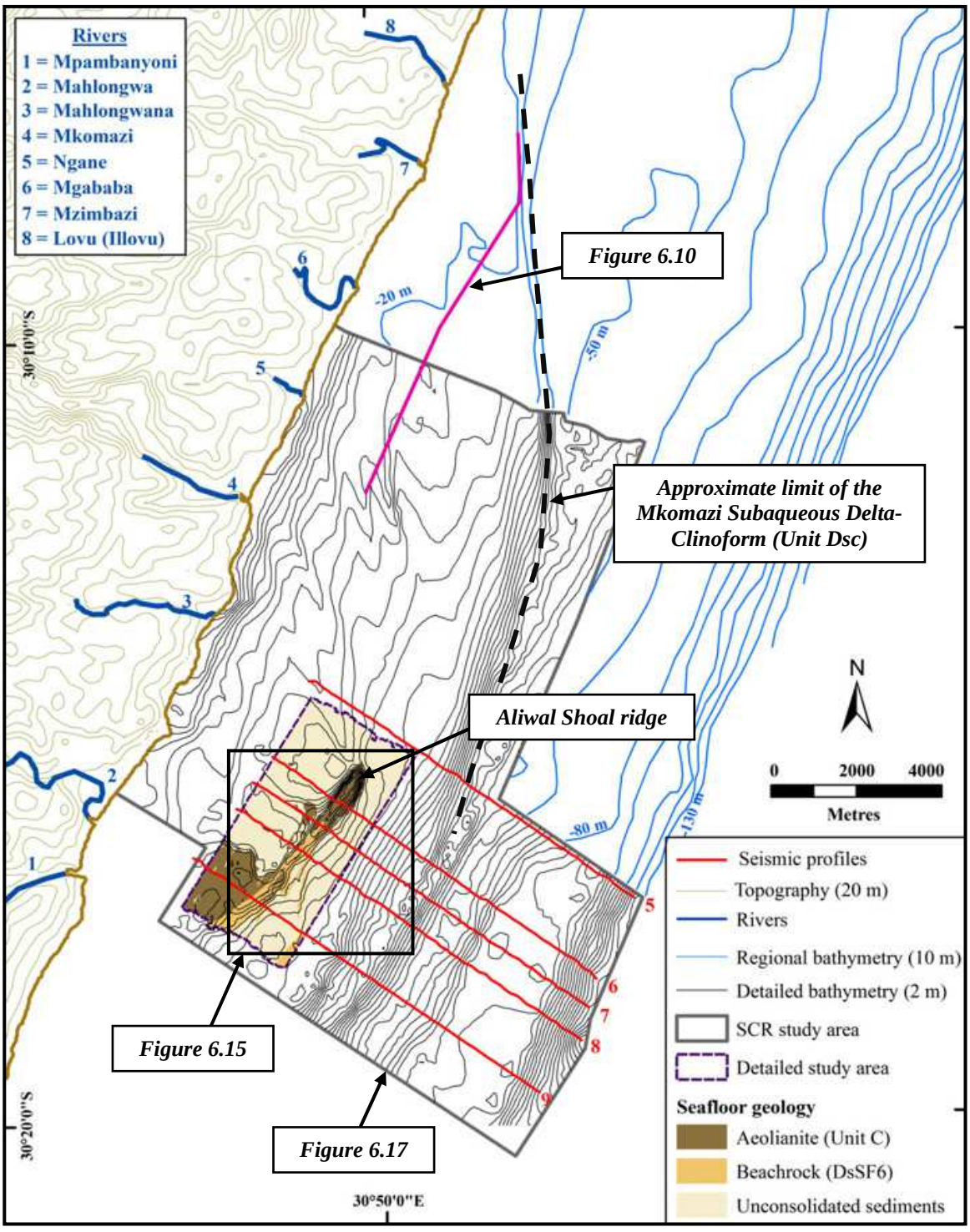

Figure 6.4 Regional setting and location of seismic profiles 5 to 9 used to delineate the shallow shelf stratigraphy. Also shown is the onshore topography, rivers, shelf bathymetry and seafloor geology of the Aliwal Shoal ridge (Unit C) within the detailed study area outline. For more detail regarding the different study areas refer to Chapters 1 and 7. Note the steep hinterland and lack of a well developed coastal plain, the latter of which is in part due to the current highstand sea-level regime. The red numbering refers to the seismic profiles, SCR = shoreface-connected ridge. The contour interval for each respective contoured dataset is listed in brackets in the legend (regional bathymetric dataset courtesy Council for Geoscience).

Seismic unit boundary reflectors formed by unconformities or lateral persistent disconformities were designated **US** and numbered from oldest (stratigraphically lowest) to youngest e.g. **US1** (Table 6.2). Unit D is further subdivided into Dl (landward) and Ds (seaward) based on its location relative to the Aliwal Shoal ridge. Seismic facies resolved within seismic units were designated numbers e.g. seismic facies 2 of Unit Ds is notated as DsSF2 (Table 6.2). Multiple similar superimposed seismic facies were labelled a - x (stratigraphically bottom to top) if present e.g. DsSF2c is the third encounter of facies DsSF2 from the bottom of the sediment pile, where the first would be designated DsSF2a. It is important to note that, although these seismic facies are numbered from a-x, these are not necessarily laterally correlated due to the poor chronological control, lateral facies variation and the fact that an unknown number of facies were possibly removed by transgressive ravinement processes. Facies DSF6 are thin, unresolved middle, outer shelf and slope transgressive deposits mapped for illustrative purposes. Facies DSF6 is correlated to DlSF5 and DsSF6 of Unit D sub-units Dl and Ds, respectively.

Prominently developed and stratigraphically important reflector surfaces present within a specific seismic unit have a prefix comprising the seismic unit and the letter R e.g. reflector a within unit Dl is notated as DlRa. The last preserved transgressive (marine flooding) surface considered to have formed at the specific location during the last-deglacial transgression is labelled surface T e.g. DRT, DlRT and DsRT. Surface DLS is present only on profile 5 (Figure 6.5). Within unit Ds high order or local flooding surfaces are labelled as within-trend facies contacts (WTFC). Even though there is no unique relationship between types of reflection configuration and specific lithology the combination of the internal reflection parameters, the external form and the three dimensional facies associations allows for the reasonable interpretation of the seismic facies units in terms of depositional environment, sedimentary processes and prediction of lithology within the chronostratigraphical connotation of the seismic depositional sequence framework (Appendix II; Mitchum *et al*., 1977b; Mitchum and Vail, 1977). As interpreted in similar settings by Foyle and Oertel (1997), and Green (2009a), the seismic facies assemblages were interpreted to represent depositional environments rather than their constituent lithofacies. Seismic interpretations were supported by published data where possible.

Note that the seismic profile lines are vertically exaggerated and in most instances the vertical exaggeration (V.E.) is approximately 17x and between 6 - 8x for the detailed interpretation of Unit Ds. The reader is advised to refer to each seismic profile for scale.

Table 6.2 Summary of the seismic stratigraphic interpretation of the Aliwal Shoal continental shelf. Unit D, subdivided into Dsc, Dss, Dl and Ds, varies laterally but is considered to have formed contemporaneously but in different palaeo-environmental settings. CEC = central estuary complex.

Underlying surface	Seismic unit			Seismic stratigraphic description	Thick-ness (m)	Seismic facies	Stratal characteristics	Interpreted depositional environment		Inferred age
US3, DLS	**D**		Dsc	Inner to mid shelf prograding sediment body with complex shore-attached bedforms	20-30	-	Very low amplitude, semi-transparent aggrading to prograding clinoforms, downlap DLS in places, overlies Ds, Dl, Dss	Aggradational to progradational subaqueous-delta clinoform		Holocene - Present
DLS				Inner to middle shelf reflector		DLS	Unit Dsc clinoform downlap (apparent?) surface	Localised surface of progradation (local MFS)		Holocene
US3	**D**	Strike variable sub-unit considered contemporaneous to Units Ds & Dl	Dss	Inner to outer shelf sediment deposits	< 14	DSF6	Low amplitude, continuous, sub-horizontal seaward-inclined, parallel to sub-parallel reflectors, onlap Unit C	Foreshore to shallow marine relict transgressive deposits	Trans-gressive shoreface	Latest Pleistocene - Holocene
						DRT - transgressive ravinement surface/marine flooding surface				
						DSF5	Low amplitude, continuous, seaward-inclined to horizontal parallel to sub-parallel reflectors	Paralic/lagoonal-estuarine deposits?	Predominant open shoreline setting	
						DSF2	Low amplitude, channel features with draped fill	Lagoonal/estuarine tidal- and abandoned-channel deposits		
						DSF1	Low/medium amplitude, discontinuous horizontal reflectors	Fluvial (estuarine?) channel fill and floodplain facies		
			Dl	Inner shelf aggradational sediment body dammed landward of Unit C	<10 - 40	DlSF5	Low amplitude, continuous, sub-horizontal seaward-inclined, parallel to sub-parallel reflectors, onlap Unit C	Foreshore to shoreface	Trans-gressive shoreface	Latest Pleistocene - Holocene
						DlRb/DlRT - combined tidal/marine flooding surfaces				
						DlSF4	Low amplitude, discontinuous landward-inclined to sub-horizontal parallel-tangential clinoforms	CEC Dune slump or flank attached bar	Back-barrier estuarine lagoon system	
						DlSF3	Low amplitude, channel features with draped to chaotic to fill, truncated by DlRT	CEC Tidal- and abandoned-channel deposits		
						DlSF2	Low amplitude, continuous sub-horizontal reflectors, truncated above by DlRT	CEC Estuarine facies including tidal- and sand-flats, shoals		
						DlRa - bay ravinement surface?				

			Dl			DlSF1	Low/medium amplitude, continuous horizontal reflectors	Fluvial plain facies?		
US3	**D**		Ds	Middle shelf sediment package with retrogradational landward thickening parasequences entrained progressively southwards between two parallel ridges of Unit C.	<10 - 30	DsSF6	Low amplitude, continuous, sub-horizontal seaward-inclined, parallel to sub-parallel reflectors, onlap Unit C	Foreshore to shoreface, including beachrock deposits	Transgressive shoreface	Latest Pleistocene - Holocene
						DsRT - transgressive ravinement surface/marine flooding surface				
						DsSF5	Low amplitude, continuous, seaward-inclined parallel to sub-parallel reflectors, truncated by DsRT	Paralic deposits	Embayed back-barrier lagoon	
						DsSF4	Low amplitude, mounded reflectors, truncated by DsRT	Lagoonal macroform facies		
						DsSF3	Low amplitude, continuous sub-horizontal to converging reflectors, truncated by DsRT	Lagoonal facies; sand/tidal flats		
						DsSF2	Low amplitude, channel features with draped and onlapping fill, truncated by DsRT	Lagoonal tidal- and abandoned-channel deposits		
						DsSF1	Low/medium amplitude, discontinuous, sub-horizontal reflectors and channel features with chaotic to draped fill	Fluvial (lagoonal?) channel fill and floodplain facies		
US3				Inner to outer shelf reflector		US3	Erosional truncation of Units A, B, C and reworking of US1, US2	Subaerial unconformity surface		Pleistocene
US2	**C**			Inner to outer shelf shore-parallel ridge complexes	<60	-	High to medium amplitude discontinuous, strongly chaotic internal reflectors. Produces characteristic acoustical blanking of underlying strata	Aeolianite and beachrock palaeo-shorelines		Pleistocene
US2				Inner to outer shelf reflector		US2	Erosional truncation of Units A and B and reworking of surface US1 in places	Subaerial unconformity surface		Pleistocene
US1	**B**			Seaward-thickening, shelf edge and slope sediment wedge	≤ 11	-	Low amplitude, high angle (3° - 6°) complex prograding to aggrading oblique parallel to tangential clinoforms. Downlap, onlap onto US1.	Shelf edge wedge		Late Pliocene - early Pleistocene?
US1				Most prominent reflector spanning the entire shelf		US1	Erosional truncation of Unit A	Major subaerial unconformity surface		Palaeocene - Pliocene
Not observed	**A**			Seaward dipping strata present along entire shelf	> 110	-	Dense, high to moderate amplitude, continuous, divergent, parallel to sub-parallel reflectors. Dip gently towards the SE (1 - 2°).	Cretaceous marine sequence		Campanian - Maastrichtian

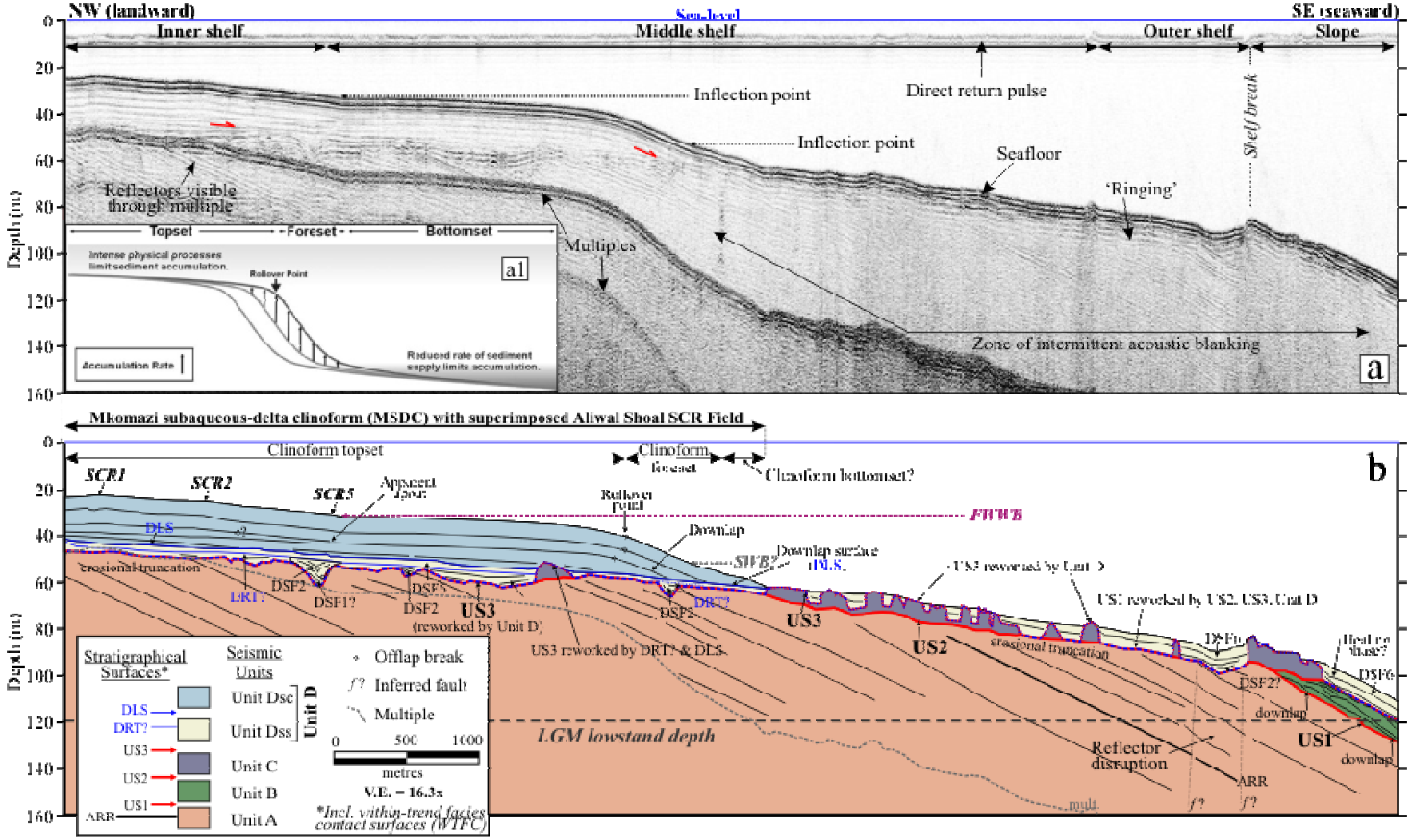

Figure 6.5 Downdip uninterpreted **(a)** and interpreted **(b)** seismic profile for line 5. (**a1**) Cartoon showing the fundamental clinoform architectural elements (from Walsh, *et al.*, 2004). Unit D only includes sub-units Dss and Dsc as the lateral equivalents Dl and Ds are not present on this line. Unit Dsc comprise the *Mkomazi Subaqueous-Delta Clinoform* (MSDC), the topset of which is organised into the Aliwal Shoal shoreface-connected ridge (SCR) system which is dealt with in Section 7.4. Refer to Figures 7.10 and 7.14 for positions of SCR crests 1, 2 and 5. Successive positions of the clinoform rollover point or offlap break indicate an initial aggradational geometry which changed to a progradational geometry. Also shown here are reworked major stratigraphical surfaces which are illustrated to highlight the general relationships and complexity of these surfaces. In the interested of clarity the remaining interpreted seismic sections will only note the major reworked stratigraphical surfaces. The Last Glacial Maximum (LGM) sea-level lowstand is shown to draw attention to the fact that the entire shelf is subaerially exposed during sea-level minima exceeding -85 m below MSL. Mult. = multiple, V.E. = vertical exaggeration, incl. = including, FWWB = fair-weather wave base, SWB = storm wave base, WTFC = within-trend facies contact.

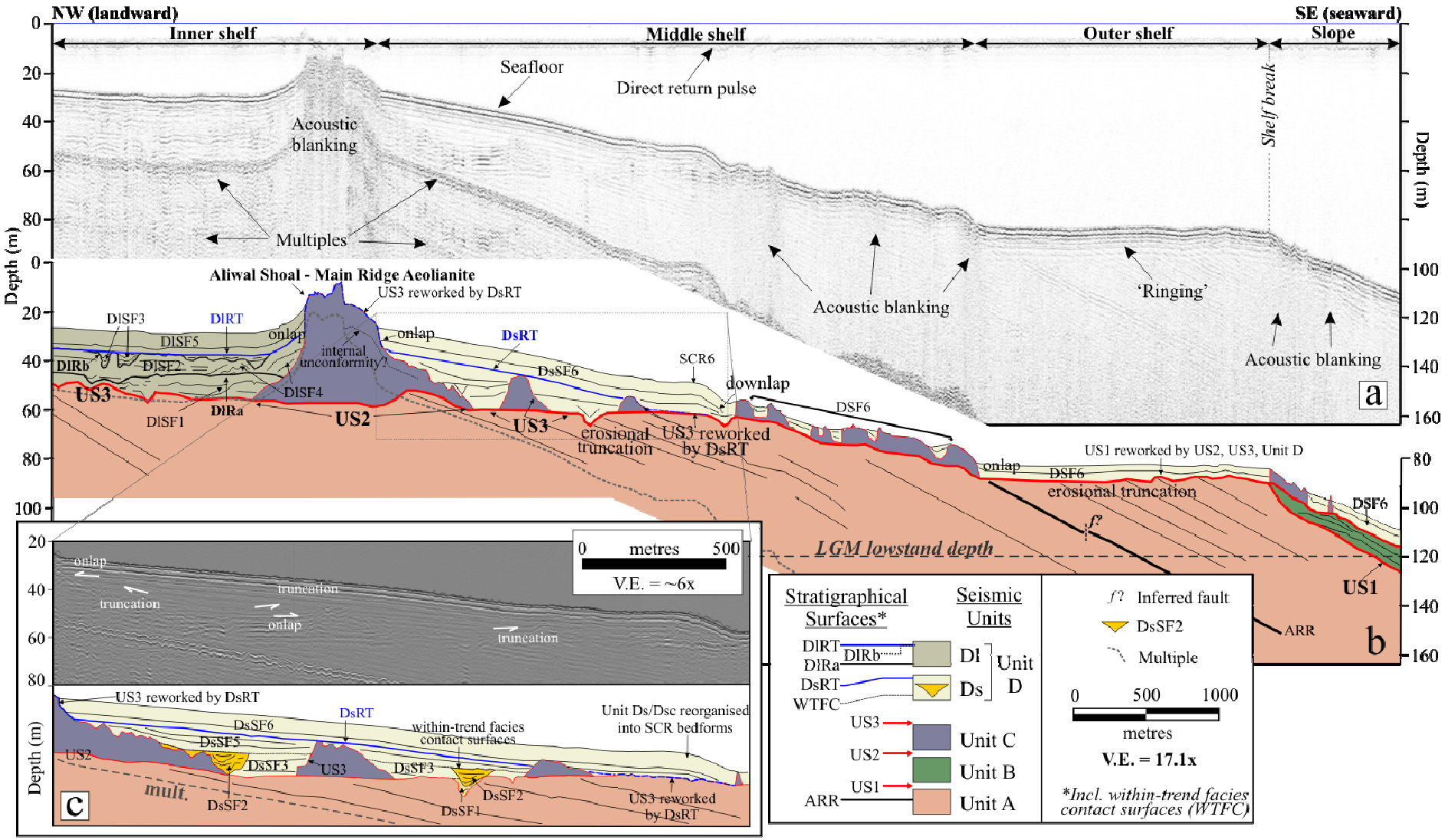

Figure 6.6 Downdip uninterpreted **(a)** and interpreted **(b)** seismic profile for line 6. Unit D is subdivided in Dl (landward) and Ds (seaward) based on its position relative to the Aliwal Shoal aeolianite ridge. **(c)** Inset showing a detailed uninterpreted (top) and interpreted (bottom) seismic profile of Unit Ds. The geomorphological domain of the Main Ridge Aeolianite is dealt with in Chapter 8.3.3 and Figure 8.7. The MRA or Unit A1 aeolianite yielded an OSL age range from 134 - 127 ka (Chapter 9). Seaward termination of Unit Ds is re-organised into SCR 6 of Unit Dsc. Due to resolution of the seismic tool used in this study it is not possible to ascertain the lateral relationship between Unit Ds and Dsc. Refer to Chapter 7.4 and Figures 7.10 for more details regarding shoreface-connected ridges. V.E. = vertical exaggeration, SCR = shoreface-connected ridge (also see Figure 6.5), Mult. = multiple, Incl. = including, LGM = Last Glacial Maximum, WTFC = within-trend facies contact.

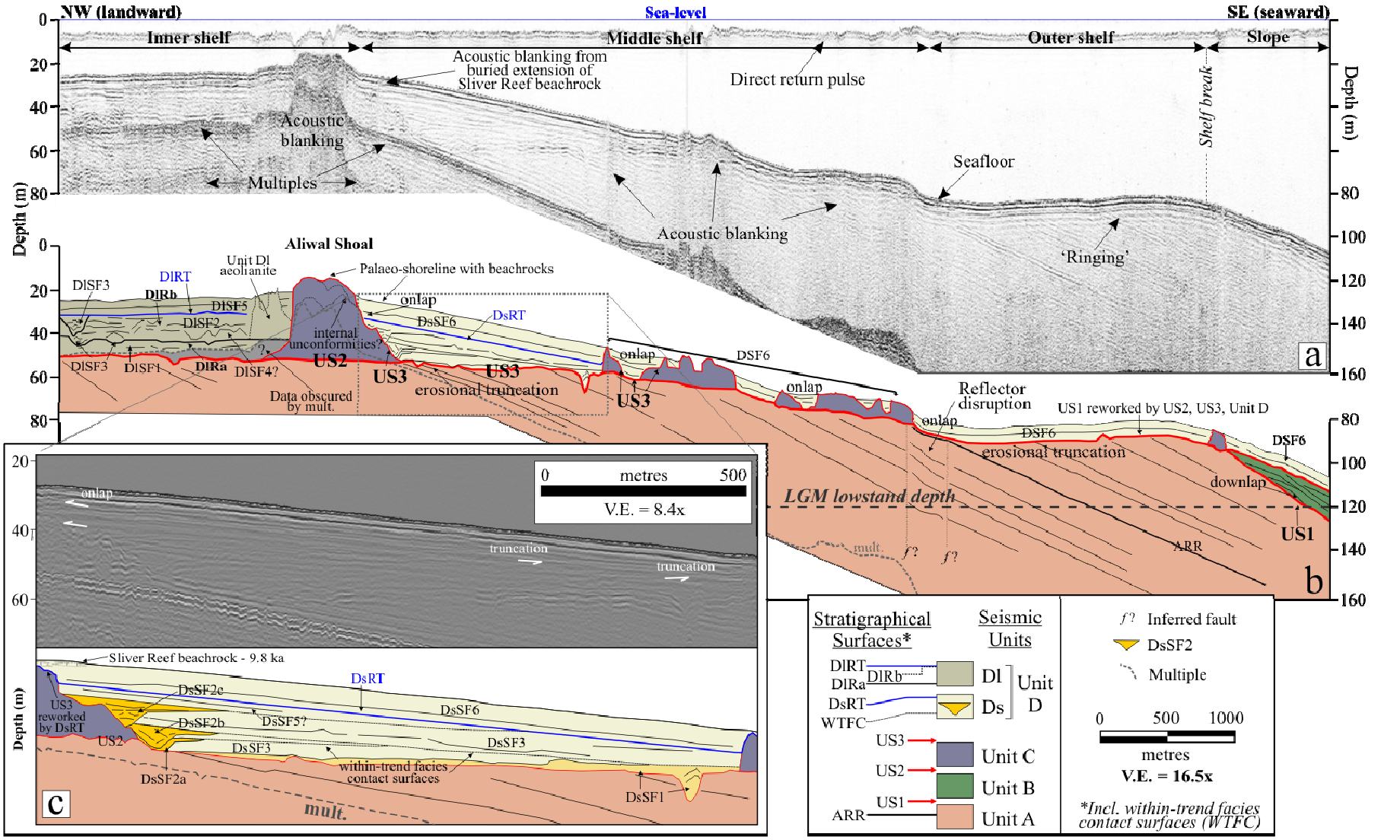

Figure 6.7 Downdip uninterpreted **(a)** and interpreted **(b)** seismic profile for line 7. Unit D is subdivided in Dl (landward) and Ds(seaward)based on its position relative to the Aliwal Shoal aeolianite ridge. **(c)** Inset showing a detailed uninterpreted (top) and interpreted (bottom) seismic profile of Unit Ds. Palaeo-shoreline lithofacies capping Unit Ds is interpreted from preserved beachrocks deposited unconformably on top of older aeolianite cores of Unit C (refer to Chapters 8.3 and 9). The carbonate-cemented aeolianite (Unit C) and beachrock (Unit D) lithofacies could not be separated due to the acoustic blanking nature of their acoustic signatures and the resolution of the seismic method used in this study. However, it is possible that the upper internal unconformity surface evident in the Aliwal Shoal ridge of Unit C (see **(b)**) may represent the boundary between the aeolianite and overlying younger transgressive beachrock. Mult. = multiple, V.E. = vertical exaggeration, incl. = including, LGM = Last Glacial Maximum, WTFC = within-trend facies contact.

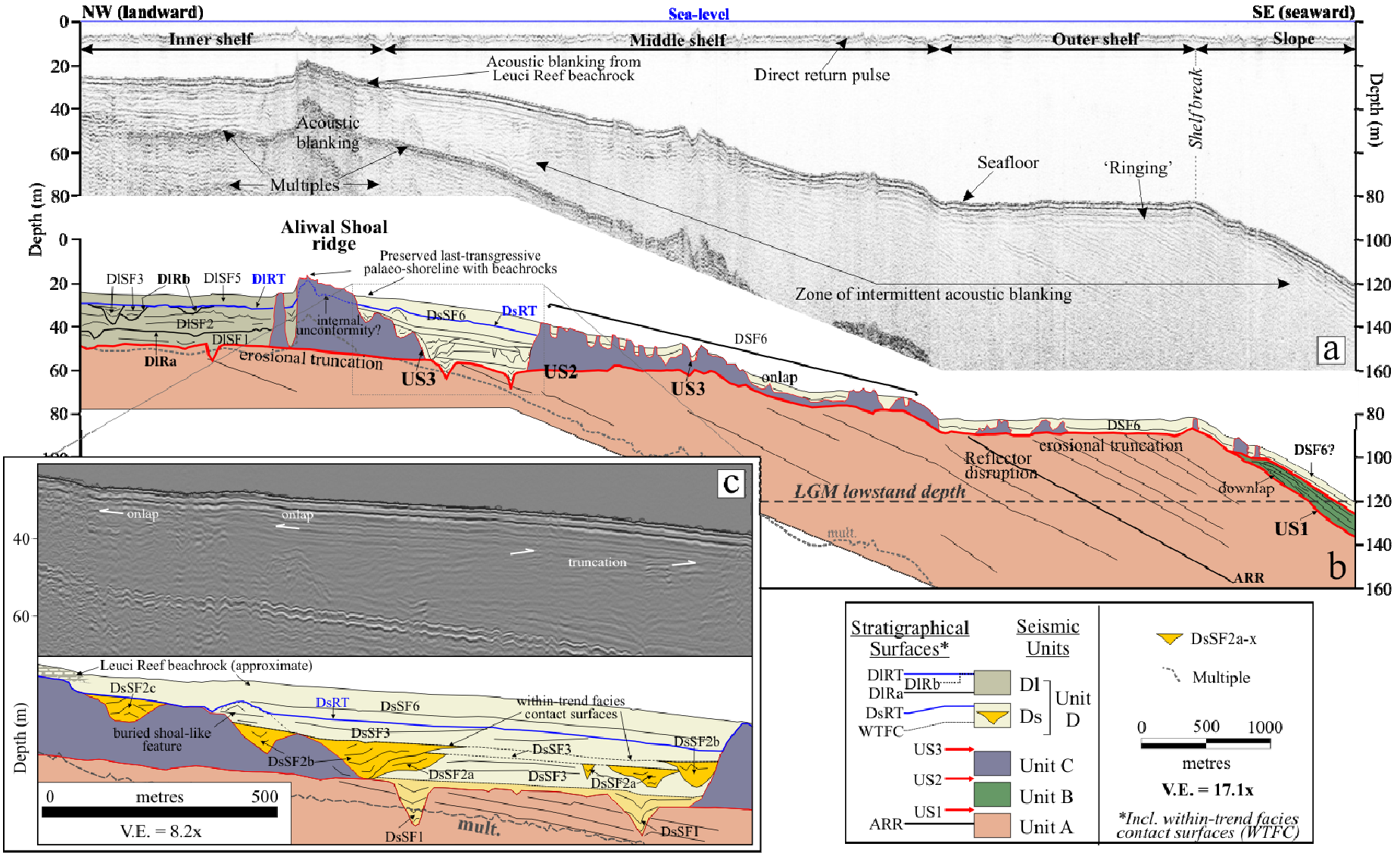

Figure 6.8 Downdip uninterpreted **(a)** and interpreted **(b)** seismic profile for line 8. Unit D is subdivided in Dl (landward) and Ds (seaward) relative to the Aliwal Shoal ridge. **(c)** Inset shows a detailed uninterpreted (top) and interpreted (bottom) seismic profile of Unit Ds. Note that the vertical exaggeration of (c) is approximately half of **(a)** and **(b)**. Leuci Reef **(a)** is a transgressive beachrock unit (dealt with in Section 8.3) deposited during the last deglacial transgression at ~9.9 ka (optically stimulated luminescence age - Chapter 9). Due to the resolution of the system the reef was not imaged but is identified by characteristic acoustic blanking. Mult. = multiple, V.E. = vertical exaggeration, Incl. = including, WTFC = within-trend facies contact, LGM = Last Glacial Maximum.

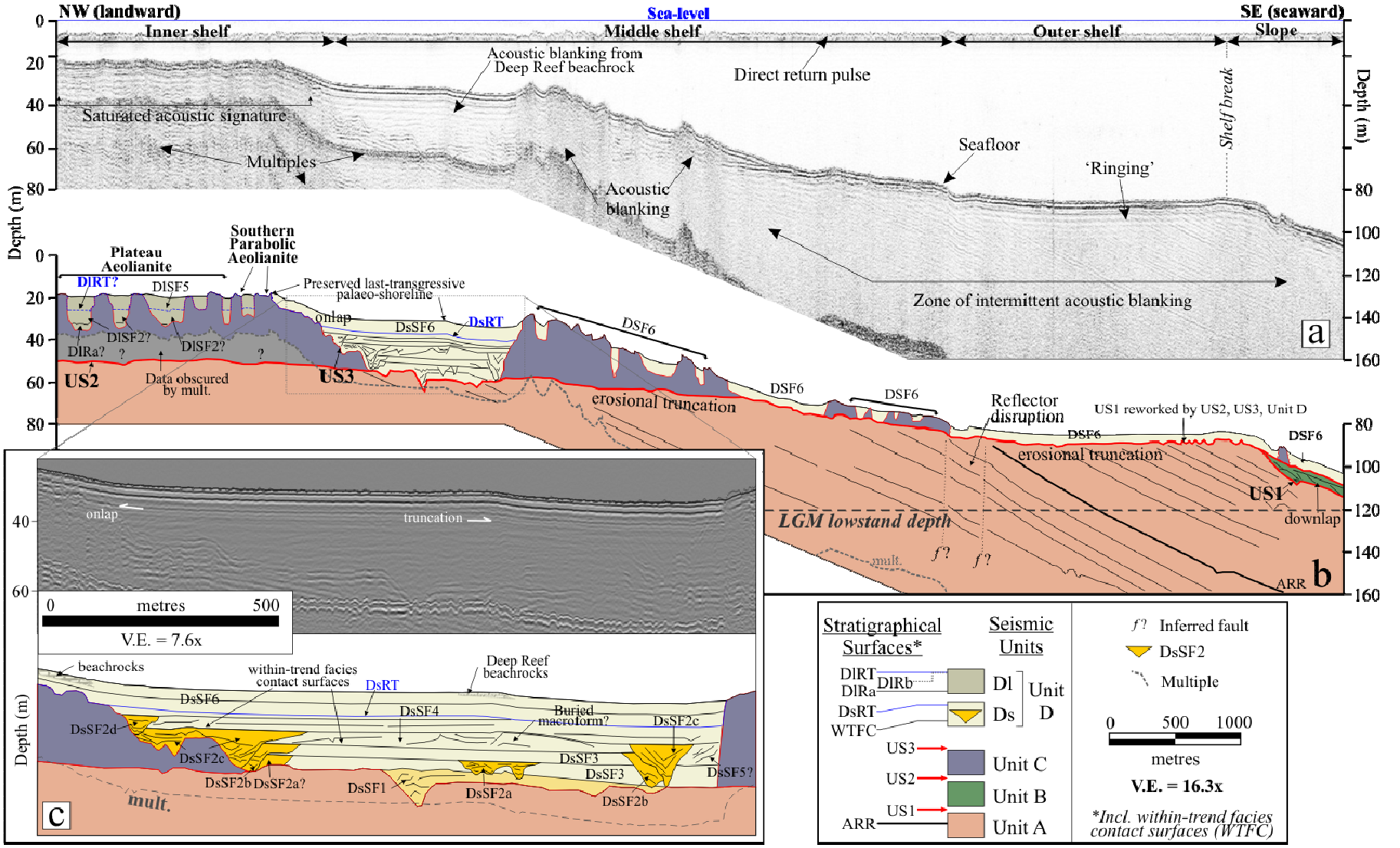

Figure 6.9 Downdip uninterpreted **(a)** and interpreted **(b)** seismic profile for line 9. Unit D is subdivided in Dl (landward) and Ds (seaward). The palaeo-shoreline occupations seaward of the Aliwal Shoal ridge extension (represented by the Southern Parabolic Aeolianite - Figure 8.7) capping Unit Ds are interpreted from preserved beachrocks deposited unconformably on top of older aeolianite dune cores of Unit C (refer to Section 8.3 and Chapter 9). **(c)** Inset showing a detailed uninterpreted (top) and interpreted (bottom) seismic profile of Unit Ds. Note the macroform feature of facies DsSF4. Deep Reef beachrock is the oldest of the last deglacial transgression beachrocks with an OSL age of 11.0 ± 0.67 ka (Chapter 9). Mult. = multiple, V.E. = vertical exaggeration, incl. = including, LGM = Last Glacial Maximum, WTFC = within-trend facies contact.

6.3.1 Unit A

Unit A (Table 6.2) is the deepest seismic unit recognised and forms the *acoustic* basement for this study. It is the most extensive and well represented unit underlying the inner, middle and outer shelf and continental slope (Figures 6.5 to 6.6). Characteristic dense high amplitude, continuous parallel, sub-parallel and divergent reflectors dip gently seawards (SE) at 1° to 2°.

The parallel reflector continuity suggests a consistently stratified deposit which underwent uniform rates of deposition on a uniformly subsiding shelf or basin setting, whilst the divergent reflector pattern is due to lateral thickening accomplished by thickening of individual units within a cycle, suggesting a lateral variation in the rate of deposition, or progressive tilting of the depositional surface (Mitchum *et al*., 1977a; 1977b). The high amplitude of the reflectors signify strong velocity-density contrasts indicating the presence of intra-formational disconformities and hiatus surfaces representing periods of nondeposition or changes in the depositional regime (Mitchum, 1977; Mitchum and Vail, 1977). Observed disruption morphologies of the reflectors are most likely related to basin subsidence and/or later tectonic instability. The dip of the reflectors within Unit A ranges from an average value of 1.26° beneath the inner shelf, 1.68 below the middle shelf to 2.02° under the outer shelf (Figures 6.8) indicating an overall steepening in the dip angles upwards in the stratigraphic succession, similarly observed by Birch (1996; Figure 6.1a, Line 165).

The upper boundary of Unit A (US1 - US3), is an easily recognisable high amplitude surface showing erosional truncation along its entire extent and fluvial incision in the inner and mid shelf regions. It is the most pronounced unconformity surface across the shelf and has very similar elevation values as those given by Birch (1996) and Martin and Flemming (1986; 1988) (Figures 6.1 and 6.2). The fluvial incision or palaeo-river channels indicate that the shelf has been subaerially exposed in the past during times of substantially lower sea-levels. Since the seismic profiles are downdip profiles, fluvial channel features incised into Unit A are coast-parallel features that most likely represent the incised tributaries of a larger river system. Generally Unit A is buried by younger sediments but it is nearly exposed on a broad plateau area forming the outer shelf (Figures 6.6 to 6.9). The erosional morphology of US1 varies from an overall convex surface in the north (Figure 6.5) to two concave surfaces on the inner and outer shelf separated by a well-developed middle shelf seaward-sloping terraced-ramp commonly occurring between -60 to -80 m (Figures 6.6 to 6.9). The seaward inclined terraced-ramp terminates on the upper part of the outer shelf as a 10 - 15 m high escarpment. At the base of the escarpment is a very well developed and laterally extensive erosional plateau that continuous to the shelf break (Figures 6.5 to 6.9). Reflector ARR is a sub-parallel, continuous, medium amplitude reflector within Unit A which is traceable across the entire study area and possibly further afield (Figures 6.1a and 6.2b). On most

seismic sections the extension of reflector AAR corresponds with the seaward termination of the escarpment and also has a similar dip (Figures 6.5 to 6.9). The true thickness of Unit A is unknown due to erosion and the limitations of the seismic system but has a seismic thickness of at least 110 m and a projected dip-corrected profile thickness of >2.9 km in the study area.

Interpretation and Correlation

Based on seismic reflection configuration and depth of occurrence, Unit A is equated to Unit M (Figure 6.1) of Birch (1996), the seaward-dipping strata (Figure 6.2) of Martin and Flemming (1986; 1988) and Units A, B and C (Figure 6.3) of Cawthra (2010; Table 6.1). Birch (1996) interpreted his Unit M as marine strata of Tertiary or Cretaceous age. Martin and Flemming (1986) interpreted their equivalent unit to a Palaeozoic to Tertiary 'pre-Quaternary' age and later revised this to a Tertiary Age (Martin and Flemming, 1988; refer to Chapter 6.2.2). Cooper and Liu (2006) assigned a Palaeozoic or Neoproterozoic age to the strata upon which the Aliwal Shoal (Unit C) rests. Cawthra (2010), assigned Cretaceous ages to her three units (Figure 6.3; Table 6.1) ranging from Santonian (Unit A), Campanian (Unit B) to Maastrichtian (Unit C). The discrepancy in the age for the marine sequence among the various workers stems from the fact that there was no direct sampling of these strata and consequently no reliable litho- and chrono-stratigraphic analysis. Interpretation is based on onland exposures and boreholes (sometimes not even in the same vicinity) and far-field oil exploration boreholes all of which is then inferred to the offshore sites. In addition, extrapolation along the coast between sites is tentative due to local sedimentary basins each with different geotectonic evolution (see Chapter 3) and differential uplift in the Tertiary age (Chapter 3.5.1).

None of the seismic units identified crop out directly onshore from the study area (Figure 3.1) nor is there any borehole control available for these units. However, age inferences for Unit A is made from nannofossil assemblages obtained from seafloor samples in the study area. Results show that samples from Unit C, which rests directly upon Unit A (Figures 6.5 to 6.9), contain several reworked Cretaceous Campanian to Maastrichtian nannofossil forms (Chapter 9). Additionally, the seismic profiles clearly show that the top surface of Unit A has been subaerially exposed and may have cropped out on the outer shelf where it is only buried by a veneer of Unit D. Based on these relationships it is suggested that the Cretaceous forms were eroded during sea-level regressions exposing the entire continental shelf and subsequently incorporated into the Unit C (Aliwal Shoal) lithologies during the ensuing transgressions. This study therefore proposes a Cretaceous Campanian to Maastrichtian age for the seaward dipping marine strata of Unit A underlying and seaward of Unit C. The interpretation is further supported by the stratal characteristic indicating widespread deposition of sandstone and siltstone within a subsiding basin

as was the case for the evolution of the proto-Indian Ocean during Cretaceous times (Chapter 3.3.1 and 3.4). This contradicts the Tertiary age of Martin and Flemming (1988) and Birch (1996) and the Neoproterozoic to Palaeozoic age assigned by Cooper and Liu (2006). Unit A is thus chronologically equivalent to Cawthra's Units B and C (Figure 6.3). Further support for a Cretaceous age for Unit A is provided by strata located underneath the Durban Harbour with Santonian to Campanian faunal assemblages (Kennedy *et al*., 1973; SACS, 1980; Tankard *et al*., 1982 and Dingle *et al*., 1983; McMillan, 2003) and Middle Santonian to Late Campanian outcrops onshore at Trafalgar (Dingle *et al*., 1983; Shone, 2006), approximately 100 km south of the Aliwal Shoal on the KwaZulu-Natal south coast (Figure 3.9).

Although the exact nature of reflector ARR is unknown, its amplitude and continuity imply that it represents a major change in the depositional regime or basin. ARR has a reflector configuration consisting of an apparent toplap of strata below ARR and downlap of strata from above suggesting it might represent a correlative conformity (Coe and Church, 2003b), possibly a maximum flooding surface (MFS) or even a basal surface of forced regression (BSFR; Catuneanu, 2006). The dip of reflector ARR varies from 1.85° (Figure 6.5), 1.69° (Figure 6.7) to 1.99° (Figure 6.10), with a progressive increase in the dip southwards. Bosman (2006) interpreted the strata above reflector ARR to possibly reflect prograding continental slope strata deposited over a Cretaceous palaeoshelf break.

6.3.2 Unit B

Unit B unconformably overlies Unit A on subaerial erosional surface US1 underlying the shelf break and continental slope (Table 6.2; Figures 6.5 to 6.9). External seismic geometry of Unit B is that of a seaward-thickening wedge with the landward pinch-out depth commonly located at approximately -100 m. Unit B consists of low amplitude, high angle (3° - 6°) prograding oblique parallel to oblique tangential clinoforms that downlap and apparently onlap onto the underlying subaerial unconformity surface US1 (Figures 6.5; 6.7; 6.8). The internal reflector configuration suggests a complex pattern of progradation and aggradation whereas the lateral variation in the reflector pattern most likely indicates strike-variability of the strata. The top surface of Unit B shows erosional truncation by the high amplitude composite subaerial erosional surface (US2 and US3). Unit B has a maximum thickness of 11 meters in the study area but as it comprises a seaward-thickening wedge it thickens basinward.

Interpretation and Correlation

An equivalent to Unit B is not recognised by other workers that undertook previous surveys in the area (e.g. Martin and Flemming, 1986; 1988 and Birch, 1996). However a similar shelf edge wedge-type deposit was recognised by Martin and Flemming (1988) offshore Durban, by Green *et al.* (2008) in the Zululand Basin offshore Maputaland (~300 km north, see Figure 3.9) and by Cawthra (2010) offshore the Durban Bluff (Unit D, Figure 6.3). Martin and Flemming (1988), observed complex sigmoid oblique clinoforms forming a shelf-edge prograding sequence offshore Durban and assigned it either as Late Pliocene or Pleistocene in age. Green *et al*. (2008) provided a Late Pliocene to early Pleistocene age for the shelf-edge wedge in the Zululand Basin based on nannofossil biostratigraphy. Cawthra (2010) also assigned the shelf-edge unit offshore the Durban Bluff to a Late Pliocene age based on correlation to other workers.

As with Unit A, age inferences for Unit B are made by using nannofossil assemblages extracted from overlying Unit C (see Chapter 9). Seismic profiles (Figure 6.5 to.6.9) indicate that the upper surface of Unit B is a subaerial erosion surface and that Units C and D directly overlie Unit B on the shelf break. Reworked Pliocene to Pleistocene forms are found in Unit C lithologies and as for Unit A, their occurrence is ascribed to erosion during sea-level minima and incorporation into Unit C during subsequent transgressions. Unit B is thus interpreted as a Late Pliocene to early Pleistocene prograding shelf-edge wedge.

6.3.3 Unit C

Unit C unconformably overlies Units A and B on the composite subaerial unconformity surface of US2 (Table 6.2; Figure 6.5 to 6.9). Unit C comprises inner to outer shelf distinct, linear and sometimes isolated shore-parallel ridge complexes. The reflector configuration comprises high to medium amplitude discontinuous, strongly chaotic internal reflectors which produce a characteristic acoustical blanking of underlying strata. The inner shelf Aliwal Shoal ridge is the most prominent developed ridge complex within Unit C and attains a maximum stratigraphic thickness of ~58 m (Figure 6.6). This ridge complex terminates in the north between seismic line 5 and 6 and becomes subdued where it merges with other ridges of Unit C in the south (Figure 6.4). Seaward on the middle shelf another ridge system, named the Middle Shelf Ridge (MSR), with a maximum thickness of 30 m (Figure 6.9b) is parallel to the Aliwal Shoal ridge but is covered by sediments of Unit D. Where observed the top of Unit C is truncated by the subaerial erosion surface US3 which is also reworked by the overlying Unit D.

Interpretation and Correlation

This study (see Chapter 8) confirmed Unit C to comprise carbonate cemented aeolianite and beachrock complexes representing palaeo-coastline events. Unit C is therefore correlated with Unit P of Birch (1996) (Figure 6.1; Table 6.1), the aeolianites of Martin and Flemming (1986; 1988) and Unit E of Cawthra (2010). McCarthy (1967) provided the first evidence that these features were palaeodune cordons whereas Ramsay (1991; 1995; 1996) showed that beachrock may also be present and that these complexes can be used to delineated palaeocoastline events. Ramsay's (1991; 1995) work provided the basis for the only relative sea-level curve for the eastern seaboard of South Africa (Ramsay and Cooper, 2002).

Most workers consider the age of these aeolianite ridges to be Pleistocene (Table 6.1), although some controversy surrounds the age of the Aliwal Shoal. This issue is thoroughly explored in Chapter 9 and will not be dealt with here. The most reliable age prior to this study is provided by Ramsay (1991; 1996) which showed that the offshore ridges on the Sodwana Bay continental shelf (Figure 1.1) ranged in age from 117 - 22 ka B.P. formed during the Late Pleistocene regression leading to the Last Glacial Maximum (LGM). Bosman *et al*. (2007) using nannofossil biostratigraphy assigned a late Middle Pleistocene to Holocene age (< 290 ka B.P.) to the Aliwal Shoal lithologies (see Chapter 9). Cawthra (2010) also used nannofossil biostratigraphy and obtained the same result for the Bluff aeolianites (Figure 6.3). She also attempted to apply infrared stimulated luminescence but, with the exception of one sample that was tentatively dated as 60 - 70 ka B.P., the results were unreliable due to the feldspar showing anomalous fading (Cawthra, *Pers. Comm.*). This study showed that the aeolianites of the Aliwal Shoal ridge complex alone range in age from 134 ± 5 ka to 79 ± 5 ka B.P., thereby indicating that one aeolianite ridge is a complex assemblage of multiple ages (Chapter 9). The beachrock lithologies that were dated in this study form part of Unit D (DsSF6; also see Chapter 9).

6.3.4 Unit D

Unit D is further subdivided into sub-units **Dl**, **Ds**, **Dss**, and **Dsc** (Table 6.2). Units Dl (landward) and Ds (seaward) are discriminated based on their relative position to that of the Aliwal Shoal ridge (Unit C; Figures 6.4 to 6.9) and internal reflector configuration. Units Dsc and Dss are best represented on the seismic profile of line 5 (Figures 6.4 and 6.5).

Unit Ds is a middle shelf sediment package which becomes progressively entrained southwards between two parallel ridges of Unit C. It ranges in thickness from <10 - 30 m (Table 6.2) and

unconformably overlies Units A and C on the composite subaerial unconformity surface of US3 (Figures 6.6 and 6.7). In the north the external seismic geometry of sub-unit Ds is that of a landward-thickening wedge banked on the seaward-side of the Aliwal Shoal ridge with lateral pinch-out along strike (Ds and Dl is represented by Dss on line 5). However, it attains a more even thickness southwards as it is increasingly entrained between the Aliwal Shoal ridge to the west and another parallel ridge of Unit C, the MSR, to the east (Figures 6.8 and 6.9). Unit Ds seems to continue southwards of the study area boundary and will most likely thin and eventually pinch-out along strike as is the case to the north. Detailed interpretation of Unit Ds allows for the identification of six seismic facies (Table 6.2; Figures 6.6c to 6.9c). DsSF1 is the lowermost facies characterised by low to medium amplitude discontinuous sub-horizontal and chaotic to draped channel fills. It is not recognised on the seismic profile for line 6 (Figure 6.6) and is progressively better preserved towards the south. DsSF1 seems to be associated with localised depocentres created in topographic lows and earlier incised river channels (up to 10 m deep) within Unit A. DsSF2 comprises low amplitude, channel features with draped, onlapping, sub-horizontal to concave-upward fill. In terms of lateral frequency, vertical stacking and individual channel size (compare Figure 6.6c with 6.9c) facies DsSF2 is also enhanced southwards as it is increasingly entrained between two parallel ridges of Unit C. DsSF2 onlaps the seaward flank of the Aliwal Shoal ridge in a retrogradational or backstepping geometry so that each younger channel generation migrates progressively in an upward and landward direction. Facies DsSF3 comprises continuous, sub-horizontal to converging clinoforms generally occurring adjacent and superjacent to DsSF2. DsSF4 constitutes low amplitude, discontinuous, mounded reflectors developed laterally from DsSF3 (Figures 6.8c and 6.9c). DsSF3 increases in concert with DsSF2 southward as entrainment is enhanced. DsSF5 consists of low amplitude, continuous, seaward-inclined, parallel to sub-parallel reflectors (Figures 6.6c and 6.7c), generally superjacent to DsSF2 and DsSF3. DsSF6 is a low amplitude, continuous sub-horizontal, seaward-inclined, parallel to sub-parallel reflector arrangement that onlaps Unit C. The top-most part of DsSF6 comprises beachrocks that represent palaeo-coastline episodes (Chapter 8) formed during the last deglacial sea-level rise (Chapter 9). The number and volume of beachrock outcrops systematically increase southwards (Figure 6.4; also compare Figure 6.6c with Figure 6.9c). Facies DsSF1 to DsSF5 are truncated by DsRT, which again is onlapped by DsSF6 (Figures 6.6c to 6.9c). Reflector DsRT dip seaward with angles ranging from 0.74° (line 6; Figure 6.6), 0.67° (line 7; Figure 6.7), 0.44° (line 8; Figure 6.8) to 0.2° (line 9; Figure 6.9). This gradual southward decrease in dip angle for DsRT also results in a more conformable relationship between DsRT and the underlying facies of DsSF1 to DsSF5. Thus all stratigraphic components of Unit Ds show a general trend of southwards modification as entrainment between the two ridges of Unit C increases. Erosional surface DsRT is observed reworking US3 and subsequently also the Aliwal Shoal ridge (Figures 6.6c to 6.9c).

Unit Dl is an inner shelf sediment package which onlaps (draped) the landward edge of the Aliwal Shoal ridge (Table 6.2; Figure 6.6 to 6.9). It range in thickness from <10 - 40 m and unconformably overlies Units A and C on the composite subaerial unconformity surface US3. The apparent external geometry of Unit Dl is that of a sheet that pinches out along strike to the north, confirmed by the fact that Unit Dl is not found on line 5. The continuation of Unit Dl to the south of the study area is uncertain as it appears to be banked against the broad plateau formed by laterally-coalesced ridges of Unit C (Figures 6.4 and 6.9). It was not possible to interpreted unit Dl in the same detail as Unit Ds due to the shallower depth range of Unit Dl and its complex lateral relationship with Unit C, which together resulted in a shallower multiple and an oversaturated seismic signal which obscured interpretation. However, five seismic facies were identified in Unit Dl (Table 6.2). DlSF1 is the lowermost facies unconformably resting on Unit A and comprises low to medium amplitude, continuous, horizontal to slightly inclined reflectors (Figures 6.6 to 6.8). DlSF1 is capped by DlRa, a prominent, high amplitude, continuous, sub-horizontal, channel incised reflector. DlRa is thus separated from the underlying subaerial unconformity surface (US3) and Unit A by DlSF1. The seismic acoustic multiple commonly occurs close to DlRa which complicates interpretation (Figure 6.7) and separation from surface US3 but in Figure 6.8 it is clear that US3 and DlRa are locally two separate reflector surfaces. DlRa is flanked predominantly by facies DlSF2 and the laterally constrained DlSF4. Facies DlSF2 comprises low amplitude, continuous, sub-horizontal reflectors, whereas DlSF4 downlaps DlRa and consists of low amplitude, discontinuous, landward-prograding clinoforms (Figures 6.6 and 6.7). DlSF3 is a low amplitude, discontinuous reflector package with characteristic channel features showing draped to clinoform fill. DlSF5 is the uppermost facies of Unit Dl and comprises low amplitude, continuous, horizontal to slightly seaward-inclined parallel reflectors that onlap the western or landward margin of the Aliwal Shoal ridge of Unit C (Figures 6.6; 6.7 and 6.8). DlSF5 is separated from the underlying sediment package (DlFS1 to DlSF4) by DlRb, a medium amplitude horizontal channel incised reflector similar to DlRa, which is mostly replaced by the erosional truncation surface DlRT.

Unit Dss unconformably overlies Units A, B and C mantling the entire continental shelf from the inner shelf to the shelf slope (Figure 6.5). It is irregular in thickness ranging from <2 - 14 m, the thickest deposits found in localised depocentres comprising topographic lows created by differential erosion of Unit A strata, the more resistant layers forming dip-slope hardgrounds, in the lee of which, the eroded softer layers provided the increased accommodation space for accumulation (Figure 6.5 - middle shelf). Four seismic facies were identified (Table 6.2) and designated as; DSF1, DSF2, DSF5 and DSF6, so as to conform to similar seismic facies identified in Units Ds. DSF1 is the lowermost seismic facies consisting of medium amplitude, discontinuous, horizontal reflectors. DSF2 is a low amplitude, discontinuous facies with channel

features showing draped fill. DSF5, present only on the middle shelf landward of a low ridge of Unit C, comprise low amplitude continuous, seaward-inclined to horizontal, parallel to sub-parallel reflectors. Facies DSF6 is the uppermost facies identified and also the most widely distributed occurring from the inner shelf to the shelf slope where it unconformably overlies Unit B. Surface DRT is tentatively mapped underlying DSF6 and considered as the lateral equivalent of DsRT and DlRT. The upper surface of Unit Dss (DSF6) is capped by surface DLS which also forms the base to Unit Dsc (Table 6.2; Figure 6.5).

Unit Dsc is best observed on seismic profile 5 to the north of the Aliwal Shoal ridge where it overlies and in places downlap Unit Dss on surface DLS (Table 6.2; Figure 6.5). To the south Unit Dsc overlies both Units Dl and Ds but occurs as a thin sediment veneer (see Chapter 8.4) which is below the detection resolution of the seismic tool and as such is not shown in Figures 6.6 to 6.9. External seismic geometry of Unit Dsc is that of an inner to middle shelf shore-attached prograding sediment body with complex bedforms superimposed predominantly above the fair-weather wave base (FWWB; -30 m). Unit Dsc comprise very low amplitude, semi-transparent, sigmoid, continuous clinoforms which overlie Unit Dss on surface DLS with the downlap angle decreasing in a landwards direction.

The down-dip seismic profile shows that morphologically the sediment body comprises a low angle (0.2°) topset, a higher angle (1.6°) foreset and a poorly developed/resolved bottomset (Figure 6.5), defining a sigmoid or clinoform geometry (Figure 6.5a1; Cattaneo *et al*., 2003; Walsh *et al*., 2004). Although the term 'clinoform' has various meanings (see Walsh *et al*., 2004; Palinkas and Nittrouer, 2006) for the purpose of this study it is a continental margin accretionary feature with a sigmoidal shape varying in size from bedform features centimetre in size to continental-margin accumulations that are kilometres high and hundreds of kilometres wide (Walsh *et al*., 2004; Palinkas and Nittrouer, 2006). On seismic profile 5 (Figure 6.5) Unit Dsc is generally 22 m thick and pinch-out at approximately -60 m. It generally slopes seaward at a similar inclination to that of Unit Dss which again is controlled by Unit A. The internal reflector configuration of Unit Dsc suggests phases of aggradation concurrent with progradation separated by retrogradation. Unit Dsc is separated from the underlying Unit Dss by reflector DLS (Figure 6.5b) comprising a downlap surface upon which Unit Dsc is deposited. The angle of downlap decreases landwards and hence the unit becomes more conformable. This might indicate that the downlap surface is apparent and that in a transgressive setting it may mark the seaward extent of the sedimentary unit (Unit Dsc) at its erosional rather than depositional limit (Catuneanu, 2006). However, this study considers the downlap of Unit Dsc to reflect the depositional limit of the unit but a limit which is controlled by the along and across shelf hydrodynamic processes. The top surface of Unit Dsc constitutes the modern seafloor and is organised into a complex system of

shoreface-connected bedforms (see Chapter 7, section 7.4). Two inflection points are noticeable on the clinoform, the upper occurring on the topset at -30 m directly above the internal point of apparent clinoform lapout and the lower on the foreset at approximately -50 m (Figure 6.5).

Interpretation

Six facies types were interpreted from **Unit Ds** (Table 6.2). DsSF1 is interpreted as either an aggradational fluvial or lagoonal channel fill and floodplain facies based on its basal position, chaotic to draped and medium amplitude reflections (Foyle and Oertel, 1997). DsSF2 represents tidal and abandoned channel deposits floored by channel-base diastems caused by erosional scour (Foyle and Oertel, 1997; McBride *et al.*, 2004; Hijma and Cohen, 2011). These channels converge in a northerly direction (less channels northwards) where subsequent tidal inlets are inferred (as per Hijma and Cohen, 2011). DsSF3 is assigned as lagoonal tidal- and sand-flats facies based on its reflector configuration and lateral association with DsSF2 (Foyle and Oertel, 1997; Nordfjord *et al.*, 2006; Hijma and Cohen, 2011). DsSF4 is limited in extent (Figures 6.8 and 6.9) and interpreted as lagoonal macroforms (including tidal bedforms and point bars; Catuneanu, 2006; Fruergaard *et al.*, 2011). DsSF5 is seaward-inclined to concave parallel reflectors interpreted as paralic deposits (Catuneanu, 2006). Locally these facies is separated by within-trend facies contact surfaces which might also be considered as local flooding surfaces (*sensu* Cattaneo and Steel, 2003; Catuneanu, 2006). Facies DsSF1 to DsSF5 is truncated in various degrees by DsTR which again is onlapped above by facies DsSF6, interpreted as foreshore/shallow marine deposits (e.g. the beachrocks).

DsRT forms a regional transgressive erosion surface (marine flooding surface) and is interpreted as the shoreface ravinement surface (SRS; *sensu* McBride *et al.*, 2004) or transgressive ravinement (TRS; Storms *et al.*, 2008). It is also known as the oceanic ravinement surface (ORS; Foyle and Oertel, 1997) which forms by wave reworking and which is more recently specifically referred to in literature as a wave ravinement surface (WRS; Catuneanu, 2006). The SRS/TRS is considered an erosional contact that separates non-marine deposits below from overlying marine deposits (Walker, 1992; Cattaneo and Steel, 2003; McBride *et al.*, 2004). It may also be considered a transgressive surface (TS) if defined based on the abrupt increase in marine influence across it (Cattaneo and Steel, 2003), but the diagnostic features of the TS is a change in stratal geometry from progradation below to retrogradation above - which is clearly not the case here. DsRT has a higher gradient in the north (0.013; Figure 6.6) of Unit Ds than in the south (0.0032; Figure 6.9c) which is also accompanied by a shallower bathymetric occurrence. In summary, Unit Ds is interpreted as a backstepping or retrograding back-barrier lagoon system (DsSF1 to DsSF5) ultimately drowned by a rapid transgressing sea-level (forming DsRT) which in the process

scoured and buried the lagoonal sequence underneath foreshore to shoreface deposits lithified in places into beachrock (DsSF6) which as such documented the passage of the transgressive palaeo-shoreline.

Unit Dl comprise five seismic facies (Table 6.2) interpreted as fluvial (DlSF1; Foyle and Oertel, 1997), central estuarine/lagoonal deposits (DlSF2; Cooper, 1994a, 2001; Catuneanu, 2006; Green, 2009b), fluvial, tidal and abandoned channel-fill deposits (DlSF3; Foyle and Oertel, 1997; McBride *et al*., 2004), dune slump deposits or estuarine channel side-attached bar (DlSF4; Green, 2009b) and foreshore/shallow marine deposits (DlSF5; Cattaneo and Steel, 2003; Catuneanu, 2006). The lowermost fluvial facies DlSF1 rests on the subaerial erosion surface of US3 and is separated from the overlying facies by reflector DlRa. Facies DlSF2 to DlSF4 are considered to form the central estuary complex (CEC; Catuneanu, 2006). Facies DlSF2 to DlSF4 are variably truncated by DlRT interpreted as the landward extension of DsRT and hence a flooding surface created by the erosion of the oceanic ravinement. In Figures 6.7 and 6.8 it can be observed that DlRT can be traced and connected to DsRT through acoustic discontinuities within the Aliwal Shoal ridge (Unit C). These acoustic discontinuities within the Aliwal Shoal are tentatively interpreted as internal unconformities created by the passage of the transgressive oceanic ravinement across the pre-existing aeolianite which in the process of transgression deposited coastal lithofacies, preserved as beachrocks, onto the pre-existing aeolianite (Unit C) core. This interpretation is supported by field evidence (Chapter 8) and geochronological results (Chapter 9) for the locations in Figure 6.7 and 6.8 where last deglacial transgression beachrocks (DsSF6) have been found unconformably overlying the older Unit C aeolianites (not shown on seismic profiles). However, DsRT does not match the internal acoustic unconformities of the aeolianite on seismic profile 6 (Figure 6.6), consequently caution must be advised in the general extrapolation of the transgressive ravinement through internal acoustic unconformities of aeolianite ridges as these might also be related to internal discontinuities within the aeolianite units.

DlRa is tentatively interpreted as a bay ravinement surface (BRS) based on its stratal configuration, position above fluvial deposits but below the tidal (tRS) and transgressive (TRS) ravinement surfaces as a consequence of the retrograding facies during transgression (Allen and Posamentier, 1993; Cattaneo and Steel, 2003; Catuneanu, 2006). The BRS is cut within estuarine settings by wave and/or tidal scour (Foyle and Oertel, 1997). The possibility that DlRa might represent an earlier tidal ravinement surface cannot be discounted. DlSF5 is the uppermost facies in Unit Dl and interpreted as shallow-marine facies based on ground-truthing and sample analyses (Chapter 8). DlSF5 is separated from the central estuary complex by reflector DlRb which is subsequently replaced by the erosive scouring of the transgressive ravinement (DlRT) only preserving the estuarine channel fills. A similar situation was observed by Nordfjord *et al*. (2009)

on the New Jersey shelf which ascribed the tidal channel preservation to (1) pauses in sea-level rise that resulted into back-barrier systems that could not be destroyed by subsequent transgressive ravinement and (2) antecedent topography controlling rates of transgression and preservation. Unit Dl is interpreted to have formed in response to a transgressive sea-level regime evolving from a fluvial inter-dune deposit (DlSF1) into a back-barrier estuarine-lagoon (DlRa; DlSF2 to DlSF4, DlRb) before eventual drowning by a rapidly transgressing sea-level (DlRT) and burial by foreshore and shoreface sands (DlSF5). The relationship to Unit Ds is inferred to be contemporaneous (albeit slightly younger due to the landward shift of facies during transgression) with Unit Dl increasingly functioning as a back-barrier system behind the Aliwal Shoal ridge (Unit C) connected by tidal-inlets as transgression proceeded.

Unit Dss is separated into four seismic facies (Table 6.2) based on similar interpretation criteria as for Units Ds and Dl. Fluvial/fluvial plain (DSF1), tidal or abandoned channel (DSF2), paralic (DSF5) and transgressive marine sands (DSF6; sheet sands of McBride *et al*., 2004) depositional systems are inferred. Facies DSF6 onlap Unit C and is present across the entire shelf (line 5; Figure 6.5), on the middle and outer shelf (forming possible healing phase deposits) on lines 6 - 9 (Figures 6.6 - 6.9) where it is also equated along dip to facies DsSF6 of Unit Ds and DlSF5 of Unit Dl. It is interpreted to represent marine sands diachronously deposited across the continental shelf as the transgression proceeded. DSF1, DSF2 and DSF5 are truncated by the overlying low to medium amplitude reflector DRT. DRT is correlated to DsRT and DlRT and hence interpreted as a transgressive ravinement and as such subjacent to the onlapping shoreface/shallow marine deposits of DSF6. In some locations on the outer shelf where the isolated ridge structures of Unit C is not resolved, zones of intermittent acoustic blanking (Figures 6.8a and 6.9a) are present within facies DSF6. This may be representative of Unit C deposits or possibly the relict carbonate facies of Flemming (1980; 1981) consisting of outer shelf current dominated basal biogenic conglomerate lag deposits formed during the Holocene transgression by the reworking of fossil algal-reef bioherms. Seismic facies of Unit Dss are inferred to have formed in an open shoreline setting during a relative sea-level transgression and are interpreted to comprise fluvial, small localised estuarine/lagoonal and beach-barrier palaeo-depositional environments.

The thick sediment accumulation representing **Unit Dsc** forms part of a large aggrading and prograding unconsolidated sediment deposit (see Chapter 2.2.3, Figure 2.12 and Chapter 3.5.2, Figure 3.17) and has previously been termed the ‘Illovu submerged spit bar’ (Martin and Flemming, 1986) and the ‘Umkomaas sediment deposit’ (Birch, 1996). Martin and Flemming (1986) suggested that this shore-attached prograding sediment depocentre formed at the convergence of sediment paths generated by the Agulhas Current, the counter current and long-shore drift (Figures 2.4 to 2.6) from sediment supplied mainly by local rivers and the northward

littoral drift. They further postulated that upwards sediment accumulation is limited by the prevailing swell energy consequently forcing progradation onto the open shelf. Martin and Flemming (1986) also presented a coast-parallel seismic profile showing northward progradation of the sediment deposit (Figure 6.10). They based their classification of this sediment body as a submerged spit bar on its progradational nature, depth of occurrence and resemblance to subaerial sand spits.

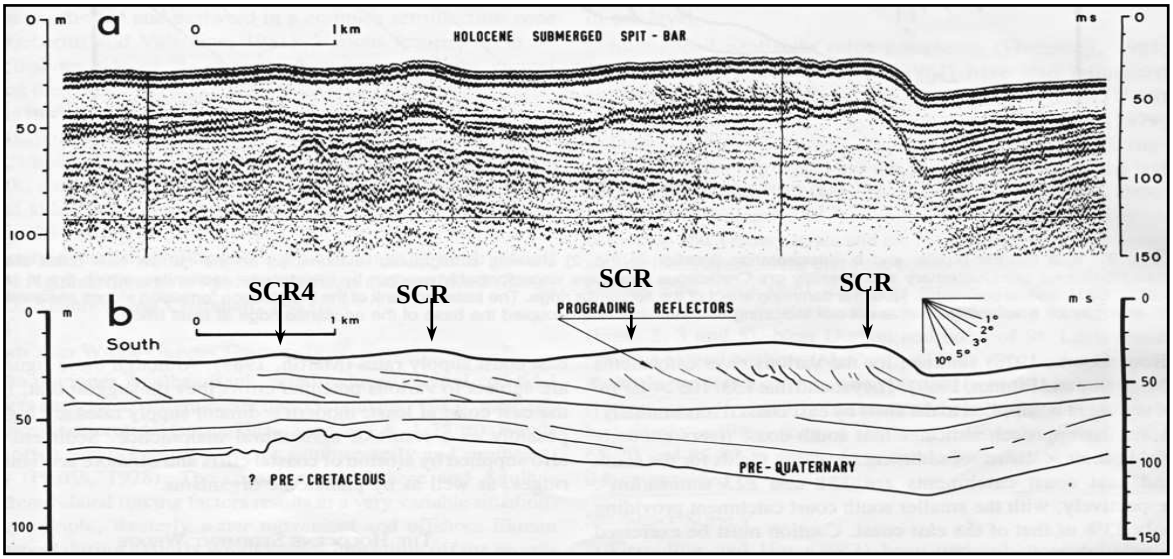

Figure 6.10 a) Uninterpreted and **b)** interpreted strike-parallel sparker seismic profile (see Figure 6.4 for locality) across the newly named Mkomazi submerged-delta clinoform (previously Illovu submerged spit bar; from Martin and Flemming, 1986). Also shown are the crests of the Aliwal Shoal SCRs as identified in this study (Chapter 7.4; Figures 7.9 and 7.10). Note the absence of Unit Dss below the prograding Unit Dsc. This may be due to the fact that the profile is further to the north and inshore and as such Unit Dss is not present. Alternatively, it is possible that the thinly developed Unit Dss is not resolved by the sparker seismic method.

However, it is suggested here that this sediment deposit be renamed the ***Mkomazi Subaqueous-Delta Clinoform*** (**MSDC**) based on its clinoform shape in dip-orientated profiles (Figure 6.5), its occurrence offshore a major river (Mkomazi, Figure 6.4; Chapter 2.1.4) and that it comprises a depositional sequence that accretes/progrades due to variations in the rate of sea-level changes and sediment supply (Walsh *et al*., 2004). Although the term subaqueous-delta can refer to the subaqueous part of a deltaic system (prodelta) or as more recently used and for the purpose of this study, adopting the definition of Cattaneo *et al*., (2003) as 'a wedge-shaped prograding body that may or may not be linked to a specific source at the shoreline (a delta *sensu stricto*) and with a relatively flat topset region occurring in variable water depths, depending on the limiting oceanographic regime'. The MSDC does however show some deviation from the adopted

definition insofar the topset is not 'relatively flat' but defined by a system of shoreface-connected ridges with high relief reflecting a complex hydrodynamic system (see Chapter 7 section 7.4). The MSDC has a poorly developed or thin bottomset which is indicative of the effect of bottom water flowing along the contour (Cattaneo *et al*., 2003; 2007), proposed here to be the impact of the southerly flowing Agulhas Current (see Chapter 2.1.3). The asymmetrical nature (sigmoidal shape) of the MSDC in plan-view (Figure 6.4) and the lack of a well developed subaerial delta are characteristic for subaqueous delta deposits on high energy shelf environments (Columbia River, Wright and Nittrouer, 1995; Amazon River, Driscoll and Kraner, 1999) and reflects the regional oceanographic processes that redistributes fluvial sediment along the shelf (Cattaneo *et al*., 2007). This is further supported by the spatial separation of the shoreline and the clinoform rollover (6.5 km, line 5, Figure 6.5) which combined with the lack of a subaerial delta component classifies the MSDC, according to the model of Swenson *et al*. (2005), as a 'purely subaqueous delta end-member' and reflects a coastal storm dominated system where large waves and intense currents are strong enough to remove all sediment delivered to the surf zone, thereby preventing subaerial delta formation. Unit Dsc is thus interpreted as a prograding shore-attached subaqueous-delta clinoform sediment deposit based on the change from retrogradational (Dss, Ds) to overlying progradational stacking patterns (Dsc). As such it marks a change, albeit local, in the nature of the depositional systems from transgressive to regressive as a result of the local rate of sediment supply keeping pace with the rate at which relative sea-level rise generated accommodation space.

Thus in summary, Unit D comprises four sub-units (Dl, Ds, Dss and Dsc). Units Dl and Ds are dip variable units with Units Dss and Dsc considered lateral strike variable units and as such, for the purpose of this study, are regarded to form a depositional continuum (Table 6.2) evolving diachronously in different palaeoenvironmental settings during a sea-level transgression. Units Ds and Dl are considered to represent palaeo-depositional settings including a retrogradational back-barrier lagoon and a fluvial inter-dune deposit which evolved into a back-barrier estuary, respectively. Lateral equivalents, Unit Dss and the subsequent Unit Dsc, comprise palaeo-depositional settings including an open linear shoreline system (Dss) and a prograding subaqueous-delta clinoform (Dsc) with its topset re-organised by oceanographic processes into a complex system of shore-connected shoreface-connected ridges and its bottomset limit by bottom currents.

Correlation

Unit D forms part of the sediment package which is commonly referred to as the Holocene unconsolidated sediment wedge (Martin and Flemming, 1986; 1988; Birch, 1996; also see Chapter 3.5.2). It is therefore generally assigned a Holocene age (Table 6.1) and is correlated to Unit Q

(Figure 6.1) of Birch (1996), the Holocene unit (Figure 6.2a) of Martin and Flemming (1986; 1988) and Unit G (Figure 6.3) of Cawthra (2010).

OSL geochronological analyses of beachrocks capping seismic facies DsSF6 indicate sequential formation from ~11 to 9.9 ka B.P. during the last deglacial sea-level rise (Chapter 9). In addition, all the sub-units of Unit D (except Dsc) show an onlapping relationship with the ~134 to 79 ka B.P. Unit C. Based on this constraining age data it is suggested that Units Dl, Ds, Dss were deposited diachronously during the post-LGM sea-level rise (Flandrian transgression). This interpretation is further supported by seismic facies within these various sub-units of the lower division of Unit D showing a retrogradational stacking of coastal facies subjacent to the transgressive ravinement which is again subjacent to onlapping shallow marine deposits, all which are characteristic of transgression (Coe and Church, 2003b; Catuneanu, 2006). The age of the overlying prograding Unit Dsc is less well constrained by absolute dating methods. However, the active stage of Unit Dsc is interpreted to post-date Units Dss, Dl and Ds but there were some minor lateral temporal overlap between the *initialisation* of Dsc and the end of formation of Units Dl and Ds (see the section on the MSDC under Sequence 4, Chapter 6.4.3; Figure 6.13b). The present active part of Unit Dsc has formed after Units Dss, Ds and Dl as evident by a thin veneer of sediment (Section 8.4) overlying the beachrock (DsSF6) outcrops. Also, redistributed sediment of the Sandridge (SCR crest 1 and 2; Section 7.4.1 and Figure 7.10) occurs as sediment starved bedforms above Unit Dl within the North Basin (Chapter 7.2; Figure 7.3).

In conclusion, the sub-units of Unit D are considered to comprise a continuum of strike-variable depositional systems reflecting changes in the antecedent geology and local variations in the balance between relative sea-level rise and sediment supply and all of which were formed sequentially during the post-LGM sea-level transgression with deposition of Unit Dsc still continuing today.

6.4 SEQUENCE STRATIGRAPHIC INTERPRETATION

6.4.1 Introduction

Results from the seismic stratigraphic analyses (section 6.3) were used to construct a sequence stratigraphic model for the Aliwal Shoal Shelf. However, the application of sequence stratigraphic principles to the study area proved difficult. The reasons for the limitations can be summarised as follows;

1) Paucity of all types of data, not only from the shelf, but also from the adjacent coastal areas. There is a complete lack of lithological sample data from Units A and B thereby complicating lithological identification of identified seismic units. In addition none of the seismic units identified crop out directly onshore of the study area nor is there any borehole control available. Furthermore, chronological control on all of the seismic units is also almost non-existent. The exceptions are that of the exposed Aliwal Shoal portion of Unit C, beachrocks deposits capping Unit Ds and cautious age inferences for Units A and B from nannofossil biostratigraphy (refer to Chapter 9). This lack of chronological control was compensated by drawing comparisons to similar dated deposits elsewhere on the eastern South African continental shelf and coastal areas and with comparison to published local sea-level curves. In addition, no previous regional sequence stratigraphic model exists for this part of the continental shelf, the nearest being that of Cawthra (2010), located 50 - 60 km north, but that too is interpretive and lacks robust chronological control for the various seismic units.
2) The concept of sequence hierarchy. Results from the seismic stratigraphic interpretation indicated that the shelf stratigraphy can divided into four seismic units, representing four incomplete sequences. These varies significantly with respect to the hierarchal order they represent e.g. Unit A is interpreted to represent a 3^{nd} order cycle, whereas parts of Unit C is interpreted to consist of 4^{th} - 5^{th} order glacio-eustatic cycles and Unit Ds possibly represents 5^{th} - 6^{th} order high frequency sea-level changes. This issue is further complicated by the fact that Unit C is diachronous and consists of amalgamated aeolianite dune cores with superimposed beachrocks, all of which show different ages
3) Due to a combination of a unique physiography of the upper continental shelf, coverage of the study area and relatively shallow penetration and low resolution of the seismic instrument, this study only pertains to a section of the studied shelf basin feature. In addition there has been significant Tertiary uplift and erosion, the most recent to over 900 m during the Pliocene (see Section 3.5.1).
4) Interpretation of seismic profiles is further limited by the resolution (~4 m) and single channel nature of the seismic system which results in the generation of 'multiple' reflector returns obscuring the data. Hence, working in shallow water, as for this study, reliable interpretation is mostly limited to areas above the multiple reflections.

The sequence stratigraphic interpretation model of the Aliwal Shoal presented here is thus an interpretive conceptual framework from which to assess the stratigraphic evolution of this section of the South African continental shelf. Confirmatory sample data are required to further support the interpretations from this study and to test the stratigraphic assumptions from previous investigations, especially with reference to inferred ages for the major units.

6.4.2 Sequence Stratigraphic Terminology

The seismic stratigraphy presented in the previous section is interpreted in a sequence stratigraphic model using established procedures (Mitchum and Vail (1977), Vail (1987), Coe and Church, 2003b), Catuneanu (2006) and Catuneanu *et al*., (2009). In the interest of standardising seismic sequence stratigraphic interpretations from the east coast of South Africa and reduce the proliferation of sequence stratigraphic terms and models this study will adhere to the terminology established by Green (2009a) and subsequently also adopted by Cawthra (2010).

Accordingly, four systems tracts are recognised in each sequence which comprise a complete cycle of base-level change (Figure 6.11a): the highstand systems tract (HST), the falling-stage systems tract (Plint and Nummedal, 2000), also termed the forced regressive systems tract (FRST; Hunt and Tucker, 1995), the lowstand systems tract (LST) and the transgressive systems tract (TST).

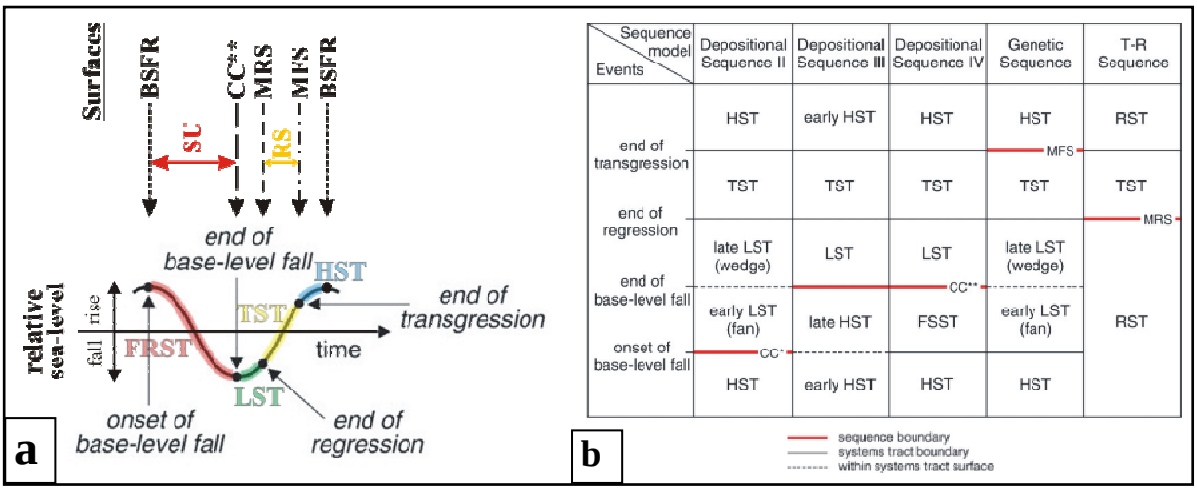

Figure 6.11 a) Timing of the systems tracts and sequence stratigraphic surfaces relative to the main events within a full cycle of base-level change (modified from Catuneanu, 2006). **b)** Timing of systems tracts and the sequence boundary as defined by the various sequence stratigraphic models (from Catuneanu *et al*., 2009). This study is based on depositional sequence model IV. LST = lowstand systems tract, FRST = forced regressive systems tract, TST = transgressive systems tract, HST = highstand systems tract, FSST = falling-stage systems tract, RST = regressive systems tract; T-R = transgressive–regressive, CC* = correlative conformity *sensu* Posamentier *et al*. (1988), CC** = correlative conformity *sensu stricto* Hunt and Tucker (1992), BSFR = basal surface of forced regression, SU = subaerial unconformity, MRS = maximum regressive surface, MFS = maximum flooding surface, RS = transgressive ravinement surface. Note that the BSFR is equivalent to the correlative conformity of Posamentier *et al*. (1988).

The HST is considered to form during the late stage of base-level rise when the rates of sediment supply outpaces the rates of relative sea-level rise resulting in depositional trends and stacking

patterns dominated by aggradational and progradational processes (Catuneanu, 2006). FRST forms in response to a falling relative sea-level (or forced regression) resulting in erosion and a lowering of the depositional profile of the shoreline and a subsequent basinward progradation of facies belts with high sediment supply to the shallow and deep marine environments (Coe and Church, 2003b; Catuneanu, 2006). The LST forms between the end of base-level fall (minimum sea-level) and during the early stage of base-level rise when the rate of relative sea-level rise is less than the sedimentation rate and as such are associated with low-rate aggradational and progradational depositional trends and stacking patterns (Coe and Church, 2003b; Catuneanu, 2006). The TST forms during a rise in relative sea-level when the rate of rise exceed the sedimentation rate and consequently is characterise by the landward migration of the shoreline and subsequent diagnostic retrogradational facies stacking patterns (Coe and Church, 2003b; Catuneanu, 2006, Catuneanu *et al*., 2009).

Although sequence stratigraphic interpretation is mostly model-independent the placement of the sequence boundary (SB) is not. Consequently this study follows depositional sequence model IV (Figure 6.11b) and as such considers the SB an unconformity surface that occurs above the regressive FRST deposits and which is formed by subaerial erosion and correlated distally to a correlative conformity (*sensu* Hunt and Tucker, 1992). Although the position of SB relative to the FRST is controversial (see Plint and Nummedal, 2000; Coe and Church, 2003b), its placement here is on the subaerial unconformity (or correlative conformity) following that of Catuneanu (2006) and Green (2009a) above the basinward prograding FRST deposits. Definition of the correlative conformity follows that of Hunt and Tucker (1992) as a surface that forms in the marine environment at the end of base-level fall as the seaward continuation of the subaerial unconformity. The basal surface of forced regression (BSFR; Hunt and Tucker, 1992) forms at the onset of base-level fall, flooring all forced regressive deposits in the marine environment and is also equivalent to the correlative conformity of Posamentier *et al*. (1988). Transgressive ravinement surfaces form by wave and tidal erosion during a shoreline transgression (Catuneanu, 2006).

6.4.3 Sequence- and Chronostratigraphic Model

Sequence stratigraphic interpretation of the four seismic units described, interpreted and correlated in Chapter 6 indicate that these units comprise at least 4 incompletely preserved sequences. The sequence stratigraphic model for the study area is presented in Table 6.3 and schematically illustrated in Figure 6.12.

Table 6.3 Sequence stratigraphical interpretation and chronostratigraphical model for the four seismic units (Section 6.3) identified in the study area. The seismic stratigraphic numbering of the unconformity surfaces is bracketed behind the sequence stratigraphic designation. Although Unit C contain at least two high order sequence boundaries based on geochronological analyses (Chapter 9; Figure 6.13b) it is grouped here as one sequence for simplicity and comparison to other studies. SB = sequence boundary; FRST = forced regressive systems tract, LST = lowstand systems tract, TST = transgressive systems tract, HST = highstand systems tract, MFS = Maximum Flooding Surface, ** = correlative conformity *sensu* Hunt and Tucker (1992).

Seismic unit	Sequence	Systems tract	Chronostratigraphical model
Dsc	*4*	HST (local)	Holocene
Localised MFS2 (Reflector DLS)			
Ds, Dl, Dss	*4*	TST	Latest Pleistocene (LGM) - Holocene
SB3 (US3) LGM forced regression			
C	*3*	TST, FRST	Pleistocene, diachronous, ~139 - 74 ka B.P.^
SB2 (US2) Complex subaerial unconformity surface spanning most of the Quaternary			
B	*2*	LST (FRST?)	Late Pliocene
SB1 (US1) Complex subaerial unconformity surface spanning most of the Tertiary			
A	*1*	FRST	Maastrichtian
MFS1 (reflector ARR)			
A	*1*	TST (HST?)	Campanian

^Age data from this study (see Chapter 9).

The four sequences are separated by three sequence boundaries (SB1 - SB3) comprising complex reworked subaerial unconformity surfaces. The partial preservation and lack of representative units is highlighted by the fact that, with the possible exception of Unit A which might comprise two sequences, each of the different seismic units identified (Section 6.3) constitute a separate sequence (Table 6.3). The poor preservation is ascribed to removal of an unknown amount of strata during the Tertiary uplift (see Section 3.5.1) and a shallow shelf morphology resulting in the entire shelf becoming subaerially exposed and subjected to denudation during sea-level regressions exceeding -85 m (Figures 6.5 - 6.9), a common occurrence during the high frequency and amplitude sea-level oscillations of the Quaternary.

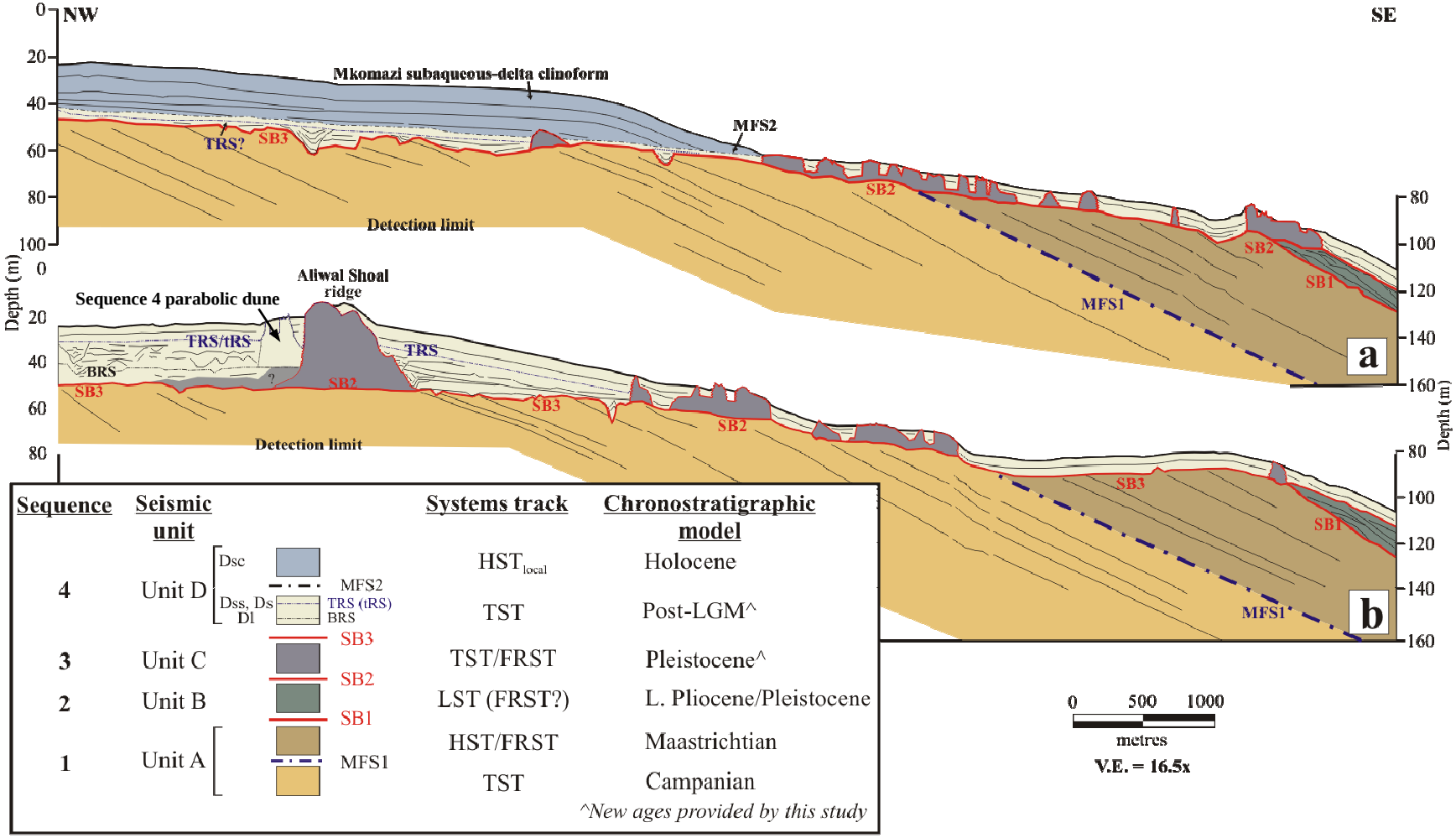

Figure 6.12 a) and **(b)** Down-dip sequence stratigraphic interpretation and chronostratigraphic model for the study area. Also shown are the end-member examples of strike variability of inner and middle shelf TST units of Sequence 4. In the south **(b)** TST Units Ds and Dl are very well developed and preserved between parallel ridges of Sequence 3 where they comprise retrograding back-barrier lagoonal and estuarine deposits. To the north **(a)** TST deposits of Sequence 3 are represented by Unit Dss where it is thin, poorly preserved and occupies palaeo-topographic lows eroded within Sequence 1.,Here it is interpreted as an open shoreline depositional environment where it is also subjacent to the HST prograding shore-attached clinoform of Unit Dsc. The HST is designated 'local' as it occurs off a major river mouth and as such indicates only a change in the character of deposition due changes in the balance between the rates of relative sea-level rise and sedimentation along strike. Overall, the shelf is still within a transgressive regime. Unit Dsc thins southwards and is present above units Dl and Ds but below the resolution of the seismic tool used. Interpretation **(a)** is seismic line 5 and **(b)** is line 7, refer to Figure 6.4 for locality. FRST = forced regressive systems tract, TST = transgressive systems tract, HST = highstand systems tract, SB = sequence boundary, MFS = maximum flooding surface, TRS = transgressive ravinement surface, BRS = bay ravinement surface, tRS = tidal ravinement surface.

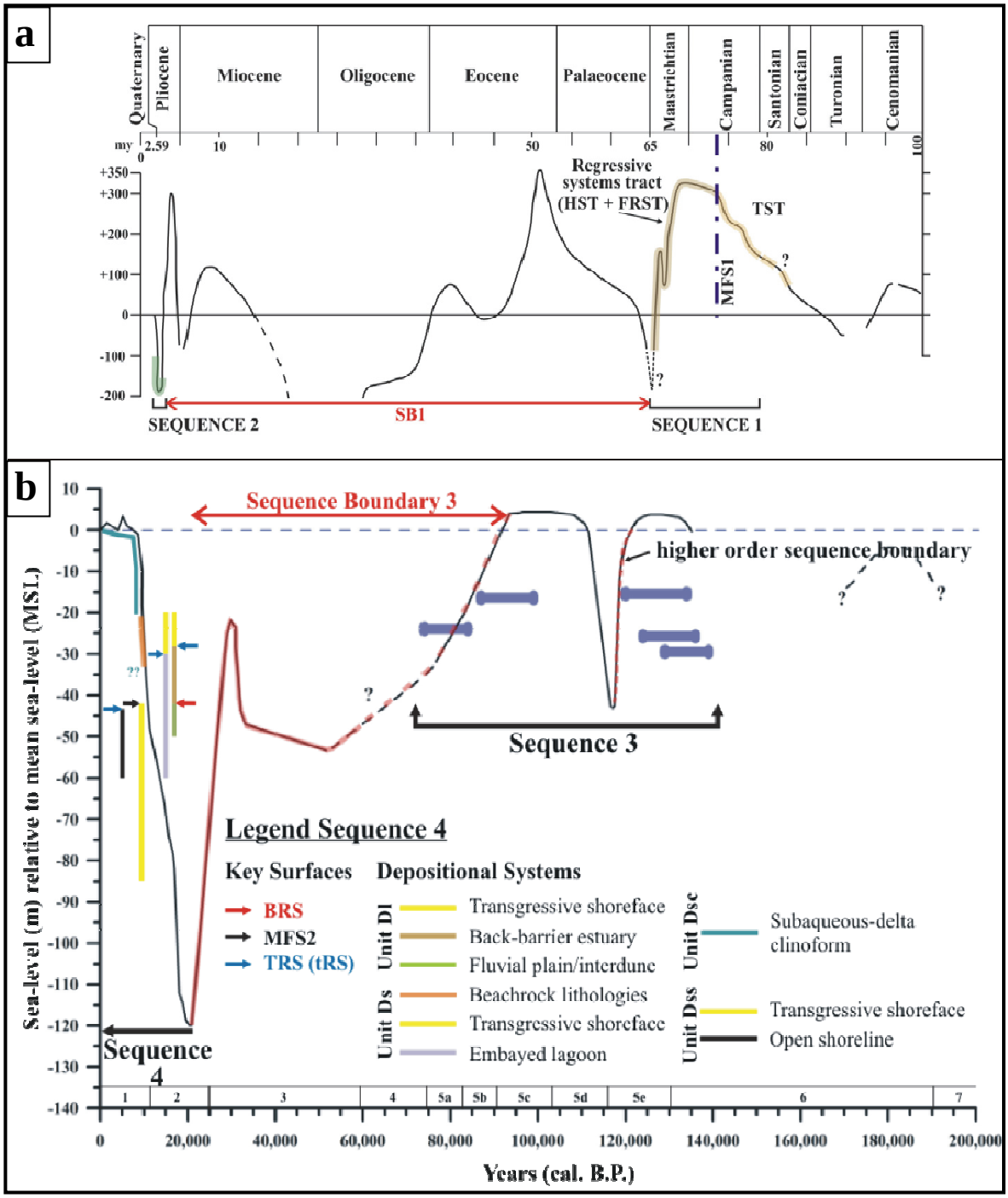

Figure 6.13 Sequence- and chrono-stratigraphic models for Sequences 1 to 4. **a)** Graphic representation of Sequences 1 and 2 on the sea-level curve of Dingle *et al*. (1983). **b)** Detailed illustration of Sequence 3 (also see Chapter 9) and the transgressive systems tract Sequence 4 (see Table 6.4 for ages) plotted on the calibrated sea-level curve of Ramsay and Cooper (2002). Refer to Chapter 9 for details on the calibration. TRS = transgressive ravinement surface, tRA = tidal ravinement surface, MFS = marine flooding surface and BSR = bay ravinement surface, FRST = forced regressive systems tract, TST = transgressive systems tract, HST = highstand systems tract.

This has the further consequence that SB1 to SB3 are complex composite reworked erosional stratigraphic surfaces e.g. the transgressive ravinement surface DsRT reworking SB3 (US3; Figure 6.6c - 6.9c) and SB1 reworked by SB2, SB3 and Unit D (outer shelf, Figures 6.5 - 6.9). In these cases where the sequence boundaries are superimposed, the name of the youngest boundary surface is used. Strike variability in terms of thickness and stratal characteristic are common for Sequences 3 and 4, whereas Sequences 1 and 2 seem to display more uniform lateral characteristic. The chronostratigraphic model for the various system tracts is based on correlation to new geochronological data from this study (Chapter 9), pre-existing local sea-level curves (Figure 6.13) and published stratigraphic data (see Section 6.3).

Sequence 1

Sequence 1 (Table 6.3) comprises Seismic Unit A which shows the presence of a basin-wide high amplitude reflector, reflector ARR, interpreted to represent a major change in the depositional basin at the time. Based on reflector configuration (Section 6.3.1) and nannofossil data (Chapter 9), Unit A is interpreted as Campanian to Maastrichtian in age where Unit A strata lies below and seaward of Unit C (Section 6.3.1). From the Cretaceous sea-level curve (Figure 6.13) three possible sequence stratigraphical surfaces may be represented by reflector ARR. These are; 1) the unconformity surface related to the Maastrichtian forced regression, 2) the basal surface of forced regression (BSFR) separating Campanian HST strata below from Maastrichtian FRST strata above, or 3) the maximum flooding surface (MFS) relateded to the end of the Campanian transgression.

During the mid Campanian to early Maastrichtian sea-level was ~400 m above (Dingle *et al*., 1983; Figure 6.13) of reflector ARR (-90 m below MSL). Also the present position for the top of reflector ARR, is also stratigraphically higher than during deposition due to the Tertiary uplift (Section 3.5.1). Thus, reflector ARR represents conditions that were prevalent deeper in the basin. Reflector ARR also lacks the typical reflector configuration (truncation, incision etc.) associated with a subaerial unconformity. Consequently, if reflector ARR is interpreted as an unconformity surface related to the Maastrichtian forced regression the only option left is that of a correlative conformity formed in the marine portion of the basin at the end of base-level fall (Figure 6.11a). But recognition of a correlative conformity is difficult due to conformable sedimentation continuing unabated during formation and as such it would show small density-velocity contrasts resulting in a low amplitude seismic surface, thereby ruling out a correlative conformity origin for reflector ARR. The sequence stratigraphic reflector ARR might possibly be a BSFR (*sensu* Hunt and Tucker, 1992) which forms the base to all strata deposited in the marine environment during a forced regression and as such separates the progradational HST below from the progradational

FRST above (Catuneanu, 2006). However, as with the correlative conformity, the conformable BSFR is not easily recognisable on seismic data (Catuneanu, 2006), especially when it cannot be correlated with the FRST deposits where it forms the oldest clinoform associated with offlap. Subsequently the BSFR origin for reflector ARR is also not favoured.

At the end of the Campanian transgression (Figure 6.13a) the shoreline and the associated locus of sedimentation reached its maximum landward position (~400 m above present top surface of reflector ARR) subsequently greatly reducing or even cutting-off terrigenous sediment supply to the shelf and deeper basin environments. This sediment starvation resulted in the formation of a condensed section (hardgrounds) or submarine unconformity, the top of which formed the MFS (Coe and Church, 2003b; Catuneanu, 2006). Its high preservation potential, broad areal extent and ease of recognition (unconformity surface within fine-grained low energy systems; Catuneanu, 2006) makes the MFS a more prominent seismic surface than the correlative conformity and BSFR. As such this study interprets reflector ARR as a maximum flooding surface (MFS1) formed distally in the basin in response to the Campanian HST. MFS1 is overlain by downlapping and prograding shelf-building Maastrichtian regressive deposits (Figure 6.12). Sequence 1 can thus be subdivided into a lower TST separated by MFS1 from overlying HST/FRST regressive deposits prograding over a postulated Campanian palaeoshelf break.

This sequence stratigraphic interpretation of the Cretaceous strata differs from that of Cawthra (2010; Figure 6.3) insofar no Santonian units were identified (although these possibly are present below the Campanian and Maastrichtian strata of Sequence 1) and in the placement and interpretation of sequence boundaries and stratal characteristics. Cawthra (2010) assigned a *subaerial* unconformity bounded sequence boundary (SB 1; Figure 6.3c) on the Campanian - Maastrichtian (mid-HST) boundary and another subaerial unconformity bounded sequence boundary (SB 2) at the end of the Maastrichtian forced regression (Figure 6.3c). Thereby assigning a subaerially exposed sequence boundary to the beginning (SB 1) and the end (SB 2) of the Maastrichtian forced regression (Figure 6.3b and c). This is clearly not possible and is not in accordance with sequence stratigraphic principles. Although Cawthra (2010) does not clarify the sequence boundary model used, she places SB 1 between the Campanian HST and the Maastrichtian FRST (Figure 6.3b and c), something which is not likely either, as the subaerial unconformity will overlie and erode subjacent FRST (FSST) deposits. Also on Cawthra's (2010) seismic interpretation, reflectors are seen to onlap MFS 1 (Figure 6.3a). As this is a down-dip seismic line, reflectors are by definition expected to downlap and not onlap the maximum flooding surface. In addition, Cawthra (2010) interpreted 'subordinate incisions' and palaeo-river channels from the late Santonian (Figure 6.3a, Unit A). However, even during the late Santonian the palaeosea-level was more than 100 m above the present level not considering that the 'palaeo-river

channel' is at least 50 m below present sea-level. It seems unlikely that sea-level can regress >150 m and only incise river channels during an overall transgression (Figure 6.3c) without leaving other evidence.

From the foregoing discussion it is clear that much work is needed to resolve the uncertainties related the different Cretaceous units that volumetrically dominate the shallow shelf stratigraphy. Until such time, the various sequence stratigraphic interpretations (this study; Cawthra, 2010) can only be considered models awaiting further validation.

Sequence Boundary 1 (SB1)

Sequence 1 is separated from overlying Sequence 2 by the subaerially exposed unconformity of SB1 (Figure 6.12; Table 6.3). SB1 is equivalent to surface US1 (Section 6.3), underlies strata from Sequence 2 (Late Pliocene; Unit B) and is presumed to have formed since the end of the Maastrichtian forced regression (Figure 6.13a). As such SB1 is a ~60 million year old surface representing multiple erosional events that is interpreted here to be responsible for bevelling the Cretaceous strata and the removal of Palaeogene and Miocene units. These erosional events include the significant Tertiary uplift (Partridge and Maud, 2000) and a major forced regression which resulted in subaerially exposing the continental shelf for a period spanning almost the entire Oligocene and lower Miocene (Figure 6.13a). The Oligocene sea-level lowstand was interpreted to have reached as low as 530 m below present sea-level (Siesser and Dingle, 1981).

Sequence 2

Sequence 2 comprises Unit B (Table 6.3) showing a shelf edge and slope complex with prograding to aggrading reflectors, downlapping SB1 (Table 6.2, Section 6.3.2) and is interpreted as a Late Pliocene to Early Pleistocene (considering that the Pleistocene now includes the Galasian Stage) LST shelf edge wedge. The LST forms at the early stage of base-level rise (Figure 6.11a) and as such is characterised by low-rate aggradational and progradational stacking patterns and hence depositional systems (Catuneanu, 2006). Due to the creation of accommodation space during the rising sea-level the lowstand wedge can include the entire range of depositional systems from fluvial to deep marine (Catuneanu, 2006). Basal prograding offlapping units are interpreted as shelf building early LST normal regressive shoreface deposits which evolved into overlying late LST aggradational facies possibly related to the sea-level turn-around from regression to transgression (Figures 6.5 to 6.9).

Since there is no evidence for palaeo-river channel incision landward of the shelf edge deposits (Figures 6.5b to 6.9b) and all major tectonics ceased after the Pliocene, this area of the shelf would have been an area of sediment bypass during the lowstand responsible for deposition of Unit B. Consequently, the shelf edge wedge can thus not be a lowstand shelf edge delta as there is no river directly onshore. Instead, the shelf edge wedge is interpreted here as a prograding and aggrading strandplain in an open shoreline setting (Catuneanu, 2006). As such sediment was provided from palaeo-river mouths and associated shelf edge deltas located south- and north-wards of the study area. Sediment distribution from these deltas to the strandplain depositional environment is attributed to longshore currents (Catuneanu, 2006). This interpretation is further corroborated by the fact that the fluvially incised inner and middle shelf channels (Figures 6.5b - 6.9b) are coast-parallel, commonly constrained between Sequence 3 ridges and therefore comprise incised tributaries of a larger river system (e.g. Mkomazi River) located either to the north or south of the study area.

Sequence Boundary 2 (SB2)

Sequence boundary 2 (SB2) is subjacent to Sequence 3 (Unit C) erosionally truncating Sequences 1 and 2 (Figure 6.12; Table 6.3). SB2 is interpreted to span most of the Pleistocene and formed by repeated subaerial exposure related to the numerous sea-level oscillations especially the high amplitude sea-level fluctuations prevalent since the Middle Pleistocene (see Chapter 4). The surface represented by SB2 is thus a complex surface that reworked SB1 in places and as such represents many erosional events, the last of which predates formation of Unit C (Table 6.2). It is clear that the present shelf break position was already established following the erosional period of SB1 with minor modification in the form of progradation of Sequence 2 only slightly increasing the shelf width.

Sequence 3

Sequence 3 (Figure 6.12; Table 6.3) consists primarily of coast-parallel, carbonate cemented aeolianite palaeoshoreline ridges of various ages (Table 6.2; Section 6.3.3) overlying Sequence 1 and 2. The study area is dominated by two major ridge systems; an inner shelf Aliwal Shoal ridge and a seaward middle shelf ridge (MSR). Smaller less pronounced ridge systems are present intermittently along the outer shelf and slope (Figures 6.6 to 6.9). A relationship exists between the palaeo-land surface of SB2, which represent the bevelled Sequence 1 and 2 strata and the occurrence of the inner and middle shelf Sequence 3 barrier ridges. These well developed Sequence 3 ridges are observed to be predominantly located on terraced areas of SB2 (Figure 6.14a). On the Adriatic shelf Storms *et al*. (2008) also observed drowned barrier-lagoon systems

present on areas of terraced antecedent topography. They subsequently produced a model for barrier evolution during a sea-level transgression (Figure 6.14b) involving barrier development on the edge of the seaward-facing steep part of the terrace with incremental upward and landward growth ultimately resulting in barrier overstep due to the rapid increase in back-barrier depth and width. Although interpreted as a single unit (Unit C) and Sequence (3) geochronological analyses (Chapter 9) of one such ridge, the Aliwal Shoal ridge, showed that it comprises a compound feature formed over three 5th to 6th order sea-level cycles (Figure 6.13b) both during TST and FRST sea-level regimes. As such the Aliwal Shoal ridge of Sequence 3 can be divided into two sequences, however due to seismic and geochronological data limitations this is impractical. Nonetheless, although these ridges have been dealt with in previous studies (Ramsay, 1991; Birch, 1996; Martin and Flemming, 1986; Green, 2009a,b; Cawthra, 2010) this is the first evidence that a single ridge comprises a compound structure forming time transgressive units during both transgressions and forced regressions. As such the difference between the modelled evolution of the Adriatic barrier-lagoon systems (Storms *et al.*, 2008) and the Aliwal Shoal barrier ridge is that the latter formed during both transgressive and regressive sea-level regimes (Figure 6.13b).

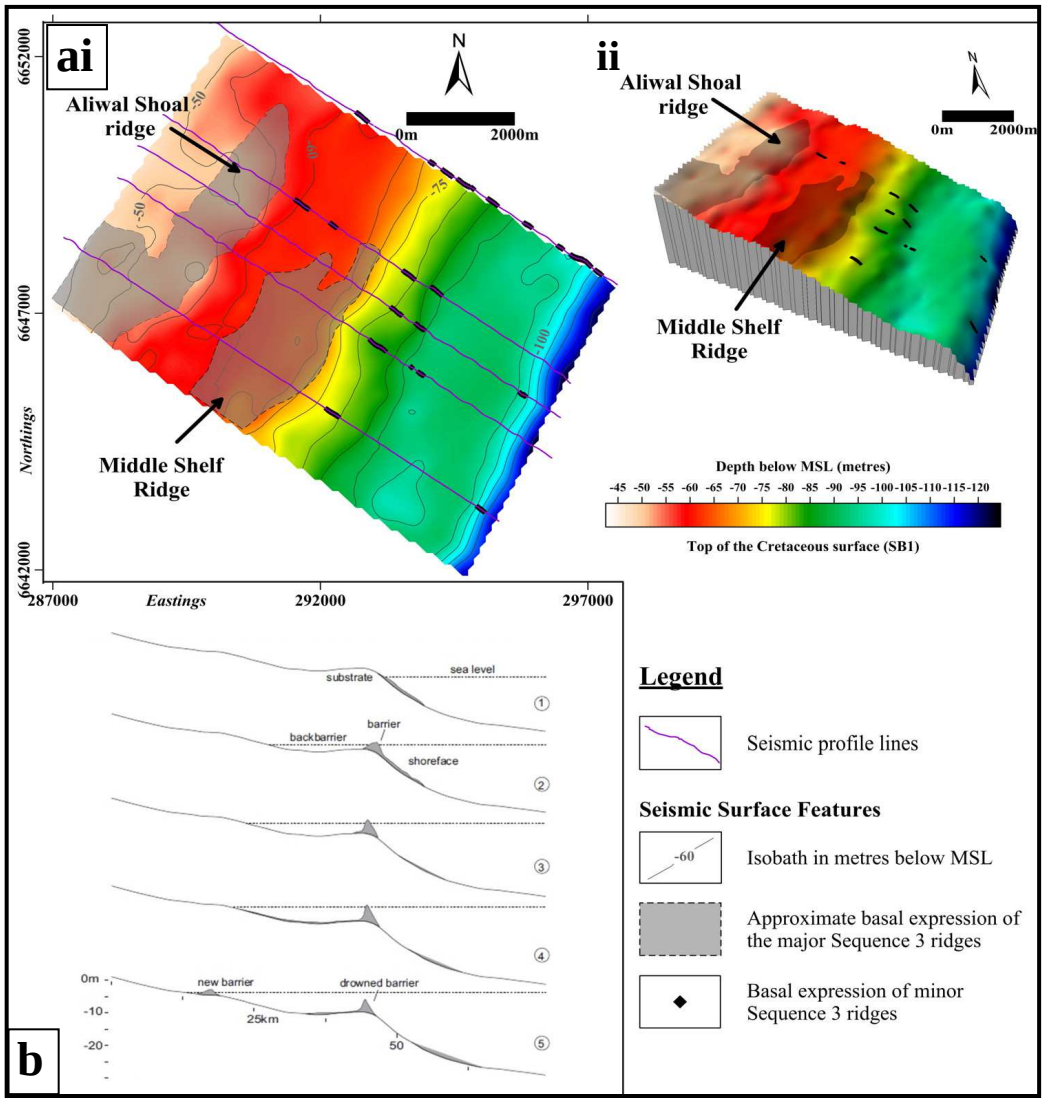

Figure 6.14 a i) Map showing the depth to the top of the Cretaceous surface (SB1) below MSL with the inferred basal expression of the major Aliwal Shoal and MSR ridges of Sequence 3. The base locations of the minor Sequence 3 ridges are plotted as points. Note the occupation of Sequence 3 ridges on terraced areas of the Cretaceous surface. **ii)** 3D model of the seismic surface in **(a i)**. **b)** Model of formation of barrier ridges on terraces controlled by palaeo-topography during a sea-level transgression (from Storms *et al*., 2008).

Although the Sequence 3 Aliwal Shoal barrier system shows a more complex evolutionary history (Figure 6.13b) than its Adriatic counterparts, the antecedent topography is possibly responsible for exerting a fundamental control on the location for the development of the Sequence 3 ridges. The other controlling factor for establishment of these aeolianite ridges would have been the presence of fluvial systems, but this also would at least in part be controlled by the antecedent geology and subsequent physiography. This is supported by observations of the coast-parallel nature of the fluvial network which is constrained to the inner and middle shelf regions (Figures 6.5 to 6.9) often located landwards and in-between dip-slope hardgrounds of Sequence 1 (Figures 6.5, 6.6 and 6.8 - middle shelf; Figure 6.7 - inner shelf).

Sequence Boundary 3 (SB3)

Sequence boundary 3 (SB3) comprises the subaerial unconformity surface formed during the depression of sea-level from peak interglacial highstand conditions (MIS5) towards the lowstand conditions (-120 m) of the LGM ~20 ka B.P. (Figure 6.13). It probably spans MIS5b to 2 (~72 ka) representing an overall deterioration of global climate and associated sea-level instability characterised by 10 - 15 m changes in sea-level (Figures 4.5 and 4.6) every ~6 - 7 ka (see Section 4.4.2). However, it is also possible that the actual subaerial unconformity surface was formed only during MIS 3 i.e. < 60 ka B.P. (Hijma and Cohen, 2011).

Incised palaeoriver channels are coast-parallel (Figures 6.15) and constrained mostly between Sequence 3 ridges indicating that these are incised tributaries of a larger river system. Interestingly, these are expected to be tributaries of the large Mkomazi River however, interpreted channel convergence (Figure 6.15) suggests flow towards a major river located to the south, possibly the Mzinto River, ~10 km south of the study area which shows deeply incised river gorges. Similarly to the earlier sequence boundaries, SB3 is a complex surface reworking not only Sequences 1 to 3 but also the previous sequence boundaries in places.

Sequence 4

Sequence 4 (Figures 6.12 and 6.13b; Table 6.3) is divided into a lower TST component (seismic Units Ds, Dl, Dss) displaying characteristic retrogradational stacking patterns and an upper local HST clinoform component (seismic Unit Dsc) showing progradation and downlapping. Inner and middle shelf TST Units Dl and Ds further show a progression from lagoonal and lower fluvial-estuarine deposits overlain by foreshore and shoreface sands (Section 6.3.4), thereby documenting the changing depositional environments in response to a sea-level transgression. Lateral equivalent, Unit Dss does not fully preserve this record especially on the outer shelf where it comprises a thin transgressive sand sheet similar to that found by Green (2009a) and Cawthra (2010). Not only is Sequence 4 highly variable along strike due to the variability of depositional systems but also highly diachronous along dip due to the deposits becoming younger in a landward direction as transgression proceeded.

Sequence 4 is interpreted as transgressive sediments deposited during the last deglacial sea-level rise with deposition still ongoing today (Figure 6.13b; Section 6.3.4). The possibility that the middle and inner shelf unconsolidated sediments of Sequence 4 (especially Units Dl and Ds) represent sediments deposited during earlier regressive systems tracks is ruled out on the basis that there is no indication of a subaerial unconformity surface within these deposits. In addition, these deposits onlap the Aliwal Shoal Sequence 3 ridge (Figure 6.14), the age of which is constrained to the previous sea-level cycle (Figure 6.13b) implying deposition after the Sequence 3 subaerially exposed boundary (SB3). Furthermore, the lack of palaeo-river channels on the outer shelf indicates that this was an area of sediment bypass during the last glacial sea-level regression (SB3), thereby suggesting that if any shallow marine normal or forced regressive deposits were present, that these were thin and subsequently reworked in a landward direction by the ensuing last deglacial transgression. LST deposits are considered absent from the shelf environments as the LGM sea-level lowstand (-120 m below MSL) occurred well below the modern shelf edge (Figures 6.6 to 6.9). In addition, the continental slope deposits (above -120 m) exhibit the same thickness and seismic signature as TST sediments (DSF6) on the outer shelf.

Figure 6.13b shows the chronological model for the development of Sequence 4 TST depositional environments based on key seismic stratigraphic surfaces (Figure 6.13b). Note that the ages quoted are approximate (except for the beachrocks and Sequence 3; see Chapter 9) and derived from a bathymetric position relative to the local relative sea-level curve (Figure 6.13b). In the interest of simplicity the physically continuous but diachronous transgressive ravinement surface (TRS, Figures 6.12, 6.13b, 6.15 and 6.16) is plotted as a single time event (Figure 6.13b) indicating the inferred marine overstepping of the retrograding embayed lagoon (DsSF1 - 5) and

aggrading back-barrier estuary (DlSF2 - 4) depositional systems, thereby providing an upper age limit for the embayed barrier-lagoon and back-barrier estuarine systems. Due to the high strike and dip variability of the depositional systems, variable palaeo-topography and the differential erosional scour of the ravinement process, the transgressive ravinement laterally may occupy the same depth range as the depositional systems it oversteps and as such appears to be of an overlapping age when depicted on a sea-level curve (Figure 6.13b). This is clearly not the case with the ravinement surface being younger than the underlying facies but illustrates the problem of plotting a diachronous ravinement surface on an age-depth plot. A similar problem occurs when trying to plot the lagoonal sequence with a depth range of ~60 to 30 m. It for instance shows overlap in bathymetry and hence age with the superjacent and younger beachrock units - a result due to the seaward dip of the palaeo-topographic surface of the lagoonal system. To this extent the annotation of the Sequence 4 depositional systems in Figure 6.13b is illustrative and prioritises bathymetric occupation over age. However, the interpreted age constraints for the different depositional systems are presented in Table 6.4 and are also used in the evolutionary model in Chapter 9.

The general development of the Sequence 4 depositional systems during the last deglacial sea-level rise (Table 6.4 and Figure 6.13b; ages given in cal. B.P.) are interpreted and summarised as follows;

i) Outer and middle shelf environments show an early TST (~20 - 14 ka B.P.) back-stepping sequence comprising deposition of linear shoreline depositional systems followed by reworking and erosion by the transgressive shoreface which deposited a thin transgressive sand sheet on the outer shelf and possible transgressive ‘healing-phase’ deposits on the slope.
ii) Initiation of embayed back-barrier lagoonal conditions in between the Sequence C ridges of Aliwal Shoal and the MSR at ~12.3 ka cal. B.P. This lagoonal system evolves under continuous aggradational and retrogradational depositional regimes as the Holocene sea-level rise ensues. Along strike to the north an open shoreline setting prevailed with small localised estuarine/lagoonal and beach-barrier palaeo-depositional environments preserved only in areas where palaeo-topography provide accommodation space.
iii) Continued aggradation and retrogradation of the lagoonal sequence during the last deglacial transgression is accompanied by the formation of a bay ravinement surface (BRS) at ~11 ka B.P.in the back-barrier area landward of the Aliwal Shoal ridge and as such signified a change from fluvial to estuarine conditions. As a result the Aliwal Shoal ridge is flanked on its seaward side by an embayed back-barrier lagoonal system and on its landward side by a back-barrier estuary. Both these systems are inferred to have had open shoreline connections to the north with the estuarine system also connected with the lagoonal system through a tidal inlet cut into the Aliwal Shoal ridge south of Unit A1 aeolianite (Figure 8.18).

Table 6.4 Summary table of the chronological criteria used in constraining the ages for the various depositional systems of Sequence 4. The age model is based on new data and the calibrated (refer to Chapter 9) sea-level curve of Ramsay and Cooper (2002) compatible with the beachrock and aeolianite ages from this study. Note that all ages are calibrated calendar ^{14}C ages before AD 1950 (cal. ka B.P.). OSL = optically stimulated luminescence; other abbreviations are as for Figure 6.13 and Table 6.2.

Depositional system/surface	Seismic designation		Depth range (metres below MSL)	Age criteria (cal. ka B.P)*		Notes
				Max	Min	
Shoreface-attached subaqueous delta clinoform	Unit Dsc		~62 - 22	<9.5? to present		Initialisation is assumed to be in a water depth of at least 20 m. Age uncertain based on post dating DlSF5/DLS and on depth of 'core' clinoform at ~ -40 m..
MFS2		DLS	~62 - 42	~12 to 9.5?		Diachronous surface, post transgression of Dss shoreface.
Transgressive shoreface	Unit Dss	DSF6	~120 - 42	~20	9.5	Lateral equivalent to DsSF6/DlSF6.
TRS		DRT	~<60 - 44	~11.2 - 10		Diachronous surface. Age is based on lateral inference from DsRT & DlRT
Open shoreline setting		DSF1, 2,5	~60 - 44	~12.3	~11.2	Depth ranges from seismic profiles.
Transgressive shoreface	Unit Dl	DlSF5	~38 - 20	~10	~9.5?	Ages are minima, oldest deposits cannot pre-date estuary. Also includes overlying unresolved Unit Dsc deposits
TRS (+tRS)		DlRT/ DlRb	~38 - 28	~10		Depth range is for occurrence above estuarine deposits only, age is a minimum. Diachronous surface.
Embayed back-barrier estuary		DlSF2, 3,4	~42 - 28	~10.9	~10	Depth ranges from seismic profiles, minimum age (OSL) from youngest beachrock.
BRS		DlRa	~50 - 42	~11		Diachronous surface, age is a maximum
Fluvial deposits		DlSF1	~50 - 42	~11.5	~11	Depth ranges from seismic profiles.
Transgressive shoreface	Unit Ds	DsSF6	~60 - 20	~11	~9.8	Ages are the OSL mid-point ages for the beachrocks (Table 9.7). DsSF6 also includes unresolved overlying Unit Dsc deposits.
TRS		DsRT	~60 - 30	~10.3		Depth range is for occurrence above lagoonal deposits only, age is a minimum. Diachronous surface.
Embayed back-barrier lagoon		DsSF1 -5	~60 - 30	~12.3	~10.3	Depth ranges from seismic profiles.

iv) Northwards along strike, slightly preceding the change to estuarine conditions (~11. ka B.P.), the open shoreline depositional environments were being overstepped by the transgressive shoreface, the passage of which formed the transgressive ravinement surface which was subsequently buried by a thin transgressive sediment sheet. Coeval with creation of the BRS in the south, the shelf above the now buried open shoreline deposits were rapidly deepening, its shallow gradient (Figure 6.14) resulting in a rapid landward shift in facies due to the wide

area being transgressed (see following section for transgression on low vs. high gradient) consequently forming surface DLS.

v) In the south the retrogradational lagoonal and aggradational estuarine systems were progressively overstepped by the transgressive shoreface, the passage of which was documented above the lagoonal deposits as a sequence of beachrock deposits. The lagoonal system was finally drowned by ~10.3 ka B.P. followed shortly afterwards by the estuarine system at ~10 ka B.P. The relatively short life span and abrupt transgression of the estuarine system was probably due to the rapid increase in back-barrier width and depth (no further Sequence C ridges landward and an even palaeo-topography, e.g. Storms *et al*., 2008; Figure 6.14b) resulting in the complete overstepping and drowning of the Aliwal Shoal barrier ridge system.

vi) To the north the rapidly deepening water column provided accommodation space which was filled with sediments delivered from the numerous fluvial systems (<9.5 ka B.P.). Locally, this sediment supply matched the relative sea-level rise resulting in an overall change from retrogradational to progradational stratal architecture and formation of a local highstand systems tract represented by the *Mkomazi Subaqueous-Delta Clinoform*. As is the case for the Shadong clinoform (Liu *et al*., 2007) the seaward growth of MSDC is proposed to occur by overlapping alongshore and cross-shore sediment transport (Figure 6.17a). Oceanographic processes not only limit the clinoform bottomset but also shape the topset into a complex system of shoreface-connected ridges (refer to the section below for the depositional history of the MSDC).

vii) Foreshore and shoreface deposition was active until <9.8 ka ca. B.P. across the lagoonal system and ~9.5 ka cal. B.P. across the estuarine system whereafter sea-level finally drowned this part of the shelf.

viii) Presently the shelf is still in a transgressive regime but deposition on the MSDC is still ongoing and comprises aggradation concurrent with progradation. The long term stability of the clinoform will be determined by the relative balance between the rate of sea-level change and sediment availability whilst oceanographic process such as swell and currents are considered secondary controls affecting the sediment transport pathways (Figure 6.17a) and hence morphological evolution of the MSDC.

Unit Ds: Antecedent geology, TST sedimentation and the transgressive ravinement surface

As discussed above the lower TST dominated unit shows high strike-variability in the depositional environments (Table 6.2) ranging from embayed back-barrier lagoonal (Ds) and back-barrier

estuarine (Dl) to open shoreline facies (Dss, northern Ds). This change in the character of the shoreline along strike parallels the modern shoreline setting and is due to variations in sedimentation rates controlled by fluvial input and accommodation space controlled by antecedent geology (controlling the antecedent topography) and sea-level. The pre-existing geology provided accommodation space in between or landward of barrier ridges of Sequence 3 (Unit C) which functioned essentially as incised valleys allowing for subsequent deposition and preservation of thick sediment packages (Units Ds, Dl) during transgression. Laterally, in the absence of major Sequence 3 ridges transgressive sediments are thin (Unit Dss), a consequence of the coastal depositional systems that developed in an open shoreline palaeoenvironment and subsequent reworking by the passage of the transgressive shoreline. The geometry of the Sequence 3 ridges further control the inherited physiography of the depositional basin, which in seismic Unit Ds (Figure 6.15), was one of the main factors controlling the dominant depositional systems and hence the sedimentary architecture, expressed by a change from aggradational lagoonal dominant facies in the south (more protection and confinement between barriers) to more open strongly retrogradational shoreline facies in the north (only a landward Aliwal Shoal ridge forming a major barrier; see Chapter 6.3.4).

This is further illustrated by the change in thickness of the lagoonal sequence ranging from <5 to 18 m in the north to 25 m in the south, a lack of lagoonal facies (DsSF2 to DsSF4) in the north and the formation of backstepping lagoonal channels instead of backstepping bayhead deltas in the south, indicative of the lower energy environment of an embayed back-barrier lagoon (Catuneanu, 2006). Thus, aggradation increased with increasing confinement between the high gradient Sequence 3 ridges as it afforded accommodation space and protection from the transgressive ravinement (Figure 6.15, also compare Figure 6.6c with 6.9c).

The topographic gradient of Sequence 3 ridges also controlled the area available for transgression as for the same rise in relative sea-level there is a more rapid landward shift in facies and a wider area transgressed in a low-gradient setting relative to that of a high-gradient setting (Cattaneo and Steel, 2003; Coe and Church, 2003b). This is well illustrated by comparing the landward shift of facies DsSF2 on the relatively lower topographic gradient of the seaward edge of the Sequence 3 Aliwal Shoal ridge (Figure 6.8c) with the relatively higher gradient of the same ridge (Figure 6.9c). On the lower topographic gradient the facies are strongly retrogradational whereas the higher gradient promoted aggradation.

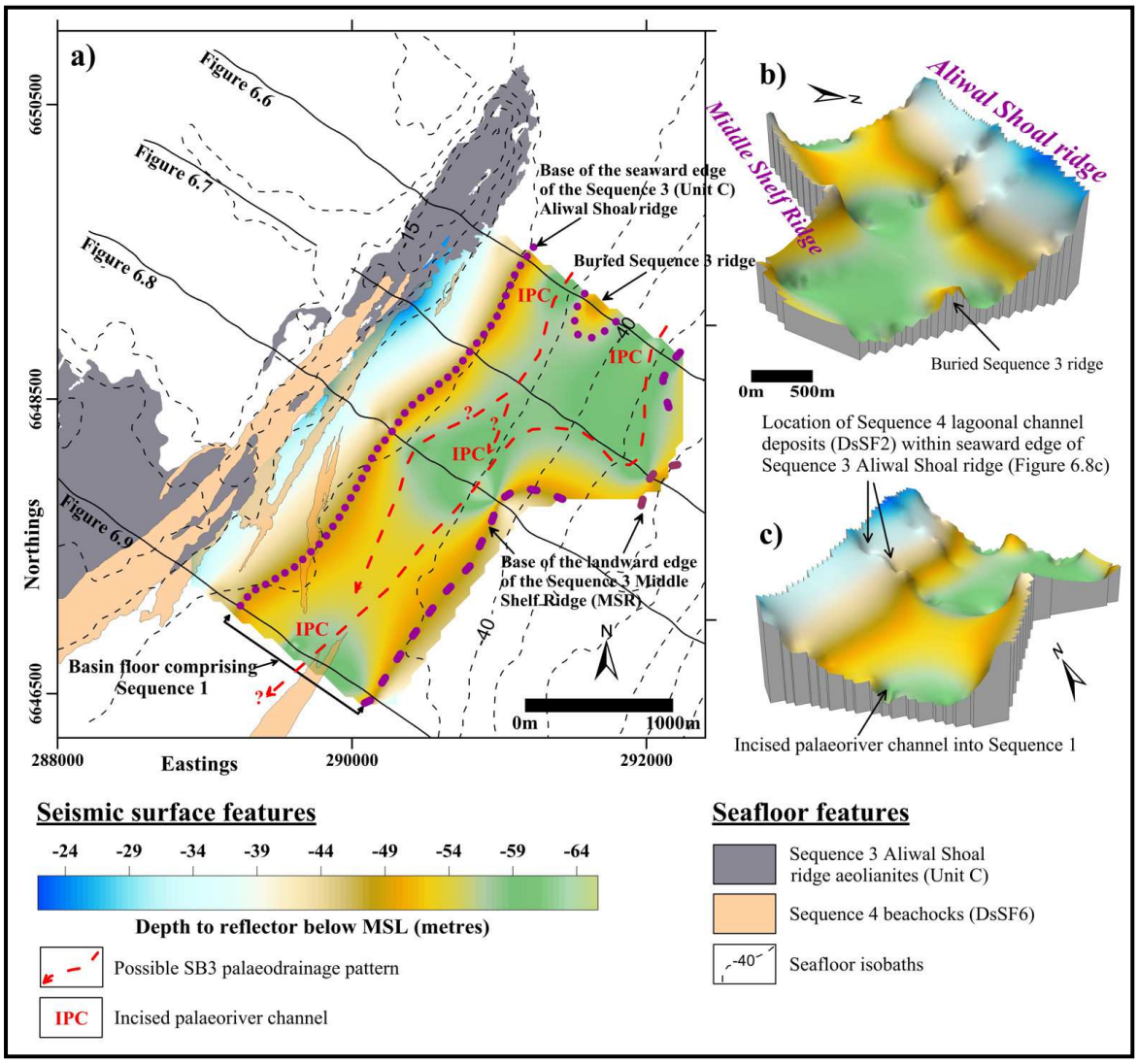

Figure 6.15 **a)** Depth to reflector map showing the physiography of the Sequence 4 Unit Ds basin which is flanked by Sequence 3 ridges and floored by Sequence 1 strata showing SB3 palaeoriver channel incisions possibly converging to the south. The topography of the Unit Ds basin controlled the subsequent sedimentary basin fill architecture and subsequently the oceanic ravinement surface and preservation of the beachrock facies. Also, note the similarity between the ravinement surface and the modern seafloor bathymetry (Figure 6.16). **b) and c)** 3D views of the seismic surface constituting the basin for Sequence 4 Unit Ds depositional systems. Note that on the seismic surface model the channel fill (DsSF2) will only show up on the actual seismic profile line and not in the areas in between due to the lack of data. Vertical exaggeration for the 3D models is 18x and the horizontal scale is the same. Locations for the seismic profiles are indicated but note that the lines extend beyond the limits of this figure (refer to Figure 6.4).

The 3D shape of the transgressive ravinement surface TRS (Figure 6.16) illustrates two important points; 1) in the north the absence of a *prominent* protective seaward barrier in an open shoreline setting, the TRS oversteps retrogradational deposits (mostly paralic; Figure 6.6; Figure 6.16bii), has a steeper shoreline trajectory (0.74°; 0.01 gradient) and possibly was associated with major erosion of the underlying deposits (directly overlying SB3/Sequence 1; Figure 6.6c) , whereas 2) in the south the TRS is sub-horizontal (0.2°; 0.003 gradient) and more conformably overlies aggradational deposits (mostly lagoonal) located, in part, behind a protective seaward barrier.

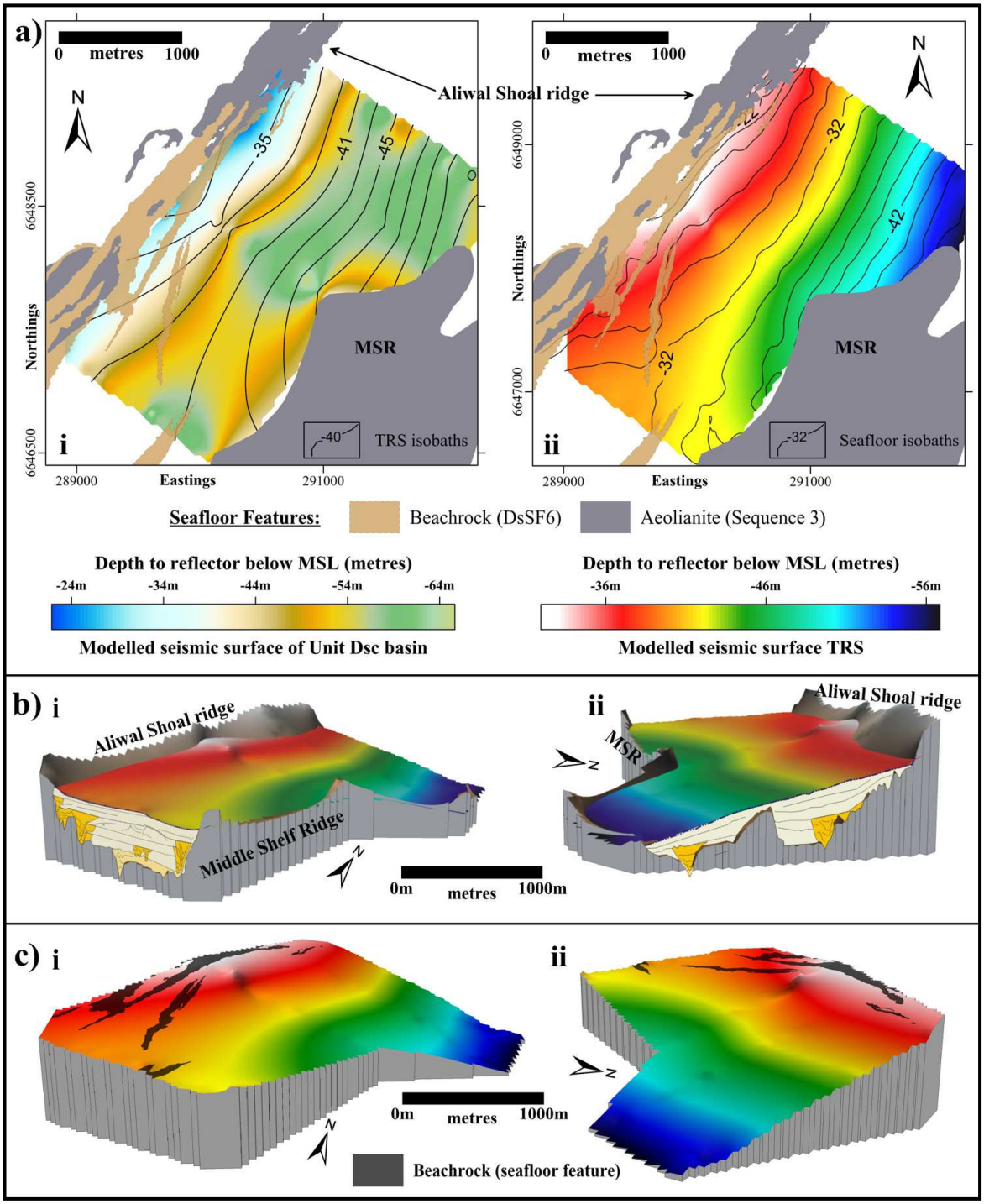

Figure 6.16(cont.) a) i) Map comprising depth to reflector surface Unit Ds (refer to Figure 6.15a) overlain by the depth to reflector isobaths lines of the transgressive ravinement surface (TRS; 2-metre interval). Also shown are the Sequence 3 ridges of the Aliwal Shoal ridge (compare with Figure 6.14), the beachrock seafloor outcrops of Sequence 4 and the basal surface expression of the Middle Shelf Ridge (MSR). Note the steeper gradient of the transgressive ravinement surface in the north (no offshore barrier) relative to that in the south (confined between Sequence 3 ridges). Also note the apparent control that the antecedent topography of the Aliwal Shoal ridge exerts on the expression of the transgressive ravinement by controlling the underlying sedimentary architecture. **ii)** Map showing the depth to reflector surface of the transgressive ravinement surface (TRS) overlain by the depth to reflector isobath lines of the modern seafloor (2-metre interval). Note the similarity between surface TRS and the modern seafloor. **bi and ii)** 3-dimensional surface models for the transgressive ravinement and the subjacent lagoonal deposits (for interpretation of **(bi)** refer to Figure 6.9 and for **(bii)** see Figure 6.6) illustrating the relationship between antecedent topography, underlying sedimentary architecture and ravinement gradient. **ci and ii)** 3-dimensional models of surface TRS and positions of the overlying beachrock units. Note that the beachrocks are separated from the ravinement surface by DsSF6 (not shown). Colour depth scale for the transgressive ravinement surface model in **(aii)** is also applicable to the surface models of **(b)** and **(c)**.

Thus, the antecedent geology controlled the subsequent sedimentary basin fill architecture which again exerted an influence on the subsequent shoreline trajectory of the transgressive ravinement surface (Figure 6.15). In addition, the shallower gradient (0.003 vs. 0.01) imparted to the ravinement surface in the south by the underlying topography, is also postulated to be responsible for preservation of the beachrocks (DsSF6; Chapter 8). The beachrocks are predominantly located on the shallower gradient of the southern thick aggradational lagoonal sequence (Figure 6.16a, c) which allowed not only a relatively faster sea-level transgression but also, initially, here had protection by the seaward barrier. The combination of a fast sea-level transgression and barrier protection resulted in a higher preservation potential for the beachrocks as reworking subsequent to formation was minimised.

Although the transgressive ravinement surface changes gradient overall it is still considered a high gradient topography for a continental shelf (>0.001; Cattaneo and Steel, 2003). Observations in similar settings (Cattaneo and Steel, 2003; Zecchin, *et al*., 2011) suggest slower rates of shoreline retreat resulting in an increase in ravinement and subsequent shoreface retreat, creation of a laterally constrained ravinement surface with a complex geometry and possibly thicker overlying marine deposits. Surface TRS (comprising DsRT and DlRT) agrees with these observations and shows a relatively thicker overlying marine deposit (DsSF6 thicker than DSF6) and a complex irregular surface but diverges insofar as the observed ravinement surface seems to be present throughout the study area and hence laterally continuous. Additionally, the contrast in the gradients of the transgressive shoreline further illustrates the contrast between the stratigraphic

result of a barrier in-place drowning (Sanders and Kumar, 1975; Units Dl and Ds) and an open shoreline transgression (Unit Dss) along this section of the South African continental shelf.

The Mkomazi Subaqueous-Delta Clinoform

Unit Dsc, named the Mkomazi Subaqueous-Delta Clinoform (MSDC) is a prograding shore-attached subaqueous-delta clinoform sediment deposit (Figures 6.17 and 6.18; also Figures 6.4 and 6.5) characteristic of sediment input (fluvial and coastal erosion) onto a high energy storm-dominated continental shelf. Oceanographic processes are responsible for its northward directed asymmetry in plan-view (longshore drift and counter-current from the return flow gyre), for the lack of a well defined bottomset (counter current and Agulhas Current) and for the re-organisation of its topset into shoreface-connect ridges (swell, storms and counter current). As opposed to the retrogradational stratal stacking geometry of the underlying units (Ds, Dl and Dss) the MSDC shows an aggradational (topset)/progradational (foreset) stratal stacking pattern with downlap (Figure 6.5) thereby marking the change, albeit local, in the nature of the depositional systems from transgressive to regressive.

As suggested by Osterberg (2006), this study also deems the internal clinoforms to most likely define the former seaward edge of the shore-connected sediment body. As such, the internal clinoform apparent lapout within the unit is not only considered to be bed thickness, not resolved due to the resolution of the system, but is also interpreted to document a temporary retrogradational response of the clinoform due to changing parameters related to the rate of sea-level rise and sediment supply. As a result the evolution of the MSDC is characterised by an initial development phase followed by an aggradational/retrogradational event (reflecting a change in the balance between sediment supply and sea-level rise) before resuming a progradational to aggradational phase which is still active today (Figure 6.18b). Unfortunately due to limited available data and the lack of a well constrained local sea-level curve it is not possible to accurately determine the cause of these sedimentary changes, such as the sudden back-stepping of the MSDC. However, as the clinoform is primarily controlled by the relative balance between accommodation space and sediment supply (considered relatively constant during the Holocene transgression) these changes are tentatively suggested here to be the sedimentary response of the clinoform to changes in the rate of sea-level rise (accommodation) brought about by climatic events during the Holocene transgression.

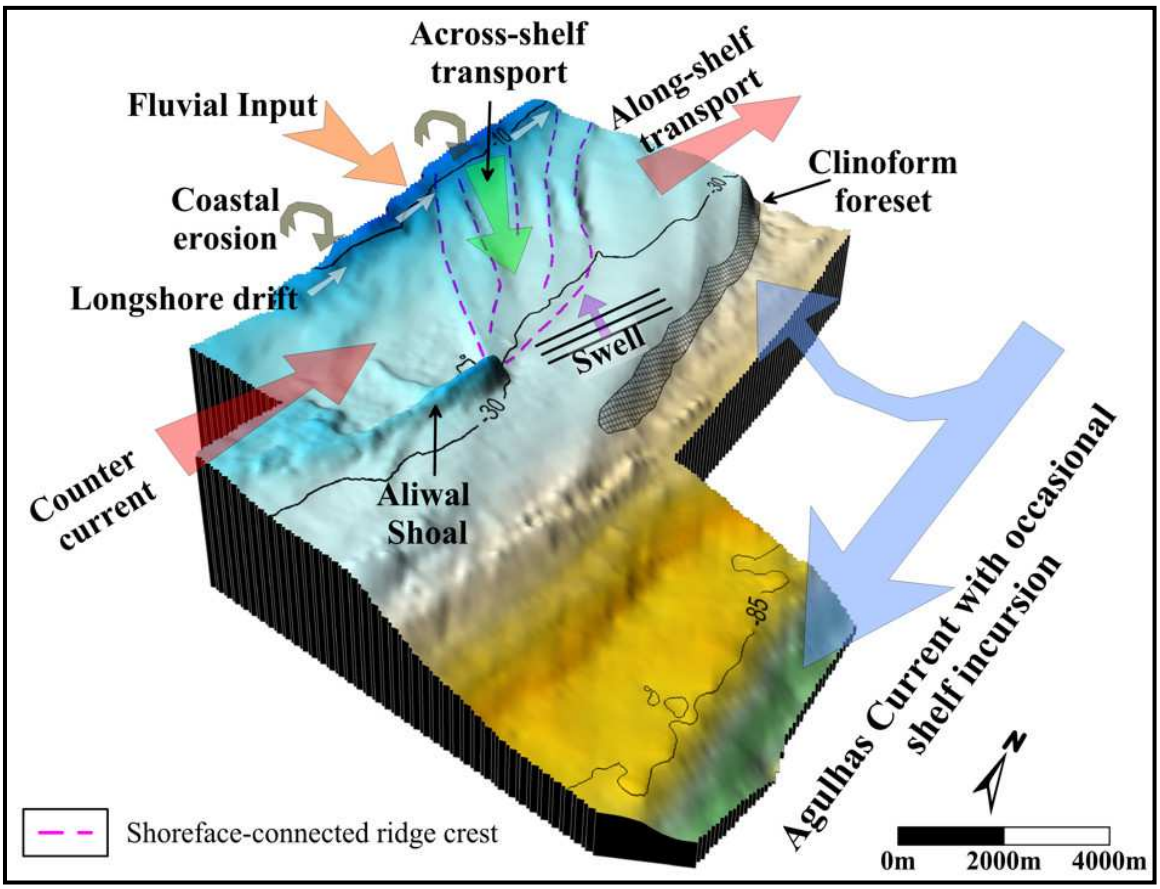

Figure 6.17 The 3 dimensional model of the shelf bathymetry showing the sedimentary processes impacting on the morphology of the Mkomazi Subaqueous-Delta Clinoform (MSDC). Sediment input (from fluvial systems and coastal erosion sources) is transported both along- (counter current) and across-shelf (via shoreface-connected ridges). The Agulhas Current is suggested to limit the development of the bottomset of the clinoform. The clinoform foreset is shaded and derived from a slope angle model (Figure 7.12). Also shown is the present day shoreface-connected ridge crests, the occurrences of which are tentatively linked to the Stage 2 retrogradational clinoform morphology (Figure 6.18). The 30 m and 85 m isobaths represent the fair-weather wave base and shelf break, respectively. Refer to Figure 6.4 for locality and fluvial systems.

The step-like nature of the last deglacial sea-level rise is characterised by relative slower rates of rise punctuated by short rapid accelerations of sea-level rise generally ascribed to meltwater pulses (Bard *et al*., 2010; Bird *et al*., 2010; Stanford *et al*., 2011; also see Section 4.4.2). From previous discussions the age for the initiation of the MSDC is placed at younger than ~9.5 ka cal. B.P. (Table 6.4) which means it post-dates the major classic meltwater pulse (MWP-1a). Liu *et al*. (2004) observed a rapid sea-level rise between 9.8 to 9.0 ka cal. B.P. in the Yellow River subaqueous delta and surrounding Yellow Sea sedimentary records which they termed Meltwater Pulse 1c (MWP-1c, overlap MWP-1b). Woodroffe and Horton (2005) also found a meltwater pulse (termed MWP-2) at ~9.1 ka cal. B.P. from the Caribbean and north Atlantic records although they question the global significance of this event. According to Liu *et al*. (2007) the remainder of

the Holocene transgression after MWP-1c was characterised by a general deceleration in the rate of sea-level rise but interrupted by multi-decadal to centennial scale meltwater pulse events associated with climatic fluctuations (Bond *et al*., 1997). One such major meltwater pulse was identified at ~8.4 - 8.2 ka cal. B.P. (Liu *et al*., 2007).

Recently, Hijma and Cohen (2010) presented evidence from the Dutch continental shelf of an abrupt global eustatic sea-level jump of 3 ± 1.2 m constrained between 8.45 to 8.25 ka cal. B.P. as such precluding the 8.2 ka cal. B.P. climatic cold event (hereafter 8.2 ka event) and thereby also confirming the major meltwater pulse event observed by Liu *et al*. (2007). In their subsequent paper Hijma and Cohen (2011) links this abrupt sea-level rise to worldwide observations of a 'marked transgressive contact' associated with drowning and backstepping events in major marine deltas in Asia (Liu *et al*., 2004; 2007) and even that of the Mississippi Delta (Törnqvist *et al*., 2004). In addition, the observations of Hijma and Cohen (2011) support the notion first put forward by Stanley and Warne (1994) of a global synchronous initiation of the bulk of the world's marine deltas between 9.5 - 7.4 ka cal. B.P. (8.5 - 6.5 ^{14}C ka B.P. in original paper). According to Hijma and Cohen (2011) the modal age of the base of the deltaic deposits recognised by Stanley and Warne (7.5- 7 ^{14}C ka B.P.) corresponds to their 8.45 to 8.25 ka cal. B.P. sea-level jump. But, whereas Stanley and Warne (1994) ascribed the coeval delta initiation to a deceleration in sea-level rise, Hijma and Cohen (2011) ascribed it to acceleration in the rate of sea-level rise.

In the absence of evidence to the contrary the conceptual model of the evolution of the MSDC (Figure 6.18) is linked to these global observations of fluctuating rates of sea-level rise and the subsequent sedimentary response of the clinoform system. It therefore follows the application of 'event stratigraphy' as suggested by Hijma and Cohen (2011) when comparing worldwide deltaic sequences and synchronising the geological evolution of coastal regions with deglacial climatic variability. The depositional history of the MSDC can be divided into four stages (Figure 6.18a);

Stage 1; ca. 9.5 - 8.4 ka cal. B.P.

The suggested age of <9.5 ka B.P. for development of the MSDC is within range of the Stanley and Warne (1994) estimates and also corresponds to initiation of development of the Shandong Clinoform (9.6 ka cal. B.P; Liu *et al*., 2007) and MWP-1b/c (9.8 to 9.0 ka cal. B.P.). The local relative sea-level curve from South Africa generally lacks reliable data for this period and as such cannot confirm nor refute the existence of a meltwater pulse (Figure 6.18b). However, three lines of evidence may lend support to an increase in the rate of sea-level rise around the time frame for MWP-1c; i) the beachrock data suggests an acceleration in the rate of sea-level rise towards 9.8 ka cal. B.P., (Table 9.7), ii) beachrocks possibly indicate two flooding events associated with

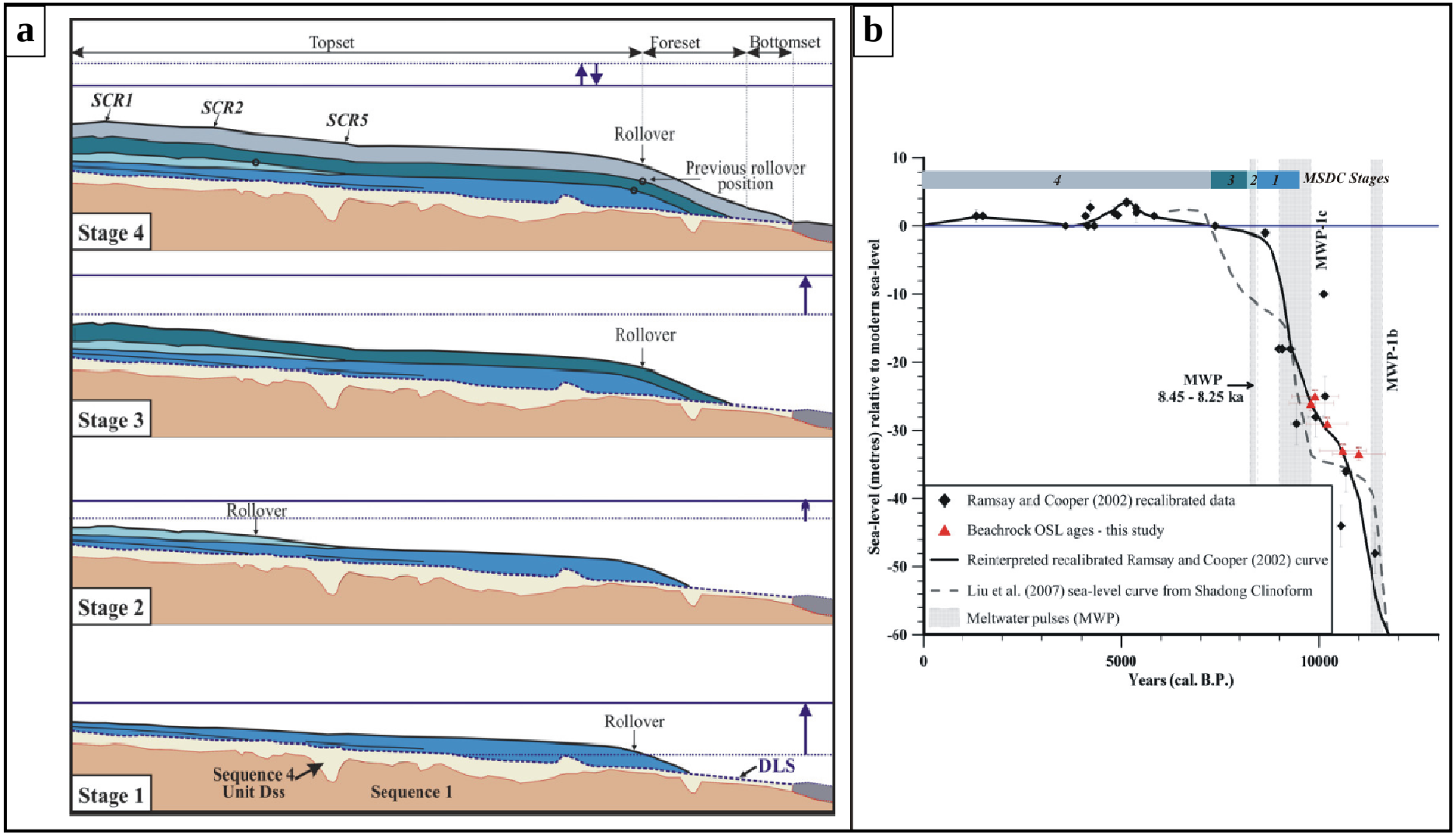

Figure 6.18 a) Conceptual four stage evolutionary model for the Mkomazi Subaqueous-Delta Clinoform (MSDC) based on event stratigraphic correlation of global observations of the Holocene sea-level fluctuations and the sedimentary response of the clinoform. Refer to the text for details. **b)** Developmental stages of the MSDC plotted in relation to the sea-level curves of Liu *et al*. (2007) and the recalibrated and reinterpreted local relative sea-level curve of Ramsay and Cooper (2002). Note the almost complete lack of data points for the local sea-level curve between the depths of 0 m and -20 m, and thus unable to resolve events such as meltwater pulses. Refer to Chapter 9 for the details regarding the recalibrated Ramsay and Cooper (2002) curve.

different pulses of enhanced rates of sea-level rise (Sections8.3.5 and 9.5.2) the youngest dated at ~9.8 ka cal B.P. which also most likely resulted in iii) the generally fast drowning of the lagoonal and estuarine systems following the beachrock deposition (see Sequence 4 above). Nonetheless, a major phase of rapid subaqueous-delta progradation (Figure 6.18a) occurred <9.5 ka cal. B.P. (Table 6.4) indicating positive accommodation space on the shelf (Catuneanu *et al*., 2009). Deceleration in the rate of sea-level rise following the meltwater pulse (<8.8 ka cal. B.P.) most likely resulted in continued progradation but with concurrent topset aggradation resulting in the sigmoid stratal configuration (Appendix II, Table II.2).

Stage 2; ca. 8.4 - 8.2 ka cal. B.P.

The retrogradational phase of MSDC development (Figure 6.18a) is ascribed to the rapid 8.4 - 8.2 ka cal B.P. (Liu *et al*., 2007; Hijma and Cohen, 2010) sea-level rise which resulted in backstepping and retrogradation and which is also observed in many large subaqueous delta systems worldwide (Hijma and Cohen, 2011). In addition, bedrock attached oysters were found at -18 m (Ramsay and Cooper, 2002) in the Mkomazi River estuary (Figures 3.1, 6.4) and dated at 8.8 to 8.3 ka cal. B.P. (recalibrated ages; Appendix XIV). Thus, marine or at least estuarine conditions were established at a position close to the present coastline by at least 8.3 ka cal. B.P., indicating the magnitude of the sea-level rise event. Backstepping of the clinoform controlled the subsequent overlying topset morphologies resulting in the later stages inheriting a stepped appearance (nickpoint). This might indicate that the sigmoidal plan-view appearance of shoreface-connected ridge (SCR) crests 1 - 5 (Figures 6.17 and 7.10) may be a surficial expression of the subjacent retrogradational phase and hence might possibly reflect the subsurface extent of the retrogradational phase (Figure 6.17). The Stage 2 topset also shows a possible erosional morphology but whether this is due to relict proto-shoreface-connected ridges or erosion related to shoreface transgression is not certain.

Stage 3; ca. 8.2 - 7.5 ka cal. B.P.

Clinoform progradation followed the backstepping event (Figure 6.18a) and is attributed to a general deceleration in sea-level rise relative to the preceding eustatic jump with subsequent associated sediment accumulation and progradation. This apparent contradiction of progradation following the 8.2 ka event when the Holocene transgression was characterised by relative slower rates of sea-level rise (compared to the meltwater pulses) is also observed in other far-field locations (e.g. Asia; Yim *et al*., 2006; Liu *et al*., 2007; Tamaru *et al*., 2009).

Stage 4; ca. 7.5 - 0 ka cal. B.P.

Stage 4 was initiated with a sea-level similar to present which subsequently, along the east coast of South Africa, rose to +3.5 m above the present level during the mid-Holocene highstand (mHH) at ~5.1 ka cal. B.P. (4480 ^{14}C ka B.P. in original Ramsay and Cooper, 2002 article). Although the timing and amplitude of this highstand is controversial (see Section 4.5) the important aspect for the development of the MSDC is that accommodation space was created (mHH) and later destroyed when sea-level finally reach the present level which was the same level as that of the

beginning of Stage 4 (Figure 6.18b). As a consequence the clinoform is expected to show an overall aggradational configuration, an observation supported by the occurrence of shoreface-connected ridges on the topset and vertical, not lateral, migration of the clinoform rollover point from Stage 3 to Stage 4 (Figure 6.18a). In addition, the stratal configuration in both Stages 3 and 4 show a change from 'proximal' topset aggradation to 'distal' foreset progradational downlap. It is possible that this stratal change may be reflecting a change in the dominant sedimentary transport mechanism i.e. from aggradational along-shore to progradational cross-shore transport (also observed by Liu *et al.*, 2004). This postulation of variable sediment transport in the near shore versus offshore zone is further supported by recent current measurements on the shelf indicating periods of stronger current velocity inshore than offshore (Roberts, *Pers. Comm.*). This variation between cross-shore and along-shore transport (Figure 6.17) is also postulated to be responsible for the changes observed in the stratal configuration of the clinoform along strike (Figure 6.10).

6.5 SYNTHESIS

The shelf margin in the vicinity of the study area is characterised by an extremely narrow (10 km) and shallow (-85 m) continental shelf (Bosman, 2003b) when compared to the global average width of 78 km and an average shelf break depth of 130 m (Kennett, 1982). The development of this narrow continental shelf and its straight coastline of the eastern continental margin as far north as Durban (Figures 3.6, 3.8 and 3.9) is the result of the rifting and extraction of the Falkland Plateau (Dingle and Scrutton, 1974; Martin, 1984) along the transform fault known as the Agulhas-Falkland Fracture Zone (AFFZ; see Section 3.2.1). Following Gondwana breakup uplift along the rift shoulders formed a marginal escarpment, the erosion of which provided the epeirogenic sedimentation, which again ultimately resulted in the deposition of the thick marine Cretaceous sequences on the subsiding newly formed continental shelf (Dingle *et al.*, 1983).

This part of Gondwana breakup is documented in Sequence 1 of the proposed seismic stratigraphic model (Figures 6.12, 6.13a and 6.19) for the continental shelf in the vicinity of the Aliwal Shoal. Campanian (and possible Santonian) TST and Maastrichtian regressive (HST and FRST) strata are interpreted to represent the local preservation of diachronous southerly directed Cretaceous transgression in the newly created proto-Indian Ocean. Sequence 1 is the deepest sequence recognised and thus the acoustic basement for this study underlying the entire continental shelf and slope. Basin-wide Reflector R is interpreted as a maximum flooding surface (MFS1) subdividing Sequence 1 into a lower TST and an upper combined regressive systems tract comprising HST/FRST deposits prograding over a postulated Campanian palaeo-shelf break and thereby signalling the onset of the major late Maastrichtian - Early Palaeocene forced regression resulting

in the initial formation of SB1 and the arrival of the Tertiary. Major movements of sea-level typified the Tertiary (Figure 6.13a; also refer to Section 3.5.1) around southern Africa with regional uplift or subsidence resulting in relative sea-level changes affecting local areas differently (Dingle *et al*., 1983).

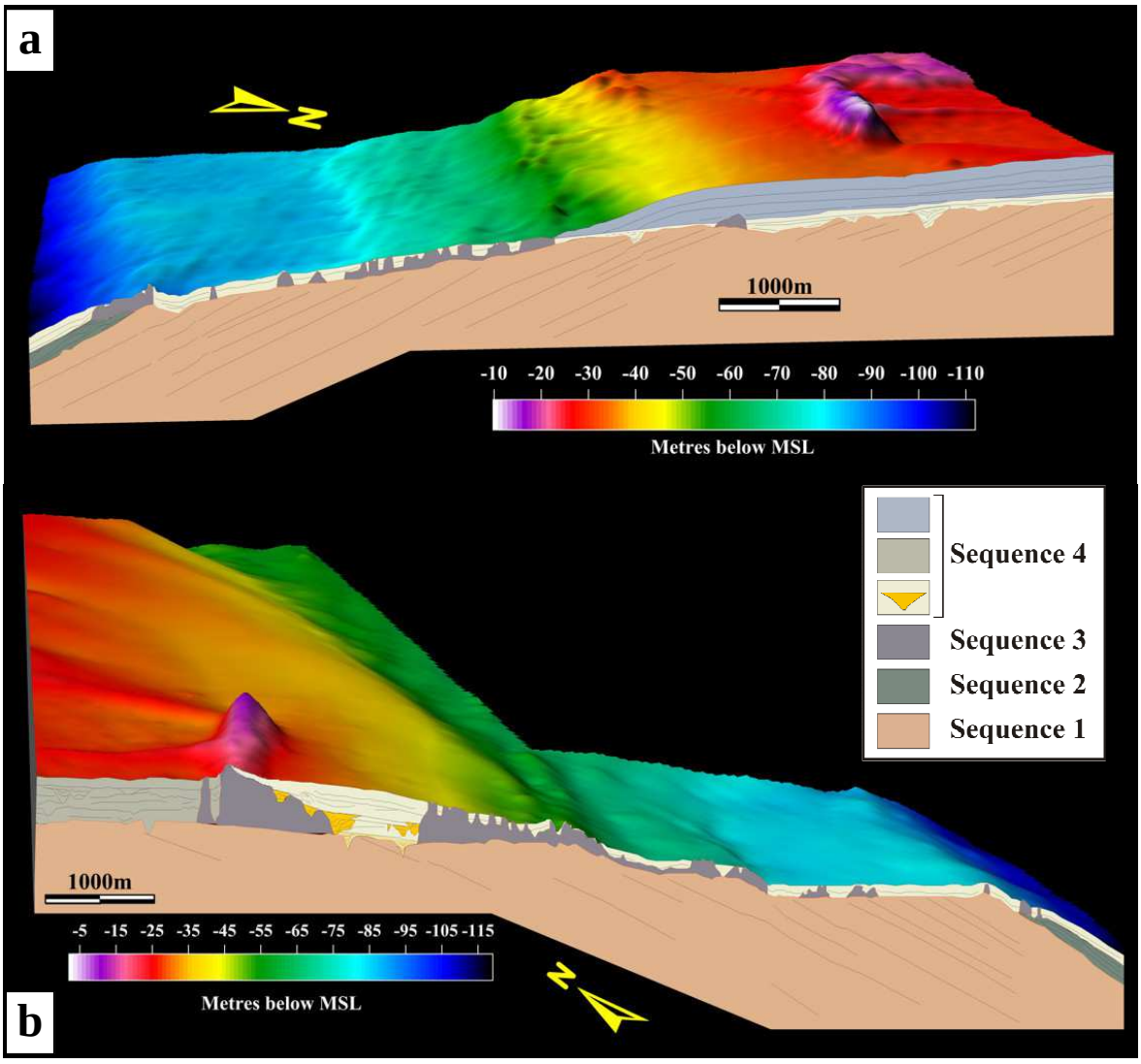

Figure 6.19 a) and (b) Digital terrain models of the shelf bathymetry integrated with the seismic sequence stratigraphic framework for seismic profile 5 (**a**) and 8 (**b**). Refer to Figure 6.5 and 6.8 for the interpretations of lines 5 and 8, respectively and to Figure 6.4 for the locations of these seismic lines. Sequence 4 is subdivided into its various sub-units for consistency and ease of referral to related figures. Refer to Section 6.3 and 6.4, for detailed discussions of the seismic stratigraphy.

As a consequence the shelf was predominantly an area of non-deposition during the Tertiary. This lack of Tertiary strata on the shelf is explained in terms of the location of the study area relative to the coast-parallel axis of maximum movement, which resulted in non-deposition in the proximal zones (study area) and increased deposition in distal areas such as the lower continental slope and deep ocean basins. A similar observation was made by Cawthra (2010) from the Durban area. SB1 evolved throughout the Tertiary to create the pre-Sequence 2 shelf break and to shape the continental shelf into a series of terraces (Figure 6.14) which would ultimately control subsequent deposition of Sequence 3, which again controlled the development of Sequence 4.

Sequence 2 (Figure 6.19) is interpreted as a Late Pliocene to early Pleistocene LST prograding shelf-edge wedge deposited as a prograding and aggrading strandplain in an open shoreline setting which were fed by longshore current-derived sediments from shelf edge deltas. Sequence 2 deposition did not alter the shelf break position as established following SB1 but only slightly increased the shelf width. For most of the Quaternary the shelf was in an erosive regime characterised by the formation of SB2 as a consequence of global climatic fluctuations. These climatic fluctuations resulted in high frequency and amplitude glacio-eustatic sea-level oscillations which produced glacial maxima sea-level lowstands down to 120 m below MSL (Ramsay and Cooper, 2002; Green and Uken, 2005) thereby not only exposing the entire continental shelf but also parts of the slope.

Glacio-eustatically driven sea-level fluctuations were primarily responsible for development of both Sequence 3 and the uppermost and final seismic sequence, Sequence 4. Sequence 3 comprise coast-parallel, inner shelf to slope, semi-continuous ridge structures observed to be predominantly located on terraced areas of SB2. This study confirmed Sequence 3 to comprise carbonate cemented aeolianite and coastal lithofacies representing palaeo-coastal barrier systems. The age of one such ridge, the Aliwal Shoal, ranges from 134 ± 5 ka to 79 ± 5 ka B.P., indicating formation before and after the fluctuating sea-levels associated with the last interglacial highstand. During the forced sea-level regression towards the LGM lowstand the Aliwal shelf comprised an interfluve area which was characterised by subaerial exposure, fluvial incision of coast-parallel tributary river systems and general sediment starvation. The Sequence 3 Aliwal Shoal ridge and most likely the MSR (Figures 6.14 and other ridges, formed during the previous sea-level cycle (Figure 6.13b), were prominent inner and middle shelf features. LST sediments of the LGM were most likely deposited on the continental slope below -120 m.

Rapid deglacial sea-level rise following the LGM (~18 - 20 ka B.P.) resulted in the deposition of Sequence 4 (Figure 6.13b), commonly referred to as the Holocene unconsolidated sediment wedge. TST deposits of Sequence 4 comprise a complex arrangement of strike and dip variable

depositional systems. On the slope and outer shelf environments Sequence 4 predominantly consists of thin retrogradational open shoreline and onlapping shallow marine depositional systems of Unit Dss. On the middle and inner shelf the development of the TST depositional systems are not only diachronous along dip but show a marked change along strike. Whereas in the north the Unit Dss TST is only preserved as a thin sand sheet, to the south thick TST deposits were preserved in accommodation space created by the palaeo-topography of the Sequence 3 ridges. A linked system comprising an embayed back-barrier lagoon (Unit Ds) and an embayed back-barrier estuary (Unit Dl) developed seaward and landwards of the Aliwal Shoal ridge, respectively. To the north the low gradient and relatively featureless shelf facilitated an earlier, relative simplistic and rapid drowning of the open coastline setting compared to the shelf in the south where the antecedent topography and subsequent sedimentary fill architecture influenced the ensuing transgressive ravinement process and the subsequent deposition of the transgressive shoreface. The passage of the transgressive palaeosea-level across the lagoonal system was documented by the deposition of a series of beachrocks.

Approximately coeval (Table 6.4) with the final transgression of the lagoonal and estuarine systems in the south, the north experienced a deepening water column and initialisation of the local HST (Unit Dsc) of Sequence 4 (Figure 6.19). This HST comprises a prograding shore-attached subaqueous-delta clinoform sediment deposit, named here the *Mkomazi Subaqueous-Delta Clinoform* (MSDC). Previous investigations interpreted the clinoform as a submerged spit bar (Martin and Flemming, 1986) and an unconsolidated sediment depocentre (Birch, 1996). As opposed to the retrogradational stratal stacking geometry of the underlying TST units (Units Ds, Dl and Dss) the MSDC shows an aggradational (topset)/progradational (foreset) stratal stacking pattern with downlap thereby marking the change, albeit local, in the nature of the depositional systems from transgressive to regressive. Morphologically the MSDC is characteristic of a sediment input onto a high energy storm-dominated continental shelf where oceanographic processes are responsible for its northward directed asymmetry in plan-view, for the lack of a well defined bottomset and for the re-organisation of its topset into shoreface-connect ridges (Figure 6.17). The conceptual evolutionary history of the MSDC is divided into four stages (Figure 6.18a) based on event stratigraphy by linking it to global observations of fluctuating rates of sea-level rise and the subsequent sedimentary response of the clinoform system. Initial progradation is interrupted by backstepping of the clinoform which controlled the subsequent overlying topset morphologies resulting in later stages inheriting a stepped appearance upon which the shoreface-connected ridges are developed. Stages 3 and 4 show a change from ‘proximal’ topset aggradation to ‘distal’ foreset progradational downlap, linked to a change in the dominant sedimentary transport mechanism from aggradational along-shore to progradational cross-shore transport.

Deposition on the MSDC is still ongoing today whilst overall the continental shelf is still in a transgressive regime.

Interestingly, Sequence 4 or the Holocene sediment wedge thus forms a complex feature consisting of both TST and local HST sedimentation, which are not only diachronous along dip but markedly variable along strike, including depositional systems ranging from embayed lagoonal and estuarine, open shoreline and submerged-delta clinoform depositional settings. Previous seismic investigations (Martin and Flemming, 1986; Birch, 1996; Green, 2009a, b; Cawthra, 2010) have not recognised the intrinsic complexity of the sediment wedge and have for instance ascribed thick accumulations of sediment banked landward of Sequence 3 ridges to these ridges presenting physical barriers to cross-shelf sediment transport (Martin and Flemming, 1986; 1988) and not to evolving depositional systems.

In addition, antecedent topography of the Sequence 3 ridges created accommodation space which sedimentologically acted as palaeo-valleys, the transgressive fill of which mostly shows coherence to the local models of transgressive incised valley fill (IVF; Green, 2009b) and as such provides a novel documentation of transgressive sedimentation analogous to that of smaller palaeo-river valley fills but on a much larger scale.

CHAPTER 7
SEAFLOOR MORPHOLOGY

7.1 INTRODUCTION

Five separate dataset sources (Figure 7.1) all of different degrees of accuracy and resolution were used for this study. Technical details relating to the collection and integration of these datasets are provided in Sections 5.2.2 and 5.3.2, whilst a comprehensive review of the theoretical background to single beam echo-sounding is presented in Appendix 1. Although, the collected and seismically derived datasets (datasets 1 to 4) cover the detailed study area, a fifth bathymetric dataset (Figure 7.1) is included to provide a historical comparison of sediment movement on the shelf. To the author's knowledge it is the first time that shoreface-connected ridges (SCRs) were identified from the South African continental shelf (Bosman *et al*., 2008). Recently, Cawthra (2010) found SCRs off the Durban Bluff (see Figure 6.1a for locality) although not comparable in size to the larger and more numerous Aliwal Shoal SCR system. The discovery of the Aliwal Shelf SCRs provides new insights into shelf sediment dynamics and continental shelf evolution.

The high resolution bathymetric map serves as a georeferenced base map for a large part of the continental shelf and is useful to a wide variety of end users, including recreational divers, biologists and oceanographers. The dataset was crucial as a decision support tool for delineating the Critical Zone (Figure 1.1) of the Aliwal Shoal Marine Protected Area (MPA) (RSA Government Gazette, 2004) and was also used as a baseline dataset to map the biological zonation of the Aliwal Shoal (Brash, 2007).

7.2 HIGH RESOLUTION COLLECTED BATHYMETRIC DATASET

This dataset is the most accurate and dense bathymetric dataset (Sections 5.2.2 and 5.3.2) covering the primary area of interest for this investigation and was published in Bosman *et al*. (2005; Appendix III). The Aliwal Shoal forms part of seismic Units C and D (Chapter 6).

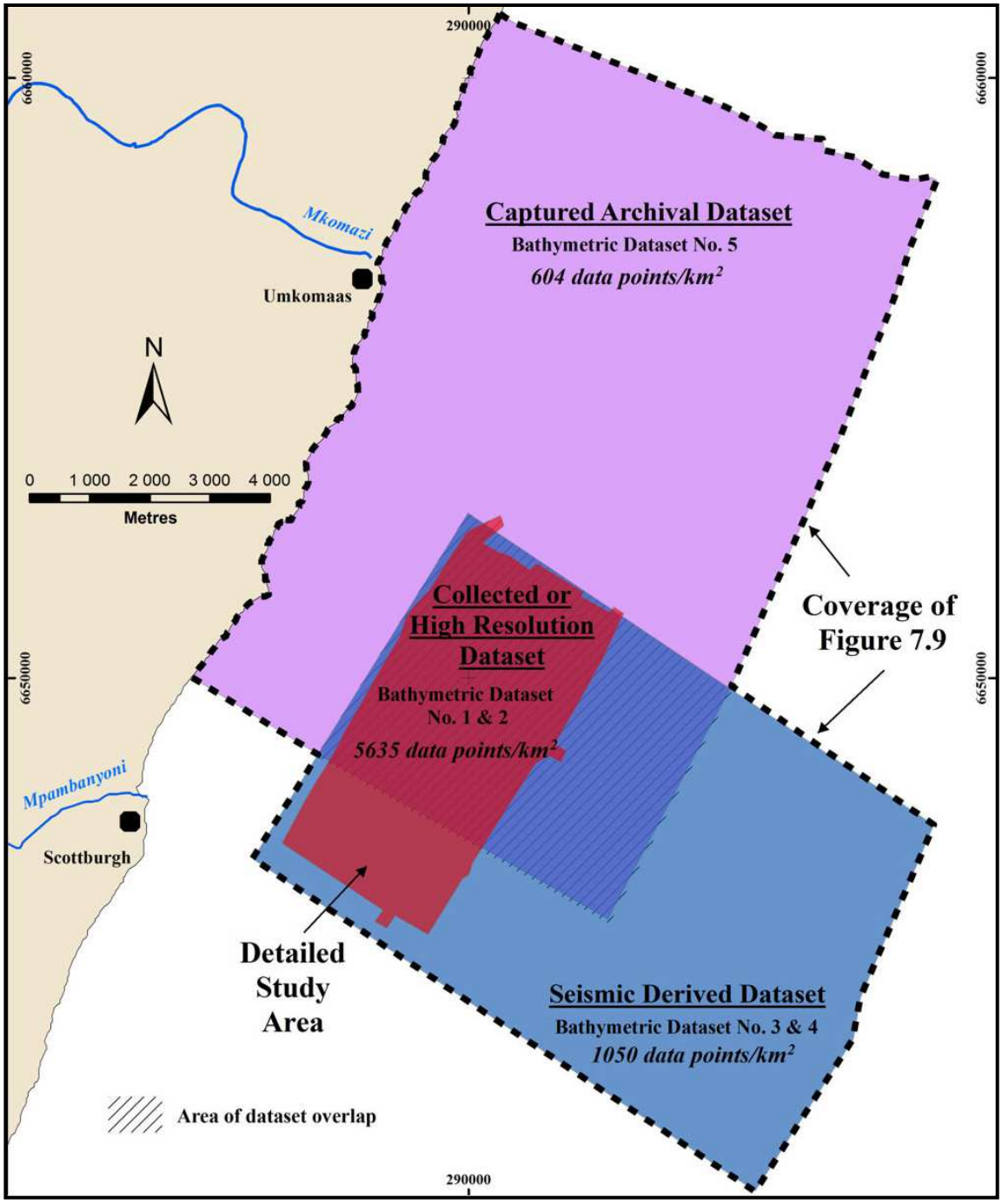

Figure 7.1 Map showing the coverage of the five bathymetric datasets and the respective data density in data points/km^2 for each bathymetric area. Also shown is the area of dataset overlap - wherein only the 'best' data was retained (refer to Section 5.3.2 for explanation).

7.2.1 Seafloor Morphology

The bathymetry map (Figure 7.2) shows that Aliwal Shoal is part of a much larger reef complex compared to previous studies (Belderson, 1961; McCarthy, 1967) revealing several new bathymetric features. Where possible the existing terms (e.g. the *Ridge* - McCarthy, 1967;

SAN 131) and colloquial names that are known to the diving and spearfishing community (e.g. Towering Inferno's) have been retained.

Considering that the shoal is Quaternary in age (this work) and that there is no direct evidence for neotectonics (Section 4.5), sea-level changes (including oceanographic influence) and lithology are assumed to be responsible for the present bathymetric expression of the Aliwal Shoal.

The detailed study area is dominated by the coast parallel Aliwal Shoal ridge (Figure 7.2) as well as several other distinctive features viz:

- smaller less pronounced linear ridges similar to, but south of the Aliwal Shoal ridge,
- a low relief shoreward widening submerged isthmus area or the *Ridge*,
- two distinctive ridge features on the landward side of the shoal, the *Spur* and the *Sandridge*,
- three distinct and separate basin features which deepens northwards,
- a N-S trending ridge on the seaward side of the shoal complex, or the *Deep Offshoot Reef*

The Aliwal Shoal ridge or *Crown* (name used by MPA; Unit A1 MRA in this study, Chapter 8) forms the narrow linear shallow coast parallel ridge section of the Aliwal Shoal complex (Figure 7.2). It is the most prominent and shallowest (-6 m) feature in the study area and has been responsible for numerous shipwrecks. Although the whole study area forms part of the "Aliwal Shoals" or Aliwal Shoal complex, this very shallow linear part is colloquially known as the Aliwal Shoal.

The general trend of the Aliwal Shoal ridge is coast parallel, northeast - southwest (037°/217°). It has an abrupt northern edge termination and exhibits a narrow (average 380 m), strongly linear character in the northern and central part of the study area but in the south it widens shoreward forming the *Ridge*. The bathymetry of the *Crown* area displays a gradual increase in depth from -6 m in the north to -20 m in the south. Inversely, it decreases in width from an average of approximately 380 m in the north to approximately 130 m in the south. The ridge is at its narrowest (100 m) at the point where the inside edge of the shoal undergoes a 90° change in direction to form the shallow submerged plateau area of the *Ridge*. The shoal is thus most rugged and well defined at its northern limit immediately south of its abrupt end.

A striking feature of the Aliwal Shoal ridge is the fact that the inside edge or landward side of the shoal is steeper than the outside edge or seaward side (Figure 7.3, cross-sections B-B' and C-C'). This is also a common characteristic of most of the aeolianite ridges found on the continental shelf and present day coastal dunes (refer to the Durban Bluff, Figure 7.5). A possible reason may be

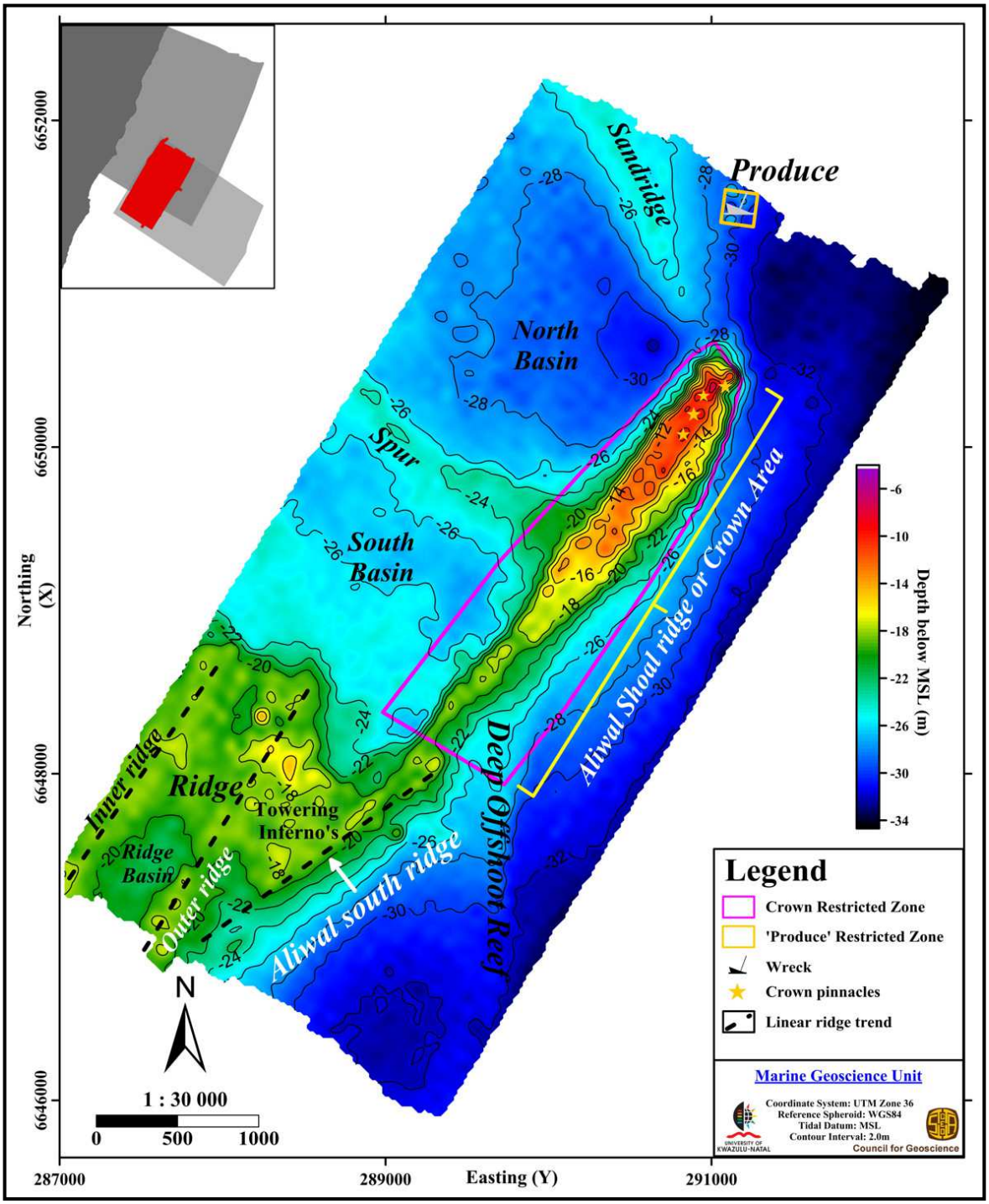

Figure 7.2 2-metre contour interval bathymetric map showing the main morphological features characterising the seafloor in the study area. Also shown is the restricted zone within the Marine Protected Area and the wreck of the Produce. Smaller less prominent ridges south of the Aliwal Shoal ridge are indicated.

related to the palaeo-environmental setting of barrier-dune systems. The landward side of barrier dunes almost always retains an estuarine system which during flood periods may undercut and steepen the inside edge of the dunes. This morphology is then inherited during subsequent dune

cementation and preserved in the resulting aeolianite. In addition, these coastal barriers are mostly constructed by sediment moved from the beach into a landward direction, which as a result of the back-barrier environment would be steeper on its landward side. Whereas the landward side of the shoal has an average gradient of 8°, the seaward facing slope has an average gradient of 6.4°. The steepest gradient for the Aliwal Shoal is 18° and is present at the northern extremity of the ridge. Not only do the landward and seaward slopes differ in gradient but they also differ remarkably in form.

While the trend of the inside edge is linear, the outside edge has a curvilinear sinusoidal trend, accentuated by the north - south trending ridge or *Deep Offshoot Reef*. This difference is most likely related to the seaward edge being exposed to the high energy environment of wave attack whereas the landward side was a embayed back-barrier estuarine environment during periods of lower sea-level (refer to Chapter 6).

Numerous pinnacles are present on the Aliwal Shoal ridge (Figure 7.2). In the northern sector of the ridge the distribution of pinnacles is very dense forming a prominent feature known as "Pinnacle Ridge" (Figure 7.3 cross-section Y-Y'). These pinnacles range in depth from -10 m to -6 m below MSL and represent the area where most of the SCUBA-diving activity takes place. In the southern sector of the ridge the distribution of pinnacles decreases drastically and the depth range is also deeper (-12 m to -18 m). This trend is consistent with the general morphology of the shoal ridge which increases in relief and becomes more rugged from the south to the north.

The wreck of the Norwegian bulk carrier Produce is located north of the northern extremity of Aliwal Shoal where it is expressed as a localized anomalous bathymetric high with a chaotic character (Figure 7.2). The Produce was wrecked in 1974 when she struck the north-eastern pinnacles on Aliwal Shoal.

In the south, the linear narrow Aliwal Shoal ridge widens shoreward to form a broad undulating plateau area (the *Ridge*, Unit A2 in Chapter 8) extending beyond the limits of the study area (Figure 7.2). The northern edge of this plateau region shows the development of a cuspate "embayment-like" form adjacent to the Aliwal Shoal ridge related to fluvial/estuarine erosion during lower sea-levels (Chapter 6). The seaward or eastern edge of the plateau (the *Aliwal south ridge;* Units A3, B5 and B6 in Chapter 8) forms the southern extension of the seaward edge of the Aliwal Shoal ridge but changes orientation and departs from the 037°/217° trend exhibited by the Aliwal ridge edge and assumes a 55°/135° trend. It is this that separates the Aliwal Shoal ridge from the *Ridge*. The northern edge of the plateau region has an average gradient of approximately 3.8° although a maximum gradient of 6° is present.

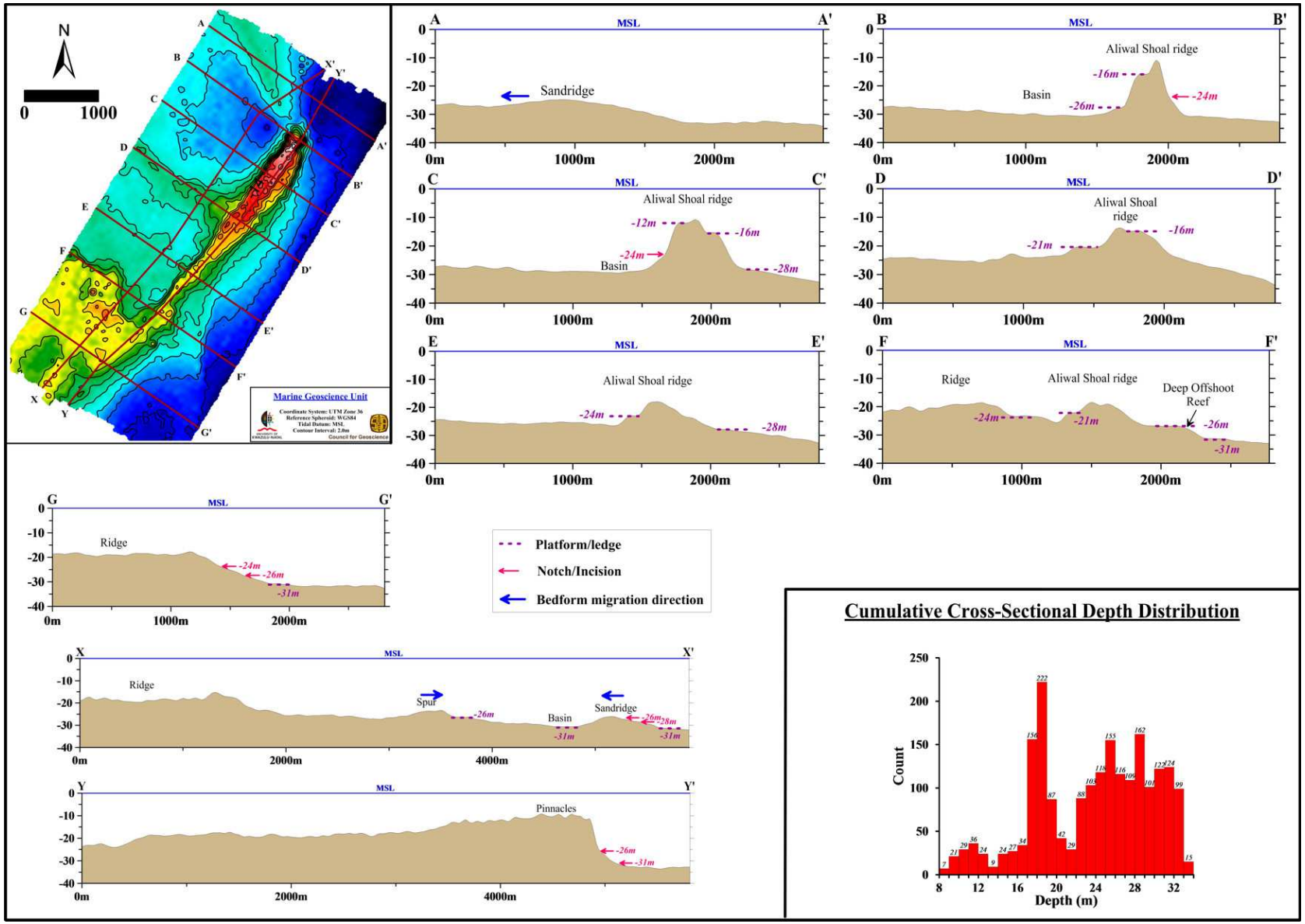

Figure 7.3 Selected cross-sections of the Aliwal Shoal with A - G coast perpendicular and X and Y coast parallel. Depth distribution is also shown in histogram form in 1 m bins. Histogram bins are read as follows: e.g. 19 - 20 m bin = 20 m depth values. Vertical exaggeration is ~20x for profiles A-A' to G-G' and 22x for X-X' and Y-Y'.

In comparison, the eastern or seaward edge has an average gradient of 2° with a maximum gradient of 5.3°. This is interesting considering that the average seaward edge gradient on the Aliwal Ridge is 6.2° with a maximum of 18°. The different seaward slopes are due to different lithological units (see Chapter 8) with different ages (Chapter 9). Thus, the morphological expression of the seaward edge of the Aliwal Shoal system is a reflection of the different depositional environments formed during the last transgression with the beach environment of the Holocene beachrocks resulting in a low topographic gradation relative to the older aeolianites which formed a steeper rocky coastline.

Although the *Ridge* area is deeper (average depth of -19.5 m) than the Aliwal Shoal ridge area (average depth of -13 m), it still represents a prominent shallow bathymetric feature in the study area (Figure 7.2 and 7.4) extending westwards towards the coast continuing well beyond the study area forming a prominent shallow region (refer to Section 7.2.3 below). At its southern extremity the Aliwal Shoal complex is interpreted to be joined to the coast by the shallow area of the *Ridge* and this would have acted as a land bridge to the Aliwal Shoal during sea-level lowstands approximately 16 to 19 metres below present. Belderson (1961) also recognised this and suggested that Aliwal would have been joined to the mainland by a 'spit' at its southern end during periods of falling sea-level - thereby implying a possible spit origin for the *Ridge* area. Results from this study (refer Chapter 8, Section 8) however suggest that this area initially formed as two parallel aeolian ridges (see below).

The shallowest recorded depths occur in the north-eastern limit of the *Ridge*, at a site known as "Towering Inferno's". At this location the seafloor rises from a depth of ~ 19 m to 14 m forming two prominent pinnacles (Figure 7.2). To the southwest of the pinnacles the undulating plateau region exhibits a small elongated localised basin feature (the *Ridge Basin*) with a maximum depth of 2 m relative to the surrounding areas. This small elliptical depression separates two parallel and low relief (< 3m) linear ridges (the *Inner and Outer ridges*) crossing the plateau-like area of the *Ridge* with a NNE-SSW trend. Since both these linear ridges have a similar morphology to the Aliwal Shoal ridge they most likely have a similar origin, although they have a different orientation, suggesting slightly different processes active during formation.

The *Ridge* is separated from a low relief NW-SE trending ridge (the *Spur*) in the north by a broad, undulating low relief depression (the *Southern Basin*). This depression attains a relative depth of only 3 m. Where the *Spur* merges with the linear Aliwal Shoal ridge it attains its maximum bathymetric relief. Relief decreases landward with increasing distance from the Aliwal Shoal ridge such that by the time the western limit of the study area is reached, the *Spur* structure is almost absent. Cross-sectional profiles indicate that the Spur is most likely a bedform feature with

an asymmetry that suggests movement towards the north (Figure 7.3, cross-section X-X'). Seismic interpretation suggests that the *Spur* had its origins as a cuspate foreland formed due to either a tidal-divide within the estuarine Unit Dl sequence or due to the segmentation of coastal lakes (Cooper, 1994a), both instances forming a platform for later dune and subsequent bedform development (see Chapters 6 and 8). The *Spur* is separated from the *Sandridge* by a deep basin feature, or the *Northern Basin* (Figure 7.2). This basin feature is located on the landward side of the Aliwal Shoal ridge and is bounded on three sides by prominent bathymetric features. The basin achieves a maximum depth of 31 m, which is also the deepest bathymetric point of the area landward of the Aliwal Shoal. Belderson (1961) ascribed the formation of the *Northern Basin* to excavating streams which would also run out to sea at the northern termination of the Aliwal Shoal ridge. In the north the basin is bounded by a NW-SE (340°/160°) trending linguoid ridge, referred to as the *Sandridge*. The *Sandridge* (Unit E in Chapter 6) attains a width of ~800 m in the north-western limit of the study area and tapers out towards the SSE over a distance of ~1500 m. It is interpreted as a large subaqueous bedform from the bathymetric profiles (Figure 7.3, cross-sections A-A' and X-X') with an apparent south-eastward migration direction. It extends north-westwards towards the coast, continuing beyond the study area forming part of the shoreface-connected ridge system developed on the very prominent bathymetric feature (refer to Section 7.2.3 below) called the Mkomazi submerged-delta clinoform (Sections 6.3.4 and 6.4.3). The gently undulating seafloor topography of the *Sandridge* is in strong contrast with the rugged nature of the Aliwal Shoal ridge further supporting the unconsolidated sedimentary nature for it.

The -26 m to -30 m isobaths of the seaward edge of the Aliwal Shoal ridge define an unconsolidated sedimentary apron deposit, the shape of which is strongly controlled by the presence of a N-S trending ridge, referred to as the *Deep Offshoot Reef* (Unit B2). This feature is not laterally extensive and pinches out between the -31 m and -32 m isobaths. The region offshore (east) of the Aliwal Shoal complex (represented by dark blue to black colour shading on the bathymetry map), is characterised by a gently undulating seafloor inclined offshore with a gradient of up to 0.6°. Although this area mostly comprises a sand sheet, its surficial expression is controlled by the underlying deposits which represent a retrograding back-barrier lagoon system (Sections 6.3.4 and 6.4.3). The slope of 0.6° of the seafloor is representative of general continental shelf morphology (gentle gradients ~0.1°, Bates and Jackson, 1984).

Several platforms and notches are evident from the constructed bathymetric cross-sections (Figure 7.3). This is not surprising as sea-level changes would have exposed and drowned the study area repeatedly during the Quaternary (refer to Chapters 4 and 6) producing erosional features such as notches and wave-planed terraces cut into rock outcrops. The bathymetry data suggests that major past sea-level occupations occurred at -12 m, -18 to -19 m, -21 to 22 m, -24 m, -26 m, -28 m and -

31 to -32 m below MSL on the Aliwal Shoal shelf (Figure 7.3). Ramsay (1991, 1996) also identified several wave-planed terraces incised into shelf lithologies on the Sodwana Bay continental shelf. These were found at -12 m, -17 to -18 m, -22 m, -26 m, -32 m and 47 m below MSL, which he ascribed to the Flandrian Transgression. Cawthra (2006) inferred similar levels from geophysical data obtained from the seafloor lithologies directly offshore the Durban Bluff. However, Richardson (2005) only identified four prominent wave-cut terraces at -30 m, -34 m, -53 m and -68 m below MSL incised into the seaward margin of a reef system present within the Durban Bight - directly north of Cawthra's (2006) area. Both Cawthra (2006, 2010) and Richardson (2005) also inferred the Holocene Transgression as the event responsible for the formation of these features. The agreement of the -12 m, -18 m, -22 m, -26 m and -32 m depth levels between Ramsay's (1991, 1997) data and that obtained from the Aliwal Shoal, ~350 km south, is good evidence that similar sea-level events were recorded over a wide area of the south-eastern African continental shelf, but however, does not necessarily prove tectonic stability across the area (see Section 4.5).

7.2.2 Comparison to the Durban Bluff dune system

Comparable coast-parallel linear ridges are common features on the eastern and southern continental shelf of South Africa (refer to Section 3.4.2, Figure 3.11). The type of morphology displayed by the Aliwal Shoal is strikingly similar to that of coastal barrier dune and associated estuarine systems found along the southern and eastern seaboard of South Africa. Belderson (1961) was the first person to draw attention to the this fact by showing that the depth contours defining the Aliwal Shoal (Figure 7.4) are essentially similar in shape to the Durban Bluff topography. He used this morphological resemblance to suggest that the Aliwal Shoal and other similar coast parallel offshore reefs are remnants of cemented coastal sand dunes that formed during lower sea levels. This was later proven by McCarthy (1967) which analysed a rock specimen from the shoal (refer to Chapter 1).

Figure 7.5 shows a comparison between the topography of the Durban Bluff (Figure 7.5a) and the bathymetry of the Aliwal Shoal (Figure 7.5b). The higher resolution bathymetric data makes the similarities even more apparent than seen on Belderson's (1961) map. Although the scale varies (Table 7.1) between some of the features of the Durban Bluff and the Aliwal Shoal, the morphological resemblance is remarkable with similar features present in both examples.

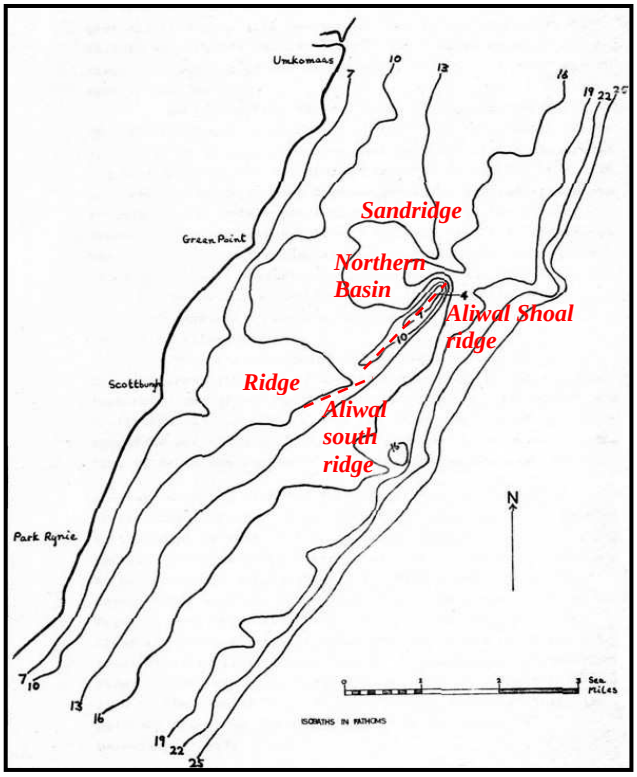

Figure 7.4 Belderson's (1961) map of the Aliwal Shoal which he used as a comparison to the coastal dune barrier system of the Durban Bluff. Note that the isobaths are in fathoms and scale in nautical miles. 1 fathom = 1.83 m and 1 nautical mile = 1.852 km. Some morphological features corresponding to those as identified by this study (Figure 7.2) are labelled.

This suggests that the Aliwal Shoal can be considered a submerged counterpart of the Durban Bluff although the Durban Bluff is wider and higher (Table 7.1). This is due to the fact the Durban Bluff is composed of both unconsolidated sediment and aeolianite whereas the Aliwal Shoal is composed only of aeolianite, the unconsolidated portion would have been removed during submergence. Assuming that Aliwal Shoal was once similar in size to the present day Durban Bluff, the aeolianite component approximates only 25% of the height and 70% of the width of the original barrier dune system and is controlled by the lithification process which only occurs below the water table. The reader is referred to Section 8.3.4 for a more detailed discussion of aeolianite diagenesis. The position of the water table within the interior of the dune is thus critical in determining the degree and extent of vertical lithification of the original aeolian sediment. Since the orientation of the coastline is parallel to two opposing wind directions (Section 2.1) the dominant sediment migration direction is coast parallel resulting in vertical aggradation and barrier dune systems that are some of the highest in the world. The water table however, remains in the lower parts of the dunes and even in a very high dune, the bulk of the unconsolidated sediment remains unlithified and is then easily removed during sea-level rise.

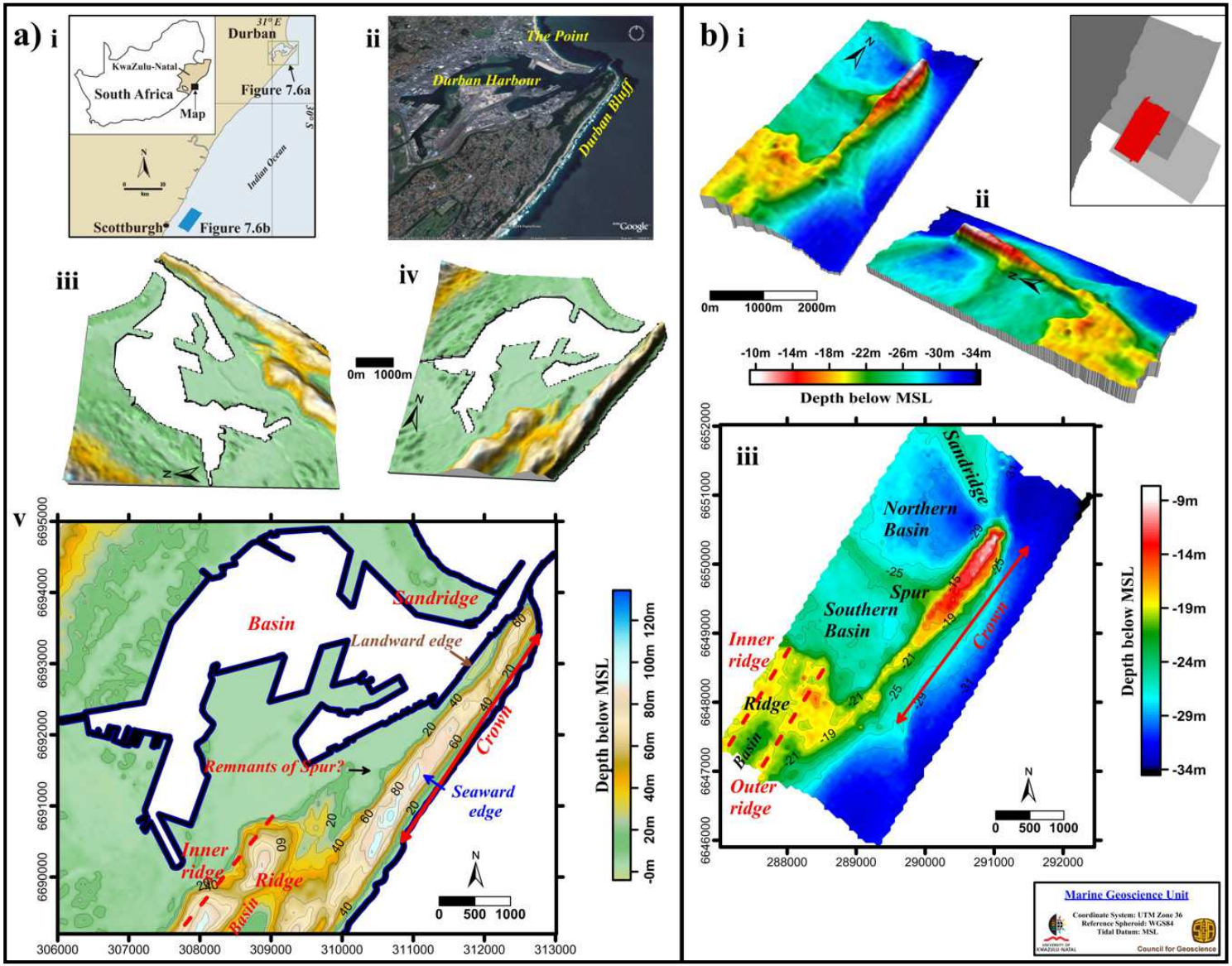

Figure 7.5 Morphological comparison between the onland coastal barrier dune system of the Durban Bluff (**a**) and the Aliwal Shoal (**b**). **ai**) locality map, (**ii**) oblique satellite image of the Durban Bluff (from Google Earth), **iii and iv**) 3D terrain models of the map area in (**av**) (data courtesy Council for Geoscience), **v**) colour coded 10 m contour map of the Durban Bluff with some of the common morphological features labelled for comparison (data courtesy Council for Geoscience). **bi and ii**) 3D terrain models of the Aliwal Shoal, (**iii**) colour coded 2 m contour map of the Aliwal Shoal annotated with the same features as on (**av**).

Unlike the Aliwal Shoal, the Bluff does not show any systematic decrease in the width of the crown southwards from the abrupt northern end termination. The extremely narrow southern end of the Aliwal Shoal Crown is most likely a result of original dune-building processes and/or an indication of a palaeo-fluvial breach and subsequent erosion of the dune barrier. Seismic interpretation indicates that there was a back-barrier estuarine system behind the Aliwal Shoal ridge (Chapter 6). Lateral migration of fluvial channels is common and estuaries along the KwaZulu-Natal coastline frequently change mouth or outlet position (Begg, 1978, Cooper, 1991b, 2001). It is most likely that the breach was due to flood conditions which resulted in a more direct estuary mouth opening (Cooper, 1994b), as opposed to water discharge at an estuary mouth opening north of the Aliwal Shoal (see Cooper 1991a for estuaries under flood conditions). In addition, the Aliwal system is interpreted to have had two fluvial outlets, responsible for a tidal divide which initialised the Spur and possibly started the process of lake segmentation as described by Cooper (1994).

Table 7.1 Tabulated morphological feature comparison between Durban Bluff and the Aliwal Shoal.

Morphological Feature	Durban Bluff	Aliwal Shoal
Abrupt northern end termination	✓	✓
Height (from base level to highest point)	>100 m	25 m
Orientation of linear ridge or 'Crown'	NE-SW (036°/216°)	NE-SW (037°/217°)
Length of 'Crown'	~3200 m	~3200 m
Average width of 'Crown'	Min: 390 m, Max, 720 m Average: 535 m	Min: 100 m, Max, 530 m Average: 380 m
Width of plateau area or 'Ridge'	>2000 m (anthropogenic alteration)	>2000 m (extends beyond study area)
Linear ridges present on 'Ridge' (orientation)	Yes (040°/220°)	Yes (033°/213°)
Approximate size of landward basin	16.2 km^2	6.3 km^2

As for the Bluff, the Aliwal Shoal system also shows the presence of linear ridges backed-up against the landward side of the main ridge system (Figure 7.5). This morphology is typical of coastal barrier dune systems which commonly display several parallel to semi-parallel ridge systems, each ridge normally representing dune development during a different sea-level. The number and the extent of dune ridges that develop are primarily controlled by the presence of rivers and availability of sediment and accommodation space (coastal plain). This is well illustrated by comparing the Maputaland coastal barrier dunes with the Durban Bluff (Figure 3.14). In Maputaland several distinct dune cordons are present on the wide coastal plain which has few major river systems. However, further south, such as at the Durban Bluff, dune ridges are limited to a coastal belt situated on a very narrow coastal plain adjacent to a steep hinterland. Interesting

to note here is that the Durban Bluff deviates slightly from the average coastline orientation and this change in orientation is what generated the accommodation space, in the form of a large coastal plain, on which the Durban Harbour is situated.

7.3 SEISMICALLY DERIVED BATHYMETRIC DATASET

The bathymetric map (Figure 7.6) and profiles (Figure 7.7) presented in this section are derived from a combination of the high resolution dataset (Section 7.2.1) and seismically derived bathy data. It covers a larger area than the high resolution dataset (Figure 7.1) and extends to the continental shelf break.

7.3.1 Continental Shelf Morphology

Apart from the Aliwal Shoal complex the most noticeable feature covered by this dataset are 3 terraces and the presence of the shelf break (Figure 7.6a, b). The shelf break occurs at a depth of 85 m, 10.5 km from the coast and is narrow and shallow compared to the global average width of 78 km, and average depth of 130 m (Kennett, 1982). The shelf morphology is characterised by the relict dune ridges, steep gradients and an extensive outer shelf planation surface (Figure 7.6bi - iii) and can be subdivided into three distinct regions: the inner, middle and outer shelf (Table 7.2).

The inner continental shelf extends from the coast (nearshore, ca. -10 m) to the -30 m isobath (refer to the next section on shelf classification) and is dominated by the Aliwal Shoal complex. Although the shoal complex has been described in detail the following observations are better made and explained in this section. On the profiles (Figure 7.7, profiles N-N' and C-C') it can be observed that the exposed inner (landward) edge of the Aliwal Shoal is at a greater depth than the outer (seaward) edge. Seismic profiles indicated that during the Holocene transgression the Aliwal Shoal ridge was flanked landwards by a back-barrier estuarine system and seawards by an embayed barrier-lagoonal system (Sections 6.3.4 and 6.4.3). As transgression proceeded, the Aliwal Shoal ridge presented a physical barrier to the landward retreating shoreface with the result that the TST sedimentation was banked up against the seaward edge of the Aliwal Shoal. This was in contrast to the aggradational estuarine system which maintained its basin structure during the transgression and which was rapidly overstepped (see Section 6.4.3) thereby preserving its morphology. The bathymetric map (Figure 7.6) also a shows that the area offshore of the Aliwal

Shoal forming a gentle undulating seaward sloping terrace which also corroborate the seismic interpretation (Sequence 4, Unit Ds) of unconsolidated sediments in this area.

The area adjacent to the northern extremity of the Aliwal Shoal shows the development of a crescentric scour trough (Figure 7.7, sunshaded relief image). Scour troughs usually develop on the stoss side of the object (Collison and Thompson, 1982) embedded in or surrounded by unconsolidated sediment (such as is the case with the Aliwal Shoal - refer to Chapter 6). This implies the presence of a strong northeast-southwest current in the study area, indicating the influence of the southerly-flowing Agulhas Current in this area of the inner shelf. It is interesting to note that although, the study area is located within a bedload parting zone where a south to north counter-current is active (Flemming, 1981; Flemming and Hay, 1988; Section 2.3.2), the Agulhas Current still affects this section of the shelf. This lends support to 1) a migratory position for the bedload parting zone and 2) that the Agulhas Current periodically transgresses close to the outer portion of the inner shelf zone with enough erosive power to create scour troughs.

The middle shelf (-30 m to -80 m) ranges in width from 500 m in the north to over 3000 m in the south. Relict dune ridges, orientated sub-parallel to the Aliwal Shoal ridge, are well defined by their rugged bathymetric expression (Figure 7.6). These ridges are best developed in the southern portion of the middle shelf between the -34 m and -62 m isobaths. At least three sub-parallel ridges can be identified with a maximum relief of 10 m to 15 m locally. In the northern portion of the middle shelf, the relict ridges consist of a single narrow linear ridge between the -57 m and -62 m isobaths. Unconsolidated sediment from the MSDC is banked against the buried seaward flank of this ridge resulting in a steep slope on the seaward termination of the sediment wedge (seismic line 6, Figure 6.6 and Figure 7.7, profile N-N'). The unconsolidated sediment wedge is thus bounded by the Aliwal Shoal Ridge and the Middle Shelf Ridge system (refer to Sections 6.3 and 6.4 for more evidence) producing a sediment wedge with a gently offshore sloping terrace area, terrace T1 (Figure 7.7). The seaward slope of the relict dune ridge is the steepest at 2.5° (average 1.7°). Offshore this evens out into a terrace between the -69 m and -72 m isobaths - terrace T2. Terrace T2 is not continuous but pinches out to the north of the study area (Figure 7.6). Although T2 contains relict dune ridges (refer Chapter 6, seismic lines 6, 7, 8, 9) they do not attain the bathymetric relief exhibited by ridges at shallower depths. There is a paucity of well developed ridge structures on the northern middle shelf area (Figures 7.7 and 7.8; Section 6.3) which is due to the combination of these ridges being of low bathymetric relief and also being buried the southern extremity of the MSDC (Section 6.3; seismic line 5).

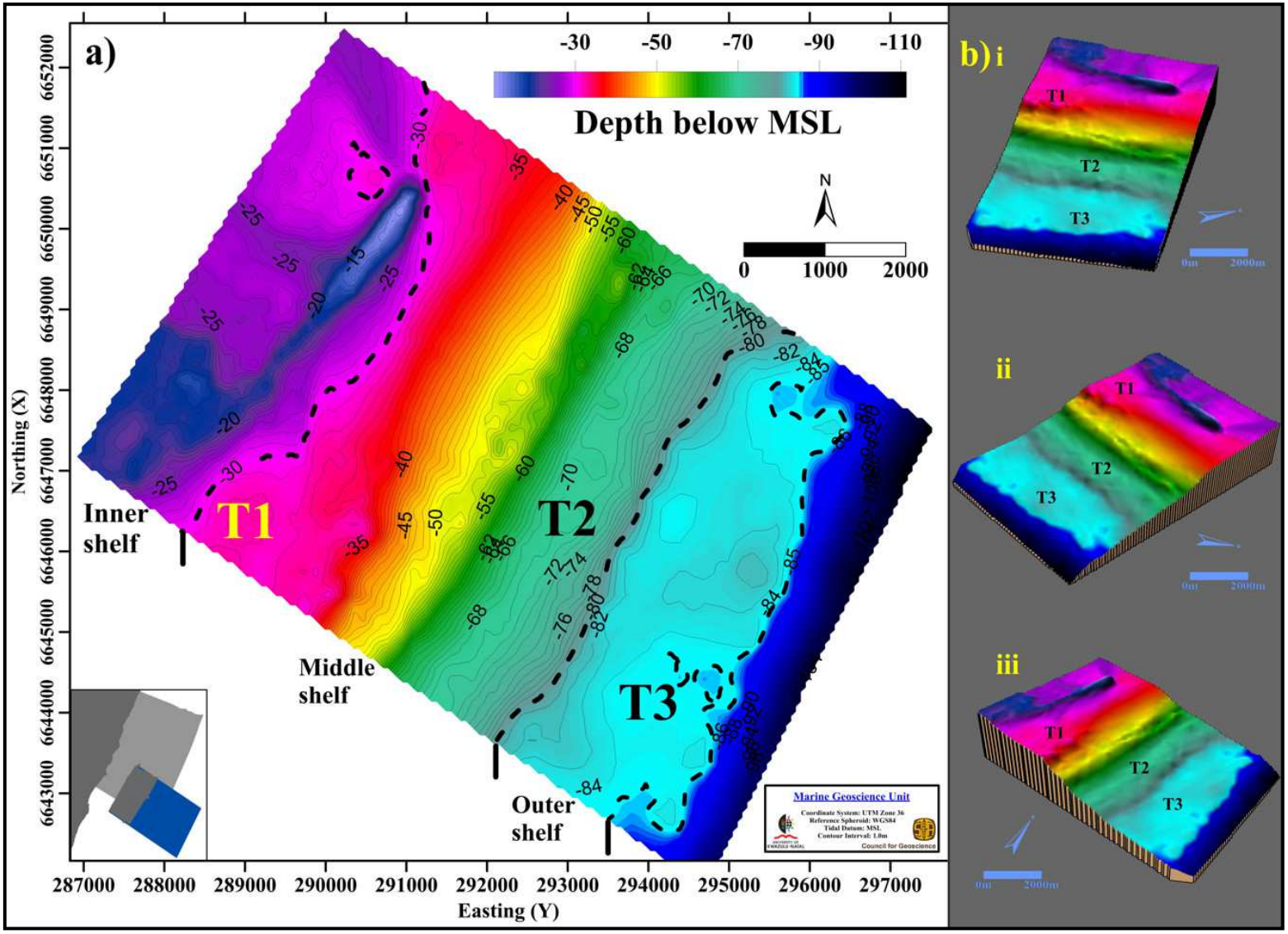

Figure 7.6 a) 1-metre contour interval bathymetric map of the continental shelf surrounding the high resolution study area based on seismic data. Data integration is discussed in the text and in Section 5.3.2. Terraces T1-T3 annotated. **bi-iii**) 3D digital terrain models from various viewing angles. Colour coded depth scale is applicable both to figures (**a**) and (**b**). Vertical scale exaggeration is 20x. Small inset map shows the coverage and locality of this dataset relative to the other bathymetric datasets (refer to Figure 7.1).

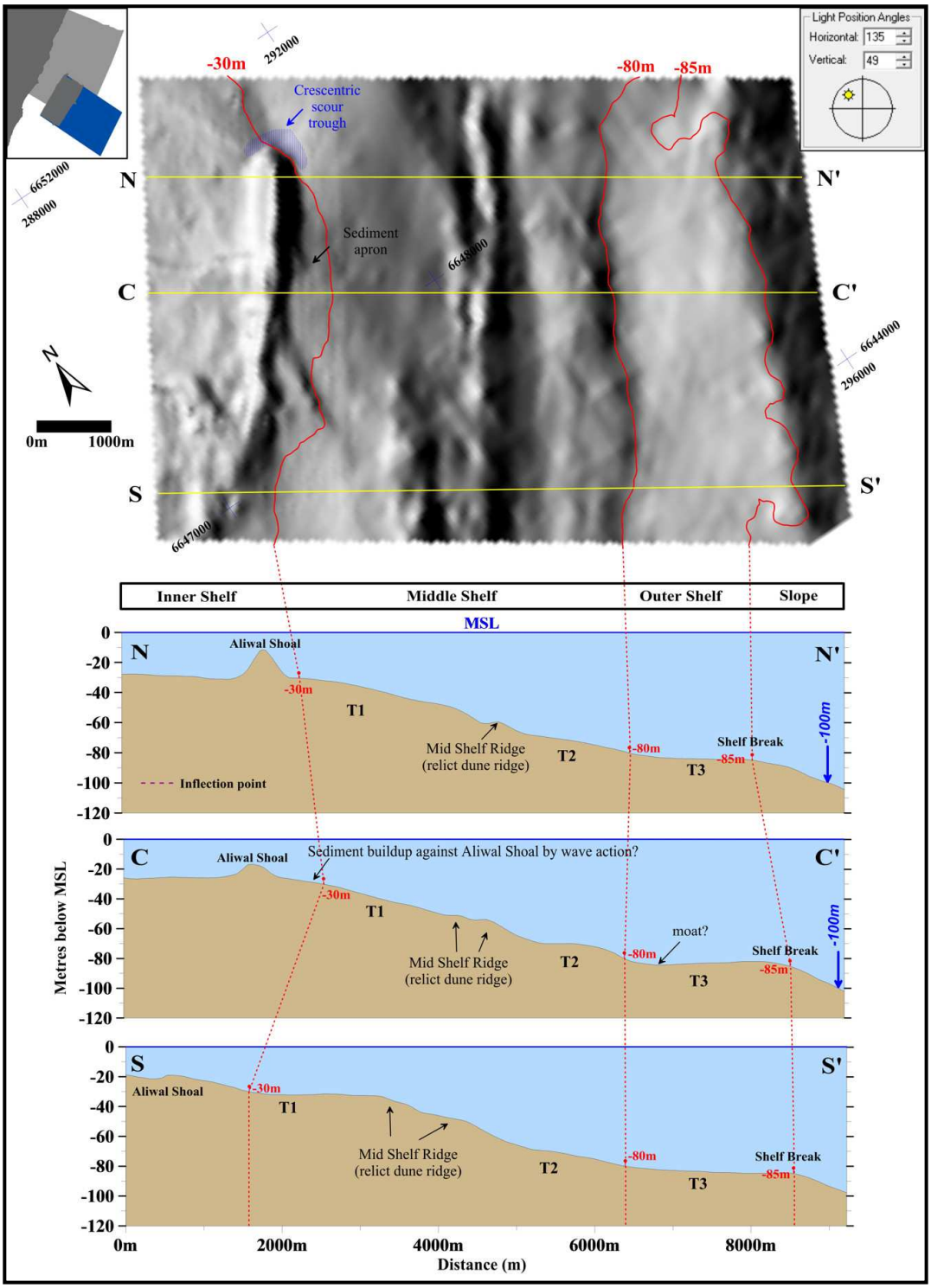

Figure 7.7 Shaded relief bathymetric map of the continental shelf with selected bathymetric profiles of the Aliwal Shoal and adjacent areas. Vertical exaggeration for the bathymetric profiles is 18.5x. Profiles N-N' and C-C' shows the 100 m isobath as this contour was used by previous workers (Goodlad, 1978; Birch, 1981) to define the shelf break. T1-3 denotes terrace 1 to 3.

The middle - outer shelf boundary is placed at the -80 m bathymetric level. Except for its northern extremity, the -80 m isobath is sub-parallel to the relict dune ridges and represents an inflection

point on the bathymetric profiles (Figure 7.7) an obvious boundary between the middle and outer continental shelf. Due to the steeper slopes associated with the well developed relict dune ridges located in the southern half of the middle shelf, the knick-point is better accentuated on the southern shelf. The well developed slope is most likely an erosion scarp formed during a sea-level stillstand event. The outer shelf is dominated by a broad well developed terrace area (terrace T3) with an average gradient of 0.16° and an average width of 1850 m (Figure 7.6 and 7.8). This terrace continues further south but not to the north (Chapter 2; Figure 2.12) and most likely represents a peneplained surface bounded at its landward edge by the erosion scarp. These features are typical of a major marine erosional event of sufficient duration to completely bevel the continental shelf. The lateral outline of the erosion scarp is sinuous (Figure 7.7, -80 m isobaths) and might indicate subsequent submarine scour by the Agulhas Current. This is further corroborated by the presence of a moat feature (Figure 7.7, profile C-C') adjacent to the erosion scarp and variable depth of the surface from -80 m to -84 m suggesting recent submarine deposition and/or erosion by the Agulhas Current. The shelf break generally occurs at the -85 m isobath, beyond which the slope gradient steepens significantly (1.9°) at the start of the continental slope. Sequence 3 discontinuous elevated ridge-like structures occur near the shelf break and can be seen on the bathymetric profiles (Figure 7.7).

Table 7.2 Summary of the major morphological features on the continental shelf in the study area.

Region	Inner Shelf 0 to -30 m	Middle Shelf -30 m to -80 m	Outer Shelf -80 m to -85 m
Northern	Aliwal Shoal complex very well developed. Relief = >25 m	Ridge system very poorly developed or absent	Presence of discontinuous elevated areas
	Wide area: >2.5 km	Very wide: >3.5 km	Narrow: 1.4 km Slope of 0.17°
Central	Aliwal Shoal complex present but moderate relief 10 m - 15 m	Presence of relict dune ridge, moderate development	Wide: 2.2 km Slope of 0.14°
Southern	Aliwal Shoal complex present but subdued relief <12 m	Relict dune ridge system in 'climax' state 10 m - 15 m relief	Moderate: 1.8 km Slope of 0.15°

In essence the continental shelf in the seismic study area consists of an inner shelf dominated by the bathymetric high of the Aliwal Shoal, which extends offshore into a middle shelf zone consisting of relict dune ridges that separate two distinct terraces (T1 and T2, Figure 7.7). The offshore termination of the lower terrace (T2) is characterised by a steep erosion scarp which forms the middle-outer shelf boundary and marks the landward boundary of the well developed outer shelf terrace (T3) which extends to shelf break.

7.3.2 Continental Shelf Classification

Birch (1981, 1996) similarly subdivided the continental shelf in the vicinity of the study area into three regions, the inner shelf extending from the coast to -50 m; the middle shelf from -50 m to -70 m; and the outer shelf from -70 m to the shelf edge. His subdivisions were mainly based on the relative positions of the 'nearshore sand sheet' (termed here unconsolidated sediment wedge), the system of relict dune ridges and an extensive terrace. Flemming (1981) subdivided the shelf platform into a nearshore and offshore physiographic zone separated by the Pleistocene relict dune ridge. This classification is more applicable to the study area but the nearshore/offshore shelf boundary would vary depending on which of the relict dune system is used resulting in some ambiguity. Since both Birch's (1981, 1996) and Flemming's (1981) study areas were extremely large their classifications are more applicable to the overall morphology of the continental shelf. Due to the more detailed nature of Birch's (1981, 1996) classification system deviations are more likely as is illustrated by the Aliwal Shoal area. The Aliwal Shoal shelf can also be considered a special case or exception as there is no other occurrence of such a prominent and well preserved aeolianite ridge in the same depth range (refer to Figure 3.11).

The revised classification of the continental shelf (Table 7.2) presented here is considered more applicable to the shelf surrounding the Aliwal Shoal. The divisions still coincide with those features suggested by Birch (1996), but are adjusted for the local morphology, the system of relict aeolianite ridges and the extensive terraces found in the study area. With the exception of the Aliwal Shoal complex, the relict aeolianite ridges are confined to a broad region between the -30 m and -75 m isobaths. The -50 m isobath, or the inner and middle shelf boundary according to Birch (1981), is not appropriate for the study area in as far as it defines different morphological features in the profiles (Figures 7.7 and 7.8). In the northern profile (Figure 7.7 N-N') it defines the seaward boundary of the nearshore sand sheet. In the central profile (Figure 7.7 C-C'), the -50 m isobath is defined by a change in slope, which is caused by the appearance of the aeolianite dune cordon. In the southern profile the -50 m isobath is also defined by a change in slope, which is also caused by an aeolianite ridge, however, here the -50 m isobath does not define the seaward boundary of the and sheet nor does it define the start of the aeolianite ridges located between the -30 m to -75 m isobaths (Figure 7.7).

Herein lies the problem with using the -50 m isobath as the boundary between the inner and outer shelf in the study area. The seaward edge of the unconsolidated sediment wedge or Umkomaas sediment deposit (Birch, 1981) or Illovu submerged spit bar (Martin and Flemming, 1986), is with the exception of its northern edge (Birch, 1981, outside of study area) dammed against the aeolianite ridges located between the -30 m to -75 m isobaths. These relict ridges however, are not

only markedly varied in distribution (Figure 7.7) but also, as opposed to the prominent linear ridge of Aliwal Shoal, consist of several sub-parallel less prominent linear ridges, defining a ridge system in the study area (Figure 7.6). The -50 m isobath is thus not optimal in defining the boundary between the inner and middle continental shelf *in the study area*. The suggested -30 m isobath is preferred as it not only defines the landward edge of the ridge system (based on gradient change) but also includes the bulk of the Mkomazi submerged-delta clinoform depocentre and the Aliwal Shoal. Bosman *et al*. (2007) also used the -30 m isobath to delineate the inner/middle shelf boundary on the continental shelf offshore of the Thukela River, ~200 km to the north of the study area. Based on sedimentological facies assemblages they found that the -30 m isobath represented the fair-weather wave base in the area, which is expected to be very similar to that of the Aliwal Shoal shelf. In the same way the -70 m isobath, used by Birch (1981) to define the boundary between the middle and outer shelf, suffers the same inadequacies in the study area as the -50 m isobath. The -80 m isobath approximates the boundary between the middle and outer shelf better corresponding to a major change in morphology in the form of an inflection point in the slope, signifying the landward limit of the well developed terrace area (T3) of the outer shelf (Figure 7.6).

In summary, Birch's (1981) subdivision of the continental shelf is not suited to the study area as the depth of the inner and middle shelf boundary is better position at -30 m rather than -50 m. Although the northern extremity of the seaward edge of the unconsolidated sediment wedge transgresses the -30 m isobath, it is still consistent in morphological definition. In contrast to the difficulties in defining the inner and middle shelf boundary, the revised middle and outer shelf boundary (-80 m) is well defined by a laterally continuous point of maximum change in gradient, which is related to an erosion scarp and extensive platform forming the outer shelf. Historically the shelf break was represented by the -100 m isobath (Goodlad, 1978, Birch 1981) but this depth is well below the actual shelf break in the study area (Figure 7.7, profiles N-N' and C-C') which is found at -85 m.

7.4 ARCHIVAL BATHYMETRIC DATASET

Bathymetric data acquired from an archival fair chart is presented in Figure 7.8 and 7.10. As stated earlier this data overlaps with the bathymetric data presented in sections 7.2.1 and 7.2.2 (Figure 7.1). Due to the fact that the archival data are less accurate than the collected data, it is replaced by the more recent data (Figure 7.1, bathymetric dataset 1 - 4) in areas of overlap (refer to Chapter 5 for the methodology). The archival data provides a more extensive overview of the

continental shelf revealing processes responsible for the observed sedimentary features (Section 8.4).

7.4.1 Shoreface-Connected Ridge Morphology

The bathymetry is dominated by the presence of the Aliwal Shoal and numerous approximate northwest-southeast trending shore-attached ridge features orientated obliquely to the coastline (Figure 7.8). The unconsolidated nature of these ridge structures is established from seismic profiling (Chapter 6) and previous work by Martin and Flemming (1986). Although Martin and Flemming (1986) did not draw attention to the ridges, they did identify a large unconsolidated northwards prograding sediment body which they coined 'the Illovu submerged spit bar' complex and renamed here to the Mkomazi subaqueous-delta clinoform (MSDC; Section 6.3.4). The ridge structures present on the topset of the MSDC (Figure 6.17) are interpreted as *shoreface-connected ridges* (hereafter SCRs), also known as *shoreface-attached ridges,* the first documentation (Bosman *et al*., 2008) of this bedform from the South African continental shelf.

The shoreface is commonly defined as a zone characterised by day-to-day sediment transport occurring beneath the low tide level and above the fair-weather wave base, normally having a concave-upwards profile (Walker and Plint, 1992). By this definition the shoreface in the study area constitutes the entire seafloor located above the -30 m isobath (thus inner shelf - refer to section 7.2.2) and occupies approximately a third of the total shelf width (Figure 7.8). Due to lack of consensus in the literature on the term shoreface and its depth range (Antia, 1996) the study area will be divided into a nearshore zone ranging from 0 to -10 m and the inner shelf from -10 m to -30 m (refer to previous section). The nearshore defines the zone of littoral drift along the coast (MacKie, 2005) forming a very pronounced shore-parallel shallow bathymetric feature present between the depths of 0 to -10 m (Figure 7.8). The term *shoreface-connected ridge* is retained (rather than nearshore-connected ridges) as it is an established term in the literature. Where the term shoreface is used here it is taken to mean the nearshore zone and inner shelf as defined above.

The SCR crests are 1 - 6 m in height, spaced 500 - >1350 m apart and vary from 3 km to >8 km in length (Table 7.3, Figure 7.9). They are attached on their shoreward portions to the shoreface between depths of -10 m to -15 m (average at -13 m) and can be traced to depths exceeding -50 m, although the majority occur on the inner shelf between -20 m to -30 m (Figure 7.8). Several individual crests can be identified (Table 7.3, Figure 7.9) forming shoreface-connected sand ridge field.

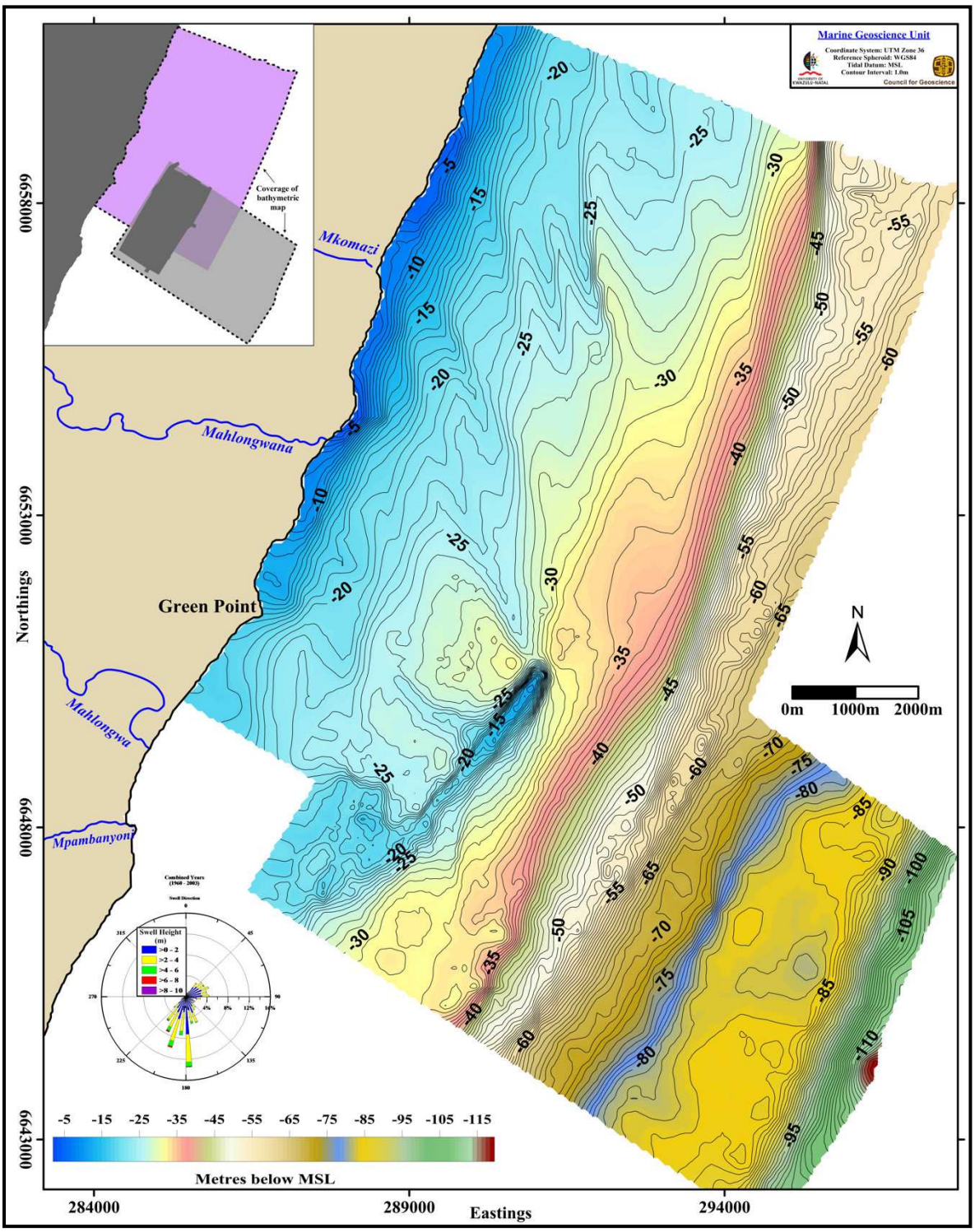

Figure 7.8 1-metre interval coloured-shaded bathymetric contour map of the continental shelf surrounding the Aliwal Shoal. Note the approximate north-south trending ridge structures attached to the shoreface (coast) and also to the northern termination of the Aliwal Shoal. These are interpreted as shoreface-connected ridges. Map inset shows relative positions of the different bathymetric datasets used to produce this chart (refer to Section 5.3.2). Yearly (1960-2003) swell height and direction data included as a rose diagram (from Figure 2.3). MSL = mean sea-level.

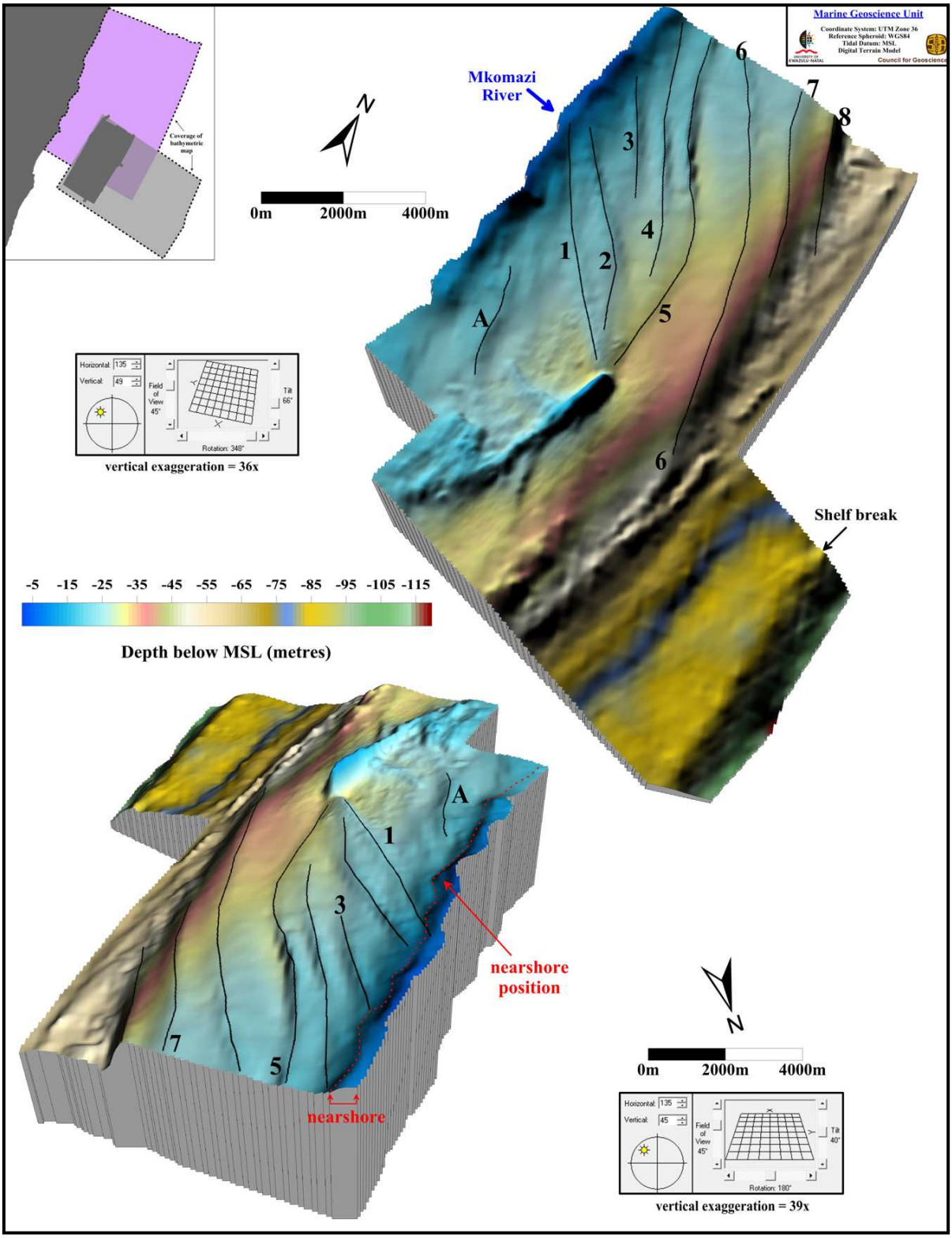

Figure 7.9 Coloured-coded sun-lit digital terrain models of the Aliwal Shoal shoreface-connected ridge (SCR) field. Approximate positions of the individual bedform crests are indicated and labelled as 1 - 6; refer to Table 7.3 for dimensions. Feature A seems to be attached to a relict dune ridge on the shoreward side of the Aliwal Shoal and does not seem to form part of the SCR system to the north. Note the sigmoidal shape that the offshore change in direction of crest 5 imparts on the composite bedform feature consisting of bedforms 1 - 5. Crest 6 seems to be attached at its offshore extremity to the Middle Shelf Ridge (MRA; Figures 6.14 - 6.16) a relict dune ridge at - 50 m. Map inset shows map coverage and the different bathymetric datasets used to produce this chart (refer to Section 5.3.2).

Table 7.3 Shoreface-connected ridge characteristics. Refer to Figure 7.9 to 7.12 for the relative positions of the individual SCR crests. Crests 5 - 8 have greater than (>) length values as they extend beyond the study area. Orientations measured as the angle between the axis of the sand ridge and the adjacent coastline following Figueiredo *et al*. (1981). Height was measured from trough to crest.

Ridge	Angle (^{0}) (decreases offshore)	Crestal Spacing (m)	Length (m)	Height (m)
Crest A	15 (increases offshore)	-	3800	1 - 4
Crest 1	50		5200	1 - 3
		540-740		
Crest 2	50		5000	1 - 5
		800 - 1200		
Crest 3	36		3000	1 - 3
		580 -650		
Crest 4	32		6000	1 - 2
		480 - 800		
Crest 5	40		>8200	1 - 6
		600 - 1850		
Crest 6	33		>9400	1 - 2
		620 - 1200		
Crest 7	30		>4800	1 - 2
		800 - 1000		
Crest 8	32		>3600	15 - 20?

Most crest orientations are approximately northwest-southeast which is parallel to the dominant swell propagation direction. As a result the SCR crests are orientated obliquely to the coastline trend at angles ranging from of 30° - 50°, with the larger crests (crests 2, 4, 5, 6), showing a decrease in this angle (i.e. become more parallel with the coastline) further offshore (Figure 7.9).

SCR crests 6 - 8 cross the junction (-30m) between the inner and middle shelf regimes with some crests merging further offshore. This is illustrated by the convergence and attachment of at least two separate SCR structures (crest 1 and crest 2, Table 7.3) to the northern extremity of the Aliwal Shoal forming one composite structure bounded at a lower depth of approximately -26 m. The southern extremity of this composite bedform feature was identified in the detailed study area and named the *Sandridge* (Section 7.2.1, Figure 7.2). The *Sandridge* is thus part of a much larger and complex system of merged bedforms extending beyond the detailed study area. In addition, to the north the *Sandridge* (crests 1 and 2) merges with another similar structure consisting of 3 ridges (crests 3 - 5). The extension of ridge 5 changes orientation at -28 m, merging southwards with the *Sandridge* and attaching to the northern extremity of the Aliwal Shoal (Figures 7.9 and 7.10).

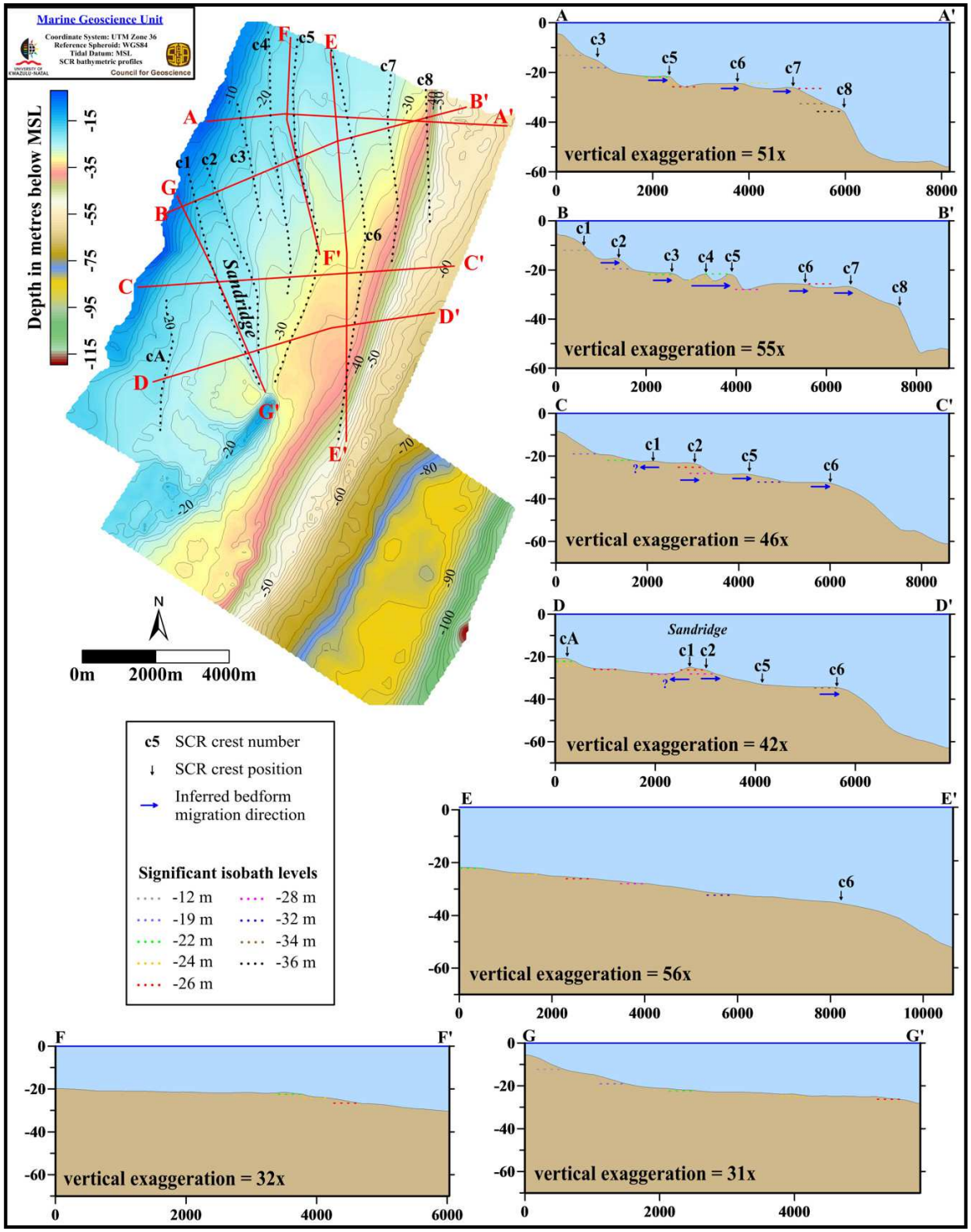

Figure 7.10 Selected bathymetric profiles of the shoreface-connected ridge (SCR) bedform field on the Aliwal Shoal shelf. Colour-shaded bathymetric contour map is as for Figure 7.8. Individual SCR crest positions are indicated on the bathymetric locality map and the profiles. Significant isobath levels correlated to those observed on the Aliwal Shoal (Figure 7.3) are indicated on the profiles as well as inferred bedform migration directions.

This imparts an overall sigmoidal shape (Figure 7.9) to the composite bedform feature consisting of SCR crests 1 to 5, the lower extremity of the sigmoidal feature ranging in depth between -30 m to -31 m with the southern limit attached to the Aliwal Shoal at a depth of -31 m (Figure 7.9 and 7.11).

Ridges represented by crests 6 - 8 bypass the Aliwal Shoal, with crest 6 abutting against a Middle Shelf Ridge system at -50 m (Figure 7.10). Both ridge crests 7 and 8 terminate on a middle shelf terrace > -50 m in depth which also represents the offshore limit of the sediment wedge on this part of the shelf (Figure 7.10, profiles A-A' to D-D' and also refer to Chapter 6). Bedforms 1 - 5 seems to be superimposed on this much larger structure represented by ridges 6 - 8 (Figure 7.10, profiles A-A' to D-D'). Ridge 6 is the longest whilst ridge 8 has the largest amplitude.

The nature of the bedform represented by crest A (Figure 7.9 and 7.11) is not certain but it does not seem to be connected to the SCR field further north. Although ridge crest A displays similar features (Table 7.3) to that of the SCRs further north, it is not attached to the northern extremity of the Aliwal Shoal, as is the case for ridges 1 - 5, but rather to the relict dune ridges (refer to description of the *Ridge* in section 7.2.1) banked against the shoreward side of the Aliwal Shoal. In addition, ridge A also displays an anti-clockwise rotated offshore termination which increases the angle of orientation with the coastline offshore. This is in contrast with the pattern exhibited by the SCRs attached to the Aliwal Shoal and may reflect a different hydraulic regime for its formation.

Slope angles from the bathymetric data (Figure 7.11) highlight the SCRs and reveal the presence of two subtle north - south trending ridges associated with ridge A. These bedforms (labelled B and C on Figure 7.11) together with ridge A provide a link to north - south directed bedform patterns observed in the detailed study area (Chapter 8). Slope analyses (Figure 7.11) suggests that crest 7 continues offshore and merges with crest 6 attaching to the northern termination of a relict palaeodune cordon located on the middle shelf resembling the configuration of crest 1 and 2. Interestingly, with the exception of crest 8, all of the SCRs seem to be directly associated and attached to ridge structures of Sequence 3 (palaeo-barrier dune cordons). Crests 6 - 8 also show overlap with the foreset of the MSDC hinting at the compound nature of the clinoform which has been continuously evolving since ~9.5 ka cal. B.P. constructed by both along- shore and across-shore sedimentation (Section 6.4.3).

The Aliwal Shoal SCRs have symmetrical and asymmetrical characteristics (Figure 7.10 and 7.12). Asymmetry is dominantly directed north-eastwards but a south-westerly asymmetry is also present.

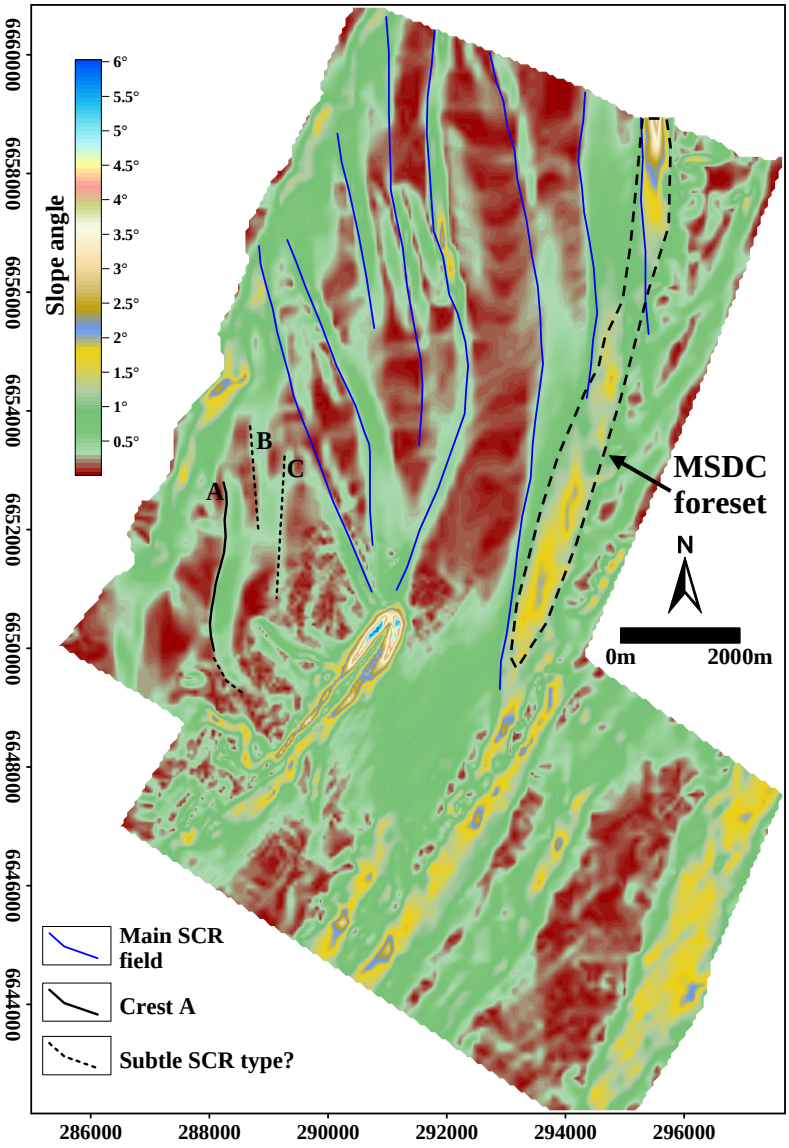

Figure 7.11 Slope angles computed from the bathymetric data aids in emphasising the major morphological components. The SCR bedform field to the north of the Aliwal Shoal is highlighted as well as the subtle bedforms, B and C, associated with ridge A. For individual crest numbers refer to Figures 7.10 and 7.11. Thick dashed black line represents the interpreted position of the MSDC foreset (refer Figure 6.17).

The composite *Sandridge* feature (crests 1 and 2, Table 7.3, Figure 7.10) shows a bi-directional asymmetry, varying with depth. Crest 2 shows asymmetry directed towards the northeast (between -13 m and -26 m), whereas the southern crest member (crest 1) displays asymmetry directed to the southwest (<-22 m to -30 m, Figure 7.10). This reversal takes place in the lee of the Aliwal Shoal (Figures 7.9 and 7.10) and might be a response to sediment transport due to wave refraction around the very shallow northern extremity of the Aliwal Shoal. Wave incidence direction (Figure 7.8) is predominantly southerly. Refraction around the Aliwal ridge redirects wave trains towards the southwest and even to the west-northwest thereby resulting in bedform

migration towards the southwest. Further evidence for this process is presented in Section 8.4. Changes in asymmetry of individual SCRs were also observed by Swift and Field (1981) on the inner shelf of the Middle Atlantic Bight of the U.S.A.

Ridge crests A and 2 - 5 show well develop northward asymmetry most likely indicating a unidirectional (or skewed bidirectional migration) direction towards the north-east. Crests 6 and 7 have a subtle asymmetry above -26 m but this is more pronounced towards the forest of the MSDC. Crest 8 constitutes the lower-most bedform unit (Figure 7.10) and imparts to overall north - easterly directed migration direction to the bedform field. The slope of the ridge flanks are generally less than 1°, although locally some lee sides show angles approaching 5° (Figure 7.11; crests 8 and 5).

Measurement of SCR migration is usually made by comparing bathymetric datasets of the same area collected at different time intervals (Swift and Field, 1981; Parker *et al*., 1982; Antia, 1996). Lateral bedform displacement must exceed the associated positional accuracy errors with the data to be meaningful. For this study bedform migration (Figure 7.12) was determined by comparing dataset 5 with the high resolution integrated dataset consisting of datasets 5 and 6 (Figure 7.1). Dataset 5 was collected in June 1986, whilst the high resolution dataset is interpreted to reflect the average conditions for the 15 month period of March 2001 to June 2002. This comparison has the following constraints;

- only one SCR, the *Sandridge* (Figures 7.3, 7.4, 7.12 and 7.13) is present in the area of overlap between the different datasets,
- the positional accuracy of the 1986 dataset can range between 50 - 200 m but is estimated to be in the 100 m range (Section 5.3.2),
- the 2001 - 2002 (referred to as the high resolution or 2002 dataset) has positional accuracy better than 1 m (Section 5.3.2).

From Figure 7.12 it can be seen that the Sandridge migration was depth dependant with the shallowest depth isobath (-25 m) showing movement of more than 800 m, the -26 m isobaths ~180 m, the -27 m isobath ~100 m and the -28 m isobath ~30 m. Only the -25 m and -26 m isobaths showed movement that can be confidently interpreted as real bedform migration, with the -25 m isobath having ~700 m and the -26 m showing ~80 m of 'real' movement. The -27 m and -28 m isobaths show the same general pattern although the actual migration distance cannot be established confidently. This indicates that over a 16 year period the bedform migrated through offshore movement of its tip (in a south-easterly direction) and seaward flank (north-easterly direction). The offshore migration of the ridge tip resulted in a general steepening of the ridge front with some associated narrowing on the ridge top above the -25 m isobath.

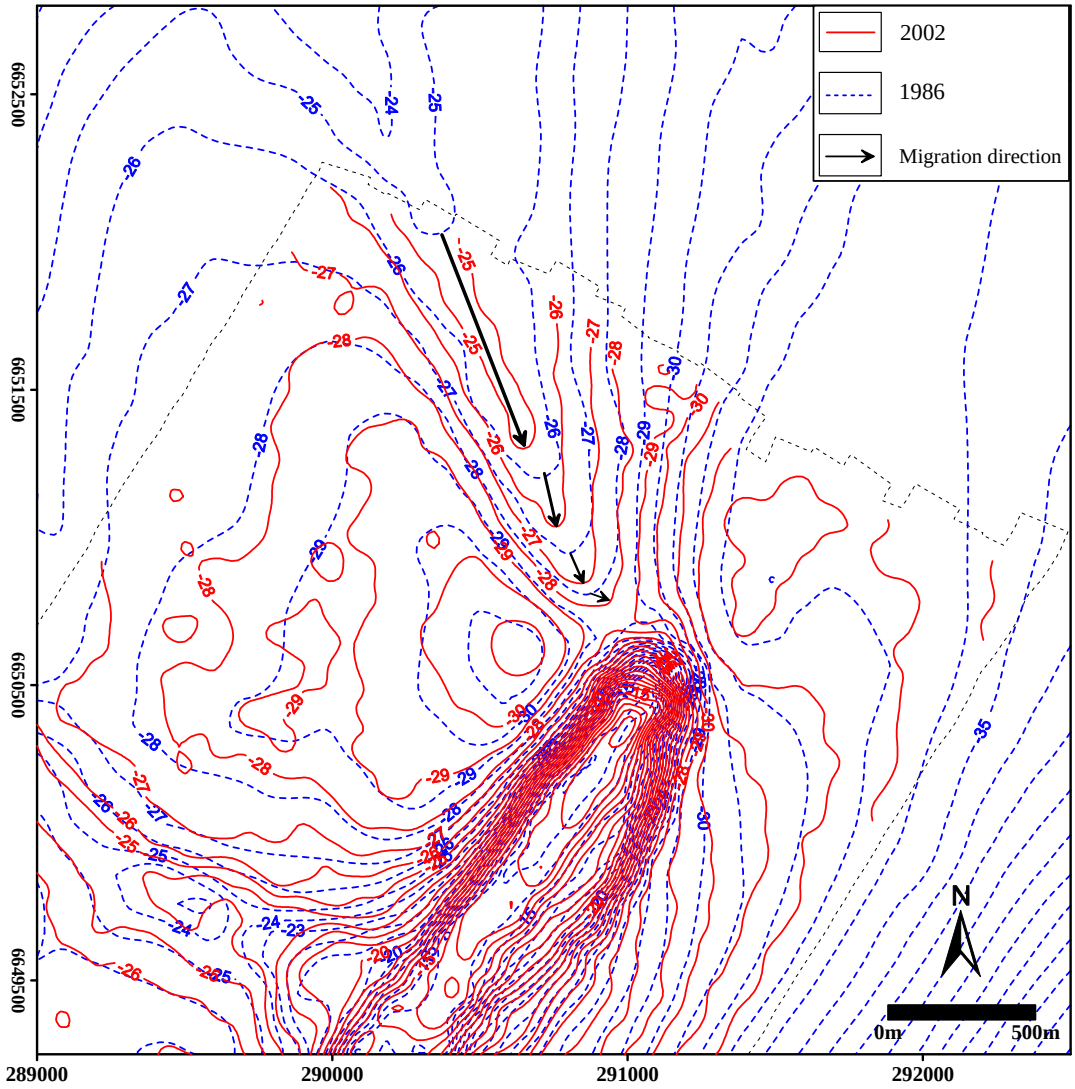

Figure 7.12 Migration of the *Sandridge* between 1986 and 2002. Most significant movement occurred on the shallowest isobath (-25 m) present in the overlap area of this feature. Migration is through ridge tip elongation and possible offshore movement of the seaward flank. Similarity between remaining bathymetric features indicates long term stability for these features.

This migration pattern is analogous to that of a prograding clinoform where highest sedimentation accumulation rates are found on the clinoform foreset as opposed to the topset considered the most energetic part where aggradation and even erosional truncation can be active (Cattaneo *et al*., 2007). Martin and Flemming (1986) also indicated that upwards growth of the bedform will be limited by swell erosion. Since the *Sandridge* forms part of seismic Unit Dsc and the local HST shore-connected prograding wedge, this interpretation of a prograding clinoform is consistent with the seismic interpretation (Chapter 6). In addition, the migration pattern is also in agreement with other SCR observations (Swift and Field, 1981; Antia, 1996). It is tentatively suggested here that significant longitudinal ridge growth was related to storm return flows accompanied by wave and/or bottom current generated shear stress at the seafloor (Pirmez, *et al*., 1998). Storm return

flows were recently observed offshore the KwaZulu-Natal coastline (Smith *et al*., 2010) and is a well documented mechanism for ridge migration (refer to next section). It is also important to note that the other bathymetric features such as the Aliwal Shoal ridge, the basin and the spur (refer to Figures 7.2, 7.3 and 7.5) show a good correlation between the two datasets (Figure 7.12) indicating long term morphological stability of these features and data reliability.

7.4.2 Shoreface-Connected Ridges

The southeast African continental shelf is generally accepted as a shelf whereupon sedimentary processes are dominated by a strong impinging current and large ocean swells (Johnson and Baldwin, 1986; Flemming and Hay, 1988). The Agulhas Current flows southwards with surface velocities exceeding 2.5 ms^{-1} subsequently, as documented by Flemming (1978, 1980, 1981), generating large south-westward directed subaqueous bedforms. Locally, gyres develop resulting in counter-currents such as the one present in the vicinity of the study area (refer to Chapter 2). Here sediment is transported northwards opposed to the predominant southerly Agulhas Current movement resulting in bedload parting zones (Figure 2.6). Although several subaqueous bedforms related to these currents have been described (Table 7.4), shoreface-connected ridges have been conspicuously absent until identification by Bosman *et al*. (2008) and later by Cawthra (2010).

Table 7.4 Summary of subaqueous bedforms described from the southeast African continental shelf. H = bedform height (trough to crest) and L = bedform spacing or wavelength. Transverse dune classification according to Ashley (1990).

Bedform type	Dimensions	Sources
Transverse dunes	Very Large: L = 700 m, H = 17 m Large: L = 170, H = 4m Medium: L = 45-90 m; H = 1-2 m 2D and 3D dunes ranging from L = 5-500 m; H = 0.3 - 5 m	Flemming (1978) Flemming (1980) Ramsay *et al*., (1996) Green (2009a, c)
Sand ridges (shoreface-detached)	L = 4 km, H = 12 m L = 1.3 km; H = 5 m	Ramsay (1994), Ramsay *et al*., (1996) Green (2009a,c)
Sand ridges (shoreface-connected)	L = 3 - >9 km, H = 1 - 20 m L = ~0.5 - 1 km; H = 12 - 22 m	Bosman *et al*., (2008) Cawthra (2010)
Submerged spit bars	H = 20-30m	Martin and Flemming (1986)

Sand ridges are massive bedforms common to most continental shelves (Belderson *et al*., 1982; Stride *et al*, 1982). Most are tidal but non-tidal examples are known (Werner & Newton, 1975; Martin & Flemming, 1986; Ramsay *et al*., 1996, Dyer and Huntley, 1999). Sand ridges are defined as composite, flow-oblique or parallel, linear accumulations of sand (usually of measureable relief) formed by the superimposition and migration of dunefields (Amos and King, 1984). They possess crests orientated sub-parallel to the dominant flow (Kenyon *et al*., 1981, Belderson *et al*., 1982; Huthnance, 1982; Harris, 1988; Yang, 1989).

Shoreface-connected ridges (SCRs) are a specific type of sand ridge attached obliquely to the shoreface and hence coastline. The general characteristics of SCRs are summarised in Table 7.5. Although SCRs are not as common as sand ridges, they are known from many continental shelves and settings worldwide: storm dominated systems (Duane *et al*., 1972; Swift *et al*., 1972; McKinney *et al*., 1974; Stubblefield and Swift, 1976; Figueiredo *et al*., 1981; Swift and Field, 1981) SCRs studies were also extended to included the North Sea; tide and storm dominated shelves (Swift *et al*., 1978, Antia, 1993, 1994, 1996, Antia *et al*., 1995, van de Meene *et al*., 1996, Van de Meene and Van Rijn, 2000a, b; Anthony and Leth, 2002); Brazilian shelf storm driven flows (Figuieredo *et al*., 1982); Argentine shelf storm driven flows (Parker *et al*., 1982) and the high intensity storm-dominated Canadian shelf (Hoogendoorn and Dalrymple, 1986; Li and King, 2007).

Most SCRs open into the prevailing coast-parallel current at an acute angle (Table 7.5; McKinney *et al*., 1974; Swift *et al*., 1978; Swift and Field, 1981). However, Antia's (1996) observations from the southern North Sea supported the view of Boczar-Karakiewicz *et al*. (1990) that ridge orientation does not necessarily need to relate to the major or net sediment transport direction. SCRs occur primarily off low unconsolidated coasts (Swift *et al*., 1978; Niederoda *et al*., 1985) and normally in clusters or complexes (Swift *et al*., 1972; Swift and Field, 1981; Saito, 1989) with their axes generally paralleling the regional wave propagation direction (Hayes and Nairn, 2004).

SCRs become larger, wider and more asymmetric (seaward directed) with increasing water depth (Goff *et al*., 1999; 2005), the latter authors suggesting that the increase in SCR width is due to the SCRs merging at depth. SCRs can also become more coast-parallel offshore as the water deepens (Swift *et al*., 1978; Goff *et al*., 1999). Some localities show two populations of SCRs, a smaller set superimposed on a larger system (McKinney *et al*., 1974; Swift and Field, 1981; Hoogendoorn and Dalrymple, 1986; Dalrymple and Hoogendoorn, 1997; Li and King, 2007). On the New Jersey Shelf (U.S.A.), McKinney *et al*., (1974) noted first-order ridges 14 m high and 2 - 6 km apart, with second-order ridges 2 - 5 m high, spaced 0.5 - 1.5 km apart. Hoogendoorn and Dalrymple (1986) and Dalrymple and Hoogendoorn, (1997) also recognised two orders on the Canadian shelf: the

first-order ridges 10 m high and spaced apart 5 - 10 km with superimposed second-order ridges spaced 1 - 2 km apart and less than 5 m in height. Swift and Field (1981) noted that second-order ridges tend to be asymmetrical with steeper landward sides.

Table 7.5 Summarised shoreface-connected ridge characteristics from worldwide localities.

Parameter	Value	Sources
Length	0.5-20 km 10-25 km	McKinney *et al*. (1974); Swift *et al*. (1978); Swift and Field (1981); Parker *et al*., (1982), Stubblefield *et al*. (1984); Gomez & Perillo (1992); Anthony and Leth, (2002); Li and King (2007) van de Meene *et al*., (1996)
Alignment	Axes parallel to wave attack	Figueiredo *et al*. (1981); Hayes and Nairn (2004)
Spacing	0.6-1 km	McKinney *et al*. (1974); Gomez and Perillo (1992); Swift *et al*. (1978);
Height	2 to >10 m 12 m	McKinney *et al*. (1974) Li and King (2007)
Depth	-3 to > -100 m Active to ~-50 m	Swift *et al*. (1978); Goff *et al*. (1999) Goff *et al*. (2005)
Angle to Coast	$10°$-60^0 50°-70°	McKinney *et al*. (1974); Swift *et al*. (1978); Figueiredo *et al*. (1981); Swift and Field (1981); Snedden *et al*. (1994); Goff *et al*. (1999); Li and King (2007)
Shape	Linear	McKinney *et al*., (1974); Swift *et al*. (1978); Niederoda *et al*. (1985); Gomez and Perillo (1992)
Slopes	1^0 or less	Swift *et al*. (1978), Antia (1995, 1996)
Migration Rates	3 to 67 m/yr 76 m in one storm 80 m/yr	Moody (1964); Duane *et al*., (1972); Gomez and Perillo (1992) Antia (1996)

Although SCRs are very stable long-lived features (Anthony and Leth, 2002) they are known to migrate down coast and offshore (Swift *et al*., 1978; Swift and Field, 1981; Antia 1996) at speeds varying from 3 - 67 m per year (Moody, 1964; Duane *et al*., 1972; Gomez and Perillo, 1992). Rapid migration is ascribed as a response to intense storm flows (Duane *et al*., 1972; Swift *et al*., 1978; Niederoda *et al*., 1985). A displacement of 76 m was recorded for one SCR, off the Delaware coast (U.S.A.), following the 1962 Ash Wednesday Storm (Duane *et al*., 1972). Antia (1996) supported Swift and Field's (1981) observation and observed 'coastwise elongation' through headward trough erosion. In the case of the southern North Sea SCRs, Antia (1996) measured migration rates 5 - 40 times those recorded for the North American Atlantic coast, however in this instance there was a tidal current component involved in the construction and propagation of these sand ridges (Antia *et al*., 1995; Van de Meene and Van Rijn, 2000a, b).

SCRs are generally steeper on their down-current margin, although this may be locally reversed near the point of shoreface attachment due to scour (Swift *et al*., 1978). Sediment is known to be coarser on the landward flank and finer and better sorted on the seaward flank of the ridges (Swift

et al., 1978; Swift and Field, 1981; Parker *et al*., 1982; Antia, 1993). Active erosion is reported from the spaces between SCRs (Stubblefield and Swift, 1976; Rine *et al*., 1991; Snedden *et al*., 1999; Goff *et al*., 2005). Termed gutters, these areas developed in response to storm-return flow (Li & King, 2007). Goff *et al*. (2005) noted that ridges and scours had a similar orientation. Active transverse bedforms, ranging from ripples to dunes and orientated at an angle to SCR crests can be superimposed on active SCRs (Swift *et al*., 1978; Antony and Leth, 2002; Hayes and Nairn, 2004; Goff *et al*., 2005; Li and King, 2007).

Models for the origin of SCRs

After more than 38 years of SCR investigations and numerous hypotheses there is still no definitive theory that can account for the origin, orientation and distribution of these bedforms (see Goff *et al*., 1999 for review; Hayes & Nairn, 2004). Generally SCR formation is linked to storm currents and coastal retreat (Swift, 1974; Swift and Field, 1981; Parker *et al*., 1982), if sufficient sand is available (Duane *et al*., 1972; van de Meene *et al*., 1996) however, no consensus on the exact process by which they form has been reached. It is widely accepted that most sand ridges observed today formed initially during the Holocene post-glacial rise in sea-level (Flandrian transgression) but have since been modified by the changing hydrodynamic setting and as a result lost their relict properties (Dyer and Huntley, 1999). Goff *et al*. (1999) suggested that the models accounting for the origin of SCRs can be divided into two classes.

The first class group together *morpho-mechanical models*, which based on qualitative approaches, explained the SCR in terms of their depositional setting i.e. sediment dispersal on Holocene shelves undergoing transgression (Goff *et al*., 1999). Swift and Field's (1981) model for the ridges on the Atlantic seaboard of the U.S. was the first of this type.

It postulates that SCRs constitutes a typological, probably even an evolutionary, sequence documenting the process from initial ridge development in the shoreface in response to alongshore storm currents to eventual ridge detachment as a consequence of the changing hydraulic regime associated with the deepening water column and retreating shoreface during the post-glacial transgression (Figure 7.13b). The evolutionary sequence consists of three arbitrary morphological transitional classes (Table 7.6): shoreface, nearshore and offshore ridges. Their model does not account directly for ridge obliquity but see it as a consequence of the different water depths occupied by the ridge which results in faster migration rates at the shallow shoreface as opposed to slow migration at the deeper and more voluminous offshore end of the ridge.

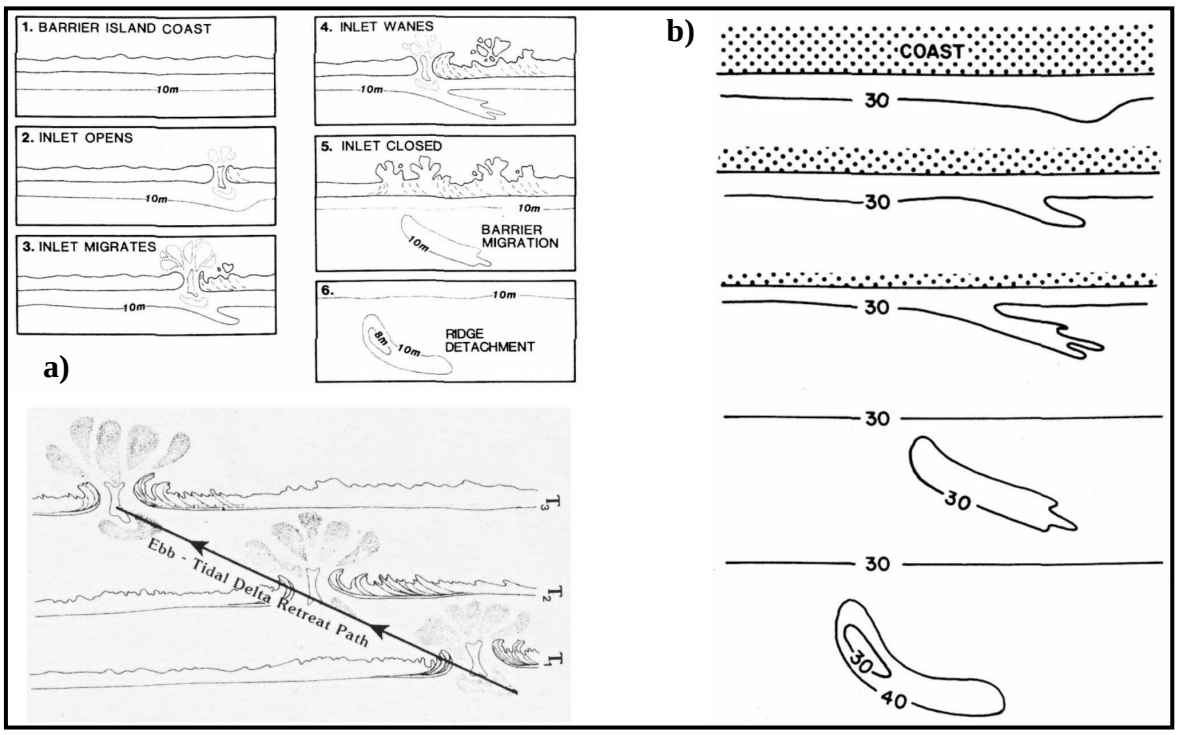

Figure 7.13 Two morpho-mechanical models for SCR formation on the Atlantic seaboard of the U.S.A. **a)** McBride and Moslow's (1991) six stage model based on ebb-tidal delta retreat and, **b)** Swift and Field's (1981) model showing their postulated ridge evolutionary sequence based on a changing hydraulic regime due to a continuing deepening water column and retreating shoreface.

Table 7.6 Swift and Field's (1981) three classes of ridge evolution constituting a suggested evolutionary sequence wherein the changing shapes of the ridges reflect changes in the hydraulic regime.

Shoreface	Nearshore	Offshore
• Occur in clusters • Merge obliquely with the shoreface • Can occur as shallow as -3m • Most symmetrical of the three classes • Systematic morphological variation along individual ridges	• Seaward asymmetry of up-current face • More massive	• Detached form • Seaward slope can be very steep in the down-current direction • Strongly asymmetric • Comma-shaped in plan-view • Broader relative to length

McBride and Moslow's (1991) proposed a two step process model for SCR formation and detachment along the U.S. Atlantic barrier island and cape coastline. Accordingly, (1) sediment is deposited along the shoreface/inner shelf as ebb-tidal deltas or river deltas prior to or during transgression, followed by (2) continuing transgression which reworks the sediment deposits into linear ridges at the lower shoreface by shelf processes (McBride and Moslow, 1991). The oblique orientation and linear from of the SCRs is thus a consequence of shoreline retreat, lateral inlet migration and wave re-working of delta deposits along the retreat path (Figure 7.13a). Although other studies (Snedden *et al*., 1994) seems to support this model and even though it has been applied with contentious success to the North Sea SCRs (Antia, 1994), existence of SCRs in areas without inlets (Hoogendoorn and Dalrymple, 1986; Li and King, 2007) point to a limited application for this model.

The second class group together fluid dynamical models which views SCRs as bedforms that initiate from fluid-substrate interactions (Goff *et al*., 1999). Huthnance (1982) used hydrodynamic stability analyses to explain ridge formation in the tidally dominated southern North Sea. According to his model both ridge spacing and obliquity to flow are innate aspects of the ridge-building process. Ridges can be formed at any depth and ridge spacing varies with depth. Huthnance's (1982) model was also applied by other researchers (Figuieredo *et al*., 1981; Parker *et al*., 1982; Dalrymple and Hoogendoorn, 1997) to storm dominated settings. Boczar-Karakiewicz and Bona (1986) and Boczar-Karakiewicz *et al*. (1987) proposed ridge formation by intragravity waves. However, this model was later discounted by Li and King (2007) who not only observed SCRs in areas not predicted but also observed that long-term SCR migration is opposite to that calculated by Boczar-Karakiewicz *et al*. (1987). Trowbridge (1995) also used stability analysis and showed that oblique ridges can be created and maintained by storm-driven flows. Although this model can successfully predict the orientation and size of ridges it is not applicable to ridge fields generated away from the shoreface (Goff *et al*., 1999).

Even though there is little consensus on SCR origin, orientation and distribution there seems to be better agreement that once formed these ridges become detached from the retreating shoreface as sea-level rises and continue to evolve within the changing hydrodynamic regime (Swift and Field, 1981; Dyer and Huntley, 1999; Goff *et al*., 2005). This implies that most SCR systems are relict to some degree but as observed today they are in hydraulic equilibrium with the present shelf processes.

7.4.3 Aliwal Shoal SCR System

The general dimensions of the Aliwal bedforms are in good agreement with the range of similar bedforms documented in the literature (compare Table 7.3 with 7.5). However, there are also some significant differences:

- Aliwal SCRs occur off a high, steep, often rocky coastline and a very narrow shelf fed by sediment from river outlets,
- they are associated with strong pulsating and reversing oceanographic current (south-westerly flowing Agulhas Current and the opposing north-easterly flowing counter current),
- the Aliwal SCR's seaward sloping flank does not necessarily become steeper offshore,
- they do not show ridge detachment and hence the offshore ridge modification (Swift and Field, 1981), unless the giant dunefields observed by Flemming (1978; 1980; 1981) on the outer shelf (>-60 m) represent that form,
- some Aliwal SCRs have a sigmoidal shape in plan-view and,
- are attached and associated with submerged bathymetric promontories (relict dune cordons)

Seismic profiling of SCRs provides information on their internal architecture and migration (Duane *et al*., 1972; Swift *et al*., 1973; Stahl *et al*., 1974; Stubblefield & Swift, 1976; Parker *et al*., 1982, Li and King, 2007). Although no high resolution seismic data are available for the Aliwal SCRs, limited seismic profiles are available across the MSDC, the topset of which comprises Aliwal SCR bedform crests 1 - 7. This includes a seismic line collected by Martin and Flemming (1986) and partial seismic coverage from this study (Section 6.3.4; Figure 6.5 and Figures 6.17 - 6.18).

Martin and Flemming's (1986) line is located shallower, orientated more perpendicular to the ridge crests but is strike-parallel to the MSDC (Figure 6.10). The seismic line from this study (Figure 6.5) is downdip orientated relative to the MSDC but only covers a part of SCR 1, 2 and 5 (the *Sandridge*) and is orientated obliquely to these bedform crest. Martin and Flemming's (1986) interpreted profile shows an internal morphology represented by large variably inclined prograding reflectors whereas the profile from this study shows vertically aggrading reflectors (Figure 6.5b). In both these studies the overall MSDC reflector configuration was imaged and not the actual SCR. However, the SCRs are intricately tied to the evolution of the MSDC (Section 6.4.3), strictly speaking the current observed SCR ridges relating to Stage 4 of the MSDC evolutionary history (Figure 6.18). As such the variance in reflector configuration as observed in these seismic profiles are suggested to be related to the evolution of the MSDC through both along-shore and

across-shore sedimentary transport which in essence is achieved by the shoreface-connected ridges (Section 6.3.4).

It is proposed here that the prograding reflectors (Martin and Flemming, 1986) represent a stratal architecture built by northerly directed climbing bedforms (along-shore transport) and that the vertically aggradational reflectors, typical of the offshore limits of the SCRs, most likely indicate longitudinal bedform processes (cross-shore transport). This implies that the shallower bedforms display growth through transverse climbing whilst the deeper portions show bedform growth by longitudinal ridge aggradation. This further supports a model whereby the Aliwal Shoal SCRs display both transverse and longitudinal characteristics as suggested by the observed bottom current patterns (Figures 2.5 and 2.6), seismic interpretation of the MSDC (Figures 6.17 and 6.18) and ridge migration (Figure 7.12).

Aliwal SCR Formation Model

A model attempting to account for the formation of the SCRs on the Aliwal shelf must take into consideration the following aspects:

- the Aliwal Shelf is a very narrow and shallow shelf compared to the global average (refer to Section 7.2.2) and even compared to other shelves showing SCR systems. This is important for three reasons; (1) it controls the available accommodation space, (2) the shelf was totally exposed during the LGM, probably covered by a wide dune cordon. This sand was available for reworking during the subsequent transgression and (3) it influences reduces the shelf width affected by currents.
- the modern coastal geomorphology shows a steep hinterland lacking a coastal plain which can store sediment,
- the shelf is swept by two strong and opposing geostrophic currents - the southerly flowing Agulhas Current and northerly directed return gyre (refer to Chapter 2),
- large ocean swells traverse this area (Figure 7.8; also refer to Chapter 2),
- longshore drift is pronounced and directed northwards (refer to Chapter 2),
- dominant wind directions are coast parallel and opposing (Chapter 2), and more-or-less coincide with the oceanic current directions,
- submerged palaeobarrier-dunes form large hard bathymetric features (reefs) at various depths. These not only influence the present hydrodynamic regime but also controlled coastal geomorphology at times of lower sea-levels,
- several large rivers provide sediment input to the shelf, which is not sediment starved.

The model is limited by the following:

- the bathymetric map that is used to analyse the SCRs is composed of various datasets (Figure 7.1) spanning more than 15 years. The different datasets have varying degrees of data density and positional accuracy,
- the bathymetric dataset does not cover the complete SCR system – e.g. ridges 5 - 8 continuous beyond the limits of the data,
- limited grain size data are available (refer to Chapter 8),
- limited side-scan sonar data coverage, covering only a small portion of SCR 1 and 2,
- limited new and historic seismic profiling is available,
- an absence of historic and long term current data (velocity, direction, depth etc) for the study area,
- very little is known of the Quaternary evolution of the southeast African continental and corroborative data is not available as is the case for the Atlantic seaboard of the U.S. and the southern North Sea to substantiate assumptions, e.g. the rate of modern/late Holocene coastal retreat is not known.

The following assumptions are made:

1. all bedforms were generated during the post-LGM sea-level rise, as commonly accepted in literature (e.g. Dyer and Huntley, 1999),
2. coastal hydrodynamics;
    - Oceanographic currents were the same throughout the transgression (some aspects of this is supported by observational evidence from this study, refer to Chapters 8 and 10). The Agulhas Current has been active throughout the Quaternary (Chapter 2) but the age of the counter current is uncertain. In the absence of any evidence pointing to the contrary, it is assumed that the counter current gyre were present at the beginning of the Holocene at least from Stage 2 of the MSDC development (first indication of SCR-like morphology; 8.2 ka cal. B.P.).
    - Tidal currents are considered negligible due to the tidal regime which is assumed to have been the same throughout the evolution of the bedforms.
    - Wind and waves during this time would have been similar although some changes are expected with palaeoclimatic fluctuations.
    - Shelf width is assumed to be dependent on the present width of the shelf, however this increased with time.
3. the SCRs are in hydrodynamic equilibrium with modern shelf processes,

4. most of the shelf sediment reworked during the transgression would have contributed to the volume of the contemporaneous shoreface (Ramsay, 1996).

A ***two stage*** process of SCR development on the Aliwal Shelf is proposed.

Stage 1: Ridge initiation

Step 1

Step 1 is characterised by the establishment of the sediment deposits which would continuously evolve from ca. 9.5 ka cal. B.P. into the present day MSDC. The evolution of shelf during the last deglacial (Holocene) transgression is presented in Section 6.4.3 (Table 6.4) and a four stage development for the MSDC is presented in Section 6.4.3 (Figure 6.18). Stage 2 of the MSDC's evolution seemed to have exerted morphological control on the subsequent developmental stages of the MSDC especially on the occurrence of SCR 1 - 5, the sigmoidal plan-view of which is a surficial expression of the extent of the retrogressive stage of clinoform development. Sediment were supplied from the reworking of barrier dune and river-dominated estuarine systems (Cooper, 1994b; Wright *et al.*, 1999) and high fluvial sediment input from the eight river systems (Figure 7.14) dominated by the Mkomazi and Lovu Rivers. Locally the sedimentation rates kept up with the rate of sea-level rise forming an aggradational to prograding sediment deposit (Unit Dsc; Section 6.3.4).

Step 2

This step entails the establishment of the shoreface-connected ridges on the topset of the evolving clinoform. As a result of the lack of corroborative data the minimum age for the establishment of SCRs are linked to Stage 2 of the MSDC development. Both along-shore and cross-shore sediment transport pathways are assumed to have been active from Stage 2 of the MSDC's development evident by subsequent Stages 3 and 4 exhibiting the same morphology (Figure 6.18) comprising a change from 'proximal' topset aggradation (SCRs 1 - 5) to 'distal' foreset progradational downlap (SCR 6 - 8) correlated to a change in the dominant sedimentary transport mechanism i.e. from aggradational along-shore to progradational cross-shore transport.

Two different options are proposed for the actual mechanism responsible for ridge initiation. The first approach is that devised by Swift and Field (1981) which suggests that sand ridge formation is initiated on the upper shoreface as a result of alongshore currents. These authors suggest storm-generated flow, but tidal flows (Antia, 1996) may also drive the process. In the case of the Aliwal Shoal coast-parallel flow is due to the counter current and not storm generated as per Swift and Field (1981). As transgression proceeded the ridges developed through alongshore and down

current migration simultaneously, thereby lowering them continuously into deeper water. Ridge obliquity is a result of the differential rates of ridge migration in shallow versus deeper water. This model implies continuing ridge response to a changing hydraulic regime.

Alternatively, as the post-glacial transgression proceeded, the shoreline and hence the river mouth bars (Mkomazi and Lovu Rivers - the others were probably tributaries at this time), migrated landward across the shelf in response to rise in sea-level. The retreat path of the mouth bar is a function of the successive positions of the fluvial outlet point. This approximates step 3 of the McBride and Moslow (1991) model (Figure 7.13).

On the KwaZulu-Natal coastline the retreat path direction would be determined by a combination of the north-eastwards directed longshore drift and west-north-westward directed translation of the shoreline during sea-level rise (using the modern shoreline orientation). Although also dependent on the rate of sea-level rise, sediment availability and coastal configuration, the net or resultant retreat path would be directed between a north-northwesterly to northerly direction. As with the model presented by McBride and Moslow (1991) the oblique initial orientation of the ridges is thus a consequence of shoreline retreat, sediment source migration and re-working along a north-northwest retreat path. From Figure 7.14 it can be seen that all of the SCRs seem to be associated with modern fluvial outlet systems; ridge A with the Mahlongwana River, ridge 1 and 2 with the Mkomazi River, ridge 3 with the Ngane River, ridge 4 and 5 with the Mgababa River, ridge 6 and 7 with the Lovu River (previously Illovu River) and ridge 8 with the Lovu/Little Manzimtoti Rivers. It is however highly unlikely that there was a continuing connection between individual rivers and their respective ridges as there is no reason for all of these river systems to converge in a south-easterly direction beyond the present coastline (Figure 7.14). The only probable but very unlikely explanation for this convergence is that all of the smaller river systems were captured by the Mkomazi River when the shelf was exposed during the LGM forced regression.

McBride and Moslow (1991) stated that regardless of geomorphic and geological variations, all examples in their study fundamentally exhibited '*the association of sand ridges with marine reworking during transgression of large, isolated deposits of sand on the shoreface or shelf*'. They further suggested that the mechanism responsible for the morphological conversion from a shoreface sand body to linear ridge consist not of a simple 'stringing together' of successive sand deposits but rather a ridge 'moulded' out of the sand body by shelf processes most likely wave and storm currents.

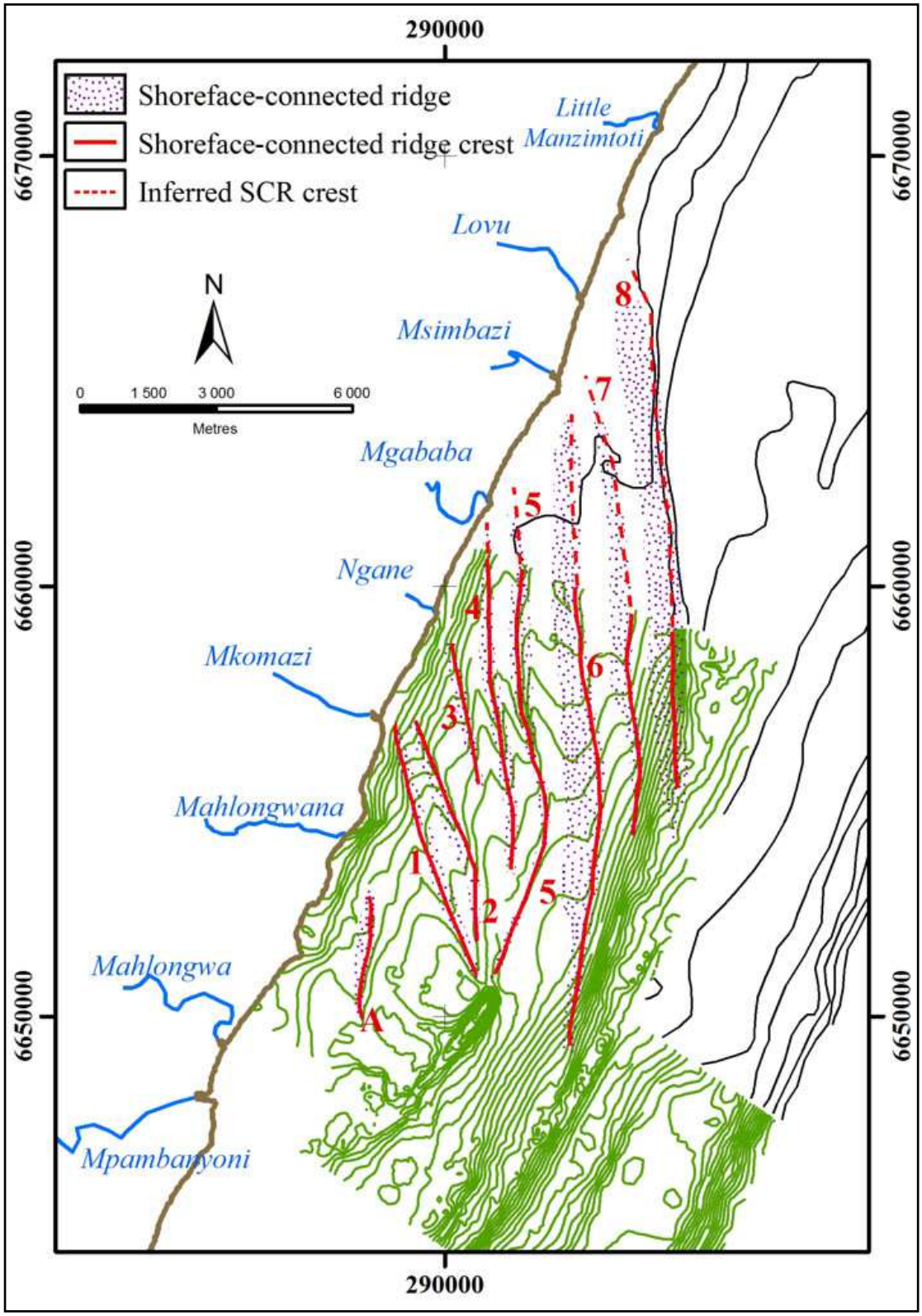

Figure 7.14 Aliwal Shoal SCR crests plotted with regional fluvial systems and bathymetry. SCR crest numbering as per previous diagrams. Green bathymetric data are from this study whereas black bathymetric isobaths are low resolution regional data (courtesy Council for Geoscience). The SCR system was previously referred to by Martin and Flemming (1986) as the Illovu submerged spit bar. Note sigmoidal shape of SCR crest 5. The Lovu River was previously named Illovu River.

Evidence presented here shows that the Aliwal SCRs are active down to at least -26 m. This is in contradiction to a 'relict' origin for these bedforms. It is noted that morphological bedform changes (Figure 7.10) in the form of base levels, knick points and plateaus occur at bathymetric levels correlated with sea-level occupation/erosion events observed from the Aliwal Shoal (also refer to Section 7.2.1). However, as stated before, most SCR systems are relict to some degree but as observed today they are in hydraulic equilibrium with the present shelf processes. Thus these sea-level indicator levels which also represent major palaeocoastline events and are also documented in the bedforms, probably represent an expression of the physical parameters active at the time (e.g. relative rate of sea-level rise, sediment volume, shoreface evolution etc.). This supports the concept of Swift (1974) that SCRs are a product of sea-level change. It is possible that each SCR is related to the rate of sea-level change which varied (due to sea-level stillstands, and slow-downs and accelerations in the rate of sea-level change related to meltwater pulses (refer to Section 4.4.2) during the last deglacial transgression. These observed bathymetric features changes not only along each bedform but also with depth. It therefore is not a consistent expression along individual ridges and is most likely indicative of later modification which is dealt with in step two of the model for the development of the Aliwal Shelf SCRs.

In summary, ***Stage 1*** in the process of SCR formation can be viewed to fundamentally consists of the deposition and concentration of significant amounts of sediment on the shoreface (step 1 - development of Stage 1 of the MSDC) with subsequent ridge initiation (step 2) following the MSDC Stage 2 retrogradational event (Figure 6.18) through marine reworking by shelf processes simultaneously with a deepening water column and evolving clinoform system showing proximal along-shore aggradation and distal across-shore progradation during the last post-glacial sea-level rise (from ca. 8.4 ka cal. B.P.).

Stage 2: Modern maintenance

Aliwal Shelf SCR bedforms are continually modified and maintained by shelf processes during transgression. It must be noted that although a two stage process is suggested these processes form part of a continuum and are active together. Previous discussions established that the SCR field is dominated by the northerly flowing counter current and evidence from ridge migration (measured, Figure 7.12) and internal seismic structure (Chapter 6) shows that the Aliwal SCRs function both as transverse and longitudinal bedforms. Stage 2 of the model accounts for these observations and consists of two physical states; state 1 considers SCR maintenance during fair-weather conditions and state 2 during storm conditions.

State 1: fair-weather conditions

During fair-weather transverse ridge migration is dominant (Table 7.7) driven by shelf circulation by the north-easterly flowing counter current. Inshore seismic data show bedform climbing under these conditions, producing an overall northerly movement of the Aliwal Shelf SCR system. Previously only coast-parallel storm currents were believed to be involved in the formation of SCRs (Swift *et al*., 1978). The evidence presented here suggests that coast-parallel oceanic currents (Agulhas and counter current) are involved in SCR construction and maintenance during fair-weather conditions and supports similar observations in the North Sea (Anthia, 1996). .

Table 7.7 Longitudinal and transverse aspects of the Aliwal Shoal SCRs.

Longitudinal Aspects (Cross-shore sedimentation)	**Transverse Aspects (Longshore sedimentation)**
Extreme length	Cross-sectional asymmetry
Positional stability	Structure of shelf bar [Allen's (1980) type 3 or 4]
Crests parallel to storm swell	Crests normal to reverse current flow
Storm erosion in swale parallel to crests	Current reversal of geostrophic flow

State 2: storm conditions

Longitudinal ridge growth (Table 7.7) is suggested to occur during storm return flow. Storm related origin of ridge migration is preferred by most workers (refer to previous section) as is cross-shelf sediment transportation on the southeast African Shelf (Flemming, 1981) derived from marine storm-erosion of the shoreface (Bosman *et al*., 2007), beach and coastal dunes (Smith *et al*., 2007; Smith *et al*., 2010). During severe storm and flood events the Mkomazi River and the other smaller fluvial outlets provide large volumes of sediment to the nearshore zone and erode the coast and shoreface transporting the sediment offshore. It is suggested that this mechanism involves offshore ridge tip elongation and offshore movement of the seaward flank with storm erosion in the intervening swales explaining the observed narrowing of the ridge. Following the storm, the regional coast-parallel current system is restored and the fair-weather state then moulds the SCRs into a transverse bedform.

The model of SCR formation presented here accounts for most of the morphological features observed from the Aliwal Shelf with the available data, but the degree of complexity of the system is sure to become much greater as new data becomes available. In the absence of any evidence to the contrary it is suggested here that the Aliwal shelf SCRs have climbed and coalesced coevally

since ca. 8.4 ka cal. B.P. to form the Mkomazi subaqueous-delta clinoform through both proximal along-shore and distal cross-shore sedimentation (Figure 6.17; also refer to Section 6.3.4 and 6.4.3; Figure 6.17). Martin & Flemming (1986; 1988) suggested that the MSCD depocentre formed where the Agulhas Current, the counter current and longshore drift converge - a concept supported by this work.

The discovery of the SCR field has a further implication for the sediment dynamics of the continental shelf insofar as it provides a mechanism by which cross-shelf sediment movement occurs. Flemming (1980) realised from his south-east African shelf sediment model (Figure 7.15) that a mechanism of cross shelf sediment movement is needed to address the way in which large quantities of sediment are made available from the nearshore to outer shelf over relatively short periods of time. He proposed a model (Figure 7.15) whereby the migrating Agulhas Current periodically erodes the seaward edge of the sediment wedge. The recognition of SCRs provides an alternative mechanism delivering sediment from the coastal zone and nearshore sediment wedge into the middle and outer shelf regimes at the rate and quantity required by Flemming's (1980) model.

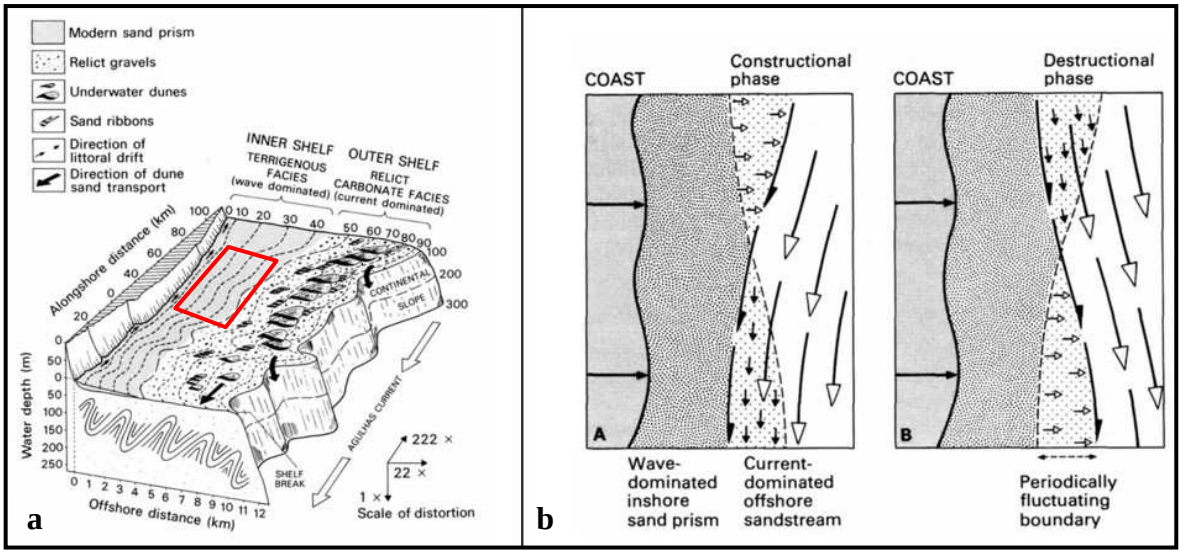

Figure 7.15 **a**) Model of sedimentary dynamics on the SE African continental shelf (from Flemming, 1978 in Johnson and Baldwin, 1986). Red box is the hypothetical position of the high resolution study area showing the position of the Aliwal Shoal ridge system predominately located within the inner shelf wave-dominated terrigenous facies. **b**) Cross-shelf sediment movement model from the wave dominated inner shelf to current dominated middle and outer shelf; (**A**) seaward growth of sediment wedge and (**B**) erosion of the outer margin of the sediment wedge due to lateral migration of the current-controlled zone (from Flemming, 1980).

CHAPTER 8
SEAFLOOR GEOLOGY

8.1 INTRODUCTION

Prior to this study little was known about the rocky seafloor that constitutes the Aliwal Shoal except that a part was carbonate-cemented aeolianite (Belderson, 1961; McCarthy, 1967) and postulated to be Tertiary or younger in age (Carter, 1966, McLachlan and McMillan, 1979). Although limited, these were the only studies that drew attention to the submerged coast-parallel complexes present on the southeast African continental shelf. This was followed by seismic profiling of these systems (Martin and Flemming, 1989; Birch, 1996) and more notably the work of Ramsay (1991) who undertook a detailed study of the submerged dune and beach complex at Sodwana Bay (Figure 1.1). Ramsay's (1991, 1995 and 1996) research demonstrated that these systems can be used to reconstruct palaeocoastline events and define a relative sea-level curve (Ramsay, 1995; Ramsay and Cooper, 2002).

This chapter presents the seafloor geology and sedimentology of the detailed study area surrounding the Aliwal Shoal. It is based on the integration of the side-scan sonar mosaic acoustic facies interpretation with the results from an extensive seafloor sampling and petrographic study (Sections 5.4, 5.5). The seafloor geology map presented here was the first map of its type (Bosman *et al.*, 2007) for a submerged aeolianite and beachrock sequence, although other notable investigations, of shallow shelf geology around southern Africa, include those of De Decker (1986), Terhorst (1987), Woodborne (1987), Lenhoff (1995) and van den Bossche (2006). Previous maps from the KwaZulu-Natal shelf provided only the distribution of the reef and seafloor sediments (Durban area by Richardson, 2005 and Cawthra, 2006), or as reef consisting of 'beachrock/aeolianite' units (Sodwana Bay by Ramsay, 1991, 1996). Most recently, Cawthra (2010) produced a detailed seafloor map of aeolianite and beachrock units offshore of Durban. Further afield no comparable detailed studies on submerged aeolianite/beachrock systems were found by the author, although similar deposits are known to exist at least off the southern and western Australian and north-eastern Brazilian coasts (Fairbridge, 1950, Sprigg, 1979; Guilcher, 1988; Brooke *et al*., 2003; Caldas *et al*., 2006, Viera and De Ros, 2006).

Geological mapping of the Aliwal Shoal seafloor resulted in the identification of the major lithological units which were further analysed geochronologically (Chapter 9).

8.2 SIDE-SCAN SONAR MOSAIC AND ACOUSTIC FACIES

The Aliwal Shoal side-scan sonar mosaic (Figure 8.1) was compiled from 23 survey lines providing a complete coverage of the detailed study area (Figures 5.1 and 7.1) which approximates 18 km^2. The individual survey lines were digitally combined into one mosaic image with a resolution of 0.25, rendering each pixel on the mosaic to represent 25 cm of seafloor (refer to Chapter 5.2.3 for more details). The resulting mosaic image is a greyscale graphical representation of the seafloor showing the acoustic shadows as white, as opposed to normal (optical) and multibeam echo-sounder pseudo-sonar backscatter imagery where shadows are black. Details relating to the methodological application of side-scan sonar as applied in this study are presented in Section 5.3.3 and a comprehensive theoretical review of the side-scan sonar method is provided in Appendix I.

Side-scan sonar backscatter imagery is capable of capturing subtle changes in seafloor texture and geology. These differences are expressed as a function of the amount of acoustic backscatter or the acoustic reflectivity of the features (Blondel and Murton, 1997, Barnhardt *et al*., 1998). The side-scan sonar mosaic of the Aliwal Shoal was used to quantify the nature of the seafloor based on interpretation principles of acoustic imagery as suggested by De Decker (1987), Barnhardt *et al*. (1998) and Blondel and Murton (1997) which classifies sonar imagery in terms of acoustic facies based on: (i) the degree of reflectivity or amount of acoustic backscatter that features produce, and (ii) the amount of surface relief or acoustic morphology. Rock, for example, yields a strong surface return on side-scan sonar records. Bioclastic gravels also produce a similarly strong acoustic return. These vastly different materials can thus be grouped together by their acoustic reflectivity, even though the features themselves are different (De Decker, 1987).

Although rock and gravel yield similar amounts of acoustic backscatter, the differentiating factor in this case mostly is surface relief. Surface relief or acoustic morphology refers to the "ruggedness" or microtopography of a feature, which can be deduced from the acoustic shadow cast by the feature and bathymetric data if available (De Decker, 1987; Ramsay, 1991; 1996; Blondel and Murton, 1997). Acoustic morphology also includes surface texture, which is expressed differently by different features e.g. sediment composed of broken shell hash, bedforms, joints and fractures.

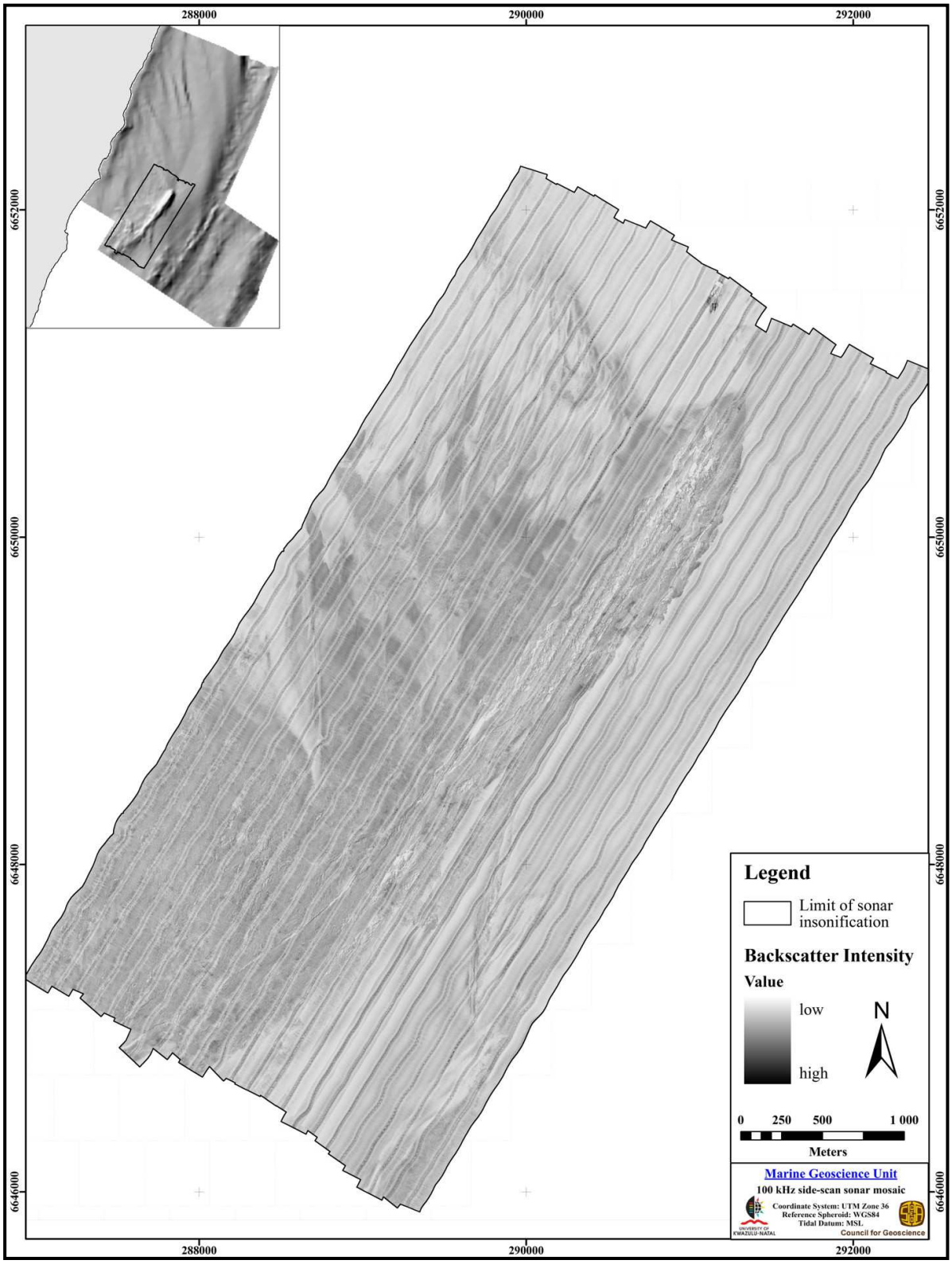

Figure 8.1 100 kHz side-scan sonar mosaic of the Aliwal Shoal and surrounding seafloor compiled from 23 individual survey lines. Inset map shows the area of sonar insonification plotted on a sunshaded relief image of the shelf bathymetry (refer to Figures 7.8 and 7.9).

Based on the principles discussed above six acoustic facies, notated A - F (Figure 8.2, Table 8.1) were identified. These were mapped on an approximate scale of 1 to 20 000. The choice of scale, for this study, is constrained by the resolution of the sonar system, the accuracy of the positional system, size of field area and the regional shelf-mapping nature of this project. In addition, the sample coverage density was also taken into account as it provided the ultimate control for the geological interpretation of the acoustic data. The delineated acoustic facies were combined to form a side-scan sonar acoustic facies interpretation map (Figure 8.3) reflecting the spatial distribution and relationship of each of the acoustic facies.

Table 8.1 Description of the acoustic facies as identified from the 100 kHz side-scan sonar mosaic.

A.	Dark and light alternating to blotchy, moderately extensive, linear, high (ridge) to low (shadows) reflective acoustic facies with small and large shadows indicating varying vertical relief fluctuations ranging from <1 m but which mostly exceeds 2 m. Interpreted as high relief rock outcrop.
B.	Speckled to granular, extensive, moderate to high reflective acoustic facies displaying vertical relief predominantly less than 2m. Interpreted as low to medium relief rock outcrop.
C.	Even toned to occasionally granular, extensive and predominantly weak to moderately reflective planar acoustic facies showing small to very large bedforms in some areas. Interpreted as unconsolidated quartzose shelf sediment.
D.	Even toned to occasionally granular, highly localised and dispersed highly reflective acoustic facies. May also incorporate small bedforms. Interpreted as unconsolidated reef-associated bioclastic-rich sediments in gullies and reef-flats.
E.	Blotchy, extensive, moderate to very highly reflective acoustic facies association. Mostly, low to very low relief showing no acoustic shadowing. Interpreted as unconsolidated lag deposits overlain by heterogeneous shelf and bioclastic-rich sediment.
F.	Dark and light, highly localised, rectangular, highly reflective acoustic facies showing pronounced unnatural relief with a distinct geometric shape. Interpreted as a wreck.

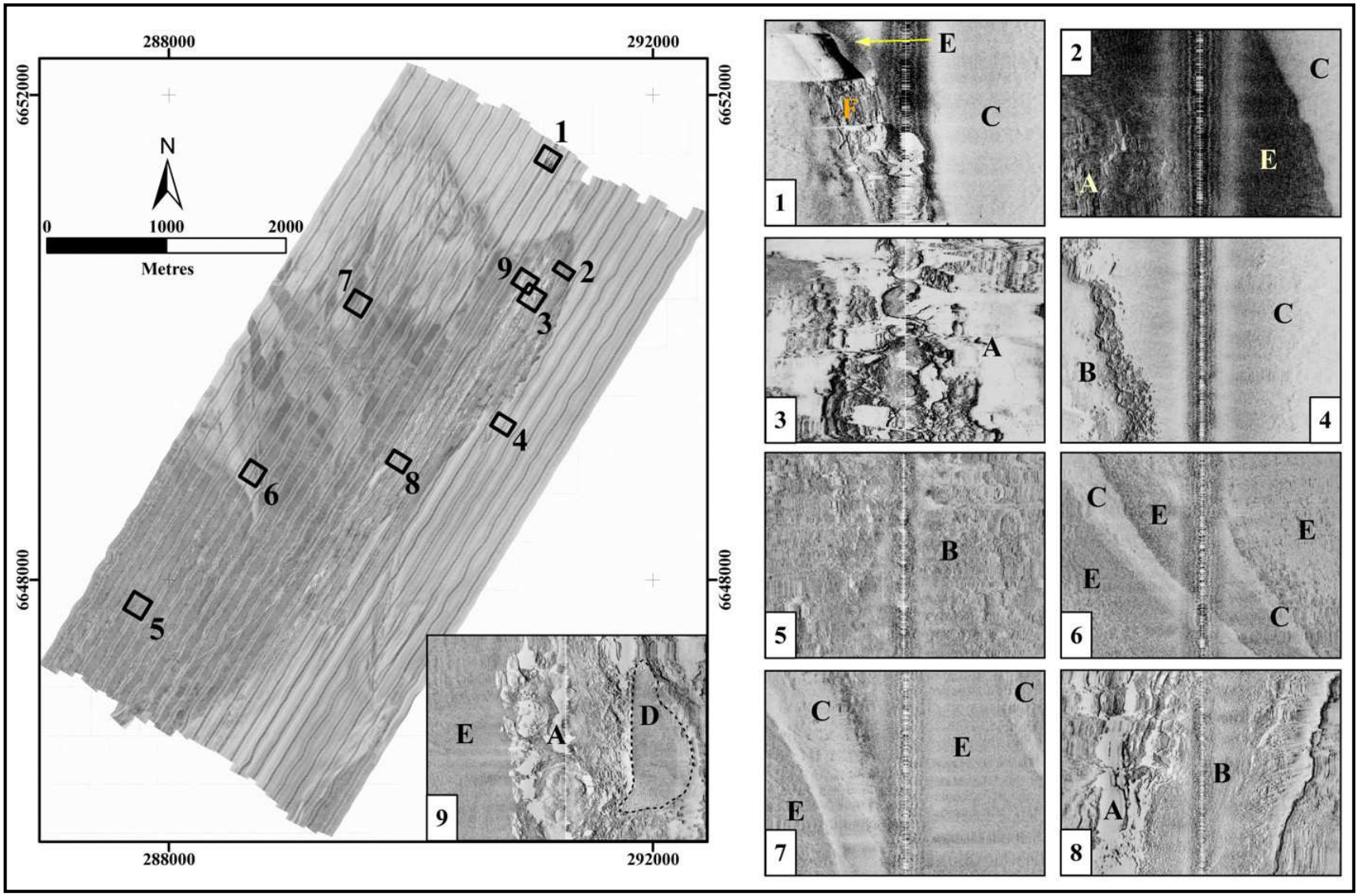

Figure 8.2 Selected examples of the various acoustic facies identified from the 100 kHz side-scan sonar mosaic, refer to Table 8.1 for facies description. The sonograph images are slant range corrected for accurate image proportions, the nadir zone is the vertical line in the centre of the image. Numbers next to the boxes on the sonar mosaic correspond to numbers on the sonograph images. Sonographs are north up and the scale varies as follows (width by height); **1**) 166 x 97 m, **2**) 171 x 167 m, **3**) 168 x 161 m, **4**) 164 x 151 m, **5**)167 x 170 m, **6**) 169 x 168 m, **7**) 167 x 167 m, **8**) 169 x 157 m, **9**) 169 x 148 m.

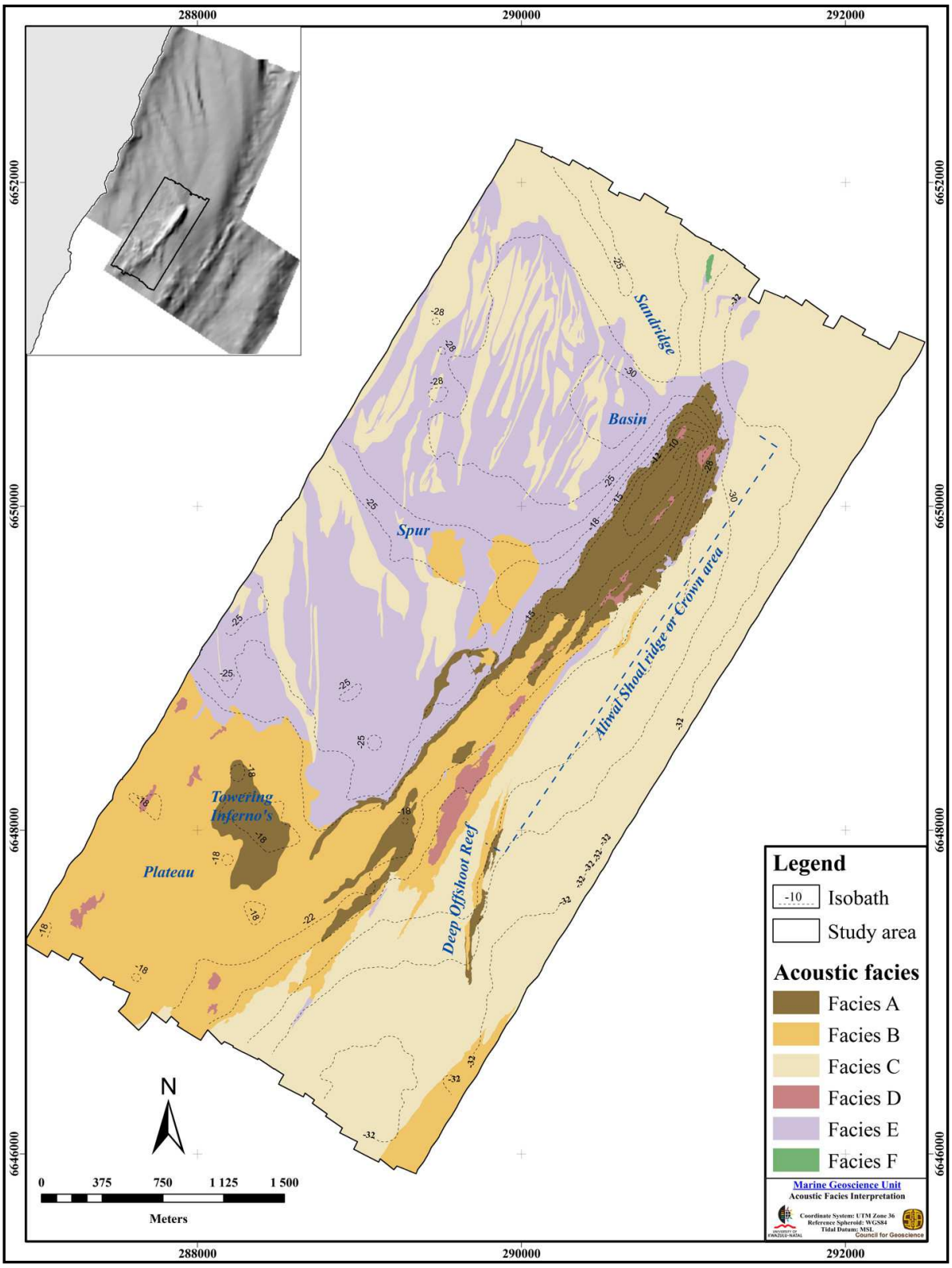

Figure 8.3 Acoustic facies interpretation map of the 100 kHz side-scan sonar mosaic (Figure 8.1). Morphological features identified from the bathymetry data are annotated for reference (refer to Chapter 7, Figure 7.2). Note that the isobaths are not in constant intervals. Inset map shows study area plotted on a sunshaded relief image of the shelf bathymetry (refer to Figures 7.8 and 7.9).

Facies A and B exerts the strongest control on the seafloor morphology (Figure 8.2, sonographs 3, 5 and 8). Although Facies A corresponds to the area of maximum seafloor relief in the study area (Figure 8.3) it is not as extensive as Facies B, which dominates the southern half of the map (Figure 8.2, sonograph 5). Facies C is the most extensive acoustic facies (Figure 8.2, sonographs 1, 2, 4, 6 and 7) and is conspicuously absent from the south-western sector of the map area. It shares common boundaries with all other acoustic facies.

Facies D was defined based on acoustic signature, sampling and association with Facies A and B, forming highly reflective distinct outcrops and sheet coverings within A and B (Figure 8.2, sonograph 9). Facies E is best developed in the confines of the two *Basin*-features located landward of the bathymetric highs created by Facies A and B, showing alternating inter-fingering linear patterns with Facies C suggesting an intricate relationship. The distribution pattern of Facies C and E located within the *Basin* features is complex but can be divided into two domains, separated by the *Spur*. North of the *Spur* and south of the *Sandridge* within the confines of the *Basin*, Facies C and E forms alternating NNE-SSW trending linear features (Figure 8.2, sonograph 7). Whereas south of the *Spur* and north of the *Plateau*, Facies E dominates forming N-S and NE-SW orientated linear features (Figure 8.2, sonograph 6). In addition, thin linear outcrops of Facies E seem to be banked against the seaward margin of the Facies A ridge feature (Figure 8.2, sonograph 2).

Facies F is highly localised and is correlated to the wreck of the *MV Produce* (Figure 8.2, sonograph 1).

Major lithological lineament trends were also traced from the side-scan sonar mosaic (Figure 8.4). These lineament patterns were primarily interpreted from regular shadows/hard acoustic returns which form consistent linear and parabolic features. The inside and outside edge of the reef were not mapped as lineaments. The inside or landward edge of the reef does intersect an approximately NE-SW trending linear underwater sea-cliff with >2 m relief in places.

8.3 SEAFLOOR LITHOLOGIES

8.3.1 Lithological Sampling

The side-scan sonar acoustic facies map (Figure 8.3) is a remotely-sensed interpretation that, as established from the previous section, may group together vastly different material types. To generate an accurate geological interpretation, each acoustic facies must be ground-truthed by

direct observation and/or sampled. As all of the acoustic facies occur within favourable diving depths, SCUBA-diving was employed to groundtruth, map and sample the seafloor (Appendix IV, Figure IV.1). A comprehensive review detailing the methods applied to the ground-truth programme is provided in Section 5.4.

A total of 130 seafloor samples were retrieved from the study area. This included 51 sediment samples (the unconsolidated sediments are briefly dealt with in Section 8.4), 69 hand specimen-sized rock samples (Appendix IV; Figure 8.5) and 10 large rock samples (~40 - 80 kg; Figure 8.5d;) collected from representative lithological units for geochronological analysis (Chapter 9).

The shallow rocky seafloor in the study area is almost completely covered by epifaunal growth which mostly consists of encrusting sponges and algae (for an inventory see Schleyer, 2006 and Brash, 2007). The anomalous high encrustation of the reef by especially sponges is attributed to a wood pulp effluent marine outfall pipeline (Schleyer, 2006) situated to the north of the study area. Hand specimen samples were generally sampled from overhangs, ridges and rocky ledges (Figure 8.5a) as these represented the most frequent type of free surface along which to induce a fracture during hammering and thus easiest to obtain during a time-limited dive. Unfortunately these samples were then often biologically attacked from more than one side resulting in limited fresh sample material (Figure 8.5c).

This was especially the case with the very shallow samples (<15 m) which would also be frequently subjected to breaking waves. As expected a decrease in epifaunal growth is observed with an increase in water depth related to reduced light intensity, nutrients and water temperature. However, some of the deeper samples showed the presence of boring molluscs. To negate these issues the geochronological samples were sampled at a sufficient size to produce representative fresh and undisturbed sample material (Figure 8.5d).

As will be dealt with in the following two sections of this chapter and the next (Chapter 9), results from the rock sample analyses indicated, that the seafloor in the study area only consists of two lithologies: carbonate-cemented aeolianite and beachrock. Hence, the consolidated lithologies will be discussed according to this division based on rock type.

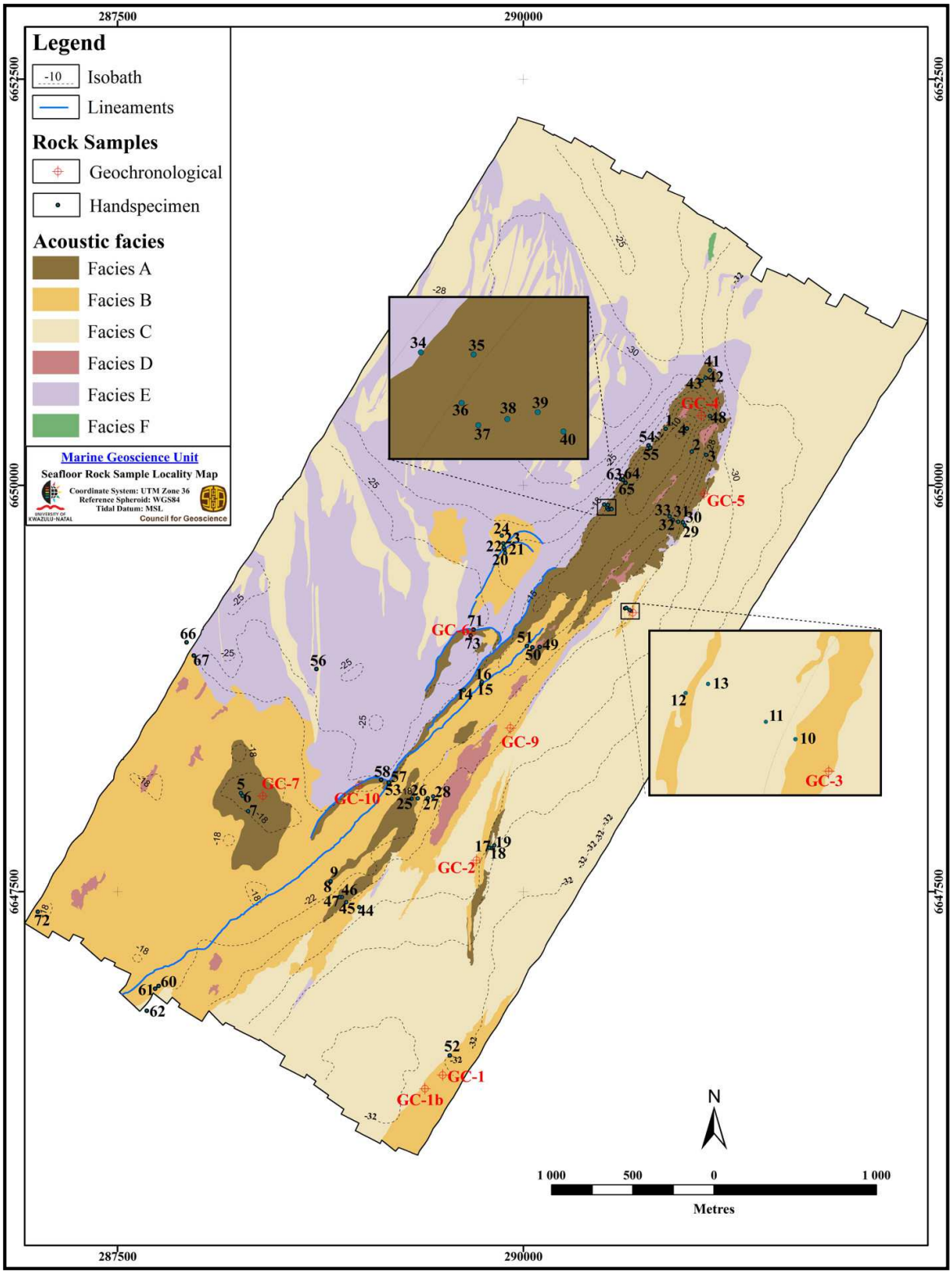

Figure 8.4 Rock sample localities plotted on the acoustic facies interpretation map. Note: isobaths not in constant intervals. All rock samples (with the exception of sample 56) are obtained from either Facies A and B, constituting the consolidated lithologies. This is also in strong agreement with the bathymetry, indicating that seafloor morphology is predominantly controlled by the consolidated lithologies of Facies A and B. Also refer to Appendix IV, Tables IV.I and IV.II for additional information.

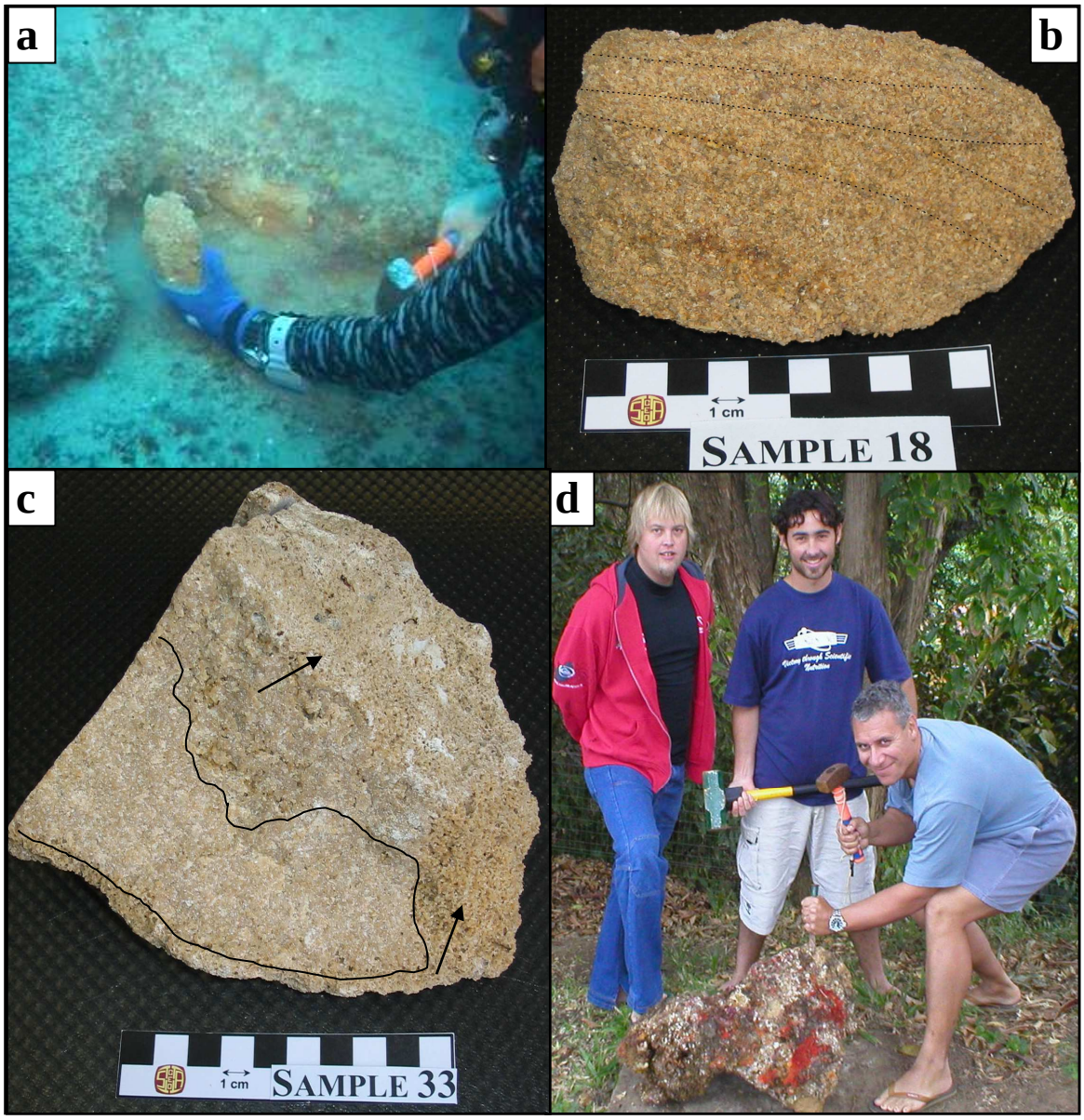

Figure 8.5 Selected examples of aeolianite and beachrock samples from the study area. **a)** Underwater photograph of a diver obtaining a hand specimen sample from a beachrock (sample 18) at -29 m below MSL (bmsl), note the low-angle dip on beachrock surface. **b)** Close-up of the sample obtained in (**a**), note subtle bedding defined by normal graded units which terminates with a coarser layer from the next cycle (highlighted with dashed lines). **c)** Aeolianite hand specimen (-17 m) showing biologically attacked surface (arrows) and approximate extent of fresh sample material (area within solid line). **d)** Example of a geochronological sample, note the surface cover of epifaunal growth and size of sample (author on the left).

8.3.2 Brief Introduction to Aeolianites and Beachrocks

Aeolianite (eolianite in some literature) is generally understood to be a carbonate-cemented wind-blown accumulation of sediment. Although the term 'eolianite' was first used to describe any sediment that was deposited by wind and later lithified (Sayles, 1931), at present it is commonly

used to indicate a dune calcarenite (Fairbridge and Johnson, 1978). Coastal and inland types (Abegg *et al*., 2001) are distinguished, while this study strictly relates to submerged coastal aeolianites.

Although aeolianites are globally found between 50° N and 45° S, the bulk of the world's aeolianite is located in the southern hemisphere (Brooke, 2001) specifically in Australia and South Africa where it forms coastal barrier-dune deposits often backed by estuaries (refer to Figure 7.5a). Coastal aeolianite deposits on the east coast of South Africa represent some of the highest coastal dunes in the world (>150 m), a likely consequence of the prevailing wind direction not only being bidirectional and opposing but also parallel to the coastline orientation (see Section 3.4.2). Globally, preserved coastal aeolianite deposits generally form shore-parallel, elongate transverse ridges often comprising multiple dune generations resulting in a compound aeolianite complex consisting of coalesced and stacked dunes (Cooper and Flores, 1991; Maud and Botha, 2000; Brooke, 2001; Frébourg *et al*., 2008). Palaeodune-forms typical include oblique, parabolic and barchanoid types (Brooke, 2001). Discontinuities in aeolianite complexes are normally marked by palaeosols and to a lesser degree by littoral, back-barrier and cave sediments (Brooke, 2001; Frébourg *et al*., 2008). Consequently, the term aeolianite now also includes shallow marine and terrestrial deposits incorporated in coastal carbonate rocks of predominantly aeolian origin (Brooke, 2001). During sea-level lowstands coastal aeolianite sediments are derived from the deflation of beach deposits and newly emerged shelf sediments, whilst during sea-level highstands sediments are sourced from wave-induced littoral input and reworking of washover and estuarine sediments (Abegg *et al*., 2001, Aagaard *et al*., 2004; Frébourg *et al*., 2008).

Aeolianites undergo early meteoric (and sometimes marine) diagenesis (Friedman, 1964; Longman, 1980; Cooper and Flores, 1991; Ramsay, 1991, 1996; Frébourg *et al*., 2008) thereby increasing its preservation potential during sea-level changes, as exemplified by submerged ridges (Ramsay 1991, 1996; Richardson 2005, Cawthra, 2010, this study). Aeolianites form during glacials (see Brooke 2001 for index), interglacials (Armitage *et al*., 2006; also see Frébourg *et al*., 2008 for inventory) and fluctuations during interstadials (Brooke, 2001; Bateman *et al*., 2004). The fundamental control on aeolianite formation has been ascribed to sea-level changes (Ramsay 1991, 1996; Armitage *et al*., 2006; Moura *et al*., 2007), margin architecture (Frébourg *et al*., 2008) and carbonate production on adjacent offshore areas (Brooke, 2001). For these reasons aeolianites represent a record of shallow-marine carbonate production, shoreline changes and the changes in the volume of littoral sediment reworked into coastal dunes (Darwin, 1851; Brooke, 2001). Darwin (1851) first described the process of aeolianite formation, studying these deposits on the island of St Helena.

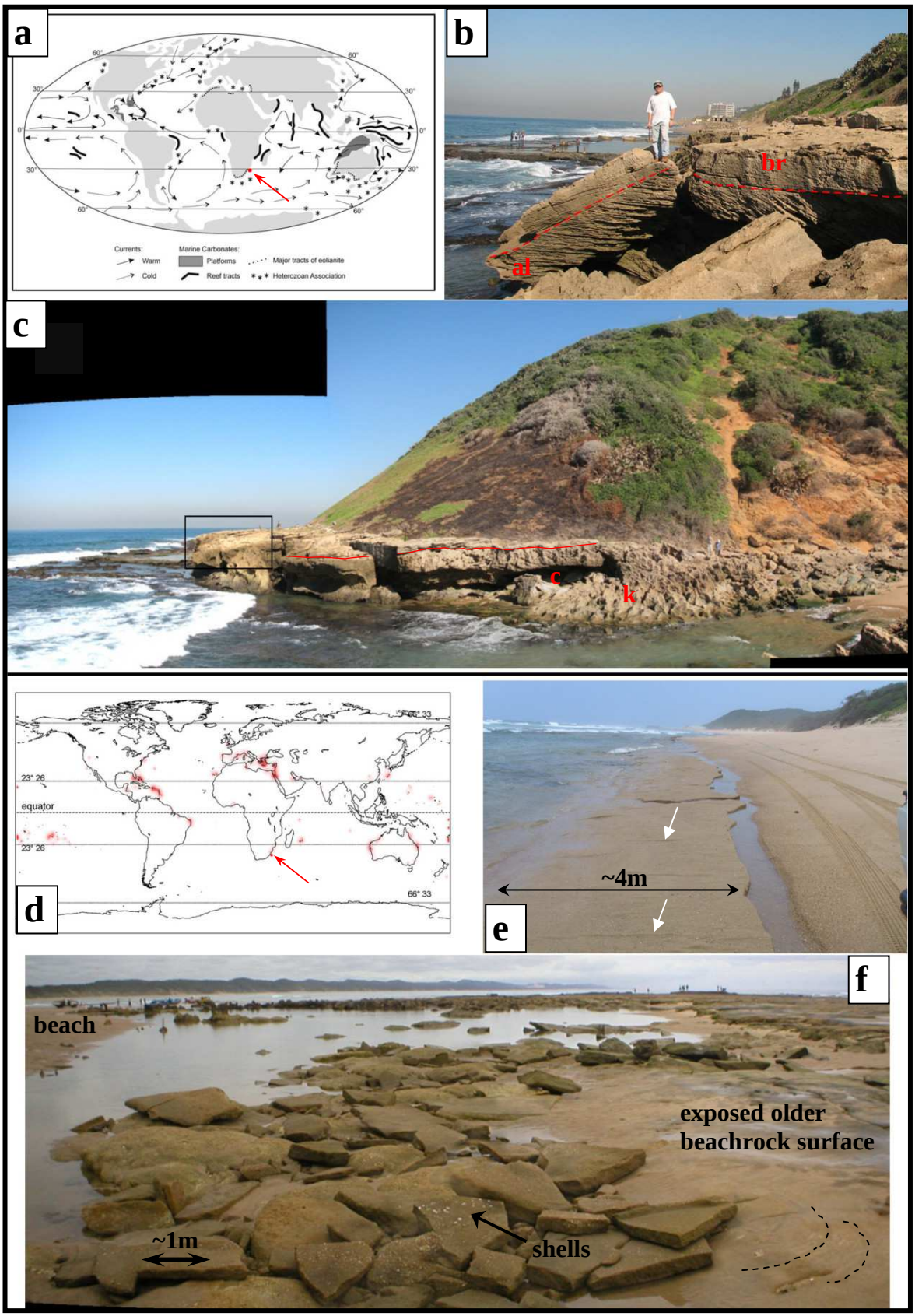

Figure 8.6 **a)** Global distribution of major carbonate aeolianite tracts located marginal to major shallow marine carbonate provinces (from James, 1997 in Brooke, 2001), arrow points to study area. **b)** Intertidal to supratidal aeolianite and beachrock facies at Isipingo Beach, Durban Bluff (see Figure 3.12 for locality). Red line separates ~182 ka B.P. (Ramsay and Cooper, 2002; also equivalent to Cawthra's, 2010 Unit 1 Aeolianite) high-angle tabular planar cross-bedded aeolianite (al) from ~125 ka B.P.

Figure 8.6 (cont.) (Ramsay and Cooper, 2002) trough cross-bedded raised beachrock (br). Person standing on undercut and collapsed block. View towards SSE. **c)** Typical coastal aeolianites forming a compound barrier complex at Isipingo. Coastal aeolianite complex forms a rocky coastline with inter- to supratidal outcrops overlain by ~130 m high vegetated stacked dune. Red line is same contact as in (b). Note seaward thickening wedge shape and irregular nature of the contact. k = karst weathered aeolianite, c = cave formed by undercutting, black box = approximate position of photograph (b), view towards SSE. **d)** Global distribution of beachrock (from Vousdoukas et al., 2007), arrow = study area. **e)** Freshly exposed intertidal Holocene beachrock outcrop at Sodwana Bay (view towards SSE, see Figure 1.1 for locality). Note similarity to surrounding beach sediments, gentle seaward dip and abrupt irregular landward margin. Possible swash marks (white arrows) preserved on upper surface. Beach is backed by a high dune barrier (photograph courtesy of Mr. W. Kidwell). **f)** Lateral continuation of beachrock in photograph (**e**) after being exhumed and eroded by a storm. Eroded beachrock overlie an older beachrock (~3.3 ka B.P.; Ramsay, 1995) with upper bedding surface showing trough cross-beds (dashed lines) defined by heavy mineral laminae. Note the beachrock forms a rocky point with a log-spiral bay to the north. Also note incorporated shell material. View towards NNE (photograph courtesy of Mr. W. Kidwell).

Brooke (2001) presented an updated and comprehensive review on the distribution of aeolianites whilst Frébourg *et al*. (2008) provided a benchmark publication on the variability of aeolianite facies assemblages and its possible misinterpretation as shallow marine deposits at core scale.

Beachrocks are loosely- to well-consolidated beach sediments formed in the intertidal to supratidal zones (including sea spray) by rapid *in situ* cementation through precipitation of carbonate cements typically derived from evaporating seawater (Bricker, 1971a; Reijers and Hsu, 1986; Vousdoukas *et al*., 2007). Globally beachrocks can be found on coasts located between the latitudes of 0° to 40°, however the majority of beachrocks occur on warm tropical/subtropical microtidal coasts (Scoffin and Stoddart, 1983; Cooper, 1991c; Vousdoukas *et al*., 2007). In South Africa beachrocks normally occur as slabs of seaward-dipping strata tens of metres wide and extending laterally for kilometres (Cooper, 1991c, Ramsay, 1997). Outcrops are generally located in the surf and swash zones but can extend onshore under the unconsolidated sedimentary cover (Cooper, 1991c; Ramsay, 1997; Vousdoukas *et al*., 2007).

Submerged beachrock deposits offshore South Africa are generally less than 2 m thick (Ramsay, 1991) although in global examples thickness can range from <0.5 to >2.5 m (Vousdoukas *et al*., 2007). Beachrock cementation can be extremely fast as exemplified by Pacific Ocean tropical island inhabitants who sustainably harvest beachrock for building material on a yearly basis (Bricker, 1971a). Cements usually consists of aragonite, high-magnesium (also called magnesian) calcite (HMC) and micrite (Bricker, 1971a), although after decades of study it is still not apparent which factors primarily control the mineralogy and the crystal habit of these cements (Vousdoukas *et al*., 2007). Also, no singular mechanism for beachrock genesis exists and beachrock formation is generally ascribed to either a physio-chemical and/or biological mechanisms (see Vousdoukas *et*

al., 2007 for detailed review). Beachrocks provide evidence for diagenetic processes in the shallow marine and mixing environments (Bricker, 1971a; Scoffin and Stoddart, 1983). They are a useful palaeosea-level indicator on microtidal coasts (Ramsay, 1995; this study) and can control coastal evolution (Cooper, 1991c; this study). Vousdoukas *et al*. (2007) provided a recent and very comprehensive review on the occurrence, cement types and formation of beachrocks.

8.3.3 Aliwal Shoal Aeolianites

Aeolianite lithologies in the study area can be subdivided into 3 different units (Figure 8.7) based on combining morphology, field relationships and sedimentary structures with the results from the geochronological analyses (Chapter 9):

1. **Unit A1** or the **Main Ridge Aeolianites (MRA)**,
2. **Unit A2** or the **Parabolic Aeolianites (PA)** which is subdivided into the **Northern Parabolic Aeolianites (NPA)** and the **Southern Parabolic Aeolianite (SPA)** and
3. **Unit A3** or the **Plateau Aeolianites (PLA)**.

Acoustically the aeolianite outcrops produce a distinctive highly reflective sonar image showing blotchy linear rugged microtopography (Figures 8.2; 8.8b to d) which can be clearly distinguished from surrounding unconsolidated sediments (Figure8.2). Beachrocks display a moderate to low reflectivity with a subdued microtopography and blocky to granular patterns. For illustration compare Figure 8.2 sonograph 3 (Unit A1) with Figure 8.2 sonograph 4 (Unit B3) and also refer to Figure 8.11b.

It may be difficult in some cases to acoustically differentiate between beachrock and aeolianite e.g. a low microtopography aeolianite outcrop such as a wave-planed aeolianite surface covered by epifaunal growth or a veneer of sediment. However, in most cases it is relatively simple to make an acoustically-based distinction, especially when ground-truth results can be integrated. Distinctive acoustic signatures of Units A1 to A3 correspond well with acoustic Facies A (Figure 8.1, Table 8.1), whilst Unit A3 also shows a less rugged microtopography corresponding to acoustic Facies B. Similar acoustic signatures of submerged aeolianite outcrops where noted by Ramsay (1991, 1996) on the Sodwana Bay continental shelf and by Richardson (2005) and Cawthra (2006) offshore of Durban.

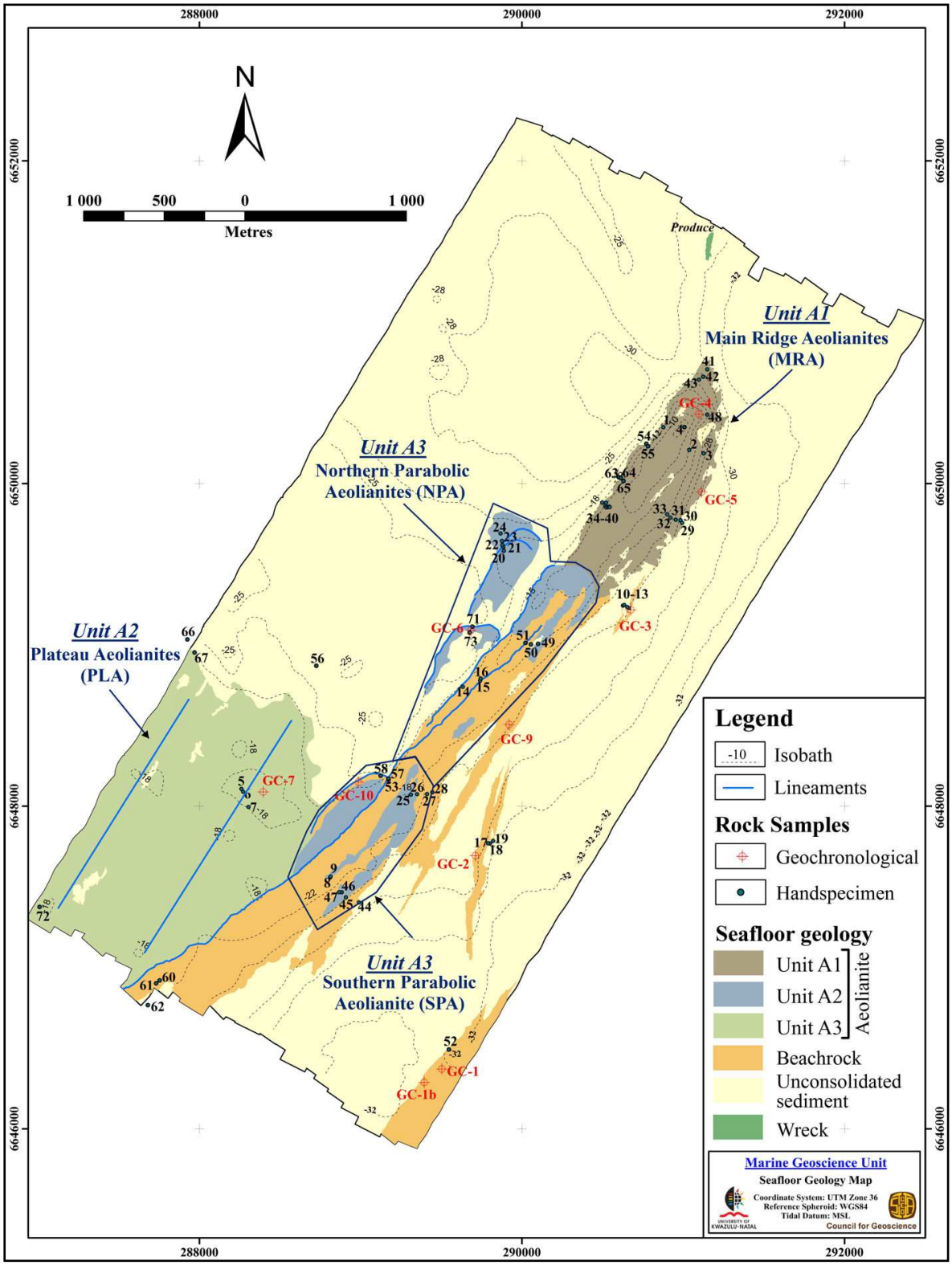

Figure 8.7 Simplified geological map of the study area showing aeolianite Units A1 to A3. Note that the Northern and Southern Parabolic Aeolianites (Unit A3) are also collectively referred to as the Parabolic Aeolianites (PA) in the text. The two parallel blue lines trending NE-SW in Unit 3 are trend-lines of two low relief ridges (see Figure 7.2). Note isobaths are not in constant intervals.

Unit A1 - The Main Ridge Aeolianites

Geomorphology

Unit A1 or the Main Ridge Aeolianites (MRA) constitutes the ~1 km long coast-parallel linear ridge that is colloquially known as the Aliwal Shoal ridge (Figures 7.2, 8.2 and 8.7). It forms the most prominent seafloor feature in the study area, is approximately 571 300 m^2 in size and covers the shallowest (-6 m) and deepest (-30 m) depths occupied by aeolianite lithologies, thereby providing the most comprehensive stratigraphic record of aeolianite deposition in the area. It achieves maximum relief in the north where it also terminates abruptly and gradually deepens southward where it borders a Northern Parabolic Aeolianite, the boundary of which could not be accurately established by field and acoustic mapping (Figure 8.7). Seismic data indicates that Unit A1 extents a further 30 m below the seafloor (Chapter 6.3.3).

Unit A1 may be subdivided into three geomorphic zones based on depth, average gradient (refer to Section 7.2.1) and position i.e. a shallow *reef crest* comprising pinnacles and gullies, a jagged irregular *seaward margin* including the *reef front* and a linear steep *landward margin* or inside edge (Figure 8.8aii).

Some of the most rugged seafloor microtopography is best developed along the northern *reef crest* which forms the shallow central axis of the reef comprising pinnacles, deep gullies, overhangs and other erosive features generally developed parallel to the strike of Unit A1 (and modern coastline) at depths between -5 and -15 m (Figure 8.8h). This very rugged microtopography is clearly visible on the side-scan sonar mosaic image by the amount of 'washed-out' (white) record due to the shadow effect (Figure 8.1, 8.8c). Pinnacle formation is ascribed to subaerial solution weathering of the carbonate-cemented lithologies during periods of lower sea-levels which commonly results in karst-like weathering features (Miller, 1992; Maud and Botha, 2000). Southwards the reef crest deepens and between -10 to -15 m the rugged microtopography of the northern reef crest is replaced by a flat terraced area completely covered by encrusting sponges and algae (Figure 8.8k) extending to the NPAs and which shows only localised small ledges and potholes ranging in diameter from 1 to 3 m.

The steep *landward margin* outlines the western extremity of the MRA (Figure 8.8a, e). Acoustically it has a strong linear expression commonly showing extensive acoustic shadowing. It forms a NW-SE trending underwater cliff (Figure 8.8e) with more than 10 m relief (-12 to -22 m) in places comprising rugged microtopography punctuated by ledges and caves (Figure 8.8l).

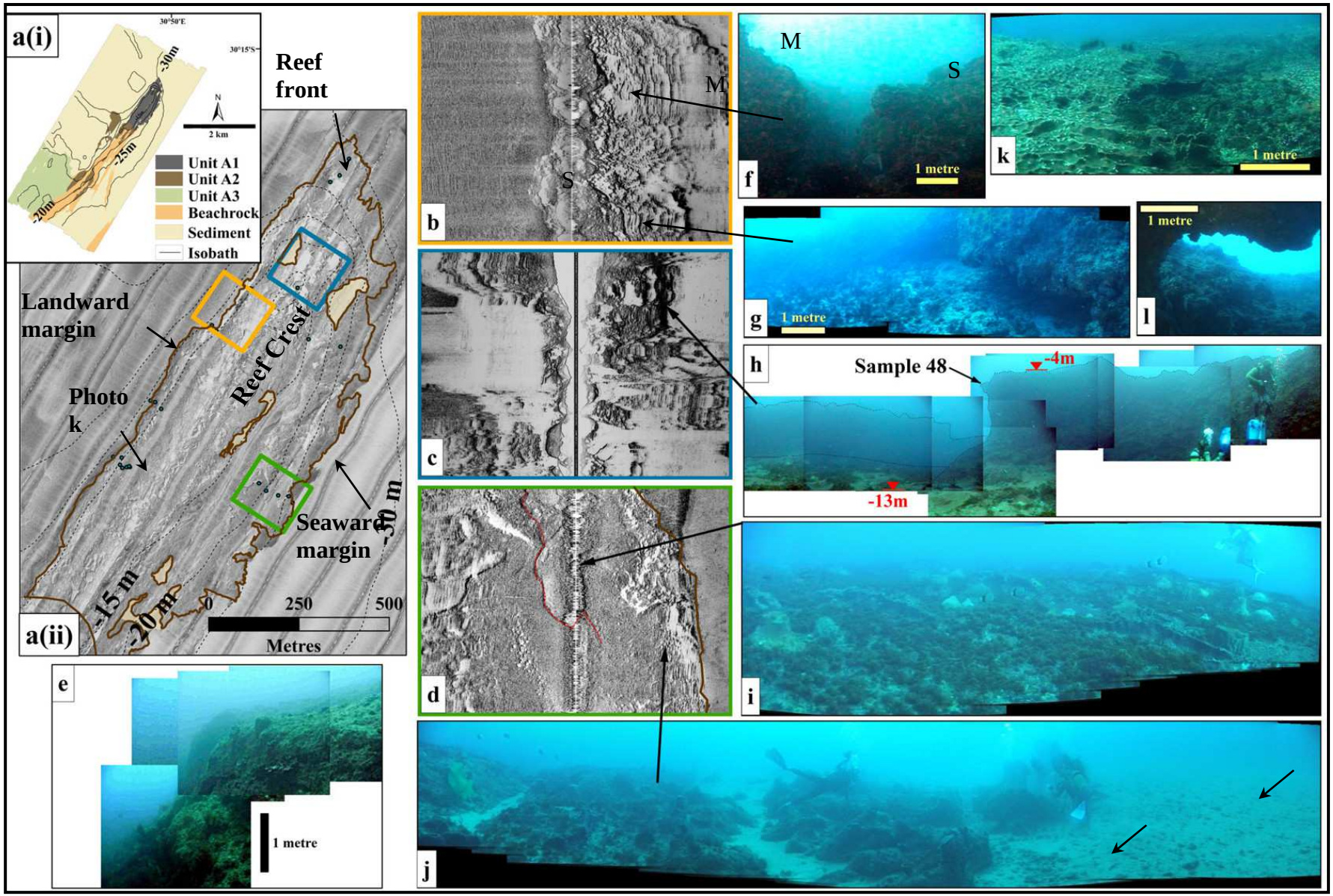

Figure 8.8 Geomorphology and side-scan sonar acoustic expression of the Unit A1 Main Ridge Aeolianites (MRA). **a)** Locality map; (i) study area with MRA outline, (ii) 100 kHz side-scan sonar mosaic of the MRA, colour boxes correspond to sonographs (b) to (d). **b to d)** 100 kHz side-scan sonar sonographs of selected areas

Figure 8.8 (cont.) in (aii) for comparison with photographs. Scale (width by height) = b) 166 x 150 m, c) 170 x 164 m, d) 167 x 154 m. Colour lines in sonograph (d): red = ledge with -22 m sea-level notch at base, brown = seaward edge of MRA reef. **e)** Photo mosaic of the steep landward margin of the reef. **f)** Undercut and slumped blocks (S) collapsed and detached from the landward margin (M), -22 m to -18 m. See (b) and Figure 8.2, Sonograph 9 for the acoustic signature. **g)** Erosional notch at the base of the landward margin (-22 m) with lag deposits. **h)** Photo mosaic of the very rugged and shallow reef crest. Note large gully bisecting the aeolianite. **i & j)** Photo mosaics of the gently sloping seaward margin (-29 m to -26m). Note the transgressive sediment deposits (arrows, -29 m) ranging in size from cobble to coarse sand banked against the aeolianite in (j) and covered with a thin veneer of sediment from the MSDC (Chapter 6). Also note the karst-like appearance similar to Figure 8.6c and gullies parallel to the reef margin. **k)** The deeper reef crest is characterised by a flat terraced morphology and completely covered by encrusting sponges and algae, -14m. **l)** Sea-level notch (-16 m) cut into the steep landward edge of the MRA.

The base of the underwater cliff between -22 to -23 m, is typically eroded forming a cave or overhang (Figure 8.8g) against which are deposits of sediment with epifaunal growth and scattered reef debris (Figure 8.8g) ranging in size from undercut and collapsed aeolianite boulders (Figure 8.8f) in places to cobbles and pebbles. The linear landward margin can be traced beyond the MRA and merges southwards, in the area between the northern and southern PAs, with another ledge feature (Figure 8.7).

In contrast, acoustically, the *seaward margin* has an irregular bowing surface showing less shadowing than the landward margin and reef crest. This is related to a gentler gradient and a series of small terraces and ledges shaping the seaward margin. Murray-Wallace *et al*., (1999) also noted a similar irregular appearance of the seaward margin of an exposed Last Interglacial (LIG) aeolianite barrier and equated it to attack from high energy waves that, as with the eastern South African coastline, characterise south-eastern Australia. The base of the forereef margin is generally encountered between -27 to -29 m typically showing rugged 'dragon's teeth' (karst) topographic features (Figure 8.8j) and strong pothole development at -26 and -28 m. A lag deposit consisting of unconsolidated pebble to cobble sized clasts covered by fine to medium grained sediment is banked against the forereef margin (Figure 8.8j, also refer to Section 8.4). The seaward margin slope exhibits a gentle gradient between -27 m to -23 m and shows little microtopography except for small gullies transecting the reef slope (Figure 8.8j). At -22 m a knick/inflection point occurs in the sloping forereef margin resulting in a ~40 m wide wave-planed surface. This planation surface is bounded in the west by a prominent ledge with a -22 m sea-level notch at the base, signifying a marked transition in the morphology of the reef. In places the ledge is clearly visible on the mosaic as dark line trending parallel to the reef margin (Figure 8.8d). At depths shallower than 22 m the reef is increasingly characterised by rugged microtopography consisting of ledges and cliffs (1-3 m high) punctuated by gullies and marks the transition zone (-22 m to -15 m) from the seaward margin to reef crest (<15 m).

Minor scattered remnant beachrock outcrops are present below -22 m on the seaward margin of the MRA but due to their limited size and occurrence do not constitute mapable units for this study. These are most likely variables of beachrock Units B3 to B5.

The presence of beachrock and erosional features such as potholes and wave-planed surfaces at distinct bathymetric levels is evidence of sea-level change across Unit A1. The major erosional events preserved on the seaward margin occur at -26, -21, -18, -16, and -14 metres below MSL, which is in good agreement with those reported by Ramsay (1991), Richardson (2005) and Cawthra (2010).

Sedimentary Structures and Features

Primary sedimentary structures (Figure 8.9) observed in Unit A1 predominantly consist of spectacular large-scale (5 - 10 m) high-angle tabular planar cross-bedding with minor low-angle tabular planar cross-bedding (Figure 8.9a-d). Foreset laminae of the cross-bedding ranges in thickness from 2 to 10 cm and are always parallel to each other with no evidence of being asymptotic either at the top or base of cosets. Dip of foreset beds ranges from 14° to 32°, similar to the angle of repose for dry sands. These observed sedimentary structures are indicative of an aeolian depositional environment. Foreset and cross-bed set thickness were only observed in a few localities and range from 5 cm to 60 cm and 2 m to 8 m, respectively. No palaeosol horizon or major erosional discontinuities were observed within Unit A1.

Field observations on the steep landward edge (Figure 8.8e, f) and the shallow reef top from aeolianite cliff sections (up to ~10 m high; Figure 8.8h) revealed the simple tabular large-scale steeply dipping unidirectional foreset beds, with palaeowind reversal constrained to a separate overlying unit. Palaeowind vectors are consistent over a linear lateral distance of ~1.5 km. Based on these field observations it is tentatively suggested that the aeolianite of Unit A1 accumulated as an oblique (or transverse) dune ridge, similar to that observed by Ramsay (1991, 1996) offshore Sodwana Bay. However, a parabolic origin cannot be completely discounted as large-scale steeply dipping planar cross-bedding may also form by progradation of the nose and trailing arms of parabolic dunes (Illenberger, 1996; Roberts *et al*., 2008) and parabolic dunes can coalesce laterally to form linked transverse dune complexes normal to the wind direction (Catto *et al*., 2002). Nonetheless, Unit A1 does not show clear trailing arms nor the complex internal structures observed in Unit A2 and some onland parabolic dunes of comparable size (e.g. Roberts *et al*., 2008 and Figure 2b in Bateman *et al*., 2011).

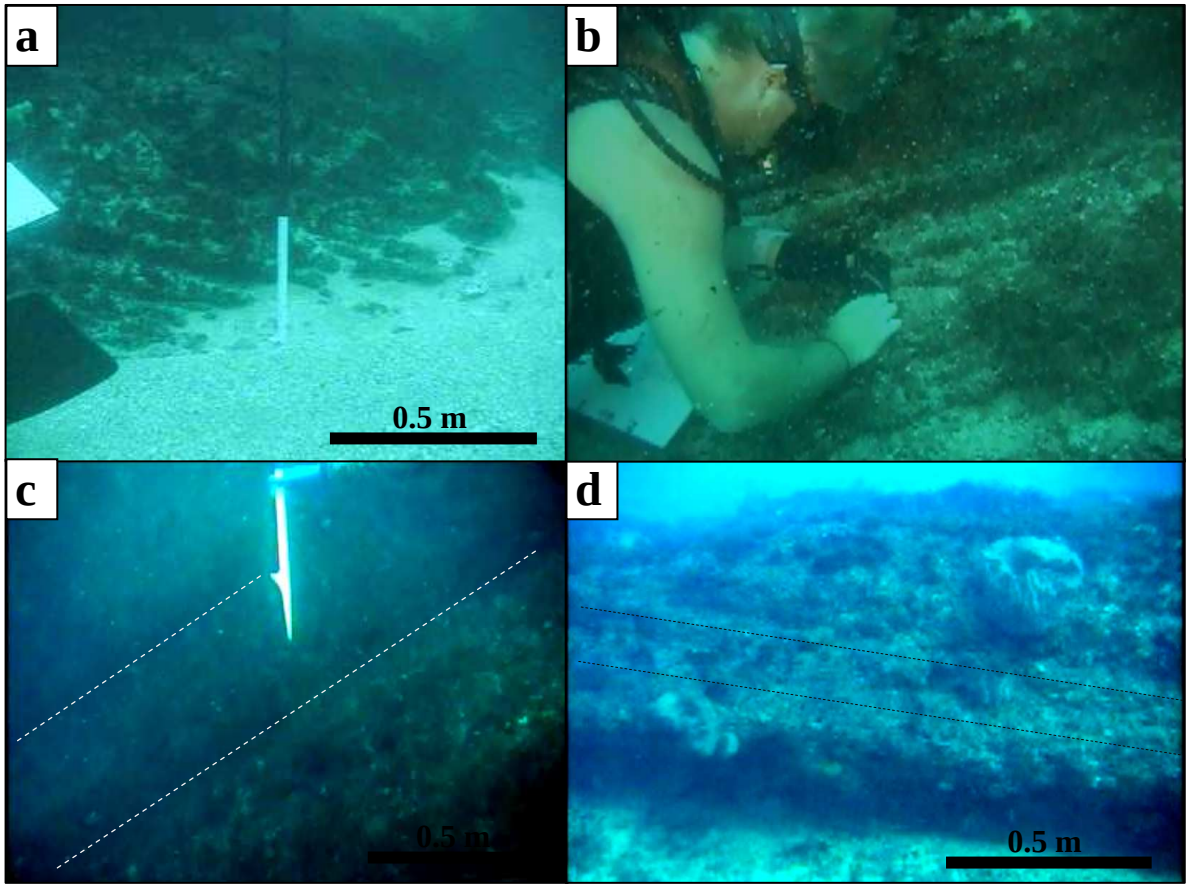
a
0.5 m
b
c
0.5 m
d
0.5 m

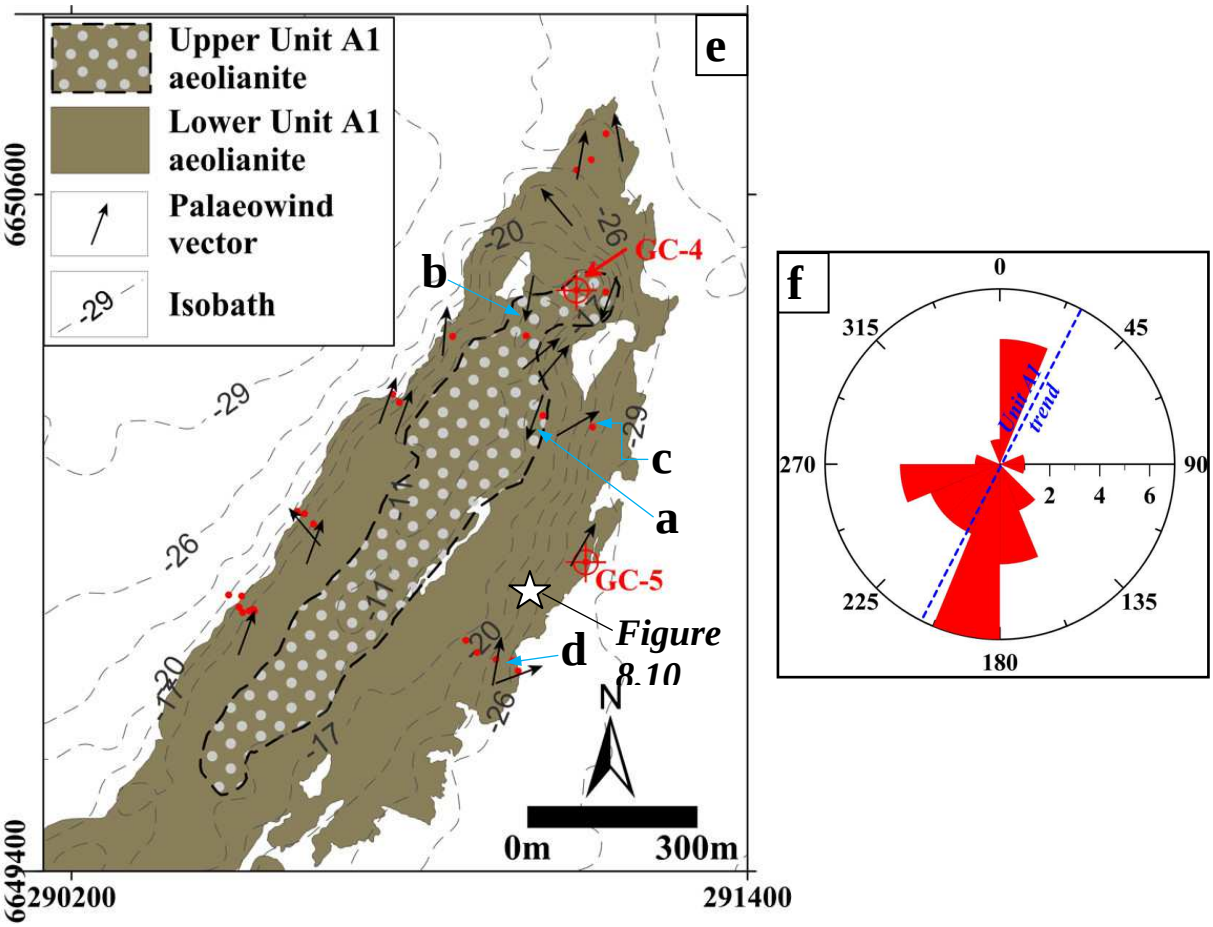
e
Upper Unit A1 aeolianite
Lower Unit A1 aeolianite
Palaeowind vector
Isobath
-29
6650600
6649400
290200
291400
GC-4
GC-5
b
c
a
d
Figure 8.10
N
0m
300m

f
0
45
90
135
180
225
270
315
2
4
6
Unit A1 trend

Figure 8.9 (cont.) Sedimentary structures of Unit A1 aeolianites. **a - d)** Underwater photographs of planar cross-bedded aeolianite foresets. For localities refer to Figure 8.9e, depths as follows (**a**) -20 m, (**b**) -10 m, (**c**) -17 m and (**d**) -23 m. **e)** Seafloor map of Unit A1 showing the dominant palaeowind vector distribution and inferred extent of the upper and lower aeolianite sub-units. Letters a - d correspond with the localities for photographs a to d. Isobath levels are in 3 m intervals. Red dots = sample localities; refer to Figure 8.7 for sample numbers. GC-4 and GC-5 are the geochronological samples for Unit A1. Star symbol indicates the locality for Figure 8.10b and d. **f)** Combined palaeowind rose diagram (22.5° bins) based on 30 strike and dip measurements taken from foreset beds of Unit A1. MRA = Main Ridge Aeolianites ≡ Unit A1.

Dip azimuth measurements from Unit A1 planar foreset cross-bedding were plotted to obtain the distributions of the mean palaeowind vector trends and indicated deposition from dominantly southerly (SSW, SW, S, SSE and SE) and opposing northerly (N and NNE) winds (Figure 8.9f). Additional minor vectors also include west-northwest and easterly components, although these are probably related to minor later beach facies (especially the westerly azimuths) and variability related to the location of the measurement (Collison and Thompson, 1982). The almost opposing bimodal distribution of the palaeowind directions approximates the present day wind regime (Figures 2.1 and 2.2) although the directions vary slightly. The dominance of the southerly components suggests that dune mobilisation and climbing primarily occurred during periods of high southerly winds (Figure 8.9 small map). Presently, similar patterns are observed along the coast with the southerly winds generally attaining higher velocities (especially in winter) than the northerly components (Section 2.1.2). The palaeowind patterns suggest that Unit A1 comprise at least two dune units (Figure 8.9e, f), a lower unit dominated by southerly palaeowind directions (from -30 to ~ -10 m) and an upper unit comprising northerly palaeowind directions (forming predominantly the shallow pinnacle region above -10 m, although the base varies), an observation which is also supported by the geochronology.

The palaeowind data trends for Unit A1 are not comparable to either Ramsay (1991; 1996) or Cawthra (2010), none of them finding the dominant wind direction distribution to be bipolar (opposing bimodal). The lower Unit A1 dune unit is similar to Cawthra's (2010) Unit 1 Aeolianite which extends from the littoral zone (Figure 8.6b, c) to mid continental shelf showing very similar palaeowind vectors. Ramsay (1991, 1996) reported comparable northerly palaeowind vectors from the reef top of Four Mile Reef (located above -25 m) an aeolianite complex offshore Sodwana Bay (see Figure 1.1 for locality). According to Flemming *et al*. (1983) palaeowind regimes measured from aeolianites in the southern Cape indicates dominant south-westerly and north-westerly directions with subordinate south-easterly and easterly directions.

Optical age data (Chapter 9) indicate formation of Unit A1 from at least 134 ± 5 ka cal. B.P. (GC-5, -29.5 m; lower unit) to 127 ± 7 ka cal. B.P. (GC-4, -15.5 m; upper unit) during the penultimate deglacial sea-level rise towards the last interglacial (Chapter 9). This supports the field observations of two different dune units within Unit A1 which were deposited fairly continuously as exemplified by a lack of development of palaeosols and other major erosional surfaces between the two dune units.

The palaeowind data suggest that climatic conditions were broadly similar to the present but that cooler climatic conditions (reflecting a post-glacial climate) or possibly a stronger climatic gradient prevailed when the lower Unit A1 dune was deposited. Presently, southerly wind conditions are characteristic of northward migrating low pressure cells and associated cold front conditions, the frequency and intensity of which increase during winter (Section 2.1.2) and glacial climatic conditions (Porat and Botha, 2008). Conversely, at present northerly wind conditions are characteristic of climatic conditions dominated by the ridging of the South Indian Ocean High - comprising anticyclonic circulation typical of summer conditions.

The postulation that climatic conditions during deposition of Unit A1 approximated the present is not unlikely considering that the formation of Unit A1 (and A2; Chapter 9) only slightly preceded the climatic optimum of the last interglacial (MIS 5e) and as such global climates should have recovered from the penultimate glacial and attained a state not too dissimilar to that of the present. Roberts *et al*. (2008) also found that last interglacial (MIS 5e to 5b) wind patterns from coastal aeolianites in the southern Cape were similar to the present.

Erosional features (Figure 8.10) observed on Unit A1 include gullies (Figure 8.8j), potholes, overhangs, caves, sea-level notches and wave-planed surfaces with lag deposits (see Section 8.4). Gully formation is most likely related to a combination of solution weathering and wave erosion in the intertidal zone during periods of changing sea-levels (Miller, 1992). Potholes, sea-level notches and wave-planed terraces are related to extensive sea-level occupations (Ramsay, 1991). Major pothole development was observed on the seaward margin and reef top, the latter displaying larger dimensions and which generally were filled with prolate and oblate pebbles and cobbles.

Similar erosional features can be observed in exposures of intertidal coastal carbonate-cemented lithologies (Figure 8.6b, c and f) present along most of the KwaZulu-Natal coastline and were studied by Miller (1992), Miller and Mason (1994) and Cawthra (2010). In addition, present day wave-action also contributes to the weathering of the shallow pinnacle areas.

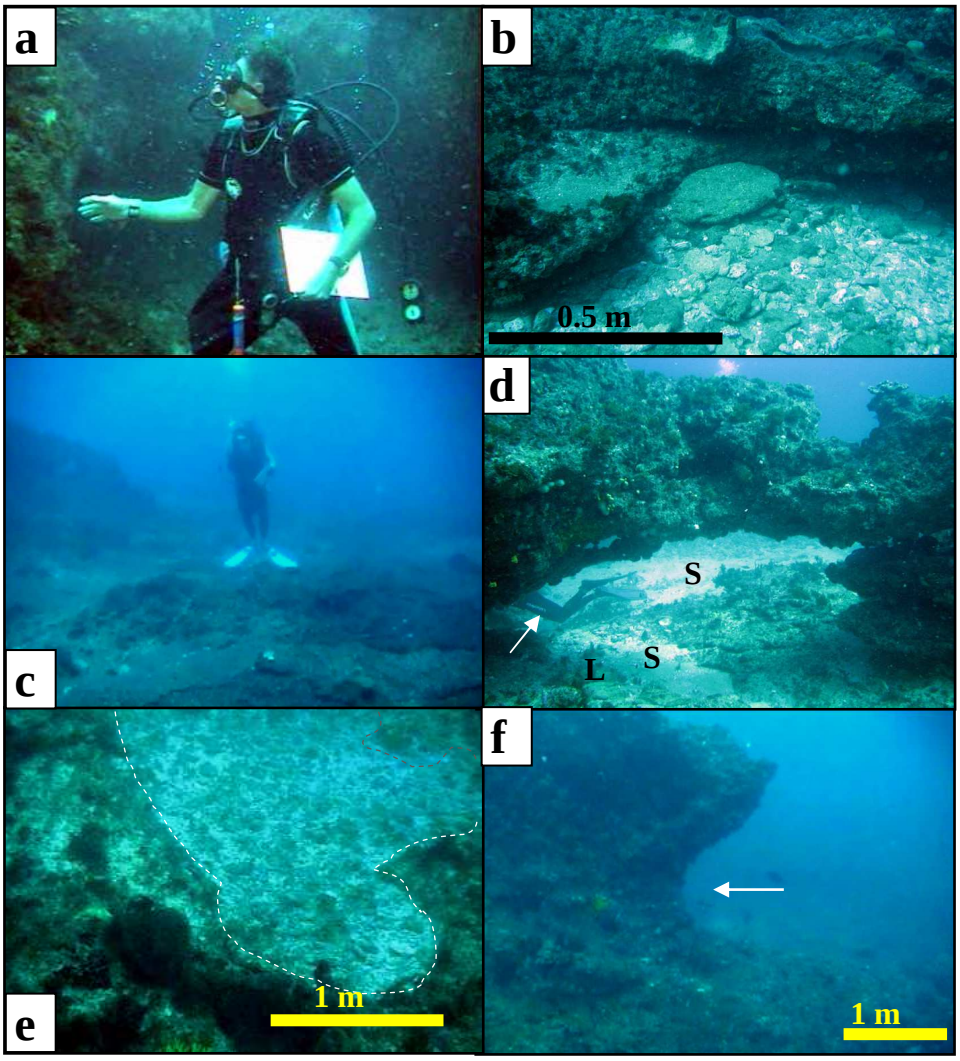

Figure 8.10 Examples of common erosional features of Unit A1. **a)** Diver in a 3 m deep pothole located on the reef crest below sample 48 in the lower Unit A1 at -14 m. **b)** Typical lag deposits found as pothole fill comprising oblate and prolate cobbles and pebbles, -22 m, see Figure 8.9e.for locality. Photograph courtesy of Andrew Richardson. **c)** Wave-planed terrace at -22 m, seaward of sample 48. **d)** Large arch formed by aeolianite foresets, -23 m, arrow points to diver for scale, see Figure 8.9e.for locality. Also note large pothole filled with bioclastic-rich sediments (S) and lag deposits (L). Photograph courtesy of Andrew Richardson. **e)** Coalesced potholes filled with lag deposits (dark) and finer grained bioclastic-rich sediments (light), -26 m at sample locality 3. **f)** Sea-level notch (arrow) incised into the lower Unit A1 close to sample locality 3 at -26 m.

Unit A2 - The Parabolic Aeolianites

Geomorphology

Unit A2 comprises the parabolic aeolianites (PA) which are ~509 565 m^2 in extent size and located in a distinctive NNE-SSW corridor separating Unit A1 from Unit A3 (Figure 8.7). The parabolic aeolianites unit is further be subdivided into the Northern Parabolic Aeolianites (NPA) and the Southern Parabolic Aeolianite (SPA) domains which are separated by the flat wave-planed surface of beachrock Units B4 and B5 representing an area of remnant high relief topography infilled and blanketed by these transgressive beachrocks (Figure 8.11).

The NPA (Figures 8.7 and 8.11aii) comprise a group of at least three preserved parabolic dune cores (Figures 8.7 and 8.11aii), the north-eastern member abutting Unit A1, a prominent south-western member, named Bosman's Reef and a north-western member comprising low relief units located on the Spur morphological feature (Figure 7.2). Conversely, the SPA consists of a large isolated parabolic form showing a complex arrangement comprising two seaward trailing arms inter-fingering with Unit B4 and a landward trailing arm overlain by Unit B5 (Figure 8.11). The north-eastern member of the NPA also shows the same configuration of two seaward trailing arms but the inter-digitating association is with Units B3 and B4 (Figure 8.11b).

The parabolic aeolianites range in size from ~2 km by ~0.8 km (SPA, length by width), ~1.2 km by ~0.5 km (Bosman's Reef), ~1.5 km by ~0.75 km (NPA, north-eastern member), yielding length to width ratios ranging from 2.4:1 to 2:1. The Unit A2 parabolic aeolianites do not achieve the same bathymetric prominence as Unit A1 with the SPA showing the maximum vertical relief consisting of ~9 m (-16 m to - 25 m). In general the morphological expression of the PA comprise prominent but isolated cross-bedded rugged flat topped ledges and overhangs bisected by deep gullies (Figure 8.11k) surrounded by broad flat sediment and epifaunal-growth covered platforms (Figure 8.11f) with numerous sediment filled potholes and conspicuous lag deposits (Figure 8.11l) comprising oblate to prolate discs ranging from coarse sand to cobble in size. Lag deposits are commonly associated with the -22 m planation surface which is a prominent feature for the PA associated with the beachrock units.

Two seismic profiles cross the PA (Bosman's Reef, Figure 6.8b; NPA, northeast and northwest members, Figure 6.7b) indicate that it extends a further 25 m below the seafloor, resting on SB3 which is comparable with the Unit A1 aeolianites. In addition, the seismic profiling also suggests that the north-eastern member of the NPA formed not as part of Sequence 3, as all the other Unit A2 aeolianites, but as part of seismic Unit Dl, Sequence 4 (Figure 6.7b).

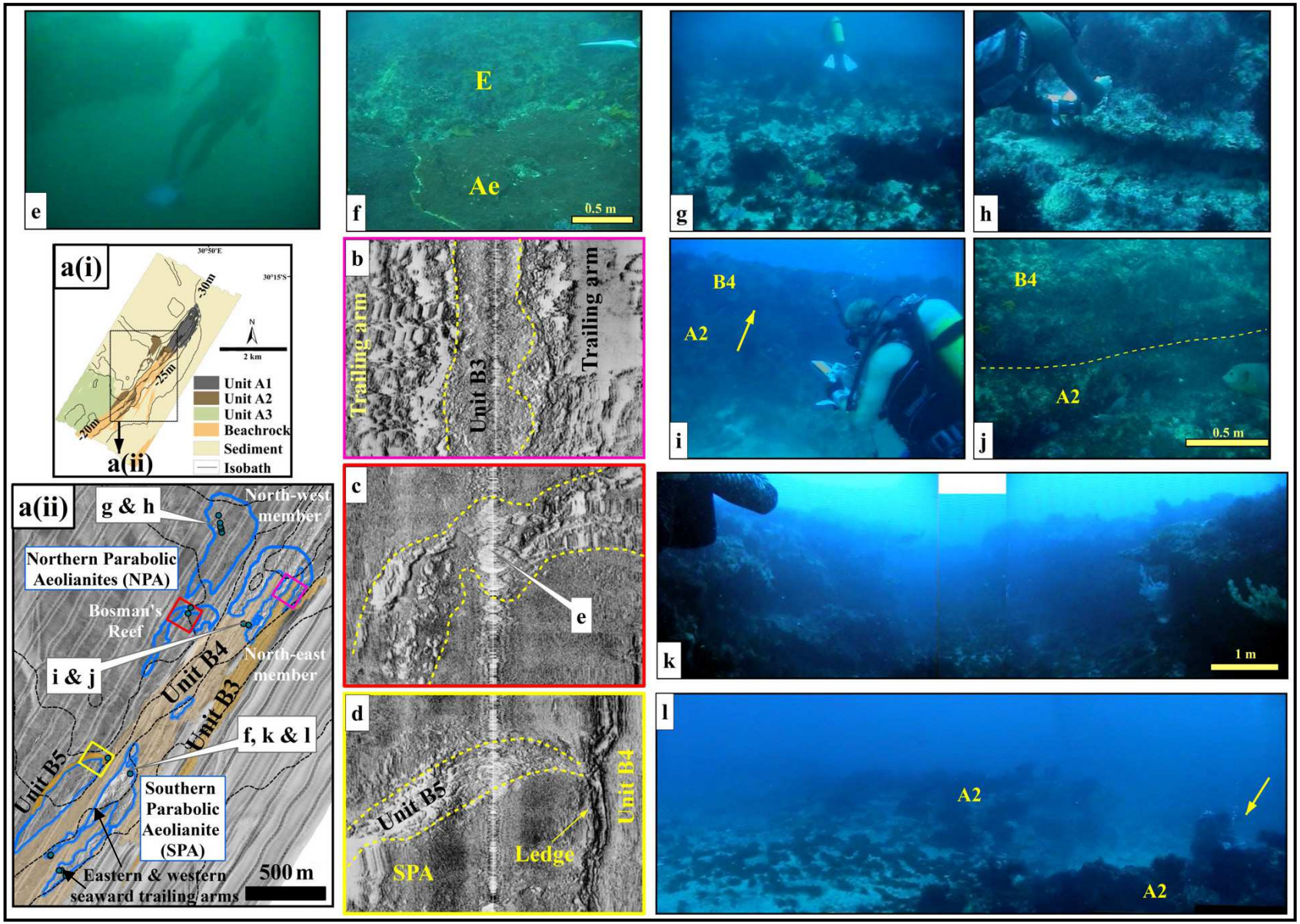

Figure 8.11 Geomorphic and side-scan sonar acoustic expression of the Unit A2 Parabolic Aeolianites (PA). **a)** Locality map; (i) study area with Unit A2 distribution, (ii) 100 kHz side-scan sonar mosaic of Unit A2, colour boxes correspond to sonographs (b) to (d). Note that the Unit A2 parabolic aeolianites are divided into the Northern

Figure 8.11 (cont.) Parabolic Aeolianites (NPA) and Southern Parabolic Aeolianite (SPA). Seafloor samples indicated for numbers refer to Figure 8.7. **b to d)** 100 kHz side-scan sonar sonographs of selected areas in (aii) for comparison with photographs. Scale (width by height) = b) 169 x 157 m, c) 166 x 156 m, d) 168 x 158 m. Note inter-fingering relationship of Unit B3 in (b). Sonograph (c) shows the nose and western trailing arm of Unit A2 Northern Parabolic Aeolianites Bosman's Reef member. In (d) Unit A2 (SPA) is overlain by both beachrock units B4 and B5. The ledge is formed by erosional undercutting during lower sea-level occupations which resulted in a cliff section exposing the relationship between Unit A2 and B4. **e)** 3 m high overhang formed by competently cemented aeolianite foreset, Bosman,s Reef, -24 m. **f)** Complete coverage of the seafloor by epifaunal growth (E) and encrusting algae (Ae), see (aii) for locality, -18 m. **g)** The low relief seafloor constituting the Northwest member is covered with extensive epifaunal growth and a sediment veneer with varying thickness, -22 m. **h)** Close up of the low relief raised ridge in (g) representing the subdued relief microtopography formed by an aeolianite foreset in an otherwise low relief seafloor, sample 21, -23 m**. i)** ~2 m high former sea cliff exposing the relationship between the North-west member of Unit A2 NPA and the overlying Unit B4 beachrocks. Arrow points to unconformity surface. **j)** Close-up view of the unconformity in (i). **k)** Photo mosaic of the reef top area in the vicinity of the SPA nose, characterised by rugged microtopography without outcrops bisected by gullies, near sample 25, -17 m. **l)** Underwater photographic mosaic of the Unit B4 sea-level planation surface (-22 m) covered with sediments, lag deposits and epifaunal growth punctuated by prominent ledges. Note diver (arrow) observing a prominent ledge with aeolianite foresets, seaward of sample 25, -22 m.

Acoustically, the Unit A2 signature ranges from highly reflective with rugged microtopography to low reflectivity with subdued microtopography (Figure 8.11a to d).

Sedimentary Structures and Features

Field observations on the macro-scale features of Unit A2 were limited due to the generally subdued nature of the outcrop compared to Unit A1, although some 2 m - 4 m high cliff sections were exposed in ledge areas (Figure 8.11i and k). Primary sedimentary structures (Figure 8.12) observed in Unit A2 predominantly consisted of large (>2 m) and smaller scale (<2 m) high-angle tabular planar cross-bedding (Figure 8.12d, f) with parallel foresets ranging in dip from 17° to 42°. Due to the environmental conditions foreset and cross-bed set thickness were observed only in a few localities and these range from 5 cm to 40 cm and 1 m to 3 m, respectively. As per Unit A1, palaeosol horizons or major erosional discontinuities were not observed within Unit A2. However, as opposed to Unit A1, the small-scale planar cross-bedded units impart a localised complex internal cross-bedded character to the Unit A2 aeolianites. The large-scale planar cross-bedded units are interpreted as progradational sedimentation in the nose and trailing arm segments of parabolic dunes based on detailed observations in remnant coastal parabolic aeolianites by Illenberger (1996) and Roberts *et al*. (2008). Similarly, the smaller scale planar cross-bedded units are interpreted as the migration of smaller-scale bedforms superimposed on the larger parabolic form (Roberts *et al*., 2008).

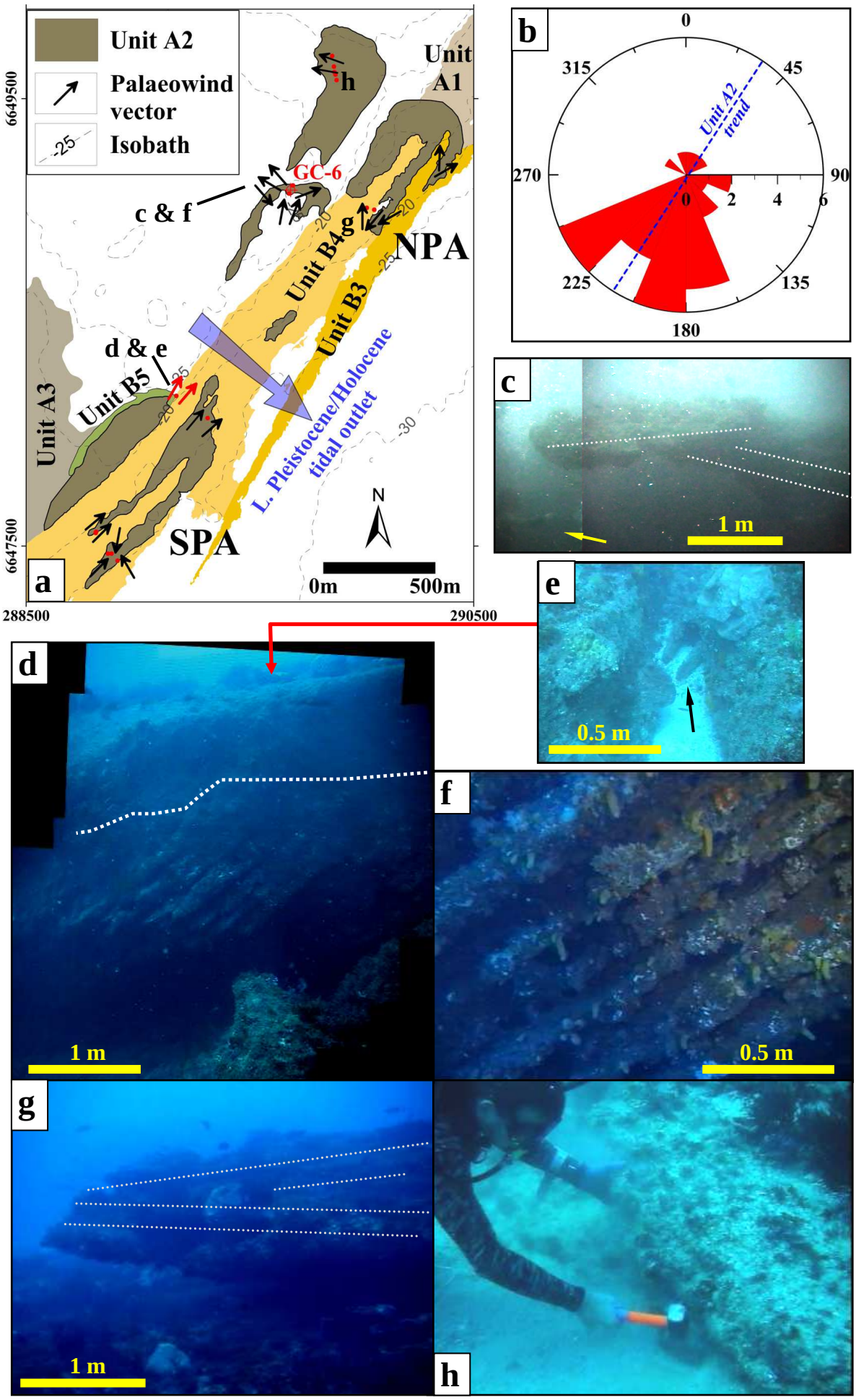
Unit A2
Palaeowind vector
Isobath
-25
Unit A1
h
GC-6
c & f
Unit B4g
NPA
Unit B3
L. Pleistocene/Holocene tidal outlet
d & e
Unit B5
Unit A3
SPA
N
0m
500m
a
6649500
6647500
288500
290500
b
0
45
90
135
180
225
270
315
Unit A2 trend
0
2
4
6
c
1 m
e
0.5 m
d
1 m
f
0.5 m
g
1 m
h

Figure 8.12 (cont.) Sedimentary structures of the Unit A2 aeolianites. **a)** Seafloor map of Unit A1 showing the dominant palaeowind vector distribution, inferred extent of Unit A2 aeolianites and proposed late Pleistocene palaeo-tidal outlet which were present during deposition of Unit A2 and re-established during the Holocene transgression (see text for details). Letters a - d correspond with the localities for photographs c - h. Two red arrows = observation of very steep foresets (42°). Isobath levels are in 5 m intervals. Red dots = Unit A2 sample localities; refer to Figure 8.7 for sample numbers. GC-6 is the geochronological sample for Unit A2. **b)** Combined palaeowind rose diagram (22.5° bins) based on 31 strike and dip measurements taken from foreset beds of Unit A2. **c)** Underwater photograph of small-scale complex aeolian foreset pattern, top foresets from the NW, bottom foreset from the S, -24 m. Arrow points to silhouette of a diver. The location is close to the dune nose it might alternatively represent the interface between the dune topset and lee-side foresets. **d)** Underwater photograph showing over-steepened dip on foresets from the nose of the SPA as revealed in a prominent sea cliff, also showing the unconformity (grey line) separating beachrock Unit B4 above from the underlying Unit A2 aeolianite (compare with Figures 8.11i, j and 8.6a). **e)** Photograph of a gully eroded into Unit B4 exposing the underlying steep foresets of the SPA. Arrow shows approximate location of photo. **f)** Underwater photograph of aeolian foresets (from the S) near sample 73, -23 m. **g)** Complex small scale aeolian foresets, bottom set from the S, top set from the N, -18 m. **h)** Example of the low relief ridges comprising aeolianite foresets, NPA north-west member, sample 24, -23 m.

The observed sedimentary structures combined with the morphological data are interpreted as indicating an aeolian depositional environment, more specifically a parabolic dune system, with hairpin parabolic dune forms. It is also similar to that observed by Sudan *et al*. (2004) and Porat and Botha (2008) from the Maputaland (Figure 3.11) coastal dunes.

Palaeowind vector trends obtained from dip azimuth measurements of the planar foresets indicate deposition from dominantly southerly (SW, SSW, S, SSE and SE) and minor opposing northerly (NNW, NNE) winds (Figure 8.12b). Additional minor vectors also include west-northwest and easterly components which are, similarly to Unit A1, also interpreted as minor later beach facies (especially the westerly azimuths) and variability related to the location of the measurement (Collison and Thompson, 1982). The palaeowind data suggest parabolic dune migration under dominant southerly winds, which as discussed previously, are associated with polar frontal systems migrating northwards along the east coast of KwaZulu-Natal. Comparably, Roberts *et al*. (2008) also found migration of last interglacial coastal parabolic aeolianites under wind regimes associated with migrating polar frontal systems.

Unit A2 southerly palaeowind vector distribution closely resembles that of the lower Unit A1, whilst the minor northerly palaeowind vector component resembles the upper Unit A1 (Figure 8.9e and f). An optical age (Chapter 9) of 130 ± 6 ka cal. B.P. (GC-6, -25.8 m; Bosman's Reef; Figure 8.11) indicates deposition of Unit A2 slightly after deposition of the lower Unit A1 (134 ± 5 ka cal. B.P., southerly palaeowinds) and slightly before the formation of the upper Unit A1 (127 ± 7 ka cal. B.P. - northerly palaeowinds). The OSL age placing Unit A2 between that of

the lower and the upper Unit A1 is also supported by the field evidence of opposing palaeowind vectors in Unit A2 which represents the opposing vectors of the lower and upper Unit A1. The Unit A2 aeolianites therefore most likely document a period of climatic transition from the predominance of southerly palaeowind directions commonly associated to glacial climates (Porat and Botha, 2008) to a more bimodal wind regime characteristic of an interglacial (present) climatic regime along this coastline. However, an alternative explanation for the predominance of the southerly wind vectors may be found in the location of the sediment source and rate of sediment supply. During the time of deposition of Unit A2 the area located to the south would have represented the shoreface from which a high rate of onshore-directed sediment (associated with the transgression) would have been supplied to the beaches and dune systems. In addition, the beach zone would have been fed by a northward-directed longshore drift as coastal conditions during the last interglacial were similar to the present (Cooper and Flores, 1991). Conversely, due to the orientation and depositional environment of Unit A1, the area to the north would have represented a back-barrier and coastal zone sediment source which could not supply sediment at the same volume and rate as that from the offshore zone. Thus it is possible that the relatively higher volume and rate of sediment supply from the south might have resulted in an apparent dominant wind direction. A similar situation was observed by Brooke *et al.* (2003) in coastal aeolianites on a volcanic island where a bias in the carbonate production area possibly skewed the dominant wind vectors. In addition, it is thus also possible that the relative difference in size between the lower and upper Unit A1 aeolianites might be due to the difference in the rate and source of a southern versus northern sediment supply.

Depositional characteristics, overall geomorphic pattern (especially the dual seaward trailing arm) and age data are interpreted to indicate that Unit A2 represents the eroded remnants of a coastal dune system most likely formed by coalesced parabolic dunes, active during a period of transitional climatic regimes between deposition of the lower and upper Unit A1. Porat and Botha (2008) also suggested parabolic dune construction of the coastal barrier in Maputaland during MIS 5 and noticeable inland dune migration during the increased desiccation and southerly windiness related to the glacial conditions of MIS 2 and 3. According to Porat and Botha (2008) the elongated parabolic dunes observed in the coastal barrier of Maputaland represent (i) a strong unidirectional wind regime, (ii) sediment movement over a relative flat terrain with sparse vegetation and (iii) sufficient precipitation to allow stabilization of the trailing arms by vegetation as the nose of the parabolic dine continues to migrate. Similar palaeo-environmental factors are observed for Unit A2, with a predominantly glacial-like southerly wind regime and increased humidity and precipitation as deglaciation proceeded representing points (i) and (iii) above whilst factor (ii) comprising flat sparsely vegetated terrain is possibly represented by the coupled area comprising of the beach and tidal/fluvial outlet (see below and Figure 8.12).

The Unit A2 parabolic dune cordon is postulated to have formed across a palaeo-estuary/lagoonal tidal outlet located north of the SPA and south of the NPA (Figure 8.12a). This is supported by the very steep foresets observed in the nose of the SPA parabolic dune (38 - 42°, Figure 8.12d, e) indicating deposition under either; high moisture content, due to undercutting or exceedingly strong winds (Allen, 1982; Collison and Thompson, 1982). Additional evidence is provided from the seismic data showing the presence of fluvial channels seaward and landward of UnitA2 incised into SB3 which postdates the formation of Unit A2 (Chapter 6). Thus, back-barrier conditions most likely existed during the deposition of Unit A2, as it did during the Holocene transgression when complex back-barrier systems developed with an estuary mouth/tidal inlet re-established in the same area (Sequence 4, Sections 6.3.4 and 6.4.3). During the Holocene this estuary mouth/tidal inlet linked the back-barrier estuary of seismic Unit Dl with the embayed back-barrier lagoonal system of seismic Unit Ds (Sections 6.3.4 and 6.4.3) until it was sealed by deposition of the Units B3 and B4 beachrocks (refer to Chapter 6, Section 8.3.4 and Chapter 9).

The Unit A2 palaeotopography was subsequently infilled during the Holocene by the deposition of the transgressive beachrock Units B3 and B4 resulting in the present appearance of Unit A2 as outcrop inliers surrounded by an extensive potholed wave-planed surface blanketed by lag deposits and sediments related to the Holocene transgression. In cliff sections it can be seen that Unit A2 aeolianites are unconformably overlain by beachrock deposits of Units B3 and B4 (Figure 8.11i and j; Figure 8.12a, d).

Unit A3 - The Plateau Aeolianites

Geomorphology

Unit A3 (Figure 8.7) or the Plateau Aeolianites (PLA) constitute the broad low relief and featureless morphological area referred to as the Plateau (Figure 7.2). It occupies ~509 565 m^2 of seafloor, is situated landwards of Unit A1 and A2 (except for the NW member of the NPA) and may extend beyond the study area (Figure 8.7).

Although, this plateau area is deeper (average depth of 19.5 m) and not along strike to the linear, coast parallel, Units A1 (average depth of 13 m) it still represents a shallow bathymetric feature. Unit A3 is characterised by a mostly flat rocky seafloor with extensive epifaunal growth (Figure 8.13e, f) interrupted by gullies and ledges formed by minor overhangs (<2m) and notches. Unconsolidated sediments occur as predominantly coarse grained reef derived bioclastic sediment concentrated as isolated ripple fields either on the rocky reef-base or in gullies and in localised

depressions. Lag deposits comprising oblate and prolate shaped pebbles including rhodoliths are common and mixed with the bioclastic-rich sediments (Figure 8.13f).

Although the seafloor morphology resembles that of the NPA northwest member (Figure 8.11g, h), the amount of sediment present is significantly less, indicating that this is an area generally starved of sediment. Unit A3 represents an extensive wave-planed aeolianite marine terrace with isolated remnants of eroded aeolianite forming higher relief outcrops. This type of morphology is very common on intertidal platforms found along the coastline (Figure 8.13g) and has also been well documented by Guilcher (1988) from Pleistocene reef systems.

Potholes and lag deposits are present at especially -16 m and -18 m on Unit A3 but these are not as well developed as those typified by the -26 m and -22 m isobaths on the seaward margin of the Aliwal Shoal. Although this might be an indication of the relative degree of reworking from the Holocene transgression and the relative duration of the sea-level occupation it can also be due to the differences in palaeo-environmental setting during the Holocene sea-level rise. As Unit A3 comprises a wave-planed terrace it must have been exposed to extensive erosion, the difference to the seaward margin is that the lag deposits were stranded predominately on the seaward margin unable to be transported onto the relatively higher topographic feature formed by Unit A3. In addition, it is likely that the contemporaneous lag deposits generated *in situ* during the erosion of the wave-plane surface and deposited on the flat intertidal platform would have been re-worked landwards as sea-level rise continued, except for those trapped in local basins such as gullies and potholes. This is supported by field observations of the localised occurrences of the lag deposits.

Sedimentary Structures and Features

Field observations on the macro-scale features of Unit A3 were very limited due to the subdued nature of the outcrop compared to Units A1 and A2, although some 2 - 3 m high rocky outcrops were exposed in an isolated area of high relief (Figure 8.7, near samples 5 - 7, GC-7). Primary sedimentary structures (Figure 8.13h to k) in Unit A3 were similar to that observed in Unit A1 and A2 comprising predominantly small-scale (<2 m), high-angle tabular planar cross-bedding (Figure 8.j and k) with parallel foresets ranging in dip from 14° to 25° and foreset thickness ranging from 5 cm to 20 cm. Rare cross-bed set thicknesses of 1 m were observed in the high relief areas. Comparably to the other aeolianite units, no palaeosol horizons or major erosional discontinuities were observed within Unit A3. An aeolian depositional environment is inferred for from the sedimentary structures although, the specific dune morphology is uncertain with the available data.

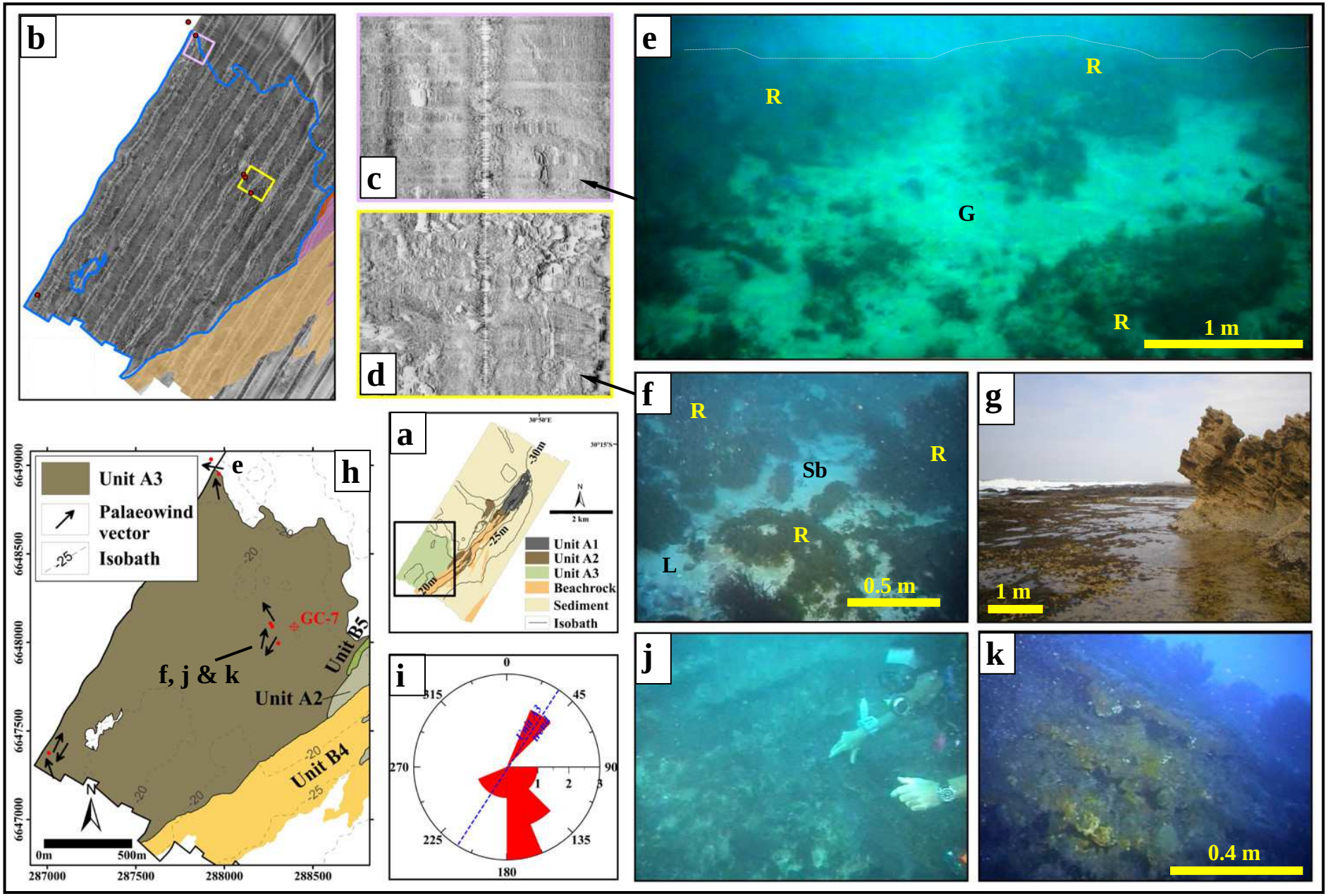
b
c
d
e
R
R
G
R
R
1 m
f
R
R
Sb
R
L
0.5 m
g
1 m
a
30°50'E
30°15'S
-30m
-25m
-20m
2 km
Unit A1
Unit A2
Unit A3
Beachrock
Sediment
Isobath
h
Unit A3
Palaeowind vector
Isobath
e
GC-7
f, j & k
Unit B5
Unit A2
Unit B4
N
0m
500m
6649000
6648500
6648000
6647500
6647000
287000
287500
288000
288500
i
0
45
90
135
180
225
270
315
1
2
3
j
k
0.4 m

Figure 8.13 (cont.) Acoustic, morphological and depositional features of Unit A3 or the Plateau Aeolianites. **a)** Locality map of the study area showing the various aeolianite units and the location of figures (b) and (h). **b)** 100 kHz side-scan sonar mosaic of Unit A3, colour boxes correspond to sonographs (c) and (d). Red circles = seafloor samples (for numbers refer to Figure 8.7). See (h) for scale. **c and d)** 100 kHz side-scan sonar sonographs of selected areas in (b) for comparison with photographs. Scale (width by height) = c) 135 x 151 m, d) 169 x 143 m. **e)** Underwater photographic mosaic of the seafloor in the vicinity of sample 67, -22 m. Note low relief rocky seafloor (R) with sediment and lag deposit filled gullies (G). **f)** Photograph of a small linear gully in between epifaunal growth covered aeolianite outcrops (R) in the vicinity of sample 7, ~ -16 m. Gully is filled with lag deposit (L) which again is mostly covered by bioclastic-rich sediment (Sb). Note the difference of the broad shallow gully morphology in the lower relief area of samples 66 and 67 compared to the narrow, deeper gullies from the higher relief area of samples 5 - 7 (Towering Inferno's, Figure 7.2). **g)** Intertidal platform at Treasure Beach (see Figure 3.1b for locality) south of Durban, cut into late Pleistocene aeolianite. Note the wave-planed platform with undulating low relief and isolated rugged relief eroded remnants of aeolianite. A similar morphological setting is inferred for the elevated region of Unit A3. High-angle planar foresets is visible in the aeolianite outcrop (equivalent of Cawthra's, 2010 Unit 1 Aeolianite; photograph courtesy of Mr Rio Leuci, view towards the SSE). **h)** Seafloor map of Unit A3 showing the dominant palaeowind vector distribution, Isobath levels are in 5 m intervals. Letters e, f, j and k indicate the localities for the correspondingly labelled photographs. Red dots = Unit A3 sample localities; refer to Figure 8.4 for sample numbers. GC-7 is the geochronological sample for Unit A3. **i)** Combined palaeowind rose diagram (22.5° bins) based on 12 strike and dip measurements taken from foreset beds of Unit A3. **j and k)** Underwater photographs of planar cross-bedded aeolianite foresets. For localities refer to (h), depths as follows (**j**) -13 m, (**k**) -17 m.

However, the variability of the small-scale foresets is representative of the parabolic dunes of Unit A2, although the outcrop morphology does not seem to resemble a parabolic form, unless the two parallel linear ridges (Figure 7.2) represent the two trailing arms, with the nose of the parabolic dune not preserved.

Palaeowind vector trends indicate deposition from primarily south-easterly (SE, SSE) and secondarily from north-easterly (NE) winds (Figure 8.13i). Additional minor vectors also include south-westerly and east-south-easterly components most likely related to palaeowind variability and some of which might be related to variation associated with the location of the measurement (Collison and Thompson, 1982). At present there is no equivalent wind distribution along the South African coastline that matches the palaeowind regime observed in Unit A3. However, Be and Duplessy (1976) analysed palaeoclimatic signals from foraminifera in a core obtained 500 km east of Durban and showed that the modern climatic conditions experienced along the east coast of South Africa are not representative of the late Quaternary, with present sea surface temperatures (SST) prevailing for only 1% of the last 540 ka.

The palaeowind distribution for Unit A3 shows similarities to that of Cawthra's (2010) Unit 2 Aeolianite, assigned a last interglacial age (MIS 5e) based on correlation to other work. Cawthra (2010) suggested that the last interglacial palaeo-climatic conditions under which her Unit 2 Aeolianite formed was associated with a SST 5° warmer than present, linking it to the present

conditions at Beira (Mozambique, 1200 km north of Durban) where south-easterly winds dominate, implying a southwards shift in climatic belts during MIS 5e.

Optical dating (Chapter 9) provided an age of 93 ± 6 ka cal. B.P. (GC-7, -16.4 m; Figure 8.13h) indicating deposition of Unit A3 on a sea-level regression during the MIS 5c warm stage, a period characterised by climatic and sea-level instability (See Chapter 9) following the maximum warmth of MIS 5e and cooler MIS 5d. As such the dunes would have been deposited at a time of relative warmth during an overall climatic deterioration possibly reflected in the variability of the palaeowind distributions (Figure 8.13i). It is therefore likely that the short-lived warmth of MIS 5c approximated climatic conditions of MIS 5e, typified by the predominance of the south-easterly wind directions but with the additional variability produced by the overall climate deterioration and instability. As such Unit A3, like the other aeolianite units, is also interpreted to indicate formation during a period of climatic transition characterised by variable palaeowind directions. However, whereas aeolianite Units A1 and A2 were deposited during an overall amelioration in climate, Unit A3 was formed during an overall climatic deterioration. It is interesting to note that the dunes developed during the transgression seem to be more prominent and better preserved than the dunes developed during the MIS 4 -2 regression towards the LGM.

Aeolianite Petrography

Composition and Texture

Unit A1 to A3 lithologies are remarkably similar in hand specimen and ranges in colour from light brown to off-white (Appendix IV). Rare conspicuous samples show red-brown colouration (Sample 41, Appendix IV) and a spotted-appearance related to diagenetic alteration (refer to diagenesis section below). Mineralogically there is minor distinction between the three aeolianite units mostly related to composition. On the whole the aeolianites exhibit a similar trend of variations in texture and composition, differing not only between aeolianite units but also within one unit. Detailed compositional and textural data for Units A1 to A3 are provided in Appendix V whilst a summary with average values are presented in Table 8.2.

The Aliwal Shoal aeolianites display a rock fabric comprising rounded to angular grains with approximately one point contact per grain all of which are set in carbonate cements showing several distinct phases. On average the three aeolianite units (A1 - A3) comprise moderately well sorted fine-skewed medium sand (Tables 8.2). Although not the typical parameters expected for a dune, the Aliwal Shoal values compares well to submerged aeolianite deposits (Ramsay, 1991) and to coastal aeolianite deposits (Bateman, *et al*., 2004, Frébourg *et al*., 2008, Roberts *et al*., 2008,

Carr *et al*., 2010 and Bateman *et al*., 2011). As grain size distributions reflect the influences of both the sediment source and the subsequent transport processes one might attempt to differentiate the depositional environments based on grains size distribution. Ramsay (1991, 1996) successfully applied depositional environment fingerprinting on offshore aeolianite and beachrock lithologies using discriminant analyses of grain size distributions. However, his study area had no direct fluvial input and hence no fluvial contamination so that he could assume that the sediment size distributions reflected the transport processes to such a degree that the effects of inheritance were removed. This same approach cannot be applied to the Aliwal Shoal samples due to the numerous fluvial systems present.

Nonetheless, sorting and skewness are useful textural parameters providing information on the transportation duration and processes. Better sorted sediments normally indicate longer transport and more homogeneous processes, whereas skewness values are linked to the influence of coastal processes (Leeder, 1982). Some broad grain size trends can be observed from the aeolianite units (Appendix V; Table 8.2). Unit A1 is a moderately well sorted, strongly fine-skewed medium sand with the upper Unit A1 showing a slightly finer grain size with better sorting (Table 8.2) relative to the lower Unit A1, possibly indicating longer transport processes. This is not unlikely as the sediment source varies for the two sub-units; upper Unit A1's sediment source is located northwards whilst that for the lower Unit A1 is located southwards and includes a nearby postulated estuarine/tidal outlet (Figure 8.12a) which could have provided the coarser grain sizes and due to its proximity, poorer sorting values.

The Unit A2 aeolianites on average comprise moderately well sorted medium sand and display the broadest range of textural parameters. This is most likely related to their unique depositional setting as a parabolic dune field within a coastal barrier system transgressing an estuarine mouth system with some dune deposition occurring within the back-barrier environment. Thus Unit A2 is associated with varied sediment sources (beach, fluvial and back-barrier) and transport distances. Units A1 and A2 show the finest and coarsest average mean grain size respectively, with Unit A2 also having the best average sorting value (Table 8.2).

Unit A3 is a moderately sorted medium sand, showing the lowest average sorting value for the aeolianite units. It has a similar sorting value to that of the NPA NWM (Table 8.2) which is interpreted as a dune deposited during the last deglacial sea-level rise within a back-barrier environment on top of a cuspate foreland which originated either due to a tidal-divide or coastal lake segmentation (refer to Section 7.2.1, description of the Spur feature). Sediments were thus most likely sourced locally from mainly the fluvial and reworked back-barrier sources with limited transport and/or by different processes.

Table 8.2 Textural and compositional data for aeolianite Units A1 to A3 obtained from petrographical analyses (Appendix V). GC-series samples are the representative geochronological samples for their respective aeolianite units (in brackets below). UW = Udden-Wentworth classification, Sk = skewness, Qtz = quartz, Fspr = feldspar, Lith Frag = lithic fragments, HM = heavy minerals (including pyroxene), Bio = bioclastic components (skeletal carbonate), Cmt Factor = cementation factor, SPA = Southern Parabolic Aeolianite, NPA = Northern Parabolic Aeolianites, BR = Bosman's Reef, NWM = north-western member, NEM = north-eastern member, AVG = average for all of the aeolianite units, A1u = upper Unit A1, A1lr = lower Unit A1, mS = medium sand, mWs = moderately well sorted, Ms = moderately sorted, Ws = well sorted, Sk = skewness, sfs = strongly fine-skewed, fs = fine-skewed, ns = near-symmetry, scs = strongly coarse-skewed. Also refer to Table 8.3 for a detailed summary of the aeolianite GC-series samples.

Unit	**Mean (phi)**	**UW**	**Sorting**		**Sk**		**Mineralogy (%)**					**$CaCO_3$ %**	**Cmt Factor**
							Qtz	**Fspr**	**Lith Frag**	**HM**	**Bio**		
Unit A1													
Upper	1.80	mS	0.61	mWs	0.50	sfs	50	3	2	2	42	60	1.4
Lower	1.67	mS	0.64	mWs	0.26	fs	57	3	2	2	35	57	1.7
Average	*1.74*	*mS*	*0.62*	*mWs*	*0.38*	*sfs*	*54*	*3*	*2*	*2*	*39*	*59*	*1.6*
Unit A2													
SPA	1.26	mS	0.62	mWs	0.41	sfs	61	15	7	3	15	49	3.5
NPA BR	1.52	mS	0.55	mWs	0.20	fs	67	12	5	5	11	50	5.0
NPA NWM	1.99	mS	0.44	Ws	0.33	sfs	54	13	5	3	25	54	2.3
NPA NEM	1.36	mS	0.74	Ms	0.76	sfs	56	17	3	6	20	50	2.6
Average	*1.53*	*mS*	*0.59*	*mWs*	*0.42*	*sfs*	*59*	*14*	*5*	*4*	*17*	*51*	*3.3*
Unit A3													
Average	*1.63*	*mS*	*0.80*	*Ms*	*-0.03*	*ns*	*58*	*21*	*2*	*6*	*13*	*46*	*3.6*
AVG	***1.63***	***mS***	***0.67***	***mWs***	***0.26***	***fs***	***57***	***11***	***4***	***4***	***24***	***53***	***2.8***
GC-series samples													
GC4 (A1u)	1.79	mS	0.65	mWs	0.31	sfs	47	3	1	3	46	70	1.5
GC5 (A1lr)	1.10	mS	0.74	Ms	0.16	fs	66	3	3	1	26	73	2.8
GC6 (A2)	1.13	mS	0.44	Ws	0.14	fs	76	7	8	2	8	47	6.0
GC7 (A3)	1.77	mS	0.82	Ms	-0.45	scs	62	20	1	3	14	53	3.8
Average	*1.45*	*mS*	*0.66*	*mWs*	*0.04*	*ns*	*63*	*8*	*3*	*2*	*24*	*61*	*3.5*

Microscopically, the aeolianites show a broad variety of depositional facies (Appendix V) comprising either heterogeneous or laminated sediment. Laminated sediments total approximately half of the aeolianite samples and are subdivided according to the scheme of Frébourg *et al*. (2008)

into the following types (Figure 8.14a - d); laminated inversely graded (Lig; pinstripe lamination), discreet laminae (Ldl), bimodal coarser/finer grained laminae (Lbl) and coarser isolated layers in heterogeneous sediment (Lci). Discreet laminae (Ldl) followed by bimodal coarser/finer grained laminae are the most common laminated facies with a noticeable complete absence of the laminated inverse grading facies (Lig) or pinstripe lamination. Frébourg *et al*. (2008) also observed the scarcity of pinstripe lamination, which is the diagnostic feature for climbing translatent wind ripples (Hunter, 1977). The general lack of microscopic sedimentary structures is most likely due to the skeletal carbonate components obscuring or even impeding formation of the fine pinstripe laminations characteristic of wind-blown sand.

The aeolianites are predominantly composed of quartz (41 to 76%; Table 8.2; Appendix V) and bioclastic fragments or skeletal carbonate (8 to 49%; Table 8.2; Appendix V), the latter alternating with feldspar (2 to 26%; Table 8.2; Appendix V) as the dominant secondary component (Figure 8.14). Other mineral components include heavy minerals (zircon, apatite and opaque Fe-Ti oxides) and lithic rock fragments comprising igneous and metamorphic constituents. Some pyroxene (Figure 8.14h) is also present especially in the landwards units such as A3 and the NPA NWM of Unit A2. Compositionally the Aliwal Shoal aeolianites are very different from those offshore Sodwana Bay (Ramsay, 1991, 1996; comprising 80 - 90% quartz) and the Durban Bluff (Cooper and Flores, 1991; comprising predominantly 73 - 78% quartz and 14 - 20% bioclastic grains). Unfortunately no quantitative compositional data were produced for the aeolianites offshore Durban by Richardson (2005) and Cawthra (2010). The Aliwal Shoal aeolianites have a characteristically high bioclastic component indicating a sediment source linked to a highly productive carbonate province.

Quartz grains are rounded to sub-rounded showing monocrystalline, polycrystalline and metamorphic or sheared varieties (Figure 8.14e). Feldspars comprise sub-rounded to sub-angular plagioclase and K-feldspar commonly showing twinning and alteration. Pyroxene, lithic fragments and sheared quartz reveal the proximity to a sediment source terrain which comprises supracrustal gneisses and pre- and syntectonic granitoids (Figure 3.1). Skeletal carbonate fragments show a range of faunal types which include varying proportions of molluscan, cirriped (barnacle), echinoid, coralline red algal, foraminiferal (miliolid, fusulinid, and rotalid forms) and bryozoan fragments (Figure 8.14a,b,f and g). The faunal assemblage is similar to that described by Siesser (1970) from coastal limestones in the southern Cape and that of Ramsay (1991, 1996) from submerged aeolianite and beachrocks offshore Maputaland.

Some broad mineralogical trend differences are observed in the various aeolianite units (Table 8.2, Appendix V). Unit A1 has an almost bimodal composition comprising quartz and bioclastic

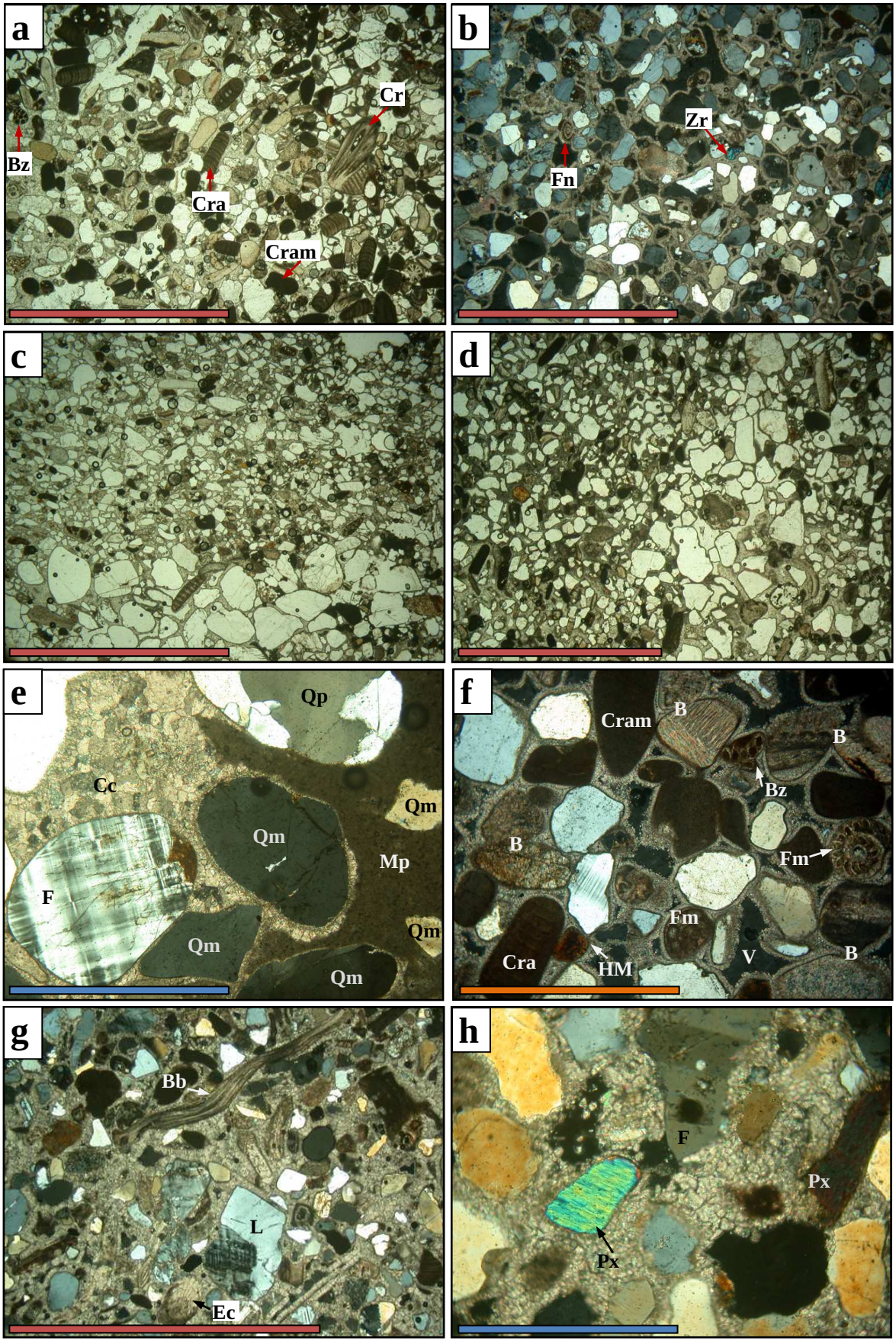

Figure 8.14 Selected transmitted light photomicrographs illustrating the petrographical characteristics of the Aliwal Shoal aeolianites. Coloured scale bars as follow; red = 5 mm, orange = 1 mm, blue = 0.5 mm. **a)** Plane-polarised light (PPL) photomicrograph of the Heterogeneous (H) microscopic facies, sample 2, -18 m,

Figure 8.14 (cont.) Unit A1. Illustrated fauna include bryozoan (Bz), coralline red algae (Cra), micritized or altered Cra (Cram) and cirriped (barnacle) fragment (Cr). **b)** Cross-polarised light (XPL) photomicrograph of the discreet laminated (Ldl) microscopic facies, sample GC-6, -24 m, Unit A2. Laminae are nearly vertical trending from top right to bottom left. Fn = nummulitid foraminifera. Zr = zircon. **c)** PPL photomicrograph of the bimodal coarser/finer grained laminae (Lbl) microscopic facies, sample 5, -14 m, Unit A3. **d)** PPL photomicrograph of the coarser isolated layers in heterogeneous sediment (Lci) microscopic facies, sample 57, -23 m, Unit A2. **e)** XPL micrograph showing the common terrigenous grains found in the aeolianites; rounded to subrounded monocrystalline quartz (Qm), polycrystalline quartz (Qp, with sutured crystal boundaries) and twinned microcline feldspar (F). Cc = calcite cement, Mp = pelleted micrite cement. **f)** XPL micrograph of the mineral and faunal assemblages of sample GC-4, -15.5 m, upper Unit A1 comprising mostly quartz and skeletal carbonate. Abbreviations as for (a) and Fm = miliolid foraminifera, B = bioclastic fragment (placed on touching bioclastic grains), HM = heavy mineral and V = void. **g)** XPL photomicrograph of sample 8, -20 m, Unit A2 SPA. Bb = bivalve fragment with foliated nature suggesting origin as an oyster (Adams and MacKenzie, 1998), L = lithic grain comprising quartz and feldspar and Ec = tangential section through an echinoid spine. **h)** XPL micrograph of sample 66, -26 m, Unit A3, showing subrounded to angular quartz, feldspar and pyroxene with minimal bioclastic components. Composition is related to the back-barrier depositional setting of this aeolianite unit dominated by fluvial input and with a limited marine input relative to Units A1 and most of Unit A2.

fragments, showing the lowest quartz and highest bioclastic component average values for the aeolianites. The upper Unit A1 shows an increase in bioclastic material and decrease in quartz relative to the lower Unit A1 (Table 8.3). The increased bioclastic component in the upper Unit A1 is largely due to a high coralline red algal content (13%; Table 8.3), but both the upper and lower Unit A1 has noticeably higher red algal values than the other aeolianite units (Table 8.3). Coralline red algae require hard substrates (Milliman, 1974) indicating the presence of a nearby rocky coastline during formation of Unit A1, indicating a source for the corallines to the south and north of Unit A1. Different sources for the red algae are supported by the different types of red algae occurring in the same thin section e.g. Figure 8.14f micritized and non-micritized forms.

Table 8.3 Composition of the aeolianite geochronological samples with subdivision of the skeletal carbonate components. CRA = coralline red algae, Forams = Foraminifera.

Sample	% CRA	% Bryozoan	% Forams	% Remaining bioclastics
GC-4 upper A1	13	2	1	30
GC-5 lower A1	7	1	1	18
GC-6 Unit A2	3	0	1	3
GC-7 Unit A3	2	1	1	10

Relative to Unit A1, Unit A2 shows increased average quartz (highest average) values, a significant decrease in the average bioclastic components, a significant increase in the average feldspar value and increased average values for heavy mineral and lithic fragments. Unit A3 displays the highest feldspar and lowest bioclastic component average values. In general, Unit A1 has a stronger marine sediment source signature due to the high values of bioclastic components, Unit A2 best represents a mixed sediment source with increased contribution from fluvial sources

and Unit A3 indicates comparably immature sediment (worst sorting value, Table 8.2) with the highest feldspar values and presence of less resistant minerals like pyroxene.

Individual and average carbonate content of the Aliwal Shoal aeolianites are much higher than that found by Ramsay (1991, 1996; 45 to 17%, average 32%) offshore Maputaland. It is however, similar to that found in coastal aeolianites from Cape Agulhas in the southern Cape by Bateman *et al*. (2004; 56 to 82%, average 67%) and Carr *et al*. (2010; 66 to 84%, average 75%).

Sudan (1999) from his work on the coastal dune and aeolianite cordon in Richards Bay (see Figure 3.11 for locality) concluded that; 1) the amount of bioclastic material within the dune/aeolianite indicates relative proximity to a marine source (i.e. the coastline) and 2) heavy mineral abundance indicates association with the beach. Based on the grain size and compositional trends the Aliwal Shoal aeolianites are interpreted to indicate aeolian deposition in a coastal barrier system in proximity to sediment delivered from the numerous sources including wave and longshore currents, deflation of beach deposits, reworking of washover and back-barrier deposits and fluvial input. For Units A1 and A2 the strongly onshore-directed sediment supply was due to a combination of a rapid sea-level transgression combined with onshore palaeowind regimes and longshore currents directly accessing the sediment source terrain. Unit A3 is also interpreted as a coastal aeolianite envisaged to have formed in a back-barrier environment, behind the pre-existing units of A1 and A2, with a more restricted sediment source that was not dominated by input from the littoral zone and where relatively limited transport processes were active.

Cementation

All of the aeolianite units display a very complex diagenetic history comprising numerous carbonate cement phases. Although the diagenetic pattern varies considerably, even on hand specimen scale, a general succession of the major carbonate cementation events in these aeolianites was established. Importantly, it was noted that samples from the inner parts of the GC sample series (geochronological samples) showed less marine cementation events (secondary cements) compared to the hand specimen samples. This is ascribed to the fact that the GC samples are much larger and sampled fresher aeolianite material as opposed to the hand specimens taken from the outer 'crust' of highly weathered aeolianite. Generally the outer surface of aeolianite shows far more decementation than the fresher interior (Figures 8.5c and 8.15c) and could thereby theoretically document more diagenetic changes due to increased porosity. As a consequence, the interpretation of the fundamental diagenetic sequence and patterns will be based on the GC samples from each of the respective aeolianite units with supplementary examples from the hand specimen samples to illustrate variation. In addition, this approach also allows for better correlation with the age data (Chapter 9).

Aeolianite primary interparticle porosity varies from 10 to 40% (Appendix V) with the secondary cement-reduced porosity values decreasing significantly to 5 to 20%, suggestive of the well-cemented character of these deposits. The open uncompacted nature of the aeolianites is typical of sediment that underwent considerable early diagenesis (Adams and McKenzie, 1998). The degree of cementation of a sample was expressed as a proportion dividing the carbonate content by the percentage of bioclastic components, a higher value indicating better more pervasive cementation of the sample (Table 8.2). The results indicate that the cementation of the aeolianites varies and that on average aeolianites are better cemented relative to the beachrocks (Table 8.8).

Fundamentally, all the aeolianite units display a cementation history involving a pattern comprising initial meteoric (mostly phreatic) cementation followed by cement erosion and porosity development which is then followed by up to 6 phases of marine cement precipitation (Figure 8.15). The patchy appearance imparted to some of the hand specimens is the macro-scale result of the variable distribution of low porosity zones containing the original sparite cement and higher porosity zones with later marine cements (Figure 8.15a). In addition, some samples do not display the patchy appearance but still exhibit the same fundamental diagenetic sequence but on a micro-scale. The cementation succession of the GC-series samples is presented in Table 8.4.

Table 8.4 Summary of the diagenetic sequences from the GC-series samples. Numbered cement phases corresponds to those in the text. Also see Appendix VI for the $MgCO_3$ mole % values for the marine cement phases.

Sample	**Meteoric Cement(s)**	**Marine Cement(s)**
GC-4 Unit A1	Phases 1 and 2 present	Clear isopachous bladed marine cement (phase 6) , 20 to 40 µm in thickness
GC-5 Unit A1	Phases 1 and 2 present	Poorly developed micritic coating (phase 3) and cloudy isopachous bladed marine cement (phase 4), 20 to 40 µm in thickness, some late stage void-infill comprising pelloidal micrite (phase 8)
GC-6 Unit A2	Phase 2	Poorly developed micritic coating (phase 3) and radial fibrous isopachous marine cement (phase 7), 40 to 80 µm in thickness
GC-7 Unit A3	Phase 2	Cloudy isopachous bladed marine cement (phase 6), 20 to 40 µm in thickness

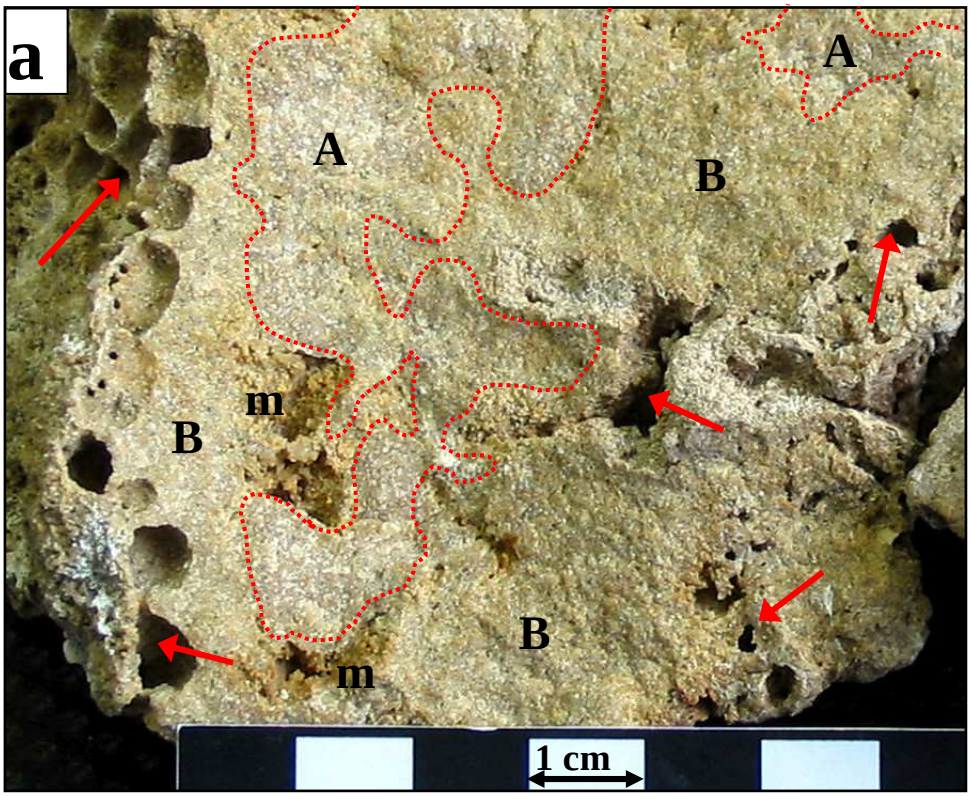
a
A
A
B
m
B
B
m
1 cm

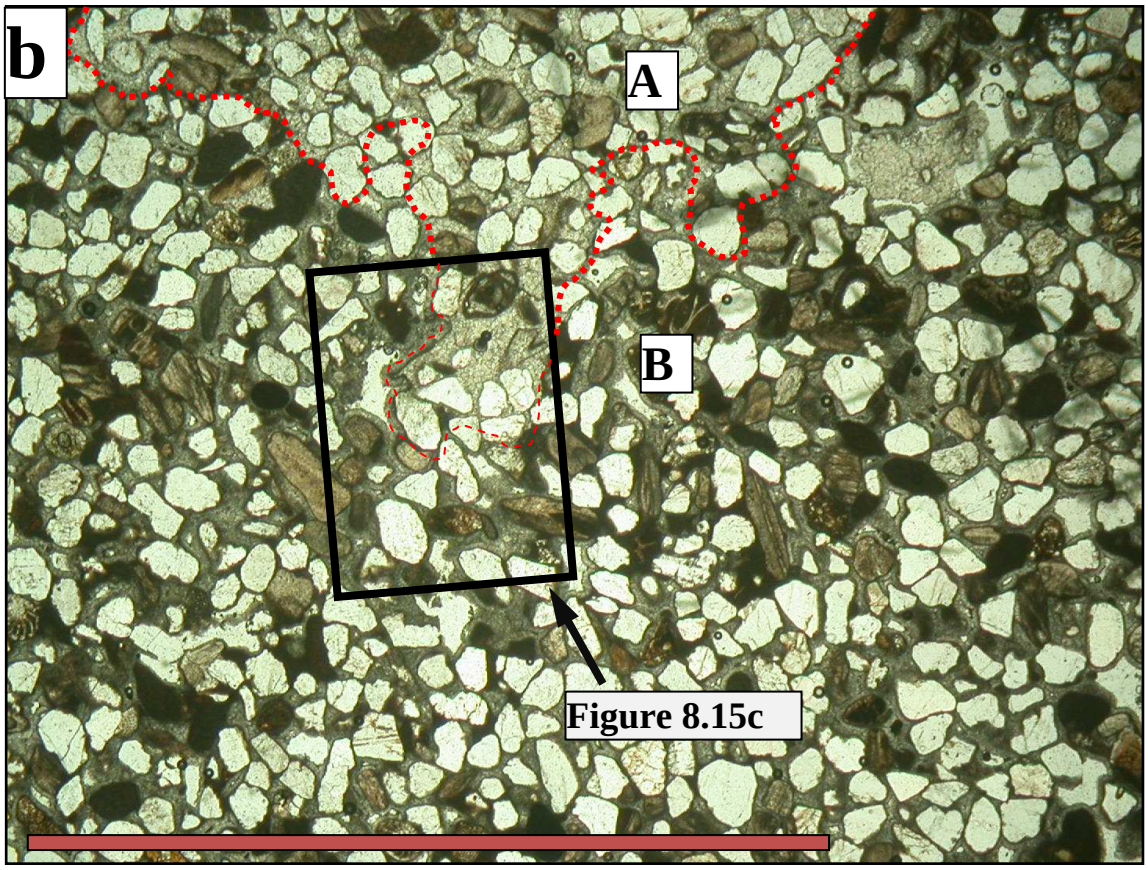
b
A
B
Figure 8.15c

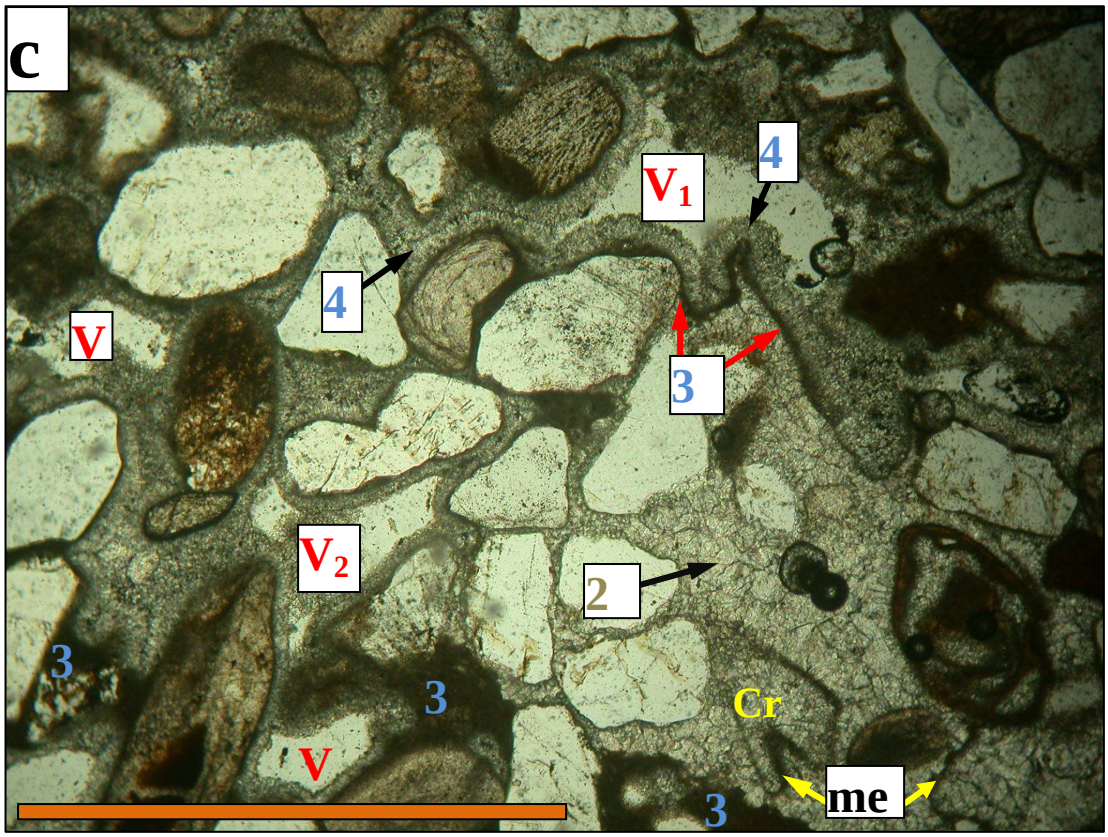

	Diagenetic Stages		
	1	2	3
Cement phase	Meteoric 1 → 2	Erosion & porosity increase —//→	Marine 3 → 4 → 5 → 6 → 7 → 8
GC-series samples	1, 2		6 (3), 4, (8)
	2		(3), 7 6
Hand specimens	(1) 2		(3), 4 or 6, (8) 3, 4, 5, 6, (8) (3), 7, (8)

d

Figure 8.15 Illustration of the fundamental diagenetic sequence and cementation history for the aeolianites. **a)** Hand specimen showing patchy appearance comprising lighter well cemented zones (domain A) and darker more porous zones (domain B). Note biologically-attacked outer surface with borings that also penetrate the samples (red arrows), m = discoloured and stained zones linked to late stage (phase 8) micrite

Figure 8.15 (cont.) cement, sample 35, -18 m, Unit A1. **b)** Transmitted light (PPL) micrograph of the same sample as in (a) showing the domains of A and B (approximately separated with red dashed line). Black rectangle indicates position of (c), scale bar = 5 mm. **c)** Higher magnification transmitted light (PPL) micrograph of the area in (b) showing the morphology and features of the various cement phases (numbers) that characterise the three diagenetic stages. Domain A comprises LMC spar (cement phase 2) which coarsens towards the pore centre and shows dissolved bioclastic grains (Cr = cirriped fragment) with micritc envelopes (me). Note that domain A is completely cemented. Domain B is observed to comprise increased porosity zones filled with at least two phases of marine cements (phases 3 and 4, with possibly phase 5 present). The junction of domain A with B is characterised by an erosional surface, coated in this example by a variable thickness micritic cement (phase 3). Note that the micritc coated irregular erosional surface cuts across both the cement (phase 2) and component grains of domain A (pointed out by the red arrows) indicating that domain A was eroded before cement phases 3 and 4 were precipitated. Cement phase 3 is not always present and shows variable morphologies including a thin coating on the erosion surface and thicker deposits between grains. Cement phase 4 is a cloudy isopachous bladed to fibrous HMC cement showing polygonal sutures and compromised boundaries. Similar cements phases in GC-5 yielded $MgCO_3$ values of 13.6 mole% (Appendix VI, Table VI.1). The phase 4 cement is thicker in larger void spaces (compare the cement thickness in V_1 with V_2). V = void/pore space, scale bar = 5 mm. **d)** Graphical illustration of the various cement phases (1 to 8) and diagenetic stages (1 to 3). Cement phases in brackets indicate variability in the presence of that phase. The illustrated sequences for the GC-series samples correspond from top to bottom to GC-4 to GC-7, also compare with Table 8.4. The cement sequences observed from the hand specimen samples are highly variable with only the more common examples shown.

Phase 1cement is a very thin (<10 µm) coating of scattered rhombic or bladed low-magnesium calcite (LMC) crystals which is typically followed, uninterruptedly, by a second phase consisting of bladed or equant spar (also LMC ; Figure 8.16) which coarsen towards and mostly fill the pore spaces (drusy mosaic). The type of cement morphology shown by phases 1 and 2 (Figure 8.16) is typical of the active meteoric phreatic zone (Longman, 1980, Scoffin, 1987; Tucker and Wright, 1990), although the scattered rhombic crystals of phase 1 may also form in the vadose zone (Longman, 1980; Gardner and McLaren, 1994). The predominance of the phase 1 cement within aeolianite units (GC-4 and 5; Unit A1) which have an established proximity to the beach might indicate that the phase 1 cement possibly has its origins as a LMC cement associated with sea spray (McLaren, 2001).

Phase 2 cement is characteristic of early meteoric phreatic diagenesis (Bathurst, 1975; Longman, 1980; Tucker and Wright, 1990). This interpretation of early pervasive phreatic meteoric cementation is further supported by characteristic meteoric phreatic zone features (Scholle, 1978; Longman, 1980; Scoffin, 1987; Tucker and Wright, 1990; Adams and MacKenzie, 1998) which include syntaxial overgrowths on echinoid spines (Figures 8.16f) and the complete replacement of grains with unstable mineralogies (aragonite and high-magnesium calcite) by calcite spar leaving only a micritic envelope (Figures 8.15c, 8.16f and 8.17a,c). The phase 1 and 2 sparry calcite cement is primary and not neomorphic spar as it fulfils the criteria developed by Bathurst (1975) to distinguish between void-filling cement and neomorphic spar (Table 8.5).

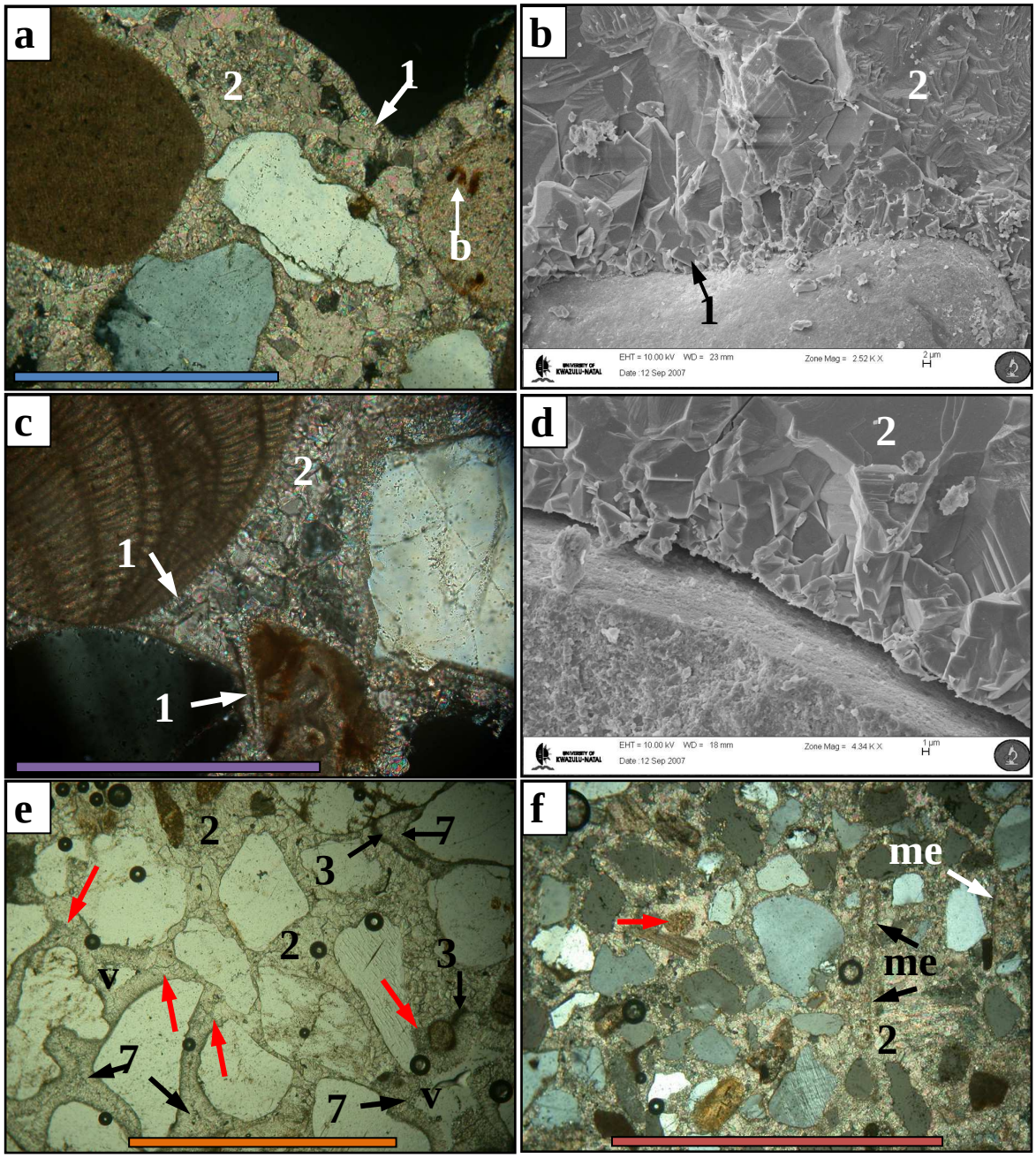

Figure 8.16 Selected examples of the meteoric cements (phases 1 and 2) of diagenetic stage 1. Coloured scale bars as follows; red = 5 mm, orange = 1 mm, blue = 0.5 mm, purple = 0.25 mm (250 µm). **a)** Transmitted light (XPL) micrograph of the phase 1 and 2 cements in GC-4 (-15.5 m, Unit A1). Note the coarsening of the crystal size of phase 2 towards the pore centre and general well-cemented nature with low primary porosity, b = borings within a bioclastic fragment. **b)** Scanning electron microscope (SEM) image of cement phases 1 and 2 in GC-4 (-15.5 m). Note the small intermittent crystals of cement phase 1 and the calcite cleavage planes in phase 2. Scale bar at bottom of image is 2 µm. **c)** High magnification transmitted light (XPL) micrograph of the phase 1 and 2 cements in GC-5 (-29.5 m, Unit A1). **d)** SEM image of the meteoric cement phase in GC-5. The separation between the grain surface and cement is due to fracturing during sub-sampling for SEM analysis. Scale bar at bottom of image is 1 µm. **e)** Transmitted light (PPL) micrograph of the cement phases in GC-6 (-25.8 m, Unit A2). The cement sequence is 2-(3)-7, refer to text for detailed explanation of the cement phases. Note that phase 3 is intermittently developed and in some instances the marine cement (7) grows directly onto the meteoric cement (2), these areas are indicated with red arrows. Note polygonal sutures in cement phase 7 and secondary porosity (V). Also compare the diagenetic history with that in Figure 8.15. The dark thick-rimmed circles predominantly found in the top left sector of the micrograph are air bubbles produced during thin section production. **f)** Transmitted light (XPL) micrograph of the cement phases in GC-7 (-16.4 m, Unit A3). Characteristic meteoric phreatic features include syntaxial overgrowth on echinoid fragment (red arrow) and replaced metastable skeletal grain fragments with preserved micritic envelopes (me).

Table 8.5 Criteria distinguishing a calcite intergranular cement from neomorphic spar (based on Bathurst, 1975 and Tucker and Wright, 1990).

Criteria	Void-filling cement	Neomorphic spar
1	Lacks relict or ghost structures	Relict ghost structures diagnostic
2	Sharp crystal boundaries to void edge	Boundaries diffuse
3	Crystals do not cut across grain boundaries	Crystals commonly transgress grain boundaries
4	Crystals increases in size towards pore centre	Crystal size is random with patchy distribution
5	Crystal boundaries straight	Crystal boundaries irregular
6	Crystals relatively clear	Crystals often cloudy with impurity rims

In the Aliwal Shoal aeolianite units, some grains are observed to undergo replacement (Scholle, 1978), also termed dissolution (Adams and MacKenzie, 1998) not to be confused with neomorphic replacement (calcitization). Dissolution is the process whereby the original skeletal grain with the unstable mineralogy is completely dissolved by undersaturated fluids and the subsequent void filled by sparry calcite. Commonly the shell outline is preserved by the micritic envelope (Figures 8.15c, 8.16f and 8.17a,c). Most micritic envelopes are produced by a process of microbial micritization (Bathurst, 1966) whereby a bioclast (skeletal fragment) are bored around the margins by endolithic algae, fungi and bacteria and the holes subsequently filled by fine-grained cement or sediment (Adams *et al*., 1984; Tucker and Wright, 1990). However, Siesser (1970) observed micritic envelopes coating terrigenous grains in aeolianites and beachrocks and suggested that micritic envelopes can also be formed as a by-product of an organism's own biological processes, whereas more recently Viera and Ros, (2007) ascribed it as a product of supersaturation of the pore waters. Micritic grain coats on terrigenous grains are also observed in the Aliwal Shoal samples (Figure 8.15c) comprising a cement following the phase 1 and 2 LMC cements (see cement phase 3 below) and rare coatings interpreted to be inherited from before the sediment was transported from the marine environment and accumulated as a coastal dune. The latter type of micritic coating is indicative of a short transport from the beach to the dune environment, further supporting observations of the relative proximity of the aeolianites to the coastal zone (see previous section).

The order for replacement of skeletal material (Bathurst, 1975), applicable to the biogenic assemblages in this study is: molluscs > pelagic foraminiferids > beach foraminiferids > larger foraminiferids > echinoids > coralline algae. Interestingly, the sequence is not controlled just by mineralogy (although aragonite is the most susceptible) but also by other factors such as wall structure and the presence of $MgCO_3$ (Bathurst, 1975). This is exemplified by the coralline algae having the highest content of $MgCO_3$ and being thus highly soluble but being the least susceptible

(Bathurst, 1975), an observation also supported by the field evidence of, especially the upper Unit A1 aeolianite, showing high concentrations of coralline algae (Figure 8.14a).

In all of the aeolianite lithologies a period of cement dissolution, decementation and an associated increase in porosity followed cement phases 1 and 2 (Figure 8.15d). This is generally represented by increased void spaces between the grains and a truncation surface developed on the phase 1 and 2 calcite cements. The dissolution surface is typically coated with a very thin dark coating, referred to here as a micritic coating or cement phase 3 (Figures 8.15c, 8.16e and 8.17a). In some instances the dissolution surface is not well represented and the subsequent marine cement seems to grow directly on the previous meteoric cement phase (Figures 8.16e and 8.17a), yet in other examples the micritic coating resembles more a void-fill morphology (Figure 8.15c). Although the coating on the erosional surface is named a micritic coating its chemical composition is not certain and as such the possibility that it might also represent a chitonic rim (pedogenetic cryptocrystalline cement; Frébourg *et al*., 2008) cannot be discarded. However, the origin of a chitonic rim is not favoured as the micritic coating is almost always followed by a marine cement and it is unlikely that a meteoric vadose zone cement will be directly followed by a marine phreatic zone cement (Longman, 1980). Thus the dark micritic coating comprising cement phase 3 is interpreted as a marine cement.

Additional marine cements follow the micritic coating (cement phase 3) showing variability in morphology and often represented by a number of successive phases. However, the GC-series samples only show the micritic rim cement (phase 3 - mostly absent) and one subsequent phase of marine cement (Figures 8.14f and 8.17e, f, g). The marine cement phases in the GC-series samples are all high-magnesium calcite (HMC) in composition and range from 8 - 22 mole% $MgCO_3$ (ascertained by SEM-EDX; Appendix VI, Table VI.1), typical for cements precipitated in the marine (Folk, 1974; Longman, 1980; Scoffin, 1987; Tucker and Wright, 1990) or possibly mixed (Folk, 1974; Csoma, 2004) diagenetic environments. The marine cement phase of GC-6 (Figures 8.16e and 8.17e,f) shows much higher Mg-values compared to the isopachous bladed to fibrous cement morphologies for the other aeolianites samples (Appendix VI, Table VI.1).

Five marine cement phases are recognised in the hand specimen samples in addition to the phase 3 micritic cement (Figure 8.17).

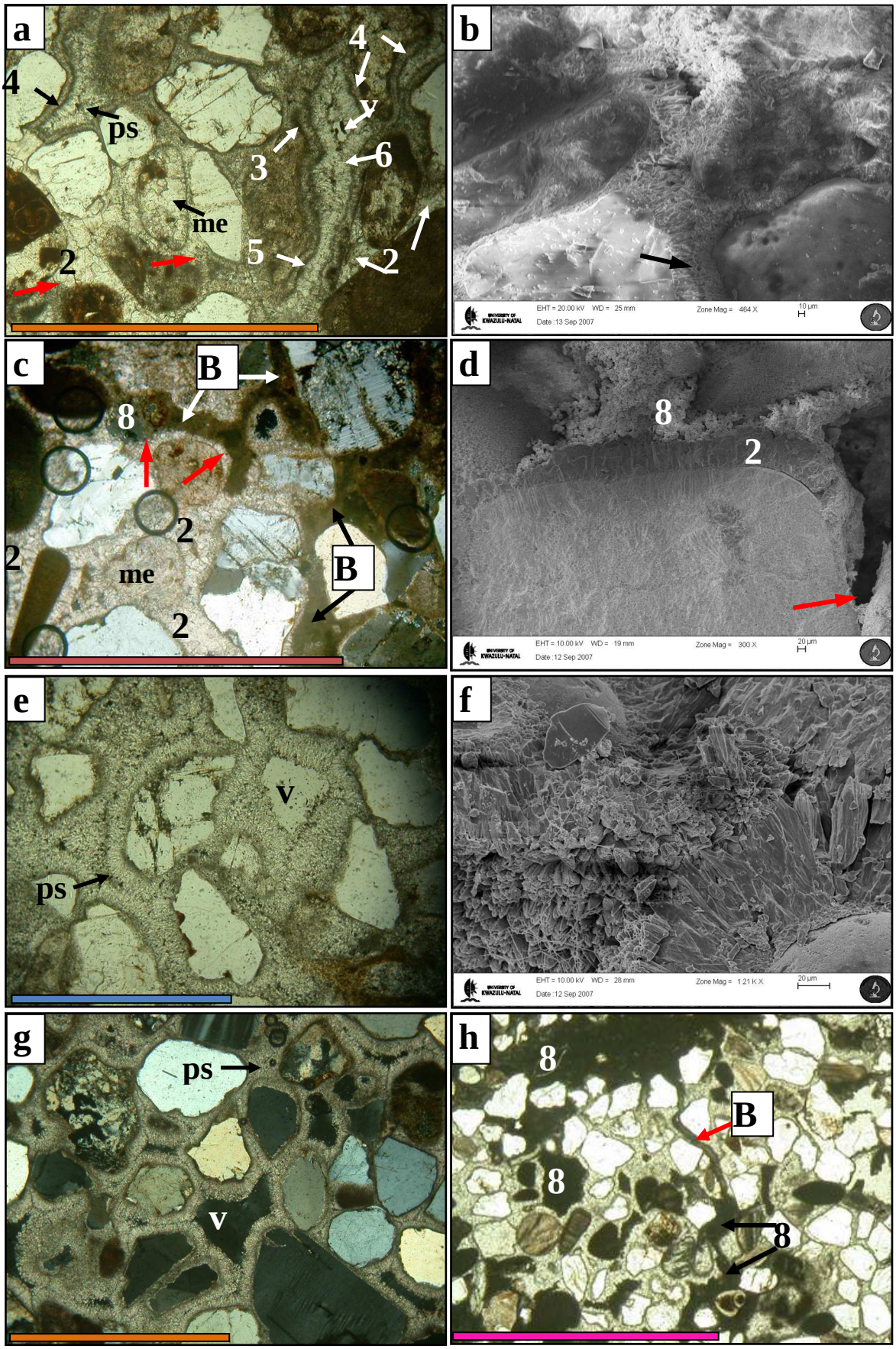

Figure 8.17 Examples of the late stage pore-lining marine cement phases of diagenetic stage 3. Coloured scale bars as follows; red = 5 mm, magenta = 2.5 mm, orange = 1 mm, blue = 0.5 mm. **a)** Transmitted light (PPL) micrograph of the multiphase marine cements preserved in some samples (sample 55, -15 m, Unit A1). Note that the cement sequence is 2-3-4-5-6. In some areas the marine phase 3 cement is absent resulting

Figure 8.17 (cont.) in phase 4 growing directly (red arrows) on the irregularly distributed remnants of phase 2, me = micritic envelope and V = void representing secondary cement reduced porosity. **b)** SEM image of GC-4 (-15.5 m, Unit A1) showing the single phase of marine cement (6). Note the polygonal suture where the isopachous cements meet (arrow). For an equivalent micrograph refer to Figure 8.14f. Scale bar at bottom of image is 20 µm. **c)** Transmitted light (XPL) micrograph of the result of boring by sponges in GC-5 (-29.5 m, Unit A1). Note the network of borings (B) resulting in a pseudo-isopachous morphology of the phase 2 cement (red arrows), borings are filled with phase 8 micrite. Similar features also present in Figure 8.14c **d)** SEM image of GC-5 showing cement erosion (red arrow) resulting in a pseudo-isopachous morphology of cement phase 2, followed by void-fill with pelloidal micrite of phase 8. Scale bar at bottom of image is 20 µm. **e)** Transmitted light (PPL) micrograph of the radial flute morphology of cement phase 7 in GC-6 (-25.8 m, Unit A2). Note micritic coating in some of the terrigenous grains, me = micritic envelope and V = void representing secondary cement reduced porosity. **f)** SEM image of GC-6 showing the marine cement in (e). Note the radiating composite fluted crystals similar to that observed in the HMC cements of beachrock Unit B3 (Figure 8.28). Scale bar at bottom of image is 20 µm. **g)** Transmitted light (XPL) micrograph of the marine cement (phase 6) in GC-7 (-16.4 m, Unit A3). Also shown are polygonal sutures (ps) forming compromised boundaries and voids representing secondary cement reduced porosity (V). **h)** Transmitted light (PPL) micrograph showing a bored conduit (B) linking two areas of phase 8 pelloidal micrite (sample 40, -12 m, Unit A1).

These five marine cement phases include a cloudy bladed to fibrous druse (cement phase 4; ranging from 15 - 50 µm in thickness), a thin irregularly developed micritic rim (cement phase 5), a clear bladed to fibrous druse (cement phase 6; ranging from 25 - 120 µm in thickness), a less common bladed to fibrous radially fluted even druse (cement phase 7; ranging from 80 - 160 µm in thickness) and a late stage void-fill micrite mostly pelloidal (cement phase 8). The sequence of marine cements following the phase 1 and 2 meteoric cements are highly variable but some rock samples shows a continuous sequence of cements from phase 1 to 8 (Figures 8.15 and 8.17a) but excluding cement phase 7. The radially fluted cement phase 7 only occurs rarely and then in the absence of cement phases 4, 5, 6 and with 8 sometimes present. The relationship of phase 7 to phase 6 is not certain but phase 7 seems to show much higher mole% $MgCO_3$ (GC-6, Table 8.4; Appendix VI). Also, the two bladed to fibrous cement phases (4 and 6) are not always present, predominant (Figure 8.15). Cement phase 5 is only developed when cement phase 6 is present. Available pore size seems to have an influence on the thickness of the isopachous (even druse) cements with thicker crusts observed in the larger pore spaces generally related to coarser component grain sizes (Figure 8.15c). In addition, the isopachous phases 4 and 6 and especially phase 7 cements commonly show polygonal sutures forming compromised boundaries (Figure 8.15c, cement phase 4). Regular straight sutures suggest cement formation in the active marine environment (Longman, 1980). Cement phase 8, or the last micritic phase (Figures 8.14e and 8.17c, d, h) is predominantly found in hand specimen samples from the shallower reef areas and interpreted as a biologically-generated modern cement related to the bio-erosive action of mainly encrusting sponges (see Figures 8.8k and 8.11f). Coudray and Montaggioni (1986) noted that rock-boring sponges produce an intensive network of galleries which can penetrate several centimetres into rock expressed in thin section as borings filled with micrite. Sponge borings filled with micrite cement resembling those observed from the Aliwal Shoal (Figures8.14e, 8.15a, 8.17c, d and h) is also presented by Scholle (1978; page 184).

In addition, only GC-5 shows the presence of the stage 8 void-fill cement which is related to the position of the thin section close to the outer surface. Thus, the lack of cement phase 8 in the fresher GC-series samples further supports a biological origin related to surface bio-erosion of the submerged aeolianites.

In summary, the cement succession or diagenetic sequence in the Aliwal Shoal aeolianites preserved three major events; 1) meteoric vadose and phreatic cementation followed by 2) cement erosion, decementation and porosity development which is finally followed by 3) the deposition of numerous marine cements with original marine composition (Figure 8.15d). The timing of formation of these carbonate cement phases is further discussed in Section 8.3.5.

8.3.4 Aliwal Shoal Beachrocks

Five different beachrock units (Figure 8.18) were identified within the study area based on morphology, field relationships, sedimentary structures and geochronological analyses (Chapter 9). Beachrock units were not as extensively covered by the ground-truth surveys as the aeolianites and this is illustrated by comparing the amount of samples viz; 28 beachrock samples versus the 50 aeolianite samples. Nonetheless, each of the beachrock units was sampled and with the exception of Unit B4, all have a representative GC-series sample (Figure 8.18; Appendix IV). Although beachrocks can change facies along strike (Viera and De Ros, 2006; Vousdoukas *et al.*, 2007; this study) the mapped beachrock depositional environment is interpreted at the relevant sample location so that the beachrocks can be corrected for their indicative meaning (see Appendix XIV and Chapter 9) and consequently plotted on a sea-level curve (Chapter 9). All the beachrocks, except Facies 2 of Unit 4 and Unit B5, conforms to the classic definition of beachrock (Bricker, 1971a) insofar being deposited and cemented in the inter-tidal nearshore zone, ranging from the berm/swash zone to low tide terrace/welded bar environments). Seismic data show that Units B1 to B3 overlie unconsolidated sediments (Section 6.3.4, Figures 6.7 - 6.8), whilst Units B4 and B5 are mainly deposited over pre-existing aeolianites units.

Geomorphology and Sedimentology

Outcrop pattern and dip and strike readings of the beachrock units are illustrated in Figure 8.18 whilst field observations of sedimentary structures and subsequent depositional environmental

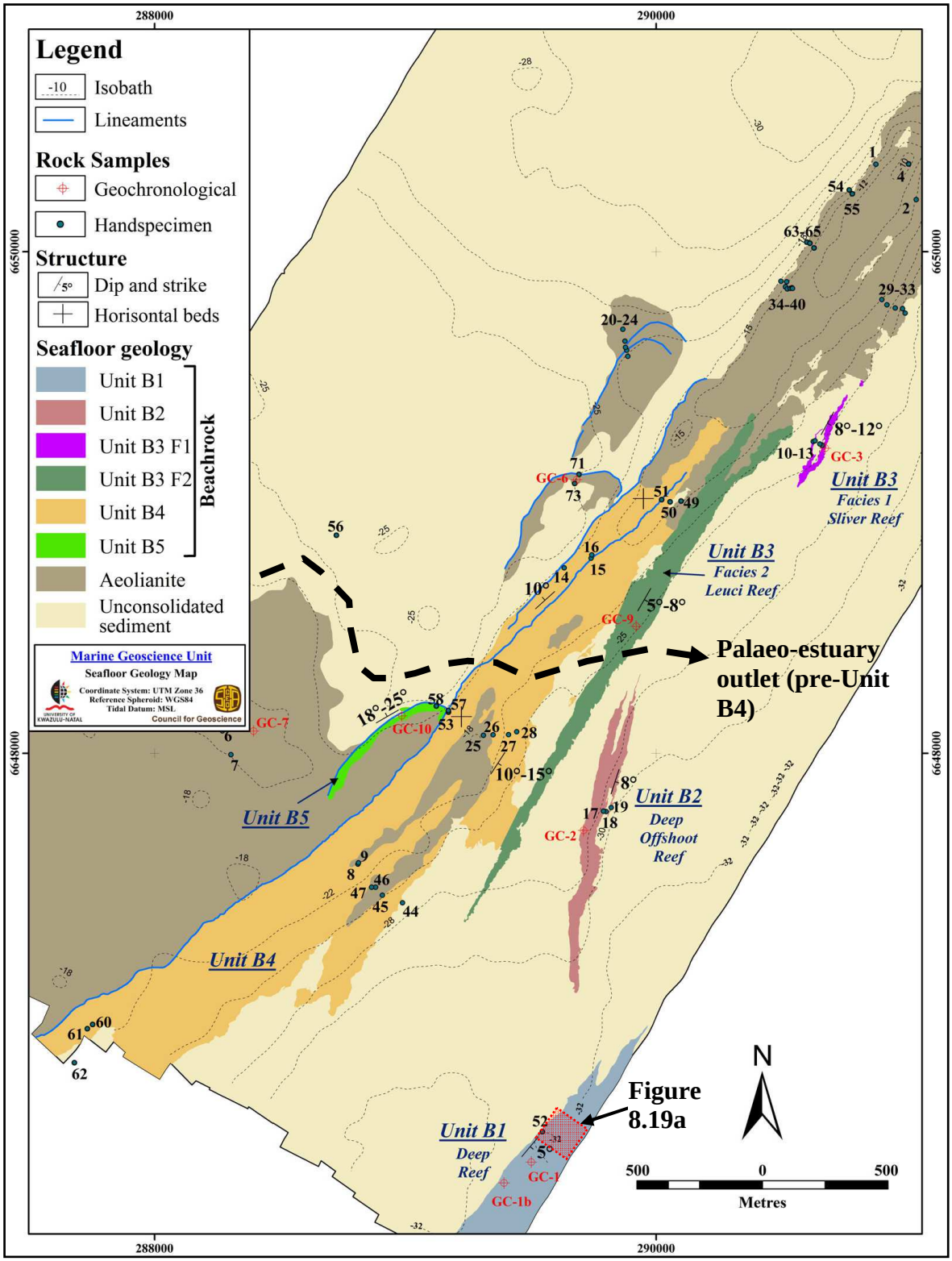

Figure 8.18 Simplified geological map of the study area showing beachrock Units B1 to B5. Note that the beachrock units occur predominantly seaward or on the aeolianites, except for Unit B5 which is landward of the SPA of Unit A2 (also see Figure 8.12). Also note that the isobaths are not in constant intervals. B3 F1 and B3 F2 refer to Facies 1 and 2 of unit B3.

interpretations are summarised in Table 8.6. Also refer to Appendix IV for sample positions (Table IV.1) and imagery (Table IV.2). Acoustically the beachrock outcrops produce a moderate to low reflectivity with a subdued microtopography and linear blocky to granular patterns (Figures 8.2; 8.11b, d) which can be distinguished from surrounding unconsolidated sediments and the more rugged relief aeolianites (Figure8.2; also see Sections 8.2 and 8.3.3). Interpretations of the sedimentary structures and depositional environments are based on comparison to the work of Cooper and Flores (1991) which studied the mainly Pleistocene MIS 5 stranded shoreline deposits (beachrocks and aeolianites) that comprise an overall transgressive-regressive sequence at Isipingo beach (Figure 8.6b, c). Their work showed that the coastal conditions in the Pleistocene were similar to the modern conditions, including that of the high wave energy, microtidal regime (palaeo-tidal range of 2 m) and actual beach morphological states. None of the Aliwal Shoal beachrock units are observed to directly overlie one another and as such combined with the age data (Chapter 9) indicate a backstepping facies arrangement sequentially formed during the Holocene transgression (Table 8.6). This is in agreement with suggestions by Cooper (1991) that rapid sea-level rise cause breaks in between bands of beachrock outcrop and that the early formation of beachrock favours overstepping during a transgression.

Table 8.6 Summary of the geomorphology, sedimentary structures, interpreted depositional environments and age for the beachrock units. The depth of beachrock units are expressed as an average or an averaged range.

Unit	Depth & size		Depositional sedimentary structures	Interpreted Depositional Environment	OSL age (ka cal. B.P.)
B1	33 m 183835 m^2		Horizontal to low angle (<5°) planar bedding defined by HM-rich laminae, seaward dip	Foreshore, possibly swash or upper surf zone	11.0 ± 0.67 to 10.6 ± 0.59
B2	29 m 72988 m^2		Planar bedding with low angle seaward dip defined by coarser laminae, shows grain imbrication	Forebeach slope or swash zone	10.2 ± 0.52
B3	184359 m^2	26 m	Facies 1: Planar beds with a 8° - 12°seaward dip (20 - 40 cm thick) with poorly defined cross laminae between the bedding surfaces defined by coarser grain sizes	Foreshore, possibly forebeach slope or swash zone	9.8 ± 0.56
		26 m	Facies 2: Planar beds with a 5° - 8°seaward dip, cross laminae between the bedding surfaces defined by HM	Foreshore, possibly between the swash and surf zones	9.9 ± 0.59
B4	1031008 m^2	~25 to 22 m	Facies 1: Planar bedding with HM laminae showing low-angle seaward dip	Foreshore; possibly swash or upper surf zone	<9.8
		<22 to ~ 18 m	Facies 2: Planar bedding, horizontal to low-angle (<8°) landwards dip, HM laminae	Backshore, possibly berm to backbeach?	
B5	24 m 1454 m^2		Planar steeply dipping beds with parabolic form in plan-view	Barrier overwash	79 ± 5

Unit B1

Unit B1, or *Deep Reef* is the deepest beachrock outcrop (-33 m) occurring in the extreme south-east corner of the study area comprising a low relief blocky outcrop covered with sediment and epifaunal growth (Figure 8.19a to c). The blocky nature of the outcrop is related to dissection of the beachrock by two joint set orientations (010°/190° and 130°/310°). Seisser (1974) also observed jointing in beachrocks from the southern Cape coast and noted that normally two directions of jointing are present one parallel and one perpendicular to the coastline. The jointing or fracturing of the beachrocks is caused by wave under-cutting (Ramsay, 1991) an observation confirmed more recently by Bezerra *et al*. (2005) from Brazil. Lag deposits comprising discoidal pebbles are present between the scattered beachrock outcrops mixed with finer grained sediments (Figure 8.18c).

Primary sedimentary structures comprise planar beds (bed sets <20 cm in thickness) with a horizontal to low-angle seaward dip (<5°) observed from the top bedding surface or dip-slope. In hand specimen the bedding is defined by alternating light and dark mineral laminae, the dark laminae comprising heavy minerals (Figure 8.19d). On average Unit B1 comprises well sorted strongly fine-skewed medium sand (Tables 8.6). With the available data a foreshore depositional environment is envisaged for Unit B1, with possible deposition in the lower swash or upper surf zone within what Clifton *et al*. (1971) term the inner and outer planar facies. According to Elliott (1986) the low seaward dip, parallel lamination comprising alternating darker (finer) and lighter (coarser) layers is characteristic of the internal structures in foreshore facies.

Due to the nature of the outcrop accurate measuring of the thickness of Unit B1 was not possible, but it is estimated at 2 - 3 m. On the seismic profile (Figure 6.9) Unit B1 is not resolved (except for its characteristic acoustic blanking) indicating its thickness is below the resolution of the seismic tool (~4 m) and/or there is no velocity-density contrast between the beachrock and subjacent unconsolidated sediment. However, Unit B1 was an important coastal feature and forms a prominent nick point on the seafloor (Figure 6.9b, c). Two OSL ages (GC-1 and GC-1b, -33 m) indicate deposition of Unit B1 from 11.0 ± 0.67 to 10.6 ± 0.59 ka cal. B.P.

Unit B2

Unit B2 or *Deep Offshoot Reef* is a narrow (90 m wide) ~1.3 km long linear beachrock outcrop located north-west of Unit B1 between the depths of 27 and 31 m (Figure 8.18). It has an approximate north-south orientation which differs from the other NE-SW or coast-parallel trending beachrock units. Unit B2 itself shows variance in strike with the northern half of the outcrop

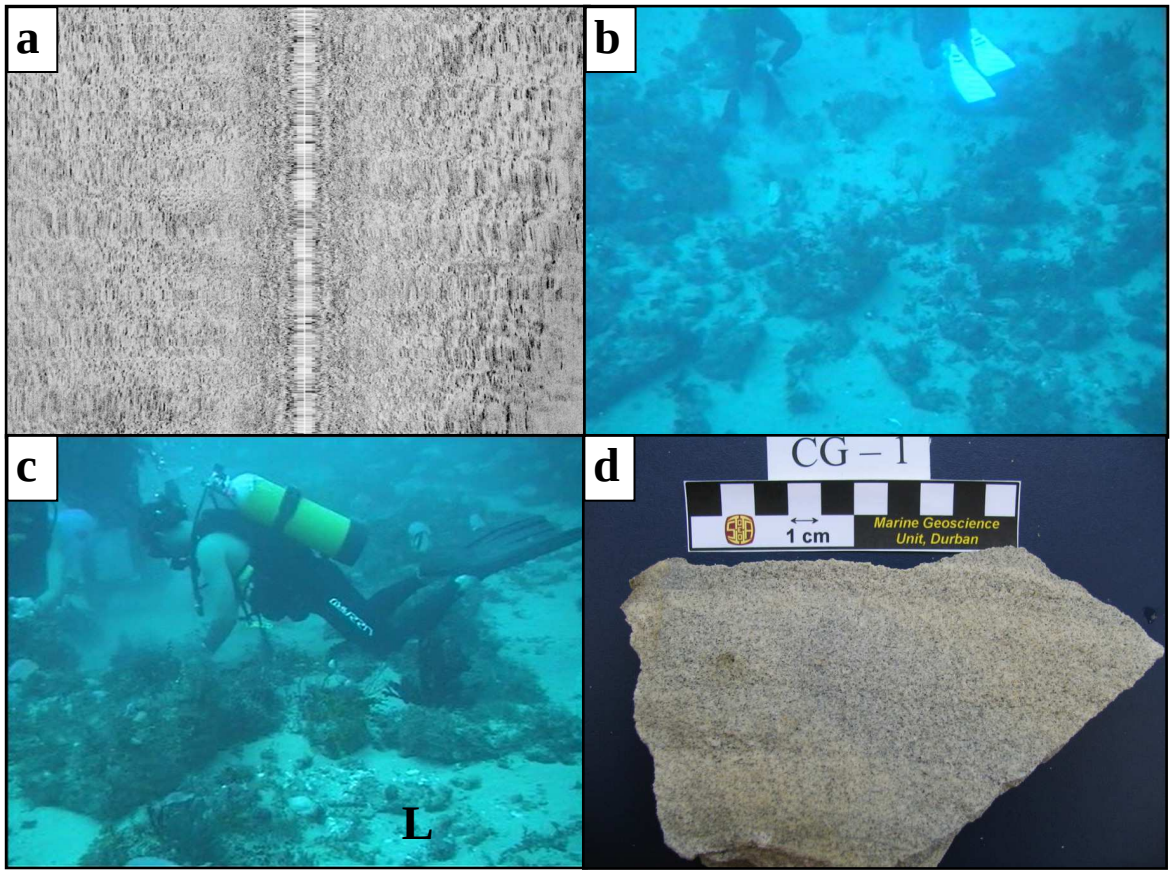

Figure 8.19 Underwater images of beachrock Unit B1. **a)** 100 kHz side-scan sonar sonograph showing the typical acoustic response of Unit B1 consisting of a low relief blocky outcrop. Locality is shown on Figure 8.18, scale (width by height) = 164 x 161 m, **b and c)** Underwater photographs of Unit B1 in the vicinity of sample 52 (-32 m). Note the sediment (c) comprising a mixed population of discoidal lag deposits (L) and medium sand. **d)** Sub-sample of GC-1 (-33 m) showing the alternating light and dark mineral laminae.

striking more NNE-SSW relative to the southern N-S trending sector (Figure 8.18). The Unit B2 outcrop is essentially flat with the exception of the reef top and reef margins that show localised microtopography. Both the seaward and landward reef margin exhibit block (also known as slab) slumping (Figure 8.20a, b), which is a characteristic feature of onshore exposed intertidal beachrocks (Figure 8.20c). Block or slab dimensions is controlled by joint sets which again are caused by wave undercutting and subsequent gravity collapse (Guilcher, 1988; Ramsay, 1991, 1996; Bezerra *et al*., 2005). The outcrop is jointed with two prominent joint sets striking 010°/190° and 105°/285° (Figure 8.20d, e). A variable thickness sediment veneer with small sediment-starved oscillation ripples and epifaunal growth covers the top surface of the outcrop (Figure 8.20).

Overall Unit B2 represents a low-angle (8°) seaward dipping surface. In hand specimen and in the geochronological samples planar lamination is defined by couplets of alternating coarser and finer grain sizes (Figure 8.5b) which sometimes show grain imbrication (Figure 8.20g) and seemingly

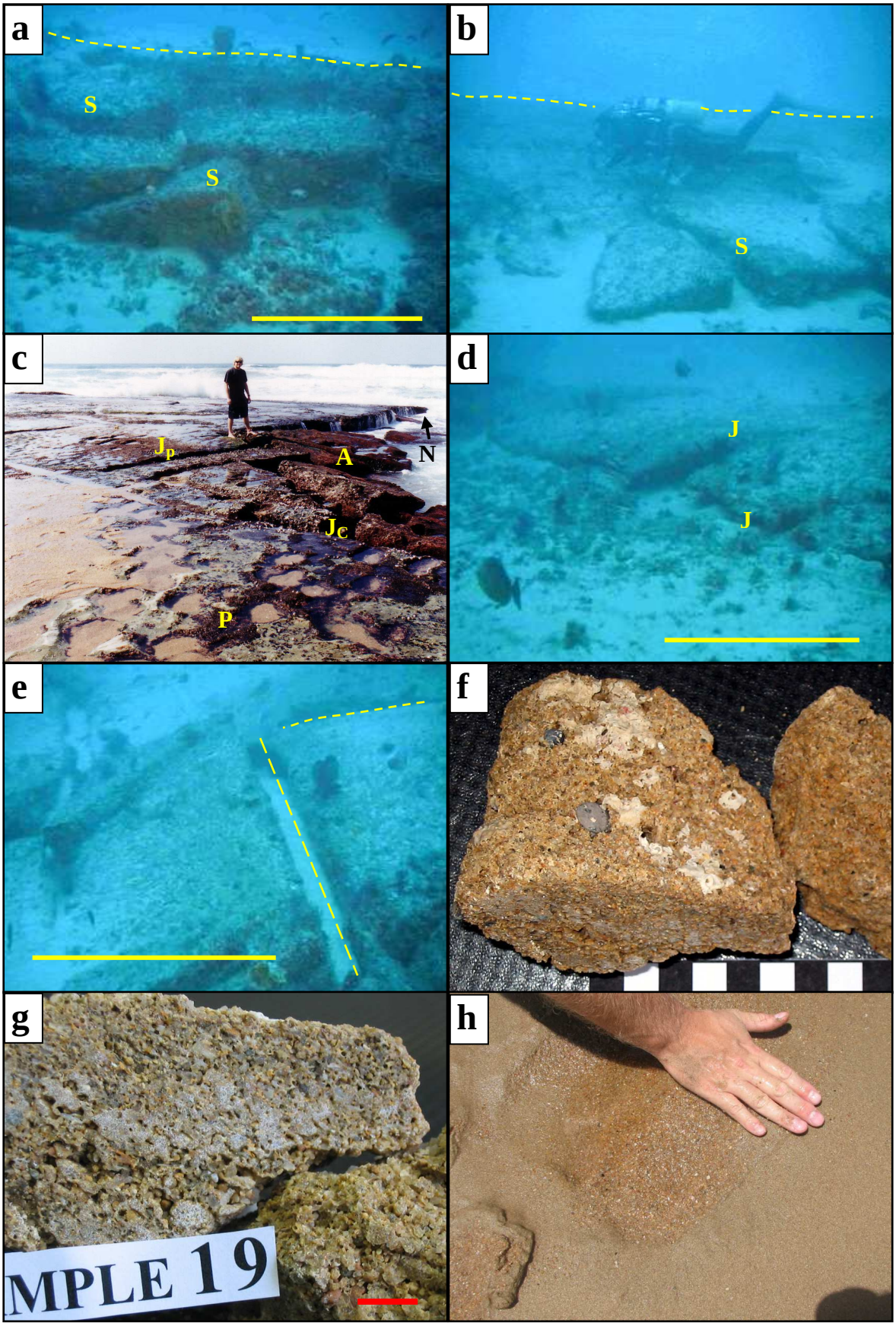

Figure 8.20 Features and characteristics of beachrock Unit B2. **a and b)** Underwater photographs of the block slumping observed from the seaward (a) and landward margin (b) of Unit B2. Dotted line indicates the reef top, S = slumped block, scale bar = 1 metre. **c)** Intertidal platform at Peace Cottage Beach, North of Durban. Note coast parallel (Jc) and coast perpendicular (Jp) joint sets, collapsed slabs

Figure 8.20 (cont.) (A) of beachrock due to wave under-cutting, present sea-level notch (N) and potholes (P). **d and e)** Block or slab dimensions are controlled by joint sets (d) and slumping (e) is caused by wave under-cutting. J = joint, dotted line = joint traces on slump blocks, scale bar = 1 metre. **f and g)** Hand specimen sample 19 (-27 m) showing the isolated discoidal pebbles (f) and grain imbrication (g; trending from top left to bottom right). Scale bar in (f) is graduated in 1 cm intervals and in (g) red scale bar = 1 cm. **h)** Photograph of the swash zone at Scottburgh beach, directly onshore of the study area. Note the normal grading with the upper layer of finer material scraped away to reveal the underlying coarser layer. Compare with hand specimen 18 in Figure 8.5b.

normal grading. Occasional individual discoidal pebbles are also found (Figure 8.20a, f). Based on these sedimentary structures and features the depositional environment for Unit B2 is interpreted as the forebeach slope or swash zone. Directly onshore from the study area at Scottburgh beach (Figure 1.1) the swash zone resembles Unit B2 and shows normal grading (Figure 8.20h), seaward dip and occasional large pebble or shell. This is also consistent with the interpretation of Facies 5 of Cooper and Flores (1991) which showed similar sedimentary structures and features deposited in a similar coastal setting.

In addition, Unit B2 is interpreted to represent the eroded remnants of a palaeo-zeta (or log-spiral) bay, with Unit B1 forming the associated headland. This interpretation is supported by the OSL age data (GC-2, -29 m) which indicates a depositional age of 10.2 ± 0.52 ka cal. B.P. for Unit B2, thus only slightly post-dating Unit B1. A submerged remnant palaeo-zeta bay was also observed by Ramsay (1991, 1996) from the Sodwana Bay continental shelf and more recently offshore Richards Bay between ~ -55 to -65 m (Ramsay, *pers. comm*).

Unit B3

Unit B3 comprises two separate beachrock outcrops named Sliver Reef and Leuci Reef occurring between the depths of ~26 to ~22 meters (Figure 8.18). These are considered lateral equivalents but with slightly different textural, mineralogical and possibly depositional parameters and assigned to Facies 1 (Sliver Reef) and Facies 2 (Leuci Reef) of Unit B3 (Figure 8.18). Facies 1 or Sliver Reef is located to the northeast of Facies 2, re-attains the NE-SW coast-parallel orientation, is surrounded by sediment and has low microtopography except for the reef margins which show block slumping according to the two joint set orientations (Figure 8.21a). The exposed landward margin of the reef seems to be thinner then the seaward margin (Figure 8.21b) but this is probably due to sediment being banked against the landward margin. The reef top is essentially flat and covered with epifaunal growth and a variable thickness of rippled sediment organised into sinuous to straight crested oscillation ripples showing interference patterns (Figure 8.21c). The presence of low relief epifaunal growth on the beachrock substrate suggests a fairly low sediment input onto the reef (Figure 8.21c).

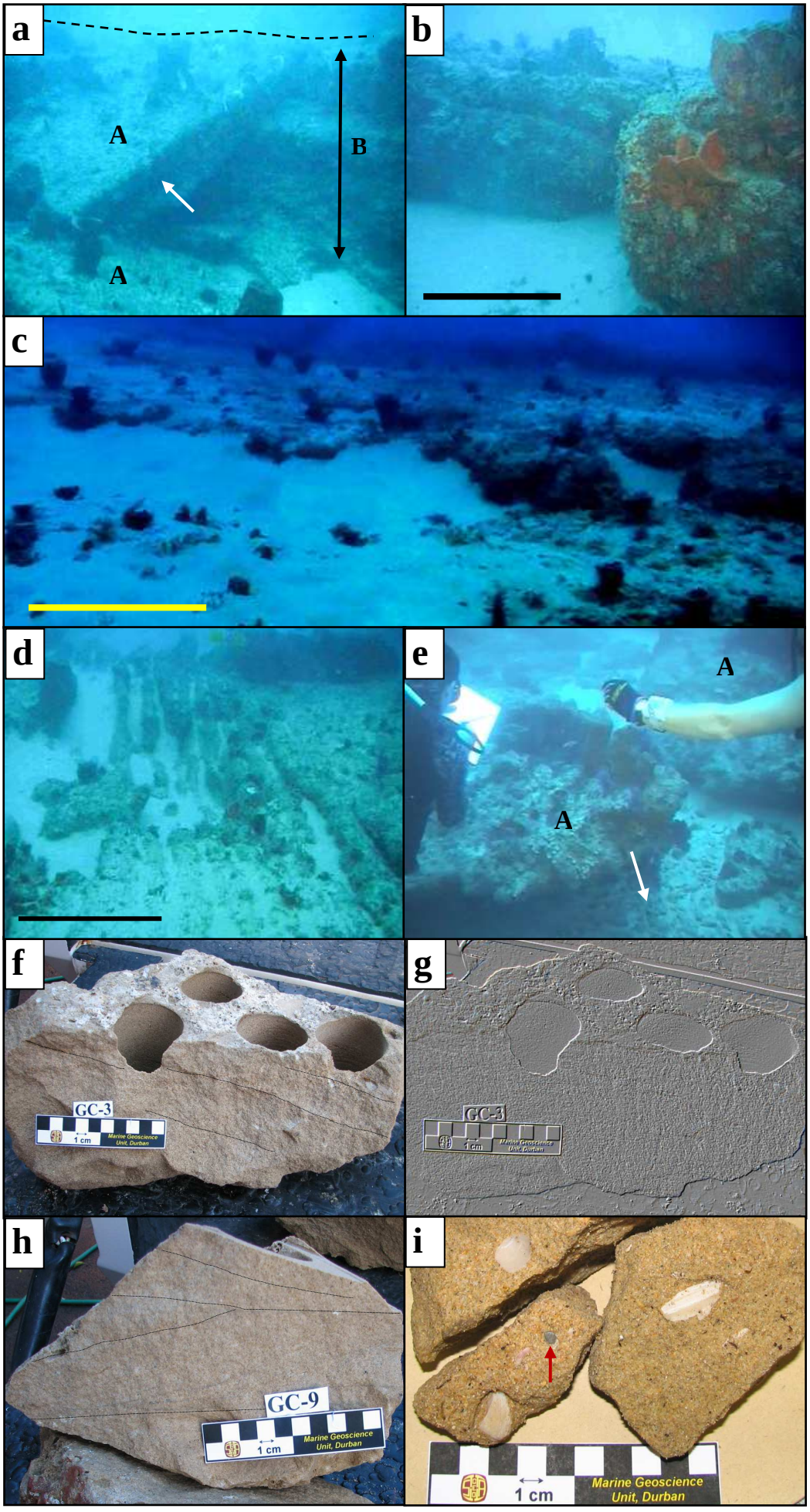
a
A
B
A
b
c
d
e
A
A
f
GC-3
1 cm
Marine Geoscience Unit, Durban
g
GC-3
1 cm
Marine Geoscience Unit, Durban
h
GC-9
1 cm
Marine Geoscience Unit, Durban
i
1 cm
Marine Geoscience Unit, Durban

Figure 8.21 (cont.) Features and characteristics of beachrock Unit B3. **a)** Underwater photograph of the seaward margin of Unit B3 Facies 1 showing flat reef top (dotted line), collapsed blocks (A) and primary planar bedding (white arrow). Outcrop thickness (B) is ~2 metres (black arrow). **b)** Underwater photograph of the thinner landward margin of Unit B3 Facies 1 showing primary bedding. Note the low-angle seaward (to the right) dip of the top surface and banking of sediment against this margin. Scale bar = 1 metre. **c)** Wave-planed top surface of Unit B3 Facies 1 showing the low microtopography, variable sediment thickness and epifaunal growth. Scale bar = 1 metre. **d)** Ridge and runnel structures observed on the landward fringe of Unit B3 Facies 1 and parallel to the margin of the reef. Scale bar = 1 metre. **e)** Collapsed blocks (A) and sediment (white arrow) comprising a mixed population of discoidal lag deposits (L) and medium sand. **f)** GC-series sub-sample of GC-3 (-26 m) showing planar bedding of Unit B3 Facies 1. **g)** Same image as in (g) but digitally enhanced to emphasize the bedding. **h)** GC-series sub-sample of GC-9 (-26 m) showing the cross-bedding defined by heavy mineral laminae. Only some of the bounding surfaces are traced so as to not obscure the laminae but still to show the general structure. **i)** Sub-samples of GC-3 showing the occasional shell fragment and discoidal pebble (arrow).

Erosive structures observed include ridge and runnel structures, coalesced potholes and reef margin collapse. Ridge and runnel structures parallel to the margin (Figure 8.21d) occur on the landward fringe of the outcrop and are typically formed on the landward side of intertidal platforms by the erosive (mechanical and chemical) action of run-off water draining the intertidal platform (Ramsay, 1991, 1996; Miller and Mason, 1994). A lag deposit comprising discoidal pebbles and cobbles are mixed with medium sand and banked on the seaward margin (Figure 8.21e). The aforementioned erosional features viz; slab slumping, ridge and runnel structures and potholes suggest that Sliver Reef comprised an intertidal platform shortly after deposition and cementation and before subsequent total submergence.

Facies 2 or Leuci Reef is parallel and along strike to Facies 1 (Figure 8.18), is a low relief linear beachrock outcrop trending NE-SW and is bounded on the seaward side by sediment and on the landward side by Unit B4. Interestingly, the Leuci Reef beachrock outcrop does not show the slab slumping of its margin, although it is most likely buried under sediment as the two typical joint set patterns (parallel and perpendicular to the outcrop trend) are present on the outcrop. Nonetheless, overall it seems that Facies 2 has not seen the same degree of post-lithification erosion as was the case for Facies 1. The reason for this is not certain although it might be related to the slightly different depositional settings occupied by the two facies; Facies 1 was located closer to a rocky coastline (Unit A1) and Facies 2 in proximity to a estuarine opening. These different settings might have influence local parameters differently during beachrock deposition.

Facies 1 and Facies 2 also show some variance in their sedimentary structures. On outcrop scale both exhibit planar bedding with a low-angle seaward dip (Facies 1 = 8° - 12°; Facies 2 = 5° - 8°), but only Facies 1 show bed thickness which ranged from 20 - 40 cm for individual beds. In the hand specimen and GC-series samples both facies displayed interbedded planar and cross lamination (Figure 8.21f to h), although the planar and the cross lamination is dominant in Facies 1

and 2, respectively. In Facies 1 the seaward inclined planar beds comprise fine lamination of alternating coarser and finer minerals (Figure 8.21f, g) whereas the cross-lamination Facies 2 is defined by heavy mineral laminae which are asymptotic to the base which may indicate trough-cross beds (Figure 8.21h). In addition, Facies 1 showed the presence of occasional shell fragments (Figure 8.21i). Based on the available data Facies 1 and 2 are interpreted to have been deposited in the intertidal environment. The planar dominated beds (Facies 1) showing the occasional shell fragment is probably indicative of a more forebeach slope or swash zone (similar to Facies 5 of Cooper and Flores, 1991) whereas the through-cross and planar laminated Facies 2 were possibly more representative of a nearshore occasionally intertidal setting between the swash and surf zones possibly in a low-tide terrace. The two facies of Unit B3 are thus linked to lateral facies variation deposited in similar depositional environments.

Optical dating (Table 8.6; Chapter 9) indicates deposition of Facies 1 at 9.8 ± 0.56 ka cal. B.P. and Facies 2 at 9.9 ± 0.59 ka cal. B.P. The depositional ages for these two facies are well within error of each other, although Facies 2 has an older central age. As the respective geochronological samples for the two facies were from the same depth, the age data support the postulation that these two facies are lateral variants of each other - formed at approximately the same time but in slightly different environments. Interestingly, if the central ages are accurate the swash zone (Facies 1) established later than the earlier intertidal setting (Facies 2) possibly indicating localised beach progradation to the north.

From a coastal evolution perspective Unit B3 represents two major changes in the coastal configuration at the time. Firstly, it signifies the change from the log-spiral bay coastal configuration established by Units B1 and B2 to a linear coastline orientation controlled by the trend of the pre-existing aeolianite units. This change in the morphology of the coastline is also documented by the shape of the underlying transgressive ravinement surface (reflector TRS, Figure 6.16) which again was controlled by the subjacent sedimentary basin fill architecture and subsequent transgressive shoreline trajectory (Section 6.4.3, Sequence 4, Figures 6.15 to 6.16). Secondly, it is envisaged that Unit B3 marks the beginning of the closure of the southern outlet of the back-barrier estuarine system (Unit Dl, Sections 6.3.4 and 6.4.3) located landwards of the Aliwal Shoal ridge. The southern opening of the estuary connected the seaward embayed back-barrier lagoonal system of Unit Ds to the back-barrier estuarine system of Unit Dl and is interpreted to have been established since ~11 ka cal. B.P. (Table 6.4). Unit B3 was deposited seawards and across the estuary opening which must have been followed shortly afterwards by Unit B4. These two units do not display a break in outcrop related to possible fluvial breach which indicates that the shoreward directed sediment transport during the transgression was sufficient to allow for deposition and cementation of the beachrock units and subsequent estuary mouth

closure. This supports a rapid sea-level rise and subsequent drowning of the estuarine system as suggested in Section 6.4.3, Sequence 4 (Table 6.4 and associated discussion).

Unit B4

Unit B4 comprises the bulk of the beachrock that directly overlies aeolianite Unit A2 (Figure 8.22a). It is parallel to Units B1 and B3, infills the aeolianite palaeo-topography, is bounded in the west by a prominent NE-SW trending ledge (Figure 8.22b) and in the east by sediment and Unit B3 (Figure 8.18). To north Unit B4 pinches out against the NPA of Unit A2 (Figure 8.12a) and seems to continue to the south beyond the limits of the study area (Figure 8.18). Morphologically B4 forms an extensive potholed wave-planed surface blanketed by epifaunal growth, lag deposits and sediments related to the Holocene transgression. No optical age is available for Unit B4, whilst the whole rock radiocarbon age on sample 27 provides a Holocene age but is considered precise but not accurate due to old carbon contamination (see Chapter 9).

Unit B4 is the most laterally extensive beachrock unit but limited sample cover and possible lateral facies variability combined with a lack of robust chronological control did not allow for a detailed interpretation. Nonetheless, a broad pattern was observed whereby the seaward margin of B4 showed planar bedding with a seaward dip (mostly <10° but up to 15°) and the landward margin showed horizontal to low-angle (<15°) landward inclined planar bedding. Both these domains showed heavy mineral laminations with thicker laminations observed from the landward margin. Unit B4 can thus tentatively be divided into two facies (Figure 8.18) with the seaward Facies 1 possibly representing deposition in a foreshore environment and the landward Facies 2 representing possible deposition in the berm or backshore environment. The boundary between the facies is based on the limited sample coverage and bathymetry but otherwise completely interpretative and mainly extrapolated. However, the subdivision is supported by the limited sample material (Table 8.7; Figure 8.22c to d).

In the absence of evidence to the contrary, the facies association is interpreted to possibly indicate that Unit B4 represents a continuous palaeo-beach system ranging from the intertidal zone (Facies 1) to the backbeach (Facies 2). Although, this is only a preliminary interpretation and must be confirmed by further sampling and dating, it does support the observation of a rapid sea-level transgression following Unit B3 to finally close the estuary mouth (see above). To this extent the sea-cliff, forming the western boundary of Unit B4, is interpreted to have initially formed the original landward diagenetic boundary of Unit B4. This was subsequently exploited by the rising sea-level and eroded into the ledge feature with ample slump blocks located on its landward margin.

Table 8.7 Summary of supportive features for the twofold facies subdivision for Unit B4.

Facies 1		**Facies 2**	
Sample and sedimentary features	Depositional interpretation	Sample and sedimentary features	Depositional interpretation
<u>Samples 44 and 27</u> 1) low-angle seaward dip, planar lamination with alternating light and dark minerals(heavy minerals), 2) textural and compositional parameters different from Facies 2 but very similar to Unit B1, 3) 44 and 27 are the only other samples that show acicular aragonite cement which has only been observed from Unit B1	Forebeach, possibly swash or upper surf zone	<u>Sample 8</u> 1) horizontal planar lamination, 2) planar-type fenestral voids - considered reliable indicators of upper intertidal and supratidal deposition (Coudray and Montaggioni, 1986)	Backshore; possibly upper intertidal to supratidal zone
		<u>Sample 16</u> 1) planar lamination with low-angle landward dip, 2) inverse grading - interpreted to be indicative of backbeach and other wash-over deposits (Cooper and Flores, 1991)	Backshore; possibly backbeach

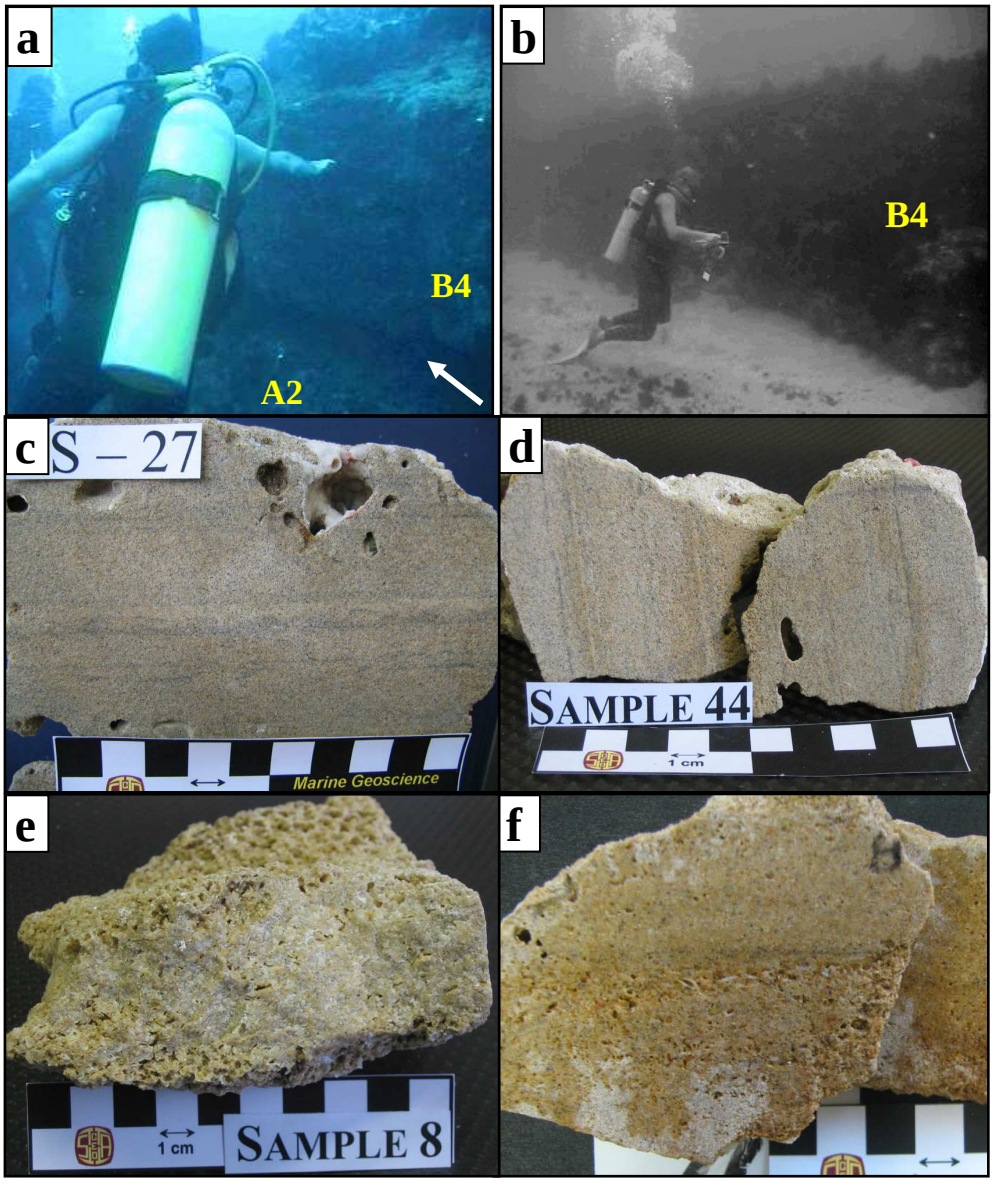

Figure 8.22 (cont.) Beachrock Unit B4. **a)** Underwater photograph of unconformable contact between Unit B4 Facies 2 and Unit A2, landward margin of Unit B4 in the vicinity of sample 16 (-20 m). Note the planar bedding in Unit B4. **b)** Underwater photograph of landward margin of Unit B4 Facies 2 comprising a ~2 m high ledge. Photo was taken along strike from (a) illustrating the highly variable thickness of Unit B4 Facies 2 which infills the palaeotopography. **c and d)** Photographs of hand specimen samples 27 (-22 m) and 44 (-25 m), also refer to Table 8.7. Note the similarity to that of GC-1 (Figure 8.19d) and holes drilled by boring molluscs. **e and f)** Photographs of hand specimen samples 8 (-20 m) and 16 (-20 m). Refer to the Table 8.7 for detailed descriptions. Sample 16 (f) is upside down with the bottom marked as 'B' (right top).

The whole-rock radiocarbon age on sample 27 indicates a Holocene age of 10.4 ka cal. B.P. (Chapter 9) which is older than expected. This age does not fall within the acceptable age range on the sea-level curve (Figure 9.6) and shows an older bias, behaviour observed from the other radiocarbon ages as well. However, seismic data, field relationships and age data from the other beachrock units suggest that the age of Unit B4 can be constrained as Holocene with deposition shortly after Unit B3. Thus Unit B4 cannot be older than ~9.24 ka cal. B.P. - which is the youngest point in the age range for GC-3. The thickness of Unit B4 is not certain but where exposed in the landward ledge it is observed to directly overlie Unit A2 and ranges in thickness from ~0.8 - 1.5 m (Figure 8.22a, b). However, as this beachrock comprises an almost sheet-like infill of the palaeotopography it is expected to vary in thickness.

Unit B5

Beachrock Unit B5 has a restricted distribution and overlies the landward or western limb of the Southern Parabolic Aeolianite of Unit A2. This imparts an arcuate shape to the beachrock outcrop (Figures 8.11aii, d; 8.12b, 8.18). Small isolated Unit B5 occurrences are represented by samples 9, 26, 58, 61 and 62, whilst a GC-series sample (GC-10) was obtained from the main B5 outcrop. The main outcrop of Unit B5 shows high relief microtopography forming a rugged flat topped outcrop with steep margins, overhangs and collapsed blocks, border to the north by a sediment and epifaunal growth covered platform with numerous sediment filled potholes and conspicuous lag deposits (Figure 8.23a).

Unit B5 unconformably overlies Unit A2 SPA (Figure 8.23b), has high-angle (18° - 25°) foresets similar to those observed in the nose area of the SPA (Figure 8.12a, d). In the vicinity of sample 58 (Figure 8.18) Unit B5 is only ~0.7 m thick (Figure 8.23b) whereas in the vicinity of sample site GC-10, the contact was not observed as B5 formed a dip slope mimicking the high-angle landward dip of the underlying aeolianite foresets. In hand specimen Unit B5 is unique, comprising poorly sorted coarse grained sediment with highly variable composition and grain characteristics (Figure 8.23 d to f). Sedimentary structures range from heterogeneous (Figure 8.23 d) to layered (Figure 8.23e), the latter including parallel to cross laminations (Figure 8.23f) comprising alternating

coarser fossiliferous layers and finer grained horizons with scattered coarser fractions. Unit B5 shows the widest variety of skeletal carbonate both in type and size, a characteristic also reflected in the nannofossil assemblage (Appendix X). Nannofossils show not only the highest diversity but also the presence of forms not represented in other samples(Cretaceous *Uniplanarius sissinghii*, *Sphenolithus* sp.). Unit B5 is interpreted as a washover deposit emplaced during an extreme depositional event such as a storm or tsunami.

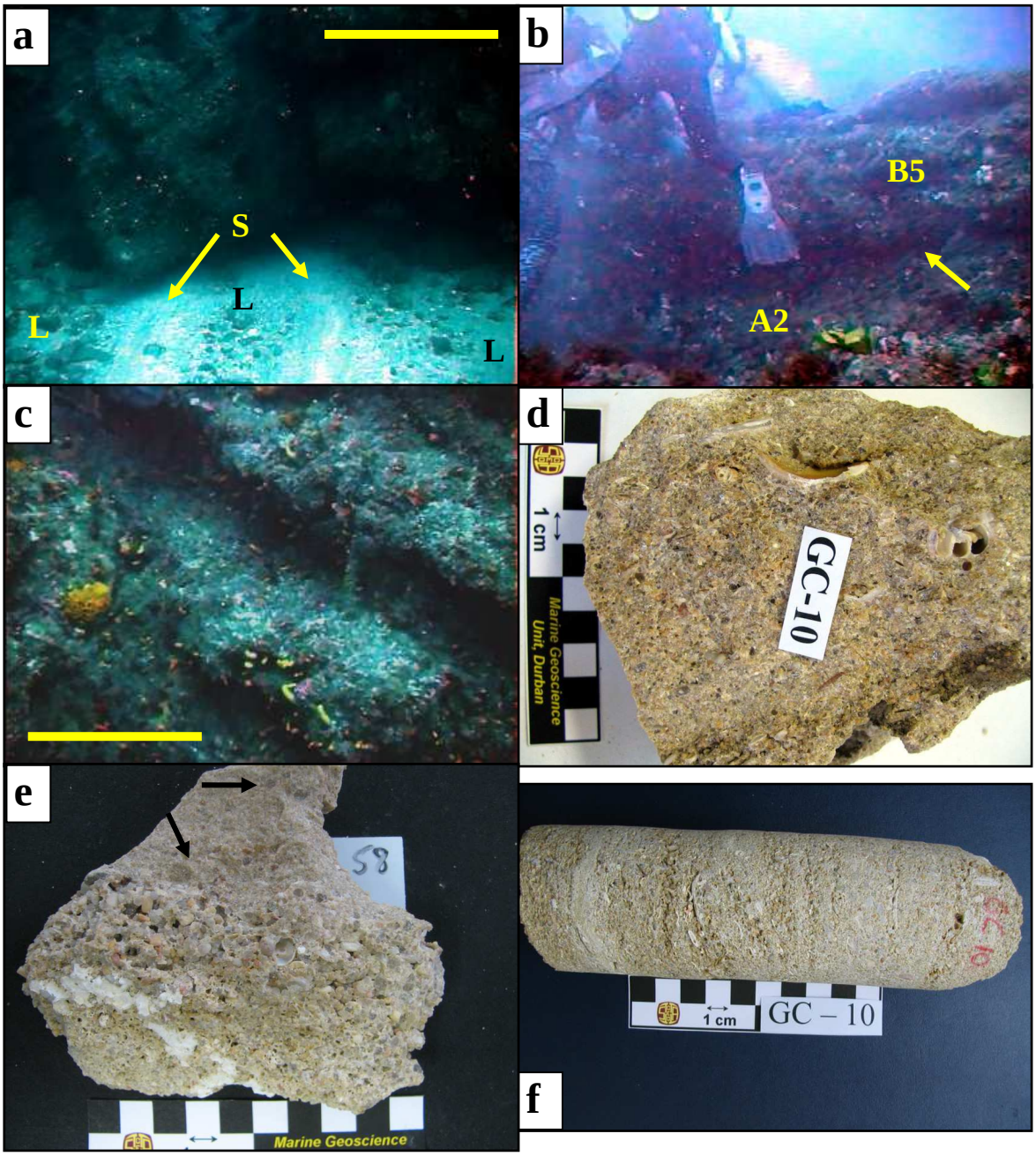

Figure 8.23 Features and characteristics of beachrock Unit B5. **a)** Seafloor at the base (-25 m)of Unit B5 showing sediment starved megaripples (S) comprising medium sand migrating over a lag (L) deposit that comprises discoidal pebbles and cobbles. Scale bar = 1 metre. **b)** Underwater photograph of the unconformable contact (arrow) between Unit B5 and A2 SPA at sample site 58 (-20 m). **c)** Underwater

Figure 8.23 (cont.) photographs of the planar cross-bedded aeolianite foresets of Unit A2 SPA below sample 58. Scale bar = 0.3 metres. **d)** Sub-sample of GC-10 (-24 m) showing high shell content and lack of sedimentary structures. **e)** Hand specimen 58 showing distinct layering comprising coarse grained shell hash overlying finer grained layer with scattered coarse pebbles (arrows; also see Figure 8.24b). Sample is upside-down; bottom is at the top of photograph. **f)** Core sample from GC-10 showing the cross-bedding observed in some samples.

Determining the origin of high-energy wash-over events requires a combination of criteria including morphological, sedimentological, palaeontological, geochemical and geochronological data that can be tied to historic records where applicable. Distinguishing storm and tsunami deposits are based on comparing known storm and tsunami events from the recent past in the same area (see Nanayama *et al*., 2000; Goff *et al*., 2004, Tuttle *et al*., 2004; Kortekaas and Dawson, 2007). These studies have shown that tsunami and storm deposits have similar characteristics and can generally only be separated by direct comparison in the same area, although tsunami deposits exclusively show rip-up clasts, boulders and a much greater landward extent than storm deposits. In most cases the product of the high-energy event is site specific and influenced by the source material, offshore bathymetry and onshore topography, the latter controling depositional environment and preservation potential (Kortekaas and Dawson, 2007).

Optical dating of Unit B5 yielded a depositional age of 79 ± 5 ka cal. B.P. during MIS 5a. This age falls within error of the Mt Toba super-eruption in Sumatra, Indonesia dated at 74.5 ± 4 ka cal. B.P. which was one of the largest explosive volcanic eruptions in geological history (Walker, 2005). It is therefore not unlikely that the Toba eruption could have produced a tsunami that reached the study area, similar to that generated by the Sumatra earthquake in 2004 (Obura, 2006). Without conclusive evidence an extreme storm event origin is preferred for the following reasons 1) correspondence of the unit to sea-level at the time (Figure 9.7), whereas tsunami generated deposits can significantly higher than than sea-level, 2) lack of observed boulders and rip-up clasts and 3) presence of foreset-like cross lamination, 4) storm events are more common along this coast than tsunamis. Nonetheless, the possibility that the local parameters at the time combined with the distance and ocean basin morphology between South Africa and Indonesia resulted in downgrading the possible tsunami waves to that resembling an extreme storm event cannot be discounted.

Beachrock Petrography

Composition and Texture

Detailed compositional and textural data for Units B1 to B5 are provided in Appendix VII, whilst a summary with average values are presented in Table 8.8. Compared to the aeolianite units (Table

8.2), the beachrock units show a higher variability in colour, texture and composition (Table 8.8). Nonetheless, on average the compositional and textural characteristic of the aeolianites and the Holocene beachrocks are very similar, both comprising moderately well sorted fine-skewed medium sand (Tables 8.2 and 8.8). It is important to note that on average, the Holocene beachrocks are slightly finer grained and better sorted than the aeolianites, although the extreme size classes are better represented in the beachrocks (Appendix VII)

Table 8.8 Summary of the textural and compositional data for beachrock Units B1 to B5 obtained from petrographical analyses (Appendix VII). The results from the individual GC-series samples are presented for comparison. UW = Udden-Wentworth classification, Sk = skewness, Qtz = quartz, Fspr = feldspar, Lith Frag = lithic fragments, HM = heavy minerals (including pyroxene), Bio = bioclastic components (skeletal carbonate), Cmt Factor = cementation factor, mS = medium sand, mWs = moderately well sorted, Ms = moderately sorted, Ws = well sorted, Sk = skewness, sfs = strongly fine-skewed, fs = fine-skewed, ns = near-symmetry, scs = strongly coarse-skewed. B3F1, B3F2 = Facies 1 and 2 of Unit B3, B4F1, B4F2 = Facies 1 and 2 of Unit B4, Avg = average, AVG = average for Units B1 to B4 (Holocene beachrocks).

Unit	**Mean (phi)**	**UW**	**Sorting**		**Sk**		**Mineralogy (%)**					**$CaCO_3$ %**	**Cmt Factor**
							Qtz	**Fspr**	**Lith Frag**	**HM**	**Bio**		
B1	1.95	mS	0.50	Ws	0.32	sfs	48	14	8	8	21	39	1.9
B2	1.25	mS	0.90	Ms	-0.15	cs	42	10	17.7	8.7	21.7	47	2.2
B3 F1	1.83	mS	0.58	mWs	0.44	sfs	51	7.6	4.4	4.6	32.4	44	1.4
B3 F2	1.93	mS	0.57	mWs	0.44	sfs	52	13	7	7	21	49	2.3
Avg B3	*1.88*	*mS*	*0.57*	*mWs*	*0.44*	*sfs*	*51.5*	*10.3*	*5.7*	*5.8*	*26.7*	*46*	*1.7*
B4 F1	2.18	fs	0.50	Ws	0.29	fs	54	12	4.5	11.5	18	43	2.4
B4 F2	1.48	mS	0.62	mWs	-0.22	cs	51.6	15.6	5.4	8.4	19	48	2.5
Avg B4	*1.40*	*mS*	*0.64*	*mWs*	*-0.01*	*ns*	*51.2*	*14.1*	*5.1*	*10.6*	*19*	*46*	*2.4*
AVG	***1.67***	***mS***	***0.64***	***mWs***	***0.21***	***fs***	***50.2***	***12.1***	***7.2***	***8.1***	***22.3***	***45***	***2.0***
B5	0.82	cS	1.28	Ps	0.94	sfs	42.2	13	8.3	5.8	30.7	57	1.9
GC-series samples													
GC-1 (B1)	1.77	mS	0.58	mWs	-0.28	cs	47	15	9	7	22	40	1.8
GC-1b (B1)	2.03	fS	0.45	Ws	0.64	sfs	48	14	8	8	22	44	1.7
GC-2 (B2)	1.20	mS	0.89	Ms	-1.01	scs	51	11	9	8	21	60	2.8
GC-3 (B3F1)	1.86	mS	0.57	mWs	0.40	sfs	51	12	4	4	29	41	1.3
GC-9 (B3F2)	1.93	mS	0.57	mWs	0.44	sfs	52	13	7	7	21	49	2
AVG	1.76	mS	0.61	mWs	0.04	ns	49.8	13	7.4	6.8	23	47	1.9
GC-10 (B5)	0.81	cS	1.28	Ps	0.61	sfs	46	13	10	5	26	59	1.9

This further supports aeolianite deposition in a coastal barrier in close proximity to a variety of sediment sources. Additionally, it may also indicate the longer evolutionary pathway of the sediment source material of the younger beachrocks relative to that what was available during deposition of the aeolianites. A possible explanation for this is that the beachrock units form part of seismic unit DsSF6 (Figures 6.6 to 6.9; Table 6.2) which overstepped and eroded the underlying embayed back-barrier lagoonal system. Sediment associated with this was probably finer grained and better sorted (reworked for duration of the lagoon, ~4 ka, Table 6.4) than that available at the time of aeolianite deposition during the previous sea-level cycle (see Chapter 6).

Although the beachrock samples vary from poor to well sorted, coarse to fine grained sand (Table 8.8; Appendix VII) some broad grain size trends can be observed. The finest grain sizes and best sorting values are represented by Unit B1 and Facies 1 of Unit B4, both of which are interpreted to have been deposited and cemented in the foreshore lower swash or upper surf zone. Unit B2 is moderately sorted, coarse-skewed medium sand and shows the poorest sorting and coarsest grain size of all the Holocene beachrock units. The relatively poor sorting value for swash zone sediment is ascribed to the proximity of the suggested fluvial sediment source (Figure 8.18) and a large proportion of coarse lithic components (Table 8.8). Unit B3 is divided into two facies based on sedimentary structures both of which show very similar grain size parameters comprising moderately well sorted, strongly fine-skewed medium sand thereby indicating a similar depositional environment and sediment source. Unit B4 is also divided into two facies based on sedimentary structures, but as opposed to Unit B3, B4 shows markedly different grain size characteristics (Table 8.8) with Facies 1 very similar to Unit B1 and Facies 2 exhibiting unique sedimentological parameters not represented in the other units. This is graphically illustrated in Figure 8.24 below. Interestingly, Unit B2 also plots separately, possibly related to the fluvial contamination. Unit B5 comprises poorly sorted strongly fine-skewed coarse sand and its anomalous nature relative to the Holocene units is clearly illustrated in Figure 8.24.

The grain size distribution data of the beachrock units are not typical of beach deposits which generally show good sorting and negative skewness (Cooper and Flores, 1991; Ramsay, 1991, 1996). However, these differences are interpreted to be related to the differences in geology of the sediment source terrain, depositional settings which controlled the transport process and sea-level characteristics during deposition.

Compared to the aeolianites the beachrocks do not show the variety of microscopic facies (Appendix VII, Table VII.2) and comprise mostly heterogeneous followed by vaguely laminated and finally laminated sediment. The laminated types include (Appendix VII, Table VII.2) discreet laminae (Ldl) and bimodal coarser/finer grained laminae (Lbl). The lack of observed lamination is

possibly due to the coarse grain size in some samples combined with the lowest available magnification still being too high and thus unable to resolve the structures obscured by the relatively larger grains.

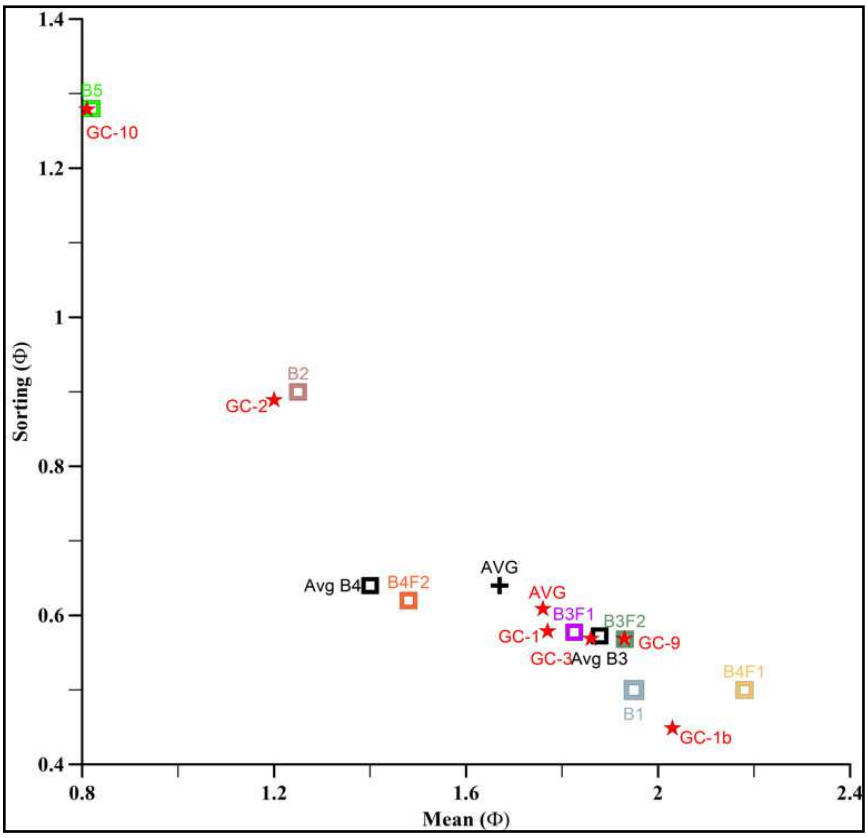

Figure 8.24 Mean grain size plotted against the standard deviation (sorting) for the beachrock data in Table 8.8. Note the distinct difference between the the cluster of Holocene beachrocks (Units B1, B2, B3 and B4) with that of Unit B5. Bx = Beachrock Unit 1 to 4, Fx = Beachrock Unit facies 1 to 4, AVG (black) = average of the sample data, AVG (red) = average of the GC-series data, Avg Bx = average for beachrock Unit 1 to 4, also refer to Table 8.8.

Mineralogically the beachrocks and aeolianites have similar framework constituents i.e. quartz, feldspar and bioclastics (Figure 8.25; Table 8.8), with the exception of glauconite (Figure 8.25a, e, f), which is present only in the beachrocks. When compared to aeolianites, beachrocks show different modal composition (compare Table 8.2 with 8.8 and Appendix V with VII). This includes an average decrease in quartz (49% vs. 57%), a significant average increase in lithic fragments (7% vs. 4%) and heavy mineral grains (8% vs. 4%) and a slight average increase in feldspar (12% vs. 11%).

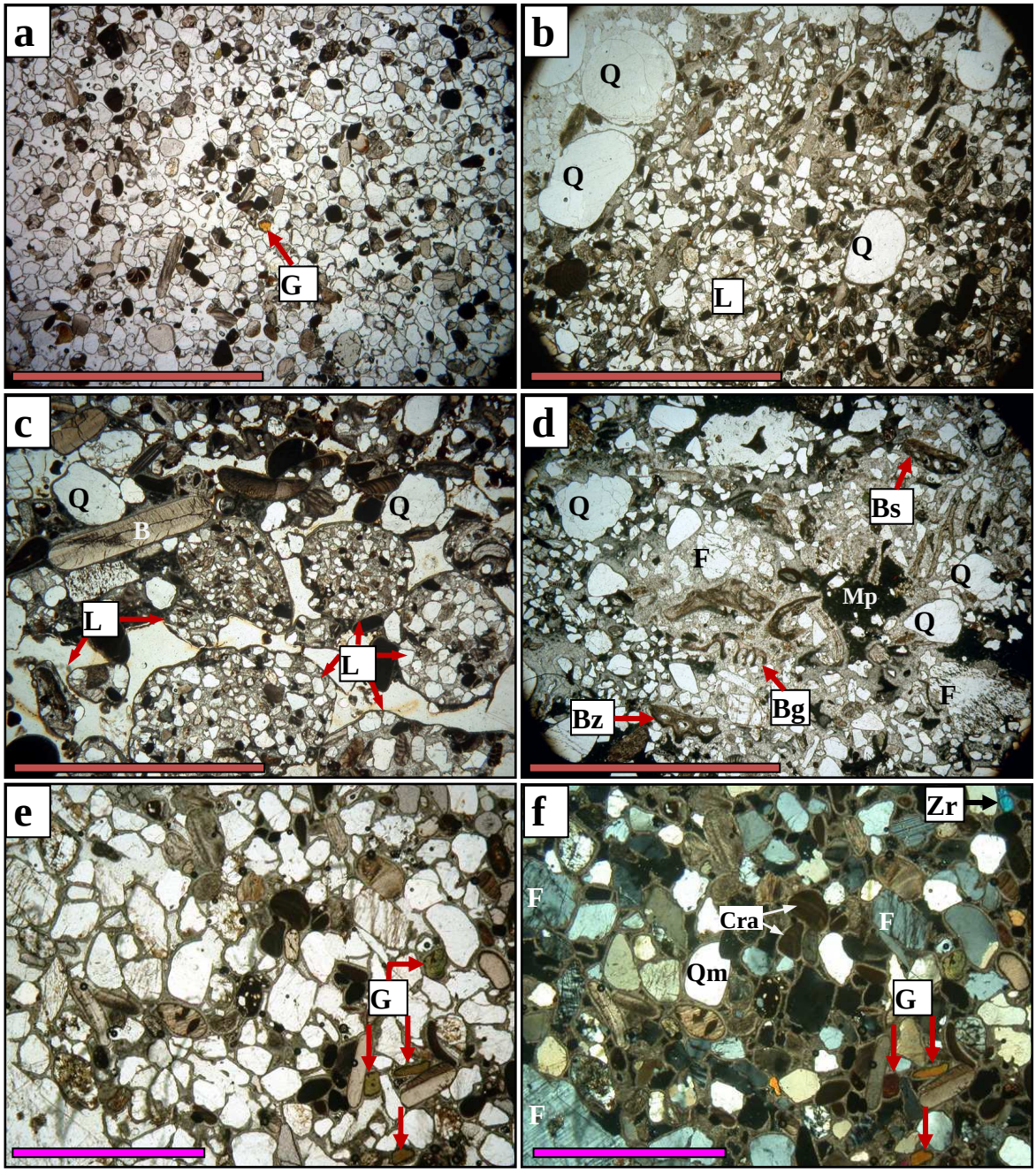

Figure 8.25 Selected transmitted light photomicrographs illustrating some of the petrographical characteristics of the Aliwal Shoal beachrocks. Coloured scale bars as follow; red = 5 mm, magenta = 2.5 mm **a)** Plane-polarised light (PPL) photomicrograph of the Heterogeneous (H) microscopic facies, sample GC-1b, -33 m, Unit B1. G = glauconite grain. **b)** PPL photomicrograph of the discreet laminated (Ldl) microscopic facies, sample 58, -20 m, Unit B5. Coarse quartz grains are set in fine grained laminae; also see Figure 8.23e for hand specimen of this sample. **c)** PPL photomicrograph of the bimodal coarser/finer grained laminae (Lbl) microscopic facies, sample 19, -27 m, Unit B2. The coarser laminae comprise aeolianite lithic fragments (L), whereas the finer laminae comprise mainly quartz (Q) and bioclastic fragments (B). **d)** PPL photomicrograph of the bioclastic rich Unit B5, note poor sorting and variety of fauna. Bz = bryozoan, Bg = gastropod, Bs = surpelid worm tube filled with fine grained sediment, Q = quartz and F = feldspar. Mp = pelloidal micrite cement related to the bio-erosive action of mainly sponges. **e)** PPL photomicrograph of sample 28, -24 m, Unit B4 Facies 2 showing glauconite grains (G). **f)** Crossed-polarised light (XPL) micrograph of (e). Cra = coralline red algae, G = glauconite, Qm = monocrystalline quartz, F = feldspar, Zr = zircon.

Interestingly, the average skeletal carbonate content (22%) is less in the Holocene beachrocks but more in Unit B5 (31%) compared to the average for the aeolianites (24%). The exceedingly high

value in Unit B5 is not unexpected as storm deposits, especially washover deposits, may contain high amounts of shell material Elliott (1986). In addition, the beachrocks show a higher proportion of angular grains and whereas the lithic grains in the aeolianites are almost exclusively igneous or metamorphic in composition (e.g. dolerite), lithic fragments in the beachrocks are predominantly aeolianite in origin (Figure 8.25c). This inclusion of aeolianite lithic fragments in the beachrocks further indicates the relative younger ages of the beachrocks supporting the geochronological results (Chapter 9). The older Unit B5 contains aeolianite lithic fragments (Figure 8.25b) further supporting the optical age data which indicate deposition of Unit B5 post-dating the aeolianites (Table 8.6; Chapter 9). Aeolianite lithic grain fragments comprise the largest proportion (ranging from 18 to 26%; Table VII.2) in Unit B2 which is also the coarsest and most poorly sorted beachrock unit (Table 8.8).

The observed assemblage of skeletal carbonate fragments are very similar to that found in the aeolianite units and include varying proportions of molluscan, cirriped (barnacle), echinoid, coralline red algal, foraminiferal (miliolid, fusulinid, and rotalid forms) and bryozoan fragments (Figure 8.25). No significant trend in the detailed subdivision of the skeletal carbonate fractions is observed between the beachrock (Table 8.9) and aeolianite samples (Table 8.3) but the greatest differences are probably related to the types of fauna represented by the undifferentiated 'Remaining bioclastic' fraction. Beachrock carbonate content varies from 32 - 67%, which, on average (45%), is lower than the average for the aeolianites (53%).

Table 8.9 Summarised subdivision of the skeletal carbonate components of the beachrock GC-series samples. CRA = coralline red algae, Forams = Foraminifera.

Sample	% CRA	% Bryozoan	% Forams	% Remaining bioclastics	Total (%)
GC-1 (B1)	4	1	1	16	22
GC-1b (B1)	5	1	1	15	22
GC-2 (B2)	2	1	1	17	21
GC-3 (B3F1)	6	1	1	21	29
GC-9 (B3F2)	2	1	1	17	21
GC-10 (B5)	3	1	1	21	26

As observed in the aeolianites, compositionally the Aliwal Shoal beachrocks are very different from those offshore Sodwana Bay (Ramsay, 1991, 1996; comprising 80 - 90% quartz and 5 - 10% feldspar) and the Durban Bluff (Cooper and Flores, 1991; comprising 47 - 77% quartz, 3 - 30% feldspar, 1 - 16% lithic fragments, 0 - 15 % heavy minerals and 6 - 13% bioclastic grains). The differences are ascribed mainly to be related to differences in the geology of the sediment source terrain and number of fluvial systems present in the different study areas. Overall the texture and

composition of the beachrock units support the field observations and depositional environment interpretations (Table 8.6).

Cementation

Compared to the aeolianites, the beachrock units (except Unit B5) show a very simple diagenetic history comprising one major phase of marine phreatic or possibly vadose cementation. Contrary to that observed in the aeolianites, the beachrocks display no difference in the cementation histories of the GC-series and hand specimen samples.

Beachrock units show significant primary and secondary porosity with primary interparticle porosity varying from 10 to >50% (Appendix VII) and secondary cement-reduced porosity values decreasing the porosity slightly to 5 to 40%, indicating the relatively poorly cemented nature of the deposits. The open uncompacted nature of the beachrocks is typical of sediment that underwent early diagenesis (Adams and McKenzie, 1998). The cementation factor (see the section on aeolianite petrology for explanation) in the beachrocks is generally lower (2.0) indicating that on average the aeolianites (2.8) are better cemented, however, GC-2 has a high cementation factor (2.8) yet shows very limited cement (see below). In this case the higher carbonate content of the sample is due to the presence of aeolianite lithic fragments which contribute to the total carbonate. Thus, the cementation factor is only a guideline and should be interpreted with caution, especially when significant lithic or bioclastic carbonate fragments are present.

<u>Unit B1</u>

Unit B1 is cemented by thin (~20 µm) generally isopachous fringes of radial aragonite needles (Figure 8.26a). Aragonite needles are pointed or square-ended, typically less than 2 µm in width and have grown radially from grain surfaces (Figure 8.26b, c). SEM imagery shows the presence of randomly orientated and inter-growing needles (Figure 8.26d) suggesting rapid precipitation in fluid-filled pores (Longman, 1980; Vousdoukas, *et al*., 2007). The aragonite composition of the needles is supported by SEM-EDX analyses indicating significant strontium (Figure VI.1) and an almost complete absence of magnesium (Appendix VI, Table VI.1). Similar aragonite needle cements were observed in intertidal, especially contemporary, beachrocks by numerous other workers, notably Stoddart and Cann (1965), Taylor and Illing (1969), Hanor (1978) Moore (1973), Gischler and Lomando (1997), Vousdoukas *et al*., (2007; review) and Cawthra (2010). According to Tucker and Wright (1990) aragonite needles constitute the most common beachrock cement and if occurring as isopachous fringes are indicative of cementation in the lower intertidal zone. For this reason acicular isopachous crusts of aragonite needles displayed by Unit B1 and Facies 1 of Unit B4 are interpreted to represent a marine phreatic cement cemented in the lower intertidal zone.

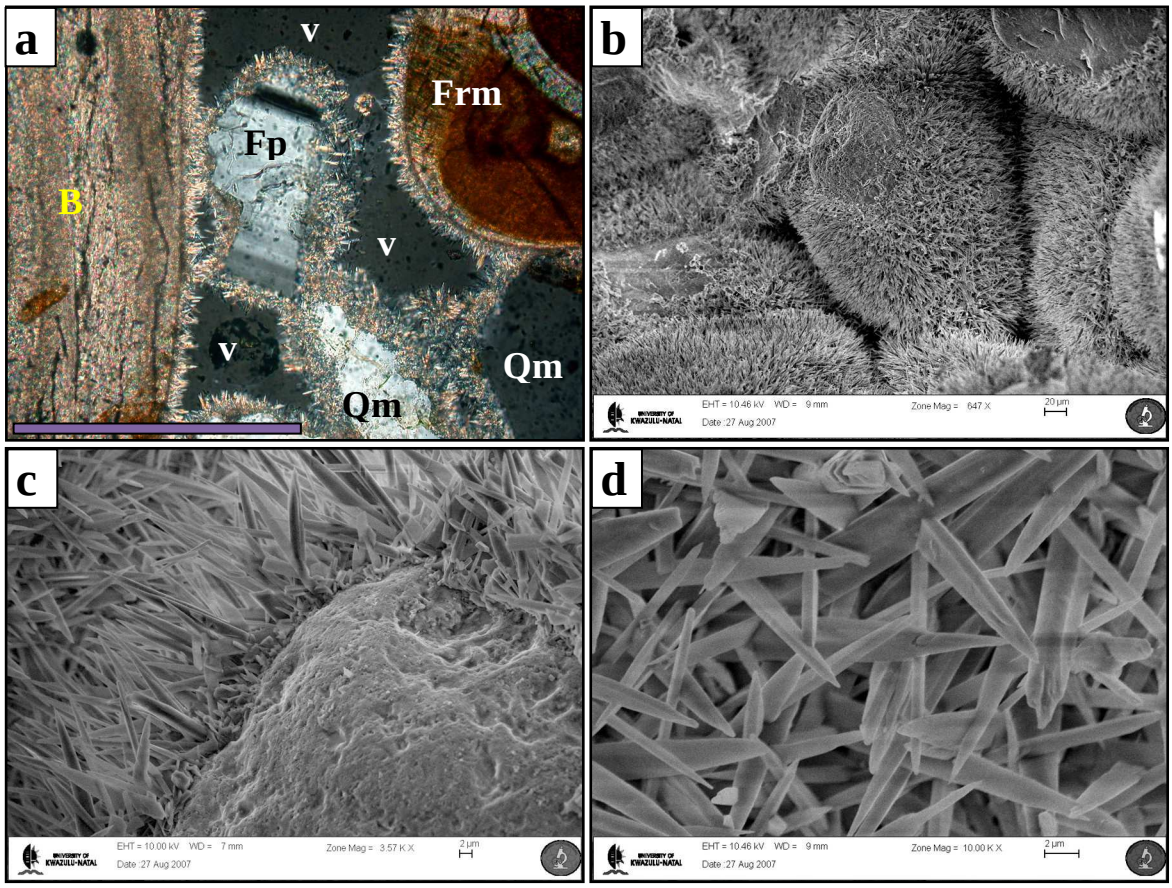

Figure 8.26 Isopachous aragonite needle cement of Unit B1. **a)** Transmitted light (XPL) micrograph of sample GC-1b (-33 m), note the high primary and cement-reduced porosity. Scale bar = 0.25 mm. Qm = monocrystalline quartz, Frm = foraminifera, Fp = plagioclase, B = bioclastic fragment, v = void. **b)** SEM image of GC-1 (-33 m) showing the isopachous needle cement and high porosity. Scale bar is 20 µm. **c)** SEM image of GC-1 (-33 m) showing the perpendicular grain attachment of the aragonite needles. Note the v-shaped percussion marks on the grain surface typical of the beach environment. Scale bar at is 2 µm. **d)** High magnification SEM image of inter-meshed aragonite crystals (GC-1, -33 m) indicating rapid precipitation in fluid-filled pores. Scale bar is 2 µm.

Unit B2

Unit B2 comprise thin (5 - 10 µm) isopachous to uneven crusts of steep-sided rhombic or scalenohedral HMC cement (Figure 8.27) containing 12.5 mole% $MgCO_3$ (GC-2). The scalenohedral form is the most common HMC cement morphology (Tucker and Wright, 1990). The SEM (EDX) analyses (Appendix VII; Figure VI.1) showed the presence of a tail of rare earth and trace elements not observed in any of the other units. The Ca position in the calcite lattice can be substituted by a variety of minor and trace constituents (Tucker and Wright, 1990) but the reason for the presence and origin of the trace elements, only in this unit, is unknown. The composition and morphology of this cement is typical for a marine precipitate however, the occasional uneven nature of the cement fringe (Figure 8.27b) with microstalactitic-like distributions (Dunham, 1971) might possibly indicate some cementation in the marine vadose zone (Longman, 1980; Scoffin, 1987; Tucker and Wright, 1990 and Vousdoukas *et al*., 2007), possibly

during low tide. Unit B2 is interpreted as being cemented in the intertidal zone predominantly within the marine phreatic zone and with occasional exposure to the marine vadose zone.

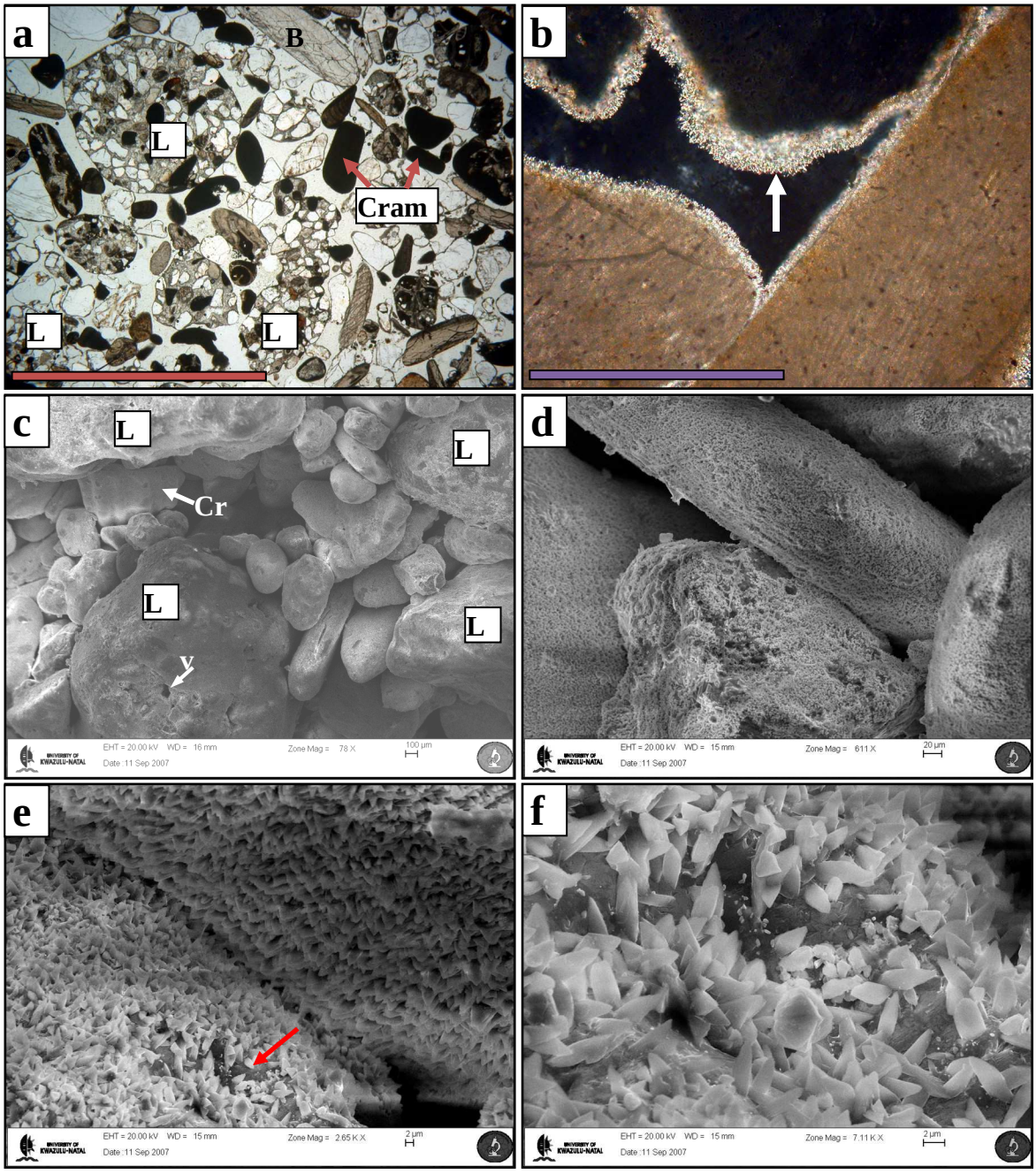

Figure 8.27 Isopachous to uneven scalenohedral HMC cement of Unit B2. **a)** Transmitted light (XPL) micrograph of sample 18 (-29 m). Despite the high primary and secondary porosity this beachrock is well lithified. L = aeolianite lithic fragment, B = bioclastic fragment, Cram = micritized coralline red algae. Scale bar = 5 mm. **b)** Transmitted light (XPL) micrograph of possible microstalactitic texture (arrow) on underside of grain (sample GC-2, -29 m). Scale bar = 0.25 mm. **c to f)** Progressively higher magnification SEM images of GC-2 (-29 m) showing the high porosity of the sediment and morphology of the HMC cement. Note the aeolianite lithic fragments (L) in image (c) showing cement-reduced porosity (v). Cr = cirriped or barnacle fragment. Image (d) shows the thin isopachous nature of the HMC cement, whereas the higher magnification image (e) shows areas with incomplete cementation (arrow). The scalenohedral morphology of the cement crystals is illustrated in the high magnification image (f). Scale bars in the SEM images are as follows; c = 100 µm, d = 20 µm, e and f = 2 µm.

Unit B3

In general Unit B3 is cemented by bladed HMC which displays a unique morphology comprising bundles of coalescing fibres which creates vertical flutings on the crystal sides terminations (Figure 8.28). This morphology was first described by Folk (1974) as '*steep rhombs of Mg-Calcite with vertically orientated flutings*' and termed fluted HMC by Flugel (2004). Folk (1974) attributed it to selective Mg poisoning of the calcite crystal lattice so that growth is inhibited in all but the c-axis direction resulting in the fibrous or steep-rhombic form. The imperfect crystal habits observed in the HMC is thus a consequence of the distortion caused by the incorporation of smaller Mg^{2+} ions (Folk, 1974; Tucker and Wright, 1990). Fluted HMC is common in hypersaline to normal marine environments and often found in beachrocks (Folk, 1974).

Although both facies of Unit B3 exhibit the bladed fluted HMC, there are morphological and compositional differences between the two facies. In Facies 1 the fluted HMC comprise a thin (<5 - 20 µm) isopachous to uneven bladed (length to width ratios of 2 - 2.5:1) grain fringes with some grain boundaries (especially terrigenous grains) showing an absence of cement (Figure 8.28a to c), whereas in Facies 2 it generally occurs as thin (10 - 20 µm) bladed (length to width ratios of 2 - 4:1) isopachous pore-lining crusts (Figure 8.28d to f). No other characteristic vadose cement morphologies were observed in Facies 1 (see Unit B5 below) and the lack of cement might be due to pore water and/or physical constraints during cementation rather than a result of inhomogeneous distribution of pore fluids typical of vadose cements. Facies 1 shows a lower $MgCO_3$ content (5.3 mole%; GC-2; Appendix VI) compared with that of Facies 2 (10.1 mole%; GC-9). However, both facies shows the same morphologies and thus the lower $MgCO_3$ content in Facies 2 is unexpected and may be due to analytical error with the SEM (EDX) spot beam possibly penetrating through the relatively thin and irregular Facies 1 cement and incorporating analyses from the underlying grain.

The fluted morphology, isopachous pore-lining nature and HMC composition of the cements of Unit B3 suggests an intertidal marine phreatic zone diagenetic environment (Folk, 1974; Longman, 1980; Scoffin, 1987; Tucker and Wright, 1990 and Adams and MacKenzie, 1998).

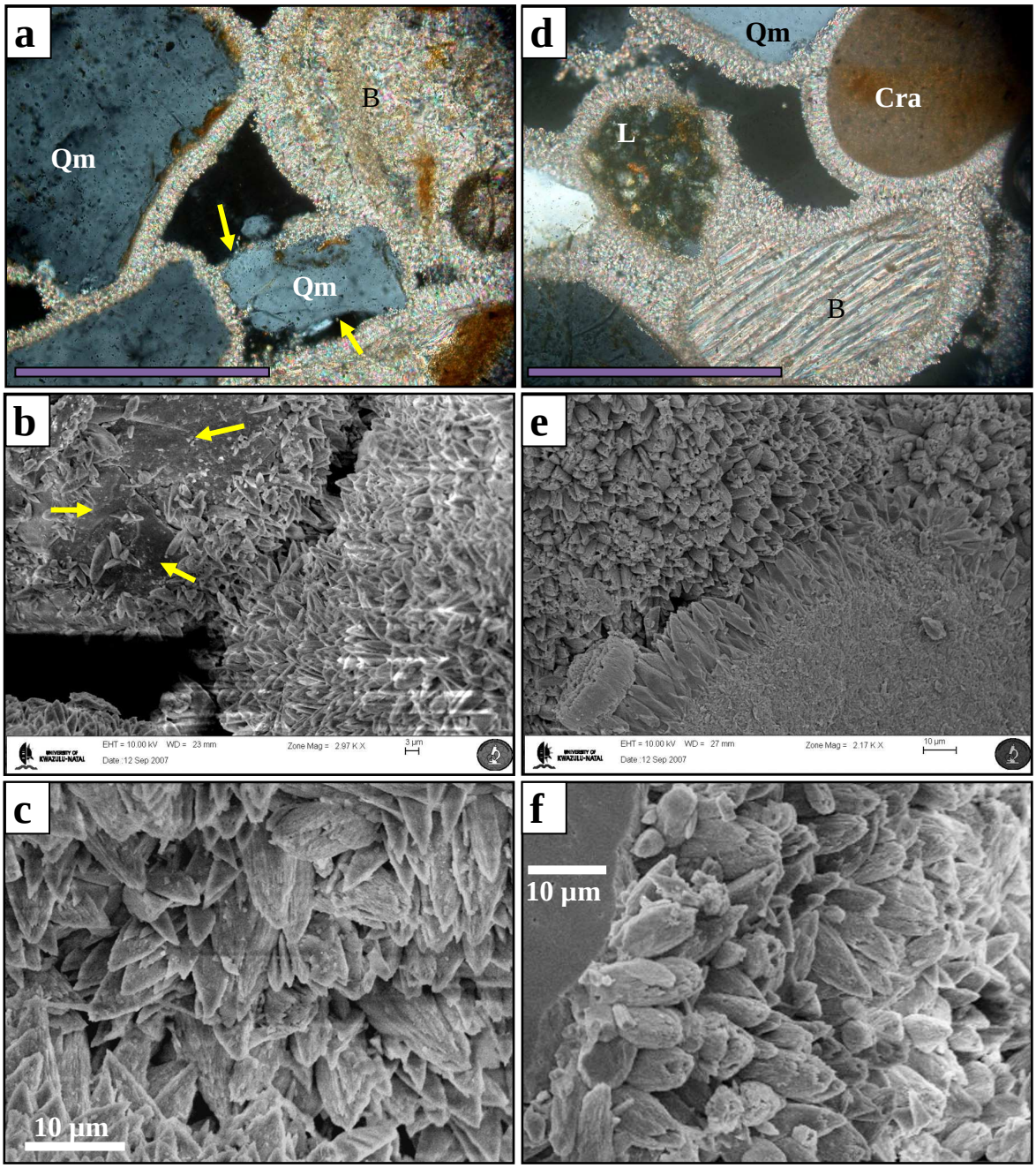

Figure 8.28 Isopachous fluted HMC cement of Unit B3. **a to c)** Images of Facies 1. **a)** Transmitted light (XPL) micrograph of GC-3 (-26 m) showing the incomplete cementation found at some terrigenous grain boundaries (arrows). Qm = monocrystalline quartz, B = bioclastic fragment. Scale bar = 0.25 mm. **b)** SEM image of GC-3 showing similar features than that observed in the thin section (a). Arrows points to areas on a terrigenous grain without cement. Scale bar at bottom of image is 3 µm. **c)** High magnification SEM image of the fluted morphology of the HMC cement. **d to e)** Images of Facies 2. **d)** Transmitted light (XPL) micrograph of GC-9 (-26 m) showing the HMC cement morphology comprising isopachous grain coatings. Qm = monocrystalline quartz, B = bioclastic fragment, L = lithic fragment, Cra = coralline red algae. Scale bar = 0.25 mm. **e)** SEM image of the dense isopachous HMC cement (GC-9, -26 m). Scale bar at bottom of image is 10 µm. **f)** High magnification SEM image of the fluted morphology of the HMC cement (GC-9).

Unit B4

Unfortunately SEM images are unavailable for Unit B4. Nonetheless, thin sections of Facies 1 are almost exact duplicates of Unit B1 (Figure 8.26a) and also interpreted as aragonite needle cement.

Facies 1 aragonite cement (Figure 8.29a, b) forms slightly thicker fringes than that observed from Unit B1 showing pointed and square-ended needle crystals and a more random orientation to the grain surface compared to the HMC cements (Figure 8.29c, b). The aragonite needle cement is interpreted, similar to Unit B1, as a marine phreatic zone precipitate (Longman, 1980; Scoffin, 1987; Tucker and Wright, 1990 and Adams and MacKenzie, 1998).

Facies 2 comprises bladed isopachous fringes ranging from 10 to 60 µm interpreted as HMC based on comparison to the other similar cement types with known HMC composition in other beachrocks (GC-2, 3 and 9) and aeolianites (GC-4, 6 and 7; Figure 8.17b, e, g; Table 8.4 and Appendix VI). Facies 2 seems to be generally better cemented than Units B2 and B3 and commonly displays polygonal or compromised boundaries (Figure 8.29c). In thin section the cement morphology of Facies 2 seems to better resemble the fluted rather than scalenohedral HMC variety. Facies 2 is also interpreted as an intertidal marine phreatic zone cement (Longman, 1980; Scoffin, 1987; Tucker and Wright, 1990 and Adams and MacKenzie, 1998).

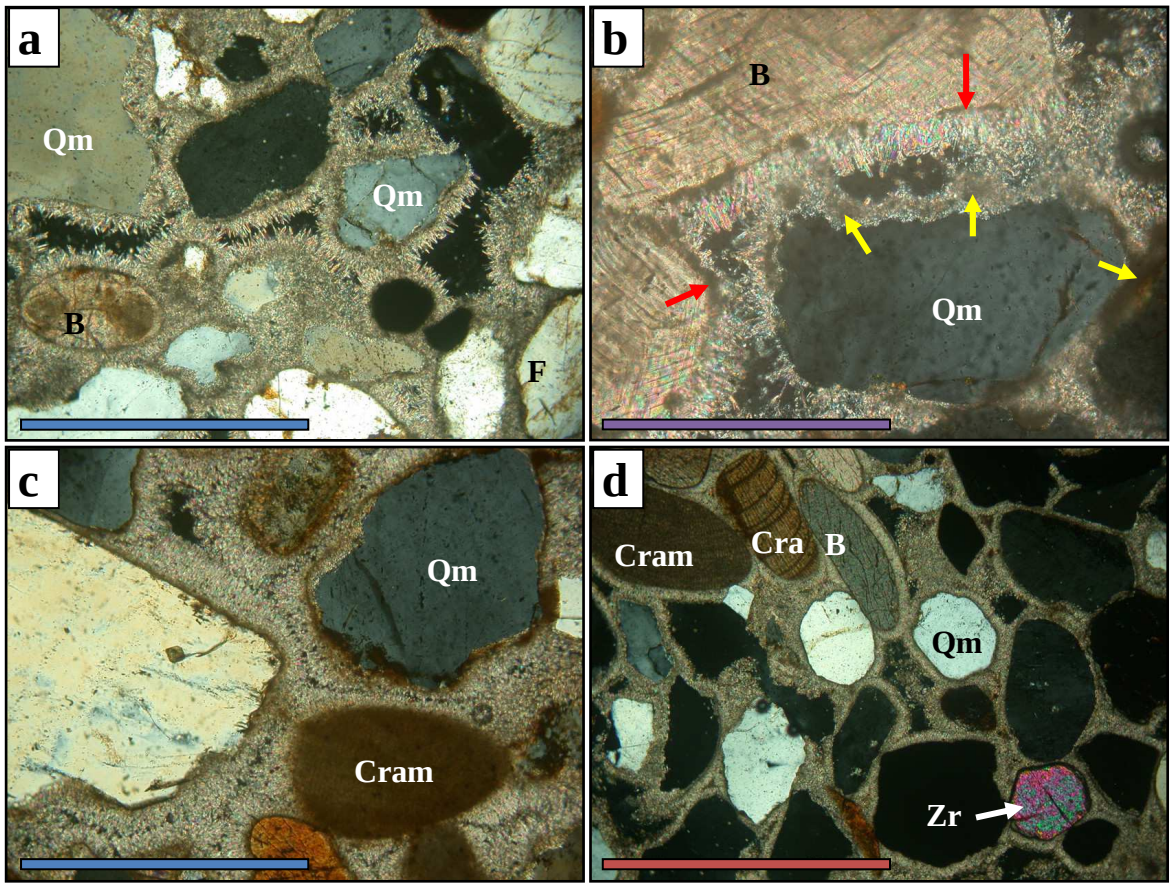

Figure 8.29 Selected examples of the cement morphologies of Unit B4. Abbreviations as follows; Qm = monocrystalline quartz, B = bioclastic fragment, Cra = coralline red algae, Cram = micritized coralline red algae, F = feldspar, Zr = zircon. **a and b)** Transmitted light (XPL) micrographs of Facies 1 samples 27 (-22 m) and 44 (-25 m), respectively showing the aragonite needle cement characteristic of Facies 1.

Figure 8.29 (cont.) Micritization of the aragonite cement is indicated by the yellow arrows and is probably related to organic activity similar to those producing the micritic envelopes (red arrows). Coloured scale bars as follow; blue = 0.5 mm, purple = 0.25 mm. **c and d)** Transmitted light (XPL) micrographs of Facies 2 samples 16 (-20 m) and 28 (-24 m), respectively. Unit B4 Facies 2 shows very similar crystal morphology to that of Unit B3 and the marine cement phases in the aeolianites. As such it is interpreted as a HMC cement. Coloured scale bars as follow; blue = 0.5 mm, red = 5 mm.

Unit B5

Unit B5 shows the presence of two possible cement phases. The first phase comprising thin (10 - 20 µm) bladed to equant uneven grain crusts mainly found at grain boundaries and the underside of grains (Figure 8.30a, b). This type of cement morphology is typical of the inhomogeneous distribution of water in the vadose zone (Longman, 1980; Scoffin, 1987), where pores are not water saturated and if present is held by capillary forces between the grains (meniscus cements; Dunham, 1971) and under the grains as pendant drops (microstalactitic). The second phase comprises thicker (30 - 60 µm) bladed to fibrous isopachous fringes of scalenohedral and fluted HMC (Figure 8.30a to d) with the highest $MgCO_3$ content (12.7 mole%; GC-10; Appendix VI) observed from the beachrocks.

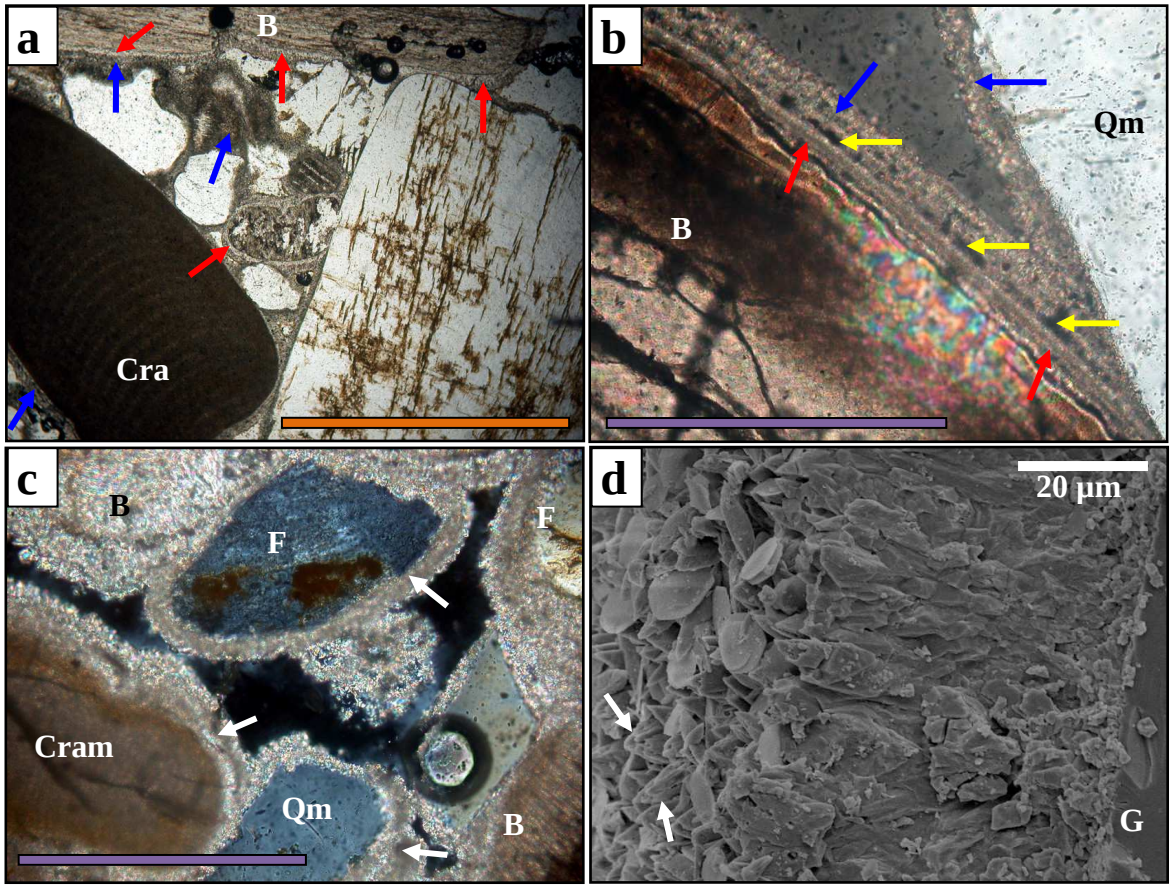

Figure 8.30 Selected examples of the cement morphologies of Unit B5. Abbreviations as follows; Qm = monocrystalline quartz, B = bioclastic fragment, Cra = coralline red algae, Cram = micritized coralline red algae, F = feldspar, G = terrigenous grain. **a)** Transmitted light (PPL) micrograph of the poorly developed

Figure 8.30 (cont.) clear cement phase 1 (red arrows) and dominant cloudy cement phase 2 (blue arrows) in sample GC-10 (-24 m). Scale bar = 1 mm. **b)** High magnification transmitted light (XPL) micrograph of cement phases 1 (red arrows) and 2 (blue arrows) separated by an irregular developed micritic coating (yellow arrows). Sample GC-10 (-24 m). Scale bar = 0.25 mm. **c)** High magnification transmitted light (XPL) micrograph of cement phase 2 in sample 58 (-20 m). White arrows indicate areas of micritization similar to that in Figure 8.29b. Scale bar = 0.25 mm. **d)** SEM image of the bladed to fibrous isopachous scalenohedral and fluted HMC cement phase 2. Fluted HMC forms are indicated by the white arrows.

In some instances the phase 1 cement is separated from phase 2 by an irregular micritic coating (Figure 8.30b) similar to that observed between the meteoric and marine cement phases in the aeolianites (cement phase 3, refer to Figures 8.15c and 8.17a). The phase 1 cement is not common and possibly indicates a limited cementation phase. Phase 2 however, is the dominant cement phase and resembles the other HMC beachrock cements.

Phase 1 is interpreted as a marine or mixed vadose HMC cement which inverted to LMC as a consequence of meteoric zone exposure (Bathurst, 1975; Longman, 1980; Scoffin, 1987; Tucker and Wright, 1990 and Adams and MacKenzie, 1998). Phase 2 is interpreted as an intertidal marine phreatic zone cement similar to Units B3 Facies 2 and B4 Facies 2.

Thus in summary, all the Aliwal Shoal Holocene beachrocks display a marine cement phase with its original marine composition intact. In addition, Units B1, B2, B3 and B4 show only one cement generation comprising a marine cement. These observations combined with the lack of subsequent meteoric zone cements and features such as replacement of grains with an unstable composition suggests 1) all the beachrock units are still in the same or similar environment to the that of cement precipitation, and 2) Units B1, B2, B3 and B4 were deposited and cemented during a fast sea-level transgression. The diagenesis therefore supports the field evidence, compositional, grain size and age data. In contrast Unit B5 displays cement inversion followed by later but prestine marine cements.

8.3.5 Discussion

Model of Aeolianite and Beachrock Carbonate Diagenesis

This study approached the investigation of the diagenesis of the Aliwal Shoal lithologies not as an end in itself but rather a means to an end based on the approach of Reijers and Hsu, (1986) which stated that; '*The considerations of the various aspects of diagenesis are not an aim in themselves but should be regarded as a step in the process that leads ultimately to a fuller understanding of what happened, where and why*'.

Diagenesis of carbonate sediments includes all the processes that have an effect on the sediment after initial deposition until metamorphism including the major processes of cementation, microbial micritization, neomorphism, dissolution, compaction and dolomitization (Longman, 1980; Tucker and Wright, 1990). Samples from this study display carbonate cements composed of two minerals: orthorhombic aragonite and rhombohedral calcite, with two varieties of calcite recognised viz: high-magnesium calcite (HMC, >5 mole% $MgCO_3$) and low-magnesium calcite (LMC, <5 mole% $MgCO_3$). Aragonite however, does not incorporate Mg^{2+} into its lattice (Scoffin, 1987). Both aragonite and HMC are metastable phases and thus commonly replaced by LMC (Folk, 1974; Bathurst, 1975; Longman, 1980; Tucker and Wright, 1990 and the references there in).

Most carbonate cementation occurs in one of four diagenetic environments (Figure 8.31a; Longman, 1980; Scoffin, 1987); the 1) meteoric vadose, 2) meteoric phreatic, 3) the mixing zone and 4) marine (phreatic and rare vadose). These four zones usually occur in a consistent sequence although some zones may be missing and other present (Longman, 1980). Importantly also is that these zones will change with sea-level change and may be independent of the depositional environment. An added consequence is that the superposition of the diagenetic environments makes it unlikely, for example, that sediment would move directly from the marine phreatic into the meteoric vadose zone, except in rare circumstances (Longman, 1980; Scoffin, 1987). The major factors controlling the type and end result of diagenesis include (Bathurst, 1975; Longman, 1980; Tucker and Wright, 1990); 1) composition and mineralogy of original sediments, 2) pore-fluid chemistry and flow rates, 3) sea-level changes and 4) climate. Sea-level changes and climate are considered the primary drivers of diagenetic change at Aliwal Shoal. Sea-level change controls the movement of the diagenetic zones, whereas climate influences the rate and nature of the various physio-chemical processes within these zones (Tucker and Wright, 1990). The model of carbonate diagenesis for the Aliwal Shoal aeolianites and beachrocks (Figure 8.31) is based on petrographical observations and depositional ages for the various units (Chapter 9). Interpreted ages for the carbonate cement phases are based on their relative age.

Aeolianite Diagenesis

The diagenetic history of the Aliwal Shoal aeolianite units are complex showing both variation in time and space reflecting their relative older ages and the consequent complex interaction of sea-level change and the associated shift in diagenetic environments. In essence, the aeolianites documented 3 major diagenetic stages; 1) initial pervasive predominantly meteoric phreatic cementation, 2) a period of cement erosion associated with decementation and increased porosity and 3) deposition of several marine cement types with pristine marine composition still intact.

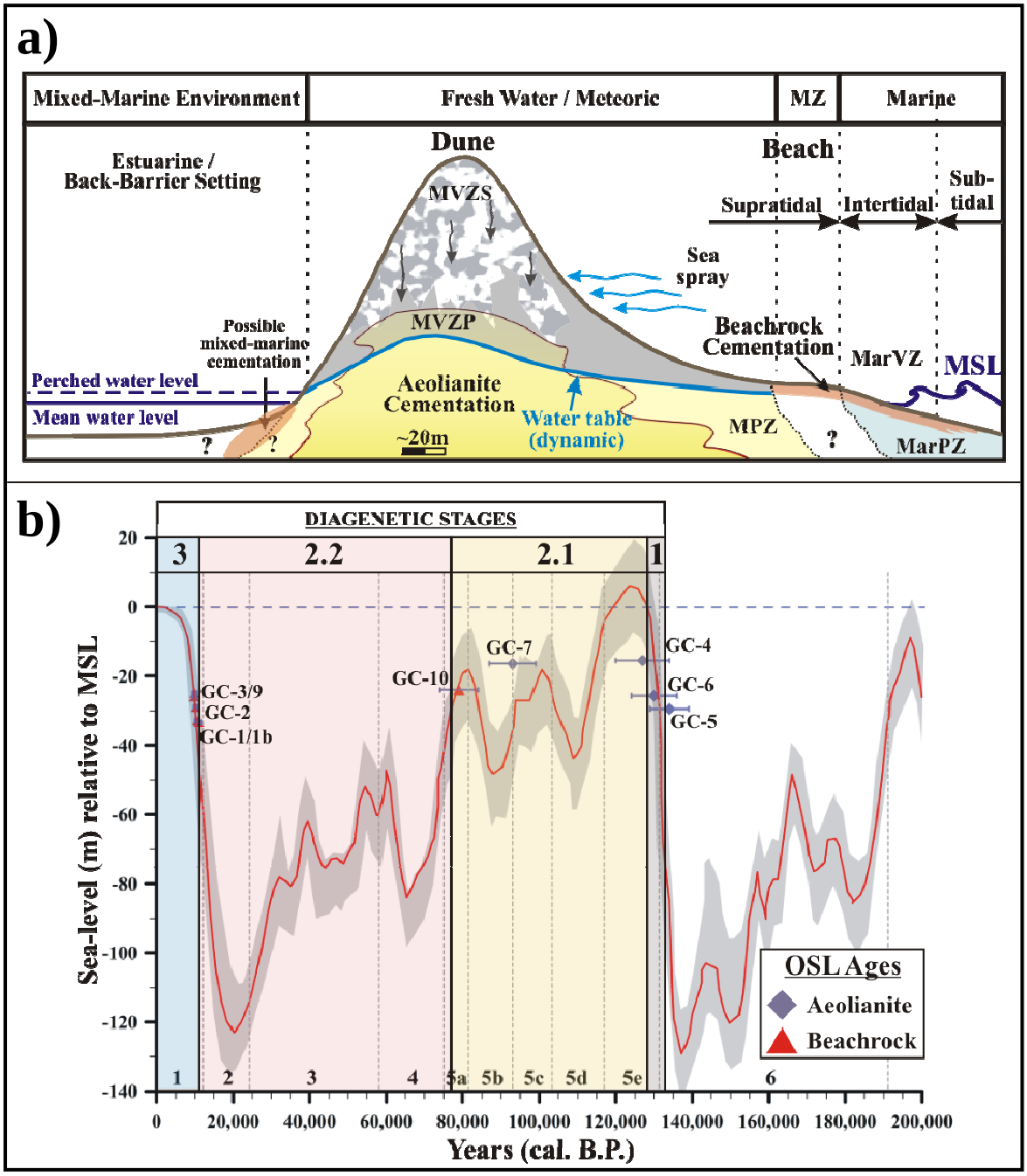

Figure 8.31 Diagenetic model for the Aliwal Shoal aeolianite and beachrock **a)** Schematic diagenetic environments related to the observed cement morphologies and compositions in the Aliwal Shoal lithologies. Note that the boundaries of the various zones are dynamic and shift in response to changes in the water table. MVZS = meteoric vadose zone of solution, MVZP = meteoric vadose zone of precipitation, MPZ = meteoric phreatic zone, MarVZ, marine vadose zone, MarPZ = marine phreatic zone, MZ = mixing zone. **b)** Proposed timing of the 3 diagenetic stages **Figure 8.31 (cont.)** responsible for the observed carbonate cement phases plotted on the global eustatic composite curve (red line) of Waelbroeck *et al.* (2002; grey area = 2σ uncertainty). The global marine isotope stages (MIS) are numbered from 1 - 6 above the age-axis. Note that for GC-7 and GC-10 stage 1 are not shown due to its short duration and the fact that it would have been followed soon after by stage 2 as a consequence of the regressive sea-level regime. For an explanation of the stages refer to the text, note that stage 3 continues to the present as cement phase 8 is related to the bio-erosion by sponges. Also refer to Chapter 9 for the OSL age data for the aeolianites and beachrocks.

Stage 1 Diagenesis

The Aliwal Shoal aeolianites display a fairly homogeneous mineralogy comprising high proportions of skeletal carbonate mixed with siliciclastic grains (quartz, feldspar etc.). Therefore, the original sediment pile constituting the Aliwal Shoal aeolianites inherently had a strong predisposition for meteoric phreatic diagenesis due to the availability of an abundant carbonate source and the intrinsic depositional setting. This is supported by the primary cement phases (Figures 8.15 to 8.17) and the abundant bioclastic components which would have supplied much of the carbonate for the meteoric cementation. (Table 8.2, Appendix V). Primary meteoric cementation of Units A1 and A2 had to be pervasive as the aeolianites survived not only the subsequent submergence (MIS 5e) shortly after formation but also the major sea-level fluctuations for the remainder of MIS 5 and 4. There is however the possibility that some unpreserved MIS 5 marine cementation might have aided preservation. In addition, while no evidence for further meteoric cementation following the initial meteoric phases (1 and 2) was observed, the aeolianite units were also well enough cemented to withstand the period of exposure related to the sea-level depression towards the LGM (stage 2) and the ensuing last deglacial sea-level rise and subsequent submergence (stage 3) (Figure 8.31b).

Aeolianite cementation is interpreted to have occurred within the interior core of the coastal dune with possibly initial sporadic sea spray-induced cementation in the meteoric vadose zone followed by dominant pervasive cementation in the meteoric phreatic zone. The meteoric phreatic zone is located between the meteoric vadose zone and the mixed meteoric-marine phreatic zone, the top marked by the water table and the base, in coastal zone, is gradational with marine waters (Longman, 1980; Scoffin, 1987; Figure 8.31a). It is characterised by dissolution, LMC cement precipitation and mineralogical transformations (Longman, 1980; Tucker and Wright, 1990) and its geometry is strongly controlled by topography, rainfall and distribution of porosity within the rocks (Longman, 1980). Typically, for every metre that the water table is above sea-level, there are ~32 m of meteoric phreatic water below the water table, assuming equilibrium and a permeable lithology (from Friedman and Sanders, 1978 in Longman, 1980). Carbonate supersaturation of the phreatic zone is interpreted to have occurred by leaching of unstable mineralogies located within the vadose zone of the aeolian sediment pile by percolating under-saturated rainwater. The rainwater became increasingly and sufficiently saturated with respect to $CaCO_3$, so that when it intersected the water table, cementation was achieved through decreasing flow rates and CO_2 release (Bathurst, 1975, Longman, 1980, Scoffin, 1987). According to McLaren (2001) vadose diagenesis in the presence of sea spray speeds up the processes of dissolution of metastable skeletal components and the precipitation of LMC. Thus, the presence of the meteoric vadose cement phase might indicate that vadose zone processes have assisted in accelerating carbonate saturation and hence the overall cementation of the aeolianites. The model of formation suggested

for the phase 1 and 2 cements is supported not only by the observed textures and LMC composition of these cements (Figures 8.15 to 8.17) but also by characteristic meteoric phreatic features such as syntaxial overgrowths and dissolution of unstable mineralogies (Figures 8.15c, 8.16f and 8.17a,c). McCarthy (1992) proposed a similar process of cementation for the Bluff dune ridge whereby initial under-saturated percolating rain water becomes progressively saturated, except he suggested cement precipitation occurred through evaporation of interstitial water during dry periods.

For Units A1 and A2 cementation must have followed soon after deposition (134 - 127 ka cal B.P.) so as to survive the ensuing transgression (Figure 8.31b). Unit A3 was deposited (93 ± 6 ka cal B.P.) either during or after the sea-level highstand of MIS 5c (Figure 8.31b) and although the timing of precipitation of the meteoric cement cannot be established with certainty it most likely followed soon after deposition as Unit A3 had to survive the sea-level transgression of MIS 5a.

Stage 2 Diagenesis

Following the initial mainly meteoric phreatic cementation of stage 1, stage 2 diagenesis is characterised by general cement erosion, decementation and associated increase in porosity. Although the exact timing of this erosional period is not certain, it has two aspects related to different palaeosea-level regimes which are interpreted not only to have time significance but also resulted in decementation and porosity changes due to;

1. groundwater table fluctuations related to alternating stages of emergence and submergence due to the high frequency MIS 5 sea-level fluctuations (refer to as stage 2.1 on Figure 8.31b),
2. complete subaerial exposure and hence carbonate solution related to the overall MIS 4 - 2 sea-level depression towards the LGM lowstand (refer to as stage 2.2 on Figure 8.31b).

Cooper and Flores (1991) and Ramsay (1991, 1996) ascribed decementation in carbonate-cemented nearshore sediments and aeolianites to changes in the groundwater table. According to Coudray and Montaggioni (1986) chemical solution of carbonate material almost exclusively occurs within the meteoric vadose and phreatic zones. These authors further also suggest that the most intense decementation and especially porosity development in carbonates can occur at the water table level. Thus, it is likely that at least some of the cement erosion and porosity improvement in especially Units A1 and A2 might be related to sea-level and associated groundwater table fluctuations which characterised diagenetic stage 2.1 (Figure 8.31b).

During the MIS 4 -2 sea-level depression the aeolianites would have been completely exposed from ~77 to 10 ka cal B.P. (Figure 8.31b) and thus stranded increasingly in the meteoric vadose zone as regression progressed. Whether meteoric cementation occurred during the earlier stages of

the sea-level lowering is not certain but there is no evidence for it. In addition, during the LGM this part of the exposed shelf formed an interfluve area (Chapter 6) with probable reduced groundwater conditions associated with the global climate desiccation related to the LGM not favouring any meteoric cementation. Climate exerts a strong influence on diagenesis if subaerially exposure occurs and in arid conditions carbonate solution generally dominates in the meteoric environments (Longman, 1980; Coudray and Montaggioni, 1986). Along the coastline further north from the Aliwal Shoal, Porat and Botha (2008) found that MIS 4 -2 was mainly a time of dune migration and not construction. These authors also linked it to increased windiness and a general desiccation of the global climate to the LGM, thereby supporting a leaching and not cementation regime. Erosion of both meteoric and possibly previous marine phases linked to the MIS5 are attributed to stage 2.2 (Figure 8.31b) with the greatest porosity increases seemingly occurring in the vicinity of the aeolianite surface with a decrease further towards the interior as is evident in the GC-series samples. In addition, the stage 2 diagenetic observations and subsequent interpretations from the Aliwal Shoal aeolianites also support the views of;

1) Melim *et al*. (2002) insofar phreatic meteoric cementation is not necessarily attributed to large-scale sea-level lowstands, and that of
2) Braithwaite and Camoin, (2011), insofar the importance of carbonate erosion and porosity development in carbonate sediments during sea-level lowstands.

Stage 3 Diagenesis

Stage 3 is predominantly characterised by last generation pore lining cements comprising bladed and fibrous isopachous crust and micritic coats and void fills. All the data indicate that the first diagenetic event in the meteoric environment is the loss of Mg^{2+} from HMC followed by solution of aragonite and precipitation of LMC (Bathurst, 1975, Tucker and Wright, 1990). Thus, HMC, especially those with >12 mole% MgCO3 (Walter, 1985) is less stable than aragonite and would be rapidly dissolved in a meteoric environment. Cement phases 3 to 8 are all HMC cements as indicated by their morphology and composition (Figures 8.15 to 8.17; Appendix VI, Table VI.1). The age of these marine phases are all ascribed to the last deglacial sea-level rise based mainly on three lines of evidence; 1) the marine cements show original metastable marine composition indicating mineral transformations to the more stable LMC have not occurred and thus these cements are still most likely in the environment of formation, 2) aeolianite marine cements are similar in morphology and composition to the marine cements preserved in beachrock Units 1 to 4, all of which are dated to have formed sequentially during the Holocene transgression (Chapter 9) and 3) no evidence of subsequent meteoric cement phases.

The rapid sea-level transgression following the LGM lowstand (see Chapters 4 and 9) progressively drowned the aeolianites depositing marine cement phases within the newly created

voids generated by subaerial exposure during the previous diagenesis stage (stage 2; Figure 8.Model). A similar diagenetic sequence was observed by Sherman *et al*. (1999) in submerged Pleistocene carbonates offshore of the Hawaiian island of Oahu. The variability and multi-layered nature of the last stage marine cement phases (only observed in hand specimens) is possibly related to variations in pore size and pore fluid according to Braithwaite and Camoin (2011), which also concluded that in these cases a lesser number of cement generations do not mean a shorter or less eventful history than a greater number and that equal numbers of cement generations do not necessarily implies the same history.

Summary

Considering the results from the three major diagenetic stages discussed above it is clear that the cementation histories of the Aliwal Shoal aeolianites are not a straightforward sum of accumulation and although some overprinting is observed it does not form a simple sequence of successive overprints. However, it was possible to group the diagenetic products into three distinctive packages of diagenetic features that are linked to discrete cycles of sea-level change (Figure 8.31b) and not to changes in the distribution of the diagenetic (hydrological) zones during an individual emergence event. Although, the approach of grouping distinctive diagenetic features together is similar to that applied by Braithwaite and Camoin (2011), it differs fundamentally insofar the Aliwal Shoal diagenesis show cement overprinting of subsequent packages by later sea-level occupations, whereas on the contrary, Braithwaite and Camoin (2011) observed no overprinting by later sea-level stands.

The complex and high variability in the type and occurrence of the carbonate cements of the Aliwal Shoal aeolianites is not an uncommon observation in diagenesis studies of carbonate sediments subjected to high-frequency glacio-eustatic sea-level changes (Tucker and Wright, 1990; Braithwaite and Camoin, 2011). Matthews and Frohlich (1987), Quinn and Matthews (1990) and Whitaker *et al*. (1997) all generated computer models of the diagenetic products of the varying hydrological zones during high-frequency glacio-eustatic sea-level changes. All of these models yielded such complex diagenetic sequences due to successive overprinting that the diagenetic history, as concluded by Whitaker *et al*. (1997) '*could not be unravelled by traditional stratigraphical and sedimentological methods*'.

Beachrock Diagenesis

The diagenetic history of the beachrock units is relatively simple when compared with that of the aeolianites. However, one beachrock unit, Unit B5, shows a different diagenetic pathway which is related to its age. Thus the beachrocks can be separated into two groups based on diagenetic history and age.

Units B1 to B4

All samples from Unit B1 to B4 exhibit only one major marine cement phase comprising either aragonite or HMC. The fact that these marine cements still show original metastable composition indicates that the beachrocks are still in their original diagenetic environment (Sherman *et al*., 1999). This inference is supported by both OSL and radiocarbon ages (Chapter 9) which indicate that the beachrocks formed during the Holocene sea-level transgression (diagenetic stage 3; Figure 8.31b). Additional marine phreatic zone cements includes micritic grain coats and some rare late stage pelloidal void-fill micrite related to the bio-erosive action of sponges, but are not considered cements responsible for beachrock lithification and preservation. Except for Unit B2 which may possibly have been cemented in the vadose zone, all the Holocene beachrocks show cementation in the marine phreatic zone.

There are differences in the chemical composition of the cements for the various beachrock units. The oldest dated beachrock unit (Unit B1) in the study area shows pristine acicular aragonite, whereas subsequent beachrock Units B2 to B3 show isopachous bladed to fibrous HMC cements. Facies 1 of Unit B4 again exhibit acicular aragonite whilst Facies 2 show isopachous bladed to fibrous HMC. After decades of research it is still not apparent which factors primarily controls the mineralogy and the crystal habit of beachrock cements, only broad trends have been found (Vousdoukas *et al*., 2007, also see Section 8.3.2). Lightly (1985) notice that aragonite precipitated before HMC in reefs offshore Florida. Whittle *et al*. (1993) observed a systematic change in cement fabric and mineralogies in the Bahamas postulated to be related to changing water chemistry. They suggested a sequence comprising; seaward micritic dominated textures, fine fibrous aragonite in a more lagoonal setting and coarser aragonite needles and HMC cements in the intertidal and supratidal zones.

There also seems to be a broad succession of cements from aragonite to HMC in the Aliwal Shoal beachrocks. The initial log-spiral bay coastal configuration comprising Units B1 and B2 show a progression from aragonite to HMC cement. Unit B3 marks the change from the previous log-spiral configuration to a linear shoreline and its position was probably influenced by the estuarine outlet which might have inhibited aragonite formation due to dilution of marine water with fresh water. Aragonite precipitation is favoured under conditions of oxygenated pore-waters, increasing ratios of ambient Mg/Ca and increasing rates of supply of CO_3^{2-} ions (Tucker and Wright, 1990) all of which are highly diminished in estuarine outlet water compared to the marine water in the active phreatic zone. Similar differences in aragonite and HMC related to environment of formation was also noted by Scoffin and McLean (1978) in the Northern Province of the Great Barrier Reef which found leeward and windward beaches cemented by aragonite and HMC,

respectively. They linked aragonite formation to an absence of trapped fines and exposure to open-shelf seawater, whilst the HMC was associated with trapped fines and a range of water chemistries (Scoffin and McLean, 1978).

Unit B4 shows the change from aragonite to HMC again and is interpreted to be responsible for the sudden closure of the estuarine outlet and as such removed the possible fresh water component which could have inhibited aragonite precipitation in Unit B3. In addition, Units B1 to B4 formed during the MWP-1b period which according to Stanford *et al*. (2011) is expressed as a broad multi-millennium period of enhanced pulses of sea-level rise following the sea-level slowdown of the Younger Dryas cold event (12.9 - 11.7 ka cal B.P; Section 4.4.2). Recent results from the Maldives carbonate platform by Paul *et al*. (2011) indicated that aragonite precipitation during the last 150 ka was linked to marine flooding events and hence related to sea-level change. As such the aragonite-HMC cycle in the Aliwal Shoal beachrocks might indicate two flooding events associated with pulses of enhanced rates of sea-level rise, which subsequently might also have been associated with changes in the seawater aragonite/calcite stability field.

Cementation of the Aliwal Shoal beachrocks is interpreted to have occurred under the following conditions (Folk, 1974; Scoffin and Stoddart, 1983; Tucker and Wright, 1990);

1) Relative stability of sediment grains and lack of mechanical abrasion to allow the delicate crystals to form,
2) Supersaturation of seawater with respect to $CaCO_3$ (direct cement precipitation model),
3) High Mg/Ca ratios,
4) Oxygenated pores waters,
5) High water exchange rates and a pumping mechanism to force large quantities of pore volumes of supersaturated seawater through the sediment, e.g. high energy shoreline with intense wave, storm and tidal processes.
6) Sufficient residence time of groundwater in the landward areas to acquire high partial pressure of CO_2 and supersaturation of $CaCO_3$, combined with sufficient residence time in forebeach areas for degassing to occur (Hanor, 1978) and modest rates of groundwater discharge in a seaward direction (CO_2-degassing model). The groundwater is allowed any chemistry including fresh, brackish and saline (Hanor, 1978).

Cementation of beachrock Units B1 to B4 is considered to have occurred under a cover of unconsolidated sediment through the mechanisms of either 1) direct inorganic precipitation from $CaCO_3$ supersaturated seawater or possibly through 2) CO_2-degassing. The mechanism of CO_2-degassing is considered the most applicable as no beachrocks are forming on the study area shoreline today. Since the present climate and seawater chemistry is not considered to be

significantly different from that which resulted in the formation of the Aliwal Shoal beachrocks some other reason must be found for the formation of beachrocks during the Holocene transgression. The most significant difference is that during formation of Units B1 to B4 a large $CaCO_3$-rich aeolianite coastal barrier system (larger than present) was situated landwards of the beachrocks. This would have supplied supersaturated $CaCO_3$ groundwater to the beach which upon mixing with the seawater in the intertidal zone would have precipitated cement as a consequence of the loss of CO_2 and which is enhanced by tidal pumping (Hanor, 1978; Ramsay 1991, 1996). Microbial processes may aid CO_2 supersaturation and carbonate cementation (Neumeier, 1999). Cementation by the CO_2-degassing mechanism is a self-regulatory mechanism, lowering the porosity of the sediments which then decreases the ability of the system to degas thereby controlling both the relative volume of pore space that can be closed-off by cementation and the maximum thickness of the cemented zone that can be developed (Hanor, 1978). This self-limiting mechanism might explain the relative variation in the amount of cementation and the variable thickness of the beachrock units. Notwithstanding the exact mechanism of formation, cementation had to be rapid and soon after deposition, if not contemporaneous with deposition to withstand the ensuing transgression.

Ramsay (1991) proposed a similar mechanism of formation for the Maputaland beachrocks on the northeast coast of South Africa where mixing of supersaturated $CaCO_3$ groundwater with seawater and/or precipitation through solar heating at low-tides results in cement precipitation. According to Ramsay (1991, 1995) contemporary beachrocks are formed beneath a 0.1 to 0.3 m cover of unconsolidated sediment, 0.1 to 0.2 m above mean sea-level. Cawthra (2010) ascribed beachrock formation offshore the Bluff to inorganic $CaCO_3$ precipitation. She also observed the formation of recent beachrock containing anthropogenic artefacts and ascribed its cementation to a chemical reaction occurring at the interface between oxidising fluids percolating through the foreshore and the reducing seawater (Cawthra, 2010).

Unit B5

Unit B5 is interpreted as a high-energy storm or possible tsunami deposit and is much older than beachrock Units B1 to B4 which formed sequentially during the last deglacial sea-level rise (Chapter 9). Unit B5's diagenesis following formation is therefore different from Units B1 to B4.

The diagenetic sequence of Unit B5 is interpreted into 3 stages;

1) Diagenetic stage 2.1 - initial marine vadose HMC cementation following deposition during the storm event. Deposition is interpreted to have occurred above MSL with the pore waters initially infiltrated by marine water due to the storm surge. The diagenetic environment during deposition

would most likely, at least initially, have been marine vadose in character resulting in the thin, uneven marine cement.
2) Diagenetic stage 2.2 - inversion of the marine HMC cement to LMC along with general cement erosion, decementation and associated increase in porosity, characteristic of this diagenetic stage.
3) Diagenetic stage 3 - deposition of pore lining cements comprising bladed isopachous crust and occasional micritic grain coating and void fills related to submergence during the Holocene transgression.

Summary

The diagenetic sequence for the Holocene beachrocks of Unit B1 to B4 comprises initial micrite grain coats followed by one major phase of either aragonite or HMC marine phreatic cement finally followed by rare late stage pelloidal void-fill micrite related to the bio-erosive action of sponges. Unit B5 shows a diagenetic sequence comprising initial marine-like (HMC) vadose cementation which inverted to LMC during a period of emergence and decementation and was finally followed by marine phreatic HMC cementation deposited during the Holocene transgression.

An oddity of the marine phreatic cementation that occurred during the last deglacial sea-level rise is that it displays multiphase isopachous forms in the aeolianite whereas in the beachrock and GC-series aeolianite samples there are is only one phase present. Although the exact reason for this is not known it is possibly related to differences in the depositional setting at the time of the transgression. Whereas the beachrocks were cemented and drowned in the same diagenetic zone, the aeolianites were already cemented with subsequent marine phreatic cementation occurring during the transgression. However, the subaerially exposed aeolianites were also subjected to different fluctuating hydrological zones dependant on the relative position of sea-level and the groundwater table (controlled by rainfall). The higher porosity of the outer aeolianite crust might have allowed for higher or differential rates of pore fluid flow and hence preservation of different phases of cements during oscillation of the hydrological zone related to changes in sea-level and climate.

Considering that an aeolianite in thin section can appear to be a beachrock with one phase of marine cement (Figure 8.14f), a useful distinguishing feature might be that aeolianites show replacement of metastable grains with associated micrictic envelopes whereas the beachrocks do not.

Aeolianite and Beachrock Formation Models from Submerged Deposits

This study proposed a model of formation of aeolianite and beachrock lithologies during times of lower sea-levels when the shelf was characterised by coastal barrier dunes and back-barrier lagoons and estuaries. Similar deposits were studied by Ramsay (1991) and Cawthra (2010), the results of which contrast from that proposed here.

Ramsay (1991; 1996) showed that the offshore reef systems on the Sodwana continental shelf comprised stacked aeolianite to foreshore sedimentary units defining a regressive sequence formed during the sea-level depression towards the LGM. Ramsay (1991, 1996) also mapped distinct linear ridges on the shelf interpreted to represent 4 palaeocoastline events at 117 ka B.P., 100 - 97 ka B.P., 97 - 23 ka B.P. and 23 - 22 ka B.P. defining a seaward younging succession deposited during the regression towards the LGM. Cawthra (2010) proposed that the onshore and offshore Bluff aeolianites also represent a seaward younging sequence comprising eight Pleistocene 'fossil dune cordons' palaeocoastline events formed in response to the sea-level regression towards the LGM. Thus, although not directly stated by Cawthra (2010) her model of aeolianite formation mirrors that proposed by Ramsay (1991, 1996).

This study investigated a single submerged dune ridge subdivided into three aeolianite and five beachrock units (Section 8.3.3). Results presented here show that the submerged Aliwal Shoal complex forms a compound coastal barrier ridge system consisting of a core of several aeolianite units deposited from MIS 6 to MIS5a, which are unconformably overlain by predominantly Holocene-age beachrocks. Aeolianite units formed during the transgression following the penultimate glacial maximum (MIS 6), slightly preceding the last interglacial, with the youngest aeolianite forming during the MIS 5c highstand during the overall regression towards the LGM. With the exception of an extreme event unit (Unit B5) all the dated beachrock units formed sequentially during the last deglacial sea-level rise, either overlying unconsolidated sediments or the older aeolianite units. Thus, aeolianite and beachrock formation and preservation occurred predominantly during fast sea-level transgressions spanning several sea-level cycles.

Whereas the Ramsay (1991, 1996)/Cawthra (2010) models require distinct dune ridges to represent discrete units of preserved palaeo-coastline events (i.e. one age per palaeocoastline event) formed on the last forced regression towards the LGM, thereby showing an overall younging in a seaward direction, the Aliwal Shoal model shows that one ridge can represent many unique palaeocoastline events deposited over several sea-level cycles with an overall younging in a landward direction.

In addition, the Aliwal Shoal data show that dune building can occur contemporaneously as vertical accretion (Unit A1) and lateral amalgamation (Unit A2) along strike, in addition to younger dunes (Unit A3) abutting older dunes (Units A1 and A3) laterally. Cawthra, (2010) also suggested vertical accretion but with lateral accretion only comprising younger aeolianites abutting older dunes in an onshore-offshore direction.

Also, shown in this study is that aeolianites can be re-cemented by subsequent marine cements increasing their preservation potential. Thus, for these submerged aeolianites to form and to be preserved one does not need to invoke a regression followed by long emergence to generate sufficient cementation to withstand the subsequent transgression. In contrast as shown by the Aliwal Shoal aeolianites, an extended regression may result in decementation and porosity increase.

The Aliwal Shelf beachrocks formed sequentially during the Holocene transgression and document the passage of the transgressive shoreface across not only the pre-existing aeolianites but also overstepping an embayed barrier-lagoon system. Both Ramsay (1991, 1996) and Cawthra (2010) observed stranded beachrock units, but these studies both lacked rigorous geochronological control. Ramsay (1991, 1996) ascribed beachrock formation to the sea-level regression and temporary stillstands during MIS 4 - 2. Cawthra (2010) assigned her submerged beachrocks (Unit 4 Beachrock to Unit 13 Beachrock), similarly to the Aliwal Shoal units, to sequential formation during the Holocene transgression. However, all of her beachrock samples show LMC cements, with Units 1, 3, 5, 8 and 9 showing low porosity related to high amounts of LMC with only Units 2 and 3 exhibiting true beachrock-like cement morphologies. Although Cawthra (2010) invoked precipitation of calcite spar in the beach environment during low tides to account for the presence of the meteoric cement it is unlikely that this would have been a primary cementation process for all of the beachrocks on a rapid sea-level transgression. As evident from the Aliwal Shoal beachrocks, if sequential formation and subsequent preservation is to occur on a sea-level transgression some important conditions are required and consequently distinctive features produced; 1) cementation must follow soon after deposition, 2) rate of sea-level transgression must be fast with a relative lower gradient setting in an overall high gradient shelf aiding in the accelerated rate of sea-level rise and beachrock preservation (Section 6.4.3), 3). Beachrock will be cemented predominantly by a single marine cement phase and thus have an associated relatively high cement-reduced porosity, 4) general absence of meteoric cement phases, although it is possible that some beachrocks may show limited meteoric void-fill cement due to a regressive sea-level phase related to a temporary beach progradation event. However, overall a transgressive sea-level regime must be implied by the cement textures and their composition and the superposition of depositional environments.

Thus, as observed from the Aliwal Shoal, the offshore submerged coastal barrier cordon represents a compound system of different types and ages of aeolian and littoral lithofacies deposited in different, albeit sometimes juxtaposed, depositional environments which were intermittently exposed to reshaping by erosion and/or deposition during numerous high frequency and amplitude sea-level fluctuations.

8.4 UNCONSOLIDATED SEAFLOOR SEDIMENTS

A detailed investigation into the nature and composition of the unconsolidated sediments is beyond the scope of this study and forms part of a continuing investigation into the sediment dynamics of the shelf, especially relating to the Mkomazi subaqueous-delta clinoform (Section 6.4.3). However, what is important here are new observations relating to the large-scale processes responsible for the observed complex patterns of sediment distribution, thereby providing new insights into the sediment dynamics on this part of the South African continental shelf.

51 sediment samples (Figure 8.32) were obtained from the seafloor sampling the various acoustic facies (Figure 8.3, Appendix VIII). Details regarding the grain size distribution data are provided in Appendix VIII, Table VIII.2 to Table VIII.4, whilst detailed mineralogical compositional data are provided in Appendix VIII, Table VIII.5 to Table VIII.5.

8.4.1 Seafloor Sedimentary Characteristics

The regional sedimentary characteristics within the study area are inferred from the grain size distribution data (Appendix VIII, Tables VIII.2 to VIII.4). Although palimpsest and relict sediments (Swift *et al*., 1971) might result in the problem of inherited characteristics, the regional sediment transport regime (at the time of sampling) can be broadly constrained by the dispersal patterns of the various grain sizes (Figure 8.33a to h).

Two patterns dominate the grain size distributions in the study area (Figure 8.33); 1) an approximate north-south trending pattern and 2) ‘bulls-eye’ patterns comprising isolated low or high values. The bulls-eye patterns are mainly attributed to the large sample spacing but it some cases it might also represent a relict or palimpsest grain size distribution.

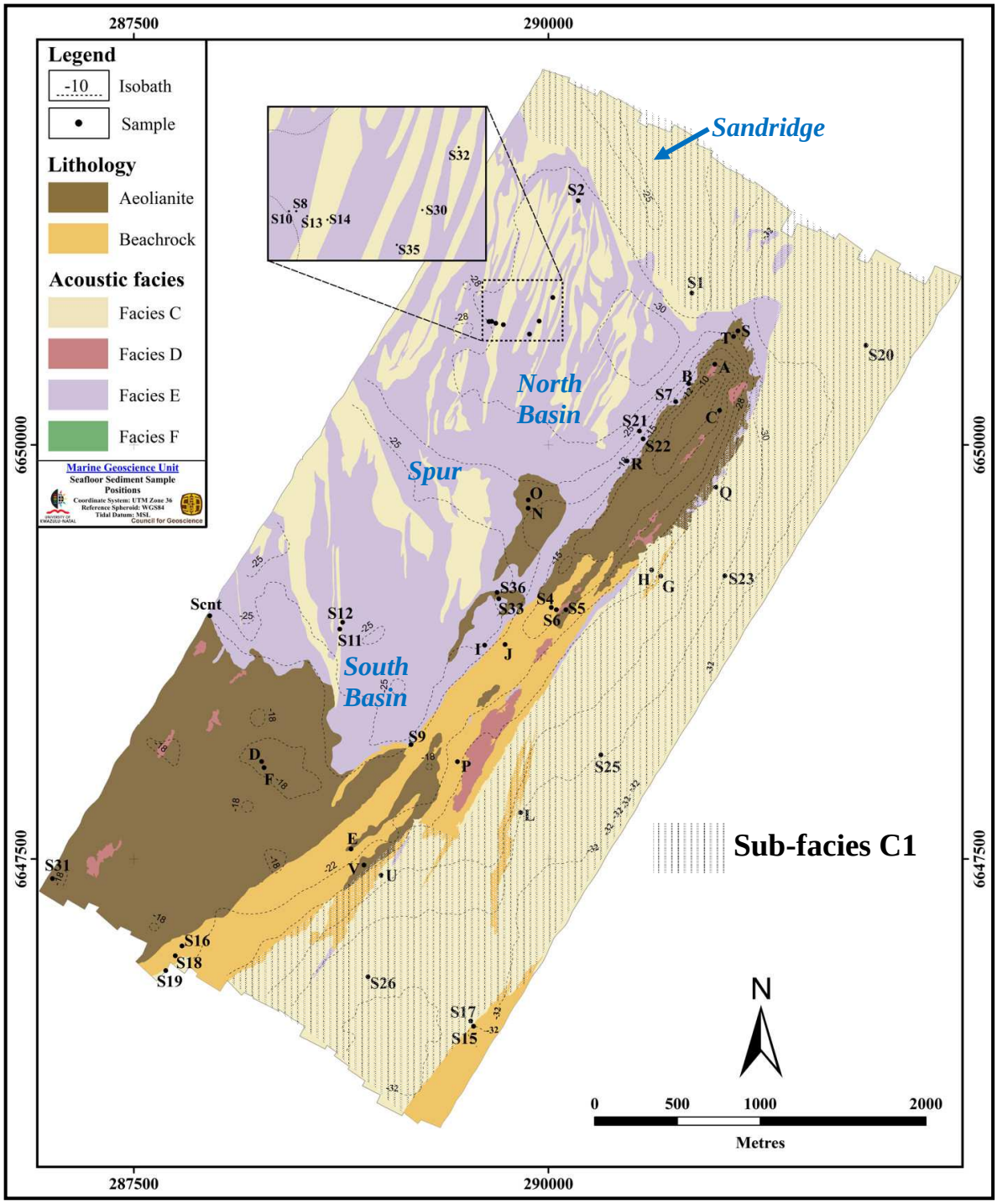

Figure 8.32 Sediment sample localities plotted on the interpreted lithologies (Section 8.3) and acoustic facies interpretation map. Also shown are seafloor morphological features (see Chapter 7) referred to in the text and the approximate coverage of acoustic sub-facies C1 (refer to text for details). The morphological features of the *North Basin* and *South Basin* are collectively referred to as the *Basin*. Note: isobaths are not in constant intervals. Also refer to Appendix IV, Tables IV.I and IV.II for additional information.

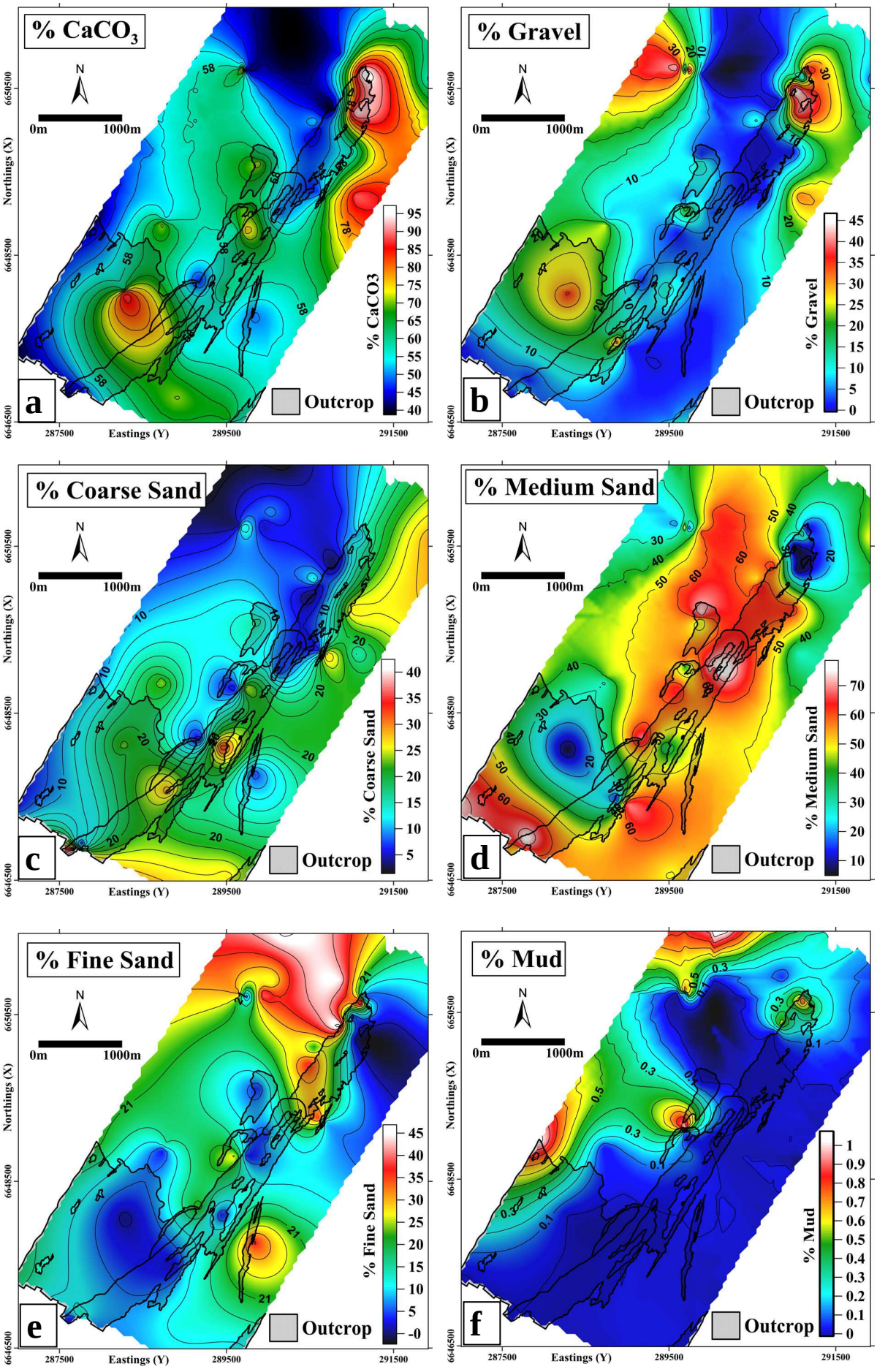
% CaCO3
% Gravel
% Coarse Sand
% Medium Sand
% Fine Sand
% Mud
N
0m
1000m
Northings (X)
Eastings (Y)
6650500
6648500
6646500
287500
289500
291500
Outcrop
a
b
c
d
e
f

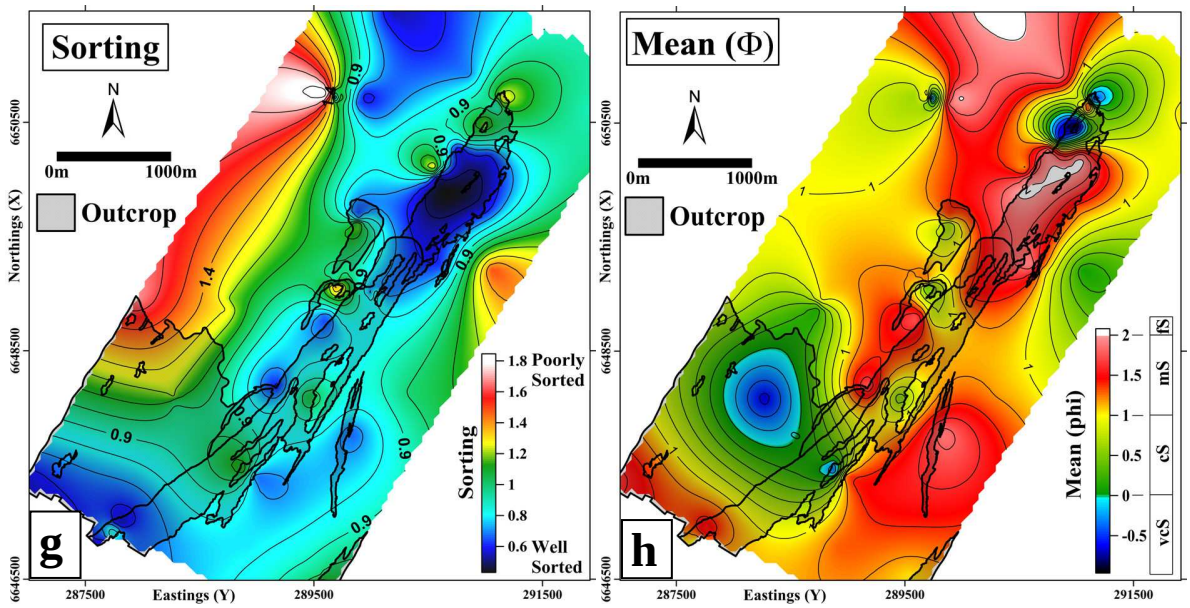

Figure 8.33 (cont.) Grain size distribution maps of surficial seafloor sediments in the study area. Abbreviations as follows; vcS = very coarse sand, cS = coarse sand, mS = medium sand, fS = fine sand, **a)** Percentage $CaCO_3$, contour interval = 4 %. Note the high carbonate content range (minimum value = 38.5 %). **b)** Percentage gravel, contour interval = 5 %. **c)** Percentage coarse sand, contour interval = 5 %. **d)** Percentage medium sand, contour interval = 10 %. **e)** Percentage fine sand, contour interval = 5 %. **f)** Percentage mud, contour interval = 0.1 %. Note the very low values (generally <1 %) for the mud fraction. **g)** Sorting (phi), contour interval = 0.1 %. **h)** Mean (phi) grains size, contour interval = 0.2 %.

$CaCO_3$, gravel and coarse sand (Figure 8.33a to c) show an inverse pattern to medium and fine sand (Figure 8.33d and e). The gravel fraction further also shows a 'bulls-eye' pattern indicating highly localised occurrences controlling the pattern. As expected there is a correspondence between high carbonate content and the occurrence of gravel (Figure 8.33a and b) indicating that at least some of the gravel fraction especially that located on the reef outcrop, is derived from coarse grained skeletal carbonate similarly as that found by Ramsay (1991, 1996), Richardson (2005) and Cawthra (2010). Uncharacteristic occurrences of gravel include sample S23 (Figure 8.32) which is located seaward of the Aliwal Shoal within Facies C, the quartzose shelf sand but probably represents the subjacent Facies E palimpsest sediment (see Figure 37). Gravel was also found in the *Basin* and is usually part of the lag deposits of acoustic facies E (Figure 8.32, Section 8.4.2).

Medium sand forms a prominent N-S trending feature across the Aliwal Shoal and study area (Figure 8.33d), whilst the fine sand fraction dominates the north-western sector of the study area, mimicking the *Sandridge* (Figure 8.32) with an associated tongue extending southwards (Figure 8.33e). An isolated bulls-eye occurrence of fine sand is due to sample L which is located seaward of beachrock Unit B2 (Figure 8.32). The distribution pattern for the mud fraction is unlike any of the other size fractions and even cut across the common bedform and other dispersal trends (NW-

SE, N-S, NE-SW). It is likely that these deposits, excluding the bulls-eye occurrences, represent settling of mud from buoyant plumes generated by river discharge (Figure 8.34).

Figure 8.34 Images of the buoyant mud-rich plume emanating from the Mkomazi River during conditions of high river discharge. **a)** Photo looking east from the bridge above the mouth of the Mkomazi River (see Figures 1.1, 2.9 and 6.4). Note the plume extending southwards. **b)** Photograph (same day) looking east towards the Aliwal Shoal from Green Point (see Figure 1.1 for locality). Note the less intense but still prominent buoyant plume and the distinct interface between the mud-rich inshore plume and clean offshore Agulhas Current dominated water. The interface is located very close to the Aliwal Shoal.

The mean and sorting size parameters (Figure 8.33g, h) summarises the overall pattern observed from the individual size fractions. In essence medium and fine sand is well dispersed and well sorted generally having an approximate NW-SE to N-S trend, whilst coarser poorly sorted fractions are localised or either on reef or within the *Basin* related to lag deposits. Some of the best and worst sorted sediment is found on the reef. The well sorted aspect is interpreted to be due to persistent wave action reworking of unconstrained on-reef sediments, whilst the poorly sorted aspect is due to sediment trapped in gullies comprising palimpsest lag deposits and/or a high percentage of reef/derived skeletal carbonate.

The origin of the fine and medium sand is linked to dispersal via the SCR system, specifically the *Sandridge* (constituting SCR crests 1 and 2; Figures 7.9 and 7.10). The grain size data thereby corroborated the ridge migration data (Figure 7.12) indicating across-shelf sediment dispersal of fine and medium sand (also see Figure 6.17) most likely through storm return flows (refer to Chapter 7, Sections 7.4.1 and 7.4.3). However, the fine and medium sand display a slightly different dispersal pattern with especially the fine sand noticeably related to the *Sandridge* SCR (Figure 8.33e). The medium sand on the contrary occurs along a north-south trend across the entire study area and even traversing the topographic feature of the Aliwal Shoal ridge (Figure 8.33d). The reason for this is not certain as it is unlikely that a storm return flow can mobilise medium grained sediment across and over the Aliwal Shoal ridge if not even the fine grained sediment shows this pattern. A possible explanation is that the medium sand fraction is the most commonly available sediment size fraction with the aeolianites, beachrocks and even unconsolidated sediments on average comprising medium sand (compare Tables 8.2, 8.8 and 8.10), which combined with the sparse sample density and presence of palimpsest sediments result in all areas except the isolated coarser areas comprising medium sand. Interestingly the fine sand not only shows an across shelf mobilisation but also a pattern of dispersal into the *Basin* (Figure 8.33e). This secondary pattern of sediment movement from the *Sandridge* into the *Basin* is also mirrored by the sorting (Figure 8.33g) and mean (Figure 8.33h) parameters.

Thus, the grain size data confirms that the SCR system provides medium and fine sand to the shelf, with the fine sand fraction almost exclusively provided by the *Sandridge*. Remobilisation of sediment from the *Sandridge* into the *Basin* indicates a secondary dispersal system not related to the storm return flows.

8.4.2 Acoustic Facies and Sedimentary Distribution Patterns

Unconsolidated sediments were classified into 3 acoustic facies (Facies C to E) based on the interpretation of the 100 kHz side-scan sonar mosaic (Section 8.2; Figures 8.1 to 8.3). A summary of the average textural and mineralogical compositional values for each of the acoustic facies are presented in Table 8.10 with detailed data provided in Appendix VIII.

Facies C

Facies C is the most extensive acoustic facies (Figure 8.32) and hence unconsolidated sediment type covering ~7 800 000 m^2 of seafloor. Sonographs of this facies (Figure 8.2, sonographs 1, 2,

4, 6 and 7; Table 8.1) are weak to moderately reflective, even toned to occasionally granular showing small (oscillation ripples) to very large (SCR, *Sandridge*) bedforms. Facies C on average comprise a moderately sorted strongly coarse-skewed medium sand composed mainly of quartz (56 %), minor feldspar (9 %) and bioclastic fragments (34 %), showing a fairly high average carbonate content of 55 % (Table 8.10).

Table 8.10 Summary of the textural and compositional data for Facies C, D and E obtained from petrographical analyses (also see Appendix VIII). UW = Udden-Wentworth classification, Sk = skewness, Qtz = quartz, Fspr = feldspar, Lith Frag = lithic fragments, HM = heavy minerals, Bio = bioclastic components (skeletal carbonate), $CaCO_3$ = carbonate content percentage, mS = medium sand, cS = coarse sand, Ms = moderately sorted, fs = fine-skewed, scs = strongly coarse-skewed. For the subdivisions of Facies C refer to the text and Appendix VIII, Table VIII.2. C Avg = average of Facies C.

Facies	Mean (phi)	UW	Sorting		Skewness		Mineralogy (%)					$CaCO_3$ %
							Qtz	Fspr	Lith Frag	HM	Bio	
C1	1.10	mS	0.98	Ms	-0.96	scs	57	10	0	1	33	64
C2	1.34	mS	0.74	Ms	-1.02	scs	58	7	0	1	34	55
C3	1.04	mS	0.87	Ms	0.14	fs	54	10	0	2	34	47
C Avg	1.16	mS	0.86	Ms	-0.61	scs	56	9	0	1	34	55
D	0.76	cS	0.92	Ms	-1.39	scs	50	5	1	1	44	67
E	1.30	mS	0.98	Ms	-2.55	scs	60	10	0	1	28	53

Facies C is interpreted as *quartzose shelf sand* and thus forms part of seismic Unit Dsc which includes the Mkomazi Subaqueous-Delta Clinoform (MSDC, Section 6.4.3). It is equivalent to Ramsay's (1991, 1996), Richardson's (2005) and Cawthra (2010) quartzose shelf sand. The major difference is that Facies C is generally coarser grained, shows lower quartz and higher bioclastic values and subsequently $CaCO_3$ content values (Table 8.11). Thus, the pattern of coarser grain sizes and higher carbonate content observed in the aeolianites and even beachrocks compared to that of similar studies is repeated in Facies C.

Facies C is further subdivided based on physiographic position of the samples (Figure 8.32). C1 (Figure 8.35a) is considered unobstructed shelf sediment comprising the area seaward of the Aliwal Shoal and the *Sandridge*, C2 (Figure 8.35b) is shelf sediment in proximity of reef outcrops and C3 (Figure 8.35c) is redistributed shelf sediment located within the *Basin* feature behind the Aliwal Shoal and which comprises sediment veneers and starved bedforms. Although there is very limited variation between the sub-facies types (Figure 8.35a-c; Table 8.10) some unexpected patterns are observed. The open shelf sub-facies C1 is not the finest grained and has the highest carbonate content, even higher than the reef-associated sub-facies C2. As C1 has the lowest

bioclastic content and almost non-existing lithic components, which might contribute carbonate, the source of the high carbonate content remains uncertain. In addition, C1 is the worst sorted sub-facies. This is unexpected as Facies C1 is the most exposed to reworking by geostrophic currents and waves and as such should have a better sorting value than at the reef-associated sub-facies C2 (Ramsay, 1991, 1996). Also, contrary to the expected, relative to the other sub-facies C2 displays the best sorting, finest grain size and a mid-range carbonate (Table 8.10). As C2 is located close to reef outcrop these are expected to show a greater amount of reef-derived skeletal bioclastic fragments which would increase the carbonate content and also should result in a worse sorting value. C3 displays a large range of textural values (Appendix VIII, Table VIII.2) resulting in an average that does not necessarily reflect the true character of the sub-facies. Nonetheless a striking feature of C3 is that it is the only sub-facies consistently displaying a positive skewness. According to Tucker (1991) sediment becomes more negatively skewed with increasing transport. Thus, the distinct positive skewness of C3 might be related to the secondary remobilisation of sediment from the *Sandridge* into the *Basin* as was found in Section 8.4.1. Alternatively it might be due to mixing with the lag deposits of Facies E.

Table 8.11 Textural parameters and carbonate content from equivalent studies of shelf sand sediments similar to that of Facies C. UW = Udden-Wentworth classification, $CaCO_3$ = carbonate content percentage, fS = fine sand, mS = medium sand, Ms = moderately sorted, Ws = well sorted, mWs = moderately well sorted. See Figure 1.1 for the locations of the various other studies.

Parameter	Aliwal Shoal	Ramsay (1991)	Richardson (2005)	Cawthra (2010)
UW	mS	fS	fS (2.2)	fS
Sorting	Ms	Ms - Ws	mWs	Ms - Ws
$CaCO_3$	39 - 90	4 - 13	10 - 36	7 -39

Sedimentary structures in Sub-facies C1 and C2 include oscillation ripples whilst C1 also contain the very large Sandridge bedform (Figure 8.32). Oscillation (wave) ripples (Figure 8.35d) generally trend either NE-SW or NW-SE are straight, sinuous and bifurcating mostly with sharp crests although rounded crest are also present and range in wavelength (L) from 4 - 30 cm and amplitude (H) from 1 to 10 cm. Interference ripples are common and related to different and superimposing swell directions (Ramsay, 1991, 1996).

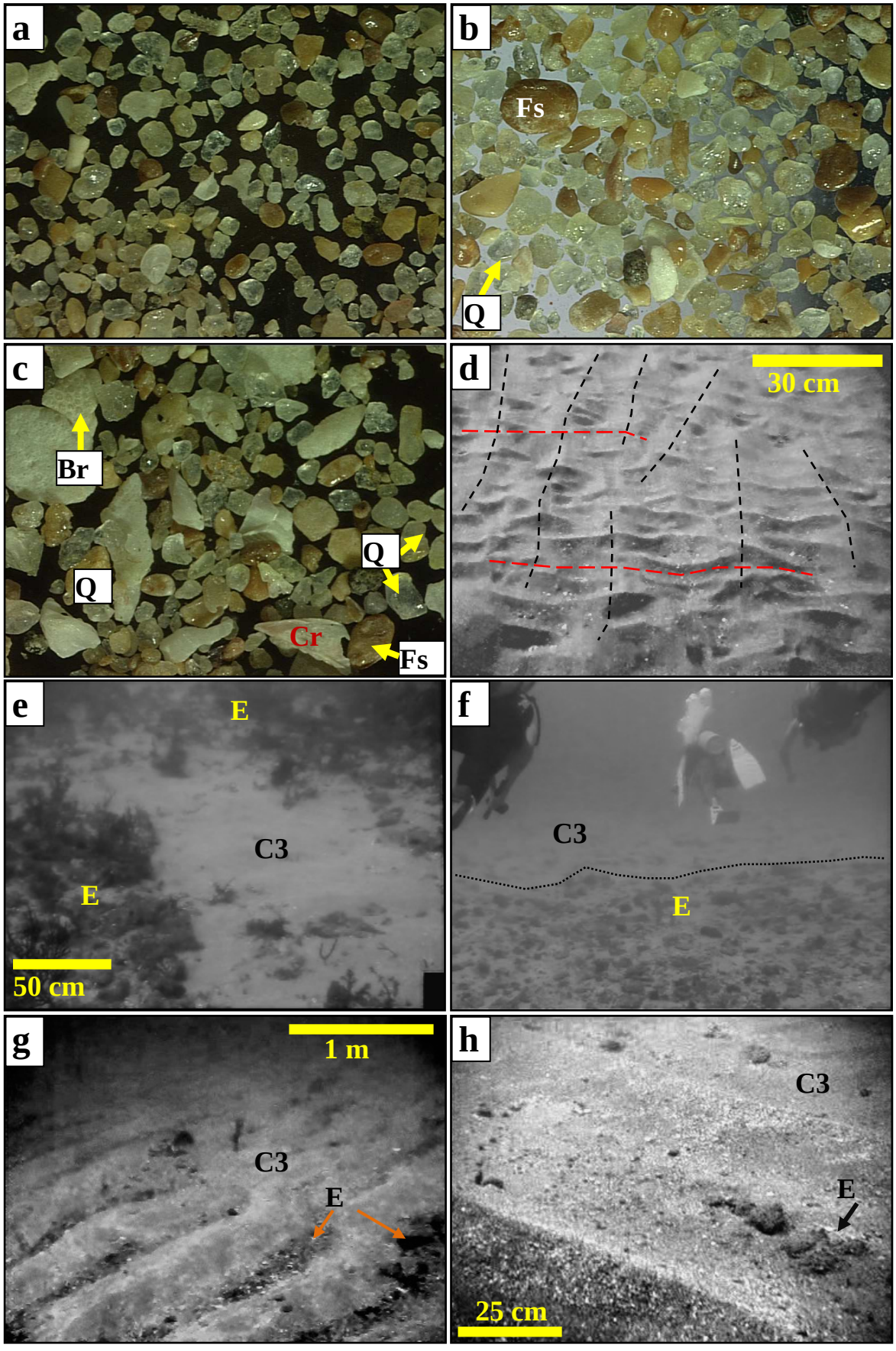
a
b
Fs
Q
c
Br
Q
Q
Cr
Fs
d
30 cm
e
E
C3
E
50 cm
f
C3
E
g
1 m
C3
E
h
C3
E
25 cm

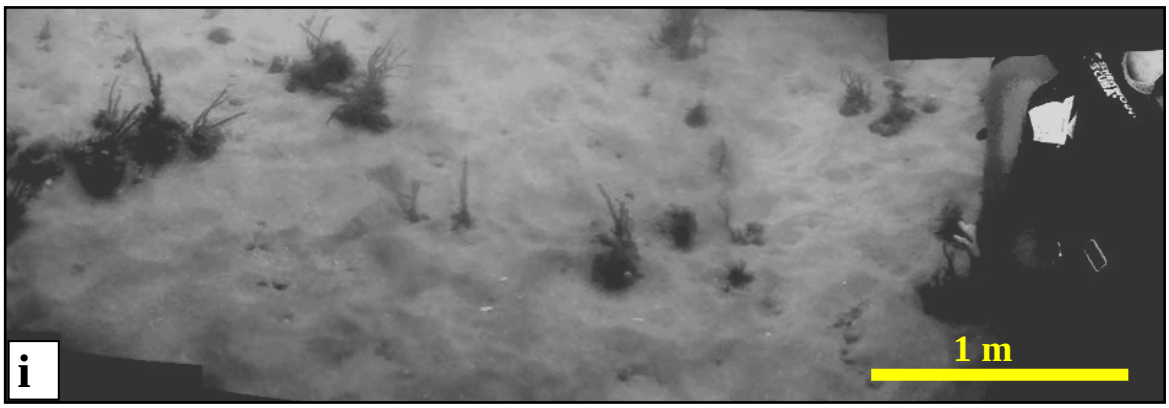

Figure 8.35 (cont.) Selected images of acoustic Facies C (quartzose shelf sand). **a - c)** Low-magnification photomicrographs of the sub-facies C1 (a), C2 (b) and C3 (c), showing the similar composition comprising mainly quartz followed by bioclastic fragments (Table 8.10). Field of view for (a) = 6 mm, (b) = 7.5 mm and for (c) = 9.5 mm. Q = quartz, Fs = feldspar, Cr = cirriped, Br = bryozoan. **d)** Underwater photograph of the two common oscillation ripple orientations observed in sub-facies C1 resulting in an interference pattern. White = straight to bifurcating NW-SE (swell from NE) and red = straight to bifurcating sharp crested NE-SW (swell from SE). Locality is close to sample Q (-28 m). **e)** Underwater photograph of a small isolated low amplitude sediment starved bedform overlying Facies E. Locality is close to sample S11 (-26 m). **f)** Underwater photograph of a gradational contact between Facies C and E. Locality is close to sample 32 (-29 m). **g)** Bifurcating sharp crested oscillation ripples constituting a low amplitude bedform (locality at sample S11, -26 m). Note the Facies E sediments in the ripple troughs. **h)** Straight sharp crested oscillation ripples within a low amplitude bedform migrating over Facies E deposits which are present within the ripple troughs. Locality at sample S14 (-29 m). Photo is digitally enhanced to compensate for poor visibility. **i)** Underwater greyscale photo mosaic of the hummocky seafloor morphology in Facies C3. Note the epifaunal growth attached to the rocky substrate provided by Facies E.

Locally at reef margins changes in the orientation of the oscillation ripples of sub-facies C2 are due to local topographic effects. The *Sandridge* is the largest bedform in the study area and comprises a NW-SE trending very large subaqueous shoreface-connected ridge (Chapter 7). Oscillation ripples are also found on top of the *Sandridge* (Figure 8.35c) and at sample S1 it was 5 cm in length, 1 cm in height and trending N-S.

Sub-facies C3 is confined to the *Basin* and observed to occur as sediment veneers and starved subaqueous dunes (Figure 8.2, sonographs 6 and 7; Figure 8.35e) which are migrating over the lag deposit of Facies E (see Facies E). The boundaries between sub-facies C3 and Facies E ranges from very distinct (Figure 8.35e) to gradational (Figure 8.35f) giving rise to a very complex pattern of sediment distribution and subsequently sonograph returns from within the *Basin* (Figures 8.1, 8.2, and 8.32). The complex distribution pattern of Facies C3 and E located within the *Basin* can be divided into two domains, separated by the *Spur* (Figure 8.32). Within domain 1 located North of the *Spur* and south of the *Sandridge* within the confines of the *Northern Basin*, Facies C3 and E forms alternating NNE-SSW trending large to very large subaqueous dunes (Figure 8.2, sonograph 7) with dimensions of L = 36 - 125 m and H = 0.2 - 0.8 m which migrate and coalesce in a predominantly westerly direction.

Evidence from the textural parameters (Figure 8.33), side-scan sonographs and bedform observations suggests secondary remobilisation of sediment from the *Sandridge* through selective erosion of the landward or southern flank of the *Sandridge.* This results in deposition of the remobilised sediments into the *Northern Basin* from where it is redistributed as low amplitude sand starved bedforms (Figure 8.35e) which migrates over the debris-lag deposits of Facies E. The mechanism of dispersion from the *Sandridge* is suggested to be through wave refraction especially of larger storm swells which moves sediment at a greater depth. The bedform migration following deposition within the *Northern Basin* is not certain but it is unlikely that the average migration rate is significant due to the physical setting of the seafloor. From field observation the sediments in the *Northern Basin* were subjected to oscillatory wave-induced motion but which is very subdued compared to other areas, even those at similar depths seawards of the Aliwal Shoal. The *Northern Basin* is thus a relatively low energy environment with sediment mobilisation probably only occurring during high energy wave events and through the counter current, although the latter mechanism seems to be dominating in the *Southern Basin*.

Within domain 2, located south of the *Spur* and north of the *Plateau* within the *Southern Basin,* Facies E dominates with sub-facies C3 forming N-S and NW-SE sediment starved, predominantly northwards migrating, large to very large subaqueous dunes (Figure 8.2, sonograph 6) with dimensions ranging of L = 50 - 300 m and H = 0.5 - 0.8 m. The interpreted northwards migration of these subaqueous dunes are most likely due to either the counter current (Figure 2.6) and/or to swell refraction across the southern section of the Aliwal Shoal ridge. Future planned sediment transport modelling combined with new oceanographic data constraining the different current regimes should clarify this ambiguity.

Oscillation ripples on top of the low amplitude subaqueous dunes of domains 1 and 2 range in size from L = 10 - 70 cm and H = 2 - 30 cm and in morphology from sinuous to straight with sharp or rounded crests (Figure 8.35g, h) to interference patterns resulting in a hummocky seafloor (Figure 8.35i). At sample S2 mud was observed draping the ripple crests further supporting the suggested postulation that mud is delivered to this part of the shelf by buoyant plumes (Section 8.4.1; Figures 8.33f and 8.34).

Facies D

Facies D was defined based on acoustic signature, sampling and association with the reef outcrop, forming highly reflective distinct outcrops and sheet deposits on top of the lithologies. For simplicity facies D was only mapped where it is constrained in major gullies within the reef base.

However, Facies D is considered as all sediment occurring on the reef outcrop, within gullies or otherwise. Commonly Facies D occurs as sediment dispersed between dense epifaunal growth (Figures 8.11g, l; 8.13e, f; 8.19b, c; 8.21c) or as sediment starved bedforms within topographic depressions, potholes and gullies (Figure 8.23a). Sonographs of the mapped segments (gully deposits) of this facies are highly reflective and even toned to occasionally granular (Table 8.1; Figure 8.2, sonograph 9). On average Facies D comprise a moderately sorted strongly coarse-skewed coarse sand composed mainly of quartz (50 %) and bioclastic fragments (44 %) (Figure 8.36a). Relative to the other facies (Table 8.10), Facies D is the coarsest grained, shows the highest average bioclastic components and subsequently also highest carbonate content (67 %), typically of that expected for the reef-associated facies where most of the bioclastics are coarse-grained reef-derived skeletal carbonate e.g. sample S showed a carbonate content of 98 % (Figure 8.36b; Appendix VIII, Table VIII.2).

Facies D is interpreted as *reef-associated bioclastic-rich sand* and is a mixture of skeletal carbonate and quartz (Table 8.10). It is equivalent to (Table 8.12) Ramsay's (1991, 1996) bioclastic sediment, Richardson's (2005) reef associated, bioclastic-rich, fine sand and Cawthra's (2010) inter-reef bioclastic sediment. Facies D compares well (Table 8.12) with equivalent units elsewhere but with higher carbonate values and a slightly better sorting.

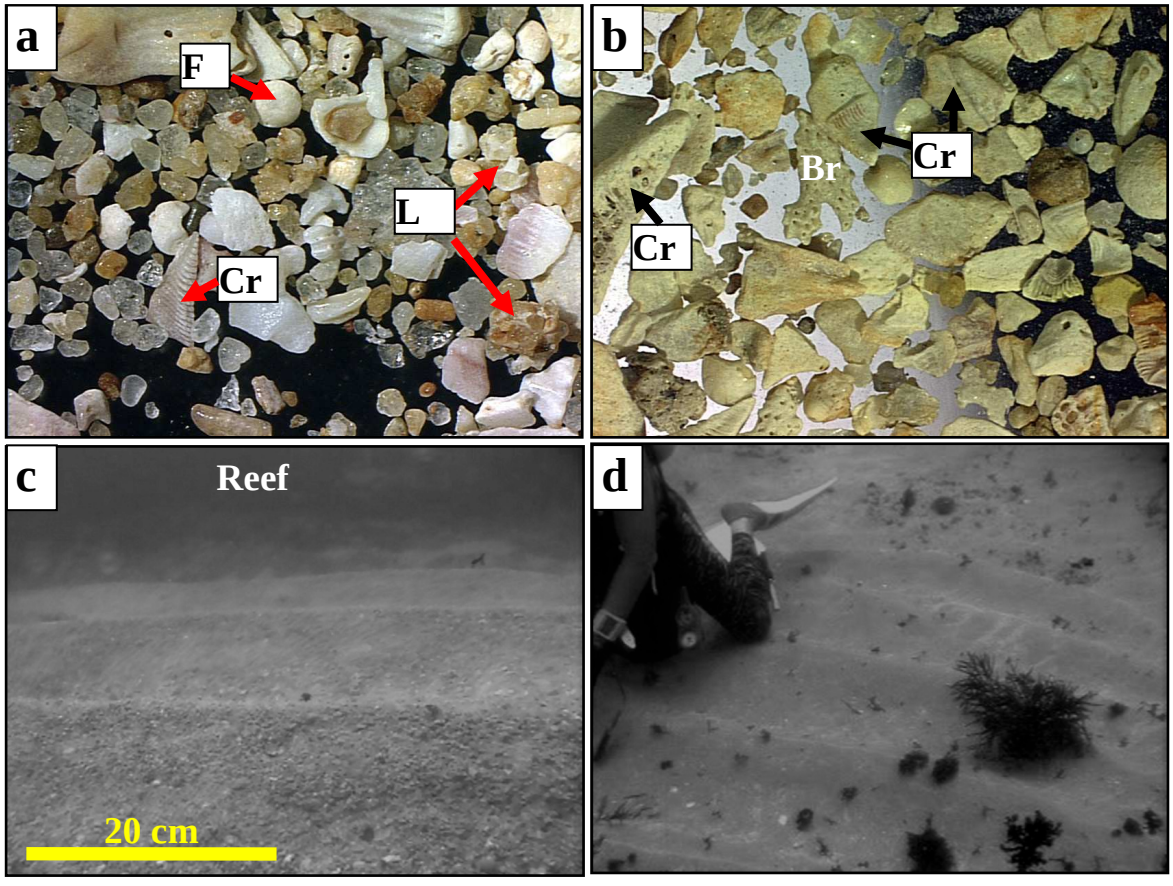

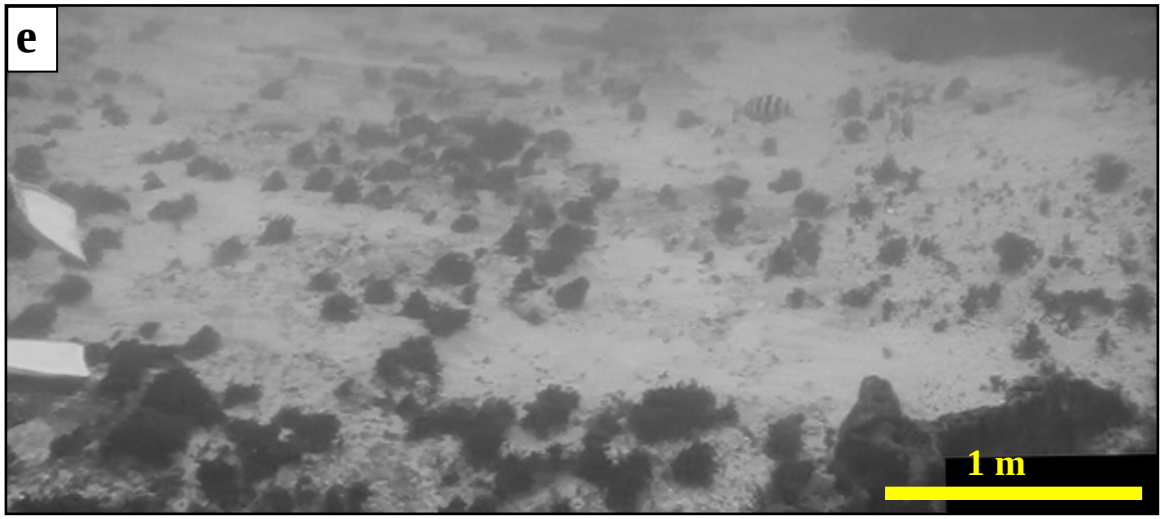

Figure 8.36 (cont.) Selected images of acoustic Facies D - reef-associated bioclastic-rich sand. Field of view for (a) = 13 mm and for (b) = 7.5 mm. L = lithic fragments from aeolianites or beachrocks, F= foraminifera, Cr = cirriped (barnacle), Br = bryozoan. **a)** Low-magnification photomicrograph of sample A (-15 m) showing the typical composition of mainly quartz and skeletal, mostly reef-derived, carbonate. **b)** Low-magnification photomicrograph of sample S (-28 m) which almost exclusively comprises bioclastic fragments and has a carbonate content of 98 % with Cirriped and bryozoan skeletal debris dominating the faunal assemblage. (Appendix VIII, Table VIII.2). **c)** Underwater photograph of the straight to bifurcating sharp crested oscillation ripples present in North Sands gully at sample A (-15 m). **d)** Underwater photograph of the straight to bifurcating, sharp crested oscillation ripples at sample locality J (-20 m). **e)** Underwater photo mosaic of Facies D sediment at sample locality S5 devoid of sedimentary structures forming a veneer draped over a substrate that comprises reef and epifaunal growth.

Sedimentary structures of Facies D (Figure 8.36c, d) comprise sharp to round crested oscillation ripples ranging in wavelength from 0.15 -1.2 m and height from 0.1 - 0.6 m, although when Facies D is present as a sediment veneer sedimentary structure may be absent (Figure 8.36e). Although ripple trend and size are variable due to depth, available sediment and local topographic parameters there is, as expected, a decrease in the size of the ripples with increasing water depth.

Table 8.12 Textural parameters and carbonate content from equivalent studies of bioclastic-rich reef associated sediments similar to that of Facies D. UW = Udden-Wentworth classification, $CaCO_3$ = carbonate content percentage, cS = coarse sand, mS = medium sand, Ms = moderately sorted, Ps = poorly sorted, mWs = moderately well sorted, N/A = not available. See Figure 1.1 for the locations of the various other studies.

Parameter	Aliwal Shoal	Ramsay (1991)	Richardson (2005)	Cawthra (2010)
UW	cS	cS	mS	N/A
Sorting	Ms	mWs - Ps	Ps	N/A
$CaCO_3$	41 - 98	56 - 82	14 – 81	N/A

Facies E

Facies E is best developed in the confines of the *Basin* (Figure 8.32) showing alternating inter-fingering linear patterns with Facies C (Figure 8.2, sonographs 6 and 7) which migrates over Facies E as low amplitude sediment starved bedforms (Figure 8.35e) consisting of heterogeneous bioclastic-rich and shelf sand (Table 8.10). In addition, thin linear outcrops of Facies E seem to be banked against the seaward margin of the Unit A1 aeolianite ridge (Figure 8.37a; Figure 8.2, sonograph 2; Figure 8.32). Sonographs of Facies E (Figure 8.2, sonographs 1, 2, 5, 6, 7, 9; Table 8.1) are moderate to very highly reflective with a low to very low relief showing no acoustic shadowing.

Although the average Facies E sediment sample (Figure 8.37b) comprises a moderately sorted strongly coarse-skewed medium sand composed mainly of quartz (60 %), feldspar (10 %) and bioclastic fragments (28 %), it is not considered a true reflection of the lag deposit. In the field Facies E comprises a poorly sorted, densely packed pavement of discoidal pebbles to boulder sized aeolianite and beachrock constituents covered by epifaunal growth and mixed with various amounts of bioclastic sediment (Figure 8.37c to e). Sample S10 (Figure 8.37b) resembles this facies the best although due to the size of the sampling bottles and size restrictions on the analyses method (sieving, Section 5.5.2) there was a bias in sampling and analysing the finer grained components.

Facies E is interpreted as an unconsolidated lag and debris deposit and forms part of seismic units DlSF5 and DsSF6 (Chapter 6). As such it is linked with ravinement processes during the Holocene transgression (refer to Chapter 6, Sections 6.3.4 and 6.4.3). The location, areal extent and morphology suggests that the deposits of Facies E situated in the Basin may possibly represent the palaeo-seafloor at that depth (-29 m) as submergence ensued. However, the Facies E sediment bank against the seaward flank of the Aliwal Shoal ridge (Unit A1; Figure 8.37a) may indicate that these deposits of Facies E are due to ravinement as the transgressive surface DsRT reworked Unit A1 (Figure 6.6b, c). Thus, Facies E does not necessarily have the same origin across the study area.

Facies E is correlated to Cawthra's (2010) bioclastic gravel pavement sediments, also interpreted as the result of the Holocene ravinement process.

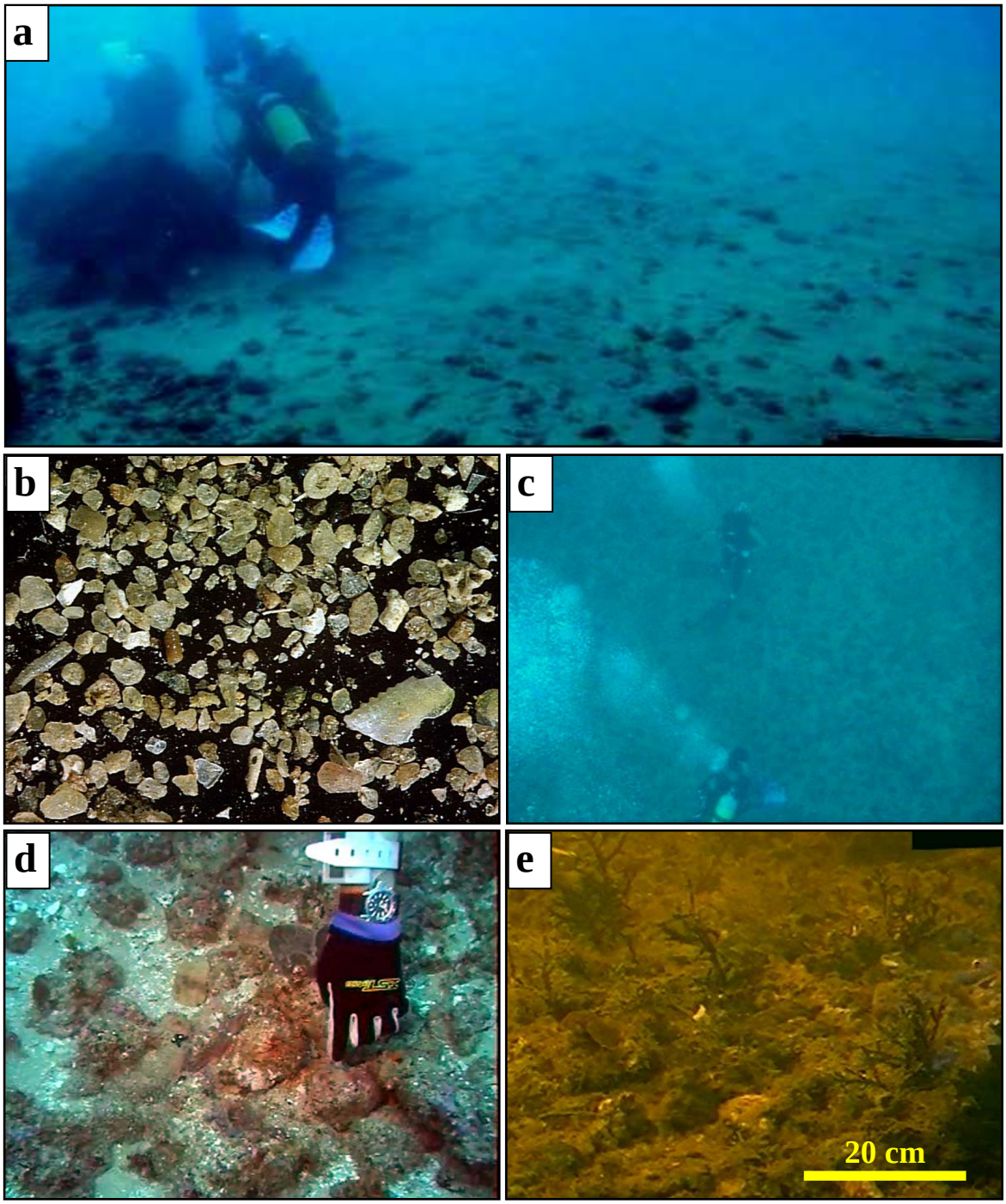

Figure 8.37 Selected images of acoustic Facies E, Holocene transgressive lag and debris deposits. **a)** Underwater photo mosaic of the seaward flank of Unit A1 showing the Facies E deposits covered by a veneer of Facies C sediment (see Figure 8.8j for locality). **b)** Low-magnification photomicrograph of sample S10 (-28 m). Field of view = 4.75 mm. **c)** Underwater photograph of the extensive and flat nature of the Facies E pavement covered by an irregularly distributed very thin veneer of Facies C sediment. Photo was taken from the top, divers are standing on the seafloor for scale, locality at sample 21 (-25 m). **d)** Close-up photograph of Facies E in image (c). Note tightly packed discoidal pebble to boulder size constituents which are mostly aeolianite, beachrock or rhodolith in composition. **e)** Close-up photo of the Facies E deposit at sample locality S10. The seafloor at this locality is covered with epifaunal growth and mud.

8.4.3 Summary and Conclusions

Fine and medium sand is delivered to the study area by the SCR system (predominantly the *Sandridge*) resulting in the general N-S trending pattern observed from all of the sedimentological parameters except for the mud fraction (Figure 8.33). The distribution of the carbonate content and gravel fraction is inversely related to that of the SCR-supplied sand fractions. The mud fraction shows a completely different distribution pattern linked to gravity settling from buoyant mud-rich plumes generated during periods of increased river outflow. Grain size distribution data further supports selective erosion of the landward flank of the *Sandridge* with deposition of the remobilised sediment in the *Northern Basin*. This was also confirmed by the results of the acoustic and sampling data.

Seafloor classification of the unconsolidated sediments based on side-scan sonar backscatter resulted in the delineation of 3 acoustic facies, C to D (Section 8.4.2; Figures 8.1, 8.2; Table 8.1). Typically differences in the backscatter of side-scan sonar data are linked to differences in grains size (Goff *et al*., 2000) although these differences in the acoustic response do not always correspond to changes in sediment properties (Nitsche et al., 2004; Rooper and Zimmerman, 2007). Sampling of the various acoustic facies indicated that some broad differences between the three facies, although the observed overlap in some sedimentological parameters (Appendix VIII) may point to a more complex relationship. Even so, with the available data, it appears that the side-scan acoustic response, in general, is related to seabed roughness, which is for the most part controlled by the grain size composition, and acoustic impedance mostly related to the composition of the substrate (sand vs. rock). This is especially illustrated by the different type of acoustic responses generated by the contrasting sediment deposits of Facies C and E. However, the acoustic mapping cannot discriminate between different genetic types of sediment e.g. modern or palimpsest unless these have significant different properties, such as is the case with Facies C and E.

Integration of the results of the side-scan acoustic mapping, field observations and textural and compositional data indicate that the present distribution of the unconsolidated sediment is the result of;

1) a highly variable distribution of a mixed sediment population comprising modern, palimpsest and possibly relict sediments which are,

2) redistributed by a complex pattern of bottom currents generated by the interaction of opposing oceanographic and swells driven circulation patterns.

The above two inferences imply that the seafloor sediments may or may not be in equilibrium with the modern shelf hydrodynamics.

The complex patterns of the unconsolidated sediment distribution indicate that numerous dynamic processes operate at different times and scales. A summary of the major dispersal processes as deduced by the data is presented in Figure 8.38. This can be summarised as follows:

1) During and after the Holocene transgression the study area was covered with paralic and shallow marine sediment deposited (including the transgressive lag) during the landwards migration of the shoreface which were subsequently covered by,
2) medium and fine sediments delivered to the inner and middle shelf by SCR processes, and
3) complemented by the addition of reef-derived skeletal carbonate sediment,
4) all of which are continually being redistribution and reworked by a combination of oceanic and wave currents.

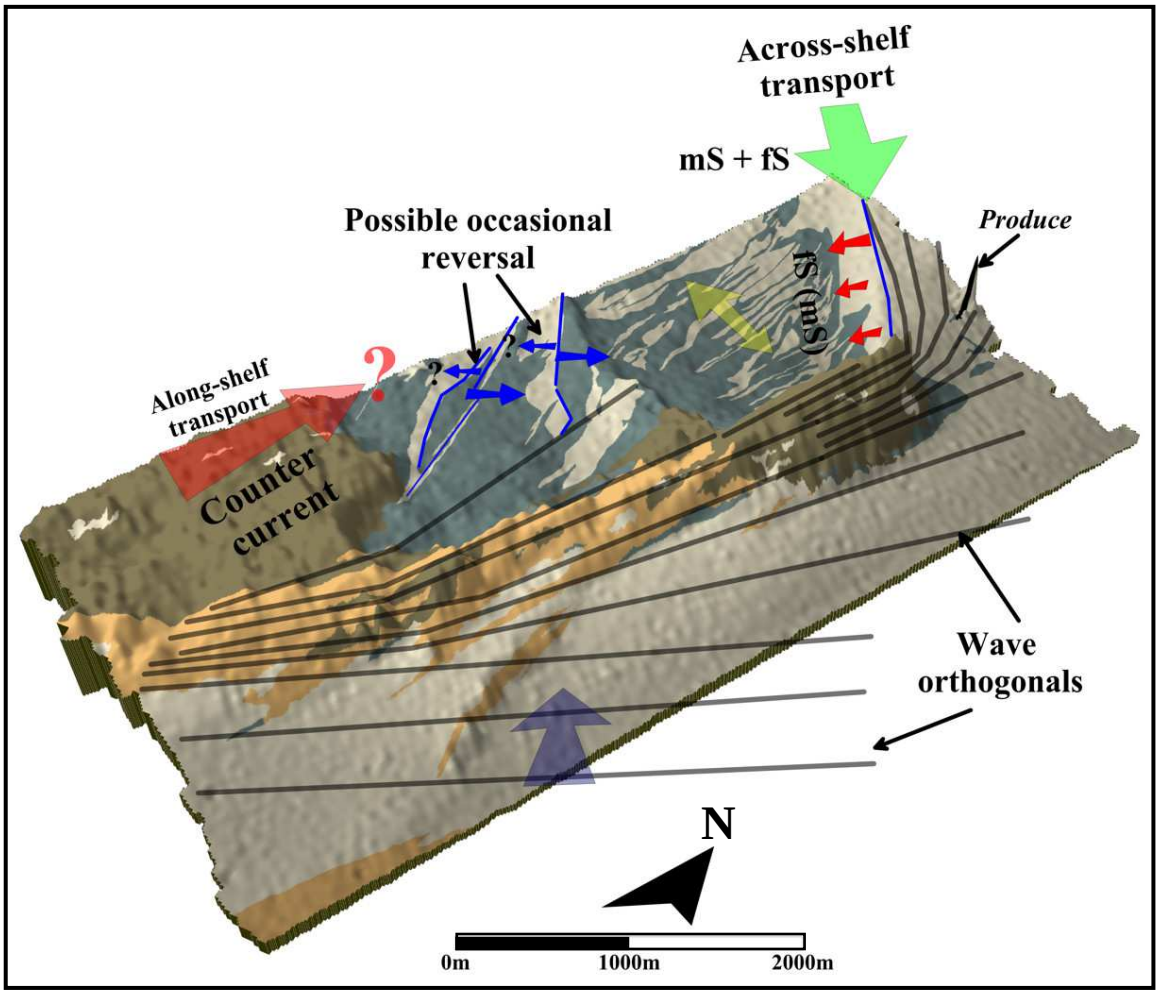

Figure8.38 Conceptual 3D-model of the large scale processes responsible for the complex distribution of the unconsolidated seafloor sediments. Refer to text for explanation. mS = medium sand, fS = fine sand. Note the refraction of the wave trains (orthogonals) around the Aliwal Shoal.

The interpretations produced here introduced new concepts of cross-shelf sediment delivery and subsequent unconsolidated sediment redistribution not observed before on the South African continental shelf. As such in explaining the shelf sediment distribution it links together the unique recent geological evolution of the shelf with subsequent submergence and a complex interaction of geostrophic and wave currents delivering, reworking and redistributing modern and palimpsest sediments.

8.5 SYNTHESIS

The seafloor geology in the study area is a result of late Pleistocene to Holocene aeolianite and beachrock lithologies, deposited as coastal barrier and transgressive shoreface depositional systems subsequently eroded and covered by mid to late Holocene transgressive deposits and redistributed MSDC sediment, the latter achieved through a complex interaction between swell and oceanographic driven circulation systems.

The aeolianites in the study area are interpreted to represent different types of dune morphologies deposited during the climatic and associated sea-level fluctuations of MIS 5. Units A1 and A2 represent contemporaneous evolution of a coastal barrier system which consisted of two different dune forms associated with a back-barrier estuarine or lagoonal system. Unit A1 most likely originated as a longitudinal coastal dune, whilst Unit A2 comprised a compound parabolic dune system which migrated across the estuary mouth/tidal inlet. The coastal configuration established by Unit A1 and A2 was most likely re-established during similar subsequent MIS 5 sea-level stands, resulting in the formation of the back-barrier dune system of Unit A3 during MIS 5c/b. Diagenesis of the aeolianite units can be divided into 3 major stages representing initial meteoric cementation followed by a long period of carbonate solution and porosity development and a final stage of pore-lining multiphase marine cementation.

Integration of morphology, field relationships and sedimentary structures with the results from geochronological analyses (Chapter 9) indicated that the Holocene Aliwal Shoal beachrocks (Units B1 to B4) were deposited and cemented sequentially during the fast Holocene sea-level rise. Diagenesis of the beachrocks occurred during diagenetic stage 3 and comprises a major phase of either aragonitic or HMC marine cement. Two cycles of initial aragonite followed by later HMC cement is tentatively linked to two marine flooding events related to different pulses of enhanced rates of sea-level rise following the Younger Dryas cold event. Interestingly, the Aliwal Shoal beachrocks conforms to the predicted model of formation under rapid sea-level rise suggested by

Cooper (1991) insofar it shows 1) early formation and overstepping of units with facies preservation and 2) breaks between bands of beachrock outcrops. Beachrock Unit B5 was deposited during MIS 5a and is interpreted to have been deposited as a result of a high energy event.

Grain size distribution patterns of the unconsolidated seafloor sediments indicate that the SCR system, specifically the *Sandridge*, delivers fine and medium sand to the inner and middle shelf and imparts a general N-S trending pattern to the gravel and sand fractions. In addition the grain size distributions support selective erosion of the seaward flank of the *Sandridge* with the remobilised sediment deposited in the *Basin* as low amplitude bedforms over the Facies E lag and debris pavement. The mud fraction is interpreted to be deposited by gravity settling from buoyant mud-rich plumes. Acoustic classification of the unconsolidated sediment samples resulted in the demarcation of 3 major acoustic facies, C to E, interpreted with sample analyses as *quartzose shelf sand* (C), *reef-associated bioclastic-rich sand* (D) and an *unconsolidated lag and debris deposit* (E). Integration of acoustic mapping, field observations and sample analyses indicate that the present distribution of the unconsolidated sediment is the result of a highly variable distribution of modern and palimpsest sediments which are continually redistributed and reworked by a complex pattern of bottom currents generated by the interaction of opposing oceanographic and swell driven circulation patterns. The seafloor sediment distribution pattern is with the exception of the migration of the Sandridge regarded to reflect the long-term regional sediment distribution pattern as corroborated by the comparative seafloor morphological data (Figure 7.12).

CHAPTER 9
GEOCHRONOLOGY AND SHELF EVOLUTION

9.1 INTRODUCTION

As for their onland equivalents, offshore aeolianite and beachrock systems are common (Flemming *et al*., 1983; Martin & Flemming, 1986, 1988; Ramsay 1991, 1995, 1996; Cawthra, 2010) on the south and eastern South African continental shelf (Figure 3.11). These relict sequences not only document relative sea-level changes (Martin and Flemming, 1987, Ramsay 1991, 1995; Ramsay and Cooper, 2002; Carr *et al*., 2010) but also have the potential to provide a palaeo-environmental record for time periods where no data are represented onland. Considering the potential scientific contribution that these offshore systems can add to our current predominantly onshore-centred understanding of the evolution of the southern African aeolianite and beachrock sequences, it was central to this investigation to develop a precise chronological framework.

The only geochronological study of such an offshore system to date was that undertaken by Ramsay (1991, 1995 and 1996) which formed the basis of the only Quaternary relative sea-level curve for southeast Africa (Ramsay and Cooper, 2002). Most recently Cawthra (2010) used infrared stimulated luminescence on feldspars to date an offshore aeolianite but the results, with the exception of one sample, were unreliable due to the feldspar showing anomalous fading (Cawthra, *Pers. Comm.*).

9.2 THE AGE OF THE ALIWAL SHOAL

The age of the Aliwal Shoal has been controversial ever since Carter (1966) published the results of a foraminiferal study in the journal *Nature*. Although the faunal assemblages gave no direct indication of an age, a Pliocene age for the Aliwal Shoal was favoured based on correlation to rocks occurring onshore with similar faunal assemblages and having similar sedimentary features. Foraminiferal forms of *Ammonia beccarii* and *Elphidium* sp. were assigned to the Tertiary based on the appearance of these forms in Australia and other parts of the world. McLachlan and McMillan (1979) revised the age of these foraminiferal forms in South Africa to the Quaternary, thereby implying a Quaternary age for the Aliwal Shoal. Recently, and perhaps most controversially, Cooper and Liu (2006) re-adopted the earlier Pliocene age. This age is based

purely on the Aliwal Shoal's inferred stratigraphic position derived from its bathymetric location and equating it with one of the early Pliocene regressive sea-level phases without any corroborative geochronological analyses. Most recently Bosman *et al*. (2007) used nannofossil biostratigraphy, the results of which placed the Aliwal Shoal lithologies in calcareous nannofossil zone NN21, indicating a late Middle Pleistocene to Holocene age (< 290 ka BP).

To finally resolve the longstanding question of the age of the Aliwal Shoal this study employed an integrated multi-method geochronological approach comprising nannofossil biostratigraphy, optically stimulated luminescence (OSL), Uranium Series (U-series) and radiocarbon techniques. To date this is the most comprehensive geochronological programme undertaken to constrain the age of an offshore aeolianite and beachrock complex and also the first time that OSL dating of quartz grains is applied to submerged lithologies of this type.

9.3 METHODS

9.3.1 Field Sampling and Sample Preparation

A total of 4 aeolianite and 6 beachrock geochronological samples were collected from the main lithological units by scientific divers from depths between 33 m and 15 m (Figure 9.1). These samples are referred to as the GC-series samples (Appendix IX, Tables IX.1 and IX.2; Figure 9.2a). Some of the GC-series beachrock samples contained embedded shell fragments, which were extracted for separate analyses (Figure 9.2b; Appendix IX, Table IX.3). In addition to these samples, *in situ* palaeo-oysters (Figure 9.2c; Appendix IX; Table IX.3) were excavated from the seaward margin of the Aliwal Shoal and palaeo-pothole fill was sampled from a beach locality at Umgababa, onshore from the study area (Figure 9.2d, e; see Figure 3.1 for locality). Hand specimens collected during the initial ground-truthing programme indicated that the outer surfaces of the seafloor lithologies were extensively bio-eroded and altered (see Section 8.3.1). As this poses problems for geochronological analyses, the GC-series of samples comprised very large sample blocks (> 80 kg) from which to obtain fresher representative sample material (Figure 8.5d). The depth of samples were accurately obtained by recording both the water depth using an Uwatec Aladin Pro dive computer and the time of sample extraction at each sample site, thereby permitting tidal correction. In the laboratory the outer part of samples containing epifaunal growth and outer surface weathering damage were manually removed and a core was drilled and its ends discarded (7 cm diameter, ~20 cm long), to ensure a fresh and representative sample (Figure 9.2f) from the

middle of the sample block. Cores were packaged in black plastic bags and consigned with applicable documentation to the various laboratories.

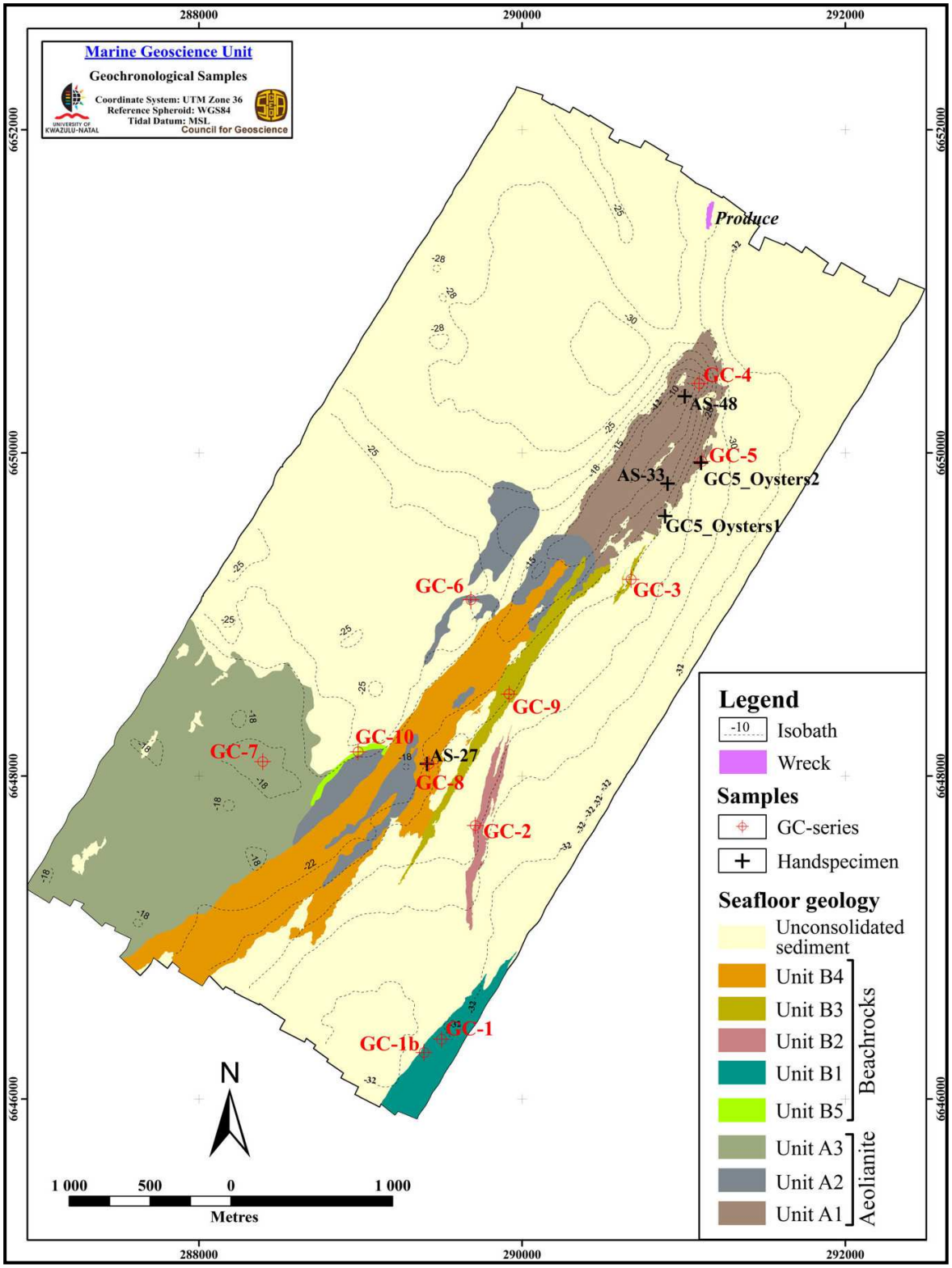

Figure 9.1 Sample locality map for the various geochronological samples discussed in the text. Note that the isobaths are not in constant intervals. Geological units are arranged from oldest at the bottom to youngest at the top in the map legend.

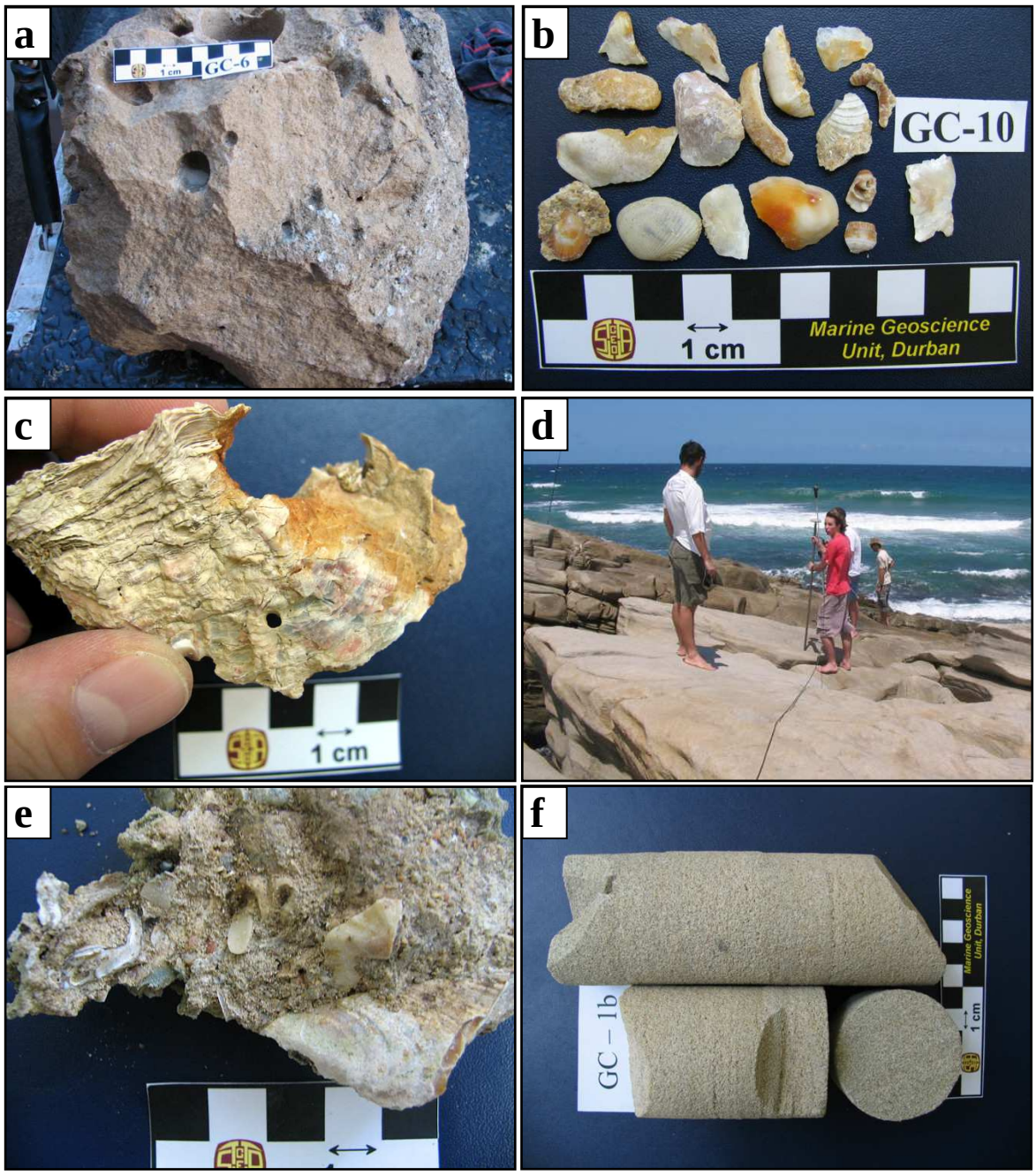

Figure 9.2 Examples of the type of materials used for age analyses in this study. Refer to Appendix IX for a complete listing and photographs of all the geochronological samples. **a)** GC-series sample blocks were obtained for most of the aeolianite and beachrock units. Sample shown is GC-6 (-26 m). **b)** Shell material extracted from selected GC-series rock samples. The subsequent shell sample is designated by placing an S behind the GC sample number, in this case it would be GC-10S. **c)** Palaeo-oysters (*Striostrea margaritacea* or the Cape rock oyster) were commonly found in living position on the seaward margin of the Aliwal Shoal. Sample GC8-Oysters, -24 m. Note the predation by a boring mollusc. **d)** dGPS surveying of the locality for the pothole-fill sample OS-5 which was obtained from a pothole incised in a dip-slope of Vryheid Formation (Figure 3.1) sandstone at a height of 2.23 m above MSL. **e)** Close up photograph of the OS-5 sample material comprising shell hash set in a fine to medium grained sandy matrix all which is cemented by carbonate cement. **f)** Sub-sampled cores were extracted from the interiors of all the GC-series samples.

9.3.2 Geochronological Programme Rationale

The geochronological programme was designed not only to constrain the age of the Aliwal Shoal but also to evaluate the usefulness and reliability of the different radiometric methods used to determine the age of the Aliwal Shoal samples. This was achieved by using multiple analyses techniques on the same samples. OSL using quartz grains was chosen as the primary dating method due to;

- its extended dating and relatively small associated error ranges with the older ages,
- its successful application to similar deposits onshore and
- the fact that it should represent a depositional age of a mineral grain and not a cementation or biogenic constituent age, which in the case of carbonated cemented aeolianites and sometimes beachrocks may consist of multiple cementation events prone to open system behaviour.

The U-series and radiocarbon methods were chosen as complementary dating methods as these have been used extensively by the detailed geochronological study of Ramsay (1991 and 1995) and Ramsay and Cooper (2002) on offshore aeolianites and beachrocks. The results from the U-series and radiocarbon methods could then be compared to the more recently developed OSL technique. Uranium series has the longest dating range and hence was used on the aeolianites which were expected to be the oldest from field observations and previous work (Ramsay 1991, 1995, 1996). The radiocarbon method was applied to beachrocks both whole rock samples and, where possible, shell material extracted from the beachrocks. All samples were dated using nannofossil biostratigraphy and provided a broad geochronological framework. The application of the various methods to either the aeolianites or beachrocks is graphically shown in Table 9.1.

Table 9.1 Table illustrating the geochronological analyses techniques applied in this study to date the various types of sample material. Note that the shell material refers to shells extracted from the beachrocks.

	Aeolianite	**Beachrock**	**Shell Material**
Nannofossil biostratigraphy	X	X	-
OSL	X	X	-
Uranium Series	X	-	-
Radiocarbon	-	X	X

9.4 RESULTS

9.4.1 Nannofossil Biostratigraphy

All nannofossil forms were identified by Dr. Maria Ovechkina (Marine Geoscience Unit, University of KwaZulu-Natal & Paleontological Institute, Russian Academy of Sciences). For the results and a full description of the methodology applied refer to Appendix X. This was the first application of nannofossil biostratigraphy to an offshore palaeo-dune and -beach sequence along the east coast of South Africa and was reported in Bosman *et al*. (2007; Appendix X). Subsequent investigations that utilised nannofossil biostratigraphy include that of Green *et al*. (2008) which was used it to constrain the age of the shelf-edge wedge in northern KwaZulu-Natal and more recently by Cawthra (2010) to constrain the age of aeolianites offshore Durban.

Nannofossil assemblages indicated that all the lithologies of the Aliwal Shoal fall within calcareous nannofossil zone NN21 thereby assigning it a late Middle Pleistocene to Holocene age (< 290 ka BP).

9.4.2 Optically Stimulated Luminescence (OSL)

OSL measurements were undertaken by Dr Zenobia Jacobs, initially at QUADRU (CSIR) in Pretoria, South Africa and subsequently completed at the GeoQuEST Research Centre, University of Wollongong, Australia. All results, methodological background and descriptions as well as discussions related to age reliability are provided in a detailed laboratory report in Appendix XI. Due to the size of this report it is provided in digital form on the back cover.

All the GC-series samples were dated by OSL (Table 9.2). The following brief method statement is distilled from Appendix XI where it is dealt with exhaustively. The environmental dose rate and the burial dose were reliably measured by a combination of methods whilst the single aliquot regenerative-dose (SAR) measurement procedure was used to determine the equivalent dose (De). Between 24 and 48 aliquots and 800 and 1 300 individual sand-sized grains were measured for each sample (see Table 9 in Appendix XI). The luminescence behaviour of each sample were further scrutinised by analysing the decay and dose response curves and by applying the recycling ratio test to check on the sensitivity correction of the measurement procedure and the OSL-IR depletion ratio test to check for contamination from feldspar grains (Appendix XI). All the analysed samples demonstrated good luminescence behaviour resulting in successful dose

recovery tests, fast decaying optical decay curves and dose response curves that were not near or in saturation and for which reliable De estimates could be obtained from each individual aliquot (Appendix XI). The ages presented in Table 9.2 are 'central' ages which are considered to be the most appropriate for the samples (see Appendix XI for a full explanation on all aspects of the optical dating). Optical dating results places the deposition of the aeolianites into two groups viz; Unit A1 and A2 deposited during the MIS 6/5e boundary and Unit A3 during MIS 5b/c. The beachrocks are all Holocene in age except for Unit B5 which was deposited during MIS 5a (Table 9.2; Figure 9.1).

9.4.3. Uranium Series

Uranium series analyses were undertaken by Dr Louise Thomas from the Open University's Uranium Series Facility (OUUSF) in the United Kingdom, whilst the open-system modelling of the raw ages was provided by Dr Peter van Calsteren, also from the OUUSF. Appendix XII is the laboratory summary report detailing the methodological description, laboratory standards and associated information.

Six aeolianite samples (GC-4 to GC-7, SA-33 and SA-48) were analysed using a Finnigan MAT262 mass spectrometer (thermal ionisation mass spectrometry or TIMS). Samples were totally dissolved, requiring HNO_3 and HF dissolution, and spiked with a mixed $^{229}Th/^{236}U$ spike. Uranium and thorium fractions were separated on 2 ml anion exchange columns using standard techniques and analysed for $^{234}U/^{236}U$, $^{235}U/^{236}U$ (a proxy for ^{238}U, assuming a $^{238}U/^{235}U$ natural ratio of 137.88), $^{230}Th/^{229}Th$ and $^{232}Th/^{229}Th$ using the TIMS method (see Appendix XII). The concentration of ^{232}Th was measured in order to assess the detrital Th component and consequently correct for it. Ages were calculated using the standard equation and the decay constants used for ^{234}U, ^{238}U, ^{230}Th and ^{232}Th were 2.82629×10^{-6}, 1.55125×10^{-10}, 9.15771×10^{-6} and 4.9475×10^{-11} yr^{-1} respectively. Detrital contamination was present ($^{232}Th/^{238}U$ value of 1.78) and constant in all samples and therefore ages are uncorrected and given with 2 sigma errors.

The Aliwal Shoal samples were dated using the daughter deficiency method which relies on the growth of an isotope that is initially absent, towards equilibrium with its parent isotope and measures the $^{234}U/^{230}Th$ ratio. It is based on the fact that uranium is co-precipitated with calcite or aragonite (constituting the cement in the Aliwal samples) from natural waters that are essentially free of thorium. This method assumes that the daughter isotopes are completely radiogenic in origin i.e. it assumes that the ^{230}Th content of the sample was 0 at the time of formation.

Table 9.2 Dose rate data, D_e values and optical ages for ten samples from the Aliwal Shoal

Sample code	Moisture content (%)	Radionuclide concentrations [a]			Dose rates			Total dose rate [e, f] (Gy kyr^{-1})	D_e (Gy)	Number of Grains [g]	σ_d [h] (%)	Optical age [i] (ka)
		U (µg g^{-1})	Th (µg g^{-1})	K (%)	Beta [b]	Gamma [c]	Cosmic [d]					
Beachrocks												
GC-1	25 ± 5	1.19 ± 0.08	1.19 ± 0.26	0.06 ± 0.01	0.17 ± 0.01	0.16 ± 0.01	0.03	0.40 ± 0.02	4.37 ± 0.12	130	23 ± 3	11.0 ± 0.67
*GC-1b	25 ± 5	1.14 ± 0.08	1.01 ± 0.24	0.10 ± 0.01	0.18 ± 0.01	0.16 ± 0.01	0.03	0.41 ± 0.02	4.32 ± 0.09	47	12 ± 2	10.6 ± 0.59
GC-2	25 ± 5	0.51 ± 0.05	0.94 ± 0.15	0.44 ± 0.02	0.30 ± 0.02	0.16 ± 0.01	0.04	0.53 ± 0.02	5.42 ± 0.16	90	13 ± 3	10.2 ± 0.52
GC-3	25 ± 5	0.72 ± 0.07	1.02 ± 0.20	0.14 ± 0.01	0.16 ± 0.01	0.13 ± 0.01	0.05	0.37 ± 0.02	3.63 ± 0.09	83	15 ± 2	9.8 ± 0.56
GC-9	25 ± 5	0.61 ± 0.05	0.98 ± 0.17	0.14 ± 0.01	0.15 ± 0.01	0.12 ± 0.01	0.05	0.35 ± 0.02	3.41 ± 0.11	94	26 ± 3	9.9 ± 0.59
GC-10	5 ± 1	0.94 ± 0.07	1.26 ± 0.23	1.00 ± 0.05	0.79 ± 0.04	0.39 ± 0.02	0.05	1.26 ± 0.04	99.3 ± 5.8	20	13 ± 5	79 ± 5
Aeolianites												
GC-4	5 ± 1	0.46 ± 0.05	0.75 ± 0.15	0.58 ± 0.02	0.45 ± 0.02	0.22 ± 0.01	0.04	0.74 ± 0.02	93.7 ± 3.8	192	27 ± 2	127 ± 7
GC-5	5 ± 1	0.64 ± 0.05	0.83 ± 0.17	0.56 ± 0.02	0.46 ± 0.02	0.23 ± 0.02	0.02	0.75 ± 0.02	99.9 ± 2.8	129	20 ± 3	134 ± 5
GC-6	5 ± 1	0.38 ± 0.04	0.51 ± 0.11	0.60 ± 0.03	0.45 ± 0.02	0.20 ± 0.01	0.05	0.73 ± 0.03	95.3 ± 3.0	134	24 ± 3	130 ± 6
*GC-7	5 ± 1	0.41 ± 0.03	0.45 ± 0.10	0.89 ± 0.04	0.62 ± 0.03	0.27 ± 0.01	0.03	0.95 ± 0.03	88.7 ± 4.4	33	25 ± 4	93 ± 6

* Only 1 mm mask size aliquots have been measured for these samples. No single-grain measurements were made.

[a] Measurements made on sub-samples of dried, homogenised and powdered samples using thick source alpha counting (TSAC) to obtain U and Th concentrations and a combination of TSAC and x-ray fluorescence (XRF) to obtain K.

[b] Measurements made on sub-samples of dried, homogenised and powdered samples by GM-25-5 beta counting and a combination of TSAC and XRF. Dry dose rates calculated were adjusted for the water content (expressed as % of dry mass of sample).

[c] Measurements made using a combination of TSAC and GM-25-5 beta counting and TSAC and XRF. Dry dose rates calculated were adjusted for the water content (expressed as % dry mass of sample).

[d] Cosmic dose rates have been calculated using the equations provided by Prescott and Hutton (1994) taking into account the latitude (-30 °S), longitude (30 °E) and a range of altitude (-33.5 to -15.5 m). We have also accounted for the different densities of the overlying water mass (1.025 g/cm^3) and sediment (2.2 g/cm^3) and the possible changes in overburden composition and thickness over time.

[e] Mean ± total uncertainty (68% confidence interval), calculated as the quadratic sum of the random and systematic uncertainties.

[f] Includes an assumed internal alpha dose rate of 0.03 Gy kyr^{-1}, with an assigned relative uncertainty of ± 25%.

[g] Number of single grains (or 1 mm single aliquots for samples indicated with a *) used for D_e derivation after grains have been rejected using the rejection criteria of Jacobs *et al*. (2006).

[h] Relative standard deviation of the D_e distribution after allowing for measurement uncertainties (Galbraith *et al*. 1999)

[i] The total uncertainty includes a systematic component of ± 2% associated with laboratory beta-source calibration.

However, in the Aliwal Shoal samples the carbonate is mixed with detrital minerals which already contain daughter nuclides and as such the Aliwal Shoal samples show detrital contamination. Normally detrital contamination can be corrected by measuring the ^{232}Th activity, which is present in the detritus but not in the calcite so that the $^{232}Th/^{230}Th$ ratio can be used to correct for the detrital addition of ^{230}Th (Walker, 2005).

The OUUSF laboratory indicated that there were problems with establishing accurate ages. This was the result of 1) all samples having detrital contributions, 2) U/Th ratios near 1 and 3) because there was as much authigenic ^{230}Th as allogenic ^{230}Th if 'normal' detrital ratios of ~3 are used. Therefore the laboratory struggled to reliably determine the initial $^{230}Th/^{234}U$ ratio which is complicated by detrital ^{230}Th contamination which essentially negates the assumption that the initial thorium content is zero. Consequently the U-Series results were modelled for open-system behaviour using the Villemant and Feuillet (2003) model. The modelling yielded results for all the samples except GC-6 which plotted outside the graph area and to which the laboratory provided no explanation. However based on the chemistry of the U-Series system GC-6 must have either suffered excessive detrital contamination and/or later uranium uptake. The Uranium series results are presented in Table 9.3, whilst the ages modelled for open system behaviour are graphically represented in Figure 9.3.

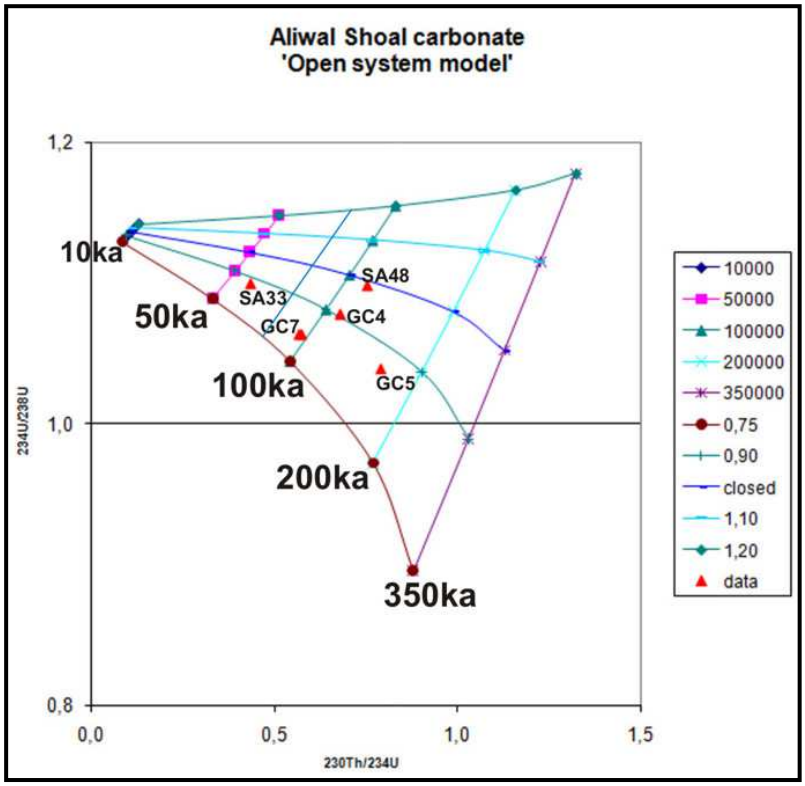

Figure 9.3 Open-system modelling of the Aliwal Shoal U-Series ages according to the methodology of Villemant and Feuillet (2003). Sample GC-6 modelled result plotted outside of the open system model parameters and hence gave a no result. Actual ages for the modelled samples are provided in Table 9.5 below.

Table 9.3 Results from the uranium series dating of the Aliwal Shoal aeolianites. Note that the ages are uncorrected for detrital contamination and as such referred to as uncorrected ages. Of the 2σ error ranges the largest will be used to quote the error range. Also refer to Appendix XII.

Sample name	**SA-33**	**SA-48**	**GC-6**	**GC-5**	**GC-4**	**GC-7**
repeated within error						
238U ppm	0.4476	0.8840	0.5299	0.6179	0.5601	0.4576
uncertainty	0.0006	0.0012	0.0008	0.0024	0.0008	0.0011
(234U/238U)	**1.099149775**	**1.097785098**	**1.028651337**	**1.038672874**	**1.077517705**	**1.06309168**
uncertainty	0.003581295	0.004365996	0.002711795	0.009894063	0.002813258	0.003971064
234U ppm	2.6546E-05	5.23641E-05	2.94154E-05	3.46315E-05	3.2566E-05	2.62507E-05
uncertainty	8.07748E-08	1.97171E-07	7.31981E-08	3.02856E-07	8.05853E-08	8.15183E-08
230Th ppb	0.003529993	0.000223137	0.005840052	0.008304475	0.006714886	0.004519122
uncertainty	5.63642E-05	3.5453E-06	0.000192921	8.46246E-05	0.000105006	4.46558E-05
232Th ppb	384.2365275	0.638563402	776.3761504	1354.664049	928.2259651	678.312124
uncertainty	30.48490917	0.04970473	140.5811487	245.9839899	167.9841169	122.7248558
(230Th/232Th)	**1.723441486**	**86.91130995**	**1.412287977**	**1.154635359**	**1.357861579**	**1.258237373**
uncertainty	0.038367059	1.907465812	0.09295935	0.049837105	0.065705644	0.053621075
(230Th/234U)	**0.438376343**	**0.014047856**	**0.654506653**	**0.790518601**	**0.679744623**	**0.567523745**
uncertainty	0.007003712	0.000223398	0.021625154	0.008116032	0.010633821	0.005613465
(234U/238U)	**1.099149775**	**1.097785098**	**1.028651337**	**1.038672874**	**1.077517705**	**1.06309168**
uncertainty	0.003581295	0.004365996	0.002711795	0.009894063	0.002813258	0.003971064
AGE ka	**62,356**	**1,545**	**115,202**	**167,602**	**121,785**	**90,526**
2σ uncertainty	2606.10	49.44	12894.20	6503.08	6623.42	2631.00
2σ uncertainty	-2633.83	-49.44	-13666.28	-6654.09	-6811.60	-2657.82
%err 2σ	4.20	3.20	11.53	3.93	5.52	2.92

9.4.4. Radiocarbon

All radiocarbon beachrock and shell samples analyses were undertaken by QUADRU (Quaternary Dating Research Unit) of the CSIR in Pretoria, South Africa. The laboratory results report is presented in Appendix XIII. It is important for later discussions to note that the radiocarbon method required complete acid digestion of the sample and is thus in the case of rock samples, referred to as a whole rock age.

Radiocarbon dating is the most widespread and commonly applied Quaternary dating method. It is based on the radioactive decay of one of three carbon isotopes, ^{14}C, hence radiocarbon. The other two isotopes of carbon are ^{12}C and ^{13}C and are stable isotopes which comprise 99.9% of all naturally occurring carbon. The basic principle of the method is the equilibrium between radioactive ^{14}C (radiocarbon) formation in the upper atmosphere and its subsequent distribution through the different carbon reservoirs in the earth, wherein the amount of ^{14}C is dependent on the rate of carbon assimilation versus the rate of ^{14}C decay (Woodborne, 2002). Therefore it is necessary to quantify the carbon reservoir effect on the radiocarbon dating if the radiocarbon ages are to be meaningful.

A review of the method falls outside the scope of this thesis and the reader is referred to the applicable journals (e.g. Radiocarbon, Quaternary Geochronology) and Walker (2005) for an updated review. A recent note on the standard radiocarbon reporting practise is provided by van der Plicht and Hogg (2006). Background related to calibration of conventional radiocarbon ages can be found in the references associated with the various calibration programs (see Appendix XIV).

Fourteen samples were dated with radiocarbon and comprise a wide variety of materials ranging from shell to whole beachrock samples. Table 9.4 presents the original radiocarbon laboratory dates which are corrected for isotope fractionation, calculated using a half-life of 5568 years for ^{14}C and reported in years Before Present (BP), i.e. before AD 1950. The conventional ages were calibrated to sidereal years using the calibration program of Fairbanks0107 (http://radiocarbon.LDEO.columbia.edu/) and the CALIB programme using the IntCal Marine09 curve. Figure 9.4 shows the correspondence between the different calibration routines. The same calibration routine was used as that applied to the recalibration of the Ramsay and Cooper (2002) data and as such the reader is referred to Appendix XIV for more details regarding the calibration process. The various calibration datasets (Figure 9.4) are within error of each other. As found during the Ramsay and Cooper (2002) recalibration, the Fairbanks 0107 calibration results are

Table 9.4 Results from the radiocarbon dating of the Aliwal Shoal beachrocks and shell material. The C14 Age (B.P.) is the original age corrected for isotope fractionation and calculated using the Libby half-life (5568 years). The preferred calibration age for the samples using the Pretoria calibration program (see Appendix XIII) is also provided. MRA = marine reservoir age, BP Age (MRA Corr.) is the original C14 B.P age corrected for the marine reservoir effect. ΔR is the Calib6.0 (calibration software) local marine reservoir age correction (refer to Appendix R&C for details). The Calib6.0 ages are provided as age ranges which are converted to the median value with an equal error for easy comparison with other data.

Sample	Lab Code	Material	C14 Age (B.P.)		Pretoria Calib. (cal. B.P.)	Fairbanks 0107 Calibration					CALIB6.0 (INTCAL Marine09 curve)					
			Age	Error		MRA	BP Age (MRA Corr.)	Error	Calib. Age FB0107	Error	MRA		Age Range (cal)		Median	
											ΔR Calib6	ΔR Err	Lower	Upper	Age	Error
GC-1	Pta-9405	BR	13380	140	15574	287	13093	140	15250	188	213	57	14415	16099	15257	842
GC-1b	Pta-9399	BR	13300	130	15501	287	13013	130	15158	177	213	57	14156	15652	14904	748
GC-2	Pta-9417	BR	10220	100	11105	287	9933	100	11359	164	213	57	10634	11196	10915	281
GC-2S	Pta-9395	BR-shell	10070	110	11089	287	9783	110	11197	120	213	57	10518	11118	10818	300
GC-3	Pta-9323	BR	12420	130	14006	287	12133	130	13932	140	213	57	13352	13940	13646	294
GC-3S	GrA-27639	BR-shell	9300	45	9913	287	9013	45	10198	34	213	57	9584	10101	9843	259
GC-9	Pta-9398	BR	7030	90	7569	287	6743	90	7598	68	213	57	7143	7543	7343	200
AS-27	Pta-9397	BR	9720	60	10387	287	9433	60	10668	89	213	57	10198	10530	10364	166
GC-10	Pta-9421	BR	15500	160	18000	287	15213	160	18425	228	213	57	17681	18558	18120	439
GC-10S	Pta-9394	BR-shell	18900	200	21913	287	18613	200	22215	215	213	57	21377	22333	21855	478
GC-5Oys1	Pta-9400	Shell	8930	70	9594	287	8643	70	9587	70	213	57	9135	9536	9336	201
GC-5Oys2	Pta-9413	Shell	8460	50	9000	287	8173	50	9106	76	213	57	8571	8987	8779	208
GC-8Oys	Pta-9402	Shell	7090	60	7626	287	6803	60	7641	46	213	57	7244	7546	7395	151
OS-5	Pta-9419	Pothole fill	2020	60	1626	287	1733	60	1642	77	213	57	1197	1537	1367	170

slightly older in age relative to the IntCal Marine09 calibration results due to differences in the MRA for the datasets (Appendix XIV). The Pretoria dataset (calibration data provided by QUADRU - see Appendix XIII) varies in correlation with the other datasets but corresponds slightly better with the Fairbanks0107 calibration dataset (Figure 9.4).

The laboratory was satisfied with all the radiocarbon ages except the age for GC-10 and GC-10S which they considered to be spurious with ages most likely beyond the radiocarbon dating range.

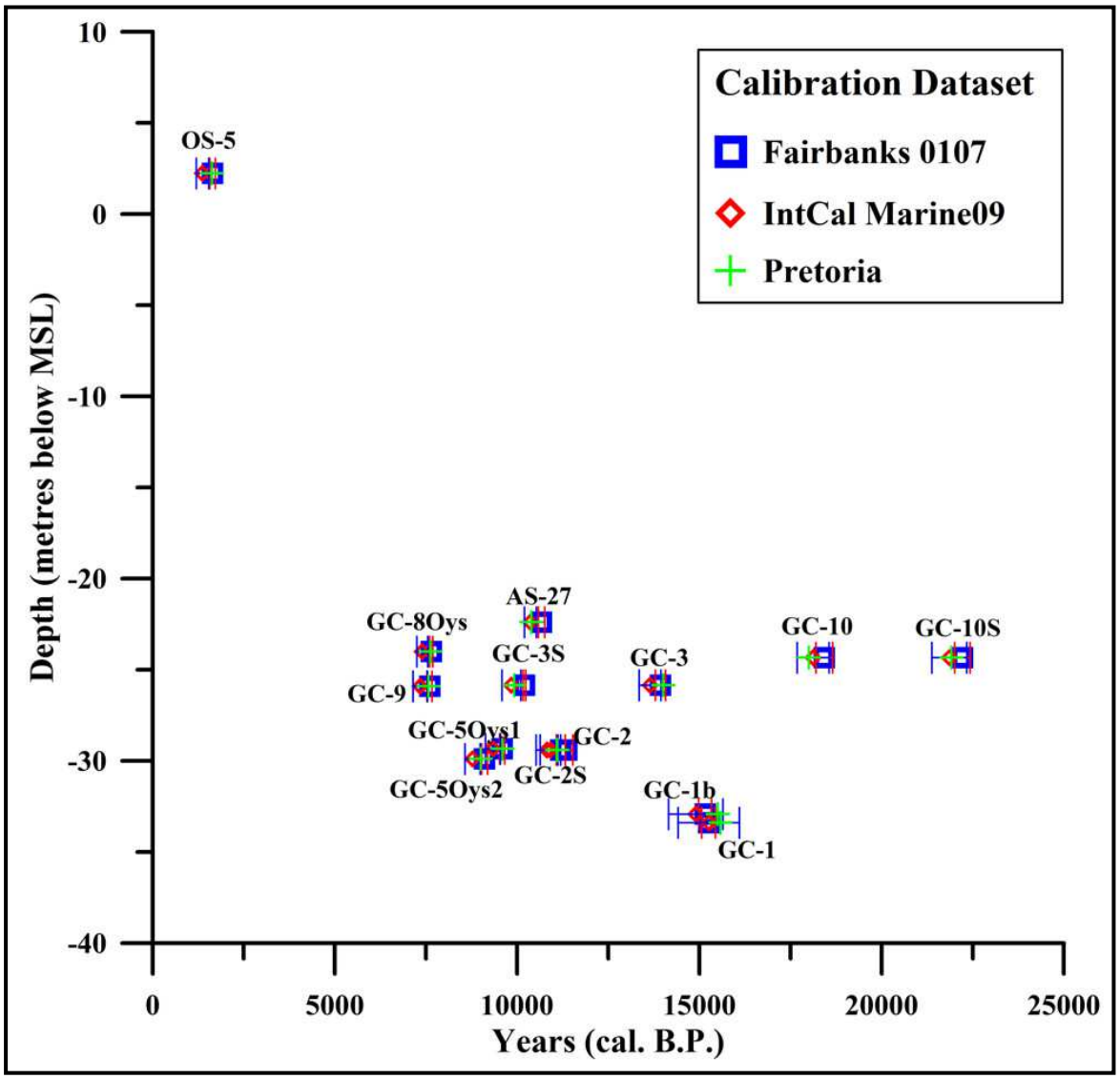

Figure 9.4 Radiocarbon calibration comparison for the Fairbanks0107, CALIB (v6.0 html) of Stuiver and Reimer (1993) using the IntCal Marine09 curve and the Pretoria calibration datasets. The three methods are within error of each other for all the data points. Refer to the text for details.

9.5. DISCUSSION

The next two sections (Sections 9.5.1 and 9.5.2) will briefly evaluate the age results in terms of comparison between the various analytical methods, whereas Section 9.5.3 considers the ages from a lithostratigraphical perspective. The significance to the record of sea-level change and the wider implications of the ages are reviewed in Sections 9.5.4 and 9.5.5, respectively.

9.5.1 Dating Aeolianites; OSL vs. U-Series

A summary of the aeolianite ages and associated analytical methods are presented in Tables 9.5, whilst the results are graphically displayed in Figure 9.5.

Table 9.5 Summary of the OSL and U-Series ages for the various aeolianite units. N/A = not analysed, N/R = no result. Note that AS-33 and AS-48 are hand specimen samples. Refer to Figure 9.1 for the location of the various units.

Sample	Unit	MSL (m)	OSL		Useries		US-Modelled Age
			Age	Error	Age	Error	
GC-4	Upper A1	-15	127000	7000	121785	6812	115000
GC-5	Lower A1	-30	134000	5000	167602	6654	168000
GC-6	A2	-26	130000	6000	115202	13666	N/R
GC-7	A3	-16	93000	6000	90526	2658	97000
AS33	Lower A1	-17	N/A	N/A	62356	2634	65000
AS48	Upper A1	-4	N/A	N/A	1545	49	110000

Independent OSL and U-series geochronological analyses of the aeolianite samples show, with the exception of GC-5, within error ages (Figure 9.5). OSL dating provides a burial or depositional age (Section 9.4.2) whereas the U-Series ages (Section 9.4.3) are considered diagenetic ages reflecting the last cementation event that fractionated thorium and uranium. As expected, with the exception of GC-5, the central U-Series or diagenetic ages seem to be slightly younger than the depositional OSL central ages (Figure 9.5).

The OSL ages are preferred and considered reliable ages for aeolianite formation due to the reasons discussed below. Since optical ages provide depositional ages, they more accurately constrain the timing of dune formation, whereas diagenetic ages are often independent of the depositional event (refer to Section 8.35). The OSL results are also compatible with international

eustatic sea-level curves (Figure 9.7). As the various aeolianite units were deposited in a coastal setting in proximity to sea-level (Section 8.3.3) there should be a fair agreement between the positions of the aeolianites, albeit above sea-level, and the position of the palaeosea-level at the time.

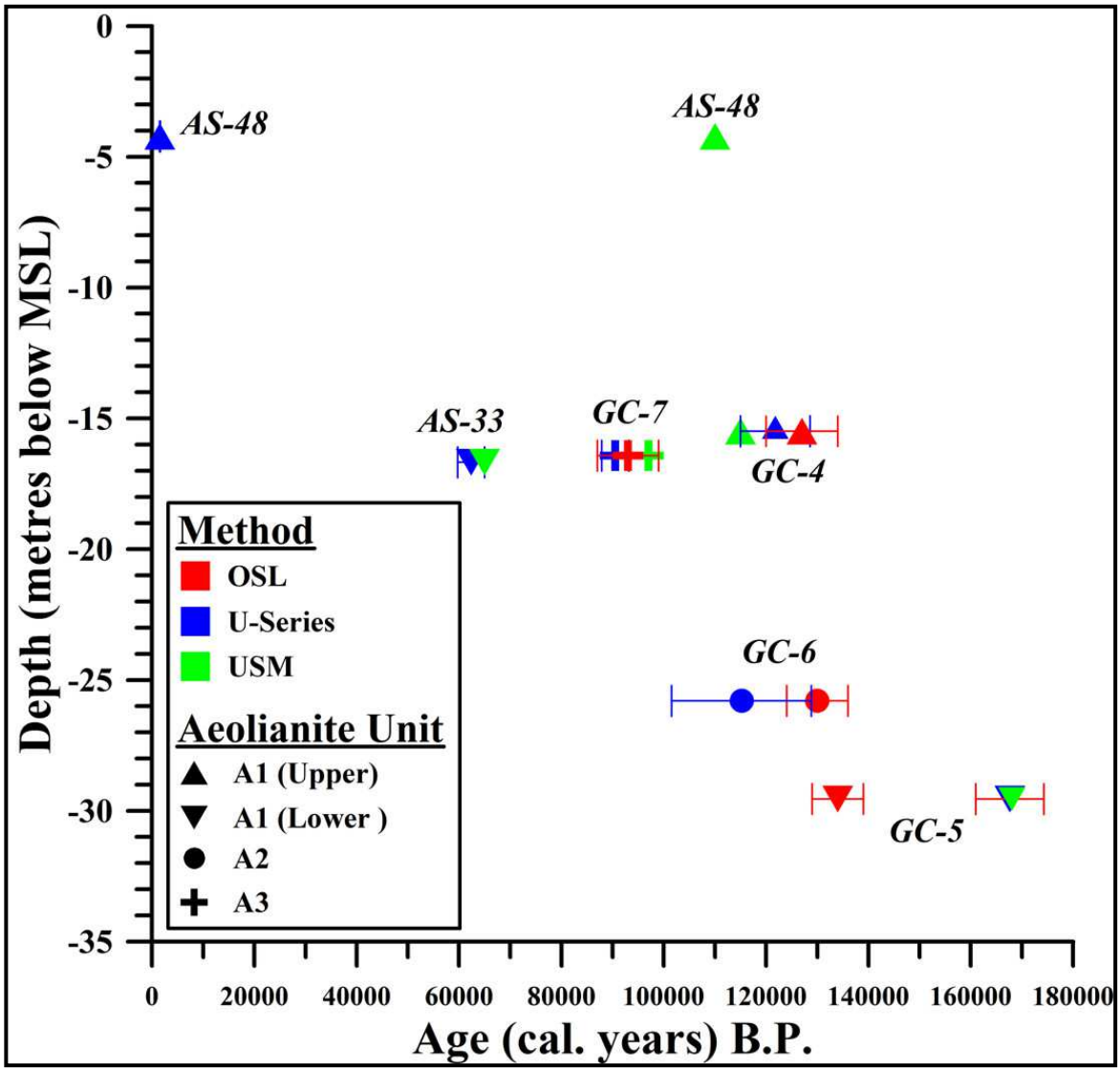

Figure 9.5 Age versus depth plot of the aeolianite samples for the various aeolianite units and the different geochronological methods. OSL = optically stimulated luminescence, U-Series = uranium series and USM = uranium series modelled age. There is no error range associated with U-Series modelled ages and there is no modelled age for GC-6.

U-Series ages for the Aliwal Shoal aeolianites involved entire sample digestion in acid. Since an accurate U-Series analysis requires measuring the U-Th disequilibrium and an assumption that all carbonate is in the cement phase. From Chapter 8, it is shown that the aeolianites have a very

complex diagenetic history which resulted in several carbonate cement phases of both meteoric and marine origin (see Section 8.3.3). Each cementation phase therefore will represent a U-Th fractionation event and as such digestion of the entire sample during U-series analyses would therefore dissolve and mix the last U-Th fractionation event of the multiple cementation events (e.g. Figure 8.15c). This problem was highlighted by the trouble experienced by the laboratory (Section 9.4.3) and the subsequent necessity for the U-Series modelling. The reliability of the resultant ages is thus questionable.

Even the results from open system modelling of the U-Series ages are questionable as the model could not account for the behaviour of GC-6. As the uncorrected GC-6 U-Series age is within error with the optical age (Figure 9.5) and thus considered reliable, it indicates that there is some deficiency in the model to account for the behaviour of the Aliwal Shoal samples. In addition, modelling may result in spurious results reflecting unknown events, as is exemplified by AS-48 (upper Unit A1; Figure 8.7). Sample AS-48 is a hand specimen sample, which as discussed Section 8.3.3 shows a greater number of cementation events compared to the GC-series samples. It has an uncorrected U-Series age of 1 545 ± 45 years cal. B.P. and a modelled age of 110 ka cal. B.P. supposedly reflecting fractionation during closed-system conditions (Figure 9.3). AS-48 is located close to GC-4 and shows similar field and sedimentological characteristics a similar but slightly younger age is expected, i.e. formation during the sea-level rise (Figure 9.7). Thus, this AS-48 age is not tied to deposition of Unit A1 but either reflects another diagenetic event or more likely, is complete nonsense as it is based on modelling an unreliable U-Series age which is flawed to begin with. The latter reason underlines the fundamental problem with the modelling insofar no matter how good a model, if the original age does not represent a single dateable event, the model age is also useless. The age of another hand specimen, sample AS-33, is also interpreted to suffer from the same problems as AS-48 and as such considered unreliable.

GC-5 shows good correspondence between the uncorrected U-Series age and the modelled age but is much older than the optical age (Figure 9.5). The older U-Series age is most likely due to detrital contamination by daughter nuclides resulting in the older apparent age (Walker, 2005).
There seems to be a good correspondence between the optical and diagenetic ages of GC-4, GC-6 and GC-7 (Figure 9.5), further supporting the interpretation of early pervasive diagenesis in the aeolianites (Sections 8.3.3 and 8.3.5). In addition it also indicates that despite the later marine cement phase, the LMC primary cement in the GC-series samples dominates as the measured fractionation event.

Thus, although it might seem that the U-Series method is well suited to dating the aeolianites this is clearly not the case. However, the U-series ages might be reliable but it will always require an

independent age check. In addition, the U-Series ages theoretically date diagenetic events, which in the aeolianites, might not be related to the aeolian depositional event. For this reason the optical age data provide the best results for this study as they are reliable and also constrain the depositional and hence formation age for the various aeolianite units.

9.5.2 Dating Beachrocks; OSL vs. Radiocarbon

A summary of the beachrock ages and associated analytical methods are presented in Tables 9.6, whilst the results are graphically displayed in Figure 9.6.

Table 9.6 Summary of the OSL and radiocarbon ages for the various beachrock units. N/A = not analysed. Note that AS-27 is a hand specimen samples. Refer to Figure 9.1 for the location of the various units.

Sample	MSL (m)	Unit	OSL		Radiocarbon			
			Age	Error	Fairbanks 0107		CALIIB Marine09	
					Age	Error	Age	Error
GC-1	-33	B1	11000	670	15250	188	15257	842
GC-1b	-33	B1	10600	590	15158	177	14904	748
GC-2	-29	B2	10200	520	11359	164	10915	281
GC-2S	-29	B2	N/A-	N/A	11197	120	10818	300
GC-3	-26	B3	9800	560	13932	140	13646	294
GC-3S	-26	B3	N/A	N/A	10198	34	9843	259
GC-9	-26	B3	9900	590	7598	68	7343	200
GC-10	-24	B5	79000	5000	18425	228	18120	439
GC-10S	-24	B5	N/A	N/A	22215	215	21855	478
AS-27	-22	B4	N/A	N/A	10668	89	10364	166

Beachrock ages show a much greater variability between the two applied methods than the aeolianites (Figures 9.5 and 9.6). This variability is mostly related to the radiocarbon ages which were not only noticeably different to the optical ages but also disagree between different materials dated from the same sample (e.g. compare GC-3 with GC-3S; Figure 9.6; Table 9.6). However, the radiocarbon shell ages, especially those corrected with the Marine09 curve (Table 9.6) are within error with the optical ages and thus show good correlation (GC-2S, GC-3S; Figure 9.6). This might indicate that the IntCal Marine09 MRA local correction factor (ΔR; also see Appendix XIV) models the east coast marine reservoir age better than the Fairbanks0107 correction.

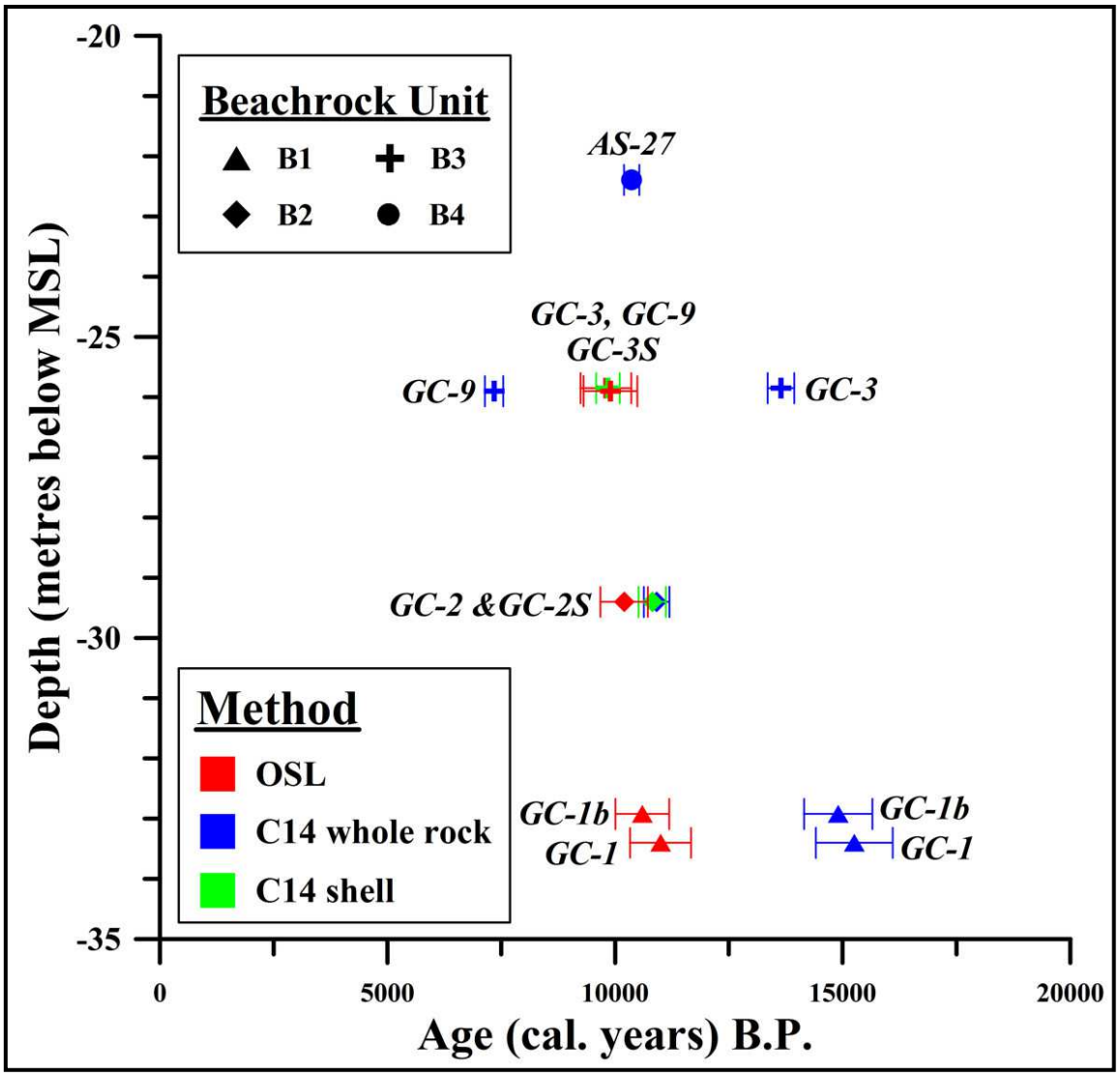

Figure 9.6 Age versus depth plot of the beachrock samples for the various beachrock units and the different geochronological methods. OSL = optically stimulated luminescence, C14 = radiocarbon method. Note that the displayed radiocarbon ages are correct with the IntCal Marine09 curve as it shows better agreement between the shell and OSL ages than the Fairbanks0107 routine (also see Appendix XIV). The OSL result for GC-10 (79 ± 5 ka cal. B.P.; Table 9.6) is not plotted as it will reduce the clarity of the Holocene beachrocks. In addition, the radiocarbon results of GC-10 and GC-10S are also not plotted due to unreliability. GC-1 and GC-1b are separated by 0.4 m for clarity.

Whole rock radiocarbon ages are at variance with the radiocarbon shell ages and the optical ages. The incompatible age results of the whole rock radiocarbon ages serve to highlight the fundamental problem in applying the radiocarbon method to date whole rock beachrock samples.

As the whole rock method requires digestion of the entire sample all carbon sources are included. The problem for the beachrocks is that they almost always contain lithic and bioclastic fragments from older sources which consequentially introduces older carbon and as such is expected to produce unreliable results. For example the lithic fragments in the Aliwal Shoal beachrocks samples comprise aeolianite fragments (Section 8.3.3; Figures 8.25c and 8.27) which are much older (Section 9.5.1) and as such incorporate older carbon into the beachrock whole rock analyses. Based on this mineralogical observation there should be a relationship between lithic fragment content of the sample and age but when comparing the lithic components in the beachrocks (Table 8.8) with the degree of correspondence/variance between the methods (Figure 9.6) there is not a clear direct or inverse relationship, as is expected.

This is exemplified by Unit B2, which displays the highest aeolianite lithic fragment content (17.7%, Table 8.8) but is within error for both the methods and sample material (Figure 9.6). Although, this might be due to the dating sample (GC-2) showing a lower average lithic fragment content (9%, Table 8.8), even so GC-3, the whole rock sample with the lowest average aeolianite lithic content (4% Table 8.8), shows a very large discrepancy to the OSL and shell ages which are within error (Figure 9.6). Thus, although the variance of the OSL and whole rock analysis must be due, at least to some degree, to incorporation of aeolianite lithic fragments, mineralogy alone is not accounting for the large age discrepancies between the methods.

In addition, Units B1 and B3 show no correspondence between the optical and radiocarbon ages. Morphological (changes in coastal configuration, Section 8.3.4) and diagenetic (aragonite-HMC cycles, Section 8.3.5, Beachrock Diagenesis) evidence have tentatively linked these two units to two flooding events associated with different pulses of enhanced rates of sea-level rise. It is therefore suggested here that the large discrepancies in the radiocarbon whole rock ages are not only due to incorporation of older carbon but possibly also due to changes in ocean chemistry and consequently the marine carbon reservoir associated with the two flooding events. It is well known that the marine carbon reservoir ages varied in space and time, a dilemma that prompted Reimer *et al*. (2009) to question '*…whether a marine calibration curve should be provided at all prior to the Holocene*'. Thus, the inconsistent behaviour of the radiocarbon whole rock method is theorised to be due to two unrelated factors;

1) the incorporation of older carbon through the inclusion of bioclastic and aeolianite lithic fragments and,
2) possible extreme and rapid changes in the apparent ages of seawater related to meltwater pulses and rapid changes in the rate of sea-level rise.

In summary, concerning dating beachrocks, optical dating has two clear and fundamental advantages over radiocarbon; 1) no need for age and marine reservoir corrections and 2) does not suffer from carbon contamination from other sources (e.g. lithic fragments) that can greatly compromise the results. The only possible drawback with applying optical dating to this type of deposits is that it might have too large an error range (normally at least 5 % of total age) to constrain recent high resolution events. Be that as it may, in the case of the Aliwal Shoal, optical dating was able to resolve the ages of the different Holocene beachrocks which shaped and document palaeocoastline events during the last deglacial sea-level rise.

9.5.3 Aeolianite and Beachrocks Ages

Several geochronological methods have been applied to date the aeolianite (Section 9.5.1) and beachrock (Section 9.5.2) units. Common to both of these is the OSL method, which as discussed previously, was the only method that produced reliable and meaningful depositional ages to the various stratigraphic units. As such this study will use the OSL results as the accepted ages for the various lithostratigraphic units.

Aeolianite Ages

Aeolianite lithologies were divided into three units based on morphology, field relationships, sedimentary structures and geochronological analyses. Unit A1 is the most prominent aeolianite unit and comprises an upper and lower unit (Section 8.3.3; Figures 8.9e). The lower Unit A1 is the oldest sampled aeolianite in the study area with an age of 134 ± 5 ka cal. B.P. (GC-5; Table 9.5; Figure 9.5) and was later followed by the overlying Upper Unit A1, dated at 127 ± 7 ka cal. B.P. (GC-4; Table 9.5). Aeolian activity is inferred to have been fairly continuous as evident by the lack of observed palaeosols and other major erosional surfaces between the two dune sub-units. Unit A2 is the most conspicuous aeolianite unit forming a distinct corridor of parabolic dunes (Figures 8.7 and 8.12a). It is dated at 130 ± 6 ka cal. B.P. (GC-6; Table 9.5; Figure 9.5) and formed during the palaeoclimatic transitional period between the lower and upper Unit A1. Unit A3 is the youngest sampled unit with an age of 93 ± 6 ka cal. B.P. (GC-7; Table 9.5; Figure 9.5) deposited in a postulated back-barrier environment.

Beachrock Ages

Beachrock outcrops were subdivided into five units based on integrating morphology, field relationships and sedimentary structures with the results from geochronological analyses (Section 8.3.4). Units B1 to B4 formed sequentially during a brief period spanning 11 to 9.8 ka cal. B.P. throughout the Holocene transgression, whilst Unit B5 is an extreme event deposit formed at 79 ± 5 ka cal. B.P.

The Holocene beachrocks therefore were deposited after the Younger Dryas cold event and during the time interval of MWP-1b (Section 4.2.2). Unit B1 is the oldest Holocene unit and was deposited between 11 to 10.6 ka cal. B.P. subsequently followed by Unit B2 at 10.2 ka cal. B.P., together representing a log-spiral bay coastal configuration. Major realignment to a linear coastal system controlled by pre-existing aeolianites is documented by Unit B3 deposited at ~9.8 ka cal. B.P. and shortly afterwards followed by Unit B4, the termination of which, signified the complete overstepping of the Aliwal Shoal coastal barrier system probably resulting in an barrier island setting and subsequent rapid complete drowning.

Correlation

All of the aeolianite units form part of the Isipingo Formation of the Maputaland Group (Table 3.1). Units A1 and A2 comprise the Cave Rock Member (pre-last interglacial aeolianite, Porat and Botha, 2008), whilst Unit A3 possibly can be grouped into the Meersig Member (<125 ka aeolianite, Porat and Botha, 2008), although it generally represents Eemian stranded beach deposits (Cooper and Flores, 1991; Cawthra, 2010). No relevant lithostratigraphic classification exists for the Holocene beachrock deposits of Unit B1 to B4, although Ramsay (1995) found a beachrock stranded on the continental shelf with a similar early Holocene age (Appendix R&C, sample Pta-6190, 9 883 ± 285 yr cal. B.P.). Considering that the Maputaland Group and subsequently Isipingo Formation have been defined based on lithostratigraphic units found onshore and then also predominantly in Maputaland (see Figure 2.11 for locality), it is thus not surprising to find that the Aliwal Shoal units do not fit into the lithostratigraphic classification of the Maputaland Group. Future amendments to the Maputaland Group should consider the results of the Aliwal Shoal and other similar offshore studies (Ramsay, 1991, 1995; Ramsay and Cooper, 2002; Cawthra, 2010).

9.5.4 Quaternary Sea-Level Changes as Documented by the Aliwal Shoal

This study produced new and accurate late Pleistocene and Holocene ages for aeolianites and beachrocks, both of which have significance to sea-level at the time of formation. The most recent and applicable relative sea-level curve for comparison is the Ramsay and Cooper (2002) relative sea-level curve (RCSLC). However, the RCSLC plots both Uranium series calendar ages with uncalibrated radiocarbon ages. Therefore, in the interest of achieving meaningful comparison between the new Aliwal Shoal data and the existing datasets, the RCSLC was essentially re-interpreted by addressing two principal issues viz; (1) recalibration of the radiocarbon data to sidereal years so as to be comparable to the uranium series ages and hence comparable to the Aliwal Shoal datasets and (2) basic reinterpretations of the radiocarbon-based sea-level index point data in accordance with international standards, thereby improving the consistency of the Ramsay and Cooper (2002) sea-level curve. Full details of the recalibration and reinterpretation procedures are presented in Appendix XIV.

Aliwal Shoal beachrock and aeolianite optical ages are plotted on the reinterpreted RCSLC and compared with the global eustatic curve of Waelbroeck *et al*. (2002) and MIS 5e data from Carr *et al*. (2010). The Holocene beachrock ages are compared with the curves from Waelbroeck *et al*. (2002) and Camoin (2004).

Indicative Meaning of the Aliwal Shoal Data

For a sea-level index point to be pertinent it must have some established elevation relationship (indicative meaning, Woodroffe and Horton, 2005) to sea-level at the time of formation. Aeolianites are deposited as aeolian sediments above sea-level but some part of the aeolianite can be cemented below the water table (Figure 8.31a). In the case of the Aliwal Shoal coastal aeolianites this type of cementation might even be below MSL. Thus, the within error depositional and diagenetic ages showed by most of the Aliwal Shoal aeolianite units (Section 9.5.1) combined with the fact that these aeolianites were deposited during a fast sea-level transgression and hence a continually upwards migrating groundwater table, suggests a close relationship with the sea-level at the time. Although the aeolianites are not actual sea-level index points, they are considered fairly accurate sea-level limiting points indicating the presence of sea-level at or below the sample position. Some notable recent studies dealing with the geochronology of onshore barrier systems used aeolianites as a constraining parameter to sea-level at the time (Bateman *et al*., 2004; 2011; Carr *et al*., 2010).

Beachrocks in microtidal open coastline settings are considered reliable indicators for sea-level (Ramsay, 1995; Ramsay and Cooper, 2002). All of the geochronologically constrained Holocene beachrock units (B1 to B3) have been deposited and cemented in the intertidal zone (Table 8.6). Ramsay (1995) found that contemporary beachrocks along the eastern South African coastline were forming at elevations of 0.1 to 0.2 m above mean sea-level. In addition the local tidal range is less than 2 metres, meaning that the beachrocks have an indicative range totalling 2 m. Thus, the indicative meaning of the Aliwal Shoal beachrocks is very close to the actual MSL at time of formation and the variability of the depositional range is also well constrained due to the microtidal regime. Thus, the beachrocks are considered reliable sea-level index points whereas the aeolianites are fairly accurate sea-level limiting points indicating a sea-level at or lower than the aeolianite sample position.

Fossil oyster specimens (Figure 9.2c) were found in living position attached as massive beds to the seaward edge of the Aliwal Shoal (Appendix IX) and constitute the first discovery of this type from the southeast African continental shelf. The oyster samples were identified as *Crassostrea margaritacea* (Lamarck, 1819) or the common Cape Rock Oyster, normally forming beds at and just below the lowest spring tide level (Herbert, *Pers Comm.*) whereof three specimens were dated by the radiocarbon method (Table 9.4; Figure 9.1) and presented here (Figure 9.8). The indicative meaning for the oysters is that MSL was ~2 m above the oysters during formation with an indicative range of 1 m related to the tidal range. According to Ramsay and Cooper (2002) fixed biological indicators such as barnacles, oysters and fossil calcareous tubeworm encrustations are good sea-level index points with their known relationship to mean sea-level and occurrence in the inter-tidal zone potentially indicating the contemporary sea-level with accuracy equal to at least the tidal range or even 0.5 m.

Palaeopothole-fill (OS-5; Table 9.4) which was obtained from a pothole incised in a dip-slope (Figure 9.2d, e) of Vryheid Formation (Figure 3.1) sandstone at a height of 2.23 m above MSL is interpreted as a sea-level index point and assigned an indicative meaning of MSL and indicative range of 2 m.

Sea-Level and Aeolianite Deposition

Results presented here show that the submerged Aliwal Shoal complex forms a compound barrier ridge system consisting of a core of several aeolianite units deposited from MIS 6 to MIS5b and which are unconformably overlain by predominantly Holocene-age beachrocks (Figure 9.7).

Relative to the global eustatic curve of Waelbroeck *et al*. (2002) the midpoint age for the lower Unit A1 (GC-5) is slightly too old, whereas the midpoint age for the upper Unit A1 (GC-4) is slightly too young (Figure 9.7). The parabolic dunes of Unit A2 (GC-6) show very good correlation with sea-level which further support the hypothesis based on field evidence of aeolian migration into an estuary (Section 8.3.3, Unit A2) as estuarine water levels generally approximate sea-level. The midpoint age for the back-barrier dune deposits of Unit A3 seems to be slightly too young relative to the global sea-level (Figure 9.7), although it is still well within error. The disparity might be related to the position of Unit A3 during deposition which was possibly not as well constrained to the sea-level at the time as that of Units A1 and especially A2.

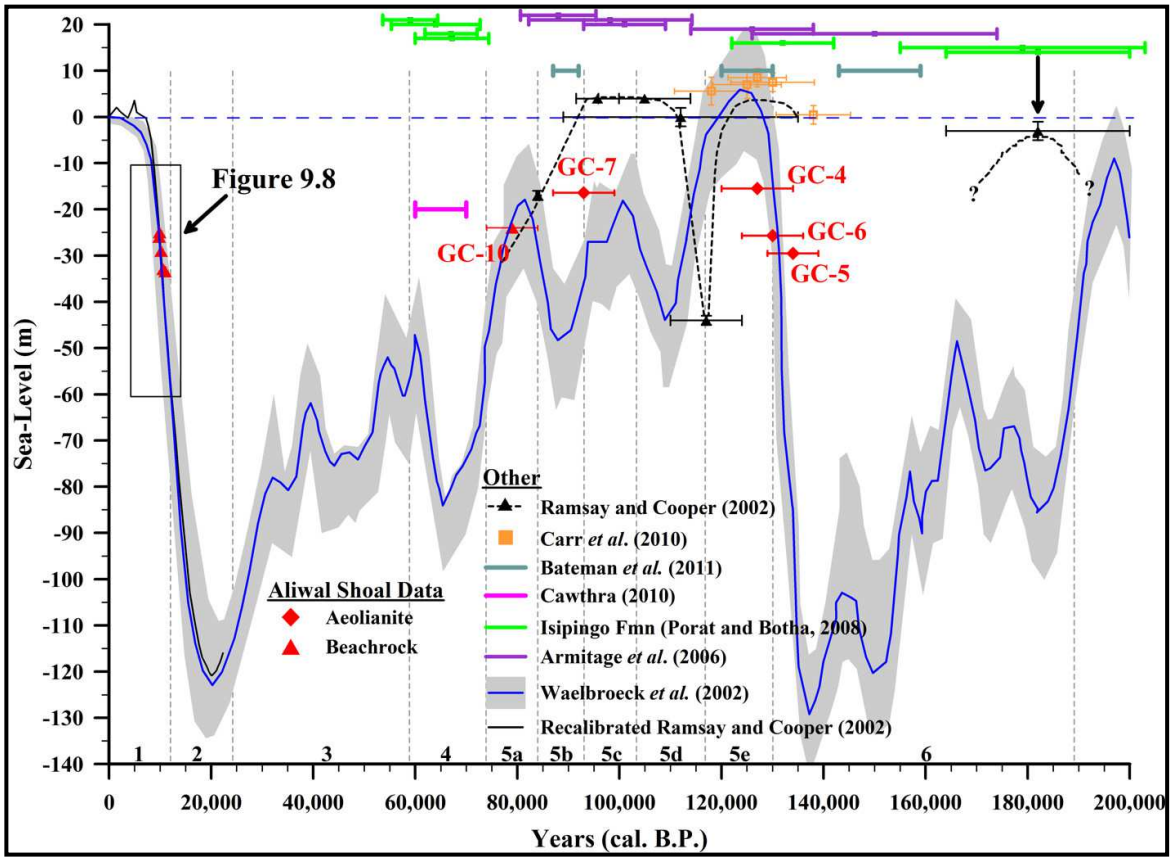

Figure 9.7 Results of the optical dating of the aeolianite and beachrock samples from the Aliwal Shoal plotted on the composite global eustatic sea-level curve of Waelbroeck *et al*. (2002). Note that the grey background to the Waelbroeck *et al*. (2002) represents the 2σ uncertainty error value. The marine isotope stages are number at the bottom of the graph. Other sea-level curves included for comparison are a partial section of the Ramsay and Cooper (2002) sea-level curve comprising only the uranium-series based index points and the recalibrated and reinterpreted Ramsay and Cooper (2002) radiocarbon-based sea-level curve (Appendix XIV). Comparative data values include; feldspar infra-red-stimulated luminescence (IRSL) age of the Unit 3 Aeolianite from Cawthra (2010), OSL ages of the major clusters of aeolian and aeolianite formation in Wilderness area after Bateman *et al*. (2011) and IRSL ages for the Isipingo Formation (Fmn) from Porat and Botha (2008). These comparative ages have an arbitrary y-value and as such separated for clarity.

Aliwal Shoal aeolian deposition occurred predominantly during rapidly changing sea-levels leading up to and following the Last Interglacial Highstand (MIS5e). This supports the findings of Bateman *et al*. (2004; southern Cape coast), Armitage *et al*. (2006; Mozambique) and Porat and Botha (2008; northern KwaZulu-Natal) who also observed onshore aeolian deposition associated with the changing sea-levels of interglacial highstands. The age data from the Aliwal Shoal aeolianites cluster into two groups, 134 - 127 ka B.P. and 93 ka B.P. separated by the last interglacial highstand (Figure 9.7). Carr *et al*. (2010) and especially Bateman *et al*. (2011) identified similar age clusters (130 - 120 ka) from the southern Cape further suggesting synchronicity of aeolian (and aeolianite) formation between the different climatic regions i.e. the winter rainfall region of the southern Cape and the summer rainfall region of KwaZulu-Natal.

The aeolianite ages presented here are the first deposits from the continental shelf and possibly, the first deposits in South Africa, found to belong to the exceedingly rapid penultimate deglacial sea-level rise. The good correspondence between the aeolianite ages of Units A1 (GC-4, GC-5) and A2 (GC-6) with the global eustatic sea-level curve (Figure 9.7) supports the notion that these aeolianites were deposited in proximity to the coastal zone and hence sea-level at the time. As supported by the findings of the compositional and textural trends of Units A1 and A2 (Section 8.3.3, Aeolianite Petrography), the deposition and preservation of these prominent units were most likely due to a combination of the rapid sea-level transgression combined with onshore palaeowind regimes and longshore currents directly accessing a similar sediment source for both units. Armitage *et al*. (2006) found a strong relationship between dune migration and rising sea-level for the Holocene in the barrier islands of Bazaruto and Inhaca in Mozambique. Similarly, Porat and Botha (2008) ascribed Late Pleistocene and Holocene dune accretion in the coastal barrier to rising sea-level during transgression. The Aliwal Shoal age data supported by the field evidence (Section 8.3.3.) indicate a similar situation for the aeolianites formed during the MIS 6/5e sea-level rise.

Following deposition and preservation of Units A1 and A2 no further evidence of dune formation is preserved during the low sea-levels associated with the MIS 5d cool period in the study area (Figure 9.7). According to the Ramsay and Cooper (2002) curve MIS 5d is characterised along the east coast by a sea-level lowstand at 117 ± 7 ka B.P. recorded by a submerged beachrock deposited at -44 m (Figure 9.7). Although this age precedes the MIS 5d lowstand of Waelbroeck *et al*. (2002) by ~7 ka, it is within error and it is of the same magnitude as that indicated to have occurred on a global scale. Thus, the submerged beachrock deposit with an adjusted age to 110 ka cal. B.P. (still within the error range) is considered a reliable indication of the timing and magnitude of the MIS 5d lowstand along the southern African coast.

The Ramsay and Cooper (2002) sea-level curve indicates that sea-level was above present levels during the latter part of MIS 5d and the whole of MIS 5c. This is not supported by this study with deposition of Unit A3 (GC-7, -16 m) occurring in MIS 5c. Carr *et al*. (2010) also noted a lack of MIS 5c ages from the southern Cape and the deposition of Unit A3 at -16 m below MSL during MIS 5c is supported by both sea-level indicators derived from coral reefs (Cutler *et al*., 2003; MIS 5c sea-level of between -14 to -10 m ± 3 m) and the oxygen isotope record (Waelbroeck *et al*., 2002; Figure 9.7). The lack of MIS 5d ages agrees with global and local records indicating a relatively brief period of low sea-level.

The last recorded Late Pleistocene depositional event in the study area is that of Unit B5 (GC-10, -24 m) at 79 ± 5 ka cal B.P. (Figure 9.7). It represents a storm event (Section 8.3.3) and plots remarkably well on the global eustatic sea-level curve. The possible extreme event origin of this unit is discussed in Section 8.3.4 which is supported by field observation, compositional and textural data and its diagenetic history (Section 8.3.4, Beachrock Petrology and Section 8.3.5 Beachrock Diagenesis). Although Unit B5 was deposited above MSL due to its storm origin, it is considered an accurate indicator of the MIS 5a sea-level along, at least, the east coast of South Africa. Following the deposition of GC-10 there are no further depositional events recorded. This supports the seismic data which indicated that during sea-level regression towards the LGM lowstand, the Aliwal shelf comprised an interfluve area which was characterised by subaerial exposure, fluvial incision of coast-parallel tributary river systems and general sediment starvation (Section 6.5).

Thus, although not as accurate as the beachrocks the aeolianite events can still be considered to represent distinct Late Pleistocene palaeocoastline events.

The Holocene Sea-Level Rise

Records of the post-LGM sea-level rise (also known as the Holocene or Flandrian sea-level rise) are very scarce and most data are derived from raised coral terraces in the Pacific and Caribbean (see Section 4.4.2). These localities however, are located in tectonically active zones resulting in large and discontinuous tectonic movements which may bias the sea-level record by variations in the rates of uplift (Camoin *et al*., 2004). The paucity of sea-level records from tectonically stable regions or areas where the vertical movements have been slow or regular or both have fuelled the continual discussion relating to the general pattern of post-glacial sea-level rise, with the occurrence of periods of accelerated post-glacial sea-level rise as one of the main controversies (Camoin *et al*., 2004).

Rapid deglacial sea-level rise following the LGM (~18 - 20 ka B.P.) resulted in the deposition of transgressive systems tract sediments (Sequence 4, Sections 6.4.3 and 6.5) which comprise a complex arrangement of strike and dip variable depositional systems including the beachrocks of Units B1 to B4.

Optical results indicate sequential formation of Units B1 to B4 during the last deglacial sea-level rise (Figure 9.8; Sections 9.5.2 and 9.5.3) thereby supporting seismic interpretations (Sections 6.3.4 and 6.4.3), field observations and sample analyses (Section 8.3.4). Each of these beachrock units is interpreted as a palaeocoastline event which can thus be used to not only constrain the coastal evolution sequence but also the rate of sea-level rise between successive palaeocoastline events (Table 9.7). In addition, the Aliwal Shoal beachrocks were deposited during, what Bard *et al*. (2010) termed '*the critical time interval*' between 14 to 9 ka cal. B.P. This period is considered important from a sea-level rise perspective as the controversial meltwater pulses 1a and 1b and the Younger Dryas (YD) cold event occurred during this time period (also see Section 4.4.2). Data from this time interval are scarce and poor resolution. In addition, during this critical time interval, there are significant discrepancies between the geophysical modelled eustatic post-LGM sea-level rise and that observed at far-field sites such as Barbados and Tahiti (Bassett *et al*., 2005).

Table 9.7 Summary table of the preserved beachrock units representing three distinct palaeocoastline events. The different average rates of change for the sea-level rise is calculated based on the mid-point optical ages for the beachrock units. Units B1 and B3 have two optical ages available and as such the average value is used. cm = centimetre.

Unit	Depth	Age	Average sea-level rise
B1 (GC-1)	-33	11000 ± 670	Unit B1 to B2 ***67 cm in 100 years*** (4 m sea-level rise in 600 years)
B1 (GC-1b)	-33	10600 ± 590	
Average mid-point age for B1		10800	
B2 (GC-2)	-29	10200 ± 520	
B3 (GC-3)	-26	9800 ± 560	B2 to B3 ***86 cm in 100 years*** (3 m sea-level rise in 350 years)
B3 (GC-9)	-26	9900 ± 590	
Average mid-point age for B3		9850	

The Aliwal Shoal beachrocks fit well into the global eustatic sea-level curve of Waelbroeck et al. (2002) and the reinterpreted Ramsay and Cooper (2002) curve (Appendix XIV). Beachrock units slightly postdate the YD event (Figure 9.8) and fall within the timeframe shared by the controversial MWP-1b event (see Section 4.2.2). The rate of sea-level rise is calculated at 67 cm per 100 years between Units B1 and B2, and 86 cm per 100 years between Units B2 and B3 (Table 9.7). These rates are averages based on the mid-point optical ages and can thus be significantly

increased or decreased if the minimum and maximum age error range values are used (Table 9.6). For example, if the Aliwal Shoal beachrock ages are adjusted (within error) to fit on the Waelbroeck *et al*. (2002) curve (Figure 9.8), the overall rate of sea-level rise (calculated from Unit B1 to Unit B3) increases to 126 cm per 100 years (where B1 = 10.4 ka cal. B.P., and B3 = 9.845 ka cal. B.P.).

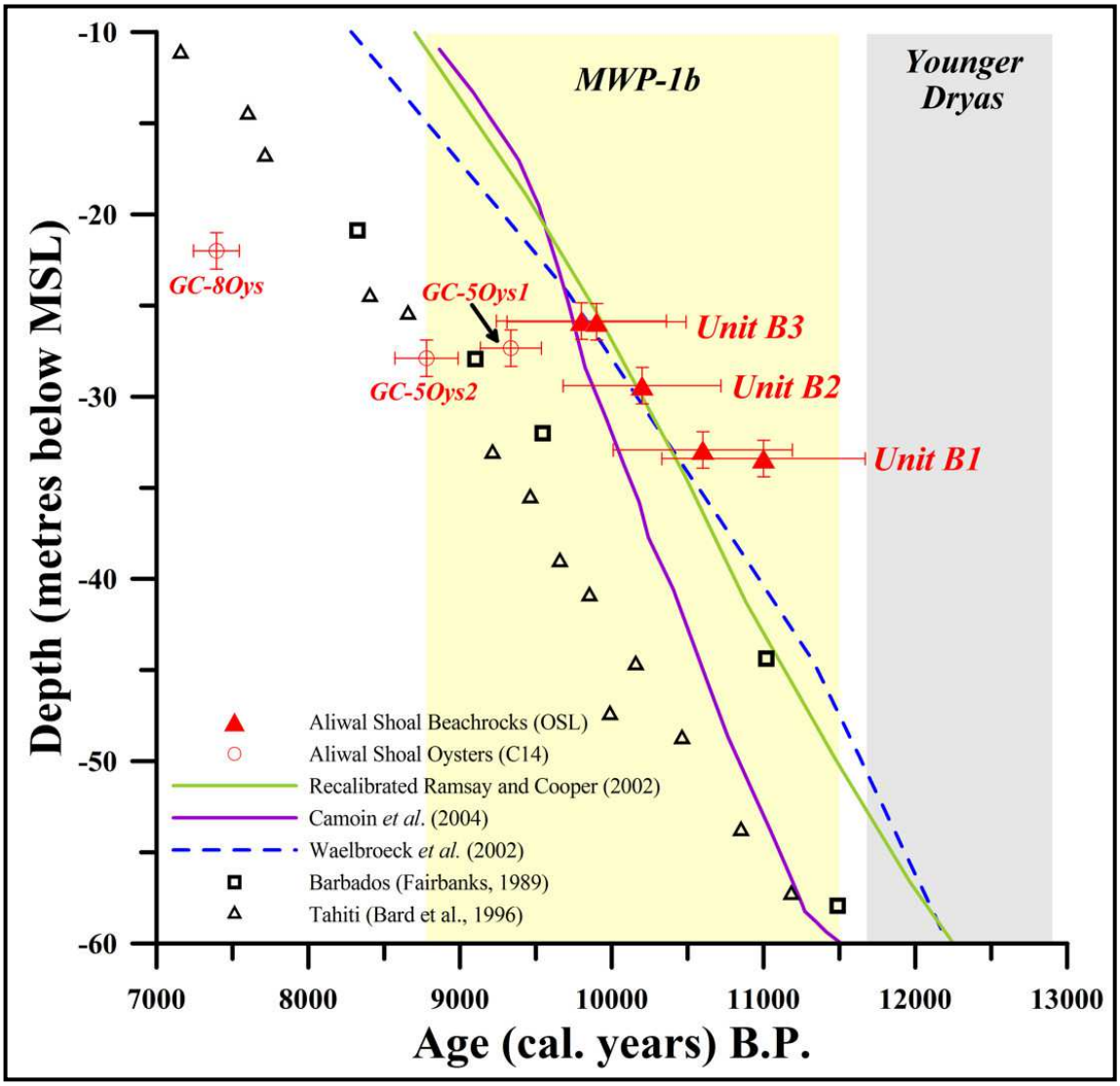

Figure 9.8 Aliwal Shoal beachrock units (Table 9.7) plotted for the critical time interval against various Holocene sea-level curves and the sea-level data from Barbados (Fairbanks, 1989) and Tahiti (Bard *et al*., 1996). Note that the Aliwal data lie above the Barbados and Tahiti data points. Also shown is the oyster samples which show poor correlation to the sea-level curves (Table 9.4; Appendix IX). Sample OS-5 (2 m above MSL) is not shown here in the interest of clarity. Refer to Figure 4.8 for a graphical representation of this sea-level index point. Timing of MWP-1b and the Younger Dryas cold event after Stanford *et al*. (2011).

Nonetheless, the average rate of sea-level rise as documented from one beachrock unit to another contrasts with that of Tankard *et al*. (1982) who suggested Flandrian sea-level rise at rates of up to 167 cm per 100 years for the transgression along the South African coast. Fleming *et al*. 1998 modelled the rate of post-LGM sea-level rise as 1 m per 100 years, whereas Lambeck *et al*. (2002a) modelled it for the periods 16 to 12.5 ka and 11.5 to 9 ka as 150 cm per 100 years. The average Aliwal beachrock data therefore show rates of sea-level rise 1.2 to 2.5 times slower than the above mentioned suggestions. However, it is compatible with that of Ramsay (1995) for the northern East Coast of South Africa calculated at 80 cm/100 years between 8 and 9 ka B.P. (~8.1 to 9.6 ka cal. B.P.) and that of Camoin *et al* (2004) from the Western Indian Ocean (Reunion, Mauritius, Mayotte, Seychelles and Madagascar) of ~60 cm per 100 years between 10 and 7.5 ka cal. B.P.

In addition, the Aliwal Shoal beachrock units show acceleration in the rate of sea-level rise from 67 to 86 cm/100 years and thus support the notion of deposition during MWP-1b. Recently, the controversy surrounded MWP-1b has intensified as Bard *et al*. (2010) found no evidence for it in Tahiti whereas conversely, Stanford *et al*. (2011) confirmed the existence of a global MWP-1b event (Section 4.4.2) which they described as a broad multi-millennial interval of enhanced rates of sea-level rise between 11.5 to 8.8 ka cal. B.P., with rates of ~130 to 150 cm/100 years at ~9.5 ka ca. B.P. Camoin *et al*. (2004) did not observe a well-defined MWP-1b event from their Western Indian Ocean records but found surges in the rate of sea-level rise especially between 11.9 and 11.3 ka cal. B.P. The Aliwal Shoal data show enhanced rates of sea-level rise between 11 and 9.8 ka cal. B.P. in line with the observations of Stanford *et al*. (2011).

However, the reason why the rate of sea-level rise for the critical time interval from records in the Western Indian Ocean localities (60 - 86 cm/100 years; Ramsay, 1995; Camoin *et al*., 2004; this study) is slower than the global values (130 - 150 cm/100 years; Stanford et al., 2011) is unknown and to the author's knowledge and has not been commented on in the literature thus far. Though, in general, most workers consider the last deglacial sea-level rise as non-uniform with marked variations in the rate of sea-level rise (Fairbanks, 1989, Fleming *et al*., 1998; Lambeck *et al*., 2002a; Clark *et al*., 2004; Bassett *et al*., 2005; Bard et al., 2010; Stanford et al., 2011). Furthermore, the Aliwal Shoal sea-level index points (Figure 9.8) also lie above the eustatic sea-level curves from Barbados (Faribanks, 1989) and Tahiti (Bard et al., 1996). This pattern was first observed by Camoin *et al*. (2004) from the sea-level records from the Western Indian Ocean. Thus, clearly the sea-level records obtained from the Western Indian Ocean differ from the generally accepted classical coral reef derived sea-level records of Barbados and Tahiti which suffer from tectonic effects.

The oyster samples all show poor correspondence to the sea-level data (Figure 9.8). Possible reasons for this may include diagenetic alteration, incorrect marine reservoir age corrections and/or sample contamination by younger carbonate. Additional explanations may be that these oyster specimens were misidentified or occupied a different ecological niche to that which is observed from the species today both of which would result in a different indicative meaning. Nonetheless, despite the poor age results the presence of these oysters as large beds attached to the seaward edge of the Aliwal Shoal suggests a marine affinity and indicates cooler water temperatures as the modern species appears to be more abundant in the Eastern Cape than in KwaZulu-Natal (Herbert, *Pers Comm*). This is not too unexpected as sea-surface temperatures (SST's) were 1° to 4° cooler in the study area during the LGM (Barrows and Juggins, 2005) and the addition of meltwater to the oceans might also have resulted in cooler SST's.

The palaeopothole-fill sample OS-5 (Figure 9.2d, e) obtained onland from the Aliwal Shoal confirms the secondary Holocene highstand observed by Ramsay (1995). It plots remarkably well on the reinterpreted Ramsay and Cooper (2002) curve (Figure 4.8).

9.5.5 Wider Implications

Precise age determination of the Aliwal Shoal aeolianite and beachrock deposits has provided a wealth of information on a range of topics, which are not only restricted to geochronology, but also pertinent to the evolution of coastal barrier systems, sequence stratigraphy, sea-level change and neotectonics on the continental margin. The wider implications of the aeolianite and beachrock ages will be briefly discussed below.

The only other detailed geochronological investigation of a similar system undertaken by Ramsay (1991; 1996) showed that the offshore reef systems on the Sodwana continental shelf comprise stacked aeolianite to foreshore sedimentary units defining a regressive sequence formed during the sea-level depression towards the LGM. The results from the Aliwal Shoal show that these systems do not necessarily form a sequentially develop regressive unit but can comprise several distinct punctuated or sequential units with greatly varying ages deposited during both regressive and transgressive sea-level regimes (Section 8.3.5; Figure 9.7).

In addition, the recent seismic sequence stratigraphic interpretations (Green, 2009a, b; Cawthra, 2010) from the KwaZulu-Natal continental margin identified similar offshore ridge systems as simple single sequences implied to have formed over one sea-level cycle. Geochronological constraints presented by this study demonstrate that a single ridge may comprise several units

formed over many high frequency sea-level cycles alternating between submergence and subaerially exposure. As such from a sequence stratigraphical point of view a single ridge might comprise more than one sequence separated by subaerially exposed sequence boundaries (refer to Section 6.4.3, Sequence 3).

The Aliwal Shoal beachrock units documented not only a changing coastal configuration (Sections 8.3.4 and 9.5.3) but also the rate of relative sea-level rise, agreeing with observations by Stanford *et al*. (2011) of enhanced rates of sea-level rise during the MWP-1b time interval. In addition, the Aliwal Shoal sea-level rise data further indicate that, on average, the Western Indian Ocean seemed to have experienced slower rates of sea-level rise during the critical time interval relative to the global values. The beachrock data further also confirmed observations by Camoin *et al*. (2004) for the critical time interval of sea-level records from the Western Indian Ocean that lie consistently above the generally accepted Barbados and Tahiti eustatic sea-level curves (Figure 9.8).

Many previous studies used whole rock radiocarbon ages from beachrocks and inferred these as reliable sea-level indicators, providing the skeletal carbonate content is entirely contemporary (Ramsay and Cooper, 2002; Woodroffe and Horton, 2005; Viera and de Ros, 2006). As shown by this study (section 9.5.2) this assumption may not be true as whole rock radiocarbon dating of beachrock is problematic, even if the carbonate is contemporary, there might still be problems with MRA corrections which may even be more severe than incorporated older carbon (Section 9.5.2).

Recently, Mather *et al*. (2009) indicated that the southern African plate is undergoing uplift resulting in differential movement along the South African coastlines resulting in an uplift rate of 1.03 mm/yr in the vicinity of the study area (east coast). Mather *et al*. (2009) ascribed the uplift to '*..rebound movement on account of historical glacial ice sheet loading.'*. Although Africa was never extensively covered by ice sheets during the LGM the effects of equatorial ocean syphoning, steric expansion and hydro-isostasy on the local relative sea-level change cannot be discarded, especially in the absence of a local isostatic response study. Nonetheless, if the figure of Mather *et al*. (2009) of 1.03 mm/yr of uplift is correct and *assumed constant throughout the Holocene transgression*, then the Aliwal Shoal beachrock data should be positioned at least 10 metres above global eustatic curves. This seems to be the case for the data from Barbados and Tahiti for which the Aliwal Shoal data points are ~10 m above (Figure 9.8), thereby apparently supporting the Mather *et al*. (2009) hypothesis. However, all of the sea-level data from the Western Indian Ocean lie above the Barbados and Tahiti data points (Figure 9.8) thereby negating the premise of uplift just because of a higher position on the sea-level curve. Furthermore, the Western Indian Ocean data comprise a range of tectonic settings including continental (South Africa), micro-continental

(Madagascar), granitic (Seychelles) and volcanic (Reunion, Mauritius and the Comoros) oceanic island data sources all of which unlikely to have been affected by similar uplift.

In addition, the Aliwal Shoal data agrees with the global eustatic curve of Waelbroeck *et al*. (2002) (Figure 9.8). The Waelbroeck *et al*. (2002) curve is derived from oxygen isotopes whereas the Barbados and Tahiti data are from coral reefs in tectonically active regions. Thus, until an explanation can be found for the variance of the Western Indian Ocean sea-level data to that of Barbados and Tahiti, the Aliwal Shoal sea-level data are assumed to reflect relative sea-level change and not tectonic uplift. As such the Aliwal Shoal sea-level data thus also question the possibility of uplift of the continental margin during the early Holocene.

9.6. CONCLUSIONS: EVOLUTION OF THE ALIWAL SHOAL CONTINENTAL SHELF

The geological history of the Aliwal Shoal shelf will be summarised in three broad stages, each characterised by different events.

9.6.1 Cretaceous to Early Pleistocene Shelf Evolution

- Following Gondwana breakup and generation of the proto-Indian Ocean, thick marine Cretaceous strata of Sequence 1 (Section, 6.4.3, Sequence 1, section 6.5) were deposited on the newly formed and subsiding continental shelf during the diachronous southerly directed Cretaceous transgression.
- A basin-wide marine flooding surface (MFS1) subdivided Sequence 1 into a lower Campanian (and possible Santonian) TST and an upper Maastrichtian combined regressive systems tract comprising HST/FRST deposits (Figures 6.12 and 6.13a) which prograded over a postulated Campanian palaeo-shelf break and as such signalled the onset of the major late Maastrichtian - Early Palaeocene forced regression which resulted in the initiation of SB1 and the arrival of the Tertiary.
- SB1 spans most of the Tertiary (Figure 6.13a) and represents multiple erosional events including the significant Tertiary uplift and a major forced regression which subaerially exposed the continental shelf for almost the entire Oligocene and lower Miocene (Figure 6.13a) eroding Palaeogene and Miocene units and subsequently shaping the pre-existing Cretaceous strata into a series of terraces (Figure 6.14) which would ultimately control the

deposition of Sequence 3 (see Section 9.6.2), which again controlled the development of Sequence 4 (see Section 9.6.3).

- The Tertiary uplift resulted in non-deposition in the proximal zones (study area) and increased deposition in distal areas, such as the lower continental slope and deep ocean basins.
- Shelf sedimentation only resumed during the Late Pliocene to early Pleistocene with deposition of the Sequence 2 shelf-edge wedge (Chapter 6.4.3; Figures 6.12 and 6.13a).
- Following Sequence 2 for most of the Early and Middle Pleistocene the shelf was in an erosive regime. High frequency and amplitude sea-level fluctuations (Figure 4.4) produced sea-level lowstands that commonly subaerially exposed the entire continental shelf and parts of the slope resulting in the complex erosional surface of SB2 (Figures 6.5 to 6.9 and 6.12).

9.6.2 Late Pleistocene Shelf Evolution

- Following the preceding erosive regime, shelf sedimentation recontinued in the Late Pleistocene through deposition and preservation of inner shelf to slope, semi-continuous Sequence 3 ridges representing carbonate cemented palaeo-coastal barrier systems.
- In the study area one such ridge, the Aliwal Shoal, comprises three distinct aeolianite units (A1 to A3) which represent different types of dune morphologies deposited during the climatic and associated sea-level fluctuations of MIS 5.
- Units A1 and A2 deposited during the MIS 6/5e (~134 to ~127 ka cal. B.P.) transgression (Figure 9.7) represent contemporaneous evolution of a coastal barrier system which consisted of two different dune forms associated with a back-barrier estuarine or lagoonal system. Unit A1 most likely originated as a longitudinal coastal dune (Figures 8.8 and 8.9), whilst Unit A2 comprised a compound parabolic dune system (Figures 8.11 and 8.12) which migrated into the back-barrier area across an estuary mouth/tidal inlet of the back-barrier system (Figure 8.12a).
- The coastal barrier-dune configuration established by Unit A1 and A2 was most likely re-established during similar subsequent MIS 5 sea-level stands (Figure 9.7), which during MIS 5c/b resulted in the formation of the back-barrier dune system of Unit A3 (Figures 8.13 and 9.7).
- For Units A1, A2 and A3 pervasive early meteoric LMC cementation followed shortly after deposition and allowed for the preservation of the dune cores during subsequent sea-level fluctuations. Sea-spray induced vadose cementation in Units A1 and A2 may have been a key factor in stabilising dune sediment allowing for later intense phreatic meteoric cementation.

- The final preserved Late Pleistocene depositional event in the study area was that of the storm deposit of beachrock Unit B5. Induration followed shortly after deposition and comprised initial marine vadose HMC cementation.
- Following deposition and lithification, Units A1, A2, A3 and B5 underwent a period of cement erosion associated with decementation and increased porosity due to either 1) groundwater table fluctuations related to the high frequency MIS 5 sea-level fluctuations (refer to as stage 2.1 on Figure 8.31b), and/or 2) carbonate solution due to complete subaerial exposure related to the overall MIS 4 - 2 sea-level depression towards the LGM lowstand (refer to as stage 2.2 on Figure 8.31b). In addition to the decementation and porosity development Unit B5 also experience inversion of the original unstable HMC cement to LMC.
- The forced MIS 4 to 2 sea-level regression towards the LGM lowstand represents an overall deterioration of global climate and associated sea-level instability and resulted in the formation of the subaerial unconformity surface SB3.
- During MIS 4 to 2 the Aliwal shelf comprised an interfluve area which was characterised by subaerial exposure, fluvial incision of coast-parallel tributary river systems and general sediment starvation.
- LST sediments of the LGM were most likely deposited on the continental slope below -120 m.

9.6.3 The Last Deglacial Sea-Level Rise and Holocene Sediment Wedge

Transgressive systems tract (TST) sediments

- Rapid deglacial sea-level rise followed the LGM (~18 - 20 ka B.P.) and resulted in the deposition of Sequence 4 (Figures 6.13b and 9.7), commonly referred to as the Holocene unconsolidated sediment wedge. TST deposits of Sequence 4 comprise a complex arrangement of strike and dip variable depositional systems.
- Outer and middle shelf environments show an early TST (~20 - 14 ka B.P.) back-stepping sequence comprising deposition of linear shoreline depositional systems followed by reworking and erosion by the transgressive shoreface which deposited a thin transgressive sand sheet on the outer shelf and possible transgressive ‘healing-phase’ deposits on the slope (Figure 6.13b; Table 64).
- On the middle and inner shelf the development of the TST depositional systems are not only diachronous along dip but show a marked change along strike.
- At ~12.3 ka cal. B.P. (Figure 6.13b; Table 6.4) embayed back-barrier lagoonal conditions were established in accommodation space provided between the Sequence C ridges of Aliwal Shoal

and the MSR (Figures 6.15 and 6.16). This lagoonal system evolved under continuous aggradational and retrogradational depositional regimes as the Holocene sea-level rise ensued. Aggradational lagoonal conditions were dominant from ~12.3 to 11.5 ka cal. B.P. during the reduced rates of sea-level rise related to the Younger Dryas cold event (Figure 9.7). Along strike to the north an open shoreline setting prevailed with small localised estuarine/lagoonal and beach-barrier palaeo-depositional environments preserved only in areas where palaeo-topography provide accommodation space.

- Continued aggradation and retrogradation of the lagoonal sequence during the last deglacial transgression was accompanied by the formation of a bay ravinement surface (BRS) at ~11 ka B.P.in the back-barrier area landward of the Aliwal Shoal ridge and as such signified a change from fluvial to estuarine conditions. As a result the Aliwal Shoal ridge is flanked on its seaward side by an embayed back-barrier lagoonal system and on its landward side by a back-barrier estuary. Both these systems are inferred to have had open shoreline connections to the north with the estuarine system also connected with the lagoonal system through a tidal inlet cut into the Aliwal Shoal ridge south of Unit A1 aeolianite (Figure 8.18).
- Northwards along strike, slightly preceding the change to estuarine conditions (~11. ka B.P.), the open shoreline depositional environments were being overstepped by the transgressive shoreface, the passage of which formed the transgressive ravinement surface which was subsequently buried by a thin transgressive sediment sheet. Coeval with creation of the BRS in the south, the shelf above the now buried open shoreline deposits were rapidly deepening, the shallow gradient (Figure 6.14) resulting in a rapid landward shift in facies due to the wide area being transgressed (see following section for transgression on low vs. high gradient), consequently forming surface DLS.
- In the south the retrogradational lagoonal and aggradational estuarine systems were progressively overstepped by the transgressive shoreface (Figure 6.16), the passage of which was documented above the lagoonal deposits as a sequence of beachrock deposits (Section 8.3.4; Figure 8.18).
- Beachrock Units B1 to B4 (Figure 8.18) were deposited in the intertidal to back-beach environments and subsequently rapidly cemented by marine phreatic carbonate cements comprising either aragonite or HMC. Unit B1 was most likely deposited at 10.8 ka cal. B.P., B2 at 10.2 ka cal. B.P, B3 at 9.8 ka cal. B.P and B4 <9.8 ka cal. B.P. (Table 9.7) thereby indicating sequential formation during the MWP-1b interval (Figure 9.7).
- Unit B3 marks the major change from the log-spiral bay coastal configuration established by Units B1 and B2 to a linear coastline orientation controlled by the trend of the pre-existing aeolianite units. This change in the morphology of the coastline is also documented by the shape of the underlying transgressive ravinement surface (reflector TRS, Figure 6.16) which

again was controlled by the subjacent sedimentary basin fill architecture and subsequent transgressive shoreline trajectory (Section 6.4.3, Sequence 4, Figures 6.15 to 6.16).

- Sea-level rose at an average rate of 67 cm/100 years from B1 to B2 and 86 cm/100 years from B2 to B2 (Table 9.7) indicating an acceleration in the rate of sea-level rise supporting enhanced rates of sea-level rise during the MWP-1b interval which also seemed to have altered the coastal configuration and resulted in the closure of the southern outlet of the back-barrier estuarine system (Figure 8.18). Two cycles of initial aragonite followed by later HMC cement are tentatively linked to two marine flooding events related to different pulses of enhanced rates of sea-level rise during MWP-1b which also may have been responsible for significant changes in the marine carbon reservoir ages (Section 9.5.2).
- Foreshore and shoreface deposition was active until <9.8 ka ca. B.P. across the lagoonal system and ~9.5 ka cal. B.P. across the estuarine system whereafter sea-level rapidly drowned this part of the shelf probably due to the rapid increase in back-barrier width and depth.
- Unconsolidated sediment Facies E is associated with the passage of the shoreface and thus linked with ravinement process although it is possible that this facies may not have to same origin across the study area.

Highstand systems tract (HST) sediments

- Approximately coeval (Table 6.4) with the final transgression of the lagoonal and estuarine systems in the south, the north experienced a deepening water column and subsequent generation of accommodation space. Locally, the supply of sediments delivered from the numerous fluvial systems and coastal erosion matched and even exceeded the relative sea-level rise resulting in an overall change from retrogradational to progradational stratal architecture and initialization (Stage 1; 9.5 to 8.4 ka cal. B.P.) of the HST of Sequence 4 (Figure 6.19).
- This localised HST comprises a prograding shore-attached subaqueous-delta clinoform sediment deposit, named here the *Mkomazi Subaqueous-Delta Clinoform* (MSDC). The seaward growth of MSDC is proposed to occur by overlapping alongshore and cross-shore sediment transport (Figure 6.17a).
- Initialization and progradation was interrupted by a retrogradational phase (Stage 2) of MSDC development (Figure 6.18a) ascribed to a rapid sea-level rise between 8.4 to 8.2 ka cal B.P. which resulted in backstepping of the system. A similar pattern of retrogradation is also observed for the same time interval in many large subaqueous delta systems worldwide.
- The stage 2 backstepping of the clinoform controlled the subsequent overlying topset morphologies resulting in later stages inheriting a stepped appearance upon which the shoreface-connected ridges are developed.

- Stages 3 (8.2 to 7.5 ka cal. B.P.) and 4 (7.5 to 0 ka cal. B.P) show a change from 'proximal' topset aggradation to 'distal' foreset progradational downlap, linked to a change in the dominant sedimentary transport mechanism from aggradational along-shore to progradational cross-shore transport related to variations in accommodation space and the rate of sediment supply.
- Morphologically the MSDC is characteristic of a sediment input onto a high energy storm-dominated continental shelf where oceanographic processes are responsible for its northward directed asymmetry in plan-view, for the lack of a well defined bottomset and for the re-organisation of its topset into shoreface-connected ridges (Figure 6.17).
- The Aliwal Shoal shoreface-connected ridges are 1 - 6 m in height, spaced 500 - >1350 m apart and vary from 3 km to >8 km in length (Table 7.3, Figure 7.9). They are attached on their shoreward portions to the shoreface between depths of -10 m to -15 m (average at -13 m) and can be traced to depths exceeding -50 m, although the majority occur on the inner shelf between -20 m to -30 m (Figure 7.8). Several individual crests can be identified (Table 7.3, Figure 7.9) forming a giant shoreface-connected sand ridge field with a sigmoidal pattern in plan-view (Figure 7.9) postulated to be a surficial expression of the subjacent retrogradational phase (Stage 2) and hence might possibly reflect the subsurface extent of the retrogradational phase (Figure 6.17).
- Formation of the Aliwal Shoal SCR's is proposed to have occurred in two stages.
- Stage 1 fundamentally consists of the deposition and concentration of significant amounts of sediment on the shoreface (step 1 - development of Stage 1 of the MSDC) with subsequent ridge initiation (step 2) following the MSDC Stage 2 retrogradational event (Figure 6.18) through marine reworking by shelf processes simultaneously with a deepening water column and evolving clinoform system showing proximal along-shore aggradation and distal across-shore progradation during the last post-glacial sea-level rise (from ca. 8.4 ka cal. B.P.).
- Stage 2 comprises the modern maintenance of the SCR system which is continually modified and maintained by shelf processes. Stage 2 consists of two physical states. State 1 considers SCR maintenance during fair-weather conditions and state 2 during storm conditions.
- During fair-weather transverse ridge migration is dominant driven by shelf circulation by the north-easterly flowing counter current.
- During storm conditions longitudinal ridge growth is suggested to occur as a result of storm return flows. Ridge migration (700 m measured) occurs by offshore ridge tip elongation and offshore movement of the seaward flank with storm erosion in the intervening swales explaining the observed narrowing of the ridge.
- Following the storm, the regional coast-parallel current system is restored and the fair-weather state then moulds the SCRs into a transverse bedform.

- It is postulated here that the Aliwal shelf SCRs have climbed and coalesced coevally since ca. 8.4 ka cal. B.P. to form the Mkomazi subaqueous-delta clinoform through both proximal along-shore and distal cross-shore sedimentation (Figure 6.17; also refer to Chapter 6.3.4 and 6.4.3; Figure 6.17).
- The Aliwal Shelf SCR field has a further implication for the sediment dynamics of the continental shelf insofar as it provides an alternative mechanism delivering sediment from the coastal zone and nearshore sediment wedge into the middle and outer shelf.
- Sediments from the MSDC (unconsolidated sediment Facies C) are continually being redistribution and reworked by a complex pattern of bottom currents generated by the interaction of opposing oceanographic and swell driven circulation patterns.
- Presently the shelf is still in a transgressive regime but deposition on the MSDC is still ongoing and comprises aggradation concurrent with progradation. The long term stability of the clinoform will be determined by the relative balance between the rate of sea-level change and sediment availability whilst oceanographic process such as swell and currents are considered secondary controls affecting the sediment transport pathways (Figure 6.17a) and hence morphological evolution of the MSDC.
- This study has shown for the first time that the Holocene sediment wedge comprises a complex feature consisting of both TST and local HST sedimentation, which are not only diachronous along dip but markedly variable along strike, including depositional systems ranging from embayed lagoonal and estuarine, open shoreline and submerged-delta clinoform depositional settings.

9.7 RECOMMENDATIONS

This study has for the first time integrated geophysical data and seafloor geological sampling and observation within a robust geochronological framework. As a result the sequence stratigraphic model is constrained by new geochronological data and the seafloor lithologies are placed in their correct chronostratigraphical division. As a result of the findings of this study some considerations for future research on similar submerged palaeo-coastal barrier system are suggested;

1. Mapping, sampling and dating of similar accessible submerged systems especially on the KwaZulu-Natal south coast. Based on the variation seen between the two previous investigations and this study it is unlikely that a unified model of aeolianite and beachrock formation can be developed. However, each additional study will bring new data that can be used to generate a set of ‘first principles’ applicable to these systems.

2. Detailed mapping and sampling (with coring) and dating programme across MSDC integrated with long term oceanographic data to test the inference made on the age of formation, sediment transport mechanisms and general functioning of the MSDC.
3. Application of the newly developed 'Clumped Isotope Geothermometry' to the carbonate cements in the beachrocks to accurately constrain the palaeo-SST along the east coast for the critical time interval.
4. Sediment transport modelling of the unconsolidated sediments with reference to the effect the Aliwal Shoal has on sediment transport patterns.
5. Application of a laser ablation U-Series method to date the individual cement phases in the aeolianites and to test the diagenesis model proposed here.

REFERENCES

Aagaard, T., Davidson-Arnott, R., Greenwood, B. and Nielsen, J. (2004). Sediment supply from shoreface to dunes: linking sediment transport measurements and long-term morphological evolution. *Geomorphology*, **60**, 205-224.

Adams, A.E., MacKenzie, W.S. and Guilford, C. (1984). *Atlas of sedimentary rocks under the microscope*. Longman, Essex, 104pp.

Adams, A.E. and MacKenzie, W.S. (1998). *A colour atlas of carbonate sediments and rocks under the microscope.* Manson Publishing, London, 180pp.

Abegg, F.E., Loope, D. and Harris, P.M. (2001). Carbonate eolianites: depositional models and diagenesis. *In*: Abegg, F.E., Loope, D. and Harris, P.M. (Eds.), *Modern and Ancient Carbonate Eolianites: Sedimentology, Sequence Stratigraphy and Diagenesis*. Soc. Econ. Pal. Min., Spec. Publ., **71**, 183-203.

Allen, J.R.L. (1980). Sandwaves: a model of origin and internal structure. *Marine Geology*, **26**, 281-328.

Allen, J.R.L. (1982). *Sedimentary structures: Their character and physical basis. Volume II*. Elsevier Scientific Publishing Company, Amsterdam, 655pp.

Allen, G.P., and Posamentier, H.W. (1993). Sequence stratigraphy and facies model of an incised valley fill: the Gironde estuary, France. *Journal of Sedimentary Petrology*, **63**, 378–391.

Alley, R.B. and Clark, P.U. (1999). The deglaciation of the Northern Hemisphere: a global perspective. *Annual Reviews of Earth and Planetary Science*, **27**, 149-182.

Amos, C.L. and King, E.L. (1984). Bedforms of the Canadian eastern seaboard: A comparison with global occurrences. *Marine Geology*, **57**, 167-208.

Anderson, W. (1906). On the geology of the Bluff Bore, Durban, Natal. *Transactions of the Geological Society of South Africa*, **9**, 111-116.

Anderson, F.P., Gründlingh, M.L. and Stavropoulos C.C. (1988). Kinematics of the Natal coastal circulation: some historic measurements 1962-1963. *South African Journal of Science*, **84**, 857-860.

Andres, M.S., Bernasconi, S.M., McKenzie, J.A. and Röhl, U. (2003). Southern Ocean deglacial record supports global Younger Dryas. *Earth and Planetary Science Letters*, **216**, 515-524.

Anthony, D. and Leth, J.O. (2002). Large-scale bedforms, sediment distribution and sand mobility in the eastern North Sea of the Danish west coast. *Marine Geology*, **182**, 247-263.

Antia, E. E. (1993). Surficial grain-size statistical parameters of a North Sea shoreface-connected ridge: patterns and process implication. *Geo-Marine Letters*, **13**, 172-181.

Antia, E. E. (1994). The ebb-tidal delta model of shoreface ridge origin and evolution: Appraisal and applicability along the southern North Sea barrier island coast - a discussion. *Geo-Marine Letters*, **14**, 59-64.

Antia, E. E. (1995). Sedimentary deposits related to inlet-shoreface storm flow in the German Bight. *Estuarine Coastal and Marine Science*, **40**, 699-712.

Antia, E. E. (1996). Rates and patterns of migration of shoreface-connected sandy ridges along the southern North Sea coast. *Journal of Coastal Research*, **12**, 38-46.

Antia, E. E., Flemming, B.W. and Wefer, G. (1995). Calm-weather spring and neap tidal current characteristics on a shoreface-connected ridge complex in the German Bight (southern North Sea). *Geo-Marine Letters* **15**, 30-36.

Armitage, S. J., Botha, G. A., Duller, G. A. T., Wintle, A. G., Rebêlo, L. P. and Momade, F. J. (2006). The formation and evolution of the barrier islands of Inchaca and Bazaruto, Mozambique. *Geomorphology*, **82**, 295-308.

Ashley, G.M. (1990). Classification of large-scale subaqueous bedforms: a new look at an old problem. *Journal of Sedimentary Petrology*, **60**, 160-172.

Bard, E., Hamelin, B., Arnold, M., Montaggioni, L., Cabioch, G., Faure, G. and Rougerie, F. (1996). Deglacial sea-level record from Tahiti corals and the timing of global meltwater discharge. Nature, 382, 241-244.

Bard, E., Hamelin, B. and Delanghe-Sabatier, D. (2010). Deglacial Meltwater Pulse 1B and Younger Dryas Sea Levels Revisitedwith Boreholes at Tahiti. *Science*, **327**, 1235-1237.

Barrows, T.T. and Juggins, S. (2005). Sea-surface temperatures around the Australian margin and Indian Ocean during the Last Glacial Maximum. *Quaternary Science Reviews*, **24**, 1017-1047.

Barwis, E.J. and Tankard, A.J. (1983). Pleistocene shoreline deposition and sea-level history at Swartklip, South Africa. *Journal of Sedimentary Petrology*, **53**, 1281-1294.

Bassett, S.E., Milne, G.A., Mitrovica, J.X. and Clark, P.U. (2005). Ice Sheet and Solid Earth Influences on Far-Field Sea-Level Histories. *Science*, **309**, 925-928.

Bateman, M.D., Holmes, P.J., Carr, A.S., Horton, B.P. and Jaiswal, M.K. (2004). Aeolianite and barrier dune construction spanning the last two glacial-interglacial cycles from the southern Cape coast, South Africa. *Quaternary Science Reviews*, **23**, 1681-1698.

Bateman, M.D., Carr, A.S., Dunajko, A.C., Holmes, P.J., Roberts, D.L., McLaren, S.J., Bryant, R.G., Marker, M.E. and Murray-Wallace, C.V. (2011). The evolution of coastal barrier systems: a case study of the Middle-Late Pleistocene Wilderness barriers, South Africa. *Quaternary Science Reviews*, **30**, 63-81.

Bates, R. L. & Jackson, J. A. (1984). *Dictionary of Geological Terms*. Doubleday, New York, 571pp.

Bathurst, R. G. C. (1966). Boring algae, micrite envelopes and lithification of molluscan biosparites. *Geological Journal*, **5**, 15-32.

Bathurst, R. G. C. (1975). *Carbonate sediments and their diagenesis*. Elsevier, Amsterdam, 620pp.

Bé, A.W.H. and Duplessy, J-. C. (1976). Subtropical convergence fluctuations and Quaternary climates in the middle latitudes of the Indian Ocean. *Science*, **194**, 419-422.

Begg, G.W. (1978). The estuaries of Natal. *Natal Town and Regional Planning Report*, **41**, 657pp.

Belderson, R.H. (1961). *The size distribution characteristics of the Recent shallow marine sediments off Durban, South Africa*. MSc. thesis (unpubl.), University of Natal, Durban, 102pp.

Belderson, R.H., Kenyon, N.H., Stride, A.H. and Stubbs, A.R. (1972). *Sonographs of the Sea Floor*. Elsevier Publishing Company, Amsterdam. 185pp.

Belderson, R.H., Johnson, M.A. and Kenyon, N.H. (1982). Bedforms : *In* Stride, A.H. (Ed.), *Offshore tidal sand;, processes and deposits.* Chapman and Hall, London, 222pp

Bender, M.I., Fairbanks, R.G., Taylor, F.W., Mathews, R.K., Goddard, J.G. and Broecker, W.S. (1979). Uranium series dating of the Pleistocene reef tracts of Barbados, West Indies. *Geological Society of America Bulletin*, **90**, 577pp.

Berger, A.L. (1978). Long-term variations of caloric insolation resulting from the Earth's orbital elements. *Quaternary Research*, **9**, 139-167.

Berger, A.L. (1979). Insolation signatures of Quaternary climate changes. *Il Nuovo Cimento*, **2C**, **1**, 63-87.

Bezerra, F.H.R., Amaral, R.F., Lima-Filho, F.P., Ferreira, A.V., Sena, E.S. Jr. and Diniz, R.F. (2005). Beachrock fracturing in Brazil. *Journal of Coastal Research*, **42**, 319-332.

Birch, G.F. (1981). The bathymetry and geomorphology of the continental shelf and upper slope between Durban and Port St. Johns. *Annals of the Geological Survey of South Africa*, **15**, 55-62.

Birch, G.F. (1996). Quaternary Sedimentation off the East Coast of Southern Africa (Cape Padrone to Cape Vidal). *Bulletin of the Geological Survey of South Africa*, Council for Geoscience, **118**, 55pp.

Bird, M.I., Austin, W.E.N., Wurster, C.M., Fifield, L.K., Mojtahid, M. and Sargeant, C. (2010). Punctuated eustatic sea-level rise in the early mid-Holocene. *Geology*, **38**, 803-806.

Blondel, P. and Murton, B.J. (1997). *Handbook of seafloor sonar imagery*. John Wiley & Sons Ltd., New York. 314pp.

Bloom, A.L., Broecker, W.S., Chappell, J., Mathews, R.K. and Mesolella, K.J. (1974). Quaternary sea level fluctuations on a tectonic coast: new $^{230}Th/^{234}U$ dates from the Huon Peninsula, New Guinea. *Quaternary Research*, **4**, 185-205.

Boczar-Karakiewicz, B. and Bona, J.L. (1986). Wave-dominated shelves: a model of sand-ridge formation by progressive, infra-gravity waves. *In:* Knight, R.J. and McLean, J.R. (Eds.), *Shelf Sands and Sandstones*. Canadian Society of Petroleum Geologists Memoir, **2**, 163-179.

Boczar-Karakiewicz, B., Drapeau, G. and Bona, J.L. (1987). Sand ridges on Sable Island Bank, Scotian Shelf. *In*: Kraus, N.C. (Ed.), *Coastal Sediments '87, Proceedings of a Specialty Conference on Advances in Understanding of Coastal Sediment Processes*, vol. **2**. American Society of Civil Engineers, New York, 2157-2169.

Boczar-Karakiewicz, B., Amos, C.L. and Drapeau, G. (1990). The origin and stability of sand ridges on Sable Island, Scotian Shelf. *Continental Shelf Research*, **10**, 683-704.

Bond, G., Showers,W., Cheseby, M., Lotti, R., Almasi, P., deMenocal, P., Priore, P., Cullen, H., Hajdas, I. and Bonani, G. (1997). A pervasive millennial-scale cycle in North Atlantic Holocene and glacial climates. *Science*, **278**, 1257-1266.

Bosman, C. (2003a). Aliwal Shoal geophysical survey, Umkomaas, South Africa: Project update & preliminary geophysical data interpretation report (2002-2003) - Bathymetry and side-scan sonar. *Council for Geoscience Report*, **2003-0133**, 28pp.

Bosman, C. (2003b). Cruise Report for the Aliwal Shoal Geophysical Survey, Umkomaas, South Africa. Phase 2: Seismic Surveys. *Council for Geoscience Report*, **2003-0046**, 32pp.

Bosman, C. (2006). Seismic stratigraphy of the continental shelf in the vicinity of the Aliwal Shoal, South Africa. *Council for Geoscience Report*, **2006-0157**, 73pp.

Bosman C. and Leuci R. (2001). Cruise report for the Aliwal Shoal geophysical survey, Umkomaas, South Africa. Phase 1: side-scan sonar and bathymetry. *Council for Geoscience Report*, **2001-0072**, 15pp.

Bosman, C, and Uken, R. (2005). Sea-level fluctuations and submerged coastal dune systems: The geology and evolution of the Aliwal Shoal. *Extended Abstracts*, GSSA, Geo2005, Durban.

Bosman, C., Uken, R. and Smith, A.M. (2005). The bathymetry of the Aliwal Shoal, Scottburgh, South Africa. S*outh African Journal of Science*, **101**, 255-257.

Bosman, C., Uken, R. and Ovechkina, M. (2007). The Aliwal Shoal revisited: New age constraints from nannofossil assemblages. *South African Journal of Geology*, **110**, 647-653.

Bosman, C., Uken, R., Leuci, R., Smith, A.M. and Sinclair, D. (2007). Shelf sediments off the Thukela River mouth: complex interaction between fluvial and oceanographic processes. S*outh African Journal of Science*, **103**, 490-492.

Bosman, C., Uken, R. and Smith, A.M. (2008). Shoreface-connected ridges from the Aliwal Shelf, KwaZulu-Natal. *Extended Abstracts*, 13th South African Marine Science Symposium, Cape Town, South Africa, 1pp.

Botha, G.A. (1997). The Maputaland Group: a provisional lithostratigraphy for coastal KwaZulu-Natal. *In:* Botha, G.A. (Ed.), *Maputaland focus on the Quaternary evolution of the south-east African coastal plain*. International Union for Quaternary Research Workshop Abstracts, Council for Geoscience, South Africa, 21-26.

Bradley, R.S. (1999). *Paleoclimatology: Reconstructing the climates of the Quaternary*, 2nd Ed. Academic Press, San Diego, 612pp.

Braithwaite, C.J.R. and Camoin, G.F. (2011). Daigenesis and sea-level change: lessons from Morura, French Polynesia. *Sedimentology*, **58**, 259-284.

Brash, J. (2007). *Zonation of the benthic communities on Aliwal Shoal, KwaZulu-Natal, South Africa*. MSc thesis (Unpubl.), University of KwaZulu-Natal, Durban, 96pp.

Bricker, O.P. (1971a). Introduction: beachrock and intertidal cement. *In*: Bricker, O.P. (Ed.), *Carbonate Cements*. Johns Hopkins Press, Baltimore, 1-13.

Bricker, O.P. (1971b). Introduction: submarine cementation. *In*: Bricker, O.P. (Ed.), *Carbonate Cements*. Johns Hopkins Press, Baltimore, 47-49.

Broecker, W.S., Denton, G.H., Edwards, R.L., Cheng, H., Alley, R.B. and Putnam, A.E. (2010). Putting the Younger Dryas cold event into context. *Quaternary Science Reviews*, **29**, 1078-1081.

Brooke, B.P (2001). The distribution of carbonate eolianite. *Earth-Science Reviews*, **55**, 135-164.

Brooke, B.P., Woodroffe C.D., Murray-Wallace, C.V., Heijnis, H. and Jones B.G. (2003). Quaternary calcarenite stratigraphy on Lord Howe Island, southwestern Pacific Ocean and the record of coastal carbonate deposition. *Quaternary Science Reviews*, **22**, 859-880.

Brown, R.W., Summerfield, M.A. and Gleadow, A.J.W. (2002). Denudational history along a transect across the Drakensberg Escarpment of southern Africa derived from apatite fission track thermochronology. *Journal of Geophysical Research*, **107**, 1-18.

Browne, I. (1994). Seismic stratigraphy and relict coastal sediments off the East coast of Australia. *Marine Geology*, **121**, 81-107.

Butzin, M., Prange, M. and Lohmann, G. (2005). Radiocarbon simulations for the glacial ocean: the effects of wind stress, Southern Ocean sea ice and Heinrich events. *Earth and Planetary Science Letters*, **235**, 45-61.

Caldas, L.H.D.O., Stattegger, K., Vital, H. (2006). Holocene sea-level history: evidence from coastal sediments of the northern Rio Grande do Norte coast, NE Brazil. *Marine Geology*, **228**, 39-53.

Camoin, G.F., Montaggioni, L.F. and Braithwaite, C.J.R. (2004). Late glacial to post glacial sea levels in the Western Indian Ocean. *Marine Geology*, **206**, 119-146.

Carr, A.S., Bateman, M.D., Roberts, D.L., Murray-Wallace, C.V., Jacobs, Z. and Holmes, P.J. (2010). The last interglacial sea-level high-stand on the southern Cape Coastline of South Africa: Optically Stimulated Luminescence and Amino Acid Racemization chronologies. *Quaternary Research*, **73**, 351-363.

Carter, A.N. (1966). Age of the Aliwal Shoal, South Africa. *Nature*, **211**, 507-508.

Cattaneo, A. and Steel, R.J. (2003). Transgressive deposits: a review of their variability. *Earth Science Reviews*, **62**, 187-228.

Cattaneo, A., Correggiari, A., Langone, L. and Trincardi, F. (2003). The late-Holocene Gargano subaqueous delta, Adriatic shelf: Sediment pathways and supply fluctuations. *Marine Geology*, **193**, 61-91.

Cattaneo, A., Trincardi, F., Asioli, A. and Correggiaria, A. (2007). The Western Adriatic shelf clinoform: energy-limited bottomset. *Continental Shelf Research*, **27**, 506-525.

Catto, N., MacQuarrie, K. and Hermann, M. (2002). Geomorphic response to Late Holocene climate variation and anthropogenic pressure, northeastern Prince Edward Island, Canada. *Quaternary International*, **87**, 101-117.

Catuneanu, O (2006). *Principles of sequence stratigraphy*. Elsevier, Amsterdam, 375pp.

Catuneanu, O., Abreu, V., Bhattacharya, J. P., Blum, M. D., Dalrymple, R. W., Eriksson, P. G., Fielding, C. R., Fisher, W. L., Galloway, W. E., Gibling, M. R., Giles, K. A., Holbrook, J. M., Jordan, R., Kendall, C. G. St. C., Macurda, B., Martinsen, O. J., Miall, A. D., Neal, J. E., Nummedal, D., Pomar, L., Posamentier, H. W., Pratt, B. R., Sarg, J. F., Shanley, K. W., Steel, R. J., Strasser, A., Tucker, M. E. and Winker, C. (2009). Towards the standardization of sequence stratigraphy. *Earth Science Reviews*, **92**, 1-33.

Cawthra, H.C. (2006). *A marine geophysical study of Blood Reef, Bluff, Durban*. Hons. thesis (unpubl.), University of KwaZulu-Natal, Durban, 79pp.

Cawthra, H.C. (2010). *The Cretaeceous to Cenozoic evolution of the Durban Bluff and adjacent continental shelf*. MSc thesis (unpubl.), University of KwaZulu-Natal, Durban, 241pp.

Chappell, J. (1974). Geology of coral terraces, Huon Peninsula, New Guinea: a study of Quaternary tectonic movements and sea level changes. *Geological Society of America Bulletin*, **85**, 553-570.

Chappell, J. (2002). Sea level changes forced ice breakouts in the Last Glacial cycle: new results from coral terraces. *Quaternary Science Reviews*, **21**, 1229-1240.

Chappell, J. and Shackleton, N.J. (1986). Oxygen isotopes and sea-level. *Nature*, **324**, 137-140.

Chappell, J., Omura, A., Esat, T., McCulloch, M., Pandolfi, J., Ota, Y. and Pillans, B. (1996). Reconciliation of late Quaternary sea levels derived from coral terraces at Huon Peninsula with deep sea oxygen isotope records. *Earth and Planetary Science Letters*, **141**, 227-236.

Choquette, P.W. and Pray, L.C. (1970). Geological nomenclature and classification of porosity in sedimentary carbonates. *American Association of Petroleum Geologists Bulletin*, **54**, 207-250.

Clark, P.U and Mix, A.C. (2002). Ice sheets and sea level of the Last Glacial Maximum. *Quaternary Science Reviews*, **21**, 1-7.

Clark, J.A., Farrell, W.E. and Peltier, W.R. (1978). Global changes in postglacial sea level: a numerical calculation. *Quaternary Research*, **9**, 265-287.

Clark, P.U., McCabe, A.M., Mix, A.C. and Weaver, A.J. (2004). Rapid rise of sea level 19,000 years ago and its global implications. *Science*, **304**, 1141-1144.

Cliff, G. (1999). Amazing grace: the raggedtooth shark. *Palmutnut Post: The magazine of the Durban Natural Science Museum*, **2(2)**, 4-5.

Coe, A.L. (2003). Division of the stratigraphical record and geological time. *In* Coe, A.L. (Ed.), *The sedimentary record of sea-level change*. Cambridge University Press, Cambridge, 18-33.

Coe, A.L. and Church, K.D. (2003a). Sea-level change. *In* Coe, A.L. (Ed.), *The sedimentary record of sea-level change*. Cambridge University Press, Cambridge, 34-56.

Coe, A.L. and Church, K.D. (2003b). Sequence stratigraphy. *In* Coe, A.L. (Ed.), *The sedimentary record of sea-level change*. Cambridge University Press, Cambridge, 57-98.

Collison, J. D. and Thompson, D. B. (1982). *Sedimentary Structures*. George Allen and Unwin, London, 194pp.

Compton, J.S. (2001). Holocene sea-level fluctuations inferred from the evolution of depositional environments of the southern Langebaan Lagoon salt marsh, South Africa. *The Holocene*, **11**, 395-405.

Compton, J.S. (2006). The mid-Holocene sea-level highstand at Bogenfels Pan on the southwest coast of Namibia. *Quaternary Research*, **66**, 303-310.

Compton, J.S. (2011). Pleistocene sea-level fluctuations and human evolution on the southern coastal plain of South Africa. *Quaternary Science Reviews*, **30**, 506-527.

Cooper, J.A.G. (1991a). Shoreline changes on the Natal coast: Mkomazi River mouth to Tugela River mouth. *Natal Town and Regional Planning Report*, **77**, 57pp.

Cooper, J.A.G. (1991b). *Sedimentary models and geomorphological classification of river mouths on a subtropical, wave-dominated coast, Natal, South Africa.* PhD thesis (unpubl.), University of Natal, Durban, 401pp.

Cooper, J.A.G. (1991c). Beachrock formation in low latitudes: implications for coastal evolutionary models. *Marine Geology*, **98**, 145-154.

Cooper, J.A.G. (1994a). Lagoons and microtidal coasts. In. Carter, R.W.G. and Woodroffe, C.D. (Eds). *Coastal Evolution*. Cambridge University Press, Cambridge, 219-265.

Cooper, J.A.G. (1994b). Sedimentation in a river-dominated estuary. *Sedimentology*, **40**, 979-1017.

Cooper, J.A.G. (2001). Geomorphological variability among microtidal estuaries from the wave-dominated South African coast. *Geomorphology*, **40**, 99-122.

Cooper, J.A.G. and Flores, R.M. (1991). Shoreline deposits and diagenesis resulting from two Late Pleistocene highstands near +5 and +6 metres, Durban, South Africa. *Marine Geology*, **97**, 325-343.

Cooper, M.R. and Liu, K. (2006). The Cainozoic palaeontology and stratigraphy of KwaZulu-Natal. Part 4. The post-Karoo geology of the Durban area, with special reference to the Isipingo Formation. *Durban Museum Novitiates*, **31**, 1-23.

Coudray, J. and Montaggioni, L. (1986). The diagenetic products of marine carbonates as sea-level indicators. *In*: Van de Plassche, O. (Ed.), *Sea-level Research: A Manual for the Collection and Evaluation of Data*. Geo Books, Amsterdam, 311-360.

Cox, K.G. (1992). The Karoo igneous activity and the early stages of the breakup of Gondwanaland. *Geol. Soc. London Spec. Publ*., **68**, 137-148.

Coyne, M.K., Jones, B. and Ford, D. (2007). Highstands during Marine Isotope Stage 5: evidence from the Ironshore Formation of Grand Cayman, British West Indies. *Quaternary Science Reviews*, **26**, 536-559.

Croll, J. (1867a). On the eccentricity of the Earth's orbit, and its physical relations to the glacial epoch. *Philosophical Magazine*, **33**, 119-131.

Croll, J. (1867b). On the change in the obliquity of the ecliptic, its influence on the climate of the polar regions and on the level of the sea. *Philosophical Magazine*, **33**, 426-445.

Csoma, A.E. and Goldstein, R.H. (2004). Porosity reduction in meteoric-marine mixing zones: Case studies illustrate some of the controls on calcite and aragonite precipitation in mixing zones. *Extended Abstracts, AAPG Annual meeting 2004; Embrace the future, celebrate the past, Dallas*, 1pp.

Cutler, K.B., Edwards, R.L., Taylor, F.W., Cheng, H., Adkins, J., Gallup, C.D., Cutler, P.M., Burr, G.S. and Bloom, A.L. (2003). Rapid sea-level fall and deep-ocean temperature change since the last interglacial period. *Earth and Planetary Science Letters*, **206**, 253-271.

Dalgleish, A.N., Boulton, G.S. and Renshaw, E. (2000). The ice age cycle and the deglaciations: an application of non-linear regression modelling, *Quaternary Science Reviews*, **19**, 687-697.

Dalrymple, R.W. and Hoogendoorn, E.L. (1997). Erosion and deposition on migrating shoreface-attached ridges, Sable Island, eastern Canada. *Geoscience Canada*, **24**, 25-36.

Darwin, C.R. (1851). *Geological observations on Coral Reefs, Volcanic Islands and on South America, being the Geology of the Voyage of the Beagle, under the Command of Captain Fitzroy during the years 1832 to 1836.* Smith, Elder and Company, London.

Davies, J.L. (1964). A morphogenic approach to world shorelines. *Zeitschrift für Geomorphologie*, **8**, 27-42.

Dawson, A.G. (1992). *Ice Age Earth: Late Quaternary geology and climate*. Routledge, London, 293pp.

De Decker, R.H. (1986). *The geological setting of diamondiferous deposits on the inner-shelf sediments between the Orange River and Wreck Point, Namaqualand*. MSc. thesis (unpubl.), University of Cape Town, 258pp.

De Swardt, A.J.J. and Bennet, G. (1974). Structural and physiographic development of Natal since the Late Jurassic. *Transactions of the Geological Society of South Africa*, **77**, 309-322.

Dingle, R.V. (1976). A review of the sedimentary history of some post-Permian continental margins of Atlantic type. *Annals of the Brazilian Acadamy of Science*, **48** (supplement), 67-80.

Dingle, R.V. and Scrutton, R.A. (1974). Continental break-up and the development of post-Palaeozoic sedimentary basins around southern Africa. *Geological Society of America Bulletin*, **85**, 1467-1474.

Dingle, R.V., Goodlad, S.W. and Martin, A.K. (1978). Bathymetry and stratigraphy of the northern Natal Valley (SW Indian Ocean): a preliminary account. *Marine Geology*, **28**, 89-106.

Dingle, R.V., Siesser, W.G. and Newton, A.R. (1983). *Mesozoic and Tertiary geology of southern Africa*. Balkema, Rotterdam, 375pp.

Driscoll, N.W. and Karner, G.D. (1999). Three-dimensional quantitative modelling of clinoform development. *Marine Geology*, **154**, 383-398.

Duane, D.B., Field, M.E., Meisburger, E.P., Swift, D.J.P. and Williams, S.J. (1972). Linear shoals on the Atlantic inner continental shelf, Florida to Long Island. *In*: Swift, D.J.P., Duane, D.B. and Pilkey, O.H. (Eds.), *Shelf Sediment Transport: Process and Pattern*. Stroudsburg, Pennsylvania, Dowden, Hutchinson and Ross, 447–498.

Dunham, R.J. (1971). Meniscus cements. *In*: Bricker, O.P. (Ed.), *Carbonate Cements*. Johns Hopkins Press, Baltimore, 297-300.

du Toit, S.R. and Leith, M.J. (1974). The J(c)-1 borehole on the continental shelf near Stanger, Natal. *Transactions of the Geological Society of South Africa*, **77**, 247-252.

Dunkley, E., Schoonees, J.S. and Theron, A.K. (1998). Thukela Water Project: effects of a reduction in the Thukela sediment yield on the adjacent coastline. *CSIR Report (draft)*, **ENV/S-C 98029**.

Dyer, K.R. and Huntley, D.A. (1999). The origin, classification and modelling of sand banks and ridges. *Continental Shelf Research*, **19**, 1285-1330.

Elliot, T. (1986). Siliciclastic shorelines. *In:* Reading H.G. (Ed.), *Sedimentary environments and facies*. Blackwell Scientific Publications, 155-188.

Emery, D. and Myers, K.J. (1996). *Sequence Stratigraphy*. Blackwell Science, 297pp.

Emiliani, C. (1955). Pleistocene temperatures. *Journal of Geology*, **63**, 538-575.

Emiliani, C. (1966). Isotope palaeotemperatures. *Science*, **154**, 851-857.

Encarnación, J., Flemming, T.H., Elliot, D.H. and Eales, H.V. (1996). Synchronous emplacement of Ferrar and Karoo dolerites and the early breakup of Gondwana. *Geology*, **24(6)**, 535-538.

ESRI (2002). *Introduction to ArcGIS Version 8.3 user manual*. Environmental Systems Research Institute, Redlands, California, 138pp.

Fairbanks, R.G. (1989). A 17 000-year glacio-eustatic sea level record: influence of glacial melting rates on the Younger Dryas event and deep-ocean circulation. *Nature*, **342**, 637-642.

Fairbanks, R.G., Mortlock, R.A., Chiu, T-C., Cao, L., Kaplan, A., Guilderson, T.P., Fairbanks, T.W., Bloom A.L., Grootes, P.M. and Nadeau, M-J. (2005). Radiocarbon calibration curve spanning 0 to 50,000 years BP based on paired 230Th/ 234U/238U and 14C dates on pristine corals. *Quaternary Science Reviews*, **24**, 1781-1796.

Fairbridge, R.W. (1950). The geology and geomorphology of Point Peron, western Australia. *Journal of the Royal Society of Western Australia*, **34**, 35-72.

Fairbridge, R.W. and Johnson, D.L. (1978). Eolianite. *In*: Fairbridge, R.W. and Bourgeois, J. (Eds), *The Encyclopaedia of Sedimentology*. Dowden, Hutchinson and Ross, Stroudsburg, 279-282.

Figueiredo, A.G., Swift, D.J.P., Stubblefield, W.L. and Clarke, T.L. (1981). Sand ridges on the inner Atlantic shelf of North America: morphometric comparisons with Huthnance stability model. *Geo-Marine Letters*, **1**, 187-191.

Fleming, K., Johnston, P., Zwarts, D., Yokoyama, Y., Lambeck, K. and Chappell, J. (1998). Refining the eustatic sea-level curve since the Last Glacial Maximum using far- and intermediate-field sites. *Earth and Planetary Science Letters*, **163**, 327-342.

Flemming, B.W. (1976). Side Scan Sonar - A Practical Guide. *The International Hydrographic Review*, **26**, 65-92.

Flemming, B.W. (1978). Underwater sand dunes along the southeast African continental margin - observations and implications. *Marine Geology*, **26**, 177-198.

Flemming, B.W. (1980). Sand transport and bedform patterns on the continental shelf between Durban and Port Elizabeth (south-east African continental margin). *Sedimentary Geology*, **26**, 179-205.

Flemming, B.W. (1981). Factors controlling shelf sediment dispersal along the southeast African continental margin. *Marine Geology*, **42**, 259-277.

Flemming, B.W. (1982). A historical introduction to underwater acoustics with special reference to echo sounding, sub-bottom profiling and side scan sonar. *In*: Russel-Cargill, W.G.A, (Ed.), *Recent Developments in Side Scan Sonar*, 3-10.

Flemming, B.W. and Hay, E.R. (1988). Sediment distribution and dynamics on the Natal continental shelf. *In*: Schumann, E.H., (Ed.), *Coastal Ocean Studies off Natal, South Africa*. Lecture Notes on Coastal and Estuarine Studies, **26**, 47-80.

Flemming, B.W., Martin, A.K. and Rogers, J. (1983). Onshore and offshore coastal aeolianites between Mossel Bay and Knysna. *University of Cape Town Marine Geoscience Unit Technical Report*, **14**, 151-160.

Fish, J.P. and Carr, H.A. (1990). *Sound underwater images*. Lower Cape Publishing, Orleans, 189pp.

Fisher, E.C., Bar-Matthews, M., Jerardino, A. and Marean, C.W. (2010). Middle and late Pleistocene paleoscape modeling along the southern coast of South Africa. *Quaternary Science Reviews*, **29**, 1382-1398.

Flugel, E. (2004). *Microfacies of Carbonate Rocks: Analysis, Interpretation and Applcation*. Springer-Verlag, Berlin, Heidelberg, New York, 976pp.

Folk, R. L. and Ward, W. (1957). Brazos River bar: a study in the significance of grain-size parameters. *Journal of Sedimentary Petrology*, **27**, 3-26.

Folk, R.L. (1974). The natural history of crystalline calcium carbonate: effect of magnesium content and salinity. *Journal of Sedimentary Petrology*, **44**, 40-53.

Frankel, J.J. (1965). On the Pleistocene rocks at Burman Bush, Berea Ridge, Durban. *South Africa Journal of Science*, **61**, 183-185.

Frébourg, G., Hasler, C.A., Le Guern, P. and Davaud, E. (2008). Facies characteristics and diversity in carbonate eolianites. *Facies*, **54**, 175-191.

Friedman, G.M. (1964). Early diagenesis and lithification of carbonate sediments. *Journal of Sedimentary Petrology*, **34**, 777-813.

Friedman, G.M. and Sanders, J.E. (1978). *Principles in sedimentology*. New York, John Wiley amd Sons, 792pp.

Foyle, A. M. and Oertel, G. F. (1997). Transgressive systems tract development and incised-valley fills within a Quaternary estuary-shelf system: Virginia inner shelf, USA. *Marine Geology*,**137**, 227-249.

Fugro OmniSTAR (2000). *The OmniSTAR Satellite DGPS Service – Client Brochure*. Fugro-OmniSTAR, Cape Town, South Africa, 2pp.

Galbraith, R.F., Roberts, R.G., Laslett, G.M., Yoshida, H. and Olley, J.M. (1999). Optical dating of single and multiple grains of quartz from Jinmium rock shelter, northern Australia: Part I, Experimental design and statistical models. *Archaeometry*, **41**, 339-364.

Gardner, R.A.M and McLaren, S.J. (1994). Variability in early vadose carbonate diagenesis in sandstones. *Earth Science Reviews*, **36**, 27-45.

Gilchrist, A.R., Kooi, H. and Beaumont, C. (1994). Post-Gondwana geomorphic evolution of southwestern Africa: Implications for the controls on landscape development from observations and numerical experiments. *Journal of Geophysical Research*, **99**(B6), 12 211-12 228.

Gill, A.E.A. and Schumann, E.H. (1979). Topographically induced changes in the structure of the inertial coastal jet: application to the Agulhas current. *Journal of Physical Oceanography*, **9**, 975-991.

Gischler, E. and Lomando A.J. (1997). Holocene cemented deposits in Belize. *Sedimentary Geology*, **110**, 277-297.

Goff, J., McFaden, B.G. and Chagué-Goff, C. (2004). Sedimentary differences between the 2002 Easter storm and the 15th-century Okoropunga tsunami, southeastern North Island, New Zealand. *Marine Geology*, **204**, 235-250.

Goff, J.A., Swift, D.J.P., Duncan, C.S., Mayer, L.A. and Hughes-Clarke, J. (1999). High resolution swath sonar investigation of sand ridge, dune and ribbon morphology in the offshore environment of the New Jersey margin. *Marine Geology*, **161**, 309- 339.

Goff, J.A., Olson, H.C., Duncan, C.S., 2000. Correlation of sidescan backscatter intensity with grain-size distribution of shelf sediments, New Jersey margin. *GeoMarine. Letters*, **20**, 43-49.

Goff, J.A., Austin Jr., J. A., Gulick, S., Nordfjord, S., Christensen, B., Sommerfield, C., Olson, H. and Alexander, C. (2005). Recent and modern marine erosion on the New Jersey outer shelf. *Marine Geology*, **216**, 275-296.

Gomez, E. A. and Perillo, G. M. E. (1992). Largo Bank: A shoreface-connected linear shoal at the Bahía Blanca Estuary entrance, Argentina. *Marine Geology*, **104**, 225-292.

Goodlad, S.W. (1978). The bathymetry of the Natal Valley off the Natal and Zululand coast (southern Africa). *Joint Geological Survey/University of Cape Town Marine Geology Program Technical Report*, **10**, Geology Department, University of Cape Town, 196-204.

Goodlad, S.W. (1986). Tectonic and sedimentary history of the mid-Natal Valley (South West Indian Ocean). *Bulletin Joint Geological Survey/University of Cape Town Marine Geoscience Unit*, **15**, 415pp.

Green, A.N. (2009a). *The marine geology of the northern KwaZulu-Natal continental shelf, South Africa, SW Indian Ocean.* PhD Thesis (Unpubl.), University of KwaZulu-Natal, 216pp.

Green, A.N. (2009b). Palaeo-drainage, incised valley fills and transgressive systems tract sedimentation of the northern KwaZulu-Natal continental shelf, South Africa, SW Indian Ocean. *Marine Geology*, **263**,
46-63.

Green, A.N. (2009c). Sediment dynamics on the narrow, canyon-incised and current-swept shelf of the northern KwaZulu-Natal continental shelf, South Africa. *Geo-Marine Letters*, **29**, 201-219.

Green, A.N. and Uken, R. (2005). First observations of sea level indicators related to glacial maxima at Sodwana Bay, KwaZulu-Natal. *South African Journal of Science*, **101**, 236-238.

Green, A.N., Ovechkina, M. and Uken, R. (2008). Nannofossil age constraints for the northern KwaZulu-Natal shelf-edge wedge: Implications for continental margin dynamics, South Africa, SW Indian Ocean. *Continental Shelf Research*, **28**, 2442-2449.

Grobbler, N.G., Mason, T.R. and Cooper, J.A.G. (1988). uMgababa lagoon: Pre- and post-flood sedimentology. *Sedimentation in Estuaries and Lagoons (S.E.A.L.) Report*, **5**, 48pp.

Grootes, P.M., Stuiver, M., White, J.W.C., Johnsen, S. and Jouzel, J. (1993). Comparison of oxygen isotope records from the GISP2 and GRIP Greenland ice cores. *Nature*, **366**, 552-554.

Gründlingh, M.L. (1980). On the volume transport of the Agulhas Current. *Deep-Sea Research*, **27a**, 557-563.

Gründlingh, M.L. (1992). Agulhas Current meanders: review and case study. *South African Geographical Journal*, **74**, 19-28.

Gründlingh, M.L. and Pearce, A.F. (1984). Large vortices in the northern Agulhas Current. *Deep Sea Research*, **31**, 1149-1156.

Gründlingh M.L. and Pearce, A.F. (1990). Frontal features of the Agulhas Current in the Natal Bight. *South African Geographical Journal*, **72**, 11-14.

Guilcher, A. (1988). *Coral reef geomorphology*. John Wiley & Sons Ltd., New York, 228pp.

Hanor, J.S (1978). Precipitation of beachrock cements: Mixing of marine and meteoric waters vs. CO_2-degassing. *Journal of Sedimentary Petrology*, **48**, 489-501.

Harris, T.F.W. (1978). Review of coastal currents in southern African waters. *South African National Science Program Report*, **30,** 68pp.

Harris, P.T. (1988). Large-scale bedforms as indicators of mutually evasive sand transport and the sequential infilling of wide-mouthed estuaries. Sedimentary. Geology, **57**, 273-298.

Hay, E.R. (1984). Sediment Dynamics on the Continental Shelf Between Durban and Port St. Johns (south-east African continental margin). *Bulletin of the Joint Geological Survey/University of Cape Town Marine Geoscience Unit*, **13**, 238pp.

Hayes, M.O. (1979). Barrier island morphology as a function of tidal and wave regime. In: S.P. Leatherman. *Barrier Islands from the Gulf of Mexico*, Academic Press, New York, 3-22.

Hayes, M.O. and Nairn, R.B. (2004). Natural maintenance of sand ridges and linear shoals on the U.S. Gulf and Atlantic continental shelves and the potential impacts of dredging. *Journal of Coastal Research*, **20**, 138-148.

Helland-Hansen, W. (2009). Comments on "Towards the standardization of sequence stratigraphy" by Catuneanu *et al*. [Earth-Science Reviews, 92, (2009), 1-33]. *Earth-Science Reviews*, **94**, 95-97.

Hijma, M.P. and Cohen, K.M. (2010). Timing and magnitude of the sea-level jump preluding the 8200 yr event. *Geology*, **38**, 275-278.

Hijma, M.P. and Cohen, K.M. (2011). Holocene transgression of the Rhine river mouth area, The Netherlands/Southern North Sea: palaeogeography and sequence stratigraphy. *Sedimentology*, *doi: 10.1111/j.1365-3091.2010.01222.x.*, 33pp.

Hobday, D.K. (1973). Middle Ecca deltaic deposits in the Muden-Tugela Ferry area of Natal. *Transactions of the Geological Society of South Africa*, **76**, 309-318.

Hobday, D.K. (1982). The southeast African Margin. In: A.E.M. Nairn and F.G. Stehli (Eds.) *The ocean basins and margins, volume 6 – the Indian Ocean*. Plenum Press, New York, 149-183.

Hoogendoorn, E.L. and Dalrymple, R.W. (1986). Morphology, lateral migration and internal structures of shoreface-connected sand ridges, Sable Island Bank, Nova Scotia, Canada. *Geology*, **14**, 400-403.

Hunt, D. and Tucker, M.E. (1992). Stranded parasequences and the forced regressive wedge systems tract: deposition during base-level fall. *Sedimentary Geology*, **81**, 1-9.

Hunt, D. and Tucker, M.E. (1995). Stranded parasequences and the forced regressive wedge systems tract: deposition during base-level fall - reply. *Sedimentary Geology*, **95**, 147-160.

Hunter, I.T. (1988). Climate and weather off Natal. In: E.H. Schumann, (Ed.), Coastal Ocean Studies off Natal, South Africa. *Lecture Notes on Coastal and Estuarine Studies*, **26**, *101-130.*

Hunter, R.E. (1977). Basic types of stratification in small eolianite dunes. *Sedimentology*, **24**, 361-387.

Huthnance, J.M. (1982). On one mechanism forming linear sand banks. *Estuarine Coastal and Marine Science*, **14**, 79-99.

Hutson, W.H. (1980). The Agulhas Current during the Late Pleistocene: analysis of modern faunal analogs. *Science*, **207**, 64-66.

Hydrographic Office. (2001). *South African Tide Tables*. South African Navy, Tokai. 260pp.

Hydrographic Office. (2003). *South African Tide Tables*. South African Navy, Tokai. 260pp.

Illenberger, W.K. (1996). The geomorphic evolution of the Wilderness dune cordons, South Africa. *Quaternary International*, **33**, 11-20.

Jacobs, J., Thomas, R.J. and Weber, K. (1993). Accretion and indentation tectonics at the southern edge of the Kaapvaal craton during the Kibaran (Grenvillian) orogeny. *Geology*, **21**, 203-206.

Jacobs, Z., Duller, G.A.T. and Wintle, A.G. (2006). Interpretation of single grain De distributions and calculation of De. *Radiation Measurements*, **41**, 264-277.

James, N.P. (1997). The cool-water carbonate depositional realm. *In*: James, N.P. and Clarke J.A.D. (Eds.), *Cool-Water Carbonates*. Soc. Econ. Pal. Min., Spec. Publ., **56**, 1-21.

Jedoui, Y., Reyss, J.L., Kallel, N., Montacer, M., Ismail, H.B. and Davaud, E. (2003). U-series evidence for two high Last Interglacial sea levels in southeastern Tunisia. *Quaternary Science Reviews*, **22**, 343-351.

Jermy, C.A. and Mason, T.R. (1983). A sedimentary model for the Berea Formation in the Glenwood Tunnel, Durban. *Transactions of the Geological Society of South Africa*, **86**, 117-125.

Johnson, M.R. (1976). *Stratigraphy and sedimentology of the Cape and Karoo Sequences in the Eastern Cape Province*. PhD. thesis (unpubl.), Rhodes University, 336pp.

Johnson, H.D. and Baldwin, C.T. (1986). Shallow siliciclastic seas. *In*: Reading H.G, (Ed.), *Sedimentary Environments and Facies*. Blackwell Scientific Publications, Oxford, 229-282.

Jones, E.J.W. (1999). *Marine Geophysics*. John Wiley & Sons Ltd., New York, 466pp.

Kennedy, W.J., Kauffman, E.G. and Klinger, H.C. (1973). Upper Cretaceous invertebrate faunas from Durban, South Africa. *Transactions of the Geological Society of South Africa*, **76**, 95-111.

Kennett, J.P. (1982). *Marine Geology*. Prentice-Hall, London, 813pp.

Kenyon, N.H., Belderson, R.H., Stride, A.H. and Johnson, M.A. (1981). Offshore tidal sandbanks as indicators of net sand transport and as potential deposits. *Special Publication International Association of Sedimentologists*, **5**, 257-268.

King, L.A. (1962a). Geomorphic history in the vicinity of Durban. *South African Geographical Journal*, **44**, 28-33.

King, L.A. (1962b). The post-Karoo Stratigraphy of Durban. *Transactions of the Geological Society of South Africa*, **65**, 95-99.

King, B.C. (1970). Vulcanicity and rift tectonics in East Africa. *In* Clifford, T.N. and Gass, I.G. (Eds.), *African Magmatism and Tectonics*. Oliver and Boyd, Edinburgh, 263-284.

King, L.C. and Maud, R.R. (1964). The geology of Durban and environs. *Bulletin of the Geological Survey of South Africa*, **42**, 54pp.

Klein (1985). *Side Scan Sonar Record Interpretation*. Klein and Associates, Salem, New Hampshire, 144pp.

Klein (1999). *Klein System 2000 Operations and Maintenance Manual*. Klein and Associates, Salem, New Hampshire, 261pp.

Klein (2004). The Sonar Operators Resource Site - Menu Page. URL: http://www.naval-minesonar.com/optips/optips.html

Klinger, H.C. and Kennedy, W.J. (1979). Cretaceous faunas from Southern Africa: Lower Cretaceous ammonites including a new Bochianitid genus from Umgazana, Transkei. *Annuals of the South African Museum*, **78**, 11-19.

Kortekaas, S. and Dawson, A.G. (2007). Distinguishing tsunami and storm deposits: An example from Martinhal, SW Portugal. *Sedimentary Geology*, **200**, 208-221.

Krige, L.J. (1932). The geology of Durban. *Transactions of the Geological Society of South Africa*, **35**, 37-67.

Kukla, G.J., Bender, M.L., de Beaulieu, J.-L., Bond, G., Broecker, W.S., Cleveringa, P., Gavin, J.E., Herbert, T.D., Imbrie, J., Jouzel, J., Keigwin, L.D., Knudsen, K.-L., McManus, J.F., Merkt, J., Muhs, D.R., Müller, H., Poore, R.Z., Porter, S.C., Seret, G., Shackleton, N.J., Turner, C., Tzedakis, P.C. and Winograd, I.J. (2002). Last interglacial climates. *Quaternary Research*, **58**, 2-13.

Lambeck, K. and Chappell, J. (2001). Sea level change through the Last Glacial cycle. *Science*, **292**, 679-686.

Lambeck, K., Yokoyama, Y. and Purcell, T. (2002a). Into and out of the Last Glacial Maximum: sea-level change during Oxygen Isotope Stages 3 and 2. *Quaternary Science Reviews*, **21**, 343-360.

Lambeck, K., Esat, T.M. and Potter, E.K. (2002b). Links between climate and sea-levels for the past three million years. *Nature*, **419**, 199-206.

Leeder, M.R. (1982). *Sedimentology: process and product*. George Allen and Unwin Publishers, London, 344pp.

Lenhoff, L. (1995). *The marine geology of Walker Bay, Hermanus, SW Cape, South Africa*. MSc. thesis (unpubl.), University of Cape Town, 58pp.

Leuci, R., Perritt, S. and Miller, W. (2002). Island View channel and basin bathymetric and seismic survey. *Council for Geoscience Report*, **2002-0117**, 21pp.

Li, M.Z. and King, E.L. (2007). Multibeam bathymetric investigations of the morphology of sand ridges and associated bedforms and their relation to storm processes, Sable Island Bank, Scotian Shelf. *Marine Geology*, **243**, 200-228.

Lightly, R.G. (1985). Preservation of internal reef porosity and the diagenetic sealing of submerged early Holocene barrier reef, southeast Florida Shelf. *In*: Schneidermann, N. and Harris, P.M. (Eds.), *Special Publication International Association of Sedimentologists*, **36**, 123-151.

Liu, J.P., Milliman, J.D., Gao, S. and Cheng, P. (2004). Holocene development of the Yellow River's subaqueous delta, North Yellow Sea. *Marine Geology*, **209**, 45-67.

Liu, J., Saito, Y., Wang, H., Yang, Z. and Nakashima, R. (2007) Sedimentary evolution of the Holocene subaqueous clinoform off the Shandong Peninsula in the Yellow Sea. *Marine Geology*, **236**, 165-187.

Longman, M.W. (1980). Carbonate diagenetic textures from near surface diagenetic environments. *Bulletin of the American Association of Petroleum Geology*, **64**, 461-487.

Lutjeharms, J.R.E. and Roberts, R. (1988). The Natal pulse: an extreme transient on the Agulhas Current. *Journal of Geophysical Research*, **93**, 631-645.

Lutjeharms, J.R.E., Bang, N.D. and Duncan C.P. (1981). Characteristics of the currents east and south of Madagascar. *Deep-Sea Research*, **28A**, 879-899.

MacKie, K.P. (2005). *Basic coastal and harbour engineering.* Keith Mackie consulting coastal & harbour engineer, Llandudno, 7806, South Africa, 419pp.

Malan, O.G. and Schumann, E.H. (1979). Natal Shelf circulation revealed by Landsat imagery. *South African Journal of Science*, **75**, 136-137.

Marean, C.W., Bar-Matthews, M., Bernatchez, J., Fisher, E., Goldberg, P., Herries, A.I.R., Jacobs, Z., Jerardino, A., Karkanas, P., Minichillo, T., Nilssen, P.J., Thomspon, E., Watts, I. and Williams, H.M. (2007). Early human use of marine resources and pigment in South Africa during the Middle Pleistocene. *Nature*, **449**, 905-908.

Marshall, J.E.A. (1994). The Falkland Islands: A key element in Gondwana palaeogeography. *Tectonics*, **13**, 499-514.

Marshall C.G.A. and Von Brunn, V. (1999). The stratigraphy and origin of the Natal Group. *South African Journal of Geology*, **102**, 15-25.

Martin, A.K. (1981a). The influence of the Agulhas Current on the physiographic development of the northernmost Natal Valley (SW Indian Ocean). *Marine Geology*, **39**, 259-276.

Martin, A.K. (1981b). Evolution of the Agulhas Current and its palaeo-ecological implications. *South African Journal of Science*, **77**, 547-554.

Martin, A.K. (1983). Fault pattern of coastal Natal – A result of strike-slip motion during Gondwanaland break-up? *Joint Geological Survey/University of Cape Town Marine Geoscience Unit Technical Report*, **14**, Marine Geoscience Group, University of Cape Town, 194-214.

Martin, A.K. (1984). Plate tectonic status and sedimentary basin in-fill of the Natal Valley (S.W. Indian Ocean). *Bulletin Joint Geological Survey/University of Cape Town Marine Geoscience Unit*, **14**, 208pp.

Martin, A.K. and Flemming, B.W. (1986). The Holocene shelf sediment wedge off the south and east coast of South Africa. *In:* Knight, R.J. and McLean, J.R. (Eds.), *Shelf Sands and Sandstones*. Canadian Society of Petroleum Geologists Memoir, **2**, 27-44.

Martin, A.K. and Flemming, B.W. (1987). Aeolianites of the South African coastal zone and continental shelf as sea-level indicators,*South African Journal of Science*, **83**, 507-508.

Martin, A.K. and Flemming, B.W. (1988). Physiography, structure, and geological evolution of the Natal continental shelf. *In*: Schumann E.H. (Ed.), *Coastal Ocean Studies off Natal, South Africa*. Lecture Notes on Coastal and Estuarine Studies, **26**, 11-46.

Martin, A.K. and Hartnady, C.J.H. (1986). Plate tectonic development of the southeast Indian Ocean: A revised reconstruction of East Antarctica and Africa. *Journal of Geophyiscal Research*, **91**, 4767-4786.

Martin, A.K., Hartnady, C.J.H. and Goodlad, S.W. (1981). A revised fit of South America and and South Central Africa. *Earth and Planetary Science Letters*, **54**, 293-305.

Martin, A.K., Goodlad, S.W. and Salmon, D.A. (1982). Sedimentary basin in-fill in the northernmost Natal Valley, hiatus development and Agulhas Current palaeo-oceanography. *Journal of the Geological Society of London*, **139**, 183-201.

Martinson, D.G., Pisias, N.G., Hays, J.D., Imbrie, J., Moore, T.C. and Shackleton, N.J. (1987). Age, dating and orbital theory of the Ice Ages: Development of a high resolution 0 to 300 000-year chronostratigraphy. *Quaternary Research*, **27**, 1-29.

Mather, A.A, Garland, G.G. and Stretch, D.D. (2009). Southern African sea levels: corrections, influences and trends. *African Journal of Marine Science*, **31**, 145–156

Matthews, P.E. (1970). Palaeorelief and the Dwyka glaciation in the eastern region of South Africa. *Second Gondwana Symposium Proceedings and Papers*, Cape Town, I.U.G.S. Commission on Stratigraphy, 491-499.

Matthews, P.E. (1972). Possible Precambrian obduction and plate-tectonics in south-eastern Africa. *Nature*, **240**, 37-39.

Matthews, P.E. (1981). Eastern or Natal sector of the Namaqua-Natal Mobile Belt in southern Africa. *In* Hunter, D.R. (Ed.), *Precambrian of the Southern Hemisphere*. Elsevier, Amsterdam, 705-714.

Matthews, R.K. and Frohlich, C. (1987). Forward modelling of bank-margin carbonate diagenesis. *Geology*, **15**, 673-676.

Maud, R.R. (1961). A preliminary review of the structure of coastal Natal. *Transactions of the Geological Society of South Africa*, **64**, 247-256.

Maud, R.R. (1968). Quaternary geomorphology and soil formation in coastal Natal. *Annals of Geomorphology*, **7**, 155-199.

Maud, R.R. and Botha, G.A. (2000). Deposits of the South Eastern and Southern coasts. *In*: Partridge, T.C. and Maud, R.R., (Eds.), *The Cenozoic of Southern Africa*. Oxford Monographs on Geology and Geophysics, **40**, 19-32.

McBride, R.A., and Moslow, T.F. (1991). Origin, evolution, and distribution of shoreface sand ridges, Atlantic inner shelf, USA. *Marine Geology*, **97**, 57-85.

McBride, R.A., Moslow, T.F., Roberts, H. and Diecchio, R.J. (2004). Late Quaternary geology of the northeastern Gulf of Mexico shelf: Sedimentology, depositional history, and ancient analogs of a major shelf sand sheet of the modern trasngressive systems tract. *In:* Anderson, J.B. and Fillon, R.H. (Eds.), *Late Quaternary Stratigraphic Evolution of the Northern Gulf of Mexico Margin*. Soc. Sed. Geol. SEPM Spec. Publ. Tulsa., **79**, 55-83.

McCarthy, M.J. (1967). Stratigraphical and sedimentological evidence from the Durban region of major sea-level movements since the late Tertiary. *The Transaction of the Geological Society of South Africa*, **70**, 135-165.

McCarthy, M.J. (1988). Some observations on the occurrence of "Berea-Type" red sand along the Natal coast. *Extended abstracts*, Geocongress '88, 22nd Earth Science Congress, Geological Society of South Africa, Durban, 403b-403d.

McCarthy, M.J. (1992). *Geological excursion notes for winners of the Fact Hunt Competition at "Careers in Geology" Expo*. University of Natal, Durban, 8pp.

McCormac, F. G., Hogg, A. G., Blackwell, P. G., Buck, C. E., Higham, T. F. G., and Reimer, P. J. (2004). SHCal04 Southern Hemisphere Calibration 0-11.0 cal Kyr BP. *Radiocarbon*, **46**, 1087-1092.

McCulloch and Esat (2000). The coral record of last interglacial sea levels and sea surface temperatures. *Chemical Geology*, **169**, 107-129.

McKinney, T.F., Stubblefield, W.F. and Swift, D.J.P. (1974). Large-scale current lineations on the central New Jersey Shelf: investigation by side-scan sonar. *Marine Geology*, **17**, 79-102.

McLachlan, I.R. and McMillan, I.K. (1979). Microfaunal biostratigraphy, chronostratigraphy and history of Mesozoic and Cenozoic deposits of the coastal margin of South Africa. *Geological Society of South Africa, Special Publication,* **6**, 161-181.

McLaren, S.J. (2001). Effects of sea spray on vadose diagenesis of Late Quaternary aeolianites, Bermuda. *Journal of Coastal Research*, **17**, 228-240.

McMillian, I.K. (1987). Quaternary sub-surface stratigraphy of the Maputaland coastal plain. *In:* Botha, G.A. (Ed.), *Maputaland focus on the Quaternary evolution of the south-east African coastal plain*. International Union for Quaternary Research Workshop Abstracts, Council for Geoscience, South Africa, 70-72.

McMillan I.K. (2003). Foraminiferally defined biostratigraphic episodes and sedimentation pattern of the Cretaceous drift succession (Early Barremian to Late Maastrichtian) in seven basins on the South African and southern Namibian continental margin. *South African Journal of Science*, **99**, 537-576.

Melim, L.A., Westphal, H., Swart, P.K., Eberli, G.P. and Munnecke, A. (2002) Questioning carbonate diagenetic paradigms: evidence from the Neogene of the Bahamas. *Marine Geology*, **185**, 27-53.

Mesolella, K.J., Mathews, R.K., Broecker, W.S. and Thurber, D.L. (1969). The astronomical theory of climate change: Barbados data. *Journal of Geology*, **77**, 250-274.

Miall, A.D. (1997). *The geology of stratigraphic sequences*. Springer, Berlin, 433pp.

Miall, A.D. and Miall C.E. (2001). Sequence stratigraphy as a scientific enterprise: the evolution and persistence of conflicting paradigms. *Earth-Science Reviews*, **54**, 321-348.

Milankovitch, M.M. (1941). *Canon of insolation and the ice-age problem*. Koniglich Serbische Akademie, Belgrade. [English translation by the Israel Program for Scientific Translations, published for the US Department of Commerce, and the National Science Foundation, Washington, D.C.].

Miller, D.E. (1991). A late Quaternary sea-level curve for southern Africa. *South African Journal of Science*, **86**, 456-458.

Miller, D.E., Yates, R.J., Parkington, J.E. and Vogel, J.C. (1993). Radiocarbon-dated evidence relating to a mid-Holocene relative high sea-level on the southwestern Cape coast, South Africa. *South African Journal of Science*, **89**, 35-44.

Miller, W.R. (1992). Erosional features of coastal beachrock and aeolianite outcrops in Natal and Zululand, South Africa. *Council for Geoscience Report*, **1992-0215**, 27pp.

Miller, W.R. and Mason, T.R. (1994). Erosional features of coastal beachrock and aeolianite outcrops in Natal and Zululand, South Africa. *Journal of Coastal Research*, **10**, 374-394.

Milliman, J.D. (1974). Part 1: Marine carbonates. *In*: Milliman, J.D., Muller, G. and Forstner, U. (Eds), *Recent Sedimentary Carbonates*. Springer-Verlag, Berlin, 1-375.

Milne, G.A., Mitrovica, J.X. and Schrag, D.P. (2002). Estimating past continental ice volume from sea-level data. *Quaternary Science Reviews*, **21**, 361-376.

Mitchum, R.M. Jr, (1977). Seismic Stratigraphy and global changes in Sea-level, part 11, glossary of terms used in seismic stratigraphy. *In*: Payton, C.E. (Ed), *Seismic Stratigraphy - Applications to Hydrocarbon exploration*. Am. Assoc. Pet. Geol. Memoir, **26**, Boulder, Colorado, 205-212.

Mitchum, R.M. Jr, and Vail, P.R. (1977). Seismic Stratigraphy and global changes in Sea-level, part 7, seismic stratigraphic interpretation procedure. *In*: Payton, C.E. (Ed), *Seismic Stratigraphy - Applications to Hydrocarbon exploration*. Am. Assoc. Pet. Geol. Memoir, **26**, Boulder, Colorado, 135-143.

Mitchum, R.M. Jr, Vail, P.R. and Thompson, S III (1977a). Seismic Stratigraphy and global changes in Sea-level, part 2, the depositional sequence as a basic unit for stratigraphic analysis. *In*: Payton, C.E. (Ed), *Seismic Stratigraphy - Applications to Hydrocarbon exploration*. Am. Assoc. Pet. Geol. Memoir, **26**, Boulder, Colorado, 53-62.

Mitchum, R.M. Jr, Vail, P.R. and Sangree, J.B. (1977b). Seismic Stratigraphy and global changes in Sea-level, part 6, stratigraphic interpretations of seismic reflection patterns in depositional sequences. *In*: Payton, C.E. (Ed), *Seismic Stratigraphy - Applications to Hydrocarbon exploration*. Am. Assoc. Pet. Geol. Memoir, **26**, Boulder, Colorado, 117-133.

Mitrovica, J.X. and Peltier, W.R. (1991). On postglacial geoid subsidence over the equatorial oceans. *Journal of Geophysical Research*, **96**(B12), 20053-20071.

Mitrovica, J.X. (2003). Recent controversies in predicting post-glacial sea-level change. *Quaternary Science Reviews*, **22**, 127-133.

Moody, D.W. (1964). *Coastal morphology and processes in the relation to the development of submarine ridges off Bethany Beach, Delaware*. PhD thesis (unpubl.), John Hopkins University, Baltimore, 167pp.

Moore, C.H. (1973). Intertidal caronate cementation, Grand Cayman, West Indies. *Journal of Sedimentary Petrology*, **43**, 591-602.

Morten, R.A., Richmond, B.M., Jaffe, B.E. and Gelfenbaum, G. (2008). Coarse-clast ridge complexes of the Caribbean: A preliminary basis for distinguishing between tsunami and storm-wave origins. *Journal of Sedimentary Research*, **78**, 624-637.

Moura, D., Veiga-Pires, C., Albardeiro, L., Boski, T., Rodrigues, A.L. and Tareco, H. (2007). Holocene sea level fluctuations and coastal evolution in the central Algarve (southern Portugal). *Marine Geology*, **237**, 127-142.

Mörner, N.-A. (1971). Eustatic changes during the last 20 000 years and a method of separating the isostatic and eustatic factors in an uplifted area. *Palaeogeography Palaeoclimatology Palaeoecology*, **13**, 1-14.

Mörner, N.-A. (1976). Eustasy and geoid changes. *Journal of Geology*, **84**, 123-151.

Mörner, N.-A. (1980). Eustasy and geoid changes as a function of core/mantle changes. *In:* Mörner, N.-A. (Ed.), *Earth Rheology, Isostasy and Eustasy.* John Wiley & Sons, 535-553.

Mörner, N.-A. (1987). Models of of global sea level changes. *In* Tooley, M.J. and Shennan, I. (Eds), *Sea Level Changes*. Blackwell, New York, 333-335.

Muhs, D.R. (2002). Evidence for the Timing and Duration of the Last Interglacial Period from High-Precision Uranium-Series Ages of Corals on Tectonically Stable Coastlines. *Quaternary Research*, **58**, 36-40.

Murray-Wallace, C.V., Belperio, A.P., Bourman, R.P., Cann, J.H. and Price D.M. (1999). Facies architecture of a last interglacial barrier: a model for Quaternary barrier development from the Coorong to Mount Gambier Coastal Plain, southeastern Australia. *Marine Geology*, **158**, 177-195.

Nanayama, F., Shigeno, K., Satake, K., Shimokawa, K., Koitabashi, S., Miyasaka, S. and Ishii, M. (2000). Sedimentary differences between the 1993 Hokkaido-nansei-oki tsunami and the 1959 Miyakojima typhoon at Taisei, southwestern Hokkaido, northern Japan. *Sedimentary Geology*, **135**, 255-264.

Neumeier, U. (1999). Experimental modelling of beachrock cementation under microbial influence. *Sedimentary Geology*, **126**, 35-46.

Nicolaysen, L.O. and Burger, A.J. (1965). Note on an extensive zone of 1 000 million-year old metamorphic and igneous rocks in southern Africa. *Sciences Terres*, **10**, 497-518.

National Oceanic and Atmospheric Administration - NOAA (2000). Surface of the Earth. *National Geophysical Data Centre Image*, **MGG-5**, http://www.ngdc.noaa.gov/mgg/image/2minrelief.html

National Research Institute for Oceanology - NRIO (1986). Basic physical geography/Hydro data for Natal "Estuaries".*NRIO Data Report*, **D 8607**, 10pp.

Niedoroda, A.W., Swift, D.J.P. and Hopkins, T.S. (1985). The Shoreface. *In*: Davis Jr., R.A. (Ed.), *Coastal Sedimentary Environments (2nd Edition)*, Springer-Verlag, New York, 533-624.

Nitsche, F.O., Bell, R., Carbotte, S.M., Ryan, W.B.F. and Flood, R. (2004). Process-related classification of acoustic data from the Hudson River Estuary. *Marine Geology*, **209**, 131-145.

Nordfjord, S., Goff, J.A., Austin, J.A. and Gulick, S.P.S. (2006). Seismic facies of incised valley fills, New Jersey continental shelf: implications for erosion and preservation processes acting during the latest Pleistocene-Holocene transgression. *Journal of Sedimentary Research*, **76**, 1284-1303.

Nordfjord, S., Goff, J.A., Austin, J.A. Jr. and Duncan, L.S. (2009). Shallow stratigraphy and complex transgressive ravinement on the New Jersey middle and outer continental shelf. *Marine Geology*, **266**, 232-243.

Obura, D. (2006). Impacts of the 26 December 2004 tsunami in Eastern Africa. *Ocean & Coastal Management*, **49**, 873–888.

Odom Hydrographic Systems (1991). *EchoTrac Model 3100 Technical Manual*. Odom Hydrographic Sytems, Baton Rouge, U.S.A., 107pp.

Okuno, J. and Nakada, M. (1999). Total volume and temporal variation of meltwater from last glacial maximum inferred from sea-level observations at Barbados and Tahiti. *Palaeogeography, Palaeoclimatology, Palaeoecology*, **146**, 283-293.

Orme, A.R .(1973). Barrier and lagoon systems along the Zululand coast, South Africa. *In:* Coates, D.R. (Ed.). *Coastal Geomorphology*. State University of New York, 181-217.

Orme, A.R. (1975). Late Pleistocene and Flandrian sediments beneath Natal estuaries: A synthesis. *Annals of the South African Museum*, **71**, 77-85.

Osterberg, E.C. (2006). Late Quaternary (marine isotope stages 6-1) seismic sequence stratigraphic evolution of the Otago continental shelf, New Zealand. *Marine Geology*, **229**, 159-178.

Palinkas, C.M. and Nittrouer, C.A. (2005). Clinoform sedimentation along the Appennine River shelf, Adriatic Sea. *Marine Geology*, **234**, 245–260.

Parker, G., Lanfredi, N.W. and Swift, D.J.P. (1982). Seafloor response to flow in a southern hemisphere sand-ridge field: Argentine inner shelf. *Sedimentary Geology*, **33**, 195–216.

Parr, W.J. (1958). The foraminifera of the Bluff Beds, Durban and some other South African calcareous coastal rocks. *Transactions of the Geological Society of South Africa*, **61**, 103-109.

Partridge, T.C. and Maud, R.R. (1987). Geomorphic evolution of southern Africa since the Mesozoic. *South African Journal of Geology*, **90**, 179-208.

Partridge, T.C. and Maud, R.R. (2000). Macro-scale geomorphic evolution of southern Africa. *In*: Patridge, T.C. and Maud, R.R. (Eds.). *The Cenozoic of Southern Africa*. Oxford Monographs on Geology and Geophysics, **40**, 3-18.

Paul, A., Reijmer, J.J.G., Fürstenau, J. and Kinkel, H. (2011). Relationship between Late Pleistocene sea-level variations, carbonate platform morphology and aragonite production (Maldives, Indian Ocean). *Sedimentology*, *doi:10.1111/j.1365-3091.2011.01319.x*.

Petroleum Agency South Africa (PASA), (2003a). *Durban and Zululand Basins. Exploration opportunities offshore South Africa's east coast.* Petroleum Agency South Africa information brochure, 4pp.

Petroleum Agency South Africa (PASA), (2003b). *Exploration opportunities in South Africa*. Petroleum Agency South Africa information poster, 1pp.

Pearce, A.F. (1974). Preliminary results from a set of ten cruises out to 100 km off Durban. Part 1: Surface temperature, salinity and currents. *National Research Institute for Oceanology Report*, **IG 74/11**, 39pp.

Pearce, A.F. (1976). The gross features of the East Coast Shelf circulation. *CSIR Restricted Report*, **346**, Stellenbosch, 18pp.

Pearce, A.F. (1978). Seasonal variations of temperature and salinity on the northern Natal continental shelf. *South African Geographical Journal*, **60**, 135-143.

Pearce, A.F., Schumann, E.H. and Lundie, G.S.H. (1978). Features of the Shelf Circulation off the Natal Coast. *South African Journal of Science*, **74**, 328-331.

Peltier, W.R. (2002). On eustatic sea level history: Last Glacial Maximum to Holocene. *Quaternary Science Reviews*, **21**, 377-396.

Peltier, W.R. (2005). On the hemispheric origins of meltwater pulse 1a. *Quaternary Science Reviews*, **24**, 1655-1671.

Peltier, W.R. amd Fairbanks, R.G. (2006). Global glacial ice volume and Last Glacial Maximum duration from an extended Barbados sea level record. *Quaternary Science Reviews*, **25**, 3322-3337.

Perritt, S. and Leuci, R. (2002). Correlation of seismic and borehole data for Island View channel and Basin, Durban Harbour. *Council for Geoscience Report*, **2002-0254**, 5pp.

Perritt, S., Leuci, R. and Bosman, C. (2003). Maydon Wharf channel and Congella basin bathymetric and seismic survey. *Council for Geoscience Report*, **2004-0074**, 24pp.

Pettijohn, F.J., Potter, P.E. and Siever, R. (1972). *Sand and sandstone*. Springer-Verlag, New York, 618.

Pillans, B. and Naish, T. (2004). Defining the Quaternary. *Quaternary Science Reviews*, **23**, 2271-2282.

Pirmez, C., Pratson, L.F. and Steckler, M.S. (1998). Clinoform development by advection-diffusion of suspended sediment: modelling and comparison to natural systems. *Journal of Geophysical Research*, **103 (B10)**, 24141 - 24157.

Pisias, N.G., Martinson, D.G., Moore, T.C., Shackleton, N.J., Prell, W., Hays, J. and Boden, G. (1984). High resolution stratigraphic correlation of benthic oxygen isotopic records spanning the last 300 000 years. *Marine Geology*, **56**, 119-136.

Plint, A.G. and Nummedal, D. (2000). The falling stage systems tract: recognition and importance in sequence stratigraphic analysis. *Geol. Soc. London Spec. Publ.*, **172**, 1-17.

Porat, N. and Botha, G. (2008). The luminescence chronology of dune development on the Maputaland coastal plain, southeast Africa. *Quaternary Science Reviews*, **27**, 1024-1046.

Posamentier, H.W., Jervey, M.T and Vail, P.R. (1988). An Eustatic controls on clastic deposition, part 1, conceptual framework. *In*: Wilgus, C.K., Hastings, B.S., Kendall, C. G. St. C., Posamentier, H.W., Ross, C.A. and Van Wagoner, J.C. (Eds.), *Sea-level Changes and integrated approach*. Soc. Econ. Pal. Min., Spec. Publ., **42**, 109-124.

Potter, E.-K., Esat, T.M., Schellmann, G., Radtke, U., Lambeck, K. and McCulloch, M.T. (2004). Suborbital-period sea-level oscillations during marine isotope substages 5a and 5c. *Earth and Planetary Science Letters*, **225**, 191-204.

Prescott, J.R. and Hutton, J.T. (1994). Cosmic ray contributions to dose rates for luminescence and ESR dating: large depths and long-term time variations. *Radiation Measurements*, **23**, 497-500.

Quinn, R. (2002). Unpublished lecture notes in *Marine GeoArchaeology*, Environmental Sciences Research Institute, University of Ulster. URL address: www.geocities.com/seafloor mapping/ens824/sub.htm, accessed in 2002.

Quinn, T.M. and Matthews, R.K. (1990) Post-Miocene diagenetic and eustatic history of Enewetak Atoll: model and data comparison. *Geology*, **18,** 942-945.

Radtke, U., Schellmann, G. and Murray-Wallace, C.V. (2004). Coastal environmental change during sea-level highstands: IGCP 437 Symposium, Barbados. *Quaternary International (Preface)*, **120**, 1pp.

Rau, A.J., Rodgers, J., Lutjeharms, J.R.E., Giraudeau, J.A., Lee-Thorp, J.A., Chen, M.-T. and Waelbroeck, C. (2002). A 450-kyr record of hydrological conditions on the western Agulhas Bank Slope, south of Africa. *Marine Geology*, **180**, 183-201.

Ramsay, P.J. (1991). *Sedimentology, Coral Reef Zonation, and Late Pleistocene Coastline Models of the Sodwana Bay Continental Shelf, Northern Zululand*. University of Natal, Durban. PhD thesis (unpubl.), 202pp.

Ramsay, P.J. (1994). Marine geology of the Sodwana Bay Shelf, southeast Africa. *Marine Geology*, **120**, 225-247.

Ramsay, P.J. (1995). 9000 years of sea-level change along the southern African coastline. *Quaternary International*, **31**, 71-75.

Ramsay, P.J. (1996). Quaternary marine geology of the Sodwana Bay continental shelf, Northern KwaZulu-Natal. *Bulletin of the Geological Survey of South Africa*, **117**, 86pp.

Ramsay, P.J. (1997). Beachrock and aeolianite – what is the difference? *In:* Botha, G.A. (Ed.), *Maputaland focus on the Quaternary evolution of the south-east African coastal plain*. International Union for Quaternary Research Workshop Abstracts, Council for Geoscience, South Africa, 1pp.

Ramsay, P.J. (1998). Marine Geological Survey of Aliwal Shoal, KwaZulu-Natal. C*ouncil for Geoscience, Report No.*, **1998-0049**, 6pp.

Ramsay, P.J. (2001). Marine geophysical data post-processing manual: Amended 2000/2001. *Council for Geoscience Report*, **2001-0070**, 51pp.

Ramsay, P.J., Smith, A.M., Lee-Thorp, J.C., Vogel, J.C., Tyldsley, M., and Kidwell, W. (1993). 130 000 year-old fossil elephant found near Durban: Preliminary report. *South African Journal of Science*, **89**, 165.

Ramsay, P.J., Smith, A.M. and Mason, T.R. (1996). Geostrophic sand ridge, dune fields and associated bedforms from the northern KwaZulu-Natal shelf, southeast Africa. *Sedimentology*, **43**, 407-419.

Ramsay, P.J. and Cooper, J.A.G. (2002). Late Quaternary sea-level change in South Africa. *Quaternary Research*, **57**, 82-90.

Reijers, T.J.A. and Hsu, K.J. (1986). *Manual of Carbonate Sedimentology*. Academic Press, London, 302pp.

Reimer, P.J., Baillie, M.G.L., Bard, E., Bayliss, A., Beck, J.W., Blackwell, P.G., Bronk Ramsey, C., Buck, C.E., Burr, G.S., Edwards, R.L., Friedrich, M., Grootes, P.M., Guilderson, T.P., Hajdas, I., Heaton, T.J., Hogg, A.G., Hughen, K.A., Kaiser, K.F., Kromer, B., McCormac, F.G., Manning, S.W., Reimer, R.W., Richards, D.A., Southon, J.R., Talamo, S., Turney, C.S.M., van der Plicht, J. and Weyhenmeyer C. E. (2009). IntCal09 and Marine09 radiocarbon age calibration curves, 0 - 50 000 years Cal BP. *Radiocarbon*, **51**:1111-1150.

Republic of South Africa Government Gazette (2004). *Notice declaring the Aliwal Shoal Marine Protected Area under section 43 of the Marine Living Resources Act 18 of 1998*, vol., **468**, no. 26433, 3-10 South Africa.

Reson, (2003). *Navisound 200/400 User Manual Version 3.3.* Reson Inc., California, U.S.A, 85pp.

Richardson, A.G. (2005). *The marine geology of the Durban Bight*. MSc thesis (unpubl.), University of KwaZulu-Natal, Durban, 96pp.

Rine, J.M., Tillman, R.W., Culver, S.J. and Swift, D.J.P. (1991). Generation of late Holocene ridges on the middle continental shelf of New Jersey, USA - evidence for formation in a midshelf setting based on comparison with a nearshore ridge. *Special Publication of the International Association of Sedimentologists*, **14**, 395- 423.

Roberts, D.L., Bateman, M.D., Murray-Wallace, C.V., Carr, A.S. and Holmes, P.J. (2008). Fossil elephant trackways, sedimentation and diagenesis in OSL/AAR-dated Late Quaternary coastal aeolianites: Still Bay, South Africa. *Palaeogeography, Palaeoclimatology, Palaeoecology*, **257**, 261-279.

Rooper, C.N. and Zimmerman, M. (2007). A bottom-up methodology for integrating underwater video and acoustic mapping for seafloor substrate classification. *Continental Shelf Research*, **27**, 947-957.

Rossouw, J. (1984). Review of existing wave data, wave climate and design waves for South Africa and South West African (Namibian) coastal waters. *CSIR Report*, **T/SEA 8401**, Stellenbosch, 66pp.

Ryan, P.J. (1967). *Stratigraphic and paleocurrent analysis of the Ecca Series and lowermost Beaufort Beds in the Karoo Basin of South Africa*. PhD. thesis (unpubl.), University of the Witwatersrand, Johannesburg, 210pp.

Saggerson, E.P., Bristow, J.W. and Armstrong, R.A. (1983). The Rooi Rand dyke swarm. *South African Journal of Science*, **79**, 365-369.

Saito, Y. (1989). Late Pleistocene coastal sediments, drainage patterns and sand ridges systems on the shelf off Sendai, Northeast Japan. *Marine Geology*, **89**, 229-244.

SAN 131 (1982). South African Naval Chart 131, Government Printer, 1pp.

Sanders, J.E., Kumar, N., 1975. Evidence of shoreface retreat and in-place “drowning” during Holocene submergence of barriers, shelf off Fire Island, New York. *Geological Society of America Bulletin*, **86**, 65-76.

Sayles, R.W. (1931). Bermuda during the ice age. *Proceeding of the America Academy of Arts and Science* **66**, 381-467.

Schellman, G., and Radtke, U. (2004). A revised morpho- and chronostratigraphy of the Late and Middle Pleistocene coral reef terraces on Southern Barbados (West Indies). *Earth-Science Reviews*, **64**, 157-187.

Schellman, G., Radtke, U., Potter, E.-K., Esat, T.M. and McCulloch, M.T. (2004). Comparison of ESR and TIMS U/Th dating of marine isotope stage (MIS) 5e, 5c, and 5a coral from Barbados - implications for palaeo sea-level changes in the Caribbean. *Quaternary International*, **120**, 41-50.

Schink, J.C., Stockwell, J.H. and Ellis, R.A. (1978). An improved device for gasometric determination of carbonate in sediment. *Journal of Sedimentary Petrology*, **48**, 651-653.

Schleyer, M. H., Heikoop, J. M. and Risk, M. J. (2006). A benthic survey of Aliwal Shoal and assessment of the effects of a wood pulp effluent on the reef. *Marine Pollution Bulletin*, **52**, 503-514.

Scholle, P.A. (1978). A color illustrated guide to carbonate rock constituents, textures, cements and porosities. *American Association of Petroleum Geologists Memoir*, **27**, 241pp.

Schulze, B.R. (1965). *Climates of South Africa (Part 8, General Survey)*. South African Weather Bureau 330pp.

Schumann, E.H. (1981). Low frequency fluctuations off the Natal coast. *Journal of Geophysical Research*, **86 (C7)**, 6499-6508.

Schumann, E.H. (1987). The coastal ocean off the east coast of South Africa. *Transaction of the Royal Society of South Africa*, **46**, 215-229.

Schumann, E.H. (1988). Physical Oceanography off Natal. *In:* Schumann, E.H. (Ed.), *Coastal Ocean Studies off Natal, South Africa.* Lecture Notes on Coastal and Estuarine Studies, **26**, 101-130.

Schumann, E.H. and Orren, M.J. (1980). The physio-chemical characteristics of the south-west Indian Ocean in relation to Maputaland. *In*: Bruton, M.N. and Cooper, K.H. (Eds.), *Studies on the Ecology of Maputaland*. Wildlife Society of South Africa, Durban, 8-11.

Scoffin, T.P. (1987). *An Introduction to Carbonate Sediments and Rocks.* Blackie, Glasgow and Hall,

New York, 274 pp.

Scoffin, T.P. and McLean, R.F. (1978). Exposed limestones of the northern province of the Great Barrier Reef. *Philosophical Transactions of the Royal Society of London*, **291**, 119-138.

Scoffin, T.P. and Stoddart, D.R. (1983). Beachrock and intertidal sediments. *In*: Goudie, A.S. and Pye, K. (Eds.), *Chemical Sediments and Geomorphology*. Academic Press, London, 401-425.

Scrutton, R.A. (1973). Structures and evolution of the seafloor south of South Africa. *Earth and Planetary Science Letters*, **9**, 250-256.

Scrutton, R.A. (1979). On sheared passive continental margins. *Tectonophysics*, **59**, 293-305.

Seibold, E. & Berger, W.H. (1996). *The Sea Floor; An Introduction to Marine Geology.* Springer-Verlag, Germany, 356pp.

Shackleton, N.J. (1987). Oxygen isotopes, ice volume and sea level. *Quaternary Science Reviews*, **6**, 183-190.

Shackleton, N.J. and Opdyke, N.D. (1973). Oxygen isotope and palaeomagnetic stratigraphy of Equatorial Pacific core V28-238: Oxygen isotope temperatures and ice volumes on a 10^5 year and 10^6 year scale. *Quaternary Research*, **3**, 39-55.

Shaw, M.J. (1998). *Seismic stratigraphy of the north KwaZulu-Natal upper continental margin*. MSc thesis (unpubl.), University of Natal, Durban, 190pp.

Sherman, C.E., Fletcher, C.H. and Rubin, K.H. (1999). Marine and meteoric diagenesis of Pleistocene carbonates from a nearshore submarine terrace, Oahu, Hawaii. *Journal of Sedimentary Research*, **69**, 1083-1097.

Shone, R. W. (2006). Onshore post-Karoo Mesozoic deposits. *In*: Johnson, M. R., Anhaeusser, C. R. and Thomas, R. J. (Eds.), *The Geology of South Africa.* Geological Society of South Africa, Johannesburg/Council for Geoscience, Pretoria, 541-552.

Siegert, M.J. (2001). *Ice Sheets and Late Quaternary Environmental Change.* John Wiley and Sons, New York, 231pp.

Siesser, W.G. (1970). Carbonate components and mineralogy of the South African coastal limestones of the Agulhas Banks. *Transaction of the Geological Society of South Africa*, **73**, 49-63.

Siesser, W.G. (1974). Relict and recent beachrock from southern Africa. *Geological Society of America Bulletin*, **85**, 1849-1854.

Smith, A.M., Guastella, L.A., Bundy, S.C. and Mather, A.A. (2007). Combined marine storm and Saros spring high tide erosion events along the KwaZulu-Natal coast in March 2007. *South African Journal of Science*, **103**, 274-276.

Smith, A.M., Mather, A.A., Bundy, S.C., Cooper, J.A.G., Guastella, L.A., Ramsay, P.J. and Theron, A. (2010). Contrasting styles of swell-driven coastal erosion: examples from KwaZulu-Natal, South Africa. *Geological Magazine, doi:10.1017/S0016756810000361*, 1-14.

Snedden, J.W., Tillman, R.W., Kreisa, R.D., Schweller, W.J., Culver, S.J. and Winn Jr., R.D. (1994). Stratigraphy and genesis of a modern shoreface-attached sand ridge, Peahala Ridge, New Jersey. *Journal Sedimentary Research*, **64**, 560-581.

Snedden, J.W., Kreisa, R.D., Tillman, R.W., Culver, S.J. and Schweller, W.J. (1999). An expanded model for modern shelf sand ridge genesis and evolution on the New Jersey Atlantic shelf. *In*: Bergman, K.M. and Snedden, J.W. (Eds.), *Isolated Shallow Marine Sand Bodies: Sequence Stratigraphic Analysis and Sedimentologic Interpretation*, Soc. Sed. Geol. SEPM Spec. Publ. Tulsa., **64**, 147-163.

Southern Oil Exploration Corporation (SOEKOR), (1994). *Licensing round information brochure: Durban/Zululand Basins*, 4pp.

South African Committee for Stratigraphy (SACS). (1980). Stratigraphy of South Africa. Part 1 Lithostratigraphy of the Republic of South Africa, South West Africa/Namibia, and the Republics of Bophuthatswana, Transkei and Venda (L.E. Kent, Ed.). *Handbook of the Geological Survey of South Africa*, **8**, 690pp.

Sprigg, R.C. (1979). Stranded and submerged sea-beach systems of southeast South Australia and the aeolian desert cycle. *Sedimentary Geology*, **22**, 53-96.

Stahl, L., Koczan, J. and Swift, D.J.P. (1974). Anatomy of a shoreface-connected sand ridge on the New Jersey Shelf: Implications for the genesis of the shelf surficial sand sheet. *Geology*, **2**, 117-120.

Stanford, J.D., Rohling, E.J., Hunter, S.E., Roberts, A.P., Rasmussen, S.O., Bard, E., McManus, J. and Fairbanks, R.G. (2006). Timing of meltwater pulse 1a and climate responses to meltwater injections. *Paleoceanography*, **21**, *PA4103, doi:10.1029/2006PA001340*, 9pp.

Stanford, J.D., Hemingway, R., Rohling, E.J., Challenor, P.G., Medina-Elizalde, M. and Lester, A.J. (2011). Sea-level probability for the last deglaciation: a statistical analysis of far-field records. *Global and Planetary Change*, 79, 193-203.

Stanley, D.J. and Warne, A.G. (1994) Worldwide initiation of Holocene marine deltas by deceleration of sea-level rise. *Science*, **265**, 228-231.

Stratten, T. (1970). Tectonic framework of sedimentation during the Dwyka Period in South Africa. *Second Gondwana Symposium Proceedings and Papers*, Cape Town, I.U.G.S. Commission on Stratigraphy, 483-490.

Stride, A.H. (1992). The first geological use of side-scan sonar. *Geology Today*, **July-August**, 146-150.

Stride, A.H., Belderson, R.H. and Johnson, M.A. (1982). Offshore tidal deposits: sand sheet and sandbank facies. *In*: Stride, A.H. (Ed.), *Offshore Tidal Sands: processes and deposits*, Chapman Hall, London, 222pp.

Stoddart, D.R. and Cann, J.R. (1965). Nature and origin of beachrock. *Journal of Sedimentary Petrology*, **35**, 243-247.

Storms, J.E.A., Weltje, G.J., Terra, G.J., Cattaneo, A. and Trincardi, F. (2008). Coastal dynamics under conditions of rapid sea-level rise: Late Pleistocene to Early Holocene evolution of barrier– lagoon systems on the northern Adriatic shelf (Italy). *Quaternary Science Reviews*, **27**, 1107-1123.

Stubblefield, W.L. and Swift, D.J.P. (1976). Ridge development as revealed by sub-bottom profiles on the central New Jersey shelf. *Marine Geology*, **20**, 315-334.

Stubblefield, W.L., McGrail, D.W. and Kersey, D.G. (1984). Recognition of transgressive and post-transgressive sand ridges on the New Jersey continental shelf. *In*: Tillman, R.W. and Siemers, C.T. (Eds.), *Siliciclastic Shelf Sediments*, Soc. Sed. Geol. SEPM Spec. Publ. Tulsa., **34**, 1-23.

Stuiver, M. and Reimer, P. J. (1993). Extended 14C database and revised CALIB radiocarbon calibration program. *Radiocarbon*, **35**, 215-230.

Stuiver, M. and Grootes, P.M. (2000). GISP2 Oxygen Isotope Ratios. *Quaternary Research*, **53**, 277-284.

Sudan, P. (1999). Sedimentology, stratigraphy and geological history of part of the Northern KwaZulu-Natal coastal dune cordon. Durban, South Africa. University of Natal, MSc. thesis (unpubl.), 181p.

Sudan, P., Whitmore, G., Uken, R. and Woodborne, S. (2004). Quaternary evolution of the coastal dunes between Lake Hlabane and Cape St Lucia. *South African Journal of Geology*, **107**, 355-376.

Swart, D.H. and Serdyn, J. de V. (1981). Statistical analysis of visually observed wave data from voluntary observing ships for South African east coast. *Unpublished CSIR Report*, **9**, 141pp.

Swenson, J.B., Paola, C., Pratson, L., Voller, V.R. and Murray, A.B. (2005). Fluvial and marine controls on combined subaerial and subaqueous delta progradation: morphodynamic modelling of compound-clinoform development. *Journal of Geophysical Research, F02013, doi:10.1029/2004JF000265110*, 1-16.

Swift, D.J.P., Stanley, D.J. and Curray, J.R. (1971). Relict sediments on continental shelves: a reconsideration. *Journal of Geology*, **79**, 322-346.

Swift, D.J.P. (1974). Continental shelf sedimentation. *In*: Burke, C.A. and Drake, C.L. (Eds.), *The geology of continental margins*, Springer-Verlag, Berlin, 117-135.

Swift, D.J.P and Field, M.E. (1981). Evolution of a classic sand ridge field: Maryland sector North American inner shelf. *Sedimentology*, **28**, 461-482.

Swift, D.J.P., Holliday, B., Avignone, N., Shideler, G. (1972). Anatomy of a shoreface ridge system, False Cape, Virginia. *Marine Geology*, **12**, 59-84.

Swift, D.J.P., Duane, D.B. and McKinney, T.F. (1973). Ridge and swale topography of the Middle Atlantic Bight, North America: secular response to the Holocene hydraulic regime. *Marine Geology*, **15**, 227-247.

Swift, D.J.P., Parker, G., Lanfredi, N.W., Perillo, G. and Figge, K.(1978). Shoreface-connected sand ridges on American and European shelves: a comparison. *Estuarine Coastal and Marine Science*, **7**, 257-273.

Sydow, C.J. (1988). Stratigraphic control of slumping and canyon development on the continental margin, east coast, South Africa. Hons. thesis (unpubl.), University of Cape Town, 58pp.

Tamura, T., Saito, Y., Sieng, S., Ben, B., Kong, M., Sim, I., Choup, S., and Akiba, F. (2009). Initiation of the Mekong River delta at 8 ka: Evidence from the sedimentary succession in the Cambodian lowland. *Quaternary Science Reviews*, **28**, 327-344.

Tankard, A.J. (1976). Cenozoic sea-level changes: a discussion. *Annals of the South African Museum*, **71**,1-17.

Tankard, A.J., Jackson, M.P.A., Eriksson, K.A., Hobday, D.K., Hunter, D.R. and Minter, W.E.L. (1982). *Crustal evolution of southern Africa*. Springer-Verlag, New York, 523pp.

Taylor, J.C. M. and Illing, L.V. (1969). Holocene intertidal calcium carbonate cementation, Qatar. *Sedimentology*, **12**, 69-107.

Terhorst, A. (1987). *The seafloor environment off Simon's Town in False Bay, revealed by side-scan sonar, bottom sampling, diver operations and underwater photography*. MSc. thesis (unpubl.), University of Cape Town, 58pp.

Terry, R.D. and Chilingar, G.V. (1955). Summary of 'Concerning some additional aids in studying sedimentary formations' by M.S. Shvetsov. *Journal of Sedimentary Petrology*, **25**, 229-234.

Theberge, A.E. (1989). Sounding Pole to Sea Beam. Technical Papers 1989 ASPRS/ACSM Annual Convention, *Surveying and Cartography*, **5**, 334-346.

Thomas, R.J. (1988). The geology of the Port Shepstone area. *Explanation sheet for Port Shepstone*. Geology Survey of South Africa , 136pp.

Thomas, R.J. (1989). A tale of two tectonic terranes. *South African Journal Geology*, **92,** 306-321.

Thomas, R.J., Bullen, W.D., de Klerk, I. and Scogings, A.J. (1990). The distribution and genesis of precious and base metal mineralization in the Natal Metamorphic Province, South Africa. *South African Journal of Geology*, **93,** 683-695.

Thomas, R.J., Marshall, C.G.A., Watkeys, M.K., Fitch, F.J. and Miller, J.A. (1992). K-Ar and $^{40}Ar/^{39}Ar$ dating of the Natal Group, Southeast Africa: a post Pan-African molasse? *Journal of African Earth Sciences*, **15**, 453-471.

Trowbridge, J.H. (1995). A mechanism for the formation and maintenance of shore-oblique sand ridges on storm-dominated shelves. *Journal of Geophysical Research*, **100**, 16071-16086.

Turner, M. (1988). *Shipwrecks and Salvage in South Africa*. Struik Publishers (Pty) Ltd, Cape Town, 224pp.

Tucker, M.E. (1991). Sedimentary petrology: an introduction to the origin of sedimentary rocks. Blackwell Scientific Publications, London, 260pp.

Tucker M.E. and Wright, V.P. (1990). *Carbonate sedimentology*. Blackwell Scientific Publications, Oxford, 482pp.

Törnqvist, T.E., Bick, S.J., González, J.L., Van der Borg, K. and De Jong, A.F.M. (2004). Tracking the sea-level signature of the 8.2 ka cooling event: new constraints from the Mississippi Delta. *Geophysical Research Letters, 31, L23309. doi: 10.1029/2004GL021429.*

Urick, R.J. (1983). *Principles of Underwater Sound (3rd edition).* McGraw-Hill, New York, 444pp.

Vail, P.R. (1987). Seismic stratigraphy interpretation procedure. *In* Bally, A.W. (Ed), *Atlas of seismic stratigraphy*. Am. Assoc. Petr. Geol., Studies in Geology, **27**, vol. 1, 1-10.

Vail, P.R. and Mitchum, R.M. Jr (1977). Seismic Stratigraphy and global changes in Sea-level, part 1, overview. *In*: Payton, C.E. (Ed), *Seismic Stratigraphy - Applications to Hydrocarbon exploration*. Am. Assoc. Pet. Geol. Memoir, **26**, Boulder, Colorado, 51-52.

Vail, P.R., Mitchum, R.M. Jr and Thompson, S III (1977). Seismic Stratigraphy and global changes in Sea-level, part 3, relative changes of sea-level from coastal onlap. *In*: Payton, C.E. (Ed), *Seismic*

Stratigraphy - Applications to Hydrocarbon exploration. Am. Assoc. Pet. Geol. Memoir, **26**, Boulder, Colorado, 63-72.

Van Ballegooyen, R.C., Valentine, H.R. and Lutjeharms, J.R.E. (1991). Modeling the Agulhas Current system. *South African Journal of Science*, **87**, 569-571.

Van Den Bossche, P. (2006). *A marine geophysical and geological investigation of Robben Island, Cape Town, South Africa*. MSc thesis (unpubl.), University of Southampton, 80pp.

Van Den Bossche, P. and Bosman, C. (2004). Marine Survey Technologies - Development of new side-scan sonar processing software for the Marine Geoscience Unit/Council for Geoscience, as developed by Marine GeoSolutions (Pty) Ltd. *Council for Geoscience Report*, **2004-0039**, 13pp.

Van de Meene, J.W.H., Boersma, J.R. and Terwindt J.H.J. (1996). Sedimentary deposits of combined flow deposits from the shoreface-connected ridge along the central Dutch coast. *Marine Geology*, **131**, 151-175.

Van de Meene, J.W.H. and Van Rijn, L.C. (2000a). The shoreface-connected ridges along the central Dutch coast - part 1: field observations. *Continental Shelf Research*, **20**, 2295-2323.

Van de Meene, J.W.H. and Van Rijn, L.C. (2000b). The shoreface-connected ridges along the central Dutch coast - part 2: morphological modelling. *Continental Shelf Research*, **20**, 2325-2345.

Van Vuuren, C.J., Broad, D.S., Jungslager, E.H.A., Roux, J. and McLachlan, I.R. (1998). Oil and Gas. *In*: Wilson, M.G.C. and Anhaeusser, C.R. (Eds.), *The Mineral Resources of South Africa.* Handbook, Council for Geoscience, **16**, 483-494.

Van Wagoner, J.C., Posamentier, H.W., Mitchum, R.M., Vail, P.R., Sarg, J.F., Loutit, T.S. and Hardenbol, J. (1988). An overview of the fundamentals of sequence stratigraphy and key definitions. *In*: Wilgus, C.K., Hastings, B.S., Kendall, C. G. St. C., Posamentier, H.W., Ross, C.A. and Van Wagoner, J.C. (Eds.), *Sea-level Changes and integrated approach*. Soc. Econ. Pal. Min., Spec. Publ., **42**, 39-45.

Vernekar, A.D. (1972). Long-period global variations of incoming solar radiation. *Meteorological Monograph*, **12**, 34pp.

Viera, M.M and De Ros, L.F. (2006). Cementation patterns and diagenetic implications of Holocene beachrocks from northeastern Brazil. *Sedimentary Geology*, **192**, 207-230.

Visser, D.J.L. (1989). The geology of the Republics of South Africa, Transkei, Bophuthatswana, Venda and Ciskei and the Kingdoms of Lesotho and Swaziland. *Explanation of the 1: 1 000 000 Geological Map, Fourth Edition* (Ed). Geological Survey of South Africa, 491pp.

Visser, D.J.L. (1998). *The geotectonic evolution of South Africa and offshore areas*. Council for Geoscience, 319pp.

Von Veh, M.W. and Andersen, N.J.B. (1990). Normal-slip faulting in the coastal areas of northern Natal and Zululand, South Africa. *South African Journal of Geology*, **93**, 574-582.

Vousdoukas, M.I., Velegrakis, A.F. and Plomaritis, T.A. (2007). Beachrock occurrence, characteristics, formation mechanisms and impacts. *Earth-Science Reviews*, **85**, 23-46.

Waelbroeck, C., Labeyrie, L., Michael, E. Duplessy, J. C., McManus, J. F., Lambeck, K., Balbon, E. and Labracherie, M. (2002). Sea-level and deep water temperature changes derived from benthic foraminifera isotopic records. *Quaternary Science Reviews*, **21**, 295-305.

Waelbroeck, C., Frank, N., Jouzel, J., Parrenin, F., Masson-Delmotte, V. and Genty, D. (2008). Transferring radiometric dating of the last interglacial sea level high stand to marine and ice core records. *Earth and Planetary Science Letters*, **265**, 183-194.

Walker, M.J.C. (2005). *Quaternary Dating Methods*. John Wiley & Sons Ltd., Chichester. 286pp.

Walker, R.G. (1992). Facies, facies models and modern stratigraphic concepts. *In*: Walker R.G. and James, N.P. (Eds.), *Facies models: Response to sea-level change.* Geological Society of Canada, 1-14.

Walker, R.G. and Plint, A.G. (1992). Wave- and storm-dominated shallow marine systems. *In*: Walker R.G. and James, N.P. (Eds.), *Facies models: Response to sea-level change.* Geological Society of Canada, 219-238.

Walsh, J.P., Nittrouer, C.A., Palinkas, C.M., Ogston, A.S., Sternberg, R.W. and Brunskill G.J. (2004). Clinoform mechanics in the Gulf of Papua, New Guinea. *Continental Shelf Research*, **24**, 2487-2510.

Walter, L.M. (1985). Relative reactivity of skeletal carbonates during dissolution: Implications for diagenesis. *In*: Schneidermann, N. and Harris, P.M. (Eds). *Carbonate Cements*. Soc. Sed. Geol. SEPM Spec. Publ. Tulsa, **36**, 3-16.

Watkeys, M.K. and Sokoutis, D. (1998). Transtension in south-eastern Africa with Gondwana break-up. *Geol. Soc. London Spec. Publ*., **135**, 203-214.

Watkeys, M.K. (2002). Development of the Lebombo rifted volcanic margin of southeast Africa. *In*: Menzies, M.A., Klemperer, S.L., Ebinger, C.J. and Baker, J. (Eds.), *Volcanic Rifted Margins*. Geological Society of America Special Paper, **362**, Boulder, Colorado, 27-46.

Watkeys, M.K. (2006). Gondwana break-up: A South African perspective. *In*: Johnson, M. R., Annhauser, C. R. and Thomas, R.J. (Eds.), *The Geology of South Africa*. Joint publication of the Geological Society of South Africa, Johannesburg and the Council for Geoscience, Pretoria, 531-539.

Werner, F. and Newton, R.S. (1975). The Pattern of large-scale bedforms in the Langeland Belt. *Marine Geology*, **19**, 29-59.

Whitaker, F., Smart, P., Hague, Y., Waltham, D. and Bosence, D. (1997). Coupled two-dimensional diagenetic and sedimentological modelling of carbonate platform evolution. *Geology*, **25**, 175-178.

Whittle, G.L., Kendall, C. G. St. C., Dill, R. F. and Rouch, L. (1993). Carbonate cement fabrics displayed: A traverse across the margin of the Bahamas Platform near Lee Stocking Island in the Exhuma Cays. *Marine Geology*, **110**, 213-243.

Wolmarans, L.G. and Du Preez, J.W. (1986). The geology of the St. Lucia area. *Explanation sheet for St. Lucia*. Geological Survey of South Africa, 42pp.

Woodborne, M.W. (1987). *Geology and Holocene evolution of diamondiferous inner-shelf sediments between White Point and Stompneus Bay, North of Kleinzee, Namaqualand*. MSc. thesis (unpubl.), University of Cape Town, 96pp.

Woodborne, S. (2002). Isotope methods and dating methods. QAUDRU course notes. 32pp.

Woodroffe, S.A. and Horton, B.P. (2005). Holocene sea-level changes in the Indo-Pacific. *Journal of Asian Earth Sciences*, **25**, 29-43.

Wright, C.I., Cooper, J.A.G. and Kilburn, R.N. (1999). Mid Holocene palaeoenvironments from Lake Nhlange, northern Kwazulu-Natal, South Africa. *Journal of Coastal Research*, **15**, 991-1001.

Wright, L.D. and Nittrouer, C.A. (1995), Dispersal of river sediments in coastal seas: six contrasting cases. *Estuaries*, **18**, 494-508.

Yang, C.S. (1989). Active, moribund and buried tidal sand ridges in the East China Sea and the Southern Yellow Sea. *Marine Geology*, **88**, 97-116.

Yim, W.W.-S., Huang, G., Fontugne, M.R., Hale, R.E., Paterne, M., Pirazzoli, P.A., Ridley Thomas, W.N. (2006). Postglacial sea-level changes in the northern South China Sea continental shelf: Evidence for a post-8200 calendar yr BP meltwater pulse. *Quaternary International*, **145-146**, 55-67.

Yokoyama, Y., Lambeck, K., De Deckker, P., Johnston, P. and Fifield, L.K. (2000). Timing of the last glacial maximum from observed sea-level minima, **406**, 713-716.

Yokoyama, Y., Esat, T.M. and Lambeck, K. (2001a). Coupled climate and sea-level changes deduced from Huon Peninsula coral terraces of the last ice age. *Earth and Planetary Science Letters*, **193**, 579-587.

Yokoyama, Y., De Deckker, P., Lambeck, K., Johnston, P. and Fifield, L.K. (2001b). Sea-level at the Last Glacial Maximum: evidence from northwestern Australia to constrain ice volumes for oxygen isotope stage 2. *Palaeogeography, Palaeoclimatology, Palaeoecology*, **165**, 281-297.

Zecchin, M. (2010). Towards the standardization of sequence stratigraphy: Is the parasequence concept to be redefined or abandoned? Discussion on “Towards the standardization of sequence stratigraphy” by Catuneanu *et al*. [Earth-Science Reviews, 92, (2009), 1-33]. *Earth-Science Reviews*, **102**, 117-119.

Zecchin, M., Ceramicola, S., Gordini, E., Deponte, M. and Critelli, S. (2011). Cliff overstep model and variability in the geometry of transgressive erosional surfaces in high-gradient shelves: The case of the Ionian Calabrian margin (southern Italy). *Marine Geology*, **281**, 43-58.

Personal Communications

Ms. Haley Cawthra (2009)

Dr. Dai Herbert (2005)

Dr. Peter J. Ramsay (2004; 2009)

Mr. Mike Roberts (2010)

APPENDIX 1

Theoretical background to the geophysical methods used in this study

(Appendix is found on the back cover in digital format)

APPENDIX II

Theoretical background to seismic stratigraphic interpretation principles and procedures

(Appendix is found on the back cover in digital format)

.

APPENDIX III

Reprint of the publication entitled 'The bathymetry of the Aliwal Shoal, Scottburgh, South Africa' by C. Bosman, R. Uken and A.M. Smith (2005)

APPENDIX IV

SCUBA-diving ground-truth metadata and rock sample database

Figure IV.1; GPS diver tracks

Table IV.1; Seafloor rock sample metadata

Table IV.2; Seafloor hand specimen rock sample photographs

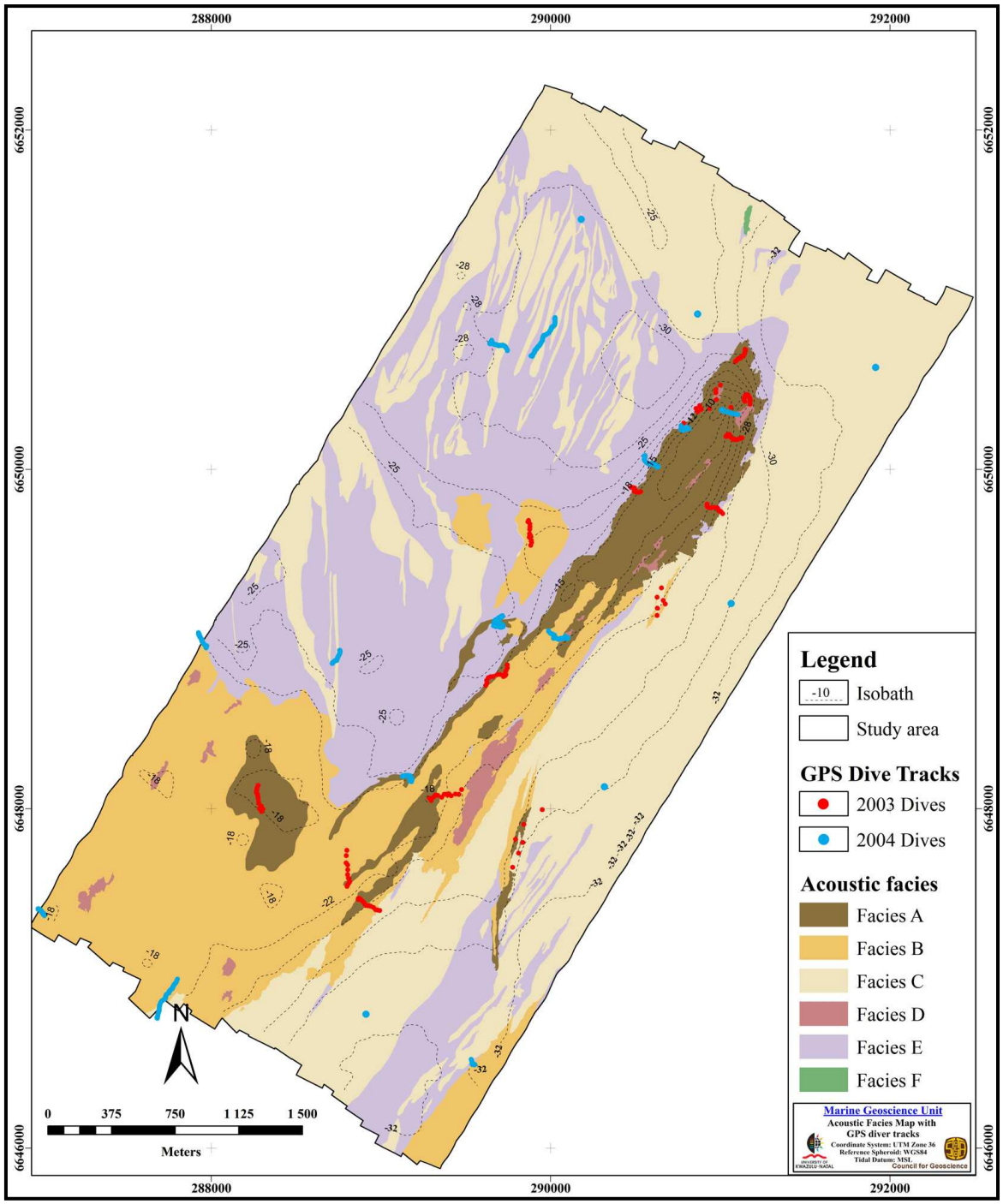

Figure IV.1 GPS diver tracks for the various dive sites visited. Note that all of the identified acoustic facies were sampled.

Table IV.1 Seafloor hand specimen rock sample metadata. OSA = outside survey area. Note that sample 56 does not belong to any aeolianite and beachrock unit as it was sampled as a sediment sample.

Sample	Northings (X)	Eastings (Y)	MSL	Acoustic Facies	Sample	Northings (X)	Eastings (Y)	MSL	Acoustic Facies
1	6650348	290877	-15	A	**36**	6649868	290497	-16	A
2	6650208	291037	-18	A	**37**	6649859	290504	-13	A
3	6650187	291125	-26	A	**38**	6649862	290516	-13	A
4	6650427	291149	-14	A	**39**	6649864	290523	-12	A
5	6648107	288261	-14	A	**40**	6649861	290525	-12	A
6	6648089	288270	-17	A	**41**	6650707	291149	-29	A
7	6647995	288304	-18	A	**42**	6650662	291123	-27	A
8	6647558	288811	-20	A	**43**	6650643	291097	-22	A
9	6647563	288813	-21	A	**44**	6647404	288989	-25	B
10	6649228	290663	-26	B	**45**	6647434	288908	-24	A
11	6649234	290653	-25	B	**46**	6647466	288881	-24	A
12	6649243	290626	-24	B	**47**	6647466	288866	-22	A
13	6649246	290634	-24	B	**48**	6650350	291007	-4	A
14	6648740	289634	-19	A	**49**	6649006	290100	-18	A
15	6648778	289741	-19	B	**50**	6649003	290056	-17	A
16	6648791	289744	-20	B	**51**	6649012	290022	-19	B
17	6647784	289821	-30	A	**52**	6646491	289546	-32	B
18	6647768	289801	-29	A	**53**	6648164	289172	-18	A
19	6647770	289790	-27	A	**54**	6650246	290770	-21	A
20	6649583	289887	-21	B	**55**	6650231	290782	-15	A
21	6649607	289883	-23	B	**56***	6648870	288725	-26	B
22	6649619	289878	-23	B	**57**	6648171	289171	-23	A
23	6649643	289876	-24	B	**58**	6648189	289124	-20	A
24	6649691	289867	-23	B	**60**	6646919	287753	-21	B
25	6648072	289311	-17	A	**61**	6646902	287732	-22	B
26	6648074	289350	-21	B	**62**	6646766	287680	-25	B
27	6648075	289412	-22	B	**63**	6650038	290601	-21	A
28	6648086	289444	-24	B	**64**	6650034	290613	-17	A
29	6649755	290993	-28	A	**65**	6650015	290630	-13	A
30	6649773	290983	-25	A	**66**	6649034	287925	-26	OSA
31	6649776	290953	-23	A	**67**	6648952	287969	-23	B
32	6649788	290920	-22	A	**71**	6649112	289692	-25	A
33	6649809	290900	-17	A	**72**	6647375	287009	-18	B
34	6649890	290479	-22	A	**73**	6649076	289675	-23	A
35	6649888	290502	-18	A					

Table IV.2 Photograph images of the hand specimen rock samples obtained from the study area. Photographs for samples 52, 54-56, 60-62, 72 not available.


SAMPLE 25


SAMPLE 26


SAMPLE 27


SAMPLE 28


SAMPLE 29


SAMPLE 30


SAMPLE 31


SAMPLE 32


SAMPLE 33


SAMPLE 34


SAMPLE 35


SAMPLE 36


SAMPLE 37


SAMPLE 38


SAMPLE 39


SAMPLE 40


SAMPLE 41


SAMPLE 42


SAMPLE 43


SAMPLE 44


SAMPLE 45


SAMPLE 46


SAMPLE 47


AS48
1 cm
Marine Geoscience
Unit, Durban


49
1 cm
Marine Geoscience Unit, Durban


50
1 cm
Marine Geoscience Unit, Durban


51
1 cm
Marine Geoscience Unit, Durban


1 cm
Marine Geoscience Unit, Durban
53


57
1 cm


58
1 cm
Marine Geoscience Unit, Durban


63
1 cm
Marine Geoscience Unit, Durban


64
1 cm
Marine Geoscience Unit, Durban


65
1 cm
Marine Geoscience Unit, Durban


Aliwal
66


67
67


71
1 cm
Marine Geoscience Unit, Durban


1 cm
Marine Geoscience Unit, Durban
73

APPENDIX V

Textural and compositional data for aeolianite units A1 to A3

Table V.1; Grain Size distribution data for Unit A1

Table V.2; Grain Size distribution data for Unit A2

Table V.3; Grain Size distribution data for Unit A3

Table V.4; Mineralogical composition data for Unit A1

Table V.5; Mineralogical composition data for Unit A2

Table V.6; Mineralogical composition data for Unit A3

Table V.1 Grain size distribution data for the aeolianite samples of Unit A1. vcS = very coarse sand, cS = coarse sand, mS = medium sand, fS = fine sand, vfS = very fine sand, Wentworth = Udden-Wentworth classification scale, Ws = well sorted, mWs = moderately well sorted, Ms = moderately sorted, sfs = strongly fine-skewed, fs = fine-skewed, ns = near-symmetrical, cs = coarse-skewed, scs = strongly coarse-skewed, AVG = average for all the samples, N/A = not available.

Sample	% Gravel	% vcS	% cS	% mS	% fS	% vfS	% mud	Mean (phi)	Went-worth	Mean (mm)	Median (phi)	Median (mm)	Sorting		Skewness	
Upper Unit A1																
2	0.00	0.24	15.45	63.16	18.13	2.92	0.10	1.58	mS	0.33	1.46	0.36	0.66	mWs	0.90	sfs
4	0.00	0.18	4.17	72.35	21.06	2.21	0.04	1.75	mS	0.30	1.70	0.31	0.57	mWs	0.55	sfs
48	0.00	0.10	4.12	48.17	46.34	1.01	0.26	2.08	fS	0.24	1.97	0.25	0.55	mWs	0.22	fs
GC-4	0.00	0.67	6.43	64.42	26.22	2.21	0.05	1.79	mS	0.29	1.73	0.30	0.65	mWs	0.31	sfs
Average	*0*	*0*	*8*	*62*	*28*	*2*	*0*	*1.80*	*mS*	*0.29*	*1.71*	*0.31*	*0.61*	*mWs*	*0.50*	*sfs*
Lower Unit A1																
1	0.00	0.15	9.88	66.47	18.56	4.79	0.15	1.71	mS	0.30	1.64	0.32	0.67	mWs	0.64	sfs
3	N/A													N/A	N/A	N/A
29	0.00	0.38	24.09	62.42	12.19	0.76	0.17	1.40	mS	0.38	1.47	0.36	0.63	mWs	0.08	ns
30	0.00	0.13	19.28	65.89	13.79	0.73	0.17	1.48	mS	0.36	1.55	0.34	0.59	mWs	0.07	ns
31	0.00	0.17	1.09	76.55	19.04	2.75	0.40	1.82	mS	0.28	1.76	0.30	0.51	mWs	0.53	sfs
32	0.00	0.00	4.99	64.56	29.71	0.73	0.00	1.90	mS	0.27	1.81	0.29	0.55	mWs	0.37	sfs
33	0.00	0.25	3.98	63.07	29.88	2.24	0.58	1.94	mS	0.26	1.83	0.28	0.57	mWs	0.48	sfs
34	0.00	0.00	1.11	67.82	29.86	0.95	0.26	1.97	mS	0.25	1.85	0.28	0.47	Ws	0.55	sfs
35	0.00	0.00	0.14	50.00	48.45	1.14	0.27	2.11	fS	0.23	2.00	0.25	0.48	Ws	0.49	sfs
36	0.00	0.23	16.23	72.62	9.75	0.93	0.23	1.45	mS	0.37	1.44	0.37	0.54	mWs	0.33	sfs
37	0.00	0.14	23.10	61.09	14.86	0.60	0.22	1.45	mS	0.37	1.53	0.35	0.62	mWs	0.09	ns
38	0.00	1.66	13.82	48.34	34.42	1.39	0.37	1.81	mS	0.29	1.81	0.28	0.78	Ms	-0.53	scs
39	0.00	0.86	19.50	51.94	25.68	2.01	0.00	1.65	mS	0.32	1.66	0.32	0.79	Ms	-0.16	cs
40	0.00	0.42	7.04	51.74	38.38	2.05	0.36	1.93	mS	0.26	1.87	0.27	0.67	mWs	0.07	ns
41	0.00	0.02	4.19	42.09	51.64	1.76	0.30	2.10	fS	0.23	2.07	0.24	0.60	mWs	-0.10	ns
42	0.00	0.55	6.00	45.62	45.23	2.31	0.30	2.02	fS	0.25	1.97	0.26	0.65	mWs	-0.11	cs
43	0.00	9.71	46.65	37.27	4.13	1.84	0.39	0.91	cS	0.53	0.85	0.55	0.80	Ms	0.61	sfs
54	0.00	0.26	32.44	46.58	18.88	1.54	0.29	1.42	mS	0.37	1.37	0.39	0.80	Ms	0.52	sfs
55	0.00	0.81	54.14	38.96	5.99	0.09	0.00	1.00	cS/mS	0.50	0.91	0.53	0.69	mWs	0.64	sfs
63	0.00	1.21	4.47	58.96	32.36	2.62	0.37	1.89	mS	0.27	1.82	0.28	0.64	mWs	0.36	sfs
64	0.00	0.21	6.25	69.67	22.66	0.92	0.28	1.77	mS	0.29	1.74	0.30	0.58	mWs	0.29	fs
65	0.10	0.20	1.94	59.17	36.26	2.21	0.12	1.94	mS	0.26	1.86	0.28	0.60	mWs	0.43	sfs

GC-5	0.00	4.70	38.92	48.20	7.35	0.84	0.00	1.10	mS	0.47	1.13	0.46	0.74	Ms	0.16	fs
Average	*0*	*1*	*15*	*57*	*25*	*2*	*0*	*1.67*	*mS*	*0.32*	*1.63*	*0.33*	*0.64*	*mWs*	*0.26*	*fs*
AVG	***0***	***1***	***11***	***59***	***26***	***2***	***0***	***1.74***	***mS***	***0.31***	***1.67***	***0.32***	***0.62***	***mWs***	***0.38***	***sfs***

Table V.2 Grain size distribution data for the aeolianite samples of Unit A2. vcS = very coarse sand, cS = coarse sand, mS = medium sand, fS = fine sand, vfS = very fine sand, Wentworth = Udden-Wentworth classification scale, Ws = well sorted, mWs = moderately well sorted, Ms = moderately sorted, sfs = strongly fine-skewed, fs = fine-skewed, ns = near-symmetrical, cs = coarse-skewed, scs = strongly coarse-skewed, AVG = average for all the samples.

Sample	% Gravel	% vcS	% cS	% mS	% fS	% vfS	% mud	Mean (phi)	Went-worth	Mean (mm)	Median (phi)	Median (mm)	Sorting		Skewness	
Southern Parabolic Aeolinaite (SPA)																
8	0.12	4.67	30.51	52.96	10.55	0.82	0.37	1.25	mS	0.42	1.27	0.41	0.74	Ms	0.09	ns
25	0.00	0.71	15.94	63.28	15.64	3.31	1.13	1.62	mS	0.33	1.61	0.33	0.69	mWs	0.35	sfs
45	0.00	0.00	38.96	53.25	6.70	0.73	0.36	1.20	mS	0.43	1.16	0.45	0.56	mWs	0.67	sfs
46	0.00	0.58	77.45	20.25	1.40	0.25	0.07	0.59	cS	0.67	0.42	0.75	0.53	mWs	1.08	sfs
47	0.00	0.37	40.84	54.12	3.41	1.17	0.09	1.11	mS	0.46	1.11	0.46	0.48	Ws	0.14	fs
57	0.00	0.00	13.28	56.57	28.67	0.97	0.50	1.77	mS	0.29	1.73	0.30	0.69	mWs	0.14	fs
Average	*0.02*	*1.06*	*36.16*	*50.07*	*11.06*	*1.21*	*0.42*	*1.26*	*mS*	*0.43*	*1.22*	*0.45*	*0.62*	*mWs*	*0.41*	*sfs*
Northern Parabolic Aeolianite (NPA) North-western member																
20	0.00	0.14	29.25	57.94	12.04	0.62	0.00	1.33	mS	0.40	1.30	0.41	0.61	mWs	0.65	sfs
21	0.01	8.88	54.25	25.81	10.80	0.24	0.01	0.88	cS	0.54	0.75	0.59	0.83	Ms	1.47	sfs
22	0.00	0.07	0.20	2.09	73.36	24.01	0.27	2.66	fS	0.16	2.76	0.15	0.17	vWs	0.27	cs
23	0.00	0.00	0.42	1.41	89.67	8.13	0.37	2.54	fS	0.17	2.54	0.17	0.30	Ws	0.10	ns
24	0.00	0.13	0.53	2.11	88.42	8.48	0.33	2.53	fS	0.17	2.53	0.17	0.30	Ws	0.10	ns
Average	*0.00*	*1.84*	*16.93*	*17.87*	*54.86*	*8.30*	*0.20*	*1.99*	*mS*	*0.29*	*1.98*	*0.30*	*0.44*	*Ws*	*0.33*	*sfs*
NPA North-eastern member																
50	0.02	1.72	32.08	53.13	10.87	1.94	0.24	1.27	mS	0.41	1.26	0.42	0.71	mWs	0.57	sfs
51	0.00	0.66	29.18	48.29	19.78	1.85	0.23	1.44	mS	0.37	1.33	0.40	0.78	Ms	0.95	sfs
Average	*0.01*	*1.19*	*30.63*	*50.71*	*15.33*	*1.89*	*0.24*	*1.36*	*mS*	*0.39*	*1.29*	*0.41*	*0.74*	*Ms*	*0.76*	*sfs*
Bosmans Reef																
71	0.00	0.09	7.90	51.97	36.35	3.52	0.17	1.95	mS	0.26	1.87	0.27	0.67	mWs	0.15	fs
73	0.00	0.00	16.10	72.56	10.76	0.58	0.00	1.46	mS	0.36	1.46	0.36	0.53	mWs	0.30	fs
GC-6	0.00	0.00	39.94	58.26	1.30	0.50	0.00	1.13	mS	0.46	1.12	0.46	0.44	Ws	0.14	fs
Average	*0.00*	*0.03*	*21.31*	*60.93*	*16.14*	*1.54*	*0.06*	*1.52*	*mS*	*0.36*	*1.49*	*0.36*	*0.55*	*mWs*	*0.20*	*fs*

AVG	***0.01***	***1.03***	***26.26***	***44.90***	***24.35***	***3.23***	***0.23***	***1.53***	***mS***	***0.37***	***1.49***	***0.38***	***0.59***	***mWs***	***0.42***	***sfs***

Table V.3 Grain size distribution data for the aeolianite samples of Unit A3. vcS = very coarse sand, cS = coarse sand, mS = medium sand, fS = fine sand, vfS = very fine sand, Wentworth = Udden-Wentworth classification scale, Ws = well sorted, mWs = moderately well sorted, Ms = moderately sorted, sfs = strongly fine-skewed, fs = fine-skewed, ns = near-symmetrical, cs = coarse-skewed, scs = strongly coarse-skewed, AVG = average for all the samples.

Sample	% Gravel	% vcS	% cS	% mS	% fS	% vfS	% mud	Mean (phi)	Went-worth	Mean (mm)	Median (phi)	Median (mm)	Sorting		Skewness	
5	0.00	13.50	35.09	23.60	26.22	1.48	0.12	1.20	mS	0.44	1.08	0.47	1.08	Ps	0.99	sfs
6	0.00	0.02	1.17	42.88	54.09	1.85	0.00	2.14	fS	0.23	2.11	0.23	0.55	mWs	-0.01	ns
7	0.11	0.63	14.08	59.59	24.40	1.06	0.13	1.68	mS	0.31	1.63	0.32	0.69	mWs	0.25	fs
66	0.07	1.41	10.77	44.53	41.76	1.46	0.00	1.90	mS	0.27	1.89	0.27	0.73	Ms	-0.36	scs
67	7.15	15.20	28.53	37.23	11.27	0.61	0.00	0.84	cS	0.56	0.97	0.51	1.10	Ps	-1.04	scs
72	0.00	0.02	4.55	57.52	36.11	1.70	0.11	1.88	mS	0.27	1.82	0.28	0.63	mWs	0.42	sfs
GC-7	0.00	0.89	18.22	41.98	36.55	2.03	0.33	1.77	mS	0.29	1.80	0.29	0.82	Ms	-0.45	scs
Avg.	**1**	**5**	**16**	**44**	**33**	**1**	**0**	**1.63**	**mS**	**0.34**	**1.61**	**0.34**	**0.80**	**Ms**	**-0.03**	ns

Table V.4 Mineralogical and compositional data for Unit A1. Roundness after Pettijohn *et al*. (1973) where A = angular; sA = subangular; R = rounded; sR = subrounded; wR = well-rounded. Microscopic facies after Frébourg *et al*. (2008) where H = Heterogeneous, L = Laminated, Lig = Laminated inversely graded, Ldl = Laminated discreet laminae, Lbl = Laminated bimodal coarse/finer grained laminae, Lci = Laminated coarser isolated layers in heterogeneous sediments. Porosity classification after Choquette and Pray (1970) and where * equals; BP = Primary Interparticle, crP = cement-reduced Primary. Cementation factor is calculated by dividing the carbonate content of the sample by the bioclastic component, a high ratio indicates a large percentage of the carbonate in the sample is cement, conversely a low percentage indicates a lower cement percentage but a higher skeletal carbonate percentage. n = number of grains counted, V.E. = visual estimation.

Sample	Depth (m)	Round-ness	Micro-scopic Facies	Mineralogy (%)						Porosity				$CaCO_3$ Content	Cementation Factor
				Quartz	Feldspar	Lithics	Heavy Minerals	Bioclastic Components	n	Type*	%	Type*	%		
Upper Unit A1															
2	-18	R-sR	Ldl	46	5	2	3	46	394	BP	20-30	crP	5-10	72	1.6
4	-14	R-sA	H	55	2	3	2	38	216	BP	20-30	crP	5-10	49	1.3
48	-4	R-sR	Ldl	53	4	3	1	39	307	BP	<15	crP	5	50	1.3
GC-4	-15	R-sA	H (L)	47	3	1	3	46	674	BP	25-	crP	10-	70	1.5

											30		15		
Average		-	-	*50*	*3*	*2*	*2*	*42*	*398*	-	-	-	-	*60*	*1.4*
Lower Unit A1															
GC-5	-30	R-sA	H	66	3	3	1	27	457	BP	25-35	crP	5-10	73	2.7
1	-15	R-sA	H - Lci	66	2	1	2	29	259	BP	>30	crP	5-10	53	1.8
3	-26	R-sR	H	45	2	3	2	49	440	BP	>30	crP	10-15	N/A	N/A
29	-28	R-A	Ldl	63	4	2	2	29	235	BP	>30	crP	15-20	67	2.3
30	-25	R-A	Lbl	66	3	2	1	27	212	BP	>25	crP	5-10	51	1.9
31	-23	R-sR	Ldl	54	4	2	2	39	256	BP	>25	crP	5-15	54	1.4
32	-22	R-sA	H	58	2	3	2	36	292	BP	>15	crP	5-10	55	1.6
33	-17	R-sA	H	53	5	4	2	36	242	BP	>30	crP	5-7	62	1.7
34	-22	R-sR	Ldl	63	3	2	1	30	257	BP	>30	crP	10-15	45	1.5
35	-18	R-sR	H (L)	62	4	2	2	30	285	BP	20	crP	5-10	59	1.9
36	-16	R-sR	H	63	3	2	3	30	279	BP	25-30	crP	10-15	51	1.7
37	-13.5	R-sA	Lci	57	3	3	1	35	202	BP	25-30	crP	5-8	51	1.5
38	-13	R-A	H	66	6	2	3	23	246	BP	>35	crP	15-20	60	2.6
39	-12	R-sA	H	58	2	2	2	37	261	BP	25-30	crP	5	62	1.7
40	-12	R-sA	H	60	3	2	1	34	301	BP	25-35	crP	5	60	1.8
41	-29	R-sA	Lbl	57	3	1	0	39	297	BP	25->30	crP	5-10	58	1.5
42	-27	R-sA	H-L	55	5	2	3	36	433	BP	25->30	crP	15-20	56	1.5
43	-22	R-A	H	41	4	8	1	46	270	BP	>40	crP	10-15	70	1.5
54	-21	R-sA	Lbl	52	6	7	6	30	284	BP	25-35	crP	5	49	1.7
55	-15	R-sA	Lbl	48	3	1	2	46	358	BP	25-35	crP	5-10	40	0.9
63	-21	R-sA	Lbl	57	4	1	2	36	281	BP	20-	crP	5	60	1.7

											30				
64	-17	R-sA	H-L	58	3	2	2	35	345	BP	25-35	crP	10-15	51	1.5
65	-13	***Thin section not available***												61	-
Average		-	-	*57*	*3*	*2*	*2*	*35*	*315*	-	-	-	-	*57*	*1.7*
Overall Average			**-**	***54***	***3***	***2***	***2***	***39***	***356***	**-**	**-**	**-**	**-**	***59***	***2***

Table V.5 Mineralogical and compositional data for Unit A2. Roundness after Pettijohn *et al*. (1973) where A = angular; sA = subangular; R = rounded; sR = subrounded; wR = well-rounded. Microscopic facies after Frébourg *et al*. (2008) where H = Heterogeneous, L = Laminated, Lig = Laminated inversely graded, Ldl = Laminated discreet laminae, Lbl = Laminated bimodal coarse/finer grained laminae, Lci = Laminated coarser isolated layers in heterogeneous sediments. Porosity classification after Choquette and Pray (1970) and where * equals; BP = Primary Interparticle, crP = cement-reduced Primary. Cementation factor is calculated by dividing the carbonate content of the sample by the bioclastic component, a high ratio indicates a large percentage of the carbonate in the sample is cement, conversely a low percentage indicates a lower cement percentage but a higher skeletal carbonate percentage. n = number of grains counted, V.E. = visual estimate.

Sample	**Depth (m)**	**Round-ness**	**Micro-scopic Facies**	**Mineralogy (%)**						**Porosity**				**$CaCO_3$ Content**	**Cementation Factor**
				Quartz	**Feldspar**	**Lithics**	**Heavy Minerals**	**Bioclastic Components**	**n**	**Type***	**%**	**Type***	**%**		
Southern Parabolic Aeolinaite (SPA)															
8	20	R-sA	H	61	13	6	4	16	160	BP	20-30	crP	<5	60	3.8
25	17	sR-sA	Ldl	63	14	4	4	15	V.E.	BP	10-20	crP	<2	51	3.4
45	24	sR-A	H	59	22	8	1	10	V.E.	BP	20-30	crP	10-15	48	4.8
46	24	R-sA	H	67	13	7	1	12	V.E.	BP	30-40	crP	3-5	40	3.3
47	22	***Thin section not available***												58	-
57	23	sR-A	Lci	56	12	8	4	20	110	BP	30-40	crP	10-15	44	2.2
Average	-	-	-	*61*	*15*	*7*	*3*	*15*	-	-	-	-	-	*49*	*4*
Northern Parabolic Aeolianite (NPA) North-western member															
20	21	R-sA	H	63	13	5	0	19	106	BP	20-30	crP	5-10	58	3.1
21	23	R-sA	Ldl	60	15	6	1	18	V.E.	BP	20-30	crP	5-10	40	2.2
22	23	R-A	Ldl	47	10	4	6	33	76	BP	20-25	crP	5-10	55	1.7
23	24	R-A	Ldl	45	12	4	5	34	V.E.	BP	20-30	crP	5-	63	1.8

													10		
24	23	R-A	Ldl	55	15	5	5	20	V.E.	BP	30-40	crP	10-15	54	2.7
Average	-	-	-	*54*	*13*	*5*	*3*	*25*	-	-	-	-	-	*54*	*2*
NPA North-eastern member															
50	17	sR-sA	H	53	15	2	6	24	V.E.	BP	20-30	crP	10-15	52	2.1
51	19	sR-A	Lci	58	18	3	6	15	210	BP	30-40	crP	15-20	48	3.2
Average	-	-	-	*56*	*17*	*3*	*6*	*20*	-	-	-	-	-	*50*	2.6
Bosmans Reef															
71	25	sR-sA	Ldl	65	15	4	6	10	V.E.	BP	25-35	crP	10-15	61	6.1
73	23	sR-sA	Ldl	60	15	2	8	15	V.E.	BP	30-40	crP	15	41	2.7
GC-6	26	sR-sA	Ldl	76	7	8	2	8	440	BP	30-40	crP	10-15	47	6.0
Average	-	-	-	*67*	*12*	*5*	*5*	*11*	-	-	-	-	-	*50*	*5*
Overall Average			**-**	***59***	***14***	***5***	***4***	***17***	**-**	**-**	**-**	**-**	**-**	***51***	***3***

Table V.6 Mineralogical and compositional data for Unit A3. Roundness after Pettijohn *et al*. (1973) where A = angular; sA = subangular; R = rounded; sR = subrounded; wR = well-rounded. Microscopic facies after Frébourg *et al*. (2008) where H = Heterogeneous, L = Laminated, Lig = Laminated inversely graded, Ldl = Laminated discreet laminae, Lbl = Laminated bimodal coarse/finer grained laminae, Lci = Laminated coarser isolated layers in heterogeneous sediments. Porosity classification after Choquette and Pray (1970) and where * equals; BP = Primary Interparticle, crP = cement-reduced Primary. Cementation factor is calculated by dividing the carbonate content of the sample by the bioclastic component, a high ratio indicates a large percentage of the carbonate in the sample is cement, conversely a low percentage indicates a lower cement percentage but a higher skeletal carbonate percentage. n = number of grains counted, V.E. = visual estimate.

Sample	**Depth (m)**	**Round-ness**	**Micro-scopic Facies**	**Mineralogy (%)**						**Porosity**				**$CaCO_3$ Content**	**Cementation Factor**
				Quartz	**Feldspar**	**Lithics**	**Heavy Minerals**	**Bioclastic Components**	**n**	**Type***	**%**	**Type***	**%**		
5	14	sR-sA	Lbl	55	24	1	10	10	V.E.	BP	30-40	crP	5	49	4.9
6	17	sR-sA	H	64	10	2	4	20	110	BP	20-30	crP	5-10	50	2.5
7	18	sR-sA	H	58	20	2	8	12	V.E.	BP	20-30	crP	5-10	43	3.6
66	26	sR-sA	H	55	25	4	6	10	V.E.	BP	20-	crP	5-	35	3.5

											30		10		
67	23	sR-sA	H	60	20	2	5	13	V.E.	BP	30-40	crP	5	47	3.6
72	18	sR-sA	H	54	26	1	5	14	V.E.	BP	20-30	crP	<5	47	3.3
GC-7	16	sR-sA	H	62	20	1	3	14	455	BP	20-30	crP	10-15	53	3.8
Average		**-**	**-**	***58***	***21***	***2***	***6***	***13***	**-**	**-**	**-**	**-**	**-**	***46***	***4***

APPENDIX VI

$MgCO_3$ mole percentage of the marine cement phases in the GC-series samples: calculation method and results

VI.1 METHOD AND RESULTS

The calculation is required to convert oxides (results from SEM-EDX analyses) into carbonates. The method is standard practise in SEM-EDX analyses and was suggested by Dr James Westley-Smith of the Electron Microscope Unit at the University of KwaZulu-Natal.

This is achieved by converting the oxide mass percentage by using the molar mass factor (MMF). The MMF is calculated by taking the following ratios:

MgCO3/MgO = 2.092

CaCO3/CaO = 1.785

1. Multiplying these factors with the oxide mass percent will yield the mass percent of carbonate. The remaining oxides were not calculated as they are trace amounts.
2. Take the sum of the mass percentage for all the components (converted and other) and use this value to normalize the results.

The results are presented in Table VI.1 below.

Table VI.1 Results of the calculation of the mole % $MgCO_3$ (bold) of the marine phase cement in the GC-series samples. * = obtained from SEM-EDX analyses.

Sample ID	MgO*	$MgCO_3$	Normalised Mole% $MgCO_3$	CaO*	$CaCO_3$	Normalised $CaCO_3$
Aeolianites						
GC4_Ox	7.03	14.71	**8.3**	90.58	161.69	91.662
GC5_Ox	10.10	21.13	**13.6**	75.52	134.80	86.450
GC6_Ox	17.33	36.25	**21.8**	73.00	130.31	78.233
GC7_Ox	8.37	17.51	**10.2**	86.29	154.03	89.792
Beachrocks						
GC1_Ox	0.09	0.19	**0.1**	96.83	172.84	99.891
GC1b_Ox	0.09	0.19	**0.1**	94.34	168.40	99.888
GC2_Ox	8.94	18.70	**12.5**	73.05	130.39	87.456
GC3_Ox	4.52	6.34	**5.3**	94.70	169.04	94.702
GC9_Ox	8.48	17.74	**10.1**	88.63	158.20	89.917
GC10_Ox	10.11	21.15	**12.7**	81.50	145.48	87.307

Graphical representations of the chemical spectra of the marine phase cements are presented in Figures VI.1. Note that the Y-axis (amount of counts) is not the same for the various spectral images and hence the height of the elemental peak is relative and not a direct measure for comparison between images.

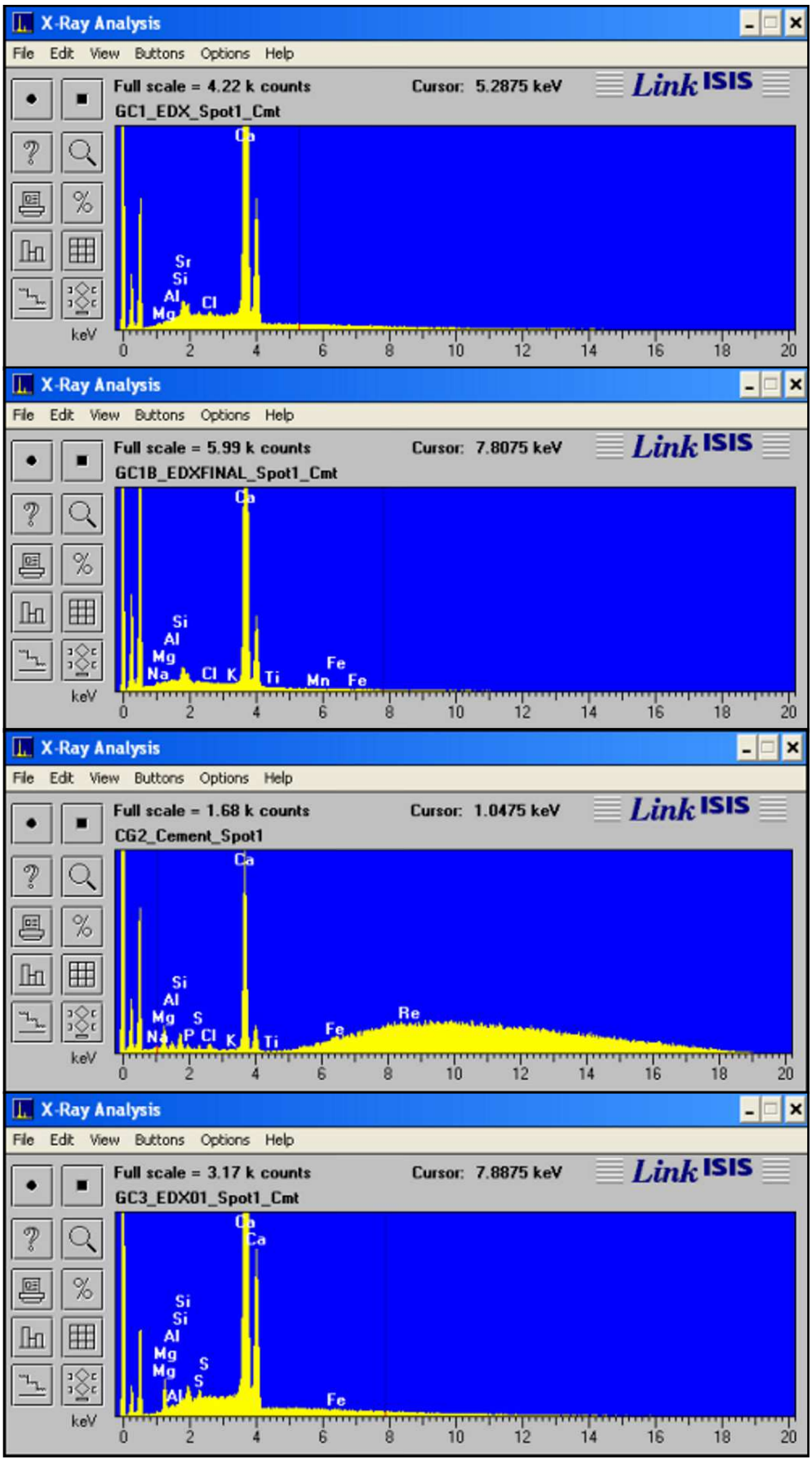
X-Ray Analysis
File Edit View Buttons Options Help
Full scale = 4.22 k counts
Cursor: 5.2875 keV
Link ISIS
GC1_EDX_Spot1_Cmt
Ca
Sr
Si
Al
Mg
Cl
keV
0 2 4 6 8 10 12 14 16 18 20
X-Ray Analysis
File Edit View Buttons Options Help
Full scale = 5.99 k counts
Cursor: 7.8075 keV
Link ISIS
GC1B_EDXFINAL_Spot1_Cmt
Ca
Si
Al
Mg
Na
Cl
K
Ti
Mn
Fe
Fe
keV
0 2 4 6 8 10 12 14 16 18 20
X-Ray Analysis
File Edit View Buttons Options Help
Full scale = 1.68 k counts
Cursor: 1.0475 keV
Link ISIS
CG2_Cement_Spot1
Ca
Si
Al
Mg
Na
S
P
Cl
K
Ti
Fe
Re
keV
0 2 4 6 8 10 12 14 16 18 20
X-Ray Analysis
File Edit View Buttons Options Help
Full scale = 3.17 k counts
Cursor: 7.8875 keV
Link ISIS
GC3_EDX01_Spot1_Cmt
Ca
Ca
Si
Si
Al
Mg
Mg
S
S
Al
Fe
keV
0 2 4 6 8 10 12 14 16 18 20

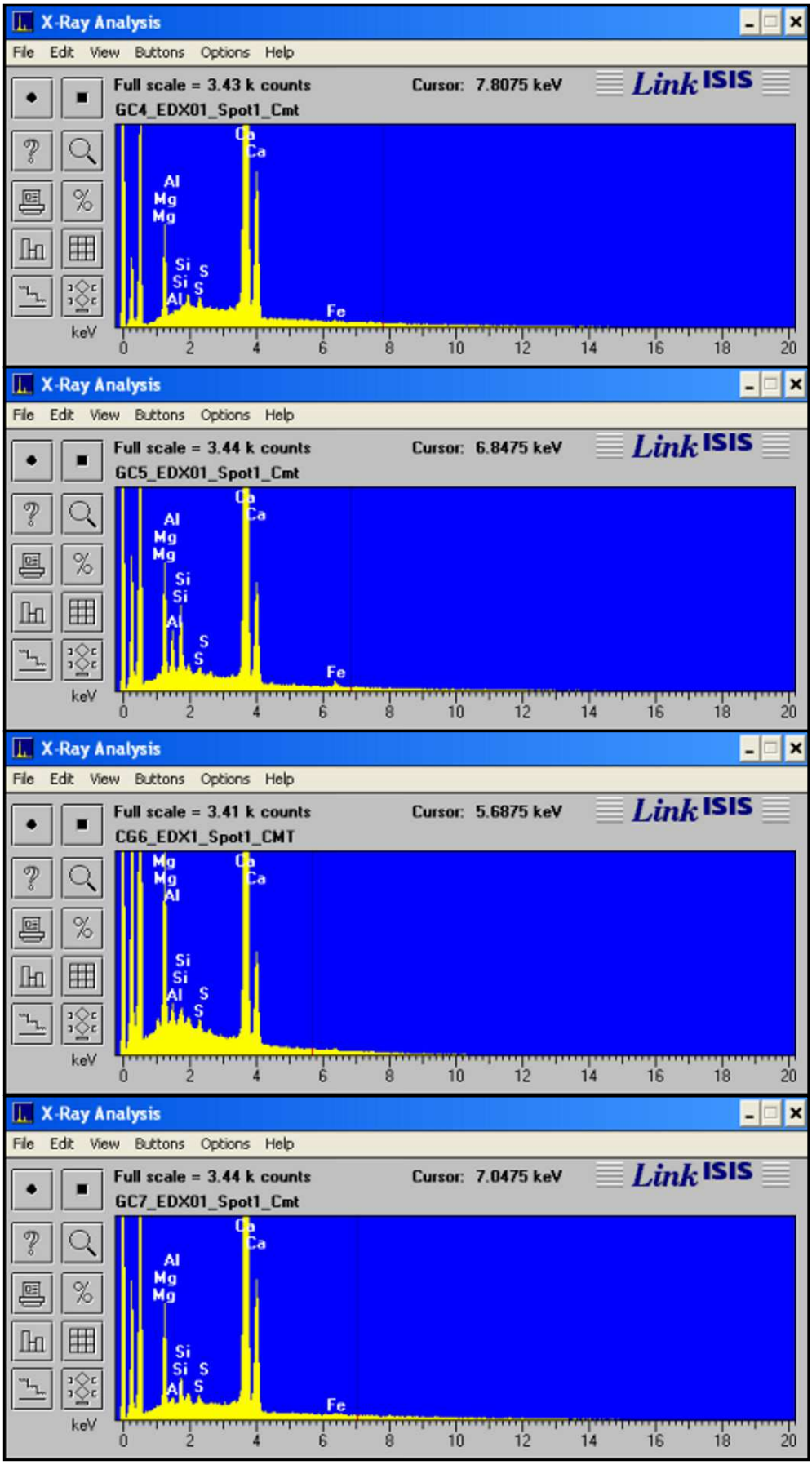
X-Ray Analysis
File Edit View Buttons Options Help
Full scale = 3.43 k counts
Cursor: 7.8075 keV
GC4_EDX01_Spot1_Cmt
Link ISIS
Ca
Al
Mg
Mg
Si
Si
S
S
Al
Fe
keV
0 2 4 6 8 10 12 14 16 18 20
X-Ray Analysis
File Edit View Buttons Options Help
Full scale = 3.44 k counts
Cursor: 6.8475 keV
GC5_EDX01_Spot1_Cmt
Link ISIS
Ca
Al
Mg
Mg
Si
Si
Al
S
S
Fe
keV
0 2 4 6 8 10 12 14 16 18 20
X-Ray Analysis
File Edit View Buttons Options Help
Full scale = 3.41 k counts
Cursor: 5.6875 keV
CG6_EDX1_Spot1_CMT
Link ISIS
Mg
Mg
Al
Ca
Si
Si
Al
S
S
keV
0 2 4 6 8 10 12 14 16 18 20
X-Ray Analysis
File Edit View Buttons Options Help
Full scale = 3.44 k counts
Cursor: 7.0475 keV
GC7_EDX01_Spot1_Cmt
Link ISIS
Ca
Al
Mg
Mg
Si
Si
Al
S
S
Fe
keV
0 2 4 6 8 10 12 14 16 18 20

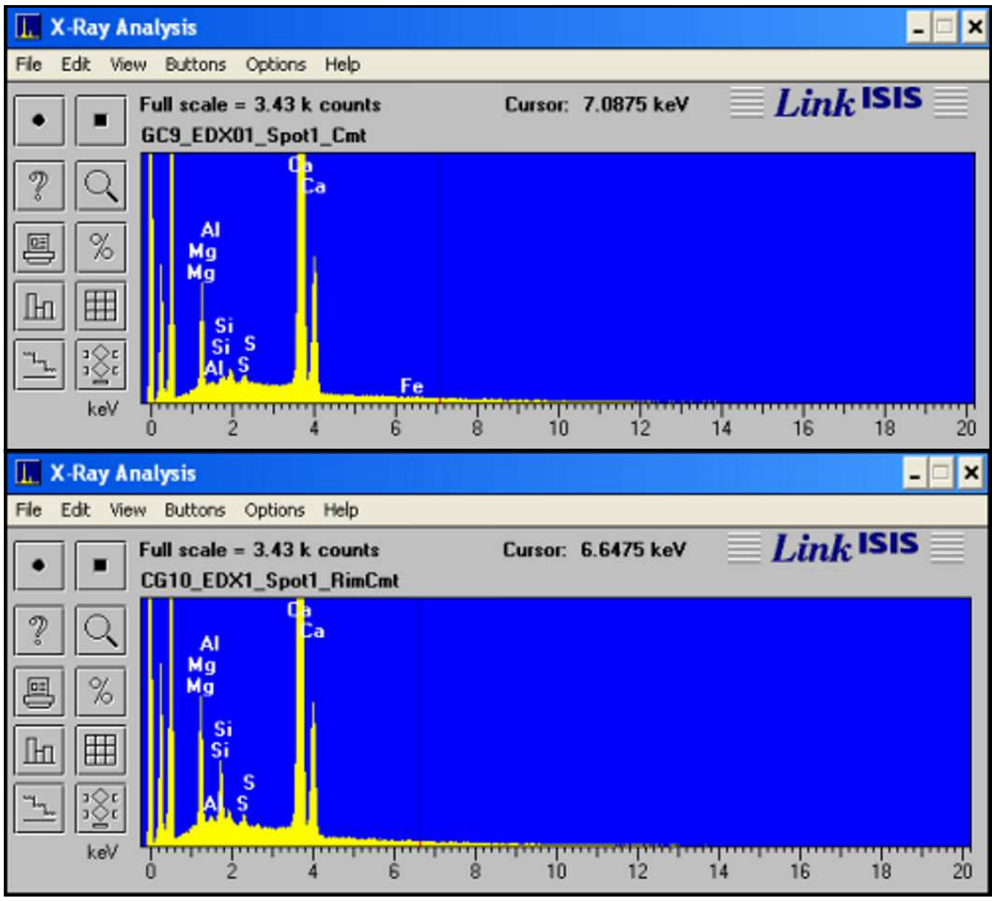

Figure VI.1 SEM (EDX) results for the marine cement phases in the GC-Series samples. For applicable sample numbers refer to the top left of each spectral graph. The Y-axis scale or number of counts are also indicated in the top left of the image.

APPENDIX VII

Textural and compositional data for beachrock units B1 to B5

Table VII.1; Grain Size distribution data for Units B1 to B5

Table VII.2; Mineralogical composition data for Units B1 to B5

Table VII.1 Grain size distribution data for all the beachrock samples. vcS = very coarse sand, cS = coarse sand, mS = medium sand, fS = fine sand, vfS = very fine sand, Wentworth = Udden-Wentworth classification scale, Ws = well sorted, mWs = moderately well sorted, Ms = moderately sorted, sfs = strongly fine-skewed, fs = fine-skewed, ns = near-symmetrical, cs = coarse-skewed, scs = strongly coarse-skewed, Avg = average, N/A = not available. * = pothole fill/lag deposits not included in grain size distribution averages.

Sample	% Gravel	% vcs	% cs	% ms	% fs	% vfs	% mud	Mean (phi)	Went-worth	Mean (mm)	Median (phi)	Median (mm)	Sorting		Skewness	
Unit B1																
52	0.00	0.04	0.35	56.83	41.66	0.98	0.15	2.06	fS	0.24	1.93	0.26	0.47	Ws	0.58	sfs
GC1	0.00	0.28	9.17	57.73	30.83	1.97	0.03	1.77	mS	0.29	1.79	0.29	0.58	mWs	-0.28	cs
GC1B	0.00	0.08	0.24	62.38	35.93	1.22	0.16	2.03	fS	0.24	1.90	0.27	0.45	Ws	0.64	sfs
Average	*0*	*0*	*3*	*59*	*36*	*1*	*0*	*1.95*	*mS*	*0.26*	*1.87*	*0.27*	*0.50*	*Ws*	*0.32*	*sfs*
Unit B2																
17	0.00	0.81	5.70	58.64	33.28	1.57	0.00	1.88	mS	0.27	1.81	0.29	0.64	mWs	0.23	fs
18	1.29	12.53	38.50	35.34	9.90	2.30	0.14	0.96	cS	0.51	0.95	0.52	0.94	Ms	0.52	sfs
19	3.44	17.20	30.03	31.51	15.35	2.47	0.00	0.95	cS	0.52	0.98	0.51	1.11	Ps	-0.36	scs
GC2	0.94	9.94	20.62	54.99	12.33	1.09	0.09	1.20	mS	0.43	1.31	0.40	0.89	Ms	-1.01	scs
Average	*1*	*10*	*24*	*45*	*18*	*2*	*0*	*1.25*	*mS*	*0.43*	*1.26*	*0.43*	*0.90*	*Ms*	*-0.15*	*cs*
Unit B3 *Facies 1*																
10	0.15	0.34	3.38	53.31	40.48	2.26	0.09	1.98	mS	0.25	1.90	0.27	0.61	mWs	0.31	sfs
11	0.00	0.11	6.43	66.26	26.95	0.25	0.00	1.77	mS	0.29	1.71	0.30	0.60	mWs	0.36	sfs
12	0.07	0.44	1.36	79.47	17.99	0.67	0.00	1.65	mS	0.32	1.61	0.33	0.50	Ws	0.54	sfs
13	0.00	0.00	3.16	66.08	27.43	3.33	0.00	1.86	mS	0.27	1.78	0.29	0.60	mWs	0.57	sfs
GC3	0.00	0.00	3.49	65.38	30.91	0.22	0.00	1.86	mS	0.28	1.79	0.29	0.57	mWs	0.40	sfs
Average	*0*	*0*	*4*	*66*	*29*	*1*	*0*	*1.83*	*mS*	*0.28*	*1.76*	*0.30*	*0.58*	*mWs*	*0.44*	*sfs*
Facies 2																
GC9	0.00	0.60	1.14	62.88	34.13	1.20	0.06	1.93	mS	0.26	1.84	0.28	0.57	mWs	0.44	sfs
Avg B3	*0*	*0*	*2*	*64*	*31*	*1*	*0*	*1.88*	*mS*	*0.27*	*1.80*	*0.29*	*0.57*	*mWs*	*0.44*	sfs
Unit B4 *Facies 1*																
27	0.00	0.03	0.29	42.50	49.28	7.75	0.14	2.21	fS	0.22	2.15	0.23	0.49	Ws	0.12	fs
44	0.00	0.03	0.18	46.97	47.92	4.77	0.12	2.16	fS	0.22	2.06	0.24	0.50	Ws	0.46	sfs
Average	*0.00*	*0.03*	*0.24*	*44.73*	*48.60*	*6.26*	*0.13*	*2.18*	*fs*	*0.22*	*2.10*	*0.23*	*0.50*	*Ws*	*0.29*	*fs*
Facies 2																

14	0.00	3.02	49.16	43.70	3.64	0.40	0.08	1.04	mS	0.49	0.97	0.51	0.57	mWs	0.22	fs
15	0.13	7.86	67.15	20.48	3.54	0.84	0.00	0.70	cS	0.62	0.66	0.63	0.62	mWs	0.49	sfs
16	0.00	0.72	18.24	67.95	12.44	0.56	0.09	1.44	mS	0.37	1.44	0.37	0.58	mWs	0.34	sfs
49	0.00	0.56	11.72	22.13	55.65	9.49	0.45	2.16	fS	0.22	2.28	0.21	0.74	Ms	-1.87	scs
53	0.00	0.00	5.89	41.01	52.42	0.68	0.00	2.07	fS	0.24	2.06	0.24	0.62	mWs	-0.26	cs
Average	*0.03*	*2.43*	*30.43*	*39.05*	*25.54*	*2.39*	*0.12*	*1.48*	*mS*	*0.39*	*1.48*	*0.39*	*0.62*	mWs	*-0.22*	*cs*
28*	7.42	7.19	48.83	36.21	0.09	0.26	0.00	0.76	cS	0.59	0.83	0.56	0.75	Ms	-1.37	scs
60*	8.27	43.97	29.21	14.73	2.35	1.32	0.14	0.08	cS	0.95	-0.05	1.04	0.92	Ms	1.79	sfs
Avg B4	*1.76*	*7.04*	*25.63*	*37.30*	*25.26*	*2.90*	*0.11*	*1.40*	*mS*	*0.43*	*1.38*	*0.45*	*0.64*	*mWs*	*-0.01*	*ns*
Unit B5																
9	4.45	18.86	8.32	17.30	48.69	2.17	0.20	1.44	mS	0.37	2.02	0.25	1.38	Ps	-6.81	scs
26	8.13	22.34	27.24	29.50	9.30	3.36	0.13	0.66	cS	0.63	0.74	0.60	1.20	Ps	0.44	sfs
58	27.34	27.34	4.27	13.77	26.40	0.65	0.23	0.38	cS	0.77	-0.28	1.21	1.44	Ps	7.99	sfs
61	0.20	25.22	18.54	31.37	22.89	1.47	0.32	1.14	mS	0.45	1.25	0.42	1.15	Ps	-0.63	scs
62	4.92	40.41	19.01	19.65	14.93	0.94	0.13	0.50	cS	0.71	0.16	0.90	1.23	Ps	4.05	sfs
GC10	6.10	28.19	19.77	25.40	19.60	0.77	0.17	0.81	cS	0.57	0.77	0.58	1.28	Ps	0.61	sfs
Average	*9*	*27*	*16*	*23*	*24*	*2*	*0*	*0.82*	*cS*	*0.58*	*0.78*	*0.66*	*1.28*	*Ps*	*0.94*	*sfs*

Table VII.2 Mineralogical and compositional data for all the beachrock samples. Roundness after Pettijohn *et al*. (1973) where A = angular; sA = subangular; R = rounded; sR = subrounded; wR = well-rounded. Microscopic facies after Frébourg *et al*. (2008) where H = Heterogeneous, L = Laminated, Lig = Laminated inversely graded, Ldl = Laminated discreet laminae, Lbl = Laminated bimodal coarse/finer grained laminae, Lci = Laminated coarser isolated layers in heterogeneous sediments. Porosity classification after Choquette and Pray (1970) and where * equals; BP = Primary Interparticle, crP = cement-reduced Primary. Cementation factor is calculated by dividing the carbonate content of the sample by the bioclastic component, a high ratio indicates a large percentage of the carbonate in the sample is cement, conversely a low percentage indicates a lower cement percentage but a higher skeletal carbonate percentage. n = number of grains counted, V.E. = visual estimation Avg = average.

Sample	**Depth MSL (m)**	**Round-ness**	**Micro-scopic Facies**	**Mineralogy (%)**						**Porosity**				**$CaCO_3$ Content**	**Cement Factor**
				Quartz	**Feldspar**	**Lithics**	**Heavy Minerals**	**Bioclastic Components**	**n**	**Type***	**%**	**Type***	**%**		
Unit B1															
52	32	R-sA	H	50	14	8	10	18	V.E.	B.P.	20-30	crP	10-15	32	1.8
GC-1	33	R-sA	H-L	47	15	9	7	22	363	B.P.	30-40	crP	10-20	40	1.8
GC-1b	33	R-sA	H-L	48	14	8	8	22	394	B.P.	30-40	crP	10-20	44	2.0
Average	-	-	-	*48.3*	*14.3*	*8.3*	*8.3*	*20.7*	-	-	-	-	-	*39*	*1.9*

Unit B2															
17	30	***Thin section not available***												43	-
18	29	R-sA	Lbl	39	10	18	8	25	231	B.P.	>50	crP	30-40	36	1.5
19	27	R-sA	Lbl	36	9	26	10	19	204	B.P.	>50	crP	30-40	46	2.4
GC-2	29	R-sA	H-Lbl	51	11	9	8	21	273	B.P.	>50	crP	30-40	60	2.8
Average	-	-	-	*42*	*10*	*17.7*	*8.7*	*21.7*	-	-	-	-	-	*47*	*2.2*
Unit B3 *Facies 1*															
10	26	R-sA	H	48	7	5	5	35	V.E.	B.P.	>40	crP	20-30	39	1.1
11	25	R-sA	Ldl	52	8	3	4	33	168	B.P.	>40	crP	20-30	60	1.8
12	24	R-sA	H-L	54	6	5	5	30	V.E.	B.P.	>40	crP	20-30	45	1.5
13	24	R-sA	H-L	50	5	5	5	35	V.E.	B.P.	>40	crP	20-30	35	1.0
GC-3	26	R-sA	H-L	51	12	4	4	29	373	B.P.	>40	crP	20-30	41	1.4
Average	-	-	-	*51*	*7.6*	*4.4*	*4.6*	*32.4*	-	-	-	-	-	*44*	*1.4*
Facies 2															
GC-9	25	R-sA	H	52	13	7	7	21	396	B.P.	>40	crP	20-30	49	2.3
Avg B3	-	-	-	*51.5*	*10.3*	*5.7*	*5.8*	*26.7*	-	-	-	-	-	*46*	*1.9*
Unit B4 *Facies 1*															
27	22	R-A	H	53	9	4	18	16	319	B.P.	20-30	crP	5-10	39	2.46
44	28	R-sA	H	55	15	5	5	20	V.E.	B.P.	20-30	crP	5-10	47	2.37
Average	-	-	-	*54*	*12*	*4.5*	*11.5*	*18*	-	-	-	-	-	*43*	*2.4*
Facies 2															
14	19	R-A	Ldl	50	20	5	5	20	V.E.	B.P.	20-30	crP	<5	57	2.83
15	19	R-A	H	52	17	7	12	12	172	B.P.	30-40	crP	10-15	38	3.16
16	20	R-A	Ldl	48	14	7	7	24	V.E.	B.P.	20-30	crP	10-15	39	1.62
49	18	R-sA	H	60	10	5	7	18	V.E.	B.P.	20-30	crP	5-10	41	2.30
53	18	R-A	H	48	17	3	11	21	184	B.P.	20-30	crP	5-10	63	2.99
Average	-	-	-	*51.6*	*15.6*	*5.4*	*8.4*	*19*	-	-	-	-	-	*48*	*2.6*
28	24	R-A	H	45	10	5	20	20	V.E.	B.P.	20-30	crP	<10	34	1.69
60	21	R-A	Ldl	50	15	5	10	20	V.E.	B.P.	30-40	crP	<15	54	2.69
Avg B4	-	-	-	*51.2*	*14.1*	*5.1*	*10.6*	*19*	-	-	-	-	-	*46*	*2.5*
Unit B5															
9	21	R-sA	H	47	15	8	5	25	V.E.	BP	10-20	crP	5-10	55	2.21
26	21	R-A	L	25	8	2	5	60	V.E.	B.P.	>50	crP	<40	66	1.10

58	20	R-A	L-Ldl	45	15	10	10	20	V.E.	BP	10-20	crP	5	50	2.49
61	22	R-A	L-Ldl	45	12	10	5	28	V.E.	BP	<20	crP	5-10	42	1.52
62	25	R-A	L-Ldl	45	15	10	5	25	V.E.	BP	<20	crP	5-10	67	2.67
GC-10	24	R-A	L-H	46	13	10	5	26	401	BP	10-20	crP	<10	59	2.27
Average	-	-	-	*42.2*	*13*	*8.3*	*5.8*	*30.7*	-	-	-	-	-	*57*	*1.85*

APPENDIX VIII

Unconsolidated sediment database

Table VIII.1; Seafloor sediment sample metadata

Table VIII.2; Sediment sample grain size data for Facies C

Table VIII.3; Sediment sample grain size data for Facies D

Table VIII.4; Sediment sample grain size data for Facies E

Table VIII.5; Mineralogical compositional data for Facies C

Table VIII.6; Mineralogical compositional data for Facies D

Table VIII.7; Mineralogical compositional data for Facies E

Table VIII.1 Seafloor sediment sample metadata. .

Sample	Northings (X)	Eastings (Y)	MSL	Acoustic Facies	Sample	Northings (X)	Eastings (Y)	MSL	Acoustic Facies
A	6650486	291004	15	D	S8	6650745	289658	28	E
B	6650370	290847	24	E	S9	6648190	289172	27	D
C	6650208	291033	18	D	S10	6650745	289642	28	E
D	6648088	288271	17	D	S11	6648888	288741	26	C
E	6648051	288286	18	D	S12	6648929	288759	26	E
F	6647560	288809	20	D	S13	6650734	289683	28	E
G	6649207	290678	27	C	S14	6650726	289729	29	C
H	6649244	290623	23	C	S15	6646490	289549	32	C
I	6648791	289616	26	E	S16	6646975	287790	20	D
J	6648795	289739	20	D	S17	6646521	289532	33	C
L	6647781	289832	31	C	S18	6646916	287750	21	D
N	6649618	289878	24	D	S19	6646826	287692	23	C
O	6649668	289879	24	D	S20	6650601	291916	33	C
P	6648087	289452	24	D	S21	6650084	290550	25	E
Q	6649745	291009	28	C	S22	6650036	290572	22	E
R	6649903	290475	23	E	S23	6649209	291064	31	C
S	6650687	291143	28	D	S25	6648129	290317	30	C
T	6650654	291117	28	D	S26	6646788	288912	32	C
U	6647402	288991	28	C	S30	6650747	289944	30	C
V	6647463	288887	27	D	S31	6647382	287008	19	D
S1	6650916	290866	27	C	S32	6650890	290027	29	C
S2	6651474	290180	30	C	S33	6649071	289701	25	D
S4	6649018	290017	19	D	S35	6650669	289886	29	E
S5	6649005	290106	19	D	S36	6649110	289691	25	D
S6	6649004	290049	18	D	SCNT	6648969	287957	25	E
S7	6650262	290768	22	E					

Table VIII.2 Grain size distribution data for samples from acoustic Facies C. Facies C is further subdivided based on physiographic position of the samples. C1 is considered unobstructed shelf sediment, C2 is shelf sediment in proximity to reef outcrops and C3 is redistributed shelf sediment located within the Basin feature behind the Aliwal Shoal and which forms sediment starved bedforms. vcS = very coarse sand, cS = coarse sand, mS = medium sand, fS = fine sand, vfS = very fine sand, Wentworth = Udden-Wentworth classification scale, Ws = well sorted, mWs = moderately well sorted, Ms = moderately sorted, sfs = strongly fine-skewed, fs = fine-skewed, ns = near-symmetrical, cs = coarse-skewed, scs = strongly coarse-skewed, AVG = average for all the samples.

Sample	% Gravel	% vcs	% cs	% ms	% fs	% vfs	% mud	Mean (phi)	Went-worth	Mean (mm)	Median (phi)	Sorting		Skewness		$CaCO_3$
Facies C1: Shelf sediment																
S1	0.68	1.51	5.55	48.15	43.92	0.15	0.04	1.93	mS	0.26	1.90	0.68	mWs	-0.26	cs	46
S20	3.34	9.32	29.31	49.18	8.85	0.00	0.00	1.06	mS	0.48	1.17	0.91	Ms	-1.32	scs	57
S23	32.59	15.41	15.60	29.32	7.08	0.00	0.00	0.05	cS	0.96	0.13	1.51	Ps	-0.21	cs	90
S25	4.24	8.84	21.21	50.51	15.19	0.00	0.00	1.17	mS	0.45	1.36	1.01	Ps	-2.37	scs	59
S26	1.78	4.19	24.16	57.16	12.71	0.00	0.00	1.30	mS	0.41	1.37	0.77	mWs	-0.62	scs	71
Average	*8.53*	*7.86*	*19.17*	*46.86*	*17.55*	*0.03*	*0.01*	*1.10*	*mS*	*0.51*	*1.19*	*0.98*	*Ms*	*-0.96*	*scs*	*64*
Facies C2: Shelf sediments at reef margins																
G	1.91	5.72	29.47	55.21	7.70	0.00	0.00	1.18	mS	0.44	1.23	0.76	Ms	-0.77	scs	67
H	0.00	0.99	5.49	56.61	36.90	0.00	0.00	1.92	mS	0.26	1.84	0.61	mWs	0.14	fs	47
L	0.56	0.82	6.52	54.91	37.20	0.00	0.00	1.90	mS	0.27	1.85	0.64	mWs	-0.04	ns	49
Q	0.50	1.00	27.41	63.52	7.57	0.00	0.00	1.29	mS	0.41	1.29	0.56	mWs	0.25	fs	57
U	0.98	3.55	16.66	69.63	9.18	0.00	0.00	1.38	mS	0.38	1.44	0.66	mWs	-0.62	scs	54
S15	10.57	4.13	23.57	52.64	8.93	0.16	0.00	1.06	mS	0.48	1.22	1.13	Ps	-4.82	scs	55
S17	4.02	10.23	27.30	48.14	10.23	0.08	0.00	1.04	mS	0.49	1.20	0.98	Ms	-1.72	scs	68
S19	1.31	5.15	45.73	47.81	0.00	0.00	0.00	0.92	cS	0.53	0.96	0.56	mWs	-0.55	scs	42
Average	*2.48*	*3.95*	*22.77*	*56.06*	*14.71*	*0.03*	*0.00*	*1.34*	*mS*	*0.41*	*1.38*	*0.74*	*Ms*	*-1.02*	*scs*	*55*
Facies C3: Sediment starved bedforms within Basin feature																
S2	0.00	0.09	1.30	50.52	47.01	0.04	1.04	2.08	fS	0.24	1.99	0.53	mWs	0.34	sfs	39
S11	25.02	20.24	23.81	28.96	1.97	0.00	0.00	0.07	cS	0.95	0.30	1.31	Ps	-2.38	scs	72
S14	42.99	30.33	14.16	10.26	1.50	0.11	0.64	-0.65	vcS	1.57	-0.84	1.20	Ps	3.14	sfs	41
S30	0.52	1.24	3.48	53.28	41.31	0.17	0.00	2.00	fS	0.25	1.89	0.58	mWs	0.25	fs	43
S32	1.30	3.09	9.19	61.66	24.75	0.00	0.00	1.69	mS	0.31	1.69	0.73	Ms	-0.63	scs	41
Average	*13.97*	*11.00*	*10.39*	*40.94*	*23.31*	*0.06*	*0.34*	*1.04*	*mS*	*0.66*	*1.00*	*0.87*	*Ms*	*0.14*	*fs*	*47*
AVG	**8.32**	**7.60**	**17.44**	**47.95**	**18.52**	**0.04**	**0.11**	**1.16**	**mS**	**0.53**	**1.19**	**0.86**	**Ms**	**-0.61**	**scs**	**55**

Table VIII.3 Grain size distribution data for samples of acoustic Facies D. vcS = very coarse sand, cS = coarse sand, mS = medium sand, fS = fine sand, vfS = very fine sand, Wentworth = Udden-Wentworth classification scale, Ws = well sorted, mWs = moderately well sorted, Ms = moderately sorted, sfs = strongly fine-skewed, fs = fine-skewed, ns = near-symmetrical, cs = coarse-skewed, scs = strongly coarse-skewed.

Sample	% Gravel	% vcs	% cs	% ms	% fs	% vfs	% mud	Mean (phi)	Went-worth	Mean (mm)	Median (phi)	Sorting		Skewness		$CaCO_3$
A	49.61	33.75	13.25	2.97	0.18	0.00	0.24	-1.12	G	2.17	-0.99	1.21	Ps	-0.97	scs	75
C	40.19	38.20	15.60	5.88	0.00	0.00	0.13	2.06	fS	0.24	1.99	0.58	mWs	0.04	ns	95
D	31.07	39.26	23.31	6.21	0.16	0.00	0.00	-0.68	vcS	1.60	-0.54	1.20	Ps	-0.97	scs	60
E	36.89	37.78	19.92	5.25	0.17	0.00	0.00	-0.63	vcS	1.55	-0.68	1.00	Ps	0.83	sfs	90
F	12.57	31.19	29.71	23.84	2.68	0.00	0.00	0.23	cS	0.85	0.24	1.09	Ps	-0.47	scs	73
J	4.76	14.14	25.24	53.31	2.41	0.00	0.14	0.81	cS	0.57	1.07	0.86	Ms	-2.46	scs	78
N	13.70	22.45	17.19	43.33	3.28	0.00	0.05	0.53	cS	0.69	0.85	1.22	Ps	-4.53	scs	73
O	1.09	4.68	13.36	74.92	5.95	0.00	0.00	1.37	mS	0.39	1.39	0.60	mWs	-0.93	scs	64
P	13.02	15.70	34.66	34.80	1.82	0.00	0.00	0.45	cS	0.73	0.76	1.10	Ps	-3.66	scs	63
S	41.47	31.87	15.94	7.63	2.57	0.23	0.30	-0.71	vcS	1.64	-0.76	1.32	Ps	1.34	sfs	98
T	1.59	3.05	9.60	37.64	46.79	0.45	0.89	1.91	mS	0.27	1.96	0.84	Ms	-1.58	scs	94
V	35.07	33.69	20.48	9.94	0.83	0.00	0.00	-0.51	vcS	1.42	-0.61	1.17	Ps	1.34	sfs	69
S4	2.36	5.03	12.90	76.05	3.65	0.00	0.00	1.31	mS	0.40	1.34	0.62	Ms	-1.53	scs	58
S5	4.42	2.13	5.99	80.60	6.86	0.00	0.00	1.45	mS	0.37	1.42	0.68	Ms	-2.04	scs	49
S6	3.11	7.46	10.88	61.21	17.22	0.12	0.00	1.42	mS	0.37	1.57	0.89	Ms	-2.36	scs	51
S9	1.13	1.00	4.58	70.10	23.11	0.09	0.00	1.80	mS	0.29	1.77	0.57	mWs	0.03	ns	46
S16	0.16	0.60	11.64	77.52	10.00	0.08	0.00	1.49	mS	0.36	1.48	0.51	mWs	0.17	fs	53
S18	10.43	0.29	3.11	68.86	17.24	0.06	0.00	1.60	mS	0.33	1.65	0.97	Ms	-6.07	scs	45
S31	0.53	1.99	5.88	73.34	18.18	0.08	0.00	1.67	mS	0.32	1.70	0.56	mWs	-0.19	cs	41
S33	24.63	19.40	11.20	36.71	8.06	0.00	0.00	0.27	cS	0.83	0.54	1.49	Ps	-2.74	scs	70
S36	4.13	8.44	13.87	59.74	12.53	0.27	1.03	1.28	mS	0.41	1.47	0.94	Ms	-2.47	scs	63
Average	*15.81*	*16.77*	*15.16*	*43.33*	*8.75*	*0.07*	*0.13*	*0.76*	*cS*	*0.75*	*0.84*	*0.92*	*Ms*	*-1.39*	*scs*	*66.76*

Table VIII.4 Grain size distribution data for samples of acoustic Facies E. vcS = very coarse sand, cS = coarse sand, mS = medium sand, fS = fine sand, vfS = very fine sand, Wentworth = Udden-Wentworth classification scale, Ws = well sorted, mWs = moderately well sorted, Ms = moderately sorted, sfs = strongly fine-skewed, fs = fine-skewed, ns = near-symmetrical, cs = coarse-skewed, scs = strongly coarse-skewed.

Sample	% Gravel	% vcs	% cs	% ms	% fs	% vfs	% mud	Mean (phi)	Went-worth	Mean (mm)	Median (phi)	Sorting		Skewness		$CaCO_3$
B	0.00	1.07	3.92	45.52	48.90	0.00	0.59	-0.71	vcS	1.63	-0.76	1.00	Ps	1.14	sfs	50
I	0.58	1.16	4.42	66.35	27.39	0.00	0.11	1.81	mS	0.29	1.77	0.60	mWs	0.17	fs	59
R	0.29	0.46	2.18	59.59	37.49	0.00	0.00	2.00	fS	0.25	1.88	0.52	mWs	0.38	sfs	45
S7	0.32	0.46	2.04	62.55	34.63	0.00	0.00	1.97	mS	0.26	1.85	0.52	mWs	0.40	sfs	39
S8	10.14	3.04	5.52	42.64	36.01	1.11	1.54	1.68	mS	0.31	1.81	1.24	Ps	-6.93	scs	51
S10	42.88	3.37	2.62	17.08	30.84	3.21	0.00	0.59	cS	0.66	1.12	1.88	Ps	-6.81	scs	60
S12	6.81	13.18	19.86	44.31	15.41	0.31	0.12	1.00	cS	0.50	1.29	1.18	Ps	-3.66	scs	54
S13	0.53	2.27	14.47	65.03	17.67	0.00	0.03	1.53	mS	0.35	1.52	0.64	mWs	0.00	ns	93
S21	12.53	5.08	13.43	49.44	19.26	0.26	0.00	1.12	mS	0.46	1.42	1.34	Ps	-6.08	scs	54
S22	0.22	0.37	3.75	66.39	29.26	0.00	0.00	1.87	mS	0.27	1.79	0.54	mWs	0.38	sfs	45
S35	0.31	1.03	6.57	61.82	30.26	0.00	0.00	1.81	mS	0.29	1.75	0.64	mWs	0.15	fs	44
SCNT	17.13	3.92	8.03	46.34	22.25	1.29	1.04	0.87	cS	0.55	1.60	1.68	Ps	-9.72	scs	41
Average	*7.64*	*2.95*	*7.23*	*52.25*	*29.11*	*0.52*	*0.29*	*1.30*	*mS*	*0.48*	*1.42*	*0.98*	*Ms*	*-2.55*	*scs*	*53*

Table VIII.5 Mineralogical compositional data for Facies C. n = number of grains counted.

Sample	n	% Quartz	% Feldspar	% Lithics	% Heavy Minerals	% Bioclasts
Facies C1: Shelf sediment						
S1	208	68.3	12.0	0.5	0.5	18.8
S20	Not available					
S23	207	54.6	9.2	0.0	0.5	35.7
S25	170	50.0	12.4	0.0	1.2	36.5
S26	171	54.4	6.4	0.0	0.0	39.2
Average	*189*	*57*	*10*	*0*	*1*	*33*
Facies C2: Shelf sediments at reef margins						
G	194	43.8	4.1	0.5	0.0	51.5
H	162	65	2.5	0.4	0.0	32.1
L	257	71.6	3.1	0.4	1.6	23.3
Q	223	53.8	1.8	0.9	0.9	42.6
U	247	60.7	6.5	0.0	0.4	32.4
S15	124	52.4	15.3	0.1	1.6	30.6
S17	268	61.9	7.5	0.1	0.0	30.6
S19	163	57.7	11.7	0.0	1.8	28.8
Average	*205*	*58*	*7*	*0*	*1*	*34*
Facies C3: Sediment starved bedforms within Basin feature						
S2	243	65.4	14.0	0.4	1.6	18.5
S11	134	39.6	14.2	0.0	0.7	45.5
S14	120	42.5	2.5	0.0	0.0	55.0
S30	166	61.4	10.8	0.0	3.0	24.7
S32	254	61.4	8.3	0.0	2.4	28.0
Average	*183*	*54*	*10*	*0*	*2*	*34*
AVG	**192**	**56**	**9**	**0**	**1**	**34**

Table VIII.6 Mineralogical compositional data for Facies D. n = number of grains counted.

Sample	n	% Quartz	% Feldspar	%Lithics	% Heavy Minerals	%Bioclasts
A	161	39.1	6.2	0.6	1.2	52.8
C	101	32.7	0.0	4.0	1.0	62.4
D	122	61.5	6.6	2.5	0.8	28.7
E	130	23.8	2.3	3.1	0.0	70.8
F	167	49.1	2.4	0.6	3.0	44.9
J	156	39.7	0.6	0.0	0.6	59.0
N	157	45.2	3.2	0.6	0.0	51.0
O	188	70.7	0.0	0.0	0.0	29.3
P	185	48.1	1.6	0.5	1.1	48.6
S	103	10.7	0.0	0.0	0.0	89.3
T	251	46.2	9.6	0.0	0.4	43.8
V	201	41.3	4.0	0.0	0.0	54.7
S4	196	63.8	5.1	0.0	0.0	31.1
S5	210	56.7	9.0	0.0	2.4	31.9
S6	157	55.4	12.7	0.0	0.6	31.2
S9	234	60.3	5.1	0.0	0.4	34.2

S16	242	67.8	6.2	0.0	1.2	24.8
S18	126	60.3	7.9	0.0	0.8	31.0
S31	208	65.9	7.2	0.0	1.0	26.0
S33	186	66.7	5.9	0.0	1.1	26.3
S36	184	51.1	6.5	0.0	0.0	42.4
Average	*175*	*50*	*5*	*1*	*1*	*44*

Table VIII.7 Mineralogical compositional data for Facies E. n = number of grains counted.

Sample	n	% Quartz	% Feldspar	% Lithics	% Heavy Minerals	% Bioclasts
B	218	72.0	6.0	0.5	1.4	20.2
I	175	56.6	2.9	0.0	0.0	40.6
R	243	70.4	0.4	0.0	0.4	28.8
S7	357	66.4	7.3	0.0	1.1	25.2
S8	202	60.9	12.4	0.0	1.5	25.2
S10	132	56.8	13.6	0.0	0.0	29.5
S12	210	57.6	14.3	0.0	2.4	25.7
S13	184	51.6	17.4	0.0	1.1	29.9
S21	177	55.4	13.6	0.0	4.0	27.1
S22	277	59.9	8.7	0.0	0.7	30.7
S35	Not available					
SCNT	189	56.6	14.3	0.0	1.6	27.5
Average	215	60	10	0	1	28

APPENDIX IX

Geochronological sample database

Table IX.1; Sample metadata

Table IX.2; GC-series sample photographs

Table IX.3; Photographs of shell material extracted from GC-series samples, oyster specimens and a pothole fill sample from an onshore locality

Table IX.1 Geochronological sample metadata.

Sample	X	Y	MSL (m)
GC-1	6646371	289502	-33
GC1b	6646288	289394	-33
GC-2	6647693	289711	-29
GC-2S	6647693	289711	-29
GC-3	6649217	290674	-26
GC-3S	6649217	290674	-26
GC4	291096.24	6650430.17	-15
GC5	291113.05	6649948.04	-30
GC6	289682.69	6649091.31	-26
GC7	288394.95	6648088.91	-16
GC-9	6648506	289921	-26
GC-10	6648150	288986	-24
GC-10S	6648150	288986	-24
GC5 Oysters1	6649608	290885	-29
GC5 Oysters2	6649938	291106	-30
GC-8Oys	6648075	289424	-24
AS-27	6648075	289412	-22
OS-5	6661822	291010	2
AS33	6649809	290900	-17
AS48	6650350	291007	-4

Table IX.2 Photograph images of the GC-series geochronological samples.


GC-4
1 cm
Marine Geoscience Unit, Durban


GC-5
1 cm
Marine Geoscience Unit, Durban


1 cm
GC-6

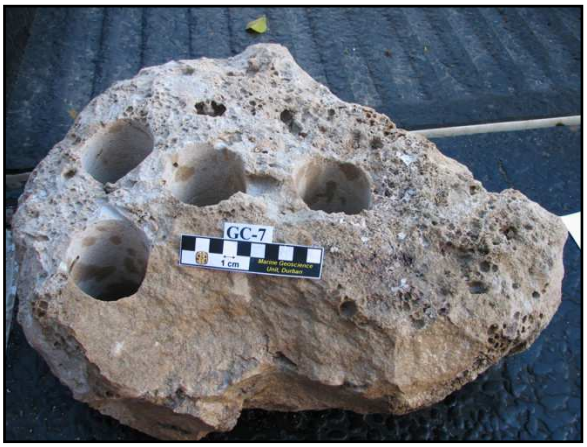
GC-7
1 cm


GC-9
1 cm
Marine Geoscience Unit, Durban


GC-10
1 cm
Marine Geoscience Unit, Durban

Table IX.3 Photograph images of shell material extracted from selected GC-series beachrock samples. The sample number refers to the GC-series sample the shells were extracted from. Note that a image of sample AS-27 is available in Appendix IV, Table IV.2, designated as sample 27.

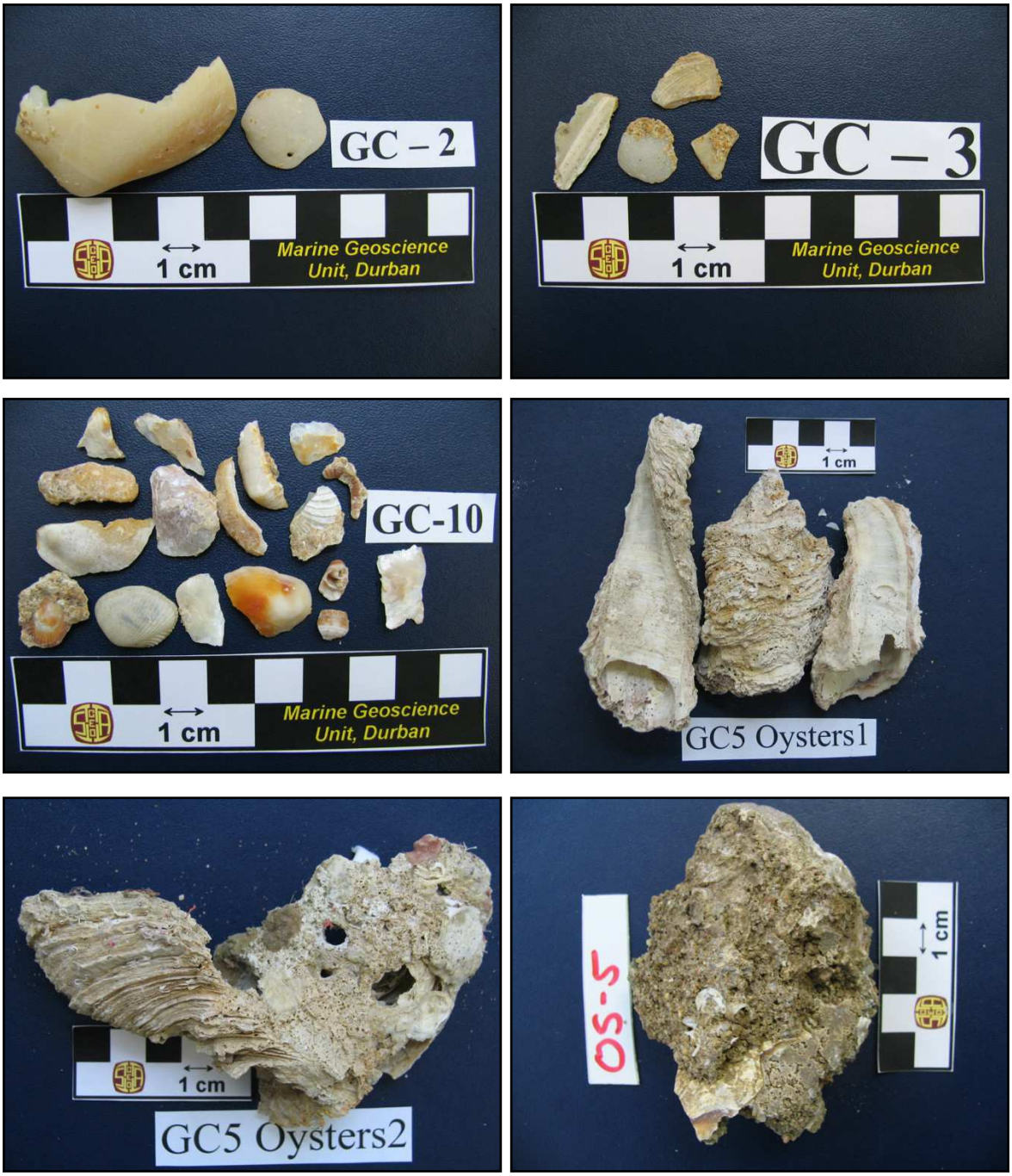

APPENDIX X

Copy of the publication entitled 'The Aliwal Shoal revisited: New age constraints from nannofossil assemblages' by C. Bosman, M. N. Ovechkina and R. Uken (2007)

APPENDIX XI

Detailed optically stimulated luminescence dating report provided by Dr Zenobia Jacobs

(Report is found on the back cover in digital format)

APPENDIX XII

Uranium series dating laboratory brief summary report provided by Dr Louise Thomas of the Open University's Uranium Series Facility (OUUSF) (Report is found on the back cover in digital format)

APPENDIX XIII

Radiocarbon dating laboratory results provided by Dr Stephan Woodborne from QUADRU

(Report is found on the back cover in digital format)

APPENDIX XIV

Summary of the recalibration and reinterpretation procedure for the Ramsay and Cooper (2002) relative sea-level curve

XIV.1 INTRODCUTION

This study produced new sea-level data (Chapter 9) for the Aliwal Shoal in calendar years before present. The most recent and locally applicable relative sea-level curve for comparison is the Ramsay and Cooper (2002) relative sea-level curve (hereafter *RCSLC*). The RCSLC plots Uranium series calendar ages with uncalibrated radiocarbon ages and in addition, has been criticised by Woodroffe and Horton (2005) as using sea-level limiting material (e.g. wood) as a sea-level indicator point. Most recently, Carr *et al*. (2010) levelled further criticisms to the validity of the RCSLC, questioning the use of Uranium series dates on mollusc shells which are prone to open system behaviour. In defence of Ramsay and Cooper (2002), oyster shells were used which have been shown by Jedoui *et al*. (2003) to provide accurate results. Given these criticisms, the RCSLC is still the most complete locally derived relative sea-level curve available, not only for the east coast but also for South Africa.

To achieve a meaningful comparison with the new Aliwal Shoal data, the RCSLC was essentially re-interpreted by addressing two principal issues viz; (1) recalibration of the radiocarbon data to calendar years so as to be comparable to the Uranium series ages and hence comparable to the Aliwal Shoal datasets and (2) basic reinterpretation of the radiocarbon-based sea-level index point data in accordance with international standards, thereby improving the reliability of the Ramsay and Cooper (2002) sea-level curve. Unfortunately it was not possible to remodel the original Uranium series age data.

XIV.2 RECALIBRATION

XIV.2.1 Rationale

The following criteria were applied to the RCSLC (Figure XIV.1);

1) East coast samples are preferred and separated from other localities along the South African coastline. This is rationalised on the basis of the recent controversy related to the tectonic stability of South Africa (Mather *et al*., 2009) suggesting that the African plate is not only undergoing uplift but that there are differences in the rate of uplift experienced along the east, south and west coast regions.
2) Sea-level index points are then classified as reliable or variable based on the presence or absence of good metadata which is required for accurate recalibration. Metadata include all the reference data associated with the radiocarbon age e.g. marine reservoir age (MRA)

corrections and other calibration terms that were applied to correct the original data. If this information is not listed an accurate recalibration cannot be completed and as such the data point is classified as variable. In the case of a missing or unknown MRA correction, the maximum MRA variance is applied to the error range of the data point.

3) Even if a sample meets the terms set by criteria 1 and 2, it does not suggest that it is a good sea-level index point, only that the confidence is high in the analytical age result. The second critical parameter is the indicative meaning of the sea-level index point. This criterion does not form part of the calibration methodology and is further discussed in Section XIV.3.1. The sea-level index points are scrutinised with reference to their relationship to the sea-level at time of formation and finally classified as either sea-level limiting points or sea-level indicator points as suggested by Woodroffe and Horton (2005). Data with unreliable relationships to the actual sea-level at the time of formation are classified as limiting points.

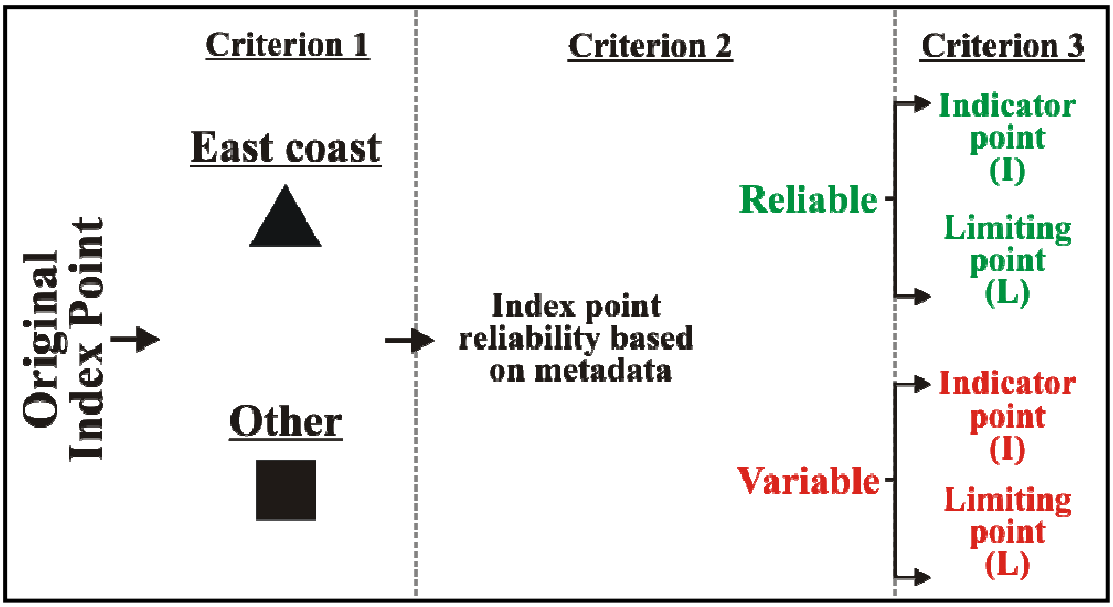

Figure XIV.1 Graphical illustration of the application of the criteria used to reinterpret the validity of the sea-level index points in the Ramsay and Cooper (2002) relative sea-level curve. Also refer to Figure XIV.2 for usage of symbols.

XIV.2.2 Radiocarbon Recalibration Terms

This study uses the marine radiocarbon calibration curves from Fairbanks *et al.* (2005) and the newer IntCal09 calibration curves. The Fairbanks *et al.* (2005) curve is referred to as the *Fairbanks0107* calibration curve, is applicable from 0 to 50 000 years and is a web-based

calibration program accessible on the website http://radiocarbon.LDEO.columbia.edu/. The accompanying marine reservoir correction program uses the Butzin *et al*. (2005) model to constrain the local marine reservoir age (MRA) or apparent age of seawater (a MRA correction value of 287 years is applicable for the Aliwal Shoal study area). For the RCSLC dataset the MRA value varied along the South African coastline from 436 (northern west coast) to 274 (northern east coast) years, therefore the maximum variance along the coast is only 162 years and not considered exceedingly significant with reference to the available data and analytical uncertainty. In situations where the marine reservoir correction cannot be applied reliably, either due to a lack of metadata or that an unknown MRA correction was applied to the original data, the applicable MRA for that sample's location is added to the age error range of the data point. Aeolianite index points are also corrected for the MRA based on the fact that these are coastal aeolianites commonly showing high proportions of bioclastic shell material derived from the marine environment. In addition as shown by this study (Section 8.3) the carbonate-cemented aeolianites commonly display marine cement phases. In the case that a known MRA value was applied, this MRA correction is removed and replaced with the Butzin *et al*. (2005) value for the location of the sample (see Table XIV.1).

In addition, the radiocarbon results were also calibrated with the more popular IntCal curves applied through the CALIB radiocarbon calibration program (currently v6.0 html) (Stuiver and Reimer, 1993). The CALIB calibration routine varies from the Fairbanks0107 calibration programme insofar it allows a user to select from five IntCal look-up curves (Intcal09, Marine09; mixed Marine09 and Northern Hemisphere Atmosphere; Southern Hemisphere Atmosphere; mixed Marine09 and Southern Hemisphere Atmosphere). In addition, whereas the Fairbanks0107 calibration program requires a MRA corrected age before calibration, the CALIB program only requires the original C14 age. Only when the Marine09 curve is used does the CALIB program applies a global MRA value of 400 years, the local variance of which is corrected by specifying the applicable deviation from the global value, expressed as ΔR. However, the ΔR data density for South Africa compares poorly to the local MRA correction values from the Fairbanks model (Butzin *et al*., 2005), although Reimer *et al*. (2009) criticised the Butzin *et al*. (2005) MRA correction model as complex and not agreeing with known ages from coastal areas. This was also found by this study insofar the IntCal Marine09 dataset corrected shell ages to within error of the applicable optical ages whereas the Fairbanks0107 ages were too old (Section 9.5.2; Table 9.6).

The RCSLC dataset is compiled from not only marine and terrestrial sample materials but also from different areas of the coastline which consequently also have different ΔR values. Hence the RCSLC dataset is divided into marine and terrestrial samples which then dictate which curve is applicable. All marine samples are corrected with Marine09 curve with the associated applicable

ΔR value (Reimer *et al*., 2009; Table XIV.2). As for the Fairbanks0107 calibration process above, in situations where the marine reservoir correction cannot be applied reliably a value of 400 years (global MRA value) is added to the age error range of the data point. The terrestrial samples are split according to age as the Southern Hemisphere curve is limited to 11 ka cal. B.P. (McCormac *et al*. 2004; Table XIV.2). Samples which were older than 11 ka cal. B.P. were corrected with the Intcal09 curve (Reimer *et al*., 2009; Table XIV.2). Although the CALIB calibration results are displayed as an age range it is converted to a midpoint with equal error to facilitate easy comparison with the Fairbanks0107 calibration results.

XIV.2.3 Results

The results from the recalibration process based on the Fairbanks0107 calibration curve are presented in Table XIV.1. Detailed analysis indicates that the Ramsay and Cooper (2002) radiocarbon age data mostly suffer from inconsistent reporting form i.e. age data were not normalised e.g. corrected MRA ages are mixed with uncorrected ages and to complicate matters sometimes the ages were captured incorrectly from their original sources Overall, the errors are mainly the result of inconsistent original reporting combined with the fact that some data were compiled from other sources which in themselves did not specify corrections or adhere to standard radiocarbon reporting practise (see van der Plicht and Hogg, 2006 for reporting standards).

The CALIB recalibrated datasets are presented in Tables XIV.2. The Fairbanks0107 calibration results compare well with the CALIB calibration (Figure XIV.2) results. Three points were not calibrated by the Fairbanks0107 program (Table XIV.1) and although there seems to be a younger bias in the CALIB calibration (Figure XIV.2) relative to that of the Fairbanks0107 calibration, the two different calibration methods are consistently within error. The younger CALIB ages being the result of the marginally greater MRA correction of the Marine09 curve relative to the *Fairbanks0107* MRA correction.

Nonetheless, both calibration programs use the same tree ring dataset from 0 to 12 410 cal yr B.P., but the Fairbanks0107 calibration curve is based on analytical data from corals for the period when the CALIB calibration uses a mix of data from corals and foraminifera in layered sediments (Cariaco Basin, Venezuela) - a part of which were retracted in the Marine04 curve due to inconsistencies (see http://radiocarbon.ldeo.columbia.edu/research/radiocarbon.htm for discussion). Nonetheless, independent optical age control from the Aliwal Shoal indicates that the Marine09 curve performs better (Section 9.5.2) and as such is used in the recalibrated RCSLC (Table XIV.4).

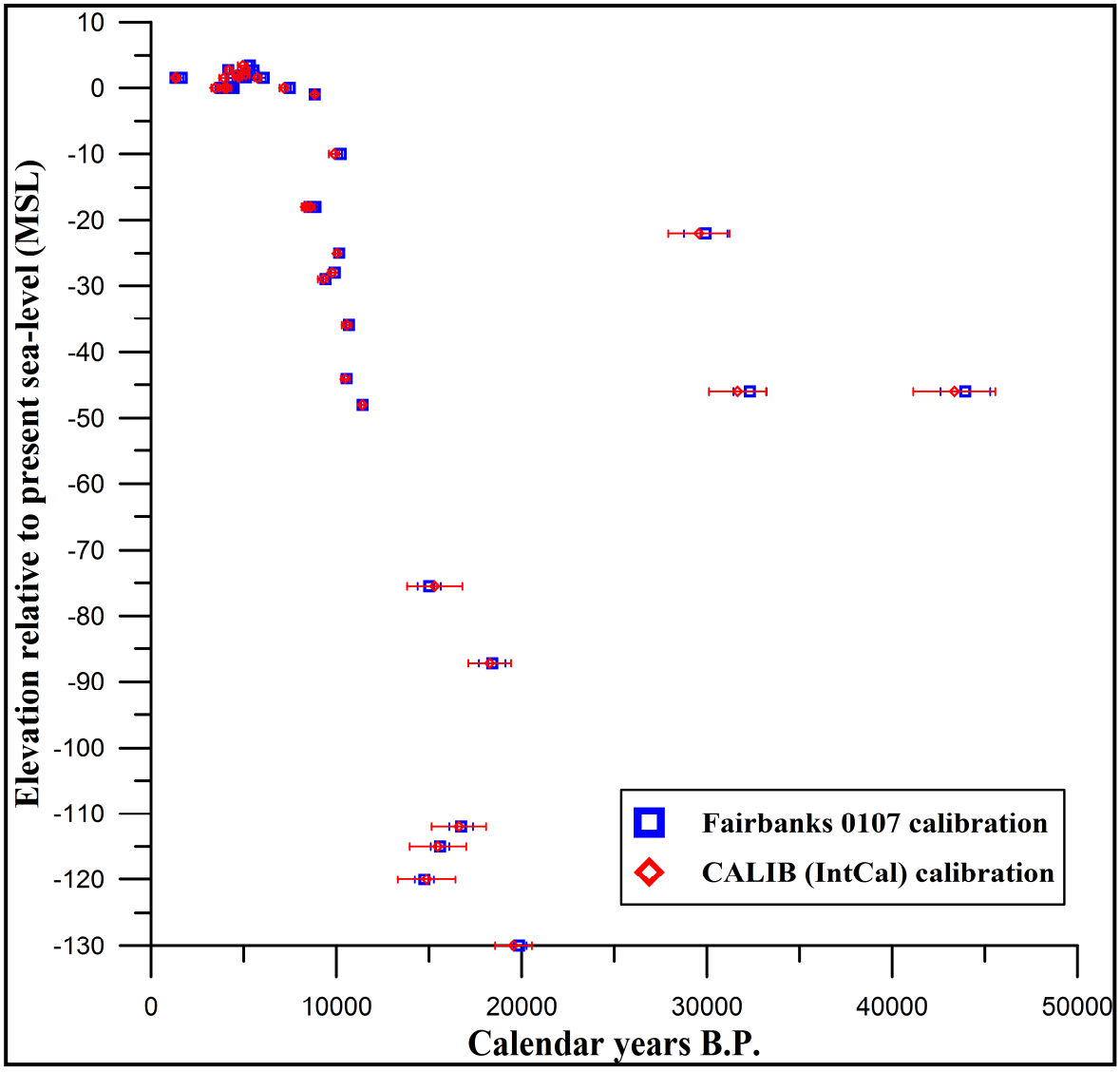

Figure XIV.2 Radiocarbon calibration comparison for the Fairbanks0107 calibration versus the CALIB (v6.0 html) of Stuiver and Reimer (1993). The two methods are within error of each other for all the data points. Refer to the text for details.

Table XIV.1 Recalibration procedure for the RCSLC using the Fairbanks *et al*. (2005; Fairbanks0107) calibration dataset. See text for explanation. OCR = outside calibration calculation range; * = applied the local MRA value to the error range; N/A = not applicable, EC = east coast, WC = west coast, SC = south coast, Moz = Mozambique, R&C2002 = Ramsay and Cooper (2002), FB0107 = Fairbanks0107 calibration curve.

Material	Sample	Criterion 1	R&C2002 C14 Age		Original C14 Age		MRA Metadata		Criterion 2 Result	MRA value	MRA Corrected C14		FB0107 Cal. Ages	
			Age	Error	Age	Error	Y/N	Value			Age	Adj. error	Age	Error
Wetland Peat	Pta-4140	EC	45200	2000	Unknown unpublished		N/A		Variable	0	45200	2000	OCR	
Wetland Peat	Pta-4142	EC	39100	1530	Unknown unpublished		N/A		Variable	0	39100	1530	43947	1342
Calcareous Algae	Pta-1104	Other (WC)	27400	440	27400	440	No	Unknown	Variable	381	27019	821*	32320	894
Wetland Peat	GaK-1390	EC	24950	950	24950	950	N/A		Reliable	0	24950	950	29933	1172
Calcareous Algae	Pta-182	Other (SC)	16990	100	16990	100	No	Unknown	Variable	281	16709	381*	19857	409
Calcareous Algae	Pta-1105	WC	15700	160	15700	160	No	Unknown	Variable	381	15319	541*	18405	711
Calcareous Algae	Pta-265	Other (SC)	14510	120	14510	120	No	Unknown	Variable	281	14229	401*	16735	643
Calcareous Algae	Pta-264	Other (SC)	13670	120	13670	120	No	Unknown	Variable	281	13389	401*	15595	498
Calcareous Algae	Pta-955	Other (WC)	13300	100	13300	100	No	Unknown	Variable	381	12919	481*	15013	619
Calcareous Algae	Pta-185	Other (SC)	12990	100	12990	100	No	Unknown	Variable	281	12709	381*	14749	516
Wood	Pta-3597	EC	9990	30	9990	30	N/A		Reliable	0	9990	30	11411	88
Wood	Pta-4344	EC	9440	90	9440	90	N/A		Reliable	0	9440	90	10687	144
Wood	Pta-4343	EC	9350	90	9350	90	N/A		Reliable	0	9350	90	10562	125
Wood	Pta-3570	EC	8950	30	8950	30	N/A		Reliable	0	8950	30	10149	64
Wood	Pta-4346	EC	8840	90	8840	90	N/A		Reliable	0	8840	90	9918	189
Wood	GaK-1389	EC	8420	140	Unknown		N/A		Variable	0	8420	140	9420	142
Attached Oyster	Pta-3622	EC	8280	80	8280	80	Y	0	Reliable	287	7993	80	8876	146
Attached Oyster	Pta-3573	EC	8140	70	8140	70	Y	0	Reliable	287	7853	70	8637	100
Attached Oyster	Pta-3575	EC	8070	80	8070	80	Y	0	Reliable	287	7783	80	8560	87
Beachrock	Pta-6190	EC	8950	80	9350	80	Y	400	Reliable	274	9076	80	10232	66
Beachrock	Pta-6431	EC	7840	90	8240	90	Y	400	Reliable	274	7966	90	8827	162
Beachrock	Pta-6248	EC	6460	80	6860	80	Y	400	Reliable	274	6586	80	7480	63

Life position Bivalve	Pta-4317	Other (SC)	5080	70	5580	70	Y	400	Variable	281	5299	70	6072	102
Aeolianite	Pta-4998	EC	4660	50	5060	50	Y	400	Reliable	274	4786	50	5536	64
Beachrock	Pta-6191	EC	4650	60	5050	60	Y	400	Reliable	274	4776	60	5522	76
Pothole fill	Pta-6252	EC	4480	70	4880	70	Y	400	Reliable	274	4606	70	5322	103
Shell in beachrock	Pta-6297	EC	4350	60	4750	60	Y	400	Reliable	274	4476	60	5120	129
Shell	Pta-4705	Other (SC)	4240	60	4640	60	Y	400	Reliable	281	4359	60	4918	87
Life position Bivalve	Pta-4462	Other (SC)	3880	60	4280	60	Y	400	Reliable	281	3999	60	4461	77
Shell	Pta-4041	Other (WC)	3820	50	4220	50	Y	400	Reliable	436	3784	50	4156	78
Coral in beachrock	Pta-5052	EC	3780	60	4180	60	Y	400	Reliable	274	3906	60	4347	91
Shell in beachrock	Pta-6300	EC	3740	60	4140	60	Y	400	Reliable	274	3866	60	4286	99
Beachrock	Pta-6429	EC	3360	60	3760	60	Y	400	Reliable	274	3486	60	3754	84
Coral in beachrock	Pta-4972	EC	1610	70	2010	70	Y	400	Reliable	274	1736	70	1646	88
Shell	Pta-4311	Other (WC)	1450	50	1850	50	Y	400	Reliable	436	1414	50	1314	31
Br	Unknown	Other (Moz)	920	145	920	145	No	Unknown	Variable	288	632	433*	OCR	
Br	Unknown	Other (Moz)	910	130	910	130	No	Unknown	Variable	288	622	418*	OCR	

Table XIV.2 Recalibration of the RC2002RSLC with the CALIB radiocarbon calibration program (v6.0 html). The various curves used include the Marine09, IntCal09 and SH Atmosphere which are originally reported as age ranges and converted here to midpoint ages with symmetrical errors for comparison reasons.

Sample	C14 Age		MRA		Marine09		Marine09		IntCal09		SHCal04 Atmosphere		Calib Terrestrial		CALIB ALL	
	Age	Error	Del R	Error	Age range		Midpoint	Error	Age	Range	Age	Range	Midpoint	Error	Midpoint	Error
Pta-4140	45200	2000	-	-	-	-	-	-	45345	50000	-	-	47673	2328	47673	2328
Pta-4142	39100	1530	-	-	-	-	-	-	41140	45576	-	-	43358	2218	43358	2218
Pta-1104	27400	840	109	28	30114	33196	31655	1541							31655	1541
GaK-1390	24950	950			-	-	-	-	27919	31224	-	-	29572	1653	29572	1653
Pta-182	16990	500	224	51	18567	20558	19563	996	-	-	-	-	-	-	19563	996
Pta-1105	15700	560	109	28	17119	19430	18275	1156	-	-	-	-	-	-	18275	1156
Pta-265	14510	520	224	51	15140	18071	16606	1466	-	-	-	-	-	-	16606	1466
Pta-264	13670	520	224	51	13949	17005	15477	1528	-	-	-	-	-	-	15477	1528
Pta-955	13300	500	109	28	13816	16797	15307	1491	-	-	-	-	-	-	15307	1491
Pta-185	12990	500	224	51	13318	16433	14876	1558	-	-	-	-	-	-	14876	1558
Pta-3597	9990	30	-	-	-	-	-	-	11284	11509	-	-	11397	113	11397	113
Pta-4344	9440	90	-	-	-	-	-	-	-	-	10290	10802	10546	256	10546	256
Pta-4343	9350	90	-	-	-	-	-	-	-	-	10250	10696	10473	223	10473	223
Pta-3570	8950	30	-	-	-	-	-	-	-	-	9888	10190	10039	151	10039	151
Pta-4346	8840	90	-	-	-	-	-	-	-	-	9555	9967	9761	206	9761	206
GaK-1389	8420	140	-	-	-	-	-	-	-	-	8999	9562	9281	282	9281	282
Pta-3622	8280	80	213	57	8337	8849	8593	256	-	-	-	-	-	-	8593	256
Pta-3573	8140	70	213	57	8191	8576	8384	193	-	-	-	-	-	-	8384	193
Pta-3575	8070	80	213	57	8114	8537	8326	212	-	-	-	-	-	-	8326	212
Pta-6190	9350	80	213	57	9598	10168	9883	285	-	-	-	-	-	-	9883	285
Pta-6431	8240	90	213	57	8820	8840	8830	10	-	-	-	-	-	-	8830	10
Pta-6248	6860	80	213	57	6937	7382	7160	223	-	-	-	-	-	-	7160	223

Pta-4317	5580	70	224	51	5565	5909	5737	172	-	-	-	-	-	-	5737	172
Pta-4998	5060	50	213	57	4884	5317	5101	217	-	-	-	-	-	-	5101	217
Pta-6191	5050	60	213	57	4863	5315	5089	226	-	-	-	-	-	-	5089	226
Pta-6252	4880	70	213	57	4672	5214	4943	271	-	-	-	-	-	-	4943	271
Pta-6297	4750	60	213	57	4503	4943	4723	220	-	-	-	-	-	-	4723	220
Pta-4705	4640	60	224	51	4396	4804	4600	204	-	-	-	-	-	-	4600	204
Pta-4462	4280	60	224	51	3866	4331	4099	233	-	-	-	-	-	-	4099	233
Pta-4041	4220	50	93	28	4010	4375	4193	183	-	-	-	-	-	-	4193	183
Pta-5052	4180	60	213	57	3728	4209	3969	241	-	-	-	-	-	-	3969	241
Pta-6300	4140	60	213	57	3680	4142	3911	231	-	-	-	-	-	-	3911	231
Pta-6429	3760	60	213	57	3240	3641	3441	201	-	-	-	-	-	-	3441	201
Pta-4972	2010	70	213	57	1167	1543	1355	188	-	-	-	-	-	-	1355	188
Pta-4311	1850	50	93	28	1177	1427	1302	125	-	-	-	-	-	-	1302	125
Unknown	920	145	171	42	61	623	342	281	-	-	-	-	-	-	342	281
Unknown	910	130	171	42	71	605	338	267	-	-	-	-	-	-	338	267

XIV.3 REINTERPRETATION

XIV.3.1 Methodology

Sea-level curves comprise an age, normally the x-axis and a position relative to a sea-level datum, normally MSL and which is plotted on the y-axis. In the previous section the RCSLC data were age calibrated and hence problems related the age or analytical components of the sea-level curve were addressed. But the vertical component or the position of data point relative to modern sea-level also needs to be precise. To this extent for a sea-level index point to be pertinent it must have some established elevation relationship (indicative meaning) to sea-level at the time of formation. For instance, Ramsay (1995) found that contemporary beachrocks along the eastern South African coastline were forming at elevations of 0.1 to 0.2 m above mean sea-level. In addition the local tidal range is 2 metres, meaning that the beachrocks have an indicative range totalling 2 m. Thus, the indicative meaning of the beachrock is very close to the actual MSL at time of formation and the variability of the depositional range is also well constrained due to the microtidal regime.

The RCSLC is compiled from a wide variety of materials all used as sea-level index points. This includes wetland peat, calcareous algae (rhodoliths) wood fragments from back barrier environments, bedrock attached oysters from back-barrier estuarine settings, in situ burrowing bivalves, beachrocks, shells in beachrock and buried beach and bar deposits. Although the indicative meaning and vertical accuracy estimates of Ramsay and Cooper (2002) in most of the cases are sufficient especially considering the large vertical error ranges (6 - 10 m), some index points should be considered as limiting points (Table XIV.3).

XIV.3.2 Results

The results of the reinterpretation of the RCSLC are presented in Tables XIV.3 and XIV.4 and graphically in Figure XIV.3.

Table XIV.3 Re-interpretation of the indicative meaning of the RCSLC index points. SL = sea-level, max. = maximum.

Sample	Material	Depositional context	Modern depositional setting relative to sea-level	Original index point (MSL)	Original vertical error	Indicative meaning	Indicative range	Criterion 3
Pta-4140	Wetland Peat	Back-barrier deposits	Forms above SL, 2 m subtracted for max. tidal range	-52	5	-50	3	Limiting
Pta-4142	Wetland Peat	Back-barrier deposits	Forms above SL, 2 m subtracted for max. tidal range	-46	5	-44	3	Limiting
Pta-1104	Calcareous Algae	Relict Rhodoliths	Forms in <20 m below SL	-46	5	-46	10	Limiting
GaK-1390	Wetland Peat	Back-barrier deposits	Forms above SL, 2 m subtracted for max. tidal range	-22	5	-20	3	Limiting
Pta-182	Calcareous Algae	Relict Rhodoliths	Forms in <20 m below SL	-130	5	-130	10	Limiting
Pta-1105	Calcareous Algae	Relict Rhodoliths	Forms in <20 m below SL	-87.2	5	-87.2	10	Limiting
Pta-265	Calcareous Algae	Relict Rhodoliths	Forms in <20 m below SL	-112	5	-112	10	Limiting
Pta-264	Calcareous Algae	Relict Rhodoliths	Forms in <20 m below SL	-115	5	-115	10	Limiting
Pta-955	Calcareous Algae	Relict Rhodoliths	Forms in <20 m below SL	-75.5	5	-75.5	10	Limiting
Pta-185	Calcareous Algae	Relict Rhodoliths	Forms in <20 m below SL	-120	5	-120	10	Limiting
Pta-3597	Wood	Wood resting on bedrock within estuary	At or above SL, 2 m tidal variance, 1 m subtracted	-48	3	-47	3	Limiting
Pta-4344	Wood	Wood within estuarine valley-fill sediment	Forms above SL, 2 m tidal variance, 1 m subtracted	-36	3	-35	3	Limiting
Pta-4343	Wood	Wood within estuarine valley-fill sediment	Forms above SL, 2 m tidal variance, 1 m subtracted	-44	3	-43	3	Limiting
Pta-3570	Wood	Wood within estuarine sediment	Forms above SL, 2 m tidal variance, 1 m subtracted	-25	3	-24	3	Limiting
Pta-4346	Wood	Wood within estuarine valley-fill sediment	Forms above SL, 2 m tidal variance, 1 m subtracted	-28	3	-27	3	Limiting
GaK-1389	Wood	Wood within estuarine sediment	Forms above SL, 2 m tidal variance, 1 m subtracted	-29	3	-28	3	Limiting

Pta-3622	Attached Oyster	Oysters adhering to bedrock within estuary	At or above SL, 2 m tidal variance, no correction to z	-18	0.5	-18	1	Indicator
Pta-3573	Attached Oyster	Oysters adhering to bedrock within estuary	At or above SL, 2 m tidal variance, no correction to z	-18	0.5	-18	1	Indicator
Pta-3575	Attached Oyster	Oysters adhering to bedrock within estuary	At or above SL, 2 m tidal variance, no correction to z	-18	0.5	-18	1	Indicator
Pta-6190	Beachrock	Beach	0.1 - 0.2 m below mean water level	-10	0.5	-10	1	Indicator
Pta-6431	Beachrock	Beach	0.1 - 0.2 m below mean water level	-1	0.5	-1	1	Indicator
Pta-6248	Beachrock	Beach	0.1 - 0.2 m below mean water level	0	0.5	0	1	Indicator
Pta-4317	Life position Bivalve	Buried bar, microtidal inlet	0.5 - 3.5 m below mean water level	1.5	0.1	4.5	1	Limiting
Pta-4998	Aeolianite	Carbonate cemented dune	Forms above SL	2	1.5	2	1	Limiting
Pta-6191	Beachrock	Beach	0.1 - 0.2 m below mean water level	2.75	0.5	2.75	1	Indicator
Pta-6252	Pothole fill	Infill of pothole (forms from mean level to storm level)	0 - 2 m above mean water level	3.5	2	3.5	1	Indicator
Pta-6297	Shell in beachrock	Beach	0.1 - 0.2 m below mean water level	1.61	0.5	1.61	1	Indicator
Pta-4705	Shell	Buried beach	At or above SL	2	1	4	3	Limiting
Pta-4462	Life position Bivalve	In situ burrowing bivalve	0.5 - 3.5 m below mean water level	0	0.1	1.5	3	Limiting
Pta-4041	Shell	Buried beach, microtidal inlet	At or above SL	2.8	1	4.8	3	Limiting
Pta-5052	Coral in beachrock	Beach	0.1 - 0.2 m below mean water level	0	0.5	0	1	Indicator
Pta-6300	Shell in beachrock	Storm beach deposit	0.1 - 0.2 m below mean water level	1.49	0.5	0.49	2	Limiting

Pta-6429	Beachrock	Beach	0.1 - 0.2 m below mean water level	0	0.5	0	1	Indicator
Pta-4972	Coral in beachrock	Beach	0.1 - 0.2 m below mean water level	1.5	0.5	1.5	1	Indicator
Pta-4311	Shell	Buried bar, microtidal inlet	0.5 - 3.5 m below mean water level	1.5	1	1.5	3	Limiting
Unknown	Beachrock	Beach	0.1 - 0.2 m below mean water level	0	1	0	1	Indicator
Unknown	Beachrock	Beach	0.1 - 0.2 m below mean water level	0	1	0	1	Indicator

Table XIV.4 Final results for the recalibration and reinterpretation of the RCSLC as set out in the text. Also refer to accompanying Figure XIV.3 and Table XIV.1. Criterion 3 abbreviations as for Table XIV.1.

Sample	Marine09 Cal. Ages		Indicative meaning	Indicative range (±)	Criterion 1	Criterion 2	Criterion 3
	Age	Error					
Pta-4140*	47673	2328	-50	3	EC	Variable	Limiting
Pta-4142	43358	2218	-44	3	EC	Variable	Limiting
Pta-1104	31655	1541	-46	10	Other (WC)	Variable	Limiting
GaK-1390	29572	1653	-20	3	EC	Reliable	Limiting
Pta-182	19563	996	-130	10	Other (SC)	Variable	Limiting
Pta-1105	18275	1156	-87.2	10	WC	Variable	Limiting
Pta-265	16606	1466	-112	10	Other (SC)	Variable	Limiting
Pta-264	15477	1528	-115	10	Other (SC)	Variable	Limiting
Pta-955	15307	1491	-75.5	10	Other (WC)	Variable	Limiting
Pta-185	14876	1558	-120	10	Other (SC)	Variable	Limiting
Pta-3597	11397	113	-47	3	EC	Reliable	Limiting
Pta-4344	10546	256	-35	3	EC	Reliable	Limiting
Pta-4343	10473	223	-43	3	EC	Reliable	Limiting
Pta-3570	10039	151	-24	3	EC	Reliable	Limiting
Pta-4346	9761	206	-27	3	EC	Reliable	Limiting
GaK-1389	9281	282	-28	3	EC	Variable	Limiting
Pta-3622	8593	256	-18	1	EC	Reliable	Indicator
Pta-3573	8384	193	-18	1	EC	Reliable	Indicator
Pta-3575	8326	212	-18	1	EC	Reliable	Indicator
Pta-6190	9883	285	-10	1	EC	Reliable	Indicator
Pta-6431	8830	10	-1	1	EC	Reliable	Indicator
Pta-6248	7160	223	0	1	EC	Reliable	Indicator
Pta-4317	5737	172	4.5	1	Other (SC)	Variable	Limiting
Pta-4998	5101	217	2	1	EC	Reliable	Limiting
Pta-6191	5089	226	2.75	1	EC	Reliable	Indicator
Pta-6252	4943	271	3.5	1	EC	Reliable	Indicator
Pta-6297	4723	220	1.61	1	EC	Reliable	Indicator
Pta-4705	4600	204	4	3	Other (SC)	Reliable	Limiting
Pta-4462	4099	233	1.5	3	Other (SC)	Reliable	Limiting
Pta-4041	4193	183	4.8	3	Other (WC)	Reliable	Limiting
Pta-5052	3969	241	0	1	EC	Reliable	Indicator
Pta-6300	3911	231	0.49	2	EC	Reliable	Limiting
Pta-6429	3441	201	0	1	EC	Reliable	Indicator

Pta-4972	1355	188	1.5	1	EC	Reliable	Indicator
Pta-4311	1302	125	1.5	3	Other (WC)	Reliable	Limiting
Unknown*	342	281	0	1	Other (Moz)	Variable	Indicator
Unknown*	338	267	0	1	Other (Moz)	Variable	Indicator

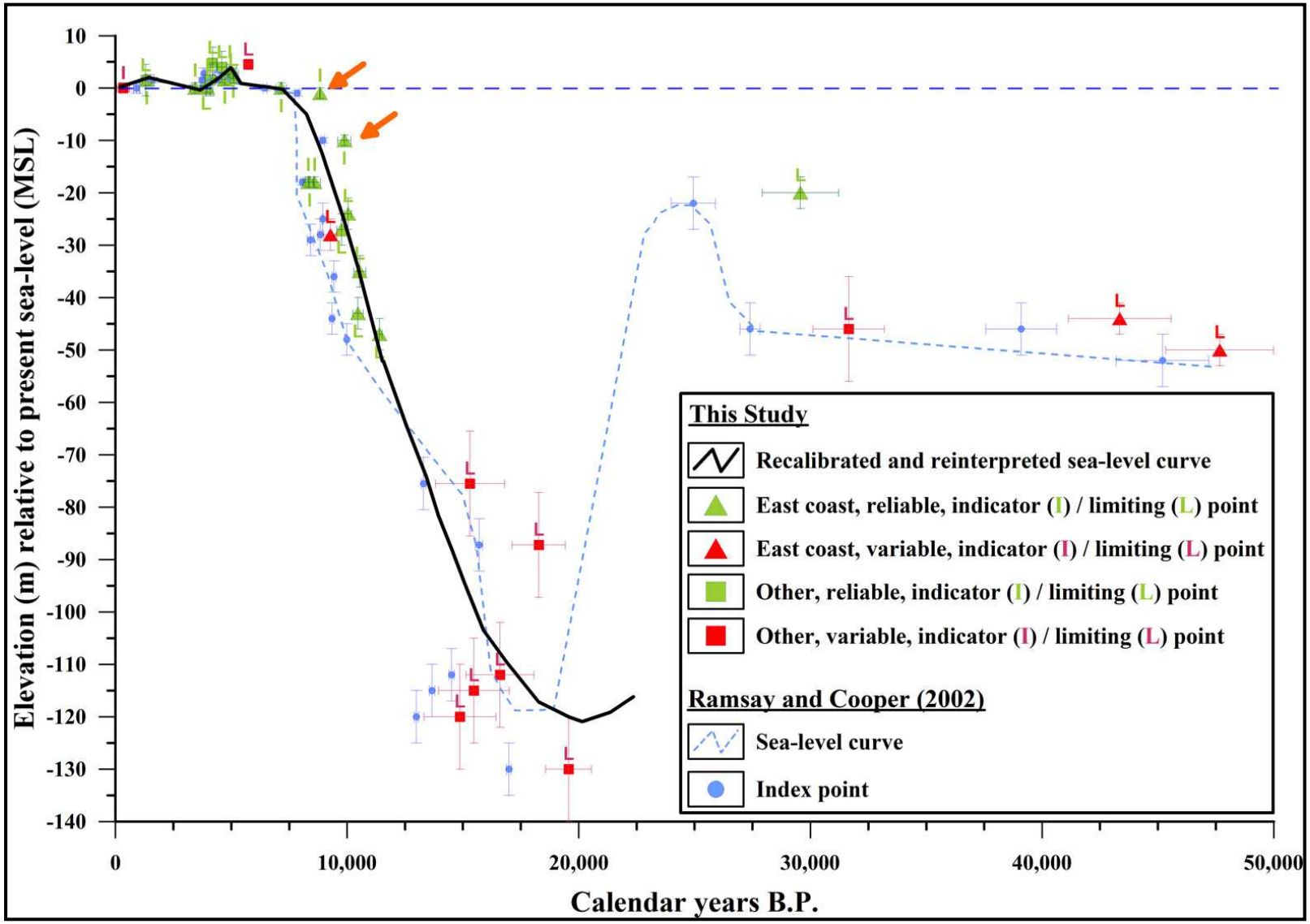

Figure XIV.3 Calibrated and reinterpreted Ramsay and Cooper (2002) radiocarbon-based sea-level data for South Africa. Also shown is the new reinterpreted curve for the last deglacial sea-level rise (Holocene transgression). Orange arrows indicate two beachrock samples not given priority based on their relative positions and the problems associated with whole-rock beachrock radiocarbon ages (see Chapter 9).